

Efficient Actuation of Load Carrying Applications by Electro-Hydraulic Compact Drives

Ketelsen, Søren

DOI (link to publication from Publisher):
[10.54337/aau488129124](https://doi.org/10.54337/aau488129124)

Publication date:
2022

Document Version
Publisher's PDF, also known as Version of record

[Link to publication from Aalborg University](#)

Citation for published version (APA):
Ketelsen, S. (2022). *Efficient Actuation of Load Carrying Applications by Electro-Hydraulic Compact Drives*. Aalborg Universitetsforlag. <https://doi.org/10.54337/aau488129124>

General rights

Copyright and moral rights for the publications made accessible in the public portal are retained by the authors and/or other copyright owners and it is a condition of accessing publications that users recognise and abide by the legal requirements associated with these rights.

- Users may download and print one copy of any publication from the public portal for the purpose of private study or research.
- You may not further distribute the material or use it for any profit-making activity or commercial gain
- You may freely distribute the URL identifying the publication in the public portal -

Take down policy

If you believe that this document breaches copyright please contact us at vbn@aub.aau.dk providing details, and we will remove access to the work immediately and investigate your claim.

**EFFICIENT ACTUATION OF LOAD
CARRYING APPLICATIONS BY
ELECTRO-HYDRAULIC
COMPACT DRIVES**

**BY
SØREN KETELSEN**

DISSERTATION SUBMITTED 2022



AALBORG UNIVERSITY
DENMARK

Efficient Actuation of Load Carrying Applications by Electro-Hydraulic Compact Drives

PhD Dissertation
Søren Ketelsen

Dissertation submitted May, 2022

Dissertation submitted: May, 2022

PhD supervisor: Professor Torben Ole Andersen
Aalborg University, Denmark

Assistant PhD supervisor: Associate Professor Morten Kjeld Ebbesen
University of Agder, Norway

Associate Professor Lasse Schmidt
Aalborg University, Denmark

PhD committee: Associate Professor Henrik Sørensen
Aalborg University, Denmark

Professor Petter Krus
Linköping University, Sweden

Professor Katharina Schmitz
RWTH Aachen University, Germany

PhD Series: Faculty of Engineering and Science, Aalborg University

Department: AAU Energy

ISSN (online): 2446-1636
ISBN (online): 978-87-7573-906-6

Published by:
Aalborg University Press
Kroghstræde 3
DK – 9220 Aalborg Ø
Phone: +45 99407140
aauf@forlag.aau.dk
forlag.aau.dk

© Copyright: Søren Ketelsen

Printed in Denmark by Stibo Complete, 2022

Preface

This dissertation has been submitted as a collection of papers to the faculty of Engineering and Science at Aalborg University, Denmark, in partial fulfilment of the requirements for the PhD degree in engineering. The dissertation work has been carried out at the Department of Energy Technology¹ at Aalborg University in the period from May 2018 to January 2022. The autumn of 2019 was spent as a visiting researcher at the Institute of Mechatronic Engineering, Technical University in Dresden, Germany, under the supervision of Prof. Dr.-Ing. Jürgen Weber.

The project is carried out as a part of the SFI Offshore Mechatronics Research Project funded by The Research Council of Norway, project number 237896/O30.

I want to thank my team of no less than three supervisors. I want to thank Professor Torben Ole Andersen, for giving me the opportunity to pursue a PhD degree, and Associate Professor Morten Kjeld Ebbesen for technical guidance and in particular a tireless and profound proof-reading of hundreds of draft pages. A special gratitude must inevitably be allocated to Associate Professor Lasse Schmidt for countless enthusiastic and interesting academic discussions and especially for crucial moral support when the going got tough in the summer of 2021.

I also want to thank my colleagues at the Department of Energy Technology, Aalborg University and at the Institute of Mechatronic Engineering, TU Dresden, for inspiring discussions and off-topic chats.

During the project period I was involved in main and co-authoring 14 scientific publications, with a total of 17 different co-authors from five research institutions and companies. I want to thank all authors for the honour of doing this together and all the insights this brought along. In particular I want to thank Dr. Sebastian Michel, TU Dresden, for providing theoretical background material and the experimental data used in Paper F, found on page 219 in this dissertation.

¹now AAU Energy

Most importantly, I want to express my sincere and greatest gratitude to my girlfriend Anne Sophie, for your loving support, patience and endless encouragements. Thank you for firmly reminding me, during abundant times of academic difficulties and doubts, that a meaningful and purposeful existence do actually consist of more than a few equations that just will not fall into line.

Søren Ketelsen
Aalborg, January 31, 2022

Reading Guidelines

This dissertation has been submitted as a collection of papers, and is split into three parts.

Part I contains an extended summary of the research carried out during the project. The summary is considered an independent text, but is mainly based on the findings in the publications.

Part II consists of six appended papers, providing additional insights, mathematical derivations and support to the extended summary in part I.

Part III is intended for the especially interested reader as it consists of five appendices providing background information to the results presented in part I. This includes detailed simulation models, their derivations and simulation parameters.

Abstract

Hydraulic actuation technology is used extensively in many industries due to well-known advantages such as the ability to generate large actuation forces and its robustness, to mention a few. Especially for applications characterized by low speed and high force operation hydraulic actuation is the preferred solution. Such applications may include mobile machinery such as excavators, wheel loaders, cranes etc. Today hydraulic cylinders are predominantly controlled by metering the flow, resulting in high power losses. This leads to low energy efficiencies being the main drawback of conventional hydraulic systems. Previous studies have found the average energy efficiency of hydraulically actuated systems to be between 21 % and 50 % on the average, across industries¹. The same study estimates that at least 1.5 % of the total energy demand in the US are consumed by hydraulic systems, suggesting that inefficient hydraulic systems is not a minor issue. This dissertation is motivated by the poor efficiency of conventional hydraulic systems, and focuses on energy-efficient hydraulic actuation using a differential cylinder for load carrying applications working in four quadrants. A medium sized knuckle boom crane is used as a theoretical case study. As the cost of energy is of increasing importance, and due to an increased political and societal awareness on energy consumption and carbon emissions, energy-efficient system designs eliminating the need for throttling control are highly needed. Several of such concepts have been developed by industry and academia recently.

The technology investigated in this study is known as pump-controlled cylinders, electro-hydraulic actuators or electro-hydraulic compact drives (ECD). Throttling losses are eliminated by removing the metering valves, such that each cylinder is equipped with a decentralised hydraulic supply. This also eliminates the need for extensive hydraulic piping to the cylinder and permits installing a fully decentralised actuator only requiring electrical power.

Replacing the valve-based hydraulic actuation system with a decentralised

¹L. Love, E. Lanke, and P. Alles, "Estimating the Impact (Energy, Emissions and Economics) of the US Fluid Power Industry", Oak Ridge National Laboratory, United States, 2012

compact actuator possesses challenges which are addressed in this dissertation. These include the reduced payload capacity of the considered crane and the need of a gasless and compact oil reservoir permitting the system to operate in tilted orientations. Further challenges include the need of a load holding functionality not preventing the ECD from recovering potential energy, as the crane lowers its load, as well as thermal considerations.

Based on a systematic review of existing system layouts, a novel system architecture is proposed to address these challenges. This system consists of a self-pressurising reservoir charged by internal system pressures and a so-called indirectly controlled hydraulic lock. The lock ensures that the cylinder is hydraulically locked in case of power loss or hose burst, but may be unlocked by properly controlling the internal pressure states. Two electrical motor-pump units are included to permit sufficient control possibilities and to increase the scalability properties. To assess the extent to which cooling of the oil is necessary, a thermo-hydraulic simulation model has been developed including a description of the passive heat transfer to the ambience. Based on experimental results obtained from a smaller version of an ECD, the modelling method has been experimentally verified to anticipate the thermal behaviour within sufficient accuracy for thermal design of ECDs.

The dissertation finds that a large potential for energy savings is present if replacing the conventional valve-technology with the developed ECD system. Theoretical studies find an efficiency of the ECD of up to 83 %. By simulating a realistic motion cycle of the crane, a reduced energy consumption of 58 % to 75 % compared to a valve-controlled system is found, while good motion tracking performance has also been established. At ambient temperatures of 20 °C, the thermo-hydraulic model finds that passive heat transfer is sufficient, thus active cooling of the oil may be avoided. This is advantageous in terms of investments cost, system compactness and to reduce the mass of the actuator. The latter is important, as the decentralised location of the actuator reduces the static payload capacity of the crane. The developed system is estimated to be 56 % heavier than the cylinder used for valve-controlled actuation, reducing the static payload capacity of the crane by around 3 %.

The dissertation contributes with knowledge to the research field by suggesting new technical solutions to the load holding and oil reservoir design challenges. Also, insights into how the thermal behaviour of ECDs may be simulated are provided. Combined, these findings may lead to an expansion of the application range to also include safety critical load carrying applications. This includes a wider acceptance of ECDs as efficient, viable alternatives to conventional valve-controlled hydraulic systems. Further studies include experimental validation of the proposed system architecture and associated control methodology, using a downscaled version of the ECD, which has been dimensioned and manufactured within the project.

Danish Resumé

Hydrauliske systemer er udbredt i mange industrier pga. velkendte fordele såsom deres evne til at generere store kræfter og deres robusthed. Særligt for applikationer der opererer ved lav hastighed og kræver store kræfter er hydraulikteknologi derfor den foretrukne løsning. Disse applikationer omfatter f.eks. gravemaskiner og kraner. Aktuelt, reguleres bevægelsen af hydrauliske cylindre hovedsageligt ved at drøvle oliestrømmen ved brug af ventiler, hvilket resulterer i høje effekttab. Den lave virkningsgrad, som dette medfører, er hydraulikteknologiens største svaghed. Et amerikansk studie har tidligere estimeret, at den gennemsnitlige virkningsgrad for hydrauliske systemer er mellem 21 % og 50 % på tværs af forskellige industrier¹. Studiet estimerer også, at mindst 1.5 % af det samlede energiforbrug i USA forbruges af hydrauliske systemer, hvilket tydeliggør at ineffektive hydrauliksystemer ikke er et ubetydeligt problem. Denne afhandling er motiveret af den lave virkningsgrad af konventionelle hydrauliske systemer, og fokuserer på energieffektiv aktivering vha. dobbeltvirkende hydrauliske cylindre til applikationer, der opererer i fire lastkvadranter. Som et teoretisk casestudie anvendes en mellemstor knæarmskran. Grundet stigende energiomkostninger og pga. større politisk og samfundsmæssig opmærksomhed på energiforbrug og kulstofudledninger, er der et stort behov for at udvikle energieffektive hydrauliksystemer, hvor drøvletab reduceres. Både industrien og den akademiske verden har i de senere år bidraget med sådanne koncepter.

Teknologien, som undersøges i dette studie, kendes under navne som pumpe-regulerede cylindre, elektro-hydrauliske aktuatorer og elektro-hydrauliske kompakte drev (ECD). Ved at fjerne styreventilerne undgås drøvletab, og i stedet udstyres hver cylinder med en decentral hydraulisk forsyning. Således fjernes behovet for rørføringer også, og resultatet er dermed en decentraliseret aktuator, der kun behøver en elektrisk forsyning. Denne afhandling omhandler de udfordringer, der er forbundet med at udskifte et konventionelt hydrauliksystem med en decentral, kompakt aktuator. Disse udfordringer

¹L. Love, E. Lanke, and P. Alles, "Estimating the Impact (Energy,Emissions and Economics) of the US Fluid Power Industry", Oak Ridge National Laboratory, United States, 2012

omfatter en reduceret lasteevne af den undersøgte kran og behovet for et gasløst, kompakt oliereservoir, der gør hydrauliksystemet i stand til at operere i varierende orienteringer. Yderligere udfordringer omfatter en lastholdefunktion, der tillader systemet at genindvinde den potentielle energi, der er til rådighed, når kranen sænker lasten, såvel som termiske overvejelser.

Baseret på en systematisk gennemgang af eksisterende systemarkitekturer, foreslås et nyt systemdesign for at adressere de nævnte udfordringer. Dette system består af et oliereservoir, der lades af tryk internt i systemet og en såkaldt indirekte styret hydraulisk lås. Låsen sikrer, at cylinderen er låst i tilfælde af strømsvigt eller slangebrud men kan låses op ved hensigtsmæssig regulering af de interne tryk. Der benyttes to elektriske motor-pumpe enheder for at frigøre den nødvendige grad af reguleringsmuligheder, samt for at øge skalerbarheden. For at vurdere behovet for olie køling, udvikles en termisk-hydraulisk simuleringsmodel, som bl.a. indeholder en beskrivelse af den passive varmeoverførsel mellem systemet og omgivelserne. Simuleringsmodellen er blevet valideret baseret på eksperimentelle resultater fra et mindre ECD-system. Dermed kan temperaturudviklingen modelleres med tilstrækkelig præcision til brug for dimensionering af kølebehov.

Afhandlingen viser et betydeligt potentiale for energibesparelser ved at udskifte det konventionelle hydrauliksystem med det udviklede ECD-system. Teoretiske studier viser en virkningsgrad på op til 83 %. Ved at simulere en virkelighedstro arbejds cyklus, ses det, at kranens energiforbrug sammenlignet med et ventilreguleret hydrauliksystem er reduceret med 58 % til 75 %. Samtidig følger cylinderen den angivne positionsreference med acceptabel nøjagtighed. Ved en omgivelsestemperatur på 20 °C, viser den termisk-hydrauliske model, at passiv varmeoverførsel er tilstrækkelig, således at aktiv olie køling kan undlades. Dette er fordelagtigt både pga. investeringsomkostninger, kompakthed og for at reducere systemets vægt. Sidstnævnte er vigtigt, da systemets decentrale placering reducerer kranens lasteevne. Det udviklede system estimeres at være 56 % tungere end cylinderen, der anvendes i det ventilregulerede hydrauliksystem, hvilket betyder en reduceret lasteevne på omkring 3 %.

Afhandlingen bidrager med viden til forskningsfeltet ved at forelå nye tekniske løsninger på lastholdefunktion og oliereservoir problematikkerne. Det belyses, hvorledes ECD-systemers temperaturudvikling kan simuleres. Disse resultater kan føre til en udvidelse af anvendelsesområdet for ECD-systemer til også at omfatte sikkerhedskritiske lastbærende applikationer. Dette kan føre til en bredere anerkendelse af ECD-systemer som effektive, funktionsdygtige alternativer til konventionelle ventilregulerede hydrauliksystemer. Fremtidige studier bør indeholde eksperimentel validering af det udviklede system, herunder den tilhørende reguleringsmetode. Hertil er en nedskaleret ECD-testopstilling, dimensioneret og fremstillet under projektet.

List of Publications

This dissertation has been submitted for assessment in partial fulfilment of the PhD degree. The dissertation is partly based on the published papers below. Co-author statements are made available to the assessment committee through the Doctoral School of Engineering and Science at Aalborg University. The following papers are appended to this dissertation and referred to as Paper A through F:

- A Ketelsen, S.,** Padovani, D., Andersen, T.O., Ebbesen, M.K., & Schmidt, L., "Classification and Review of Pump-Controlled Differential Cylinder Drives", *Energies*, 12, 1293, **2019**, doi.org/10.3390/en12071293
- B Ketelsen, S.,** Andersen, T.O., Ebbesen, M.K., & Schmidt, L. (2019). "Mass Estimation of Self-Contained Linear Electro-Hydraulic Actuators and Evaluation of the Influence on Payload Capacity of a Knuckle Boom Crane", In *Proceedings of the ASME/BATH 2019 Symposium on Fluid Power and Motion Control*, October 7-9, **2019**, Sarasota, Florida, USA, doi.org/10.1115/FPMC2019-1689
- C Ketelsen, S.,** Andersen, T.O., Ebbesen, M.K., & Schmidt, L., "A Self-Contained Cylinder Drive with Indirectly Controlled Hydraulic Lock", *Modeling, Identification and Control*, Vol. 41, No. 3, **2020**, doi.org/10.4173/mic.2020.3.4
- D Ketelsen, S.,** Kolks, G., Andersen, T.O., Schmidt, L., & Weber, J. "Bootstrap Reservoir Concepts for Electro-hydraulic Compact Cylinder Drives". In *Proceedings of the 12th International Fluid Power Conference, Online*, **2020**
- E Ketelsen, S.,** Padovani, D., Ebbesen, M.K., Andersen, T.O., & Schmidt, L., "A Gasless Reservoir Solution for Electro-Hydraulic Compact Drives with Two Prime Movers", In *Proceedings of the ASME/BATH 2020 Symposium on Fluid Power and Motion Control, Online*, **2020**, doi.org/10.1115/FPMC2020-2773
- F Ketelsen, S.,** Michel, S., Andersen, T.O., Ebbesen, M.K., Weber, J., & Schmidt, L. "Thermo-Hydraulic Modelling and Experimental Validation of an Electro-Hydraulic Compact Drive", *Energies*, 14, 2375, **2021**, doi.org/10.3390/en14092375 .

Contents

Preface and Reading Guidelines	iii
Abstract and Danish Resumé	v
List of Publications	ix
Abbreviations and Nomenclature	xv
I Extended Summary	1
1 Introduction	3
1.1 Motivation	3
1.2 Alternative System Designs	5
1.3 Electro-Hydraulic Compact Drives	9
1.4 State of the Art	12
1.4.1 Comparison of ECD Classes	15
1.4.2 Current Research Topics	19
1.5 Drive Architecture for Further Study	20
1.6 Research Hypothesis	22
1.7 Dissertation Outline	22
1.8 Project Delimitations	24
2 Knuckle Boom Crane	25
2.1 Reduction of Payload Capacity	26
2.2 Dynamic Knuckle Boom Crane Model	32
2.2.1 Joint Kinematics	32
2.2.2 Equations of Motion	34
2.2.3 Cylinder Loads	35
2.3 Chapter Summary	37

3	Energy Saving Potential	39
3.1	Benchmark Actuation System	39
3.1.1	Pump Model and Loss Models	40
3.1.2	Efficiency Calculation of Benchmark System	44
3.2	ECD Actuation Systems	46
3.2.1	Steady State Models of Eletro-Hydraulic Compact Drive Actuation System	47
3.2.2	Power Losses of Motor Drive	49
3.2.3	Efficiency Calculations of the ECD Systems	50
3.3	Comparison of Efficiencies	51
3.4	Energy Consumption for Motion Trajectory	55
3.4.1	Realistic Motion Trajectory	55
3.4.2	Steady State Solutions During Motion Trajectory	57
3.5	Chapter Summary	64
4	System Design	65
4.1	Load Holding Technology	65
4.1.1	Mini Review	66
4.1.2	Indirectly Controlled Hydraulic Lock	69
4.2	Gasless Reservoir	71
4.3	Four Quadrant Operation Diagram	75
4.4	Steady State Performance	79
4.4.1	Bootstrap Reservoir Dimensions	79
4.4.2	Selecting Pump Displacements	80
4.4.3	Energy Efficiency	82
4.4.4	Energy Consumption for Motion Trajectory	83
4.5	Chapter Summary and System Diagram	84
5	Dynamic System Modelling	87
5.1	General Considerations on Modelling of Closed Circuit Hy- draulic Systems	87
5.1.1	Valve Flows	88
5.1.2	Fluid Properties	89
5.1.3	Simulation Results	90
5.2	Model Simplifications and Assumptions	92
5.3	Hydraulic Transmission Model	94
5.3.1	Pressure and Temperature Dynamics	96
5.3.2	Motion Dynamics and Friction Modelling	98
5.4	Electrical Drive Models	99
5.4.1	Power Losses	102
5.5	Chapter Summary	102

6	System Analysis and Controller Design	103
6.1	Simplified Modelling Equations	105
6.1.1	Linear Model	108
6.2	Linear Coupling Analysis	110
6.3	Pressure Controller Design	112
6.3.1	State Space Representation	114
6.3.2	Linear Couplings in Pressure Controlled System	115
6.3.3	Time Domain Response	116
6.3.4	Controller Tuning	117
6.4	Motion Controller	119
6.4.1	State Space Representation	120
6.4.2	Time Domain Response	121
6.4.3	Controller Tuning	122
6.5	Local Stability	124
7	Simulation Results	125
7.1	Continuous Controller Implementation	125
7.2	Switching Between Operation Modes	132
7.2.1	Switching Logic	133
7.2.2	Simulation Results	136
8	Closing Remarks	141
8.1	Conclusions	141
8.2	Future Work	143
	References	145
II	Publications	157
A	Classification and Review of Pump-Controlled Differential Cylinder Drives	159
B	Mass Estimation of Self-Contained Linear Electro-Hydraulic Actuators and Evaluation of the Influence on Payload Capacity of a Knuckle Boom Crane	189
C	A Self-Contained Cylinder Drive with Indirectly Controlled Hydraulic Lock	191
D	Bootstrap Reservoir Concepts For Electro-Hydraulic Compact Cylinder Drives	215

E	A Gasless Reservoir Solution for Electro-Hydraulic Compact Drives with Two Prime Movers	217
F	Thermo-Hydraulic Modelling and Experimental Validation of an Electro-Hydraulic Compact Drive	219
III	Appendices	251
A	Parameter List	253
B	Steady State Model of Benchmark System	261
C	Steady State Model of ECD+ System	267
D	Dynamic Model Derivation	271
E	Linear Models and Model Reduction	279

Nomenclature and Abbreviations

Abbreviations

Abbreviation	Description
AC	Alternating Current
CBV	Counter Balance Valve
CPR	Common Pressure Rail
CV	Check Valve
DC	Direct Current
ECD	Electro-hydraulic Compact Drive
ECD+	Electro-hydraulic Compact Drive with load holding valves and bootstrap reservoir
EHA	Electro-Hydraulic/Hydrostatic Actuator
ESS	Energy Storage System
FOC	Field Oriented Control
HPU	Hydraulic Power Unit
IHT	INNAS Hydraulic Transformer
ISV	Inverse Shuttle Valve
LS	Load Sensing
PCCV	Pressure Compensated Control Valve
PMSM	Permanent Magnet Synchronous Machine
POCV	Pilot-Operated Check Valve
PTC-LO	Pilot-To-Close LOgic Element
PTO-LO	Pilot-To-Open LOgic Element
RGA	Relative-Gain-Array
RGA _#	Relative-Gain-Array number
RV	Relief Valve
STP	Standard Temperature and Pressure
SV	Safety Valve
VCD	Valve-Controlled cylinder Drive

Nomenclature

Common Subscripts and Overline Notations

Parameter	Description
\bullet_A, \bullet_B	Quantity evaluated in control volume A/B
\bullet_C, \bullet_R	Quantity evaluated in control volume C/R
$\bullet_{PA}, \bullet_{PB}$	Quantity evaluated in control volume PA/PB
$\bar{\bullet}$	Quantity evaluated at average conditions or time integral of signal
$\hat{\bullet}$	Estimated quantity
$\tilde{\bullet}$	Change variable of state \bullet

Parameters

Parameter	Description	Unit
α	Cylinder area ratio A_B/A_A	-
α	Thermal expansion coefficient	K^{-1}
$\alpha_{1..5}$	Angles related to crane kinematics	rad
α_B	Area ratio of bootstrap pistons A_C/A_R	-
β	Oil-air mixture bulk modulus	Pa
β_{0F}	Oil bulk modulus at p_0	Pa
β_{eff}	Effective bulk modulus	Pa
$\beta_{eff,\bullet 0}$	Effective bulk modulus in linearisation point	Pa
β_{mech}	Mechanical elasticity parameter	Pa
γ	Shaft friction directional switching parameter	s/rad
γ_F	Friction directional switching parameter	s/m
Δp	Pressure difference	Pa
$\Delta p_{\bullet,nom}$	Nominal valve pressure drop	Pa
Δp_{CV}	Fixed check valve pressure drop	Pa
ΔT	Temperature difference	K
ΔU	Change in internal energy	J
ΔV	Compensation volume	m^3
ϵ	Volumetric content of free air at p_0 or emissivity related to thermal radiation	-
ϵ_{asynch}	Ratio of sheet metal	-
ϵ_{PMSM}	Ratio of sheet metal	-
ζ_{fil}	Damping ratio of reference filter	-
$\zeta_{n,\omega}$	Damping ratio of shaft speed loop	-
ζ_{xx}	Desired damping ratio. Motion loop.	-
η_{asynch}	Induction motor efficiency	-
η_{ECD}, η_{VCD}	ECD and benchmark system efficiency	-

Nomenclature & Abbreviations

Parameter	Description	Unit
$\eta_{\text{HPU}}, \eta_{\text{pump}}$	HPU and pump efficiency	-
η_{inv}	Motor inverter efficiency	-
$\theta_{1..6}$	Angle related to crane kinematics or shaft position	rad
κ	Polytropic coefficient	-
λ	Pump losses scaling parameter	-
λ_{pm}	Flux linkage	Wb
ν	Specific volume	m ³ /kg
ρ	Density	kg/m ³
$\rho_{\text{OG}}, \rho_{\text{OF}}$	Air and oil density at p_0	kg/m ³
σ	Stefan-Boltzmann constant	W/m ² /K ⁴
τ_{δ}	Additional/unknown torque	Nm
τ_1, τ_2, τ_3	Joint torque	Nm
τ_{asynch}	Induction motor torque	Nm
$\tau_{\text{em}}, \tau_{\text{em,ref}}$	Electro-magnetic motor and reference torque	Nm
τ_{L}	Pump load torque	Nm
τ_{loss}	Hydro-mechanical pump losses	Nm
$\tau_{\text{loss,ref}}$	Friction losses losses of reference unit	Nm
τ_{rated}	Rated torque	Nm
τ_{T}	Ideal pump torque	Nm
$\boldsymbol{\tau}$	Vector of joint torques	Nm
$\varphi_1, \varphi_2, \varphi_3$	Angle/Generalised coordinate	rad
$\phi_{\text{dr}}, \phi_{\text{ds}}$	d-axis rotor and stator flux	Wb
$\phi_{\text{qr}}, \phi_{\text{qs}}$	q-axis rotor and stator flux	Wb
ω	Shaft speed	rad/s
ω_{ω}	Desired closed loop bandwidth	rad/s
$\omega_{n,\omega}$	Obtained eigenfrequency of speed loop	rad/s
ω_{Fe}	Reference speed for power loss calculation	rad/s
ω_{fil}	Eigenfrequency of reference filter	rad/s
ω_{I}	Desired bandwidth of current control loop	rad/s
ω_{L}	Desired bandwidth of pressure control loop	rad/s
ω_{M}	Desired bandwidth of pressure control loop	rad/s
ω_{r}	Electrical angular velocity of rotor	rad/s
ω_{ref}	Reference shaft speed	rad/s
$\omega_{\text{ref}\lambda}$	Reference speed for loss evaluation	rad/s
ω_{s}	Synchronous angular velocity	rad/s
ω_{V}	Bandwidth for valve dynamics	rad/s
$\omega_{\text{x}}, \omega_{\text{xx}}$	Desired frequency of motion control loop	rad/s
$\Omega_{1..7}$	Rotational velocity of body 1 to 6	rad/s
\mathcal{K}	Total kinetic energy	J

Nomenclature & Abbreviations

Parameter	Description	Unit
\mathcal{L}	Lagrangian, $\mathcal{L} = \mathcal{K} - \mathcal{P}$	J
\mathcal{P}	Total potential energy	J
A_A	Piston area	m ²
A_B	Rod side area	m ²
A_C	Small piston area of bootstrap reservoir	m ²
A_R	Large piston area of bootstrap reservoir	m ²
A_s	Surface area (heat transfer calculations)	m ²
$\mathbf{A}_{1..5}$	Rotation matrices	-
$\mathbf{A}_E, \mathbf{A}_I$	System matrices	-
$\mathbf{A}_{MC}, \mathbf{A}_p$	System matrices	-
$\mathbf{A}_{PC}, \mathbf{A}_u$	System matrices	-
B_{CM3}	Rotational viscous friction coefficient	Nm s
B_{shaft}	Viscous friction coefficient	Nm s/rad
B, B_x, B_z	Viscous friction coefficients	Ns/m
$\mathbf{B}_E, \mathbf{B}_I$	Input matrices	-
$\mathbf{B}_{MC}, \mathbf{B}_p$	Input matrices	-
$\mathbf{B}_{PC}, \mathbf{B}_u$	Input matrices	-
c_p	Isobaric specific heat	J/kg/K
$\mathbf{C}_E, \mathbf{C}_I$	Output Matrices	-
$\mathbf{C}_{MC}, \mathbf{C}_p$	Output Matrices	-
\mathbf{C}_u	Output Matrix	-
\mathbf{C}_q	Matrix of velocity dependent torques	kg m ² /s
\mathbf{C}_x	Vector of velocity dependent forces	N
d_A, d_B	Piston and rod diameter	m
d_C, d_R	Piston diameters (bootstrap)	m
D_p	Pump displacement	m ³ /rad
$D_{p,ref}$	Pump displacement of reference unit	m ³ /rad
\mathbf{D}_q	Inertia Matrix	kg m ²
e_x	Position control error	m
e_d, e_q	d- and q-axis current error ($i_{d,ref} - i_d$)	A
e_ω	Shaft speed error ($\omega_{ref} - \omega$)	rad/s
E_{asynch}	Energy input to benchmark system	J
E_{CBV}, E_{PCCV}	Throttling losses	J
E_{con}, E_{inv}	Converter and inverter losses	J
E_{Cu}, E_{Fe}	Electric motor losses	J
E_{Cyl}, E_{Rec}	Resistive and aided cylinder work	J
E_{DC}	Energy input to ECD systems	J
E_{ESS}	Energy stored in ESS	J
E_{Fr}, E_{Th}	Friction and throttling losses (ECD)	J

Nomenclature & Abbreviations

Parameter	Description	Unit
E_{HM}, E_Q	Pump energy losses	J
$F_{C,x}, F_{C,z}, F_{S,x}$	Coulomb and static friction parameters	N
F_{cyl1}, F_{cyl2}	Cylinder forces	N
F_{ext}	External force	N
F_G	Gravitational load	N
$F_{Fric,x}, F_{Fric,z}$	Cylinder and bootstrap friction forces	N
F_{req1}, F_{req2}	Required cylinder forces	N
\mathbf{F}	Vector of forces	N
$\mathbf{F}_{PC}, \mathbf{F}_{MC}$	Linear pre-filters	-
\mathbf{F}_{MCd}	Linear derivative input matrix	-
g	Gravitational acceleration	m/s ²
\mathbf{G}_x	Transfer function matrix	-
\mathbf{G}_q	Vector of gravitational loads	Nm
\mathbf{G}_x	Vector of gravitational loads	N
h_\bullet	Specific enthalpy	J/kg
h_{conv}, h_{rad}	Heat transfer coefficients	W/m ² /K
h_{comb}	Heat transfer coefficient ($h_{conv} + h_{rad}$)	W/m ² /K
\dot{H}_{sys}	System enthalpy flow rate	W
i_d, i_q	d- and q-axis currents	A
$i_{d,ref}, i_{q,ref}$	Current references	A
I_{dr}, I_{ds}	d-axis rotor and stator currents (induction)	A
I_{qr}, I_{qs}	q-axis rotor and stator currents (induction)	A
$J_{1..7}$	Mass moment of inertia of body 1 to 7 about CM ₁ to CM ₇	kg m ²
J_{shaft}	Total shaft inertia	kg m ²
\mathbf{J}	Jacobian Matrix	m
k	Thermal conductivity	W/m/K
$K_{\omega I}$	Controller Parameter	Nm/rad
$K_{\omega P}$	Controller Parameter	Nm s/rad
K_{Fe}	Parameter for power loss calculation	W/kg
K_{Leak}	Laminar leakage parameter, ISV	m ³ /s/Pa
$K_{sw,LH}$	Model switching parameter	-
$K_{sw,ISV}$	Model switching parameter	-
$K_{\ddot{x}}$	Controller Parameter	Pas/m
K_{Px}	Controller Parameter	Pa/m
K_{Ix}	Controller Parameter	Pa/m/s
$\mathbf{K}_{PC}, \mathbf{K}_{MC}$	State feedback gain matrix	-
$L_{1,min}, L_{2,min}$	Minimum length of cylinder 1 and 2	m
L_c	Chracteristic length	m
L_{sx}, L_{sz}	Stroke lengths of cylinder and bootstrap	m

Nomenclature & Abbreviations

Parameter	Description	Unit
L_q, L_d	Motor inductances	H
L_s, L_r, L_m	Induction motor inductances	H
\dot{m}	Mass flow	kg/s
\dot{m}_T	Ideal pump mass flow	kg/s
$m_{1..7}$	Mass of body 1 to 7	kg
m_{asynch}	Mass of induction motor	kg
m_{PMSM}	Mass of PMSM	kg
$m_{\text{steel}}, m_{\text{oil}}$	System mass of steel and oil	kg
M	Load mass	kg
M_z	Mass of bootstrap pistons and rod	kg
M_{eq}	Equivalent mass	kg
M_{eq0}	Equivalent mass in linearisation point	kg
\mathbf{M}_x	Mass matrix	kg
p_0	Atmospheric pressure	Pa
p_1, p_2	Minimum and maximum reservoir pressure	Pa
p	Pressure in control volume	Pa
$p_{\text{CR},\bullet}$	Valve cracking pressure	Pa
$p_L, p_{L,\text{ref}}$	Load pressure and reference	Pa
$p_{\text{LS},\text{margin}}$	Pump pressure margin	Pa
$p_{\text{min}}, p_{\text{min},\text{ref}}$	Min pressure and reference	Pa
$p_{\text{OP},\bullet}$	Fully open valve pressure	Pa
p_s	Pump outlet pressure	Pa
p_{set}	Pressure set-point	Pa
p_t	Transition pressure	Pa
p_T	Tank pressure	Pa
$\dot{p}_L^*, \dot{p}_{\text{min}}^*$	Desired pressure dynamics	Pa/s
P	Number of pole pairs	-
P_{asynch}	Power input to induction motor	W
$P_{\text{Cu}}, P_{\text{Fe}}$	Copper and iron losses	W
$P_{\text{Cyl1}}, P_{\text{Cyl2}}$	Cylinder output powers or rate of work	W
$P_{\text{CBV}}, P_{\text{PCCV}}$	Throttling losses	W
P_{DC}	Power input to motor inverter	W
P_{HM}, P_Q	Hydro-mechanical and leakage pump losses	W
P_{inv}	Power loss of motor inverter	W
$P_{\text{inv},\text{rated}}$	Rated inverter power	W
P_{PMSM}	Power input to PMSM	W
$\mathbf{P}_{\text{CM1..CM7}}$	Position vector in global frame	m
Q	Volume flow	m ³ /s
Q_{amb}	Heat to ambience	J
$Q_{\bullet,\text{nom}}$	Nominal valve volume flow	m ³ /s

Nomenclature & Abbreviations

Parameter	Description	Unit
$Q_{\text{loss,ref}}$	External leakage flow of reference unit	m^3/s
Q_T	Ideal pump volume flow	m^3/s
\dot{Q}	Rate of heat flow	W
\dot{Q}_{amb}	Natural convection and radiation to surroundings	W
\dot{Q}_{losses}	Rate of heat flow due to friction losses	W
\mathbf{q}	Vector of generalised coordinates	rad
R	Stator resistance of PMSM	Ω
R	Gas constant for air	J/kg/K
R_{acc}	Volume ratio, gas-charged accumulator	-
R_{boot}	Volume ratio, bootstrap reservoir	-
R_{CBV}	Pilot area ratio	-
R_r, R_s	Rotor/stator resistance, induction motor	Ω
$R_{\text{th}}, R_{\text{eq}}$	Thermal resistances	K/W
s	Laplace frequency	rad/s
S	Entropy	J/K
\mathbf{s}_\bullet	2D-vector for crane kinematics.	m
T_0	Constant temperature (fluid properties)	K
T_{amb}	Ambient temperature	K
T_{sample}	Controller sampling time	s
T_{sys}	Uniform system temperature	K
u	Specific internal energy	J/kg
u_1, u_2	Normalised input (benchmark system)	-
u_d, u_q	d-axis and q-axis voltage	V
u_{JS}	Normalised operator joystick signal	-
u_{JS}^*	Rate limited joystick signal	-
u_{LH}	Operation mode switch	-
u_{SV}	Control signal to safety valves	-
U_{DC}	DC-link voltage	V
$U_{\text{dr}}, U_{\text{ds}}$	d-axis rotor and stator voltage (induction)	V
U_n	Grid line-to-line voltage (RMS)	V
$U_{\text{qr}}, U_{\text{qs}}$	q-axis rotor and stator voltage (induction)	
$\mathbf{u}_E, \mathbf{u}_{\text{MC-ref}}$	Input vectors	-
$\mathbf{u}_p, \mathbf{u}_{\text{p-ref}}$	Input vectors	-
\mathbf{u}_{ref}	Input vector	-
v_{sw}	Stribeck curve decay parameter	m/s
V	Chamber volume	m^3
$V_{\bullet 0}$	Chamber volume in linearisation point	m^3
$V_{0\bullet}$	Initial chamber volumes	m^3
V_{1G}, V_{2G}	Maximum and minimum gas volumes	m^3

Nomenclature & Abbreviations

Parameter	Description	Unit
V_{boot}	Volume of bootstrap reservoir	m^3
$V_{\bullet x}$	Chamber volume at p_0	m^3
\dot{W}_{shaft}	Rate of work	W
x, x_{ref}	Main cylinder position and reference	m
\dot{x}_{max}	Maximum allowed reference velocity	m/s
\ddot{x}_{max}	Maximum allowed reference acceleration	m/s^2
\mathbf{x}	Vector of operational coordinates	m
$\mathbf{x}_E, \mathbf{x}_{\text{MC}}$	State Vectors	-
$\mathbf{x}_P, \mathbf{x}_{\text{PC}}$	State Vectors	-
\mathbf{x}_u	State Vectors	-
y	Normalised valve spool/seat position	-
y_{leak}	Leakage flow switching parameter	-
y_{ref}	Normalised reference valve position	-
$\mathbf{y}_E, \mathbf{y}_{\text{MC}}$	Output vectors	-
$\mathbf{y}_P, \mathbf{y}_{\text{PC}}$	Output vectors	-
\mathbf{y}_u	Output vector	-
z	Position of bootstrap reservoir piston	m

Part I

Extended Summary

Chapter 1

Introduction

Hydraulic actuation technology is used extensively in many industries due to the well-known advantages such as the ability to generate large actuation forces, robustness and the flexibility offered by transporting power through hoses or pipes. The latter seen in contrast to mechanical distribution of power by shafts and gears. Also compared to mechanical linear actuators, such as ball or roller screws, the hydraulic cylinder represents a much simpler mechanical device capable of realising linear motion [1]. Especially for applications characterised by low speed and high force operation hydraulic actuation technology is the preferred solution. Such applications may include large industrial machinery, e.g. injection molding machines and presses etc., and mobile machinery such as excavators, wheel loaders, telehandlers, cranes etc.

Today hydraulic cylinders are predominantly controlled by metering the flow using throttling valves resulting in high power losses, leading to a low energy efficiency being the main drawback of valve-controlled hydraulic systems.

1.1 Motivation

The current work is motivated by the poor energy efficiency of conventional hydraulic systems and focuses on energy-efficient linear hydraulic actuation using a differential cylinder for load carrying applications working in four quadrants, such as cranes and excavators. A medium sized knuckle boom crane is used as a theoretical case study throughout this dissertation, which is introduced later (see Fig. 1.7 on page 20).

Low energy efficiencies are partly a result of the power losses of the compo-

nents, e.g. pumps, pipes, hoses and actuators but the majority of the losses is in fact conceptual losses i.e. originating from the fact that the system is controlled by power dissipation [2]. This means that even if components were ideal, significant power losses would still occur due to the control principle being based on throttling.

Obtaining a high efficiency is fundamentally achieved if the supplied power is close to the power demanded by the load. Constant pressure or flow systems, now only common in low-cost and low-power machines [2], do have large power losses under part load conditions due to a mismatch between the needed and supplied pressure. For actuation of a hydraulic crane the ratio of hydraulic output energy to pump input energy for a constant pressure system is reported to be as low as 8.5 % [3]. To improve the efficiency load sensing (LS) hydraulic power units (HPU) are currently commonplace for both industrial and mobile hydraulics. This enables a closer matching of the supplied power to the needed power, as the pump outlet pressure is adjusted to the needs of the actuator requiring the largest supply pressure. If only a single actuator needs to be supplied by a single pump, a decent efficiency is obtainable despite the metering losses across the control valve. However, as a single pump is usually used to supply multiple simultaneously working actuators, load pressures may be poorly matched, leading to large throttling losses.

Another unfortunate characteristics of such a conventional valve-controlled cylinder drive (VCD), is the in-ability to recover energy in situations where the load aids the cylinder motion, e.g. when a crane lowers its payload. This energy is wasted/converted to heat as the return flow is throttled from the cylinder chamber to the oil reservoir.

As an example [4] reports an energy efficiency of 15 % of a multi-actuator mobile machine performing a typical loading cycle using an LS system. Across industries [5] estimates that the average efficiency is 21 % for mobile hydraulic systems and 50 % for industrial hydraulic systems. In 2012 [5] estimated the annual energy consumption of industrial hydraulic systems in the US alone to 1.16 EJ¹, while the annual energy consumption of mobile hydraulic machinery was estimated to range between 0.38 EJ and 1.33 EJ. With a total estimated annual energy consumption in the US in 2010 of approximately 105 EJ [5], the energy consumed by hydraulic systems represents at least 1.5 % of the total energy consumption. This is clearly showing that inefficient hydraulic systems is not a minor issue.

¹Exajoule (10^{18} J)

1.2 Alternative System Designs

Cost of energy is of increasing importance to the end user and there is an increased political and societal awareness on energy consumption and carbon emissions. Due to this it is clear that alternative energy-efficient system designs, that eliminate the need for throttling control are highly needed.

Several of such system concepts have been developed recently. The field of so-called digital hydraulics is one potential technology capable of eliminating throttling losses. It is being characterised by having replaced the conventional throttling control valve with multiple 2/2-way on/off valves. The on/off valves are used to connect the cylinder chamber with a number of pressure lines, such that the cylinder is able to deliver a number of discrete forces [6]. By increasing the number of pressure lines, the number of obtainable forces increases, at the expense of a higher number of needed components. This is visualised in Fig. 1.1a.

Equivalently, the number of cylinder chambers may be increased (multi-chamber cylinder), to increase the number of force levels per available pressure line, as shown in Fig. 1.1b. This comes at the expense of more components and a more complex and costly cylinder design [7]. For a multi-chamber cylinder system [8, 9] simulate the actuation of a knuckle boom crane. Compared to a conventional LS system a significant energy saving potential is present, but at the cost of a highly degraded motion tracking performance.

The digital hydraulic technology may conveniently be supplied by a common pressure rail (CPR), where a centralised pump is controlled to charge hydraulic accumulators, constituting a high and a low pressure line. This has several advantages, as energy aided by the load may now be recovered

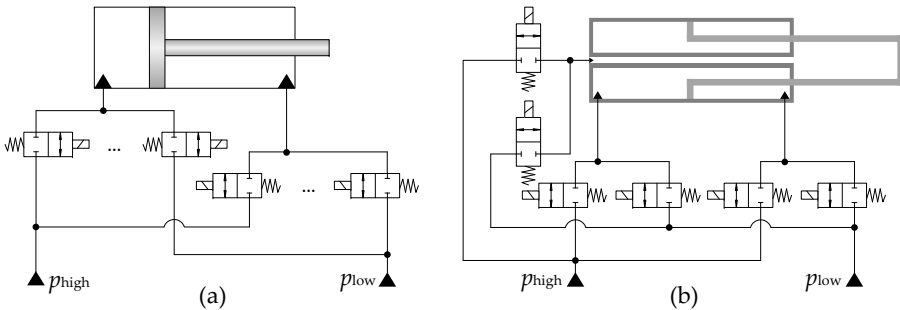


Fig. 1.1: Simple illustration of two digital hydraulic topologies. (a) On/off valves are used to connect each chamber of a standard cylinder with a number of pressure lines. (b) A multi-chamber cylinder may be used to increase the number of obtainable force levels.

and stored in the hydraulic accumulators. Furthermore the pump may be controlled to operate at an optimal speed to enhance energy efficiency and turned off when the accumulators are charged. This is advantageous as the hydraulic supply unit may be sized to meet the average power requirement and not for the peak power demand of the actuators.

Another option for controlling hydraulic cylinders supplied by a CPR is hydraulic transformers, namely throttleless control devices that transform the pressure levels of the CPR to the load pressure required by the cylinder, as illustrated in Fig. 1.2. However, [10] finds that due to a low efficiency of transformers constructed from commercially available components, hydraulic transformers are not a feasible solution yet. Even though initiatives for developing a commercially viable hydraulic transformer have been ongoing for decades, e.g. the INNAS hydraulic transformer (IHT) introduced in the late 1990s [11], further development is still needed according to [12]. A simulation study conducted in [13] finds a reduced fuel consumption of 51 % for a 33 ton wheel loader application compared to an LS-system when implementing CPR and hydraulic transformers.

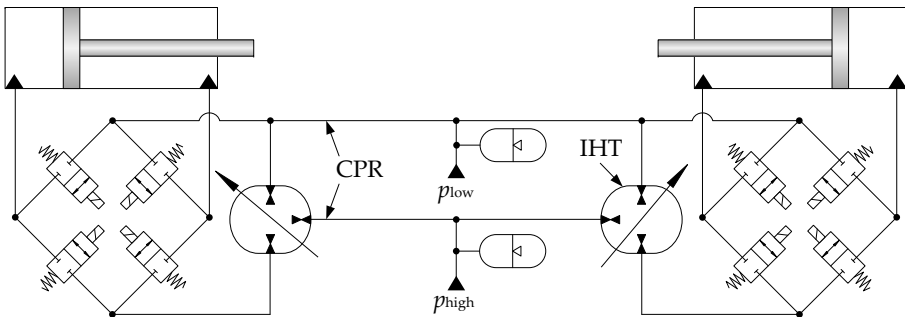


Fig. 1.2: Simplified illustration of a common pressure rail and INNAS hydraulic transformers, used to control hydraulic cylinders in four quadrant operation. Redrawn and simplified from [13].

Instead of transforming the hydraulic power from a centralised HPU by means of throttleless devices, a completely different approach to eliminate metering losses is to decentralise the hydraulic supply, i.e. to have a separate pump unit to control the motion of each cylinder. This is known as pump-controlled cylinders and may generally be divided into displacement controlled actuators and variable-speed pump-controlled cylinders, also known as electro-hydraulic actuators (EHA).

Displacement controlled actuators have been investigated mainly in the context of mobile machinery [14, 15, 16]. Variable-displacement units are connected to the same shaft and driven by a combustion engine or an electrical machine, as shown conceptually in Fig. 1.3a. Fuel savings between 15 % and

1.2. Alternative System Designs

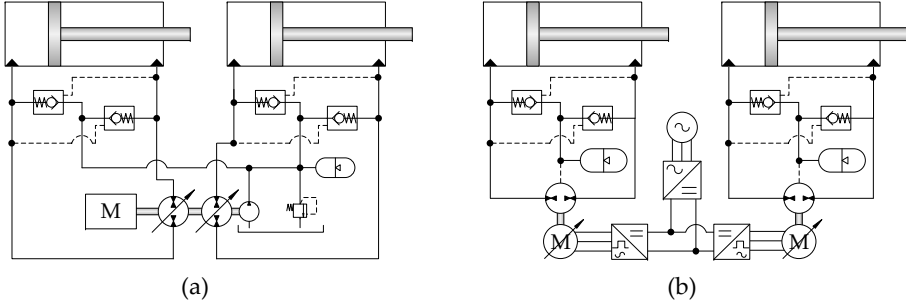


Fig. 1.3: Examples of pump-controlled cylinders. (a) Displacement controlled cylinders. The motor (M), may either be a combustion engine or an electrical machine [2]. (b) Electro-hydraulic actuators are connected on the electrical grid but do not share hydraulic connections.

40 % compared to load sensing systems are reported by [4, 17].

Due to recent developments and cost reductions of variable-speed electric motor drives, the focus on pump-controlled cylinders are shifting from variable-displacement to variable-speed pump units. This is partly due to an improved energy efficiency of variable-speed pump units compared to variable-displacement units [18, 19, 20] and partly due to variable-speed units matching industrial trends of electrification and plug-and-play capabilities.

Each cylinder is here equipped with a decentralised hydraulic supply, and the system is hydraulically isolated from the other actuators, as shown in Fig. 1.3b. These systems are coined by various names by different manufacturers and researchers. These names include electro-hydraulic actuators (EHA), electro-hydrostatic actuators (EHA), zonal hydraulics, decentralised hydraulics to name a few. As the oil volume of these actuators may be reduced significantly compared to conventional hydraulics, the oil reservoirs of these systems are often constituted by a low pressure accumulator. This ensures good suction conditions for the hydraulic units even for tilted system orientations, e.g. upside-down. As such these actuators can be seen as completely stand-alone or self-contained turnkey actuators.

Note the conceptional difference between how power is distributed for the system designs listed above. Using a CPR, either with hydraulic transformers or on/off valves, multiple actuators may be sharing power hydraulically, i.e. power regenerated from one actuator may be used by another via hydraulic power sharing or stored in hydraulic accumulators. Displacement controlled actuators distribute power mechanically via the common shaft. The low pressure hydraulic connection between the actuators, seen in Fig. 1.3a, is working to compensate pump leakages and to increase the pressure level of the actuators hence the drive stiffness and not for power sharing. Finally, the EHA concepts distribute power electrically. This means that recuperated power

from one actuator is shared to other actuators via the common DC-link. Energy storage systems (ESS) such as batteries, super-capacitors, or fly-wheels, may be connected to the DC-link, such that recuperated power may be stored, leading to minimising the peak power required by the DC-supply [21].

Each power distribution topology has certain drawbacks and benefits. The CPR concept is advantageous in terms of that the centralised supply can be sized to meet the average power demand for all actuators. The prime movers for the mechanical and electrical power distribution topologies need to be sized for the peak power. However, for the displacement controlled system, the prime mover may be sized to the combined peak power of the actuators. The electrical machines for the system based on electrical distribution need to be sized to meet the peak power of each actuator, even though these do not work simultaneously. This is disadvantageous both in terms of investment cost, but also in terms of efficiency when recuperating power from an aided load, as the power needs several stages of conversion before reaching a resistive load. This may be considered the main disadvantage of EHAs working in multi-actuator systems. On the other hand these systems offer advantages in terms of system compactness, modular or decentralised designs, and installation flexibility including plug-and-play capabilities, e.g. the avoidance of expensive piping between actuators and the centralised HPU.

Each of the presented alternative system designs offers unique characteristics and all require further development for the real industrial break-through. This includes development of cheap and reliable high performance on/off valves and control strategies for digital hydraulics and developing a viable hydraulic transformer for CPR systems. For pump-controlled cylinders this includes developing suitable hydraulic units, control strategies and system architectures.

Due to an increased industrial focus on system electrification, system compactness, installation flexibility etc., it is chosen in close cooperation with the industrial partners within the SFI Offshore Mechatronics Research Project, that the current work should focus on decentralised electro-hydraulic actuators. These are found to offer the highest extend of system electrification and flexibility. The industrial partners are associated within the offshore industry, where the electrification trend is already taking place for rotational drives such as winches and drilling top-drives [22].

Focus in the remainder of this dissertation is therefore on electro-hydraulic actuators not featuring a conventional vented hydraulic reservoir. These systems are referred to as Electro-Hydraulic Compact Drives (ECDs), in the remainder, starting with an introduction to this technology and a state-of-the-art review.

1.3 Electro-Hydraulic Compact Drives

As shown previously in Fig. 1.3b on page 7, ECDs generally consist of an electrical servo drive (motor inverter and variable-speed electric motor) supplied from a common DC-link. The motor shaft is connected to a fixed-displacement pump, which is connected to the cylinder chambers without any throttling elements in the main transmission lines. Due to the uneven flow required by the chambers of a single rod cylinder, means of flow balancing are needed. This may be constituted by passive valves connecting the low pressure side of the cylinder with the reservoir as seen in Fig. 1.3. To balance the rod, thermal expansion and compression volumes, a small volume low pressure oil reservoir is often used.

ECDs represent a promising alternative to conventional valve-controlled cylinder drives (VCD) as well as to electro-mechanical linear drive solutions. Simple illustrations of a VCD and an electro-mechanical linear drive with a planetary transmission screw are shown in Fig. 1.4.

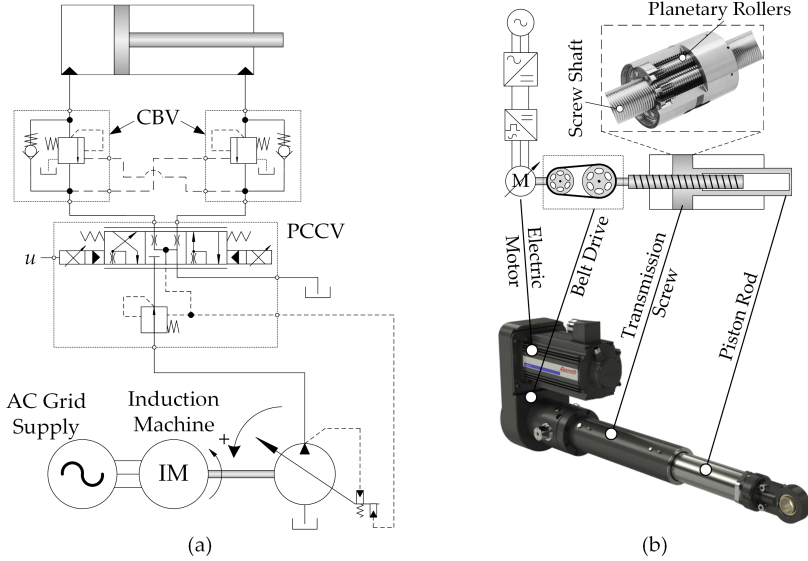


Fig. 1.4: (a) Simplified schematics of a valve-controlled hydraulic linear drive, consisting of a fixed-speed induction machine, a variable displacement pump, a pressure compensated control valve (PCCV) and counter-balance valves (CBV). (b) Simplified illustration of an electro-mechanical linear drive from Bosch Rexroth [23] consisting of a variable-speed electric motor, a belt drive and a planetary transmission screw. Illustration of planetary transmission screw is from [24].

The motion of the cylinder in the VCD shown in Fig. 1.4a is controlled using a pressure-compensated control valve (PCCV). This valve is typically used in

mobile machinery, as it is important that the input from the operator yields the same flow regardless of pump and load pressure. Counter-balance valves (CBV) are used to maintain controllability in aided load situations, to avoid load dropping if hydraulic pressure is lost or if a hose bursts, and as overload protection and shock absorption [25]. Hydraulic power is supplied through pipes or hoses from a centralised pressure controlled (LS) pump, driven by an electric induction machine or a combustion engine. In contrast to ECD systems the conventional HPU includes a voluminous vented oil tank, which is needed in order to ensure an appropriate resting time for the fluid (approximately 2-5 min). The fluid mainly needs to rest in order for air released during fluid throttling to dissolve in order to avoid pump cavitation. At STP¹ hydraulic fluid contains between 7 % to 10 % of dissolved air (volumetric) [26]. During the throttling process the fluid is accelerated, such that the fluid velocity at the valve opening is larger than downstream the valve. This means that for a steady flow along a streamline the specific kinetic energy is larger for the fluid passing the valve opening than downstream the valve. According to Bernoulli's equation this leads to the fluid pressure being smaller at the valve opening than downstream the valve. As oils ability to dissolve air is decreasing for decreasing pressures (Henry's law) [26], air is released during throttling. As no throttling elements are needed in ECDs, then theoretically no rest time is required and the oil volume can be significantly reduced for ECDs.

Fig. 1.4b, shows a simplified diagram of an electro-mechanical linear drive, consisting of a variable-speed electric motor, controlled by a motor inverter and supplied by a grid-connected rectifier. A belt drive or gearing connects the motor shaft and the screw shaft. A transmission screw which either may be a ball screw or a roller screw converts the rotational motion to linear motion. The main characteristics of the two actuation technologies shown in Fig. 1.4 are listed in Tab. 1.1.

For energy-efficient actuation of a high force, low speed application such as the knuckle boom crane used in this study, the characteristics given in Tab. 1.1 show that the conventional technologies of both VCD and electro-mechanical linear drives are unsuitable. For the former technology this is primarily due to high power losses. For the latter technology this among other reasons is due to certain limitations, such as limited reliability (e.g., impact loads damage), difficulties of implementing overload/failure protection and/or limited force capabilities [25, 30, 31].

To some extent ECDs may be regarded as the combination of electro-mechanical drives and hydraulic drives. The prime mover is a variable-speed electric machine controlled by an inverter as known from mechanical linear drives.

¹Standard temperature and pressure, defined to 0 °C and 1 bar [26]

1.3. Electro-Hydraulic Compact Drives

Table 1.1: Characteristics of conventional hydraulic drives and electro-mechanical linear drives. Composed from [27, 28, 29].

	Conventional Hydraulic Drives	Electro-Mechanical Linear Drives
Advantages	<ul style="list-style-type: none"> ▪ Robust and scalable ▪ High transmission ratio ▪ High power/force density (actuator) ▪ Easy implementation of overload protection ▪ Load holding/safety functionality ▪ Tolerance towards impact loads ▪ Heat and contamination is transferred by fluid 	<ul style="list-style-type: none"> ▪ Low power losses ▪ Plug-and-play installation ▪ Electrical and mechanical interface only ▪ Small footprint
Disadvantages	<ul style="list-style-type: none"> ▪ High power losses ▪ Centralised power unit requiring piping network ▪ Risk of oil leakage ▪ Voluminous oil tank 	<ul style="list-style-type: none"> ▪ Wear ▪ Impact absorption ▪ Overload protection ▪ Fixed transmission ratio ▪ Small load forces

The gearing or conversion from rotational mechanical energy is performed hydraulically using a hydraulic pump and cylinder instead of mechanical linear gears. Ideally this should provide a turnkey decentralised actuator combining the advantages of the conventional technologies. This includes the robustness, high power densities, high achievable transmission ratios, load holding functionalities and the tolerance towards shock loading known from hydraulic drives, with the high energy efficiency, plug-and-play capabilities and small footprint/compactness (occupied area) from electro-mechanical drives. Additionally, compared to conventional hydraulic drives, ECDs are characterised by a smaller risk of oil leakage due to short and integrated fluid lines and a much smaller oil volume [32]. The oil may be pre-filled at the manufacturing site, reducing the commissioning effort when installing the ECD in the application. Ideally no oil changes are required through the life-cycle of the actuator, thus reducing the needed maintenance effort compared to conventional systems [32].

ECDs have received a fair amount of research effort lately and recently commercial products have also entering the market e.g. the EHA from Parker Hannifin [33], the Servo-Hydraulic Axis (SHA) from Bosch Rexroth AG, and the Helax from Bucher Hydraulics [34] to mention a few. To obtain an overview of the research efforts and to classify different hydraulic circuit ar-

chitectures, a thorough state-of-the-art review has been conducted and documented in the appended paper A. In this paper both variable-displacement pump architectures and variable-speed architectures are included. In the following section a summary of the state-of-the-art review given in Paper A focusing on ECDs is given.

1.4 State of the Art

Paper A classifies ECD architectures according to Fig. 1.5, i.e. based on the type of hydraulic supply, whether the circuit architecture is an open or closed circuit architecture and based on the flow compensation method. An open circuit architecture here means that oil from one cylinder chamber needs to pass the oil reservoir before entering the other chamber, while for closed architectures there is at least one pump being connected to both cylinder chambers. This leads to three main classes of ECDs, being single pump/single prime mover (Class A), multiple pumps/single prime mover (Class B) and multiple prime mover (Class C) architectures. Examples of each class is given in Fig. 1.6.

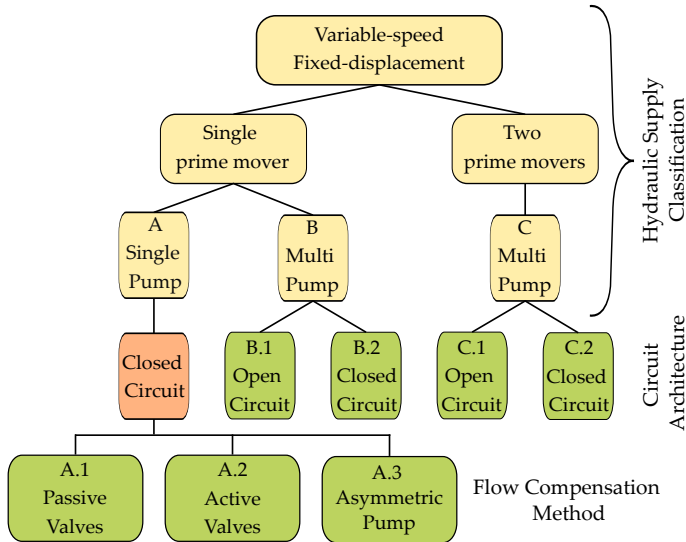


Fig. 1.5: Classification of ECD architectures proposed in Paper A.

Class A

Class A drives consist of a single prime mover driving a single hydraulic unit. This means that the circuit architecture also needs to incorporate methods to

compensate the asymmetric flow from the cylinder chambers. This may be achieved using passive valve arrangements (Class A.1) such as an inverse shuttle valve as shown in Fig. 1.6A [28, 35], which connects the low pressure side of the cylinder with the accumulator, to allow flow compensation. A similar solution is achieved by replacing the inverse shuttle valve with pilot operated check valves as investigated in [36, 37].

The ECDs based on passive valves for flow compensation are reported to suffer from mode-oscillations at certain loading conditions by numerous authors (e.g. [2, 38, 39, 40, 41]). In [2] this complicated phenomenon is explained to happen when the equilibrium point of the system is close to the switching pressure of the valves. For a poorly damped system, the switching condition is met while moving towards the equilibrium point. This causes the structure of the system to change hence moving the equilibrium point, causing undesired pressure and piston velocity oscillations as seen in e.g. [39].

A suggestion on eliminating the mode-oscillation issue is presented in [36] where two counter balance valves are used to stabilise the system in the critical loading region while allowing free flow at higher loading conditions to allow power regeneration. In [39] an under-lapped inverse shuttle valve is used to stabilise the circuit. Recently, [38, 42] presented a circuit for triggering the flow compensation valves stating that this has *"come to solve the compensation flow instabilities and provide the basis for the development of commercially viable circuits"*. The solution presented here requires five pilot operated directional valves and a pressure intensifier in addition to auxiliary valves such as pressure relief and anti cavitation valves. The natural question here is whether this represents a viable solution compared to *just* adding another pump to the shaft (class B) to circumvent the mode-oscillating challenge.

Another approach to eliminate mode-oscillations is constituted by class A.2 architectures, where actively controlled valves are used to connect the appro-

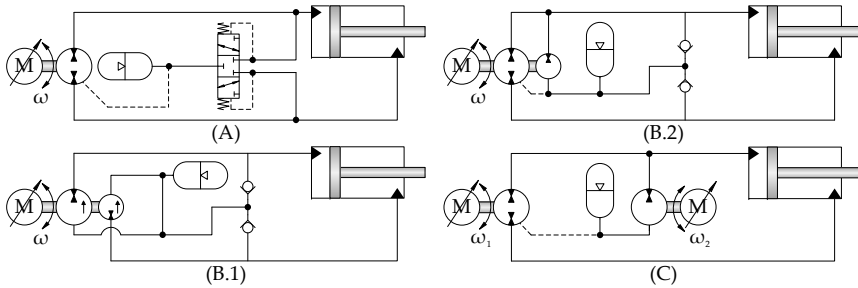


Fig. 1.6: (A) Example of a class A ECD architecture based on passive valve flow compensation. (B.1) Example of an open circuit class B architecture. (B.2) Example of a closed circuit class B architecture. (C) Example of a closed circuit class C architecture.

prate cylinder chambers to the reservoir [38, 43, 44].

Finally, a three port asymmetric pump solution is presented in [45, 46, 47, 48], and is here classified as class A.3 ECDs. The ports connected to the cylinder chambers are constructed with a displacement ratio that matches the cylinder area ratio, such that no additional components are needed for flow compensation. This is conceptually similar to using two fixed displacement pumps connected to the same shaft in an open circuit configuration, as class B.1 ECDs discussed next.

Class B

A fundamentally different approach to balance the asymmetric cylinder chamber flows is represented by using multiple pumps instead of auxiliary valves, which is especially compelling for ECDs required to work in four quadrants due to the absence of mode-oscillations.

Several researchers have investigated this, using two oppositely oriented fixed-displacement pumps in an open circuit configuration (Class B.1.), as shown in Fig. 1.6(B.1) [1, 49]. In [50] a lifting efficiency of approximately 55 % is reported for the actuation of a single boom crane. To avoid low-pressure operation, which is an inherent feature of class A and B ECDs, a third pump is added to the shaft by the researchers in [51, 52]. By further including 2/2-way proportional valves used to bleed off oil from the chambers to the reservoir, it is possible to maintain a certain minimum pressure level during piston motion to improve *"the dynamic properties of the system significantly"* [52].

The two pumps may also be configured in a closed circuit configuration as shown in Fig. 1.6(B.2), requiring a closed circuit pump, but offering smaller pump sizes compared to the open circuit configuration. In [28, 35], a low power system is compared to an electro-mechanical counterpart showing a similar energy efficiency. In [53], this architecture is used for actuating a Stewart platform, showing a highly improved energy efficiency compared to a valve-controlled system. As an example the commercially available Helax actuator from Bucher is also based on the closed circuit architecture, and the efficiency is evaluated to be up to 82 % and 84 % in resistive and aided loading conditions respectively [54].

Due to speed and pressure dependent pump leakage flows, it is not possible to maintain proper matching of pump displacement ratios and cylinder area ratios under all operating conditions. This may cause excessive pressure build up or cavitation in either cylinder chambers [55]. In [55] it is pointed out, that anti-cavitation valves and pressure relief valves are required, and it is suggested to implement 2/2-way proportional valves to bleed off oil from the chambers to the reservoir to limit the pressure build up.

1.4. State of the Art

To avoid the strict inherent geometrical constraint emerging when mounting multiple pumps on the same shaft, two variable-speed electrical motor-pump units may be used, which are classified as class C drives, seen in Fig. 1.6C and presented below.

Class C

By offering ideal matching of the pump flows to the cylinder area ratio regardless of operating conditions, the problem of uncontrolled pressure build up or cavitation may be avoided. The dual input nature of class C drives, enables to control the pressure level of the actuator, as well as the piston motion. This may have some benefits compared to single prime mover classes as discussed in Sec. 1.4.1.

Compared to class A and B, only little research effort has been focusing on Class C drives. In [18, 56, 57, 58] a 64 kW drive is experimentally tested in an injection molding machine, focusing on pump wear, energy saving potentials and control related topics.

In [59] the closed circuit configuration shown in Fig. 1.6C is compared with an open circuit counterpart, showing the former to be more energy efficient and requiring smaller pump and motor sizes for the same power output.

1.4.1 Comparison of ECD Classes

To summarise the findings of the review process, paper A compares the drive classes based on the eight criteria listed in Tab. 1.2 on page 16.

Energy Efficiency

For drive classes A and B a significantly improved energy efficiency has been reported for each drive class compared to conventional valve-controlled hydraulic systems. For instance [60] shows an energy consumption reduction of 62 % for a single boom crane compared to an LS valve-controlled system for a Class A drive. The authors in [61] simulate a reduced energy consumption of up to 62.5 % for a class B.1 ECD architecture performing a digging cycle of a 9-ton excavator compared to an LS system. As [62] points out, it is not feasible to compare the obtained relative energy savings or efficiencies reported in different studies, as these are based on different applications, assumptions and operating conditions. For drive class C no comparison study has been identified. As mentioned previously, the losses of all ECD architectures are dominated by component efficiencies, meaning that comparable energy characteristics should be obtainable for all three drive classes.

If class C drives are controlled to elevate the low pressure chamber of the cylinder above the reservoir pressure, certain load cases may lead to one

Table 1.2: Comparison of the proposed drive classes from Paper A. The derived drive classes are assessed based on eight criteria. Four different grades are used, ranging from (- -) to (+ +), with (- -) being the worst.

	Class A	Class B	Class C
Energy Efficiency	+	+	+
Ability to control drive stiffness	- -	-	+ +
Ability to handle highly dynamic/switching loads	- -	+	+ +
Drive compactness	+ +	+ +	+
Hydraulic circuit simplicity	+	+ +	+ +
Control simplicity	+	+	-
Reliability	-	-	-
Degree of scalability	-	-	+

electric machine working as a motor and the other as a generator or vice versa, as stated by [59]. Because power is shared electrically more stages of power conversion is required compared to the other drive classes under these specific working conditions. This may cause energy efficiency to be slightly lower for class C. An in-depth analysis is however needed to assess the severity of this loss mechanism compared to the (small) throttling losses for flow compensation of class A [62], and the associated valve losses to avoid cavitation or over-pressurisation of class B.

Ability to control drive stiffness

For class A and B ECDs one chamber of the cylinder is generally at a pressure level close to the reservoir pressure, i.e. at a low pressure. Low pressure operation may lead to varying dynamic properties of the cylinder, due to a highly pressure dependent bulk modulus of the oil-air mixture. At low pressures (< 25 bar), the bulk modulus is highly influenced by the free air content in the oil, causing a small bulk modulus of the mixture. For higher pressures the free air is compressed leading to the mixture bulk modulus being dominated by the high and almost constant bulk modulus of the oil. Especially, for small external loadings, the low pressure operation, causes the pressures in both cylinder chambers to be low, in turn causing a low system eigenfrequency as shown in [63]. Elevating the pressure level such that the lowest chamber pressure is 30 bar, is found to increase the eigenfrequency of the cylinder. This also leads to a less varying eigenfrequency as external loading is varied, i.e. plant uncertainty decreases or robustness increases [63].

1.4. State of the Art

It is important to keep in mind that the eigenfrequency or stiffness referred to here is the uncompensated drive stiffness, i.e. the drive dynamics has not been manipulated by closing control loops. The higher uncompensated eigenfrequency obtained in [63] by increasing the lower chamber pressure from 1 to 30 bar, enables choosing a higher proportional controller gain for a simple proportional feedback motion controller. This leads to a significantly improved motion tracking performance. The same is reported in [52], where tracking performance is improved significantly for a class B ECD architecture capable of increasing the actuator pressure level compared to low pressure operation.

Class C drives distinguish themselves from class A and B drives in terms of the ability to manipulate the drive stiffness. Multiple researchers used the additional control input to control a pressure state as well as the cylinder motion to avoid low pressure operation. This increases the uncompensated stiffness and reduce plant uncertainty (varying bulk modulus).

The importance of elevating the uncompensated stiffness, depends on the control structure desired to use. E.g. if a class A or B ECD is operated by a human operator in *hydraulic* open loop, i.e. only the closed loop speed controller of the electric motor is used, it may be advantageous to elevate stiffness to increase robustness toward force disturbances. However if operating in force or motion closed loop control, [64] recently showed how to compensate drive dynamics using pressure, position and shaft speed feedback. As such the obtained closed loop dynamics/bandwidth is ideally not limited by the pressure level i.e. the bulk modulus of the hydraulic system (or other physical parameters), but rather limited by the actuator dynamics. That is the speed-control loop or torque/current control loop bandwidth of the electric drive. Even though excellent motion tracking performance is obtained during low pressure operation, as shown in [64], simpler control structures may still benefit from increased uncompensated stiffness and decreased plant uncertainty. Additionally, as will be utilised later in this dissertation, the ability to control the drive stiffness i.e. the lowest chamber pressure, opens up novel approaches for including and controlling auxiliary components such as load holding valves in ECDs.

Ability to handle highly dynamic/switching loads

As mentioned under the previous criteria, the ability to keep the drive stiffness at a reasonable level is in some studies found to improve closed loop position control bandwidth, thus improving the performance for highly dynamic load cases or disturbances. As also mentioned here [64] presented novel methods for improving the dynamic performance of ECDs even during low pressure operation. This means that the ability to obtain high closed loop position bandwidths may not be limited by low pressure operation but rather actuation dynamics. In terms of oscillation reduction and active vibra-

tion damping, which are important aspects for modern hydraulic drives, the actuation dynamics is also the limiting factor. The actuation dynamics for class A, B and C is determined by the chosen electric drive components, and does not depend on the ECD class as such.

Nevertheless, class A drives are in the basic configuration reported to suffer from the previously mentioned mode-oscillation at certain load conditions, meaning that transition issues may arise for switching loads [28, 29]. Therefore class A drives are graded lower than class B and C in this criterion.

Drive Compactness

The drive compactness is heavily affected by the selected components. For example is the power density of a permanent magnet synchronous machine (PMSM) larger than for an induction machine, even though both topologies may be suitable for ECDs. It is however generally assessed that single prime mover architectures (class A and B) may be constructed to be more compact than class C containing two prime movers, especially for small power outputs.

Hydraulic Circuit Simplicity

The general assumption is that that multiple-pump classes (class B and C), may be constructed simpler than class A where additional valves and fluid paths are needed for flow balancing.

Control Simplicity

The control complexity is heavily affected by the requirements set by the application, meaning that closed loop control structures may be involved for all drive classes. Generally, it is however likely that the control of the multiple-input system (class C) is more advanced than controlling the single input classes. This is justified by the fact, that class A and B may be controlled in *hydraulic* open loop, i.e. by just using the closed loop speed controller of the electric drive, whereas this is not possible for class C, at least not if cavitation or over-pressurisation should be avoided.

Reliability

Long term evaluation of the reliability of ECD systems are generally absent in literature. The reliability of the systems is assessed to be determined by the extent of which components are used within their design ranges, including oil temperature and contamination management.

Especially the hydraulic pump unit is of interest, because most pump types are developed through decades to fit the need of conventional hydraulic systems i.e. constant speed operation. Therefore the majority of commercially available pumps require a certain minimum rotational speed for long term reliable operation, typically from 200-600 RPM [62]. As reliability have not been the main concern for researchers in the past, some studies ignore the minimum speed limitation. No long term evaluation of the system reliability

is presented, so the consequences are hard to assess [62]. In [65, 66, 67] valves are included in the system architecture capable of emulating pump leakage and controlled such that the pump speed is always above the minimum required speed (unless direction is changed). As this may cause substantial throttling losses, energy efficiency is reduced and cooling requirements increased. A better technical solution is therefore probably to utilise pumps optimised for variable-speed operation, which entered the market lately. The ideal pump for ECDs features small leakage and friction losses also at zero speed and high pressures, four quadrant operation without speed limitations, and a high maximum speed and pressure rating [12, 68]. Based on these requirements the newly introduced AX series pump from Bucher [69] is worth mentioning as this offers these properties.

Degree of Scalability

The scalability is primarily decided by the available component sizes. The limiting factor is typically the electric motor, especially if this is chosen to be a permanent magnet synchronous machine, as this has a lower application range than e.g. induction machines, considering standard off-the-shelf machines. Therefore if the same type of components are selected, it is clear that the dual prime mover class C configured in a closed-circuit architecture offers a larger power output than the single prime mover classes.

1.4.2 Current Research Topics

The literature review in Paper A reveals that research has previously focused on identifying and verifying circuit architectures capable of balancing cylinder chamber flows and the impact in terms of energy consumption for specific applications. More recently, some research started to focus on other aspects as well. This includes fluid management properties of ECDs. In conventional centralised hydraulic systems the fluid is cooled and filtered using dedicated circuits with its own pump and motor unit connected to the centralised oil reservoir. This is not necessarily an appropriate solution for ECDs, as this limits compactness of the system and is required for each actuator in an application. An attractive idea is the complete avoidance of both the cooling and filtration elements. In [70] it is found that after 960 hours of operation, the self-contamination resulted in a high particle load. Therefore [70] concluded that currently operating an ECD is not recommended without an oil filter. For ECDs it is therefore beneficial to include an in-line filter element, not requiring a circulation pump. In [62] it is suggested *"to filter the whole amount of circulating oil"*, which for closed circuit architectures may lead to high pressure filters, which generally is undesirable as these are *"heavier, harder to maintain and more expensive than"* [62] low pressure filters.

The lower energy losses of ECDs may permit these systems to rely solely

on passive cooling, i.e. the losses are balanced by passive heat transfer to the ambience. This is especially interesting for smaller drive powers (<10 kW), while for larger ECD drives passive cooling is unlikely to suffice. To gain knowledge and insight into the thermal behaviour required for proper thermal designs, increased research interest has recently been placed on modelling the thermal behaviour of ECDs [71, 72, 73].

To ensure durability and reliability of ECDs thermal modelling and proper thermal designs are therefore important research areas. In [74], the electric motor is cooled using oil from the hydraulic circuit, such that only one cooler is needed. Another way of reducing the number of oil coolers for an application requiring multiple actuators, is represented by systems combining the advantages of ECDs and centralised hydraulics. This means that the stand-alone nature of ECD is abandoned, which on one side limits the plug-and-play nature of the technology, as a centralised hydraulic supply with a common reservoir is used requiring piping to each actuator. However, these hybrid solutions offer some significant benefits such as centralised oil cooling and filtering and reduction of the installed electric power. Examples of such systems are given in [7, 75].

1.5 Drive Architecture for Further Study

In cooperation with the industrial partners of the SFI Offshore Mechatronics Research Project, a medium sized knuckle boom crane is selected as the focus application in this study. Examples of such cranes are shown in Fig. 1.7. Only the cylinders used for actuation of the boom structures are included in this work, i.e. the hydraulic motor for rotating the crane or the hydraulically actuated lifting yoke are not included. A more detailed description as well as a dynamic model of a specific crane is given in Chapter 2.



Fig. 1.7: Offshore knuckle boom crane examples. Left hand photo is provided by National Oilwell Vargo ©NOV. Right hand photo is made available by Geir Arne Moslått, NOV.

1.5. Drive Architecture for Further Study

The most strenuous requirements are present for actuation of the knuckle boom (outer boom) of the crane. Here both four quadrant operation is required as well as the ability for the actuation system to work in tilted orientations, as it is intended to mount the ECD system on the main boom to reduce piping. In addition to this the ECD architecture should include load holding functionality or safety valves such that the load is kept stationary during power supply failure or hose burst. The load holding functionality must comply with the safety regulations and cannot preclude the possibility for energy recuperation. The needed output power for the considered crane is roughly 65 kW per actuator, however the industrial project partners would value if the ECD is scalable to even higher power classes. Beside a high power range, the cylinders used for crane actuation also feature long strokes, meaning that a large rod volume need to be stored in a pressurised gas-charged accumulator during motion of the piston. To stay within the permissible pressure range, this leads to large gas volumes. It is therefore desirable to implement other types of accumulators to increase compactness and to avoid the need of gas, as leaking gas to the oil or the surroundings may lead to system failure.

An ECD fulfilling these requirement are not identified in the literature. Especially the requirements in terms of load holding capabilities (a review is given in Sec. 4.1) and the desire of a gasless pressurised accumulator, represent challenges. These requirements may be considered as auxiliary functionalities of ECDs whereas required functionalities include flow balancing and four quadrant operation. As the latter challenges already are solved by the presented drive classes, it is found reasonable to use one of the existing drive classes as the starting point and add innovations to this to fulfil the requirements set by the knuckle boom crane.

By holding the comparison made previously between the drive classes against the requirements, it is chosen to focus on class C architectures for the remainder of this work, i.e. architectures with two prime movers. The reason for this is due to the requirements related to scalability and four quadrant operation. Additionally, the flexibility offered by the two control inputs may enable adding load holding functionality and the gasless reservoir in a mechanically/hydraulically simple way.

1.6 Research Hypothesis

Based on the literature review and the requirements from the industrial partners of the SFI Offshore Mechatronics Research Project, the research hypothesis follows as:

It is possible to design and control an electro-hydraulic compact cylinder drive based on two electrical machines which includes load holding capabilities and a pressurised gasless oil reservoir, still offering significantly improved energy characteristics compared to a conventional valve-controlled system.

The hypothesis is supported by the following research questions (RQ):

- RQ1:** How large is the potential for energy savings if electro-hydraulic compact drives are used to actuate a medium sized knuckle boom crane compared to a conventional valve-controlled system?
- RQ2:** To what extent is the static payload capacity of a medium sized knuckle boom crane reduced if electro-hydraulic compact drive systems are installed locally on the hydraulic cylinders?
- RQ3:** How can hydraulically actuated load holding valves be included and controlled in the hydraulic architecture without leading to severe throttling losses and still fulfilling the law-enforced safety requirements for load carrying applications?
- RQ4:** How can a gasless oil reservoir deliver the required compensation flow at the required pressure level and to what extent can the reservoir volume be reduced compared to a gas-charged accumulator?
- RQ5:** How can a dynamic thermo-hydraulic modelling framework including the oil temperature state be derived which is suitable for assessing oil cooling requirements of electro-hydraulic compact drives?
- RQ6:** How can an electro-hydraulic compact drive consisting of two electric motors be controlled to obtain good motion tracking performance as well as to control the opening of hydraulically actuated load holding valves?

1.7 Dissertation Outline

The main contribution of the work in the PhD project has been to investigate the research questions. The results of this are presented in the appended papers and in this dissertation. Conclusions on the main research contributions are given in the Closing Remarks in Chapter 8.

The research activities are documented in the following chapters:

Chapter 2

A medium sized knuckle boom crane used to handle drilling pipes is presented as the focus application of this dissertation. A dynamic model of the crane is formulated based on the Euler-Lagrange formulation, and it is investigated how attaching electro-hydraulic compact drives locally on the cylinders affects the static payload capacity of the crane (RQ2). The latter is a summary of paper B where RQ2 is also the focus.

Chapter 3

This chapter is dedicated to investigate the energy saving potential of electro-hydraulic compact drives compared to conventional valve-controlled drive systems (RQ1). This is done by formulating, solving and comparing steady state hydraulic models of these. This includes power loss models of the main components of the drive systems. The energy consumption is compared based on a predefined motion trajectory defined by the industrial partners.

Chapter 4

How to include load holding capabilities (RQ3) and a gasless pressurised reservoir (RQ4) is investigated in this chapter. Based on a mini-review hydraulically actuated logic elements are inserted in the main transmission lines and the pilot pressure is selected as the lowest chamber pressure, to ensure closing in the event of electrical power loss or hose burst. RQ3 is also the main topic of Paper C. With regard to RQ4, this chapter provides a summary of papers D and E where a bootstrap reservoir is used to provide the needed compensation volume. The chapter concludes with comparing the energy consumption characteristics of the proposed system design and a system without load holding valves and bootstrap reservoir.

Chapter 5

A thermo-hydraulic modelling framework (RQ5) is derived and experimentally validated in Paper F. Based on the findings in Paper F, a dynamic thermo-hydraulic model of the system designed in Chapter 4 is formulated.

Chapter 6

Based on simplified models, control structures are designed to handle the dual input nature of the drive system. The aim of this chapter is to obtain both good motion tracking performance and the ability to control the opening of the load holding valves (RQ6).

Chapter 7

A simulation study of the knuckle boom crane modelled in Chapter 2 is presented. The crane is actuated by the electro-hydraulic compact drive modelled in Chapter 5 and controlled using the control system developed in Chapter 6. The main focus in this chapter is therefore to investigate if the research hypothesis can be verified or not.

1.8 Project Delimitations

The current dissertation is primarily based on theoretical studies. This means that only small parts of the presented material has been experimentally verified. The drive system designed during the research period has not been experimentally verified on a knuckle boom crane due to practical and economical limitations. Even though a downscaled version of the drive system has been manufactured, it has not been possible to obtain experimental data within the project period.

Due to the focus on simulation studies, the dissertation delimits itself from investigating the reliability of the drive system. This also excludes studies concerned with the requirements for components installed in offshore environments, e.g. how the reliability is affected by rain, salty water, wind, ultra-violet radiation etc.

Finally, no cost analysis or comparison with conventional drive systems has been conducted. This excludes both the investment cost of the drive systems and the operating cost, e.g. maintenance cost, energy cost etc.

Chapter 2

Knuckle Boom Crane

A knuckle boom crane as depicted in Fig. 2.1 is used as the focus application for the further theoretical studies. This is chosen because it represents a system of particular interest for the SFI Offshore Mechatronics Research Project who funded this research.

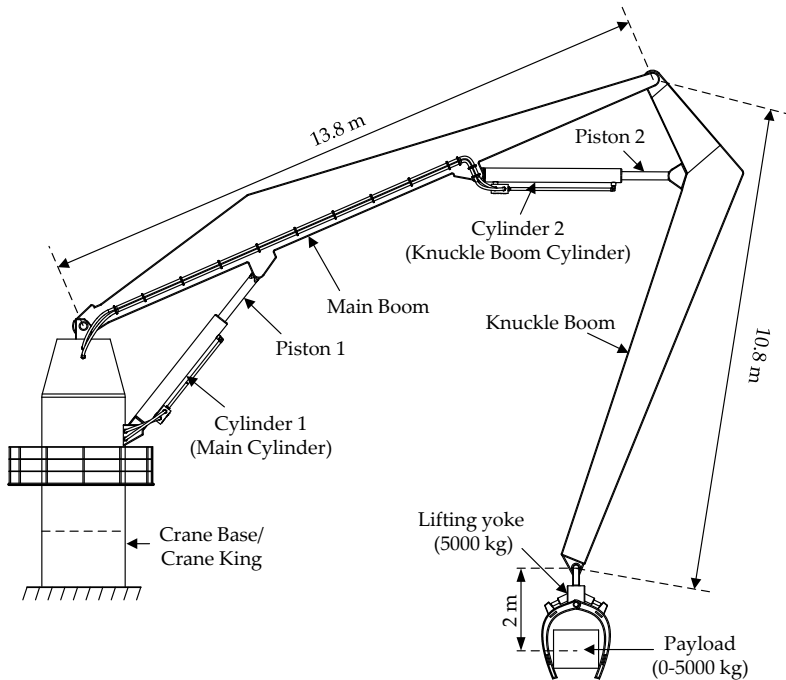


Fig. 2.1: Illustration of a knuckle boom crane used as the application for the theoretical studies in this dissertation.

In cooperation with the industrial partners in the project, it has been decided to focus on linear drive solutions for actuation of the booms of pipe handling cranes. Pipe handling cranes are special type of offshore cranes used to manoeuvre pipes onboard drilling rigs or drilling ships, and unlike many other types of knuckle boom cranes these are not equipped with a winch for load handling. Instead a lifting yoke is attached to hold the payload/pipes.

Knuckle boom cranes come in a variety of sizes and configurations. Some are equipped with three booms or jibs [76] or only two as considered in this work. Smaller or medium sized cranes use a single cylinder for actuation of each boom, while larger cranes use multiple cylinders in parallel for actuation of each boom. While large offshore knuckle boom cranes are able to carry loads of several hundreds ton (e.g. 400 t in [77]), pipe handling cranes are typically sized with a significantly smaller lifting capacity.

In this work a medium sized pipe handling crane with a lifting capacity of approximately 10 ton and a maximum working radius of approximately 17 m is utilised. A single cylinder is used to actuate each boom. An illustration of this crane is shown in Fig. 2.1. Mass moment of inertias has been approximated by assuming a uniform mass distribution over the volume of the boom.

In this chapter the knuckle boom crane is modelled and initial analyses are carried out. It is first investigated how the static payload capacity of the selected knuckle boom crane is affected by locally installing electro-hydraulic compact drives (ECDs) and how the choice of different ECD-architectures may affect this. This investigation is a summary of Paper B.

Subsequently, a dynamic mechanical model of the knuckle boom crane is derived.

2.1 Reduction of Payload Capacity

A significant benefit by installing ECDs is the reduced amount of needed hydraulic piping compared to conventional centralised hydraulic power units (HPUs). For the considered crane, the HPU is conventionally installed in the crane base and hydraulic power is transferred to the actuators by hoses or pipes. This is visualised in Fig. 2.2a.

By installing ECDs, the hydraulic hoses can be replaced by electrical power and communication cables. In Fig. 2.2b the ECD for actuation of the main boom is assumed to be installed stationary in the crane base, while the ECD for actuating the knuckle boom is attached to the outer cylinder. For practical realisation it may be possible to install the power unit inside the hollow main boom and use short hoses or pipes for connection to the cylinder.

2.1. Reduction of Payload Capacity

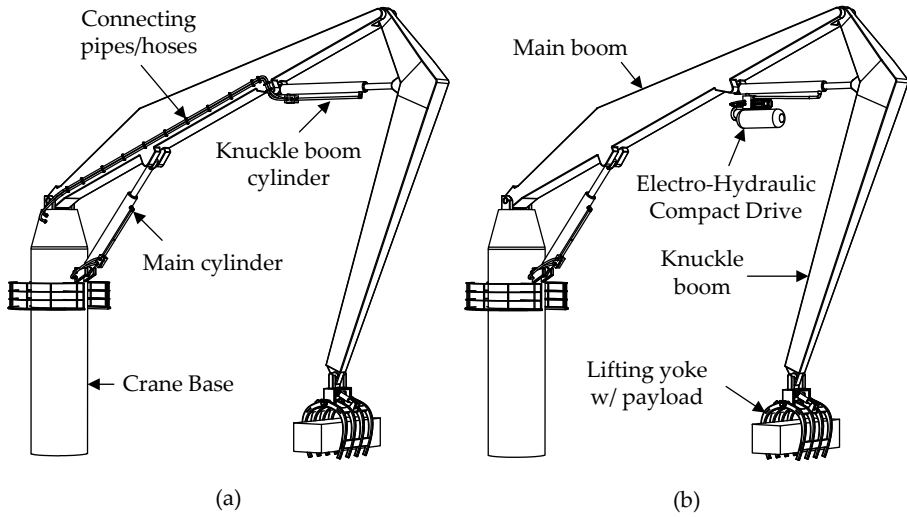


Fig. 2.2: (a) Illustration of knuckle boom crane, with conventional valve-controlled cylinder drives. Hoses are transporting hydraulic power from the centralised power unit to the knuckle boom cylinder. (b) Illustration of knuckle boom crane actuated by ECDs. To shield the ECD from harsh offshore conditions, the actuator may be installed in the hollow main boom for practical realisation. From Paper B.

Installing an ECD on or inside the main boom means, that an additional load needs to be carried by the crane, which reduces the static payload capacity of the knuckle boom crane. In paper B the static payload capacity is investigated by assuming the force capability of the hydraulic cylinders to be the limiting factor.

To investigate how different ECD architectures affect the payload capacity, the mass of seven different ECD architectures shown in Fig. 2.3 has been estimated as a function of the maximum cylinder output power.

In Paper B the required pump flows for the architectures given in Fig. 2.3, is calculated as a function of the maximum actuator power assuming ideal components, steady state conditions and defining the load pressure to 300 bar. Using pump datasheet information for Bosch Rexroth A10, A4 and A2 axial piston pumps [78, 79, 80], the needed pump displacement as a function of actuator power is estimated. This assumes the shaft speed to be limited by the allowed pump speed and not the electrical machine. As such the needed shaft torque may be calculated, which is used to estimate the mass of the required electrical machine using both asynchronous induction motors [81] and permanent magnet synchronous machines (PMSM) [82].

The estimated pump and electrical machine masses for the architectures given in Fig. 2.3 are shown as a function of actuator power in Fig. 2.4.

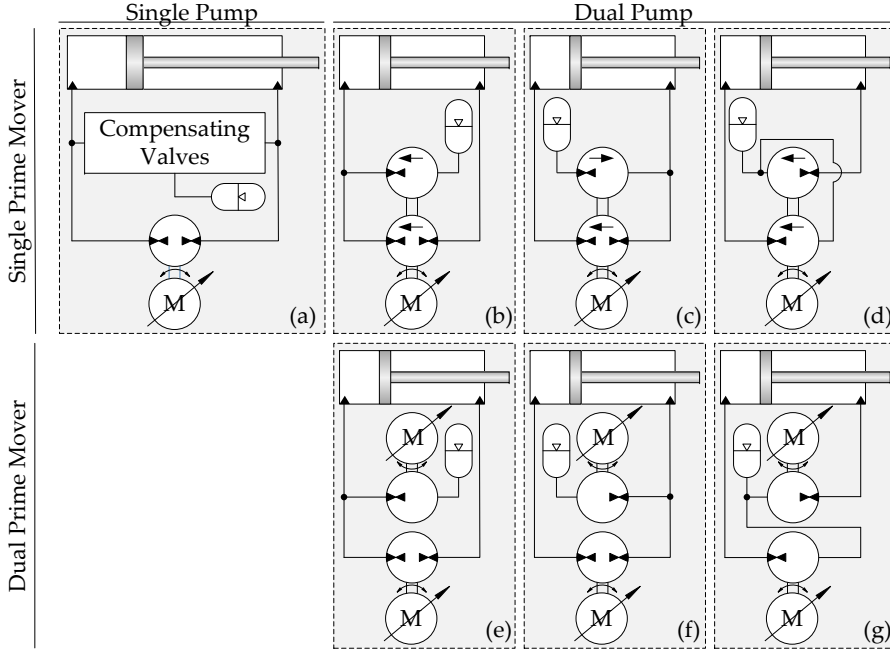


Fig. 2.3: (a) to (g): Hydraulic diagrams used for estimating the mass of different ECD architectures in paper B.

The estimated masses depend on the ratio, α , between the cylinder rod side area and the piston area ($\alpha = A_B / A_A$), as well as the assumed pressure in the chamber with the lowest pressure. In Fig. 2.4 these are defined to $\alpha=0.6$ and 0 bar respectively. A detailed description of the mass estimation procedure is given in Paper B.

From Fig. 2.4a it is found that for the single prime mover architectures, the mass of the pumps and electric motor is only a weak function of the considered architectures. However, by utilising an induction machine as the prime mover the power range may be extended compared to PMSM (Fig. 2.4b). This causes architecture (b) from Fig. 2.3 to be beneficial in terms of reduced mass. The explanation for this is that for architecture (b), the flow needed for cylinder extension is delivered by two pumps. As smaller pumps are generally allowed to rotate faster than larger pumps, the sum of the two pump displacements are smaller than the needed sum of pump displacements for the remaining architectures. This in turn requires a smaller shaft torque leading to a lighter electric machine to be used.

Considering the estimated total mass of the pumps and electric motors for the dual prime mover architectures, seen in Fig. 2.4c and d, it is seen that architecture (e) from Fig. 2.3 is beneficial in terms of reduced mass. From

2.1. Reduction of Payload Capacity

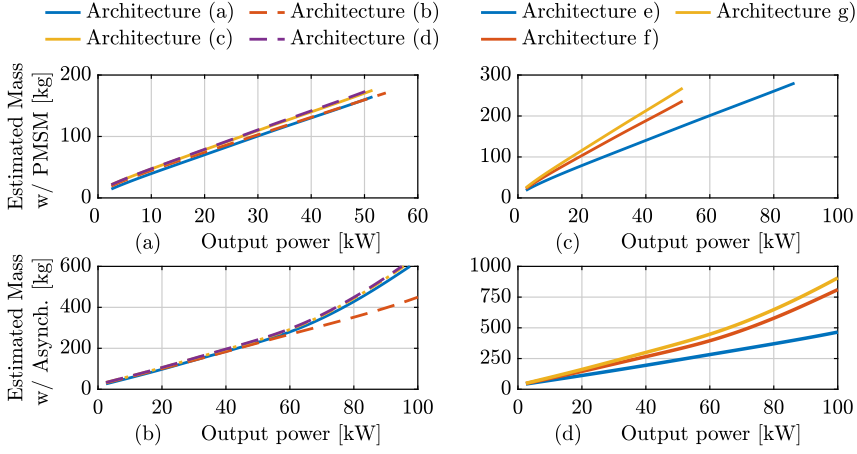


Fig. 2.4: (a) and (b) Estimated pump and electrical machine masses as a function of maximum output power for architectures with a single prime mover using a PMSM and an induction/asynchronous electric motor respectively. (c) and (d) Estimated pump and electrical machine masses as a function of maximum output power for architectures with two prime movers using PMSMs and induction/asynchronous electric motors respectively. Revised figure from Paper B. The cylinder area ratio (A_B/A_A) is 0.6, the load pressure is 300 bar and the pressure in the chamber with the lowest pressure is 0 bar.

Paper B this is explained by the fact that in this architecture the two electrical machines aid each other, meaning that the cylinder power is delivered simultaneously from both prime movers. If the rod area is half the piston area, the two prime movers are delivering the same amount of power. For the other architectures this is not the case in all operation quadrants. Take architecture (g) from Fig. 2.3 as the simplest example. If the load is carried by the piston chamber, then all the mechanical power must be delivered by the motor connected to the piston chamber, while the other motor idles. However if the load is carried by the rod side chamber, the situation changes and the cylinder power is delivered by the motor connected to this chamber. This means that the two motors do not deliver power simultaneously, leading to a higher amount of installed power than it is possible to deliver instantaneously as mechanical power by the cylinder. This causes heavier electric motors compared to architecture (e). Due to the power adding nature of architecture (e), this has the advantage of delivering higher output powers using commercially available PMSMs which are limited to approximately 50 kW in this investigation.

When evaluating the changed static payload capacity of the knuckle boom crane, it is assumed that the ECD actuating the main boom is placed stationary in the crane base, while the ECD actuating the knuckle boom is installed locally, as illustrated in Fig. 2.2b. As such only the mass of the latter ECD

is assumed to affect the payload capacity. The required actuator power is 59 kW for a maximum load pressure of 300 bar and a flow of 118 L/min. For the given cylinder piston area ($d_A=250$ mm) this corresponds to a maximum force of 1.47 MN and a speed of 40 mm/s.

Tab. 2.1 summarises the estimated pump and electrical machines masses for the seven architectures in Fig. 2.3, using components that are commercially available.

Table 2.1: Estimated masses for the electric motors and pumps for the considered knuckle boom actuator application example. From Paper B.

Architecture	Mass using available components		Installed Electric Power	
	PMSM	Asynchronous	PMSM	Asynchronous
(a)	-	264.0 kg	-	61 kW
(b)	-	336.0 kg	-	75 kW
(c)	-	279.5 kg	-	61 kW
(d)	-	279.5 kg	-	61 kW
(e)	208 kg	382.5 kg	72 kW	71 kW
(f)	-	483.5 kg	-	99 kW
(g)	-	427.0 kg	-	92 kW

From Tab. 2.1, it may be seen that only architecture (e) is capable of delivering the required amount of power using the available PMSMs. The single prime mover architectures (a), (c) and (d) have approximately the same estimated mass, while architecture (b) is significantly heavier. This is due to a mismatch between the needed pump sizes for this architecture and the available ones, leading to over-sizing of the pumps in turn causing a heavier electric machine. This is reflected by the fact that 75 kW is in fact installed, despite targeting 59 kW.

For the dual prime mover architectures, it is seen that architecture (e) has a significantly smaller mass compared to architectures (f) and (g).

As stated in the introduction the current dissertation deals with dual prime mover architectures. From the investigation in Paper B, architectures (f) and (g) are less attractive than architecture (e), if considering four quadrant operation due to the fact that the electrical machines in the former architectures do not deliver power instantaneously, as explained earlier. This leads to a larger mass and importantly also higher component costs.

Based on these findings the remainder of the dissertation focuses on architecture (e) in Fig. 2.3. Additionally in the remainder of the dissertation "ECD" refers to this specific circuit architecture, unless stated otherwise.

2.1. Reduction of Payload Capacity

Beside the mass of the pump and electrical motors also the hydraulic cylinder, accumulator, hydraulic manifold and the oil contribute with a significant mass. These masses are however assumed to be independent of the selected circuit architecture and thus not included in the above analysis.

Tab. 2.2 summarises the estimated mass of the ECD system used for actuation of the knuckle boom. For the given system, it can be seen that the masses of the pumps and motors are 7.8 % of the total ECD mass, showing that the selection of system architecture in fact only has a minor effect on the total ECD mass.

Table 2.2: Estimated masses of the main components of the knuckle boom actuator. *Estimated

Component	Mass	Relative to total mass of ECD
Hydraulic Cylinder [83]	1711 kg	64.1 %
Pumps and Motors (Architecture (e))	208 kg	7.8 %
Manifold and Reservoir	600 kg*	22.5 %
Hydraulic Oil (175 L)	150 kg	5.6 %
Total	2669 kg	

For the benchmark system (VCD) only the hydraulic cylinder is attached to the booms (neglecting mass of safety valves etc.). This mass is 1711 kg, meaning that the considered ECD system is estimated to be 56 % heavier than the benchmark.

How this affects the payload capacity is also investigated in Paper B, based on a static mechanical model presented in this paper. By assuming the maximum pressure of the cylinders to be 300 bar and assuming zero back-pressure, the maximum force of the main cylinder is 1.85 MN while it is 1.47 MN for the knuckle boom cylinder. Dependent on the configuration of the crane, the knuckle boom cylinder should also be able to deliver negative load forces. The largest negative load force is -0.71 MN. By defining the maximum force capabilities, it is possible to solve for the unknown payload mass leading to at least one of the cylinders being at their maximum force capacity.

For the benchmark system, i.e. the VCD, the static payload capacity is shown in Fig. 2.5a. The payload capacity is highly dependent on the configuration of the crane, ranging from 12.9 ton to 43.2 ton. If installing the proposed ECD on the knuckle boom cylinder the static payload capacity decreases in the majority of the operating space of the crane. This is visualised in Fig. 2.5b. The maximum reduction is 1.25 ton. The minimum reduction is found in the lower left corner of the operating space, where the reduction is 0 kg

as the payload capacity is here limited by the force capability of the knuckle boom cylinder.

Fig. 2.5c shows the relative reduction of the payload capacity, if installing an ECD on the knuckle boom cylinder compared with the benchmark solution. In the areas where the payload capacity is in fact reduced, the reduction is found to be relatively constant at 3 %.

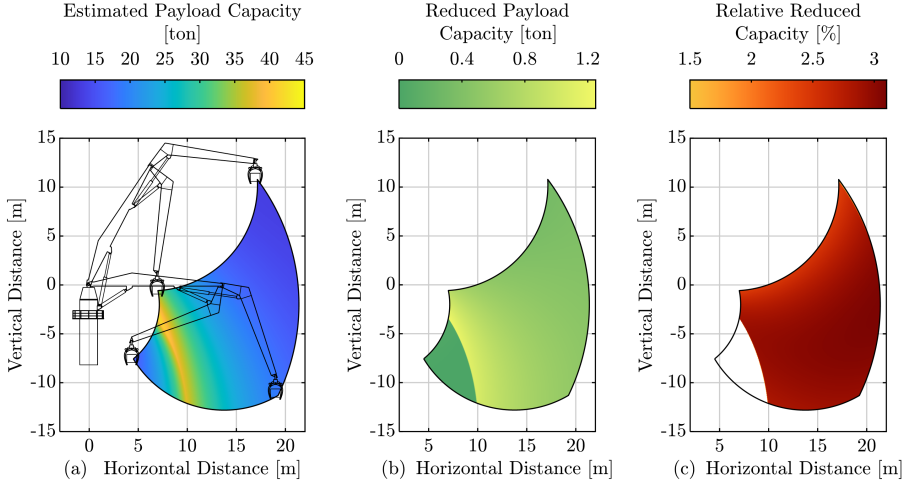


Fig. 2.5: (a) Estimated static payload capacity in the working range of the crane for the benchmark solution, i.e. valve-controlled actuation. Given in ton (1000 kg). (b) Reduced static payload capacity, if installing an ECD on the knuckle boom cylinder compared to benchmark. (c) Relative reduction in static payload capacity.

2.2 Dynamic Knuckle Boom Crane Model

A dynamic mechanical model is derived in the following, which is utilised for evaluating the performance of the designed ECD, in Chapter 7. Even though the crane is capable of rotating around its base, the crane is modelled as a planar mechanism as the main focus is evaluating the performance of the cylinder drives controlling the motion of the booms. All dimensions, masses, inertias etc. may be found in the parameter list in Tab. A.1 on page 254.

2.2.1 Joint Kinematics

The planar joint kinematics of the crane are derived based on Fig. 2.6. Here the crane components and load are considered as seven rigid bodies.

2.2. Dynamic Knuckle Boom Crane Model

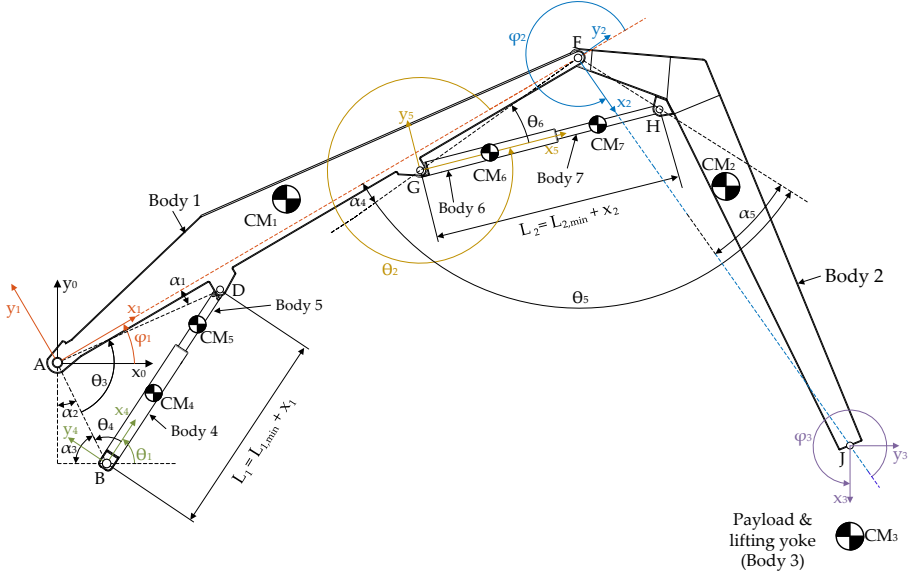


Fig. 2.6: Sketch showing the knuckle boom crane and the relevant quantities used for derivation of the crane kinematics.

The positions of the center of masses are calculated using the local coordinate frames defined in Fig. 2.6:

$$\begin{aligned}
 \mathbf{P}_{CM1} &= \mathbf{A}_1 \mathbf{s}_{A-CM1} & \mathbf{P}_{CM2} &= \mathbf{A}_1 \mathbf{s}_{A-F} + \mathbf{A}_2 \mathbf{s}_{F-CM2} \\
 \mathbf{P}_{CM3} &= \mathbf{A}_1 \mathbf{s}_{A-F} + \mathbf{A}_2 \mathbf{s}_{F-J} + \mathbf{A}_3 \mathbf{s}_{J-CM3} & \mathbf{P}_{CM4} &= \mathbf{s}_{A-B} + \mathbf{A}_4 \mathbf{s}_{B-CM4} \\
 \mathbf{P}_{CM5} &= \mathbf{A}_1 \mathbf{s}_{A-D} + \mathbf{A}_4 \mathbf{s}_{D-CM5} & \mathbf{P}_{CM6} &= \mathbf{A}_1 \mathbf{s}_{A-G} + \mathbf{A}_5 \mathbf{s}_{G-CM6} \\
 \mathbf{P}_{CM7} &= \mathbf{A}_1 \mathbf{s}_{A-F} + \mathbf{A}_2 \mathbf{s}_{F-H} + \mathbf{A}_5 \mathbf{s}_{H-CM7}
 \end{aligned} \tag{2.1}$$

The vectors \mathbf{s}_\bullet are constant vectors given in their local coordinate frames. The rotation matrices \mathbf{A}_1 to \mathbf{A}_5 are given as:

$$\begin{aligned}
 \mathbf{A}_1 &= \begin{bmatrix} \cos(\varphi_1) & -\sin(\varphi_1) \\ \sin(\varphi_1) & \cos(\varphi_1) \end{bmatrix} & \mathbf{A}_2 &= \begin{bmatrix} \cos(\varphi_1 + \varphi_2) & -\sin(\varphi_1 + \varphi_2) \\ \sin(\varphi_1 + \varphi_2) & \cos(\varphi_1 + \varphi_2) \end{bmatrix} \\
 \mathbf{A}_3 &= \begin{bmatrix} \cos(\varphi_1 + \varphi_2 + \varphi_3) & -\sin(\varphi_1 + \varphi_2 + \varphi_3) \\ \sin(\varphi_1 + \varphi_2 + \varphi_3) & \cos(\varphi_1 + \varphi_2 + \varphi_3) \end{bmatrix} & & \\
 \mathbf{A}_4 &= \begin{bmatrix} \cos(\theta_1) & -\sin(\theta_1) \\ \sin(\theta_1) & \cos(\theta_1) \end{bmatrix} & \mathbf{A}_5 &= \begin{bmatrix} \cos(\varphi_1 + \theta_2) & -\sin(\varphi_1 + \theta_2) \\ \sin(\varphi_1 + \theta_2) & \cos(\varphi_1 + \theta_2) \end{bmatrix}
 \end{aligned} \tag{2.2}$$

The considered crane has three degrees of freedom, represented by the generalised coordinates φ_1 , φ_2 and φ_3 . Note, that due to the closed kinematic chains of the crane manipulator the angles θ_1 and θ_2 are fully determined by

the generalised coordinates φ_1 and φ_2 respectively:

$$\theta_1 = f_{\theta_1}(\varphi_1(t)) \quad \Rightarrow \quad \dot{\theta}_1 = \frac{\partial f_{\theta_1}(\varphi_1(t))}{\partial \varphi_1} \dot{\varphi}_1 \quad (2.3)$$

$$\theta_2 = f_{\theta_2}(\varphi_2(t)) \quad \Rightarrow \quad \dot{\theta}_2 = \frac{\partial f_{\theta_2}(\varphi_2(t))}{\partial \varphi_2} \dot{\varphi}_2 \quad (2.4)$$

The kinematic relations $f_{\theta_1}(\varphi_2(t))$ and $f_{\theta_2}(\varphi_2(t))$ are not shown here. These have been established using standard trigonometric relations and the stroke dependent angles θ_4 and θ_6 , recognising that:

$$\theta_1 = \pi - \theta_4 - \alpha_3 \quad \theta_2 = 2\pi - \theta_6 + \alpha_4 \quad (2.5)$$

2.2.2 Equations of Motion

The equations of motion of the knuckle boom crane may be represented in the joint-space formulation as [84, 85]:

$$\boldsymbol{\tau} = \mathbf{D}_q(\mathbf{q}) \ddot{\mathbf{q}} + \mathbf{C}_q(\mathbf{q}, \dot{\mathbf{q}}) \dot{\mathbf{q}} + \mathbf{G}_q(\mathbf{q}) \quad (2.6)$$

$$\boldsymbol{\tau} = [\tau_1 \quad \tau_2 \quad \tau_3]^T \quad \mathbf{q} = [\varphi_1 \quad \varphi_2 \quad \varphi_3]^T \quad (2.7)$$

where τ_1 and τ_2 are the external joint torques applied by cylinder 1 and cylinder 2 respectively. τ_3 may represent joint friction or drag forces exerted on the payload. \mathbf{q} is the generalised coordinates in joint space, given as the rotational coordinates φ_1 , φ_2 and φ_3 defined in Fig. 2.6.

Multiple methods exist for deriving the matrices \mathbf{D}_q , \mathbf{C}_q and \mathbf{G}_q in Eq. 2.6. In this work the Lagrange formulation is utilised, which proceeds with calculation of the Lagrangian, \mathcal{L} , as [84]:

$$\mathcal{L} = \mathcal{K} - \mathcal{P} \quad (2.8)$$

where \mathcal{K} and \mathcal{P} are the total kinetic and potential energy of the mechanism, given as:

$$\mathcal{K} = \frac{1}{2} \left(\sum_{i=1}^7 m_i \dot{\mathbf{P}}_{\text{CM}i}^T \dot{\mathbf{P}}_{\text{CM}i} + \sum_{i=1}^7 J_i \Omega_i^2 \right) \quad (2.9)$$

$$\mathcal{P} = [0 \quad g] \sum_{i=1}^7 m_i \mathbf{P}_{\text{CM}i} \quad (2.10)$$

where g is the gravitational acceleration, m_i is the mass of the bodies and J_i is the mass moment of inertia about CM_i . Ω_i is the rotational velocity of the bodies, expressed in the global inertial frame, given as:

$$\begin{aligned} \Omega_1 &= \dot{\varphi}_1 & \Omega_2 &= \dot{\varphi}_1 + \dot{\varphi}_2 & \Omega_3 &= \dot{\varphi}_1 + \dot{\varphi}_2 + \dot{\varphi}_3 \\ \Omega_4 &= \Omega_5 = \dot{\theta}_1 & \Omega_6 &= \Omega_7 = \dot{\varphi}_1 + \dot{\theta}_2 \end{aligned} \quad (2.11)$$

2.2. Dynamic Knuckle Boom Crane Model

From the Lagrangian, the dynamic equations of motion are derived using Lagrange's equation for each generalised coordinate [84]:

$$\frac{d}{dt} \frac{\partial \mathcal{L}}{\partial \dot{q}_i} - \frac{\partial \mathcal{L}}{\partial q_i} = \tau_i \quad (2.12)$$

By evaluating Eq. 2.12 for the three generalised coordinates and collecting terms, the matrices in Eq. 2.6 are obtained.

The crane is controlled by applying cylinder forces. The joint torques and velocities are related to actuator forces and velocities by the Jacobian, \mathbf{J} , defined as [84]:

$$\boldsymbol{\tau} = \mathbf{J}^T \mathbf{F} \quad \dot{\mathbf{x}} = \mathbf{J} \dot{\mathbf{q}} \quad \mathbf{J} = \mathbf{J}^T \quad (2.13)$$

$$\mathbf{F} = \begin{bmatrix} F_{\text{cyl1}} & F_{\text{cyl2}} & -B_{\text{CM3}} \dot{\phi}_3 \end{bmatrix}^T \quad \mathbf{x} = \begin{bmatrix} x_1 & x_2 & \phi_3 \end{bmatrix}^T \quad (2.14)$$

where \mathbf{x} is actuator or operational coordinates, being the cylinder positions and the payload joint coordinate. F_{cyl1} and F_{cyl2} are the linear forces exerted by the hydraulic cylinders including cylinder frictions. B_{CM3} is a rotational viscous friction coefficient used to model joint friction and drag forces. For the considered crane the Jacobian matrix is diagonal, and has been established by describing \mathbf{x} as a function of \mathbf{q} using the stroke dependent angles θ_3 and θ_5 recognising that:

$$\varphi_1 = \theta_3 + \alpha_1 + \alpha_2 - \frac{\pi}{2} \quad \varphi_2 = \theta_5 + \alpha_4 - \alpha_5 + \pi \quad (2.15)$$

The angles θ_3 and θ_5 are described as functions of the cylinder strokes using standard trigonometric approaches. Doing so, \mathbf{x} may be expressed in terms of \mathbf{q} using Eq. 2.15. From this, the Jacobian matrix fulfilling $\dot{\mathbf{x}} = \mathbf{J} \dot{\mathbf{q}}$ may be established.

The dynamic simulation of the knuckle boom crane is performed in joint space by solving for the accelerations of the generalised coordinates in Eq. 2.6. The external torques exerted on the crane from the cylinder forces are calculated by Eq. 2.13.

2.2.3 Cylinder Loads

Using the definitions in Eqs. 2.13 and 2.14, the equations of motions in actuator or operational space may be represented as:

$$\mathbf{F} = \underbrace{\mathbf{J}^{-1} \mathbf{D}_q(\mathbf{q}) \mathbf{J}^{-1}}_{\mathbf{M}_x(\mathbf{x})} \ddot{\mathbf{x}} + \underbrace{\left(\mathbf{J}^{-1} \mathbf{C}_q(\mathbf{q}, \dot{\mathbf{q}}) \mathbf{J}^{-1} - \mathbf{J}^{-1} \mathbf{D}_q(\mathbf{q}) \mathbf{J}^{-1} \dot{\mathbf{J}} \mathbf{J}^{-1} \right)}_{\mathbf{C}_x(\mathbf{x}, \dot{\mathbf{x}})} \dot{\mathbf{x}} + \underbrace{\mathbf{J}^{-1} \mathbf{G}_q(\mathbf{q})}_{\mathbf{G}_x(\mathbf{x})} \quad (2.16)$$

where $\mathbf{M}_x(\mathbf{x})$ is a 3x3 mass-matrix representing the equivalent mass in actuator space, $\mathbf{C}_x(\mathbf{x}, \dot{\mathbf{x}})$ is a 3x1 vector representing velocity dependent forces and $\mathbf{G}_x(\mathbf{x})$ is a 3x1 vector representing the gravitational load in actuator space.

To visualise the strong load variations working on the cylinders, the linear actuators are considered individually for simplicity. This means that loads are evaluated by assuming the remaining bodies to be at rest and their accelerations 0. By these simplifications the force equilibrium for either cylinder may be found as:

$$p_{A,i} A_{A,i} - p_{B,i} A_{B,i} = \underbrace{M_{eq,i}(\mathbf{x})}_{\mathbf{M}_x^{i,j}(\mathbf{x})} \ddot{x}_i + \underbrace{F_{vel,i}(\mathbf{x}, \dot{x}_i)}_{\mathbf{C}_x^i(\mathbf{x}, \dot{\mathbf{x}})} \dot{x}_i + \underbrace{F_{G,i}(\mathbf{x})}_{\mathbf{G}_x^i(\mathbf{x})} + F_{fric,i}(\dot{x}_i) \quad (2.17)$$

where i is used as an index for either cylinder 1 or 2. p_A , A_A , p_B and A_B are the gauge pressures and areas of cylinder piston and rod side respectively. M_{eq} is the equivalent mass, \ddot{x} is the piston acceleration and $F_{vel} \dot{x}$ is the force acting on the piston from velocity dependent forces. F_G and F_{fric} are the gravitational load and the velocity dependent cylinder friction force respectively. In subsequent chapters Eq. 2.17 are used for analysis of the hydraulic system and for controller design purposes, as the current work is not concerned with multi-axis control of the crane.

Fig. 2.7 shows the strong variations of the evaluated cylinder loads in Eq. 2.17. Here M_{eq} , F_{vel} and F_G are depicted in the entire operating space of the crane for both cylinders. The payload m_3 is 10 ton.

Due to the slow motion of the actuators, Fig. 2.7b and e show that the velocity dependent forces, are negligible compared with the gravitational load forces in Fig. 2.7c and f.

Note that forces caused by couplings are not included in Fig. 2.7, e.g. an acceleration of cylinder 1 will result in a force exerted on cylinder 2 due to a nonzero element in $\mathbf{M}_x^{2,1}(\mathbf{x})$, where the superscript points to row 2 and column 1 of $\mathbf{M}_x(\mathbf{x})$. These coupling forces are however included in the dynamic simulation of the knuckle boom crane by Eq. 2.6.

2.3. Chapter Summary

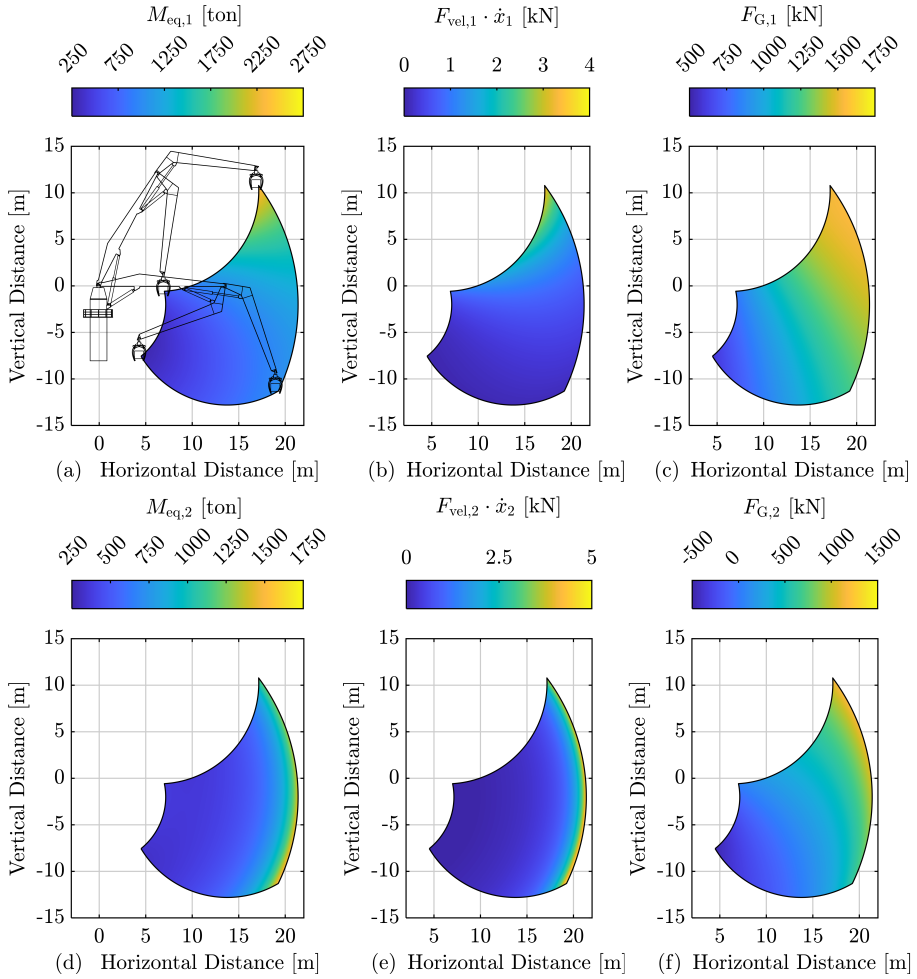


Fig. 2.7: Load variations in actuator space with a payload of 10 ton. (a) Equivalent inertia or mass for cylinder 1. (b) Velocity dependent force for cylinder 1, for $\dot{x}_1 = 50$ mm/s and $\dot{x}_2 = 0$ mm/s. (c) Gravitational load on cylinder 1. (d) Equivalent inertia or mass for cylinder 2. (e) Velocity dependent force for cylinder 2, for $\dot{x}_1 = 0$ mm/s and $\dot{x}_2 = 50$ mm/s. (f) Gravitational load on cylinder 2.

2.3 Chapter Summary

In this chapter the knuckle boom crane used throughout this dissertation has been introduced. A dynamic model of the crane, showing strongly varying cylinder loads in the working range of the crane has been derived. An ECD based on two electrical motor and pump units configured in a closed circuit architecture has been selected for further study and is denoted "ECD" in the

following chapters. It has been estimated that installing this ECD on the main boom for actuation of the knuckle boom reduces the static payload capacity by approximately 3% in most of the operating range compared to the conventional valve-controlled cylinder drive (VCD). This reduction may be accepted if considerable energy savings may be achieved by replacing the VCD which is studied in the following chapter.

Chapter 3

Energy Saving Potential

The main motivation for this dissertation is to reduce the energy consumption of the hydraulic linear actuators. The potential for energy savings, for the knuckle boom crane, is investigated in this section, before the design of load holding functionalities and an alternative reservoir are considered.

This analysis is based on steady state hydraulic drive models of the conventional valve-controlled cylinder drive (VCD) and the considered electro-hydraulic compact drive (ECD) actuation system.

3.1 Benchmark Actuation System

VCD systems are the current state-of-the-art for hydraulic actuation of off-shore cranes [6, 86] and are used as the benchmark for evaluating the energy saving potential. The benchmark system schematic is given in Fig. 3.1. The two cylinders are here controlled by pressure compensated proportional control valves (PCCV). Hydraulic power is supplied by a centralised HPU, consisting of a grid connected (approximately fixed-speed) electric induction motor and a variable displacement pump. The pump displacement is controlled using a pressure feedback, such that the pump outlet pressure is controlled to be $p_{LS,margin}$ higher than the highest pressure in a chamber requiring a flow input. To avoid uncontrolled load drop if power is lost or a hose bursts, counter balance valves (CBV) are incorporated. These also ensure that even in load aided operating conditions, the speed of the cylinder piston is controlled by the cylinder input flow. Because the input flow is controlled by a pressure compensated valve, the combination of this and the CBV ensures that a control input (u) from the operator, yields the same actuator speed independent of loading.

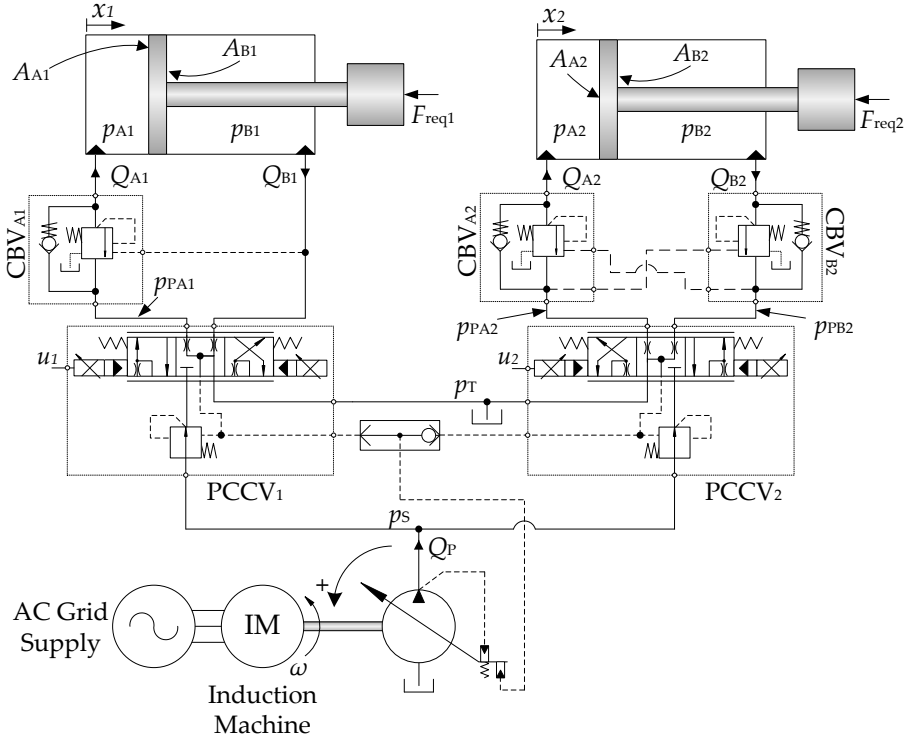


Fig. 3.1: Schematic of the hydraulic actuation system used as a benchmark. The left cylinder is actuating the main boom, while the right cylinder is actuating the knuckle boom.

The power usage of the benchmark system is evaluated using the steady state solution to the governing system equations. This means that the steady state system pressures and flow quantities for predefined required forces and cylinder speeds are used to calculate the speed and shaft torque of the induction machine in order to find the required power input to the benchmark system. The steady state model of the hydraulic transmission and the electric induction machine including loss models of the latter are given in Appendix B. All parameters introduced during the steady state model derivation may be found in Tab. A.2 on page 255.

3.1.1 Pump Model and Loss Models

The pump models and the associated loss models are presented here in the main part of the dissertation as these are common for all models to be presented in the remainder. The required pump output flow Q_p in Fig. 3.1 is calculated in Appendix B. This and the pump shaft torque τ_L are modelled

3.1. Benchmark Actuation System

as:

$$Q_p = D_p \omega - Q_{\text{loss}} = D_p \omega - \lambda^2 Q_{\text{loss,ref}}(\omega_{\text{ref}\lambda}, p_s) \quad (3.1)$$

$$\tau_L = D_p p_s + \tau_{\text{loss}} = D_p p_s + \lambda^3 \tau_{\text{loss,ref}}(\omega_{\text{ref}\lambda}, p_s) \quad (3.2)$$

$$\lambda = \sqrt[3]{\frac{D_p}{D_{p,\text{ref}}}}, \quad \omega_{\text{ref}\lambda} = \lambda \omega \quad (3.3)$$

where p_s is the pump outlet pressure calculated in Appendix B and ω is the shaft speed. D_p is the geometrical displacement of the pump. In this steady state analysis, the variable displacement pump is assumed to adjust to the required D_p ideally and without requiring actuation power. The utilised pump is an axial displacement pump with a maximum displacement of 250 cm³/rev, yielding a maximum flow of 450 l/min at 1800 RPM. Q_{loss} and τ_{loss} are the leakage and torque losses, calculated based on the measured losses of a reference unit, $Q_{\text{loss,ref}}$ and $\tau_{\text{loss,ref}}$. These are evaluated as a function of the pump pressure and the scaled reference speed, $\omega_{\text{ref}\lambda}$ [87]. The measured losses are scaled based on the scaling term λ , which depends on the current D_p and the displacement of the reference unit $D_{p,\text{ref}}$. Refer to [87] for an introduction to this loss scaling approach.

The pump losses generally depend on the pump size, the pump pressure, shaft speed, and the displacement ratio ($D_p/D_{p,\text{max}}$) for variable-displacement pumps [87]. To ensure a fair comparison between the energy consumption of the benchmark system and the ECD, the pump losses for the benchmark system are simplified to only depend on pump size, pressure, and shaft speed. The dependency of the pump size is handled by the scaling term

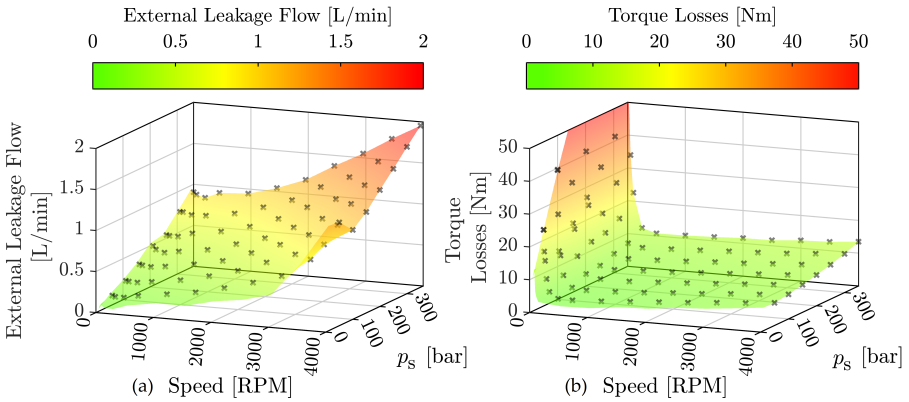


Fig. 3.2: Pump loss measurements of a 28 cm³/rev Bosch Rexroth A4FO axial piston pump, extracted from [88]. The black points are measurement points. (a) Measured external leakage flow. (b) Measured torque loss.

λ in Eqs. 3.1 to 3.3. This means that for the benchmark system, the variable displacement pump is treated as a fixed displacement pump with a varying pump size, instead of a changed displacement ratio in terms of evaluating pump losses. This is assessed to be highly in favour of the benchmark system as variable displacement pumps are most efficient at full displacement [16, 89].

Loss measurements for an 28 cm³/rev Bosch Rexroth A4FO pump is available in [88], and is used as the reference pump. From [88] the external leakage flows for 77 measurement points been extracted and is visualised as black points in Fig. 3.2a. Similarly, the measured torque losses for 98 points have been extracted from [88], and visualised in Fig. 3.2b. The coloured surfaces in Fig. 3.2, show the interpolated losses between the datapoints as well as the linearly extrapolated losses required as no datapoints for p_s below 50 bar are available.

Neglecting both fluid compressibility and the temperature change during the pumping process the losses visualised in Fig. 3.2, yields the total pump efficiency given in Fig. 3.3.

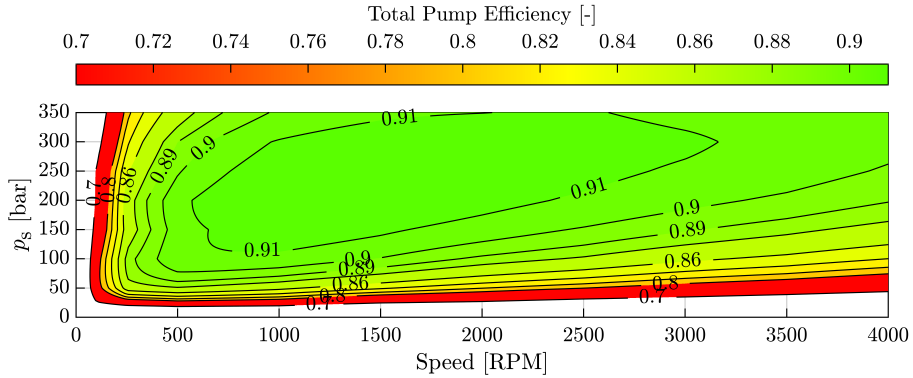


Fig. 3.3: Pump efficiency based on the loss measurements showed in Fig. 3.2.

The visualised pump efficiencies in Fig. 3.3, do not include internal leakage losses, as only external leakage are measured and shown in Fig. 3.2a. No explicit information of the internal leakage is available in [88], as this cannot be measured. However, [88] states that *"internal leakage will affect the total output flow rate, so it will be visible in the efficiency calculations"*. The efficiencies in Fig. 3.3 are found to be in close resemblance with the efficiency map in [88]. As an example the maximum efficiency is 0.917 in Fig. 3.3 and 0.916 in [88]. Based on this observation, internal leakages are not included in the considered loss model. This does not mean that internal leakages are absent in the physical pump, but based on the available information, the effect of

3.1. Benchmark Actuation System

internal leakage on the pump efficiency is found to be limited for this specific pump.

By combining the losses of the pump and the induction motor model (Appendix B), the needed pump displacement and the corresponding shaft speed needed to realise the required pump flow at the required steady state pump pressure can be found. This problem is rather tedious, because the pump outlet flow is calculated based on the leakage losses and the product of pump displacement and shaft speed. The latter is a function of the shaft torque (i.e. pump displacement) due to the well-known torque-speed curve of an induction machine (Fig. B.2 a on page 265). The shaft torque is in turn a function of pump displacement, pump outlet pressure and the torque loss. The pump losses also generally depend on the outlet pressure, the shaft speed and the pump displacement via the scaling-term λ . As the leakage losses or torque losses only exist as a look-up table based on measurements points and it has not been possible to apply a polynomial fit with an satisfactory accuracy it has not been possible to solve this problem analytically. Alternatively the problem is solved iteratively.

This means that the shaft speed and pump displacement is first calculated for the needed pump flow and pressure by assuming zero pump losses (here an analytical solution is found). In the second iteration the shaft speed and pump displacement from the first iteration are used to evaluate the pump losses, and then the shaft speed and pump displacement are re-calculated. This continues until the change in the calculated shaft speed between consecutive iterations is below 1/10000 RPM.

Fig. 3.4a shows the shaft speed as a function of the pump displacement D_p

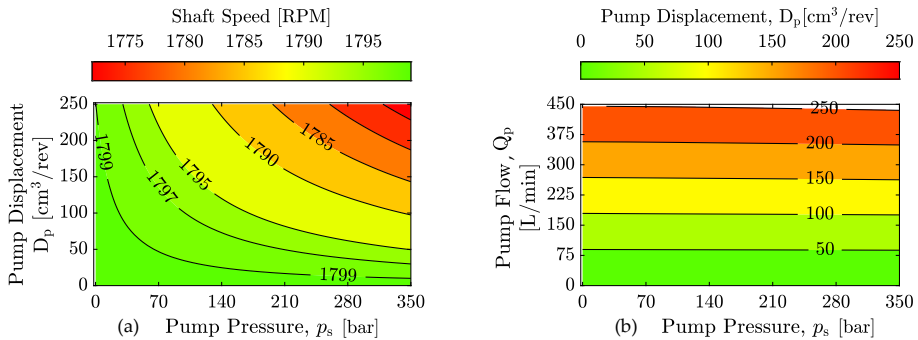


Fig. 3.4: Characteristics of the hydraulic power unit (i.e. grid connected induction motor and hydraulic pump). In both plots the pump losses from Fig. 3.2 have been included. (a) Induction motor shaft speed as a function of pump displacement and pump pressure. (b) Required pump displacement as a function of pump flow and pump pressure.

and the pump outlet pressure p_s . It can be observed that the shaft speed decreases slightly, as either pressure or displacement increases, caused by the increased shaft torque. Fig. 3.4b shows the required pump displacement as a function of pump flow Q_p and pressure p_s . It may be observed that due to increased leakage losses as well as slightly decreased shaft speeds when increasing pump displacement the relation between the pump displacement and the pump flow is not fully linear.

3.1.2 Efficiency Calculation of Benchmark System

Fig. 3.5a shows the total pump efficiency η_{pump} as a function of the required pump flow and pump pressure. The pump losses from Fig. 3.2 has been included and scaled according to Eq. 3.3. In Fig. 3.5b the losses of the grid connected induction motor have also been included, and the efficiency of the hydraulic power unit (HPU) is visualised as a function of pump flow and pump pressure. The two efficiencies are calculated as:

$$\eta_{\text{pump}} = \frac{Q_p p_s}{\tau_L \omega} \quad \eta_{\text{HPU}} = \frac{Q_p p_s}{P_{\text{asynch}}} \quad (3.4)$$

where P_{asynch} is the electric power supplied by the grid and includes motor losses as elucidated in Appendix B. Note, that the efficiency calculations in Eq. 3.4 assumes the fluid to be incompressible.

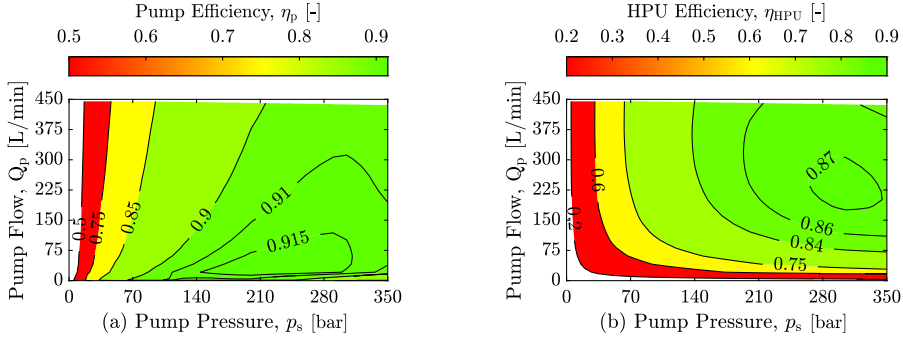


Fig. 3.5: (a) Pump efficiency and (b) HPU efficiency. Both as a function of pump outlet pressure and required pump flow.

When defining the total efficiency of the benchmark system some basic definitions and limitations need to be discussed. Fundamentally the efficiency is the ratio between output power and required input power ($\eta = P_{\text{out}}/P_{\text{in}}$). As such the efficiency is an instantaneous or time dependent measure. Obviously efficiency has a very basic definition, but challenges occur when selecting how to calculate the input and output powers. For a crane it may

3.1. Benchmark Actuation System

be relevant to define a lifting efficiency, i.e. to define the output power as the time rate of change in potential energy of the payload. However if the payload is moved horizontally, the output power is defined to be 0. Even for an ideal actuation system, power is required to perform this horizontal movement, because the center of masses of the crane bodies are moved vertically. Therefore, this definition of input power is not particularly relevant when comparing actuation systems.

Instead the output power is selected to be the cylinder power or rate of work, when the cylinder force and velocity has the same sign, i.e. when cylinder power is positively defined:

$$P_{\text{out}} = \dot{x}_{1,\text{ref}} F_{1,\text{ref}} + \dot{x}_{2,\text{req}} F_{2,\text{req}} \quad \text{for} \quad \begin{aligned} &\text{sign}(\dot{x}_{1,\text{ref}}) = \text{sign}(F_{1,\text{req}}) \\ &\& \text{sign}(\dot{x}_{2,\text{ref}}) = \text{sign}(F_{2,\text{req}}) \end{aligned} \quad (3.5)$$

As no frictional losses of the cylinders are included, the mechanical power in Eq. 3.5 equals the hydraulic cylinder power, i.e. $p_L Q_A$. p_L is the load pressure defined as $p_L = p_A - \alpha p_B$.

When none of the cylinder powers are negative, the input power is defined to be the power to the induction motor, P_{asynch} in Eq. B.29 on page 266, such that the total efficiency of the benchmark system is defined as $\eta_{\text{VCD}} = P_{\text{out}} / P_{\text{asynch}}$.

When the load is moved down, the input power to the system is the cylinder powers, now defined negatively. As the benchmark system lacks the capability of recovering the potential energy of the load back to the electrical grid, the output power is the power required by the induction motor which still demands positively defined power. This means that the efficiency is now negative due to the sign convention of the power flow. Even though negative efficiencies are well defined, they hardly bring any useful information. An efficiency close to 0 approaching from negative, may either indicate that the cylinder powers are numerically large or that the needed motor power is small. On the other hand a small efficiency, potentially minus infinity, may either indicate that a large motor power input is needed or that a numerically small amount of cylinder powers are available. Note, that defining the input power to be the motor power and the output power to be the cylinder powers brings the same ambiguity. Considering, the benchmark actuation system, efficiencies are therefore only considered when none of the cylinder powers ($\dot{x}F$) are negative, as defined by Eq. 3.5.

In Sec. 3.3 the instantaneous efficiency of the benchmark system is evaluated in the entire working range of the crane and compared to the ECD system. In Sec. 3.4 the actual energy consumption for a defined loading and unloading cycle is evaluated and compared to the ECD actuation system.

3.2 ECD Actuation Systems

Steady state models of the electro-hydraulic compact drive (ECD) actuation system are used to assess the energy saving potential of this technology compared with the benchmark system. The potential for energy savings is compared before load holding functionalities and the alternative reservoir are designed as these functions should ideally only affect energy consumption to a small extent.

Load holding valves and accumulators are therefore not considered in the following. A simplified diagram of the ECD actuation system with a vented reservoir for controlling the motion of both the main and knuckle boom cylinder is given in Fig. 3.6.

The power input to the actuation system is considered to be supplied from a common DC-link, i.e. electrical power may be shared between all four electric motors. In Fig. 3.6 numeric subscripts 11, 12, 21, 22 are used to distinguish between the four pump-motor drives. The first number refers to system 1 or 2, where system 1 is the actuation system of the main boom and system 2 is the knuckle boom. The second number is referring to pump 1 or 2 in each system, where pump 1 is connecting the A and B chamber and 2 is placed between the oil reservoir and chamber A. All parameters used to model the ECD systems in steady state are given in Tab. A.3 on page 256.

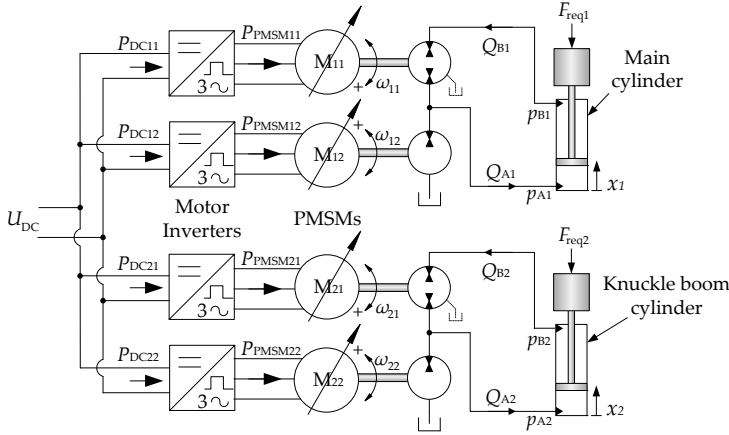


Fig. 3.6: Simplified structure of the ECD actuation system. The upper cylinder is the main boom cylinder of the crane, while the lower cylinder is the knuckle boom cylinder. Each cylinder is controlled by two pumps each connected to a PMSM, controlled by an inverter. All inverters are supplied from a common DC-link, such that electrical power sharing is possible.

3.2.1 Steady State Models of Eletro-Hydraulic Compact Drive Actuation System

The steady state solution to the equations modelling the ECD hydraulic systems is significantly simpler than for the VCD system, because there are no restrictions (i.e valves) in the transmission lines defining the pressure in the non-load carrying chamber (backpressure). For the ECD systems the back-pressure is defined to a constant value, p_{set} , which is here 30 bar:

$$Q_{A1} = \dot{x}_{\text{ref},1} A_{A1} \quad , \quad Q_{B1} = \dot{x}_{\text{ref},1} A_{B1} \quad (3.6)$$

$$Q_{A2} = \dot{x}_{\text{ref},2} A_{A2} \quad , \quad Q_{B2} = \dot{x}_{\text{ref},2} A_{B2} \quad (3.7)$$

$$p_{A1} = \frac{F_{\text{req},1} + p_{B1} A_{B1}}{A_{A1}} \quad , \quad p_{B1} = p_{\text{set}} \quad (3.8)$$

$$p_{A2} = \begin{cases} \frac{F_{\text{req},2} + p_{B2} A_{B2}}{A_{A2}} & \text{for } F_{\text{req},2} \geq p_{\text{set}} (A_{A2} - A_{B2}) \\ p_{\text{set}} & \text{for } F_{\text{req},2} < p_{\text{set}} (A_{A2} - A_{B2}) \end{cases} \quad (3.9)$$

$$p_{B2} = \begin{cases} p_{\text{set}} & \text{for } F_{\text{req},2} \geq p_{\text{set}} (A_{A2} - A_{B2}) \\ \frac{p_{A2} A_{A2} - F_{\text{req},2}}{A_{B2}} & \text{for } F_{\text{req},2} < p_{\text{set}} (A_{A2} - A_{B2}) \end{cases} \quad (3.10)$$

where $\dot{x}_{1,\text{ref}}$, $\dot{x}_{2,\text{ref}}$ are desired cylinder speeds, and Q_{\bullet} , p_{\bullet} are volume flows and chamber pressures according to Fig. 3.6, and A_{\bullet} are areas according to Fig. 3.1. Note that in the steady state analysis gauge pressures are utilised. Furthermore cylinder frictions are not included in this comparison, as it is assumed to be equivalent for both the VCD and ECD system.

The required shaft speeds of the pumps are calculated based on the required flows and the pump leakage losses. The leakage losses are modelled as described for the benchmark system, i.e. based on the leakage losses of a reference unit. However for the closed circuit/four quadrant pump, i.e. the pump connecting the A and B cylinder chambers, external leakage from both the A and the B chamber is included. This is visualised in Fig. 3.7.

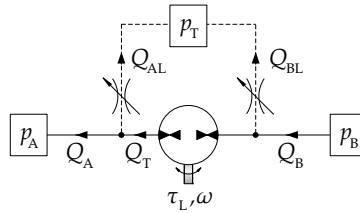


Fig. 3.7: Illustration of pump flow model. External leakage is modelled to occur from chambers A and B, whereas internal leakage between the two chambers is neglected.

Based on Fig. 3.7 the shaft speeds and torques (τ_L) are calculated based on the external leakage flows and torque losses as:

$$Q_{B1} = Q_{T1} + Q_{BL1} = \omega_{11} D_{p,11} + \lambda_{11}^2 Q_{\text{loss,ref}}(\omega_{\text{ref}\lambda 11}, p_{B1}) \Rightarrow \quad (3.11)$$

$$\omega_{11} = \frac{Q_{B1} - \lambda_{11}^2 Q_{\text{loss,ref}}(\omega_{\text{ref}\lambda 11}, p_{B1})}{D_{p,11}} \quad (3.12)$$

$$Q_{A1} = Q_{T1} + Q_{T2} - Q_{AL1} - Q_{AL2} \Rightarrow \quad (3.13)$$

$$\omega_{12} = \frac{Q_{A1} - \omega_{11} D_{p,11} + \lambda_{11}^2 Q_{\text{loss,ref}}(\omega_{\text{ref}\lambda 11}, p_{A1}) + \lambda_{12}^2 Q_{\text{loss,ref}}(\omega_{\text{ref}\lambda 12}, p_{A1})}{D_{p,12}} \quad (3.14)$$

$$\omega_{21} = \frac{Q_{B2} - \lambda_{21}^2 Q_{\text{loss,ref}}(\omega_{\text{ref}\lambda 21}, p_{B2})}{D_{p,21}} \quad (3.15)$$

$$\omega_{22} = \frac{Q_{A2} - \omega_{21} D_{p,21} + \lambda_{21}^2 Q_{\text{loss,ref}}(\omega_{\text{ref}\lambda 21}, p_{A2}) + \lambda_{22}^2 Q_{\text{loss,ref}}(\omega_{\text{ref}\lambda 22}, p_{A2})}{D_{p,22}} \quad (3.16)$$

$$\tau_{L,11} = D_{p,11} (p_{A1} - p_{B1}) + \lambda_{11}^3 \tau_{\text{loss,ref}}(\omega_{\text{ref}\lambda 11}, p_{A1} + p_{B1}) \text{sign}(\omega_{11}) \quad (3.17)$$

$$\tau_{L,12} = D_{p,12} (p_{A1}) + \lambda_{12}^3 \tau_{\text{loss,ref}}(\omega_{\text{ref}\lambda 12}, p_{A1}) \text{sign}(\omega_{12}) \quad (3.18)$$

$$\tau_{L,21} = D_{p,21} (p_{A2} - p_{B2}) + \lambda_{21}^3 \tau_{\text{loss,ref}}(\omega_{\text{ref}\lambda 21}, p_{A2} + p_{B2}) \text{sign}(\omega_{21}) \quad (3.19)$$

$$\tau_{L,22} = D_{p,22} (p_{A2}) + \lambda_{22}^3 \tau_{\text{loss,ref}}(\omega_{\text{ref}\lambda 22}, p_{A2}) \text{sign}(\omega_{22}) \quad (3.20)$$

where $\omega_{11}, \omega_{12}, \omega_{21}, \omega_{22}$ are shaft speeds according to Fig. 3.6. $D_{p,i}$ is the geometrical pump displacement for each of the four fixed displacement pumps. λ_i is a scaling factor used to scale pump losses of a reference unit evaluated at the reference pump speed $\omega_{\text{ref}\lambda,i}$ [87]. The leakage and torque losses of the reference unit are equivalent to the ones used for the benchmark system as showed in Fig. 3.2 on page 41. The scaling factors λ_i and reference speeds are found by [87]:

$$\lambda_i = \sqrt[3]{\frac{D_{p,i}}{D_{p,\text{ref}}}} \quad , \quad \omega_{\text{ref}\lambda,i} = \lambda_i |\omega_i| \quad , \quad i = \{11, 12, 21, 22\} \quad (3.21)$$

The absolute value of the shaft speed is used to evaluate the losses of the reference unit, as data are only available for positive shaft speeds and when working as a pump. Losses are assumed equivalent for all operation quadrants, and are always positively defined.

Based on the above equations it is straightforward to calculate the chamber pressures for the required cylinder forces. The shaft speeds however both depends on the required output pump flows and the leakage losses which also depend on shaft speed. As the leakage losses are only available as look up tables, the shaft speeds are found by solving the equations iteratively.

3.2.2 Power Losses of Motor Drive

The pumps are controlled by variable-speed motor drives, consisting of a permanent magnet synchronous machine (PMSM) and an inverter. Based on the required shaft speed and torque the motor and inverter losses are calculated subsequently.

The power losses of the motor inverter (P_{inv}) are modelled using the inverter efficiency η_{inv} :

$$P_{\text{invi}} = \begin{cases} \frac{1-\eta_{\text{invi}}}{\eta_{\text{invi}}} P_{\text{PMSMi}} & P_{\text{PMSMi}} \geq 0. \\ (\eta_{\text{invi}} - 1) P_{\text{PMSMi}} & P_{\text{PMSMi}} < 0. \end{cases} \quad P_{\text{DCi}} = P_{\text{invi}} + P_{\text{PMSMi}} \quad i = \{11, 12, 21, 22\} \quad (3.22)$$

where η_{inv} is the inverter efficiency evaluated using the efficiency map in Fig. 3.8a from [90] as a function of the rated inverter power, $P_{\text{inv, rated}}$, and the current normalised power. P_{DCi} is the power supplied from ($P_{\text{DCi}} > 0$) or delivered to ($P_{\text{DCi}} < 0$) the DC-link for one inverter. The total power demand of the DC-link is obtained by adding P_{DCi} of all inverters. P_{PMSM} is the electric motor power evaluated as:

$$P_{\text{PMSMi}} = \tau_{L,i} \omega_i + P_{\text{Cui}} + P_{\text{Fei}} \quad i = \{11, 12, 21, 22\} \quad (3.23)$$

where P_{Cu} is current dependent copper losses and P_{Fe} is the speed dependent iron/core losses caused by eddy currents and magnetic hysteresis [91]. These are modelled as [92]:

$$P_{\text{Cuj}} = \frac{3}{2} R \left(i_{\text{dj}}^2 + i_{\text{qj}}^2 \right) \quad P_{\text{Fej}} = K_{\text{Fe}} m_{\text{PMSM}} \epsilon_{\text{PMSM}} \left(\frac{|P \omega_j|}{\omega_{\text{Fe}}} \right)^{3/2} \quad (3.24)$$

$$j = \{11, 12, 21, 22\}$$

where R is the stator resistance, i_{d} , i_{q} is the d-axis and q-axis current, K_{Fe} is a loss model constant of 4 W per kilo sheet metal at an electrical angular velocity of ω_{Fe} . ϵ_{PMSM} is the ratio of sheet metal to total motor mass m_{PMSM} . Using the parameters of the Bosch Rexroth MS2N13-D1BNC [93] motor used for all four motors in this study and given in Tab. A.3 on page 256, the efficiency map in Fig. 3.8b is obtained. Note that the sign convention used in this work defines the power to be positive when the motor works as a motor and negative if operating as a generator. The losses of the inverter and PMSM are assumed to be equivalent in both motor and generator operation mode.

The motor currents are calculated by assuming these to be controlled ideally to be equal to their references in steady state. In this work a so-called surface mounted PMSM is utilised characterised by the d -axis and q -axis inductances to be equal ($L_{\text{q}} = L_{\text{d}}$), such that only the q -axis current is torque generating

according to:

$$\tau_{em,j} = \frac{3}{2}P \left(\lambda_{pm} i_{qj} + (L_d - L_q) i_{dj} i_{qj} \right) = \frac{3}{2}P \left(\lambda_{pm} i_{qj} \right), \quad j = \{11, 12, 21, 22\} \quad (3.25)$$

where τ_{em} is the electro-magnetic motor torque generated by the PMSM, P is the number of pole pairs of the PMSM and λ_{pm} is the flux linkage linking the rotor magnets with the stator. In this steady state analysis $\tau_{em,j} = \tau_{L,j}$ such that the currents equal [64]:

$$i_{dj} = 0 \quad i_{qj} = \frac{2}{3} \frac{\tau_{L,j}}{P \lambda_{pm}}, \quad j = \{11, 12, 21, 22\} \quad (3.26)$$

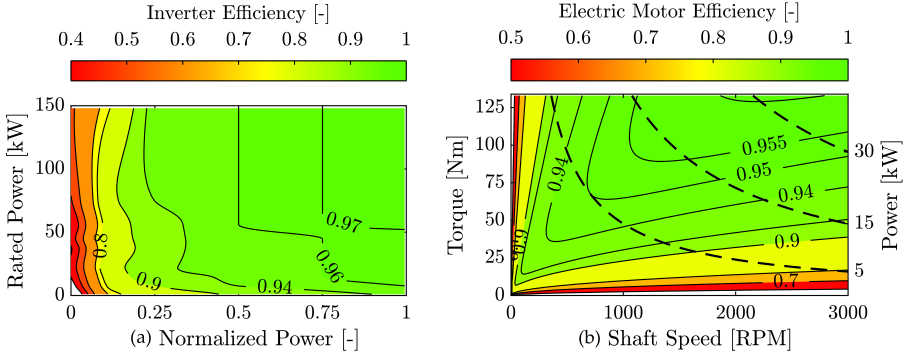


Fig. 3.8: (a) Inverter efficiency as a function of the rated inverter power and the normalised power taken from [90]. (b) Efficiency map calculated based on the copper and iron losses given in Eq. 3.24.

3.2.3 Efficiency Calculations of the ECD Systems

Opposite to the benchmark system, the ECDs are capable of recovering some of the potential energy from the load back to the DC-link when the load is lowered. The efficiency of each cylinder actuation system is calculated as:

$$\eta_{ECDi} = \frac{P_{outi}}{P_{ini}} \quad P_{outi} = \begin{cases} F_{reqi} \dot{x}_i & \text{for } \text{sign}(F_{reqi}) = \text{sign}(\dot{x}_i) \\ P_{DCi1} + P_{DCi2} & \text{for } \text{sign}(F_{reqi}) \neq \text{sign}(\dot{x}_i) \end{cases} \quad (3.27)$$

$$i = \{1, 2\} \quad P_{ini} = \begin{cases} P_{DCi1} + P_{DCi2} & \text{for } \text{sign}(F_{reqi}) = \text{sign}(\dot{x}_i) \\ F_{reqi} \dot{x}_i & \text{for } \text{sign}(F_{reqi}) \neq \text{sign}(\dot{x}_i) \end{cases} \quad (3.28)$$

When the powers are numerically small, e.g. if the input power is a numerically small negative value of the product $F_{req} \dot{x}$, the losses of the system

3.3. Comparison of Efficiencies

may have a larger numerical value. This means that the output power to the DC-link is positive (power is delivered from the DC-link to the inverter), leading to negative efficiencies. As discussed earlier negative efficiencies are ambiguous, hence negative efficiencies are disregarded here.

Due to the connection of all motor inverters to the same DC-link, the actuation system benefits from being able to share electrical power. This means that if the main cylinder is working in a motoring quadrant (power flow from DC-link to cylinder), some of this power may be delivered by the knuckle boom actuator if this works in a generator quadrant (power flow from cylinder to DC-link). In terms of efficiency calculations for the whole actuation system, this may be calculated as $\eta = (P_{\text{out1}} + P_{\text{out2}}) / (P_{\text{in1}} + P_{\text{in2}})$. Due to the sign convention of the power flow this definition may however cause η_{ECD} not to be upper bounded to 1. Therefore when considering the total efficiency of the ECD actuation system, this is restricted to only be defined in conditions where the power flow for both cylinders are either from or to the DC-link:

$$\eta_{\text{ECD}} = \frac{P_{\text{out}}}{P_{\text{in}}} \quad (3.29)$$

$$P_{\text{out}} = \begin{cases} F_{\text{req1}} \dot{x}_1 + F_{\text{req2}} \dot{x}_2 & \text{sign}(F_{\text{req1}} \dot{x}_1) = \text{sign}(F_{\text{req2}} \dot{x}_2) = 1 \\ P_{\text{DC11}} + P_{\text{DC12}} + P_{\text{DC21}} + P_{\text{DC22}} & \text{sign}(F_{\text{req1}} \dot{x}_1) = \text{sign}(F_{\text{req2}} \dot{x}_2) = -1 \end{cases}$$

$$P_{\text{in}} = \begin{cases} P_{\text{DC11}} + P_{\text{DC12}} + P_{\text{DC21}} + P_{\text{DC22}} & \text{sign}(F_{\text{req1}} \dot{x}_1) = \text{sign}(F_{\text{req2}} \dot{x}_2) = 1 \\ F_{\text{req1}} \dot{x}_1 + F_{\text{req2}} \dot{x}_2 & \text{sign}(F_{\text{req1}} \dot{x}_1) = \text{sign}(F_{\text{req2}} \dot{x}_2) = -1 \end{cases}$$

To investigate the benefits of the DC-link connection of all inverters and the associated electrical power sharing it is more informative to consider the actual energy needed to perform a given motion trajectory rather than focusing on efficiencies. This is especially true when the power flow for each cylinder have different signs.

3.3 Comparison of Efficiencies

As mentioned previously comparing efficiencies of the drive systems have some limitations due to the four quadrant operation of the crane. Nevertheless evaluating the efficiencies under certain conditions may bring some interesting knowledge. In Fig. 3.9 the efficiency of the benchmark system, the VCD system, is shown for different operating conditions. In Fig. 3.9a the instantaneous efficiency is shown for a total load mass, m_3 , of 10 ton (lifting yoke and payload), and at full cylinder piston extension speeds, which are here defined to 30 mm/s for cylinder 1 and 40 mm/s for cylinder 2. The efficiencies are ranging from 31 % to 73.7 %. Decreasing the load to 5 ton (empty

lifting yoke) and still moving at full speed lowers the efficiencies as seen in Fig. 3.9b, as the system is now working in part load conditions.

From Fig. 3.9a and b it can be observed that the efficiency increases as the payload is moved further away from the crane base, i.e. further to the right in the figure. This is partly explained by the fact that the required forces for both cylinders increase, such that the output powers increase, leading to

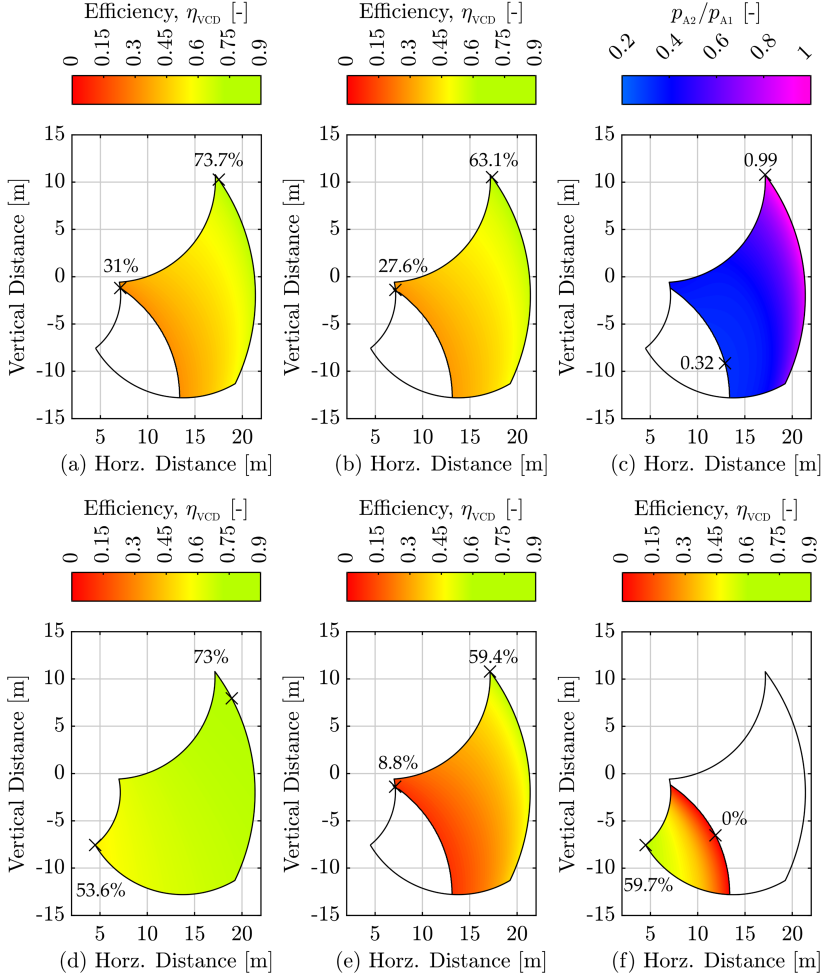


Fig. 3.9: Instantaneous efficiency of the benchmark system, calculated by Eqs. 3.5. (a) $m_3 = 10$ ton, $\dot{x}_{ref,1} = 30$ mm/s and $\dot{x}_{ref,2} = 40$ mm/s. (b) $m_3 = 5$ ton, $\dot{x}_{ref,1} = 30$ mm/s and $\dot{x}_{ref,2} = 40$ mm/s. (c) Pressure ratio for $m_3 = 10$ ton. (d) $m_3 = 10$ ton, $\dot{x}_{ref,1} = 30$ mm/s and $\dot{x}_{ref,2} = 0$ mm/s. (e) $m_3 = 5$ ton, $\dot{x}_{ref,1} = 6$ mm/s and $\dot{x}_{ref,2} = 40$ mm/s. (f) $m_3 = 10$ ton, $\dot{x}_{ref,1} = 0$ mm/s and $\dot{x}_{ref,2} = -40$ mm/s.

3.3. Comparison of Efficiencies

higher efficiencies as the losses do not scale linearly with the output powers. Another important reason is caused by the centralised HPU, supplying power to both cylinders. The pump pressure is dictated by the largest piston chamber pressure during forward motion of the cylinders, which in this case is the A chamber in cylinder 1, p_{A1} . If the A chamber pressure in cylinder 2, p_{A2} , is much smaller than this pressure, the throttling losses across the pressure compensator of PCCV₂ are large. Therefore, if the ratio of p_{A2}/p_{A1} is much lower than unity, large throttling losses for the low pressure consumer occur. Fig. 3.9c shows the ratio of p_{A2}/p_{A1} and confirms this observation. The efficiencies clearly increase as p_{A2}/p_{A1} approaches unity.

Fig. 3.9d shows how the efficiency generally increases, if only cylinder 1 is moving at maximum speed while cylinder 2 is at standstill. This is due to the pump pressure being adjusted to fit the moving actuator, and no additional throttling losses are associated with supplying a low pressure actuator.

On the other hand, the additional losses associated with simultaneous operation of the actuators are illustrated in Fig. 3.9e. Here cylinder 1 is moving at 20 % of the maximum speed and cylinder 2 is moving at full speed. This means that the pump pressure is dictated by a slow moving actuator while a fast moving unloaded, i.e. low pressure, actuator requires a large flow, leading to large throttling losses of the fast moving actuator, as clearly seen in Fig. 3.9e. Finally, Fig. 3.9f shows the efficiency, if cylinder 2 is retracting at full speed, -40 mm/s, and cylinder 1 is at standstill. Here the efficiency is only well-defined in the lower left corner of the operating range.

As a comparison Fig. 3.10 shows the instantaneous efficiency for the ECD actuation system evaluated in the entire operating range by Eq. 3.29. Fig. 3.10a shows the efficiency for a load of 10 ton and both cylinder pistons moving at maximum speeds. In 3.10b and c the efficiency is evaluated for a reduced load of 5 ton and a reduced speed respectively. Compared to the benchmark system, it is clear that the efficiency is significantly larger for the ECD systems. In fact, in the case with a payload of 5 ton, the maximum efficiency of 63.1 % for the benchmark system almost corresponds to the minimum efficiency of the ECD system of 61.4 %. Fig. 3.10d shows the efficiency in aided loading conditions. Fig. 3.10e and f shows the efficiency of the individual systems, ECD1 and ECD2. In Fig. 3.10e the efficiency of the main cylinder system, ECD1, is shown for a load of 10 ton at full speed. Fig. 3.10f shows the efficiency of the knuckle boom cylinder system, ECD2, for a load of 10 ton and retracting at full speed. In the white area of Fig. 3.10f, the efficiency is below 0. This happens in the situation where the load is aiding the motion of the cylinder, such that there is a potential for recovering some of this power, i.e. the cylinder power is defined to be negative. However the losses of the system exceed this amount of available power, such that positively defined power from the DC-link is still needed, leading to negative efficiencies,

shown as a white area.

It is clear that the ECD actuation system offers significantly improved efficiencies compared to the benchmark system. However, the efficiency characteristics of the systems when the load is lowered is not taken into account. A better alternative is to compare the actual amount of energy needed to per-

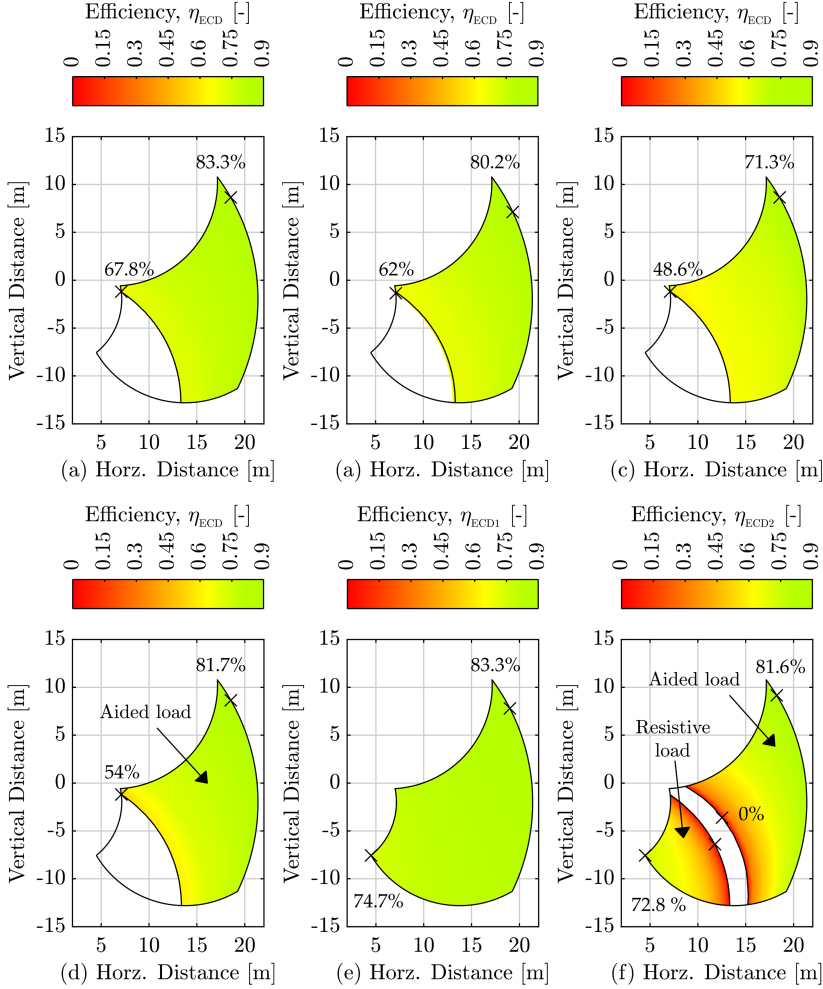


Fig. 3.10: Instantaneous efficiency of the ECD actuation system, calculated by Eqs. 3.29. (a) $m_3 = 10$ ton, $\dot{x}_{ref,1} = 30$ mm/s and $\dot{x}_{ref,2} = 40$ mm/s. (b) $m_3 = 5$ ton, $\dot{x}_{ref,1} = 30$ mm/s and $\dot{x}_{ref,2} = 40$ mm/s. (c) $m_3 = 10$ ton, $\dot{x}_{ref,1} = 6$ mm/s and $\dot{x}_{ref,2} = 8$ mm/s. (d) $m_3 = 10$ ton, $\dot{x}_{ref,1} = -30$ mm/s and $\dot{x}_{ref,2} = -40$ mm/s. (e) Efficiency for the main cylinder system, ECD1. $m_3 = 10$ ton and $\dot{x}_{ref,1} = 30$ mm/s. (f) Efficiency for the knuckle boom cylinder system, ECD2. $m_3 = 10$ ton and $\dot{x}_{ref,2} = -40$ mm/s.

form a predefined motion cycle. Doing so, the amount of energy required to lower the load will also be included in the comparison.

3.4 Energy Consumption for Motion Trajectory

To evaluate the performance of the drive systems performing a realistic motion task, the SFI project partners have specified a loading and unloading motion cycle to be performed [94].

3.4.1 Realistic Motion Trajectory

In Fig. 3.11, the considered motion trajectory is shown in operational space. The trajectory starts by lifting a 5 ton load (total payload is 10 ton including lifting yoke), from point A to point B. At point B, the load is removed and the crane returns empty to point A (payload is 5 ton), to represent a full loading cycle. After a short standstill at point A, the crane moves empty to point B, where the 5 ton load is attached and moves back to point A to represent an unloading cycle as well.

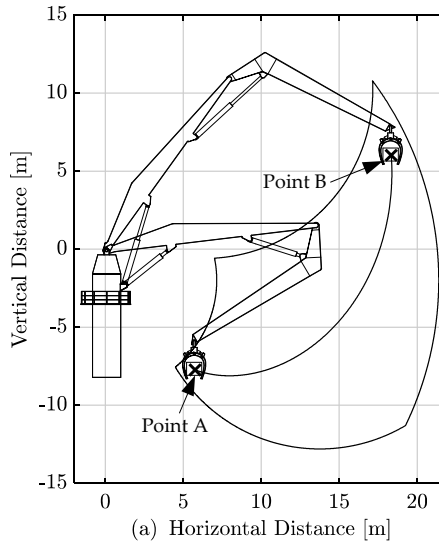


Fig. 3.11: Motion trajectory in crane operational space. The trajectory starts by moving a 5 ton load (total payload is 10 ton including lifting yoke), from point A to point B. At point B, the load is removed and the crane returns empty to point A (total payload is 5 ton), to represent a full loading cycle. After a short standstill at point A, the crane moves empty to point B, where the 5 ton load is attached, and returns to point A to represent an unloading cycle as well.

The desired crane motion is controlled by a human crane operator and Fig.

3.12 shows an overview of the proposed control structure for a single degree of freedom of the knuckle boom crane, if using the proposed ECD. Each of the two cylinder drives are controlled by the crane operator using a joystick to generate the appropriate motion references. A set-point generator converts the joystick position to a piston position reference and a velocity reference (x_{ref} and \dot{x}_{ref}) [76]. The motion references are fed to the control structures, which based on system feedback measurements, including motor currents, shaft speeds, all chamber pressures as well as piston position and speed, determines the motor control voltages.

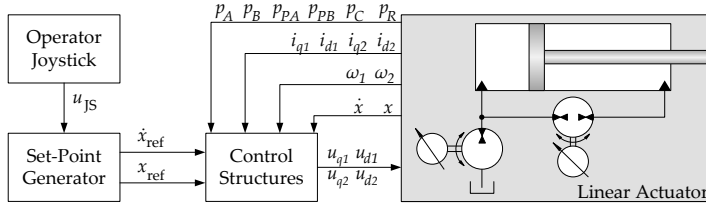


Fig. 3.12: Overview of the control structure for a single degree of freedom of the knuckle boom crane. The feedback signals include the chamber pressures, motor currents, shaft speeds, and piston position and speed. The notation of the subscripts used for the individual chamber pressures are introduced subsequently in the modelling section.

The normalised joystick position signal (ranging from -1 to 1) is filtered to avoid unobtainable motion references (e.g. infinite accelerations or jerks). The first derivative of u_{JS} is limited to limit the acceleration of the piston:

$$\dot{u}_{JS}^* = \begin{cases} \text{Rate} \frac{u_{JS} - u_{JS}^*}{|u_{JS} - u_{JS}^*|} & \text{for } \left| \frac{u_{JS} - u_{JS}^*}{\Delta T} \right| \geq \text{Rate} \\ \frac{u_{JS} - u_{JS}^*}{\Delta T} & \text{for } \left| \frac{u_{JS} - u_{JS}^*}{\Delta T} \right| < \text{Rate} \end{cases} \quad \text{Rate} = \frac{\ddot{x}_{\text{max}}}{\dot{x}_{\text{max}}} \quad (3.30)$$

where u_{JS} is the actual joystick position, u_{JS}^* is the rate limited joystick position, \ddot{x}_{max} is the maximum allowed piston acceleration and \dot{x}_{max} is the maximum allowed piston speed.

To smooth the motion references further and ensure finite jerks, u_{JS}^* is filtered using:

$$\frac{\dot{x}_{\text{ref}}}{u_{JS}^*} = \dot{x}_{\text{max}} \frac{\omega_{\text{fil}}^2}{s^2 + 2\zeta_{\text{fil}}\omega_{\text{fil}}s + \omega_{\text{fil}}^2} \quad (3.31)$$

where \dot{x}_{ref} is the reference cylinder speed fed to the control structure, ω_{fil} and ζ_{fil} are the eigenfrequency and damping ratio of the reference filter and s is the Laplace frequency.

To follow the motion trajectory from Fig. 3.11 the cylinders are commanded to extend simultaneously from point A at their maximums speed for 60s,

3.4. Energy Consumption for Motion Trajectory

stay stationary for 30s at point B, and then retract to the starting point A at maximum speed and repeating this sequence. Using the reference filters in Eqs. 3.30 and 3.31 and the filter parameters from Tab. A.4 on page 256, the motion references in actuator space are visualised in Fig. 3.13.

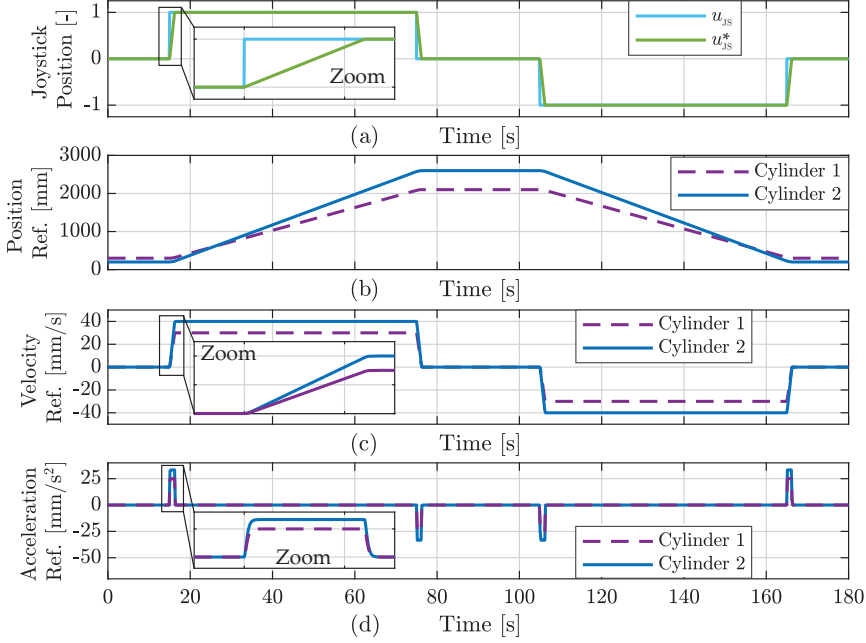


Fig. 3.13: Joystick position and cylinder motion references, for a single loading and unloading sequence. (a) Actual u_{js} and rate limited joystick position u_{js}^* . (b) - (d) Generated position, velocity and acceleration references for cylinder 1 and 2.

Fig. 3.14a shows the position references for the entire loading and unloading cycle. Fig. 3.14b shows the required actuator forces evaluated using Eq. 2.16, i.e. acceleration forces and velocity dependent forces are included. The forces have been evaluated including the mass of the ECD system mounted on the knuckle boom cylinder. For the benchmark system, the required cylinder force for cylinder 1 is between 93 % and 98 % of the shown forces, while for cylinder 2 the required forces are unchanged.

3.4.2 Steady State Solutions During Motion Trajectory

During the motion trajectory certain cylinder speeds and cylinder forces are required, as visualised in Fig. 3.14. Looping through the trajectory with a time-step of 1/1000 s, the steady state solutions to the governing equations for the benchmark and ECD actuation systems are found. Fig. 3.15 shows

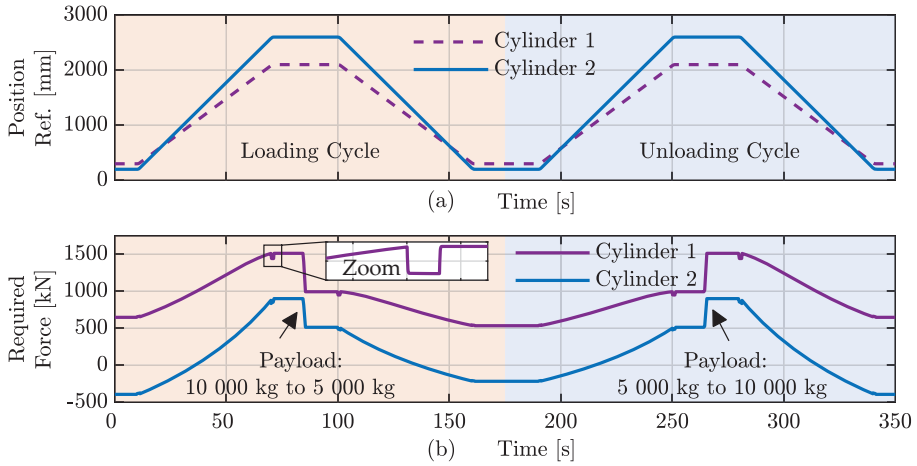


Fig. 3.14: (a) Position references during the entire motion trajectory. (b) Required actuation forces. The changed payload mass, corresponds to the lifting yoke carrying a load or not.

the steady state chamber and pump pressures as well as the shaft speed and the displacement of the pump for the benchmark system during the motion trajectory. Fig. 3.15a and b show that significant backpressures are present in the cylinders during aided load situations, e.g. p_{B1} between 100 s and 160 s in Fig. 3.15a. Furthermore, in the aided load situations there is a large pressure drop across the counter balance valves, i.e. the power supplied by the load is lost as throttling losses. This can be observed between 100 s and 160 s in Fig. 3.15a, for p_{A1} and p_{PA1} . Fig. 3.15c and d, show that the required pump pressure varies between 35 bar (standstill) and 280 bar while the pump displacement varies between 0 and 125 cm³/rev. This leads to shaft speeds

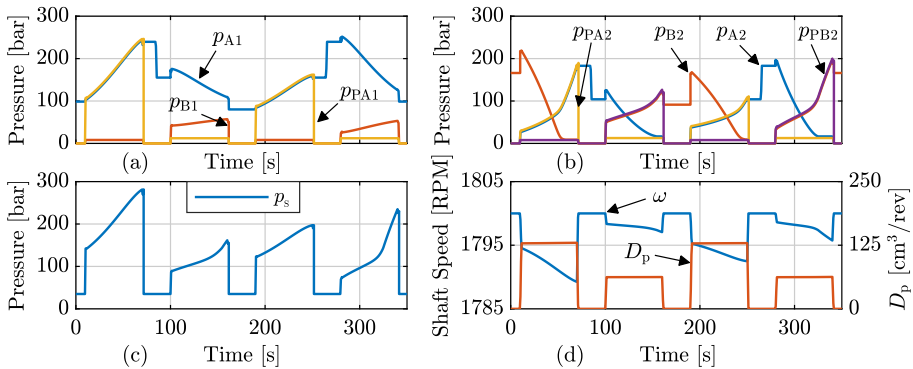


Fig. 3.15: (a) and (b) Steady state pressures for cylinder 1 and 2 during motion trajectory. (c) Required pump output pressure. (d) Pump shaft speed and pump displacement.

3.4. Energy Consumption for Motion Trajectory

ranging between 1789 RPM and 1800 RPM.

Fig. 3.16 shows the steady state power flow and power losses in the benchmark system. Fig. 3.16a shows the power supplied by the grid to the induction machine, P_{asynch} , and the sum of the cylinder output power calculated as:

$$P_{\text{cyl}} = \dot{x}_1 F_{\text{req1}} + \dot{x}_2 F_{\text{req2}} \quad (3.32)$$

If P_{cyl} is negative, power is supplied from the load. Even in this situation Fig. 3.16a shows that power still needs to be supplied by the induction motor, to fill oil into the expanding chambers.

Fig. 3.16b and d shows the throttling losses of the counter balance and pressure compensated control valves respectively. For the counter balance valves in aided load situations the power losses may become significant. For the considered conditions up to 44 kW for cylinder 1 and 36 kW for cylinder 2. For the pressure compensated control valves in Fig. 3.16d, the power loss is constant for the valve dictating the pump pressure ($Q p_{\text{LS,margin}}$), while it may be significantly higher for the cylinder requiring a smaller pressure. Fig. 3.16c shows the losses of the induction motor as the sum of the iron and copper losses ($P_{\text{Fe}} + P_{\text{Cu}}$), the torque losses of the pump P_{HM} and the pump leakage losses, P_{Q} .

The motor losses are seen to be relatively constant due to the speed dependent losses. The pump losses are dominated by the hydro-mechanical losses. In general the power losses caused by components efficiencies (Fig. 3.16c) are significantly smaller than the conceptual i.e. throttling losses.

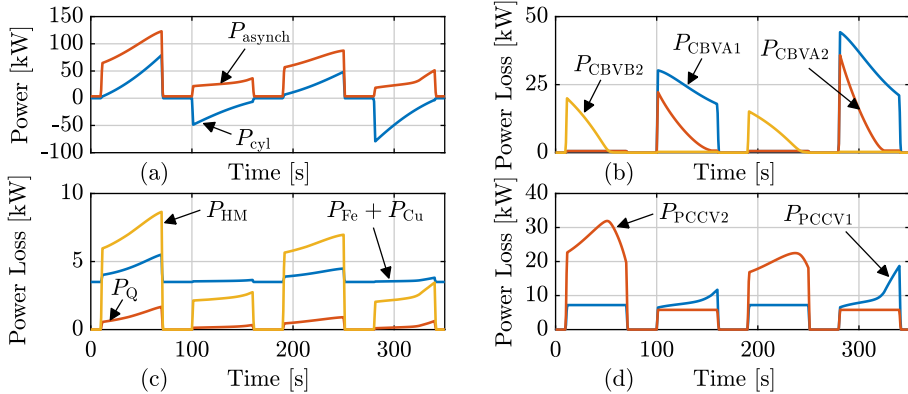


Fig. 3.16: Steady state power losses of the benchmark system during motion trajectory. (a) Induction motor power and the sum of cylinder output powers. (b) Power losses of counter balance valves. (c) Motor losses ($P_{\text{Fe}} + P_{\text{Cu}}$), pump hydro-mechanical losses (P_{HM}) and leakage losses P_{Q} . (d) Power losses of pressure compensated control valves.

The steady state chamber pressures and motor speeds for the ECD actuation systems are shown in Fig. 3.17. Due to the multiple input nature of each individual ECD system, it is possible to control the backpressure, which in this investigation is set constant to 30 bar, as seen in Fig. 3.17a and b. As seen in Fig. 3.17c and d the shaft speeds for all four PMSMs are close to each other, showing that the pump displacements are matched appropriately with the area ratios of the cylinders. The maximum speed of the pumps is 2250 RPM (ω_{22}). As the allowed maximum speed of the considered pumps is 3000 RPM this leaves a good margin for transient control efforts, compression flows and for adding further flow consuming functionalities to the drive system.

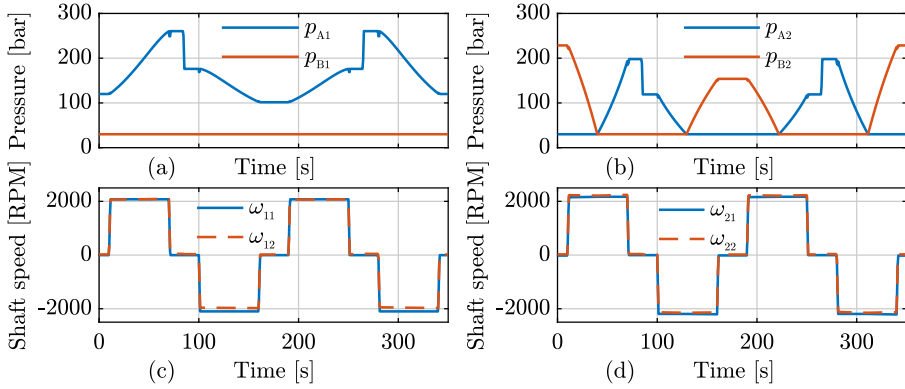


Fig. 3.17: Steady state chamber pressures and shafts speed of the ECD actuation systems during the motion trajectory. (a) Chamber pressures of main cylinder. (b) Chamber pressures of knuckle boom cylinder. (c) Shaft speeds for main cylinder actuation system. (d) Shaft speeds for knuckle boom cylinder actuation system.

The steady state power flow and power losses for the ECD actuation system are shown in Fig. 3.18. Fig. 3.18a shows the power delivered by or to the DC-link for the two inverters of the main cylinder actuation system as well as the cylinder output power or rate of work calculated as $P_{\text{cyl1}} = \dot{x}_1 F_{\text{req1}}$. Note that in aided loading conditions, the sum of P_{DC11} and P_{DC12} is negative, meaning that power delivered by the load is recuperated to the DC-link. Also, the sign of the power to or from the DC-link is always the same for the two motor inverters. On the other hand Fig. 3.18b shows the DC-link and cylinder output powers for the knuckle boom ECD actuation system. Here it can be observed that in loading situations where the rod side chamber pressure, p_{B2} , exceeds the piston chamber pressure, p_{A2} , the DC-powers for the two motor inverters have opposite sign. This happens because the sign of the power flow for motor 2, is dictated by the rotational direction of the shaft i.e. the motion direction of the cylinder piston as p_{A2} is always larger than the tank pressure. For motor 1, the sign of power flow is not only dependent on the motion direction but also the load conditions, i.e. which

3.4. Energy Consumption for Motion Trajectory

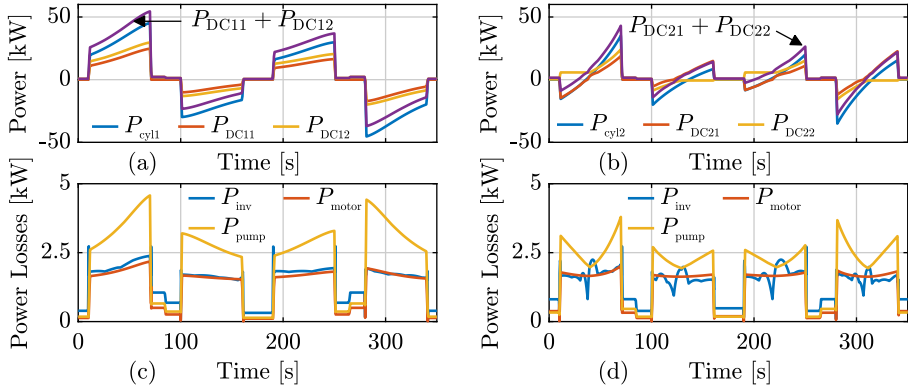


Fig. 3.18: Steady state power flow and power losses for the ECD actuation system during the motion trajectory. (a) DC-link and cylinder output power for main cylinder actuation system. (b) DC-link and cylinder output power for knuckle boom cylinder actuation system. (c) Inverter, electric motor and pump power losses for main cylinder actuation system. (d) Inverter, electric motor and pump power losses for knuckle boom cylinder actuation system.

chamber pressure is larger. For instance this happens between 10 s and 35 s in Fig. 3.18b, where $p_{B2} > p_{A2}$ and the cylinder is extending, leading to positive shaft speeds. Motor 2 delivers positive power to the system as oil pressure is increased from tank pressure to p_{A2} . Motor 1 works as a generator because oil is decompressed from p_{B2} to p_{A2} . Due to the connection of the motor inverters via the DC-link, motor 2 is driven by the recuperated power of motor 1, such that the sum of inverter powers is negative. In Fig. 3.18b it can also be observed from around 30 s to 35 s that even though the cylinder power is negative, a positive sum of inverter powers $P_{DC21} + P_{DC22}$ is needed, due to the system losses exceeding the available aided cylinder power.

Fig. 3.18c and d show the power losses of the inverter, electric motor (iron and copper losses) and pump (leakage and friction losses), for the main cylinder actuation system and knuckle boom system respectively. Note, that these losses occurring from components efficiencies, are noticeable smaller than the throttling losses of the benchmark system.

In Fig. 3.19a the efficiencies of the benchmark system are compared to the ECD actuation system during the motion trajectory. Note that by the definition, the efficiency of the benchmark system is not defined when the load is lowered. The efficiencies of the individual ECD systems are shown in Fig. 3.19b showing that the efficiency of the main cylinder actuation system is higher than for the knuckle boom actuation system.

Fig. 3.19c compares the input power to the benchmark system (P_{asynch}) with the required input power to the ECD actuation (P_{DC}). Additionally the input power to the individual ECD actuation systems are shown.

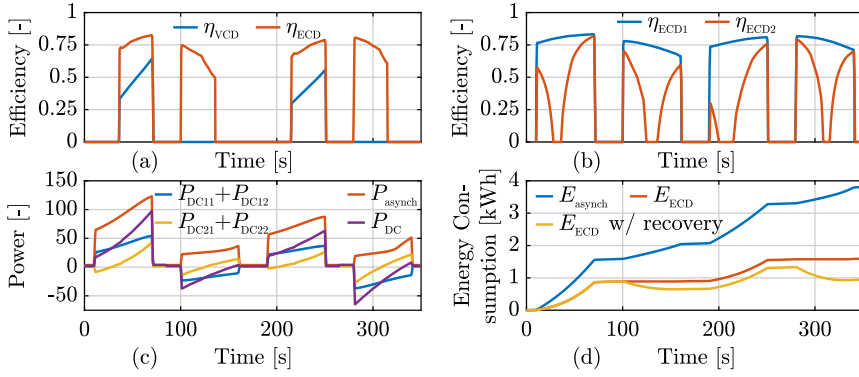


Fig. 3.19: Comparison of energy consumption during motion trajectory. (a) Efficiency of benchmark (VCD) system and combined efficiency of ECD systems. (b) Individual efficiency of main cylinder actuation system, η_{ECD1} , and knuckle boom cylinder actuation system, η_{ECD2} (c) Required input power to the VCD and ECD systems. (d) Required input energy to the VCD and ECD system with and without energy recovery to ESS.

By integrating the power curves over time, the energy needed to perform the motion trajectory can be found. Fig. 3.19d shows that the benchmark system consumes 3.8 kWh to perform the motion trajectory. For the ECD system two scenarios are considered. In the first scenario, the energy recovered in aided load situations is lost, i.e. dissipated across a braking resistor for instance. In this scenario the ECD system has a zero net energy consumption in aided load situations leading to a total energy consumption of 1.6 kWh during the trajectory. This is 58.2 % lower than for the benchmark system. In the second scenario, the energy recovered in aided load situations is not dissipated across a braking resistor. Instead the power may be consumed by other consumers connected to the DC-link, as long as there is a net consumption of power. If there are no other consumers the energy may be stored in an electrical storage element e.g. lithium-ion batteries. An ideal energy storage element is considered here by assuming a constant conversion efficiency of 94 % [60]. In this case the net energy consumption of the ECD system is 0.94 kWh, which is 75.2 % lower than for the benchmark system.

Sankey Diagram

Another way to visualise and compare the energy consumption and losses of the actuation systems is by Sankey diagrams.

Fig. 3.20 shows the Sankey diagrams for the entire motion trajectory, presented in Sec. 3.4.1. For the benchmark system 3806 Wh of energy is supplied by the grid to the induction motor and a total of 1215 Wh is aided by the load, denoted E_{Rec} here. 1215 Wh of energy is also the total energy or

3.4. Energy Consumption for Motion Trajectory

work output of the cylinders. The equality of these two numbers happens because the start and stop point of the load during the trajectory is the same, and because no cylinder friction is included in this comparison. This also explains why evaluating the efficiency of the systems by using the integral of the cylinder power as the energy or work output, does not yield an informative number, as the output energy and thereby the efficiency would yield zero. In the Sankey diagram of Fig. 3.20, E_{Fe} and E_{Cu} refer to iron and copper losses of the electrical machine and E_{HM} , E_Q to hydro-mechanical and leakage pump losses. Throttling losses of the counter balance valves and control valves are denoted E_{CBV} and E_{PCCV} respectively.

For the ECD system 1258 Wh of energy or work is aided by the load during the entire trajectory, whereof 648 Wh of energy is stored in the energy storage system (E_{ESS}) and delivered to the motor inverters in resistive load cases. This means that a net total of 944 Wh of energy need to be supplied by the DC-link to perform the trajectory. Losses of the motor inverters are denoted E_{inv} , and E_{conv} denotes conversion losses related to the energy storage system. Note that the positive cylinder work is slightly higher for the ECD system (1258 Wh) compared to benchmark system (1215 Wh), because the mass of

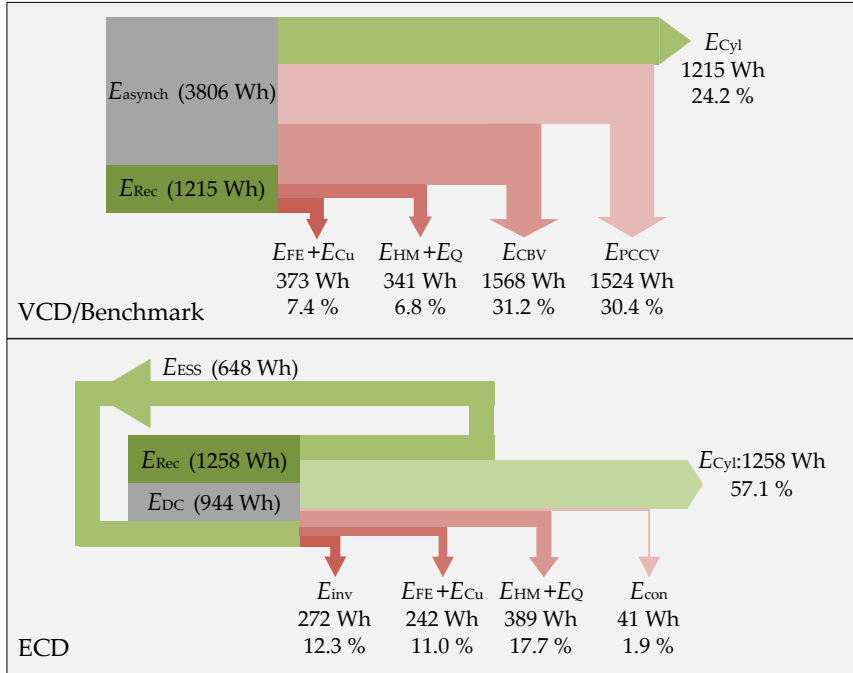


Fig. 3.20: Sankey diagrams during the entire motion trajectory defined in Sec. 3.4.1. E_{con} is conversion losses for converting power between the DC-link and the energy storage system.

the knuckle boom ECD system has been included.

One significant reason for the changed energy consumption of the two systems is the energy consumptions characteristics during load lowering. As an example the benchmark system requires 492 Wh of electrical input energy to lower a 10 ton load to fill oil into the expanding chambers. The ECD systems do not require any input energy during load lowering. In fact 394 Wh of energy may potentially be stored in the energy storage system, including a conversion efficiency of 94 %.

3.5 Chapter Summary

In this chapter the energy saving potential of the ECD actuation system compared to a conventional VCD system has been investigated, using steady state models. For a realistic loading and unloading motion cycle, the energy saving potential is found to be up to 75.2 % if recuperated energy may be stored, and 58.2 % if no storage is available. Note that this energy saving potential is found even though optimistic pump loss models have been used for the benchmark system, i.e pump losses are underestimated. Especially, the standby losses of the variable displacement pump are underestimated due to the simplifications made regarding loss scaling. Also note, that cooling systems have not been taken into account. As the power losses are larger for the benchmark systems, more cooling power needs to be installed compared to the ECD systems. Combined with the lower power consumption of the ECD system, this means that there is a significant potential for downsizing the amount of installed power. This assumes, that the actuators are operated simultaneously at their maximum speeds, as investigated here.

Due to the positive findings in this chapter, it is found reasonable to continue with maturing the ECD technology, to make it feasible for actuation of the knuckle boom crane. Specifically, this means adding load holding features, as well as a gasless reservoir technology. These are developed subsequently, and the result is denoted ECD+ to indicate additional functionalities.

Chapter 4

System Design

This chapter summarizes the development and design of the load holding technology and the gasless reservoir. These have been elaborated thoroughly in paper C (load holding) and papers D and E (gasless reservoir). Whereas the previous chapters focused on applying the ECD technology for both actuators of the knuckle boom crane to estimate the potentials for energy savings, the following chapters narrow the focus towards the knuckle boom ECD only. This is chosen as this actuator operates in four quadrants, whereas the main boom actuator only operates in two quadrants. Furthermore, the knuckle boom ECD is operated in varying orientations, highlighting the need of a pressurised reservoir. Note; this implies that the numeric subscripts {11,12,21,22}, are omitted as only a single ECD system is considered. In the remainder, the subscript 1 refers to the four quadrant pump and 2 refers to the two quadrant pump.

4.1 Load Holding Technology

Obviously the main reason for implementing load holding functionalities is safety. In case of power loss or the burst of any hose in the system the load should not be dropped in an uncontrolled manner, leading to severe danger for personnel and equipment. This is required by numerous certification authorities. Among others the American Bureau of Shipping requires [95]:

"Hydraulic cylinders used for luffing, folding or telescoping are to be provided with directly mounted lock valves that are capable of maintaining the position of the cylinder ram in the event of loss of hydraulic power. These valves are to be directly mounted on the cylinders without

the use of hoses. The valves are to be capable of closing automatically when the control lever is returned to the neutral position or upon loss of hydraulic power"

Likewise, the European Standard for Offshore Cranes (EN 13852-1) states:

"Where hydraulic cylinders are used for luffing, folding or telescoping, they shall be fitted with a device, which will hold the boom in position in the event of loss of hydraulics pressure to the cylinder or hose/pipe burst. This device shall be directly connected to the cylinder, i.e. no intermediate piping or hoses in between. Automatic overriding of this device in order to reduce oscillations etc. is not permitted."

Of secondary importance the load holding functionality may also be utilized to reduce energy consumption during standstill, i.e. the load may be kept passively without requiring input power [62].

4.1.1 Mini Review

A review of load holding solutions used in ECDs has been carried out and Fig. 4.1 summarizes the findings. The identified references, only consider single prime mover architectures, i.e. it is not possible to control the pressure level of the ECD. Fig. 4.1 divides the identified technologies into three main categories: passive valves, controlled pilot, and solenoid actuated valves. In Fig. 4.1 all architectures are shown with load holding valves on both the piston and rod side of the cylinder. All concepts can be configured to be incor-

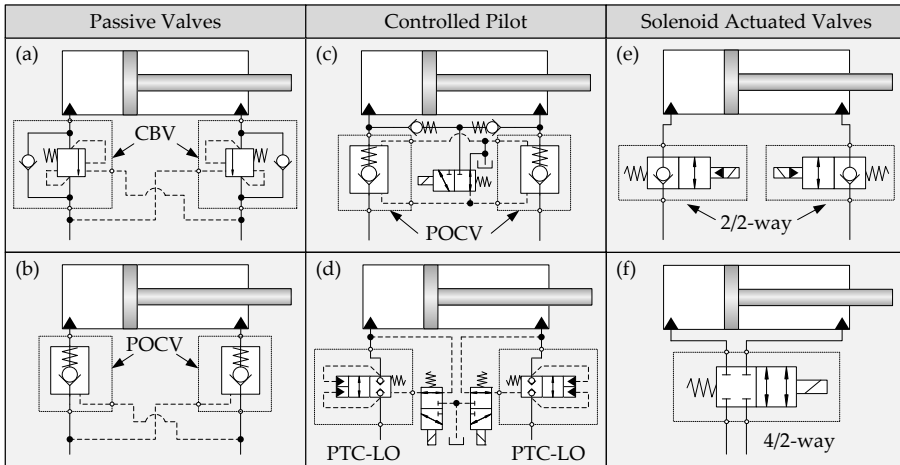


Fig. 4.1: Overview of load holding topologies for pump-controlled systems identified in literature. Abbreviations: CBV: Counter Balance Valve. POCV: Pilot-Operated Check Valve. PTC-LO: Pilot-To-Close LOogic element.

porated on one side of the cylinder, depending on the requirements.

Passive Valves

The first idea for load holding solutions suitable for electro-hydraulic compact drives, is inspired by solutions already used and accepted for conventional systems. This includes counterbalance valves (CBV), as shown in Fig. 4.1a. The CBV ensures that a flow can only leave a cylinder chamber, if a sufficient pressure in the crossport of the cylinder (back pressure) is available. In the case of power loss or hose bursts it is not possible to maintain a sufficient back pressure, and motion is stopped. CBVs are used for load holding for electro-hydraulic compact drives in [44, 96].

Note however, that a hose burst not necessarily leads to a stop of motion. Consider e.g. the situation shown in Fig. 4.2. Here the piston is retracting and a hose burst occurs downstream the CBV in the piston chamber line. As fluid is still pumped into the rod side chamber and the back-pressure is maintained motion may continue. Importantly the load does not drop rapidly due to the metering of the CBV and is as such still controlled by the pump flow. Motion stops when fluid is not filled into the rod side chamber.

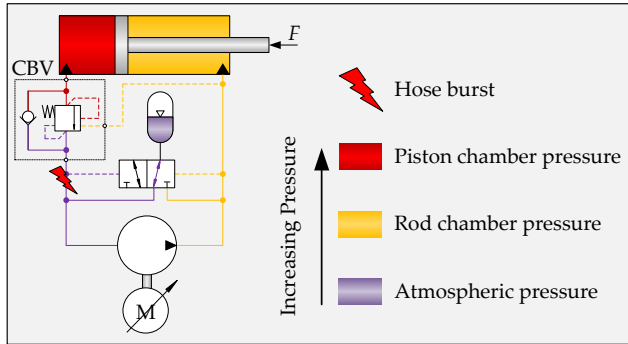


Fig. 4.2: If the counter balance valve is piloted by the crossport of the cylinder, retracting motion may continue even though a hose burst occurs in the piston line downstream the CBV as indicated by the red lightning symbol.

In [33] pilot-operated check valves (POCV) are used for load holding, which also works by blocking the cylinder chambers if the back-pressure or pilot pressure is not sufficient to open the valves.

Even though the conventional usage of passive valves for load holding is a simple solution, it suffers from the main drawback of preventing the possibility of energy recovery [62, 96], at least if the backpressure cannot be actively controlled. As stated by [97], CBVs works as hydraulic brakes as they dissipate the energy made available by the load via throttling.

The inability to recover energy provided by the load is unfortunate. Not only does it increase energy consumption but also because cooling capacity needs to be increased. Furthermore, throttling may release free air bubbles as described in the introduction. This compromises the possibility of reducing the oil amount and pressurising the oil reservoir. The considered knuckle boom application works in aided load situations in large areas of the operating range, meaning that a load holding technology preventing energy regeneration is unfeasible.

Controlled Pilot and Solenoid Actuated Valves

To enable energy recovery, solutions where the opening of the load holding valves are not determined by maintaining a certain back-pressure have been introduced. As such the opening of the valves are de-coupled from the control of oil flow into the chambers and are simply determined by additional control inputs.

One approach of doing this is by using electrically controlled directional valves to control the pilot pressure of the load holding valves. This is denoted as *controlled pilot* in this dissertation, and examples are given in Fig. 4.1c and d. In Fig. 4.1c, a 3/2-way directional valve determines whether the pilot pressure of the two POCVs equal the reservoir pressure (normal position) or the largest cylinder chamber pressure [37]. If the pilot pressure equals the reservoir pressure, the POCVs are closed by the spring force. If the largest cylinder pressure is used as the pilot pressure, the POCVs fully open due to the pilot area ratio and the vented design of the these.

Whereas the POCV are pilot-to-open types, i.e. a large pilot pressure opens the valves, a configuration using pilot-to-close valves are found in [98] and seen in Fig. 4.1d. Here two 3/2-way directional valves are used to control the pilot pressure of two pilot-to-close logic elements (PTC-LO). In the normal position the pressure of the adjacent cylinder chamber is used as the pilot pressure, which keeps the logic elements closed. If the reservoir pressure is used as the pilot pressure the load holding logic elements open.

As an alternative to control the pilot pressure using valves, electrically controlled valves may also be incorporated directly into the main transmissions lines as seen in Fig. 4.1e and f (here denoted *Solenoid Actuated Valves*). In Fig. 4.1e two internally piloted 2/2-way valves are used as load holding valves as considered in [16, 17]. Also versions using direct acting 2/2-way valves can be identified, e.g. in [61, 67, 97]. In [99] a direct acting 4/2 way directional valve is used, as shown in Fig. 4.1f.

The advantage of using the *controlled pilot* approach in Fig. 4.1c and d compared to the *solenoid actuated valves* in Fig. 4.1e and f is typically larger flow rates, especially compared to direct acting solenoid valves.

4.1. Load Holding Technology

The *controlled pilot* and *solenoid actuated valves* load holding approach enables energy regeneration because only limited throttling losses occur across the load holding valves. This is achieved by having separate control inputs, controlling the state of the load holding valves disregarding the remaining states of the system, e.g. backpressure. In other words, the load is only kept stationary if the state of the controlled valve(s) is selected accordingly. This means that a hose burst or loss of hydraulic power is not necessarily leading to the load being kept in a stationary position as required by the certification authorities. In the case of a hose burst, the load holding valves are only closed, if the burst is sensed, e.g. by a pressure sensor or if a piston speed sensor measures an excessive piston speed.

Therefore the solutions based on electrically controlled valves, are found not to immediately comply with the requirements from the certification authorities. Even though so-called hose burst valves may be included to block flow in case of a hose burst, this is undesired as these valve introduces pressure drops of up to 8 bar [100]. Instead a solution based on the additional control freedom offered by the two prime movers used in the considered ECD system is pursued. This should mainly be based on mechanical components and mechanical feedback as known from the conventional systems in Fig. 4.1a and b instead of solely by electrical components as in Fig. 4.1c to f. Additionally the throttling losses across the load holding valves must be limited, to enable energy regeneration.

4.1.2 Indirectly Controlled Hydraulic Lock

The load holding solutions depicted in the Fig. 4.1 are all identified in the literature for electro-hydraulic compact drive systems based on a single prime mover. For the solutions based on passive valves (4.1a and b), the characteristics are to some extent governed by the system in which it is implemented. For the ECD studied in this dissertation the utilization of two prime movers offers new possibilities for incorporating and controlling the load holding valves, as the pressure level of the actuator may be controlled.

Take the simple example of using two pilot-operated check valves as load holding valves, with the pilot line being connected to the cross port of the cylinder as shown in Fig. 4.3a combined with the POCV depicted in Fig. 4.3c. The considered ECD system renders the possibility of controlling the lowest chamber pressure to ensure that the POCVs are fully opening during nominal operation to decrease throttling losses and enable energy recovery. In the case of a power loss or a hose burst in the cross port of the cylinder, sufficient pressure in the pilot line is not maintained and the POCV closes such that the load is kept stationary as required by the certification authorities.

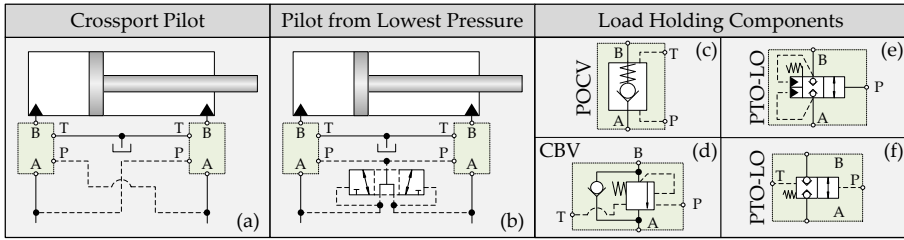


Fig. 4.3: (a) Load holding strategy using the pilot pressure from the crossport of the cylinder. (b) Load holding strategy, where an inverse shuttle valve is used to select the lowest cylinder chamber pressure as the pilot pressure. (c) to (f) Load holding components. (c) Pilot-operated check valve. (d) Counter-balance valve. (e) Pilot-to-open logic element based on an unbalanced poppet design. (f) Pilot-to-open logic element based on a balanced poppet design.

The pressure level of the actuator is controlled by a closed-loop pressure controller. The control architecture may conveniently be arranged such that the human operator joystick is used to generate motion references, i.e. piston velocity references, as depicted in Fig. 3.12 on page 56. The reference input to the pressure level controller however, may be adjusted in a binary way. For instance the level pressure reference may be set to 0 bar when the POCV should be closed and a set-point above the opening pressure of the load holding valves, e.g. 30 bar, if motion is desired. The level pressure set-points may be toggled by an operator-switch or automatically if the operator joystick position is requiring piston motion. In the latter case, the level pressure set-point should be set to 0 bar (closed load holding valves) if the joystick has been in the neutral position for a pre-defined period of time.

As the pressure level is closed loop controlled and ideally decoupled from the motion reference generated by the operator, a hose burst may in some situations lead to a rapidly dropping load, i.e. faster than required by the operator. Consider the situation where the cylinder retracts under an aided load, and a hose burst occurs in the piston chamber line downstream the POCV. This is equivalent to the situation shown in Fig. 4.2 on page 67 for a CBV and single prime mover setup. Depending on how the control structure is designed, the closed loop controllers may attempt to keep the pressure in the rod chamber at 30 bar. In the event of this being successful, the POCV will stay fully open and the load will drop rapidly.

To increase safety, an inverse shuttle valve may be used to select the lowest chamber pressure as the pilot pressure as seen in Fig. 4.3b. This means that a hose burst in any of the two transmission lines closes both load holding valves. Note, that even though the load is locked in the case of a hose burst, the control efforts will still attempt to counteract the substantial leakage occurring due to the hose burst, by supplying oil into the leaking chamber. To avoid this a simple *watch-dog* approach may be implemented, where a safe

state is engaged setting the shaft speed references to 0 RPM, if a safe state signal is triggered. This may be triggered if the position error is above a predefined limit, or if the shaft speeds are inconsistent with the measured piston speed for a certain amount of time.

As shown in Fig. 4.3c to f, several valve types may be used as load holding valves in the considered ECD-system. The only requirement is that they are leakage free, normally closed and opens when pilot pressure is applied. Candidates include pilot-operated check valves, counter balance valves and different types of pilot-to-open logic elements. One common characteristics of the POCV, the CBV, and the PTO-LO element in Fig. 4.3e is that the pilot pressure required to open the valves depends on the loading conditions. Thus it may vary significantly. To ensure predictable and load independent switching, a PTO-LO based on a so-called balanced poppet design is found to be a simpler solution from a control point of view. The balanced poppet design ensures that any pressure in the main transmission lines (A and B in Fig. 4.3f) does not affect the required opening pressure of the valve, as this is fully determined by the spring force and the pressure in the drainport (port T in Fig. 4.3f).

A load holding solution consisting of the lowest chamber pressure piloting approach visualised in Fig. 4.3b in combination with balanced poppet pilot-to-open logic elements (Fig. 4.3f) are selected for further study. In paper C this is denoted as an *indirectly controlled hydraulic lock*, as the state of the logic elements is not directly controlled by dedicated inputs such as electrically controlled valves, but rather controlled by the pressure level of the system. The balanced poppet pilot-to-open logic elements are referred to as the load holding valves in the remainder.

4.2 Gasless Reservoir

A key feature of electro-hydraulic compact drives are the closed architecture utilizing a pressurised reservoir. This ensures good pump suction conditions, the ability to work in tilted orientations and potentially a lower risk for external contamination to enter the hydraulic system [32]. To balance the rod volume as well as thermal expansion and compression volumes, the closed oil reservoir must be able to expand and contract without exceeding the tolerated pressure range. The allowable pressure range is typically restricted by the pump, as many commercially available pumps need a low pressure leakage line to avoid malfunctioning, e.g. shaft sealing blowout. Conventionally the needed flexible reservoir volume is obtained using a low pressure gas-charged accumulator. These comes in different types as shown in Fig. 4.4, where diaphragm-, bladder- and piston accumulators are depicted.

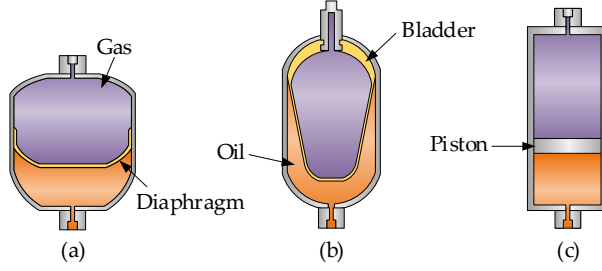


Fig. 4.4: Illustration of gas-charged accumulator types. (a) Diaphragm. (b) Bladder. (c) Piston.

Despite the type of accumulator, the variable volume is obtained by the characteristics of the gas. To stay within a narrow range of allowable pressures, this leads to large accumulators relative to the oil volume that needs to be stored. In this study the reservoir pressure is allowed to vary between 1.5 bar and 4 bar (absolute). Nitrogen is typically used in accumulators. By treating this as an ideal gas undergoing an poly-tropic process, which is reasonable for low pressures and temperatures, it may easily be shown why large gas volumes are needed to stay within 1.5 bar to 4 bar:

$$\left. \begin{aligned} p_1 V_{1G}^\kappa &= p_2 V_{2G}^\kappa \\ \Delta V &= V_{1G} - V_{2G} \end{aligned} \right\} \Rightarrow \frac{V_{1G}}{\Delta V} = R_{\text{acc}} = \frac{p_2^{\frac{1}{\kappa}}}{p_2^{\frac{1}{\kappa}} - p_1^{\frac{1}{\kappa}}} \quad (4.1)$$

where p_1 , p_2 , V_{G1} and V_{G2} are the minimum and maximum gas pressures and corresponding gas volumes. κ is the polytropic coefficient and ΔV is the oil volume that may be stored in the accumulator while staying within pressure limit p_2 . Therefore R_{acc} is the ratio of the gas volume at the minimum pressure relative to the oil compensation volume (ΔV) of the gas-charged accumulator. To stay within 1.5 bar and 4 bar ($p_1 = 1.5$ bar, $p_2 = 4$ bar), it requires an initial gas volume of 2 times ΔV if the gas process is assumed to be adiabatic ($\kappa = 1.4$ for nitrogen [101]) and 1.6 if an isothermal process is assumed ($\kappa = 1$). Especially for long stroke cylinders requiring a large compensation volume, the accumulator turns out to be large. It is desirable to implement other types of accumulators to increase compactness and even more importantly to avoid the need of gas, as leaking gas to the oil or the surroundings may lead to system failure.

Alternative reservoir types include spring-charged, mass-charged and self-pressurising reservoirs as shown in Fig. 4.5.

In the spring-charged accumulator a spring simply replaces the pressurised gas from the piston type gas-charged accumulator. The compression of the spring elevates the fluid pressure. To store large oil volumes either a large

4.2. Gasless Reservoir

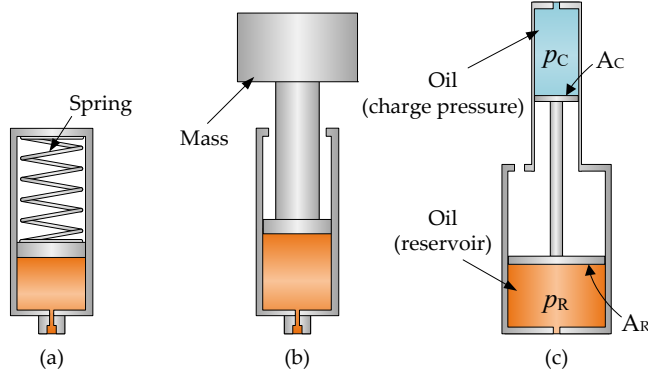


Fig. 4.5: Alternatives to gas-charged accumulators. (a) Spring-charged. (b) Mass-charged. (c) Self-pressuring or bootstrap reservoir.

area piston or a long stroke is required. In either case this leads to large and heavy springs. Therefore spring-charged accumulators are only suitable for small accumulators [102]. The mass-charged accumulator works by pressurising the oil by the gravity forces of a large mass. This means that this solution is not feasible for the knuckle boom crane application as this does not allow for working in tilted orientations.

Bootstrap reservoirs or self-pressurising reservoirs are essentially two interconnected differential hydraulic cylinders. As seen in Paper D and E, the chambers of the hydraulic cylinders may be connected in different configurations, but in this work the configuration shown in Fig. 4.5c is used, i.e. the rod chambers are vented to atmosphere. In the absence of frictional and gravitational forces, the bootstrap reservoir simply works as a volume-pressure transmission, where the reservoir pressure is elevated by the charge pressure as $p_R = p_C \alpha_B$ with $\alpha_B = A_C / A_R$ and utilizing relative pressures. Bootstrap reservoirs are used widely in both commercial and military air-crafts [103], where they form a pressurised reservoir being charged by the constant pump outlet pressure of the hydraulic system of the aircraft. The ability to contain a compensation oil volume in the bootstrap reservoir is due to the piston area ratio α_B . In commercially available bootstrap reservoirs the reservoir piston area, A_R , may be as much as 85 times larger than the charge chamber piston area, A_C [104].

The volume saving potential of a bootstrap reservoir compared to the gas-charged accumulator is investigated by calculating the required chamber volumes of the charge chamber and reservoir chamber needed to obtain a certain compensation volume ΔV as visualised in Fig. 4.6.

In the fully extended position the reservoir chamber is filled with its maximum oil volume of $V_{R,max} = A_R L_{sz}$ while the charge chamber is empty. In

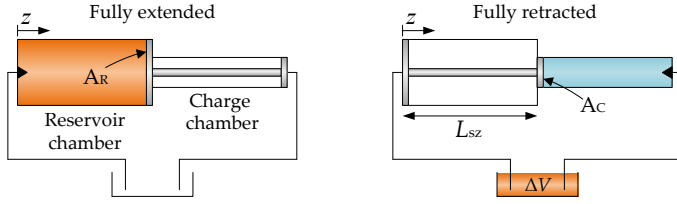


Fig. 4.6: In the fully extended position the reservoir chamber is completely filled with oil while the charge chamber is empty. As the piston retracts, fluid is displaced from the reservoir chamber to the charge chamber. Due to a larger area of the reservoir piston compared to the charge piston, some oil is available for volume compensation in the remaining system (ΔV).

the fully retracted position the reservoir chamber is empty while the charge chamber is filled with its maximum oil volume $V_{C,max} = A_C L_{sz}$. The total volume of the bootstrap reservoir is the sum of both chamber volumes ($V_{boot} = (A_R + A_C)L_{sz}$), while the compensation volume may be found as the difference of the maximum chamber oil volumes, $\Delta V = V_{R,max} - V_{C,max}$ as illustrated in Fig. 4.6. The ratio of V_{boot} to the compensation volume ΔV is given as:

$$R_{boot} = \frac{V_{boot}}{\Delta V} = \frac{(A_R + A_C)L_{sz}}{A_R L_{sz} - A_C L_{sz}} = \frac{A_R + \alpha_B A_R}{A_R - \alpha_B A_R} = \frac{1 + \alpha_B}{1 - \alpha_B} \quad (4.2)$$

Fig. 4.7 shows the volume ratio R_{boot} from Eq. 4.2 as a function of the inverse of the area ratio $\alpha_B^{-1} = A_R/A_C$.

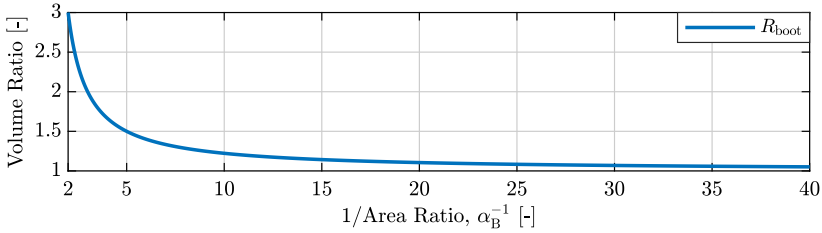


Fig. 4.7: Plot of R_{boot} (Eq. 4.2) as a function of the inverse of the area ratio $\alpha_B^{-1} = A_R/A_C$.

Recall, that for the allowed pressure range the gas-charged accumulator required a gas volume twice as big as the oil compensation volume. From Fig. 4.7 it may be seen that to obtain significant volume reductions for the bootstrap reservoirs the reservoir piston needs to be several times larger than the charge piston. Note that R_{acc} depends on the allowed reservoir pressure range, while for the bootstrap reservoir it is assumed that the charge pressure is controlled to keep the reservoir pressure within limits.

As an example $R_{boot} = 1.22$ and $R_{boot} = 1.08$ for area ratios of $\alpha_B = 1/10$ and $1/25$ respectively. This corresponds to volume savings potentials of 38 % and

4.3. Four Quadrant Operation Diagram

45 % respectively compared to gas-charged accumulator in adiabatic conditions. Note that these potential volume savings are only based on the theoretical gas and chamber volumes. This means that the material thicknesses and additional inactive lengths of the bootstrap reservoir chambers needed for practical realisation has not been included.

As noted in paper D, a controllable charge source is needed to keep the charge pressure sufficiently high during operation. This charge source may be constituted by the low pressure cylinder chamber, as this is kept at an elevated level during motion in order to keep the load holding valves fully open. The inverse shuttle valve used to select the pilot pressure of the load holding valves, may therefore be re-used to connect the charge chamber of the bootstrap reservoir with the low pressure cylinder chamber. This is also considered in paper E for a system without load holding valves. In Paper E a closed center inverse shuttle valve is used, leading to an insufficient charge pressure at some loading conditions. One of the findings from paper E is thus that an open center inverse shuttle valve should be used to ensure the charge chamber to be connected to a cylinder chamber at all times, in order to maintain a sufficient charge pressure in all loading situations.

4.3 Four Quadrant Operation Diagram

The ECD system with incorporated load holding valves developed in Sec. 4.1 and the gasless bootstrap reservoir introduced in the previous section is referred to as ECD+ to indicate the additional functionality. Simplified schematics of the ECD+ is given in the four quadrant operational diagram in Fig. 4.8.

In Fig. 4.8 the lowest chamber pressure of the cylinder is controlled such that the load holding valves LH_A and LH_B are fully open. This mode is denoted *Motion operation mode*. Chamber pressures and their adjacent transmission lines are equally coloured to indicate that the pressure drop across the load holding valves in motion operation mode is considered negligible.

In quadrant 1 and 2 of Fig. 4.8 the external load prescribes the piston chamber pressure p_A to be bigger than the rod chamber pressure p_B such that the inverse shuttle valve, ISV, connects p_B to the pilot lines of the load holding valves and to the charge chamber of the bootstrap reservoir.

In quadrant 1, the cylinder is extending and both electric motors deliver power into the system. As the cylinder is extending this will contain more fluid, which is delivered by pump 2 into the closed circuit. This means that the bootstrap reservoir piston must retract to balance this flow requirement. The steady state speed of the reservoir pistons, \dot{z} , as a function of cylinder

speed \dot{x} may, in the absent of pump leakage, be calculated as:

$$\left. \begin{aligned} Q_A &= Q_R + Q_{P1} \\ Q_B &= Q_C + Q_{P1} \end{aligned} \right\} = Q_B = Q_A - Q_R + Q_C \Rightarrow \dot{x} A_A \alpha = \dot{x} A_A + \dot{z} A_R - \dot{z} A_R \alpha_B$$

$$\Leftrightarrow \dot{z} A_R (1 - \alpha_B) = -\dot{x} A_A (1 - \alpha) \quad \Leftrightarrow \quad \dot{z} = -\frac{A_A (1 - \alpha)}{A_R (1 - \alpha_B)} \dot{x} \quad (4.3)$$

Eq. 4.3 is valid for all operation quadrants and reveals that in the case of a symmetric cylinder ($\alpha = 1$), \dot{z} is 0, which indeed is the case as no flow balancing is needed for a symmetric actuator (compression and thermal expansion absent). On the other hand if the bootstrap reservoir is symmetric, \dot{z}

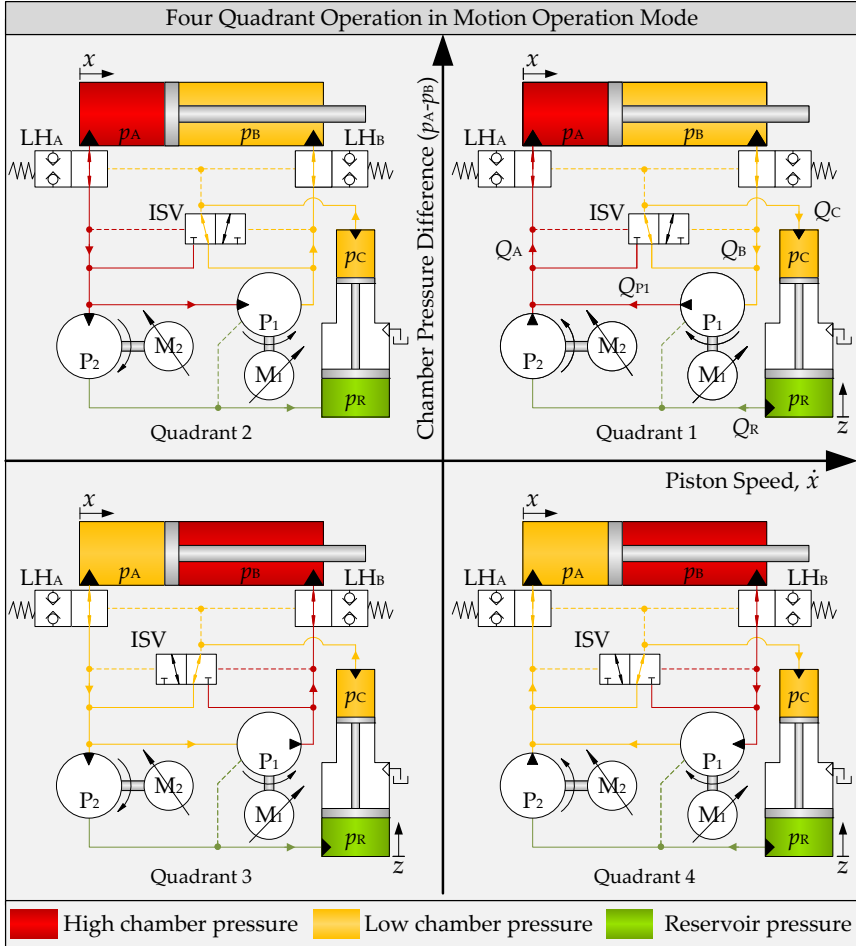


Fig. 4.8: Four quadrant operation schematics in motion operation mode.

4.3. Four Quadrant Operation Diagram

approaches infinite, which happens because a symmetric bootstrap reservoir does not have the ability of flow compensation, because all oil leaving the reservoir chamber need to enter the charge chamber (steady state).

Due to the retraction of the bootstrap reservoir pistons in the first quadrant, the charge chamber expands and a part of the flow leaving the rod chamber of the cylinder enters the charge chamber of the reservoir as these are connected by the ISV. This means that pump 1 does not need to displace as much fluid as for a system without a bootstrap reservoir. With pump leakage absent, the steady state volume flow Q_{p1} in the first quadrant may be calculated as:

$$\begin{aligned} Q_{p1} &= Q_A - Q_R = \dot{x}A_A + \dot{z}A_R = \left(A_A - \frac{A_R A_A (1 - \alpha)}{A_R (1 - \alpha_B)} \right) \dot{x} \\ &= \left(1 - \frac{1 - \alpha}{1 - \alpha_B} \right) A_A \dot{x} = \frac{\alpha - \alpha_B}{1 - \alpha_B} A_A \dot{x} \end{aligned} \quad (4.4)$$

Eq. 4.4 shows that the smaller α_B is, the smaller is the impact on the needed pump flow compared to a system with no bootstrap reservoir. If $\alpha_B = 0$, i.e the charge chamber has zero area, the required pump flow is not affected because no fluid enters the charge chamber. If the bootstrap reservoir is symmetric, $\alpha_B = 1$, the needed pump flow approaches infinity for a required cylinder speed because all flow delivered by the pump enters the charge chamber (steady state). Interestingly if $\alpha = \alpha_B$ pump 1 does not need to deliver any flow in this quadrant, independently of the actual area of the bootstrap reservoir pistons.

Compared to a system without a bootstrap reservoir pump 2 needs to displace more fluid to maintain a certain cylinder speed to compensate the smaller flow of pump 1. Neglecting leakage, the steady state flow Q_R may be found as:

$$Q_R = -\dot{z}A_R = \frac{1 - \alpha}{1 - \alpha_B} A_A \dot{x} \quad (4.5)$$

If $\alpha_B = \alpha$, Eq. 4.5 confirms that the entire piston area flow of the cylinder needs to be delivered by pump 2 as pump 1 is inactive in this case. If $\alpha_B = 0$, pump 2 must deliver the rod volume flow as the case in a system with no bootstrap reservoir.

In quadrant 2 the cylinder is retracting under an assistive load, such that both motors work as generators showing a potential for recovering the power supplied by the load. A part of the flow entering the rod side chamber is supplied from the charge chamber of the bootstrap reservoir. This means that the steady state flow supplied from pump 1 and pump 2 is changed compared to a system with no bootstrap reservoir according to Eq. 4.4 and 4.5 respectively.

In the third and fourth quadrant of Fig. 4.8 the external load prescribes the rod side chamber p_B to be larger than p_A . This means that the inverse shuttle valve connects the piston chamber of cylinder with the charge chamber of the reservoir and the pilot lines of the load holding valves. An important difference from quadrant 1 and 2, is the fact that the electric motors work in different modes. In the third quadrant motor 1 is supplying power to the system while motor 2 works as generator with the opposite being true in the fourth quadrant. This situation arises, because the pressure p_A is required to be above the reservoir pressure to keep the load holding valves fully open. If this was not needed and p_A could be controlled to equal the reservoir pressure, motor 2 would idle (losses absent) and the cylinder output power would be delivered entirely by motor 1.

The inverse shuttle valve connects the piston chamber and the charge chamber in quadrants 3 and 4. This means that the volume expansion of these chambers have the same sign, due to the opposite motion direction shown in Eq. 4.3. This means that in quadrant 3 both chambers contract while in quadrant 4 both chambers expand. In turn this means that pump 2 must displace more fluid than in a system with no bootstrap reservoir, as given in Eq. 4.5. Notice, that Eq. 4.5 is valid in all operation quadrants such that to maintain a certain cylinder piston speed, the flow requirements of pump 2 generally increases. This means that if a bootstrap reservoir is implemented in an existing system, the steady state cylinder velocity range is decreased if the flow capacity of pump 2 is unchanged. To mitigate this effect α_B should be chosen as small possible.

In quadrant 3 and 4 the flow requirement of pump 1 is not altered by the implementation of the bootstrap reservoir. In steady state conditions and in the absent of losses the flow is given as:

$$Q_{p1} = A_A \alpha \dot{x} \quad (4.6)$$

Even though it may be tempting to select $\alpha_B = \alpha$ such that pump 1 may be inactive in quadrants 1 and 2 (Eq. 4.4) this is not sensible for an application working in four quadrants. The consequence will be an increased flow requirement for pump 2 in all operation quadrants, while pump 1 cannot be inactive in quadrants 3 and 4.

Self-Locking Mode

In load holding or self-locking mode the lowest chamber pressure is controlled to be below the cracking pressure of the load holding valves. This ensures that these are fully closed and the cylinder chambers are disconnected from the remaining system. In case of a failure e.g. power loss or hose burst, the lowest chamber pressure cannot be kept above the opening pressure of the load holding valves, meaning that the system enters self-locking

4.4. Steady State Performance

mode.

The self-locking mode may also be engaged actively during nominal operation to save energy in stationary situations. In these situations it is obviously beneficial to control the pressure in the transmission lines to equal the atmospheric pressure to yield zero torque on the pump shafts. This operation mode is illustrated in Fig. 4.9.

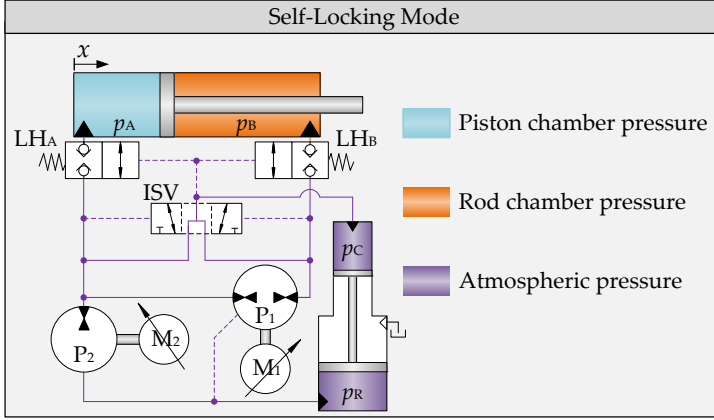


Fig. 4.9: During failure such as power loss or hose burst the system enters the self-locking mode, where the load holding valves are fully closed to keep the load stationary. This operation mode may also be used to actively save energy in stationary situations.

4.4 Steady State Performance

The steady state performance of the proposed ECD+ system architecture is investigated similarly to the steady state performance of the benchmark actuation system (VCD) and the ECD with a vented tank and without load holding valves from Chapter 3. The aim of this is to validate that the insertion of these features does only alter energy consumption to a small extent and validate that the reservoir pressure is kept within limits during steady state conditions.

4.4.1 Bootstrap Reservoir Dimensions

The dimensions of the bootstrap reservoir impact the performance of the system to a large extent. Especially the area ratio of the bootstrap reservoir, α_B , has conflicting optimization targets as investigated in Paper E. On one hand it should be low in order to decrease the volume of the bootstrap reservoir (Eq. 4.2) and to decrease the flow requirement of the charge chamber. On

the other hand a small area ratio requires a large charge pressure to maintain a certain reservoir pressure according to $p_R = p_C \alpha_B$. As the charge pressure is selected as the lowest chamber pressure of the cylinder a large charge pressure decreases the force capabilities of the cylinder.

The load holding valves selected for this theoretical study are fully open for a pilot pressure above 20 bar. To include some margin for back-pressure in the drain line and imperfect pressure control a reasonable lower chamber pressure may be selected to 25 bar. This is also beneficial in regard to the fluid bulk modulus which is highly varying for small pressure values while being almost constant for pressures above approximately 25 bar (depending on air content). The allowed reservoir pressure is 1.5 bar to 4 bar (absolute), leading to a desired area ratio of 1/13.8 for the bootstrap reservoir, aiming for a average reservoir pressure of 2.75 bar. From commercially available piston areas this ratio cannot be obtained. Increasing the area ratio to 1/16 a number of available piston areas can be combined to yield the desired ratio. Still aiming for a reservoir pressure of 2.75 bar, the lowest chamber pressure must then be controlled to 28.8 bar.

Papers D and E investigates how the selection of the piston areas affects the system dynamics. Paper D shows that selecting a bootstrap reservoir with an eigenfrequency in the vicinity of the eigenfrequency of the cylinder leads to severely changed system dynamics with regards to the position state of the cylinder. Paper E investigates the dynamic couplings of the system using the RGA-number and shows that for small piston areas the control of the reservoir pressure and cylinder motion would be close to ideally decoupled. However from a practical point of view selecting small piston areas may turn infeasible, as this requires a very long stroke length of the bootstrap reservoir. Therefore it is found more pragmatic to select piston areas yielding a feasible stroke length and handle the dynamic couplings during controller design. For this study a reservoir piston diameter of $d_R = 320$ mm and a charge chamber piston diameter of $d_C = 80$ mm is selected. This yields a stroke length of 1.15 m, such that the bootstrap reservoir is able to compensate a volume corresponding to 120 % of the rod volume of the cylinder. Note that the minimum length of the bootstrap reservoir is twice the stroke length.

4.4.2 Selecting Pump Displacements

In Chapter 3, the geometric displacements of the pumps in the system with no bootstrap reservoir were found based on the required steady state pump flows. This included a margin of 25 % of the allowed maximum pump speed

4.4. Steady State Performance

for compression flows, transient control efforts, pump leakage etc.:

$$D_{p,1} = \frac{A_B \dot{x}_{\max}}{0.75 \omega_{\max}} \quad D_{p,2} = \frac{(1 - \alpha) A_A \dot{x}_{\max}}{0.75 \omega_{\max}} \quad (4.7)$$

where $\dot{x}_{\max} = 40$ mm/s is the maximum knuckle boom cylinder speed and $\omega_{\max} = 3000$ RPM is the maximum rotational speed of the pump.

For $\alpha_B < \alpha$ including a bootstrap reservoir does not change the required displacement of pump 1, as the numerically largest pump flow is occurring in quadrants 3 and 4.

For pump 2, the required displacement when including a bootstrap reservoir may be calculated as:

$$\left. \begin{aligned} Q_R &= \frac{1-\alpha}{1-\alpha_B} A_A \dot{x} \\ Q_R &= \omega_2 D_{p,2} \end{aligned} \right\} \Rightarrow D_{p,2} = \frac{(1 - \alpha) A_A \dot{x}_{\max}}{0.75(1 - \alpha_B) \omega_{\max}} \quad (4.8)$$

The calculated and selected displacements available from the considered pump series (Bosch Rexroth A10 piston pumps [78]) are summarised in Tab. 4.1.

Table 4.1: Selection of pump displacements. The calculated values are found from Eqs. 4.7 and 4.8 aiming to obtain the steady state flow requirement at 75 % of the maximum pump speed. The *margin* is calculated with respect to the selected pump displacement and maximum allowed pump shaft speed of 3000 RPM.

Without Bootstrap Reservoir (Chapter 3)			With Bootstrap Reservoir ($\alpha_B = 1/16$)
$D_{p,1}$	Calculated	25.21 cm ³ /rev	25.21 cm ³ /rev
	Selected	26 cm ³ /rev	25 cm ³ /rev
	Margin	818 RPM / 21 L/min (27 %)	731 RPM / 18 L/min (24%)
$D_{p,2}$	Calculated	27.14 cm ³ /rev	28.95 cm ³ /rev
	Selected	28 cm ³ /rev	28 cm ³ /rev
	Margin	819 RPM / 23 L/min (27 %)	673 RPM / 19 L/min (22 %)

For the Bosch Rexroth A10 pump series, no pump between 28 cm³/rev and 32 cm³/rev is available. Therefore the displacement is selected as $D_{p,2} = 28$ cm³/rev for the system with a bootstrap reservoir as seen in Tab. 4.1, accepting that a 25 % shaft speed margin is not fulfilled (22 % instead). To obtain a fairly good steady state pump matching between pumps 1 and 2, the displacement of pump 1 is reduced from 26 cm³/rev to 25 cm³/rev .

Note that inserting the load holding valves and the bootstrap reservoir has changed the steady state characteristics of the ECD+ compared to the ECD in Chapter 3, which is partly caused by the inability to obtain a similar pump displacement matching using the considered pump series. This has caused

the maximum obtainable steady state piston speed to be decreased from 55 mm/s to 51.6 mm/s, corresponding to a decrease of 6.2 %. Additionally the basic ECD without load holding valves and bootstrap reservoir features the possibility of lowering the lower chamber pressure to increase the steady state force capabilities while still allowing piston motion. This is not possible for the ECD+ system as the load holding valves requires a minimum pilot pressure of 20 bar to be kept fully open.

4.4.3 Energy Efficiency

The steady state solution to the equations modelling the ECD+ system with load holding valves and bootstrap reservoir is given in Appendix C and used to evaluate the efficiency and energy consumption in this section. The procedure and the loss models are similar to the ones used in Chapter 3.

Fig. 4.10 shows the instantaneous efficiency of the knuckle boom actuator in the entire operating range of the crane for $m_3 = 10$ ton, $\dot{x}_{\text{ref},2} = 40$ mm/s.

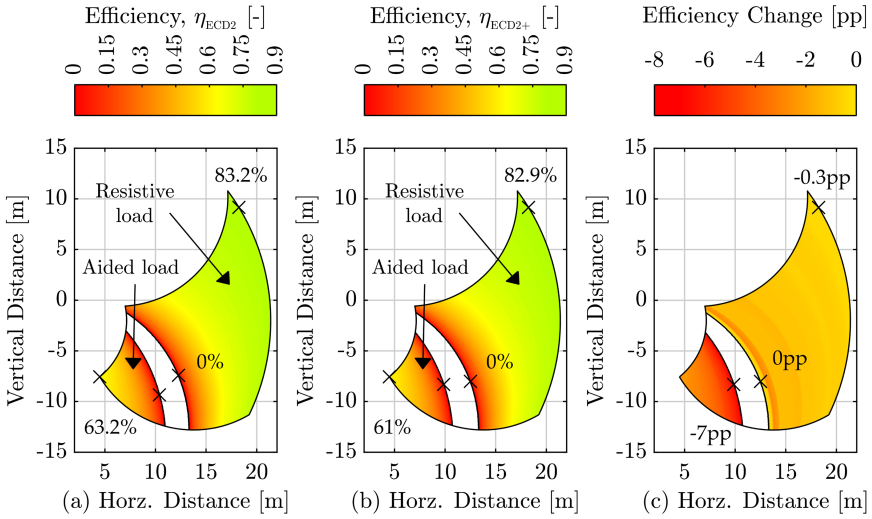


Fig. 4.10: Evaluated efficiency of knuckle boom actuation system (ECD₂) in the entire crane range for $\dot{x}_{\text{ref},2} = 40$ mm/s, $m_3 = 10$ ton. (a) ECD with a vented tank as considered in Chapter 3 and without load holding valves. (b) ECD+ system with bootstrap reservoir and load holding valves. (c) The efficiency change in percentage points [pp]. The negative sign indicate a lower efficiency of the ECD+ system.

Fig. 4.10 illustrates that the inclusion of the bootstrap reservoir and load holding valves, decreases the efficiency in the entire operating range, mainly due to throttling losses and friction losses of bootstrap reservoir pistons. The difference may be as large as 7 percentage points. This however occurs in

loading conditions with small drive powers. In the main part of the operating range the efficiency change is below 2 percentage points.

To investigate the actual additional energy consumption of the knuckle boom actuation system, the motion trajectory defined in Sec. 3.4.1 is studied in the following section.

4.4.4 Energy Consumption for Motion Trajectory

In Fig. 4.11a and b the steady state shaft speeds during the motion trajectory are compared between the ECD and the ECD+ system. Fig. 4.11a shows a change in the shaft speed of pump 1 in the ECD+ system when the external load force changes direction, i.e. due a position change of the inverse shuttle valve. This was anticipated by Eqs. 4.4 and 4.6. The change is approximately 160 RPM, and is shown in the zoom window in Fig. 4.11a. Fig. 4.11b confirms that pump 2 needs to rotate faster when the bootstrap reservoir is included, which is clearly seen in the zoom window. This is caused by the extension or retraction of the charge chamber. At maximum speed approximately 4 L/min is required by the charge chamber leading to an increase in rotational speed of pump 2 of approximately 145 RPM.

Fig. 4.11c shows that the steady state reservoir pressure is kept within the allowed range of 1.5 to 4 bar (absolute) for the ECD+ system. Fig. 4.11d shows the additional losses for the ECD+ system including throttling losses across load holding and inverse shuttle valves and friction losses of the bootstrap reservoir pistons.

Fig. 4.12 compares the energy distribution of the knuckle boom actuator for

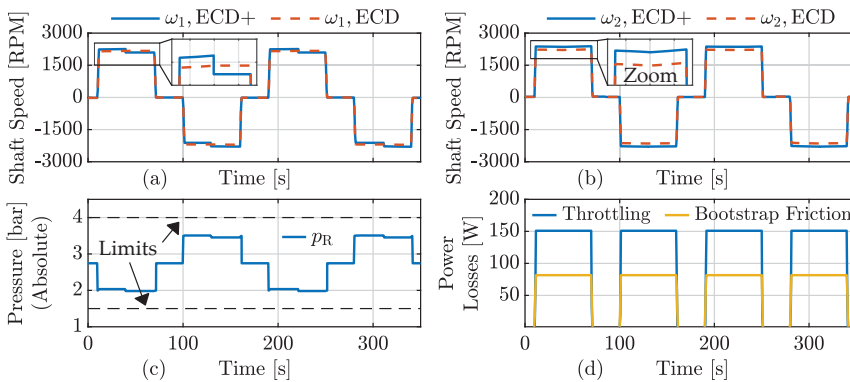


Fig. 4.11: Steady state calculation results for considered motion trajectory for ECD and ECD+ systems. (a) Steady state shaft speeds of motor 1. (b) Steady state shaft speeds for motor 2. (c) Absolute steady state pressure in reservoir chamber of bootstrap reservoir. (d) Throttling and bootstrap friction power losses.

the entire motion trajectory presented in Sec. 3.4.1 using Sankey diagrams. Note that Fig. 4.12 does not include power sharing with the ECD system actuating the main cylinder. For the basic ECD system it may be seen that 595 Wh is supplied from the DC-link to the system, whereof 335 Wh is converted to positive cylinder output work. 335 Wh is aided by the cylinder load whereof 164 Wh is stored in the energy storage system. If this energy is used in resistive loading situations the net energy demand from the DC-link is decreased to 431 Wh.

For the ECD+ system the addition of the load holding valves and bootstrap reservoir has introduced 10 Wh of throttling losses and 5 Wh of bootstrap piston friction losses. In addition to this, the changed operation conditions have lead to a changed loss behaviour of the pump and motors. This causes the energy demand from DC-link to be increased to 606 Wh, which corresponds to an increase of 1.9 % compared to the basic ECD system. 158 Wh of energy may be stored in the energy storage system for the ECD+, leading to a net demand of 448 Wh corresponding to an increase of 4 % compared to the basic ECD system.

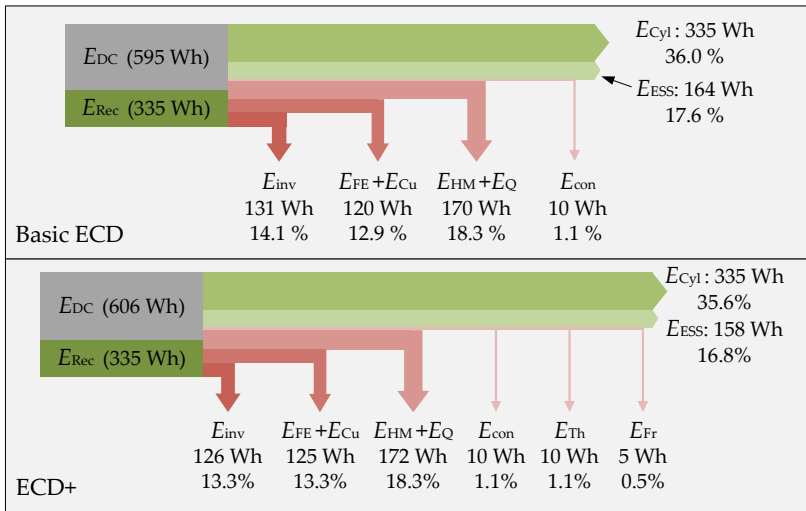


Fig. 4.12: Energy distribution of knuckle boom actuation system for the entire motion trajectory presented in Sec. 3.4.1 for the basic ECD system (no bootstrap reservoir or load holding valves) and the ECD+. Power sharing with the ECD system actuating the main cylinder is not included.

4.5 Chapter Summary and System Diagram

In this chapter the basic ECD technology has been matured such that it is found feasible for actuation of the knuckle boom cylinder. This system is

denoted ECD+ to indicate additional functionalities. It is found that the introduction of the load holding valves and the gasless bootstrap reservoir has increased the energy consumption of the ECD+ system. These additions are however necessary means in order to develop a drive system feasible for local installation and actuation of the knuckle boom cylinder. As the ECD+ system still offers a significant energy saving potential compared to the current valve-controlled actuation systems, it is found reasonable to continue with the ECD+ system. In the final chapters of this dissertation, dynamic models of the drive system are therefore developed in order to design control structures such that the motion of the cylinder piston as well as the locking mechanism may be controlled.

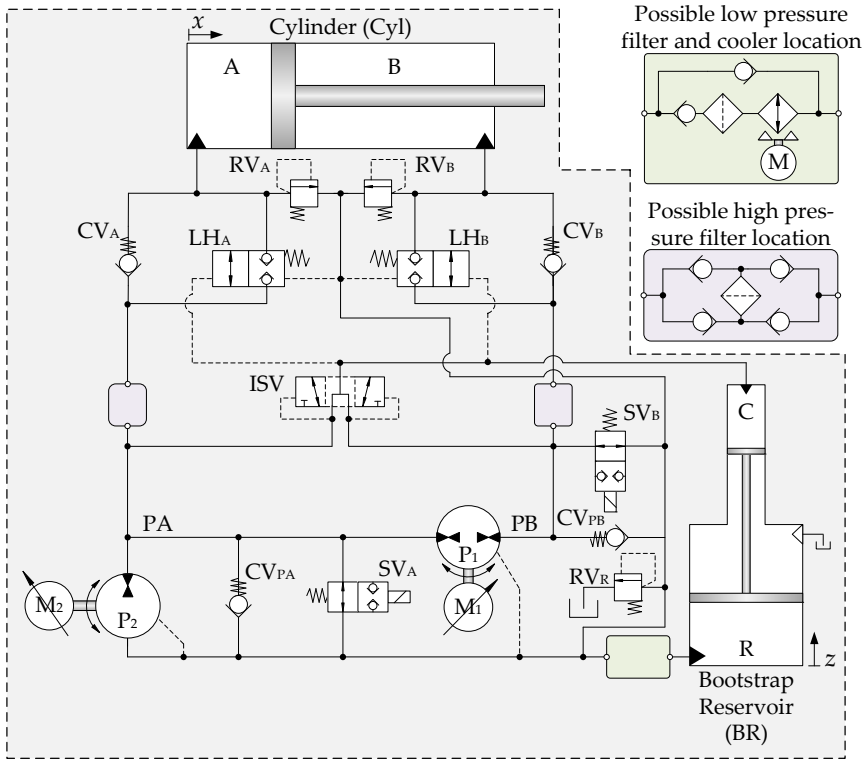


Fig. 4.13: Hydraulic diagram of the ECD+ system with bootstrap reservoir and load holding valves. Possible locations of oil filters and coolers are indicated.

The hydraulic diagram of the developed ECD+ system is shown in Fig. 4.13. Note that in addition to the already introduced components, two normally open 2/2-way solenoid operated on/off valves (denoted safety valves) are included. These are used to decompress the chambers PA and PB, which en-

sure that the load holding valves are rapidly closed in the event of electrical power loss. If not included the leakage behaviour of the pumps would determine the closing of the load holding valves. Additionally four anti-cavitation check valves and three pressure relief valves are implemented. Fig. 4.13 also shows possible locations of oil filter and coolers. The implementation of these auxiliary components are not studied further.

Tab. 4.2 shows the key information of the selected drive components according to Fig. 4.13.

Table 4.2: Main components of the proposed ECD+ system for actuation of the knuckle boom, according to the diagram in Fig. 4.13. [†]Note that the indicated dimensions of the bootstrap reservoir refer to the two piston diameters whereas the dimensions of the cylinder refer to the piston and rod diameter.

ID	Description	Model	Notes
M ₁	Permanent magnet	Bosch Rexroth	Rated torque: 133 Nm
M ₂	synchronous machine	MS2N13-D1BNC	Rated speed: 3000 RPM
P ₁	4Q hydraulic unit	Bosch Rexroth A10FZG025	Maximum speed: 3000 RPM 25 cm ³ /rev (fixed)
P ₂	2Q hydraulic unit	A10FZO028	28 cm ³ /rev (fixed)
RV _A RV _B RV _R	Pressure relief valve	Not specified	Cracking pressure: 315 bar Cracking pressure: 315 bar Cracking pressure: 5 bar
LH _A LH _B	Load holding valve	Sun Hydraulics DKJSXH	Δp : 7 bar at 375 L/min Pilot pressure: 20 bar
CV _A CV _B CV _{PA} CV _{PB}	Anti-cavitation check valves	Bosch Rexroth M-SR15KE02	Δp : 0.8 bar at 65 L/min Cracking pressure: 0.2 bar
ISV	Inverse shuttle valve	Bucher HOSV-10-N-O	Δp : 3.5 bar at 53 L/min Open transition
SV _A SV _B	2/2-way on/off valve Solenoid operated	Sun Hydraulics DTDFXH	Δp : 13 bar at 60 L/min Response time: 50 ms
Cyl	Differential cylinder	Not specified	250/180-2846 mm
BR	Bootstrap reservoir	Not specified	320/80 [†] -1153 mm Compensation volume: 87 L

Note that for the maximum allowed pressure of 315 bar the ideal pump torque is 140 Nm. According to Tab. 4.2 the rated or continuous torque of the motors is 133 Nm, showing that these are rather conservatively dimensioned, and there is a potential for downsizing in further design iterations.

Chapter 5

Dynamic System Modelling

Before the simulation model of the ECD+ system is derived, an example showing the importance of using mass flows for modelling closed hydraulic systems is given.

5.1 General Considerations on Modelling of Closed Circuit Hydraulic Systems

Consider the simple hydraulic circuit in Fig. 5.1, used as an example in this section only. It consists of two equally dimensioned hydraulic cylinders each actuating a mass against an external force F_{ext} . The cylinder rod side chambers are vented to the atmosphere, while the piston chambers are connected to each other by a pump and two orifices.

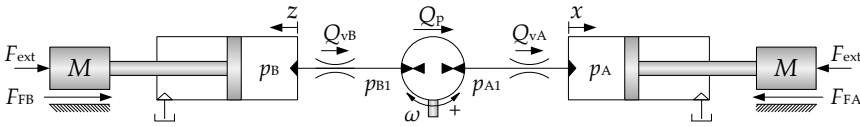


Fig. 5.1: Architecture used as a simple example for showing the importance of using mass flow models for modelling closed hydraulic circuits.

The pressure and motion dynamics of the system is modelled as:

$$\dot{p}_A = \frac{\beta_A}{V_0 + \dot{x}A_A} (Q_{vA} - \dot{x}A_A) \quad \dot{p}_{A1} = \frac{\beta_{A1}}{V_0} (Q_p - Q_{vA}) \quad (5.1)$$

$$\dot{p}_B = \frac{\beta_B}{V_0 + \dot{z}A_A} (-Q_{vB} - \dot{z}A_A) \quad \dot{p}_{B1} = \frac{\beta_{B1}}{V_0} (-Q_p + Q_{vB}) \quad (5.2)$$

$$\ddot{x} = \frac{1}{M} (p_A - F_{\text{ext}} - B\dot{x}) \quad \ddot{z} = \frac{1}{M} (p_B - F_{\text{ext}} - B\dot{z}) \quad (5.3)$$

where β_\bullet is the oil bulk modulus, V_0 is the initial volume of the control volumes and Q_{vA} , Q_{vB} are orifice volume flows. Q_p is the pump volume flow, which is modelled ideally as $Q_p = \omega D_p$ with ω being the shaft speed and D_p the pump displacement. The friction forces F_{FA} and F_{FB} are modelled as viscous friction only, using the viscous friction coefficient, B .

5.1.1 Valve Flows

For large pressure drops across the orifices, the volume flows Q_{vA} and Q_{vB} , are modelled using the orifice equation, which are derived under the assumption that viscous fluid friction losses are neglectable. According to [105, 106] using the orifice equation for modelling dynamic systems, may cause numerical issues for ODE-solvers when the pressure difference across the valve approaches 0 Pa. This may lead to infinite first order derivatives of the flow with respect to pressure. To reduce throttling losses the valves used in ECD systems, e.g. for load holding, are usually characterised by large flow gains, such that the pressure drops across the valves are close to 0 Pa. From a physical point of view it is also sensible not to use the orifice equation at low pressure drops, as the pressure drop (losses) is here mainly caused by viscous fluid friction. At low pressure drops, i.e. low Reynolds numbers, the volume flow is modelled as a laminar flow, meaning that flow is a linear function of the pressure drop [107]. A two-regime flow model is therefore utilised where a transition pressure (p_t) determines which model to use. To ensure that the volume flow and the first derivative is identical at p_t , a polynomial approach is utilised, i.e. the flow model below the transition pressure consists of a linear and second order term, according to [107]:

$$Q = \begin{cases} y \frac{Q_{\text{nom}}}{\sqrt{\Delta p_{\text{nom}}}} \sqrt{|\Delta p|} \text{sign}(\Delta p) & \text{for } \Delta p \geq p_t \\ y \left(\frac{3 Q_{\text{nom}} \Delta p}{2\sqrt{\Delta p_{\text{nom}} p_t}} - \frac{Q_{\text{nom}} \Delta p |\Delta p|}{2\sqrt{\Delta p_{\text{nom}} p_t^3}} \right) & \text{for } \Delta p < p_t \end{cases} \quad (5.4)$$

where y is the normalised valve opening, which in this example is 1. Δp is the pressure drop across the valve, Q_{nom} is the nominal volume flow at the nominal pressure drop Δp_{nom} .

In Fig. 5.2 it is visualised how the proposed two-regime flow model compares to the turbulent flow (orifice) model.

5.1. General Considerations on Modelling of Closed Circuit Hydraulic Systems

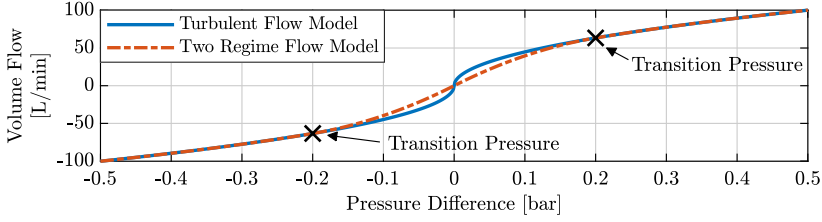


Fig. 5.2: Volume flows modelled by the orifice/turbulent flow model and the two-regime flow model from Eq. 5.4

5.1.2 Fluid Properties

The bulk modulus of the oil is modelled using the temperature independent fluid properties derived in paper F. Here the thermal expansion of the fluid is neglected ($\alpha = 0$) such that the density of the oil-air mixture is constant for varying mixture temperatures. Hydraulic oil expands approximately 3.5 % for a temperature increase of 50 K (Paper F). From paper F the temperature independent density and bulk modulus of the oil-air mixture are:

$$\rho = \frac{(\rho_{0F} + (\rho_{0A} - \rho_{0F})\epsilon)(\beta_{0F} + p - p_0)p}{(p_0 - \beta_{0F})(p - p_0)\epsilon + \beta_{0F}p} \quad (5.5)$$

$$\beta = \frac{p((p_0 - \beta_{0F})(p - p_0)\epsilon + \beta_{0F}p)(\beta_{0F} + p - p_0)}{(p_0^2 - (\beta_{0F} + 2p)p_0 + p^2)(p_0 - \beta_{0F})\epsilon + \beta_{0F}p^2} \quad (5.6)$$

where ρ_{0F} , ρ_{0A} , β_{0F} is the oil density, air density and oil bulk modulus respectively at pressure p_0 . ϵ is the volumetric content of free air at p_0 , and p is the current absolute pressure. Note that this model assumes the fluid density to be a function of pressure and approximates this with a first order Taylor series expansion as elucidated in Paper F. Furthermore the air is modelled as an ideal gas, such that the air density may be found as $\rho_A = p(RT_0)^{-1}$. Here R is the gas constant for air, T_0 is the constant temperature. A detailed derivation of the fluid properties is found in Paper F.

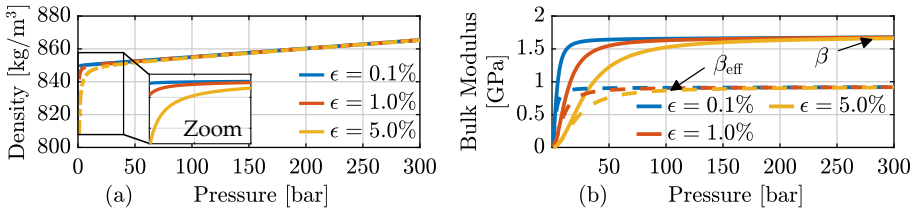


Fig. 5.3: Modelled density and bulk modulus of fluid-air mixture as a function of pressure. (a) Density. (b) β is evaluated using Eq. 5.6, while β_{eff} includes mechanical elasticity.

In Fig. 5.3, the oil-air mixture densities and bulk moduli are given as a

function of pressure and for three volumetric air contents. In this dissertation a volumetric content of free air at atmospheric pressure of 1 % is used. In Fig. 5.3b, the effective bulk modulus β_{eff} is also given, which includes mechanical elasticity introduced in Eq. 5.9 on page 96.

5.1.3 Simulation Results

No shaft speed dynamics is included and the shaft speed is found as:

$$\omega = K_x(x_{\text{ref}} - x) + K_{\dot{x}}\dot{x}_{\text{ref}} \quad (5.7)$$

where $K_x, K_{\dot{x}}$ are controller parameters and $x_{\text{ref}}, \dot{x}_{\text{ref}}$ are position and velocity references, such that one of the cylinder pistons is feedback controlled. The parameters used in this example study, is given in the Tab. A.5 on page 257. x_{ref} is a sinusoidal position reference with a frequency of 0.2 Hz. The simulated position and chamber pressures are given in Fig. 5.4.

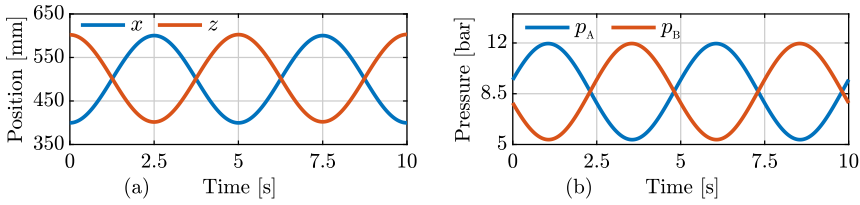


Fig. 5.4: (a) Simulated piston positions. (b) Simulated chamber pressures.

In the first 10 s of the simulation, Fig. 5.4a shows that the piston positions equal each other with a phase shift of 180°, which is as expected. This is also true for the chamber pressures in Fig. 5.4b. Note that the pressures p_{A1} and p_{B1} almost resembles the shown pressures p_A and p_B due to a large flow gain of the orifices. If continuing the simulation, here for 60 minutes, unanticipated behaviour occurs. The piston position of the uncontrolled cylinder is drifting, as shown in Fig. 5.5a. It can be shown that the pressures are not drifting, i.e. the position drift cannot be explained by compression flows. Thermal expansion is not included, so this cannot be the explanation either.

By evaluating the total oil-air mass in the system it can be observed that the oil mass increases in Fig. 5.5b. This happens despite the system is sealed from the surroundings, i.e. the simulation violates the conservation of mass principle. This happens because the pressure dynamics is modelled using a compressible fluid leading to a finite bulk modulus. The transfer of oil through the orifices and the pump however assumes the density to be constant leading to an infinite bulk modulus (incompressible fluid). This means

5.1. General Considerations on Modelling of Closed Circuit Hydraulic Systems

that the oil volume is preserved in the fluid transfer process, but as the densities in the control volumes are not equal, mass is not preserved. As the changes in density is small as pressure increases, this does not constitute a significantly problem in terms of accuracy for most short time simulations. However, if simulating for longer, e.g. to simulate thermal behaviour, this may cause problems such as drifting accumulator pressures if a gas-charged accumulator is used, or position drift as seen here.

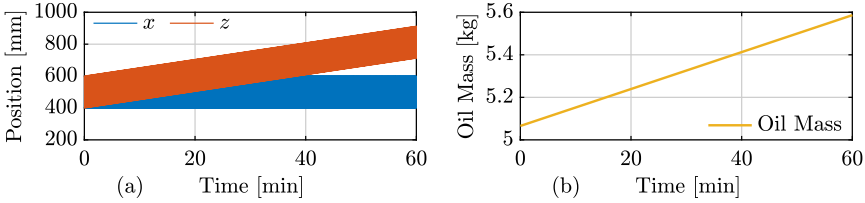


Fig. 5.5: (a) Simulated piston positions. (b) Simulated oil-air mixture mass.

For the orifice equation, the mass-drift problem occurs because the oil density is assumed equal upstream and downstream the orifice as well as in the vena-contracta. This leads to significant simplifications of the Bernoulli equation, laying the theoretical foundation of the orifice equation. For a complete theoretical solution of the mass-drift problem, one may want to reformulate the orifice equation without using the incompressibility assumption. However, as the mass-drift problem is primarily a concern in long term simulations and does not affect *short term accuracy* significantly, this problem is probably primarily of academic interest. This is supported by the simple observation that volume flow models derived by assuming incompressible fluids, have been used for decades to simulate hydraulic systems and for model based controller design with satisfying results in terms of pressure and motion dynamics. Therefore a very simple solution to the problem is proposed here to make the simulation models operational and stable for long term simulation usage. Instead of treating the components (orifices, pumps) as volume-preserving, they are modelled as mass-preserving by compensating the calculated volume flow by the average density in the adjacent chambers $\bar{\rho}$, as done in [108]:

$$\dot{m} = \bar{\rho}Q \quad (5.8)$$

Using Eq. 5.8 to calculate mass flows from the presented volume flow equations, a new simulation has been performed. Comparing the simulated pressures and piston speeds of this new model shows insignificant differences compared to the original volume flow formulation.

Fig. 5.6a shows no piston drifts during a 60 minutes simulation, while Fig. 5.6b shows that the oil-air mass is constant within numerical accuracy

during the entire simulation.

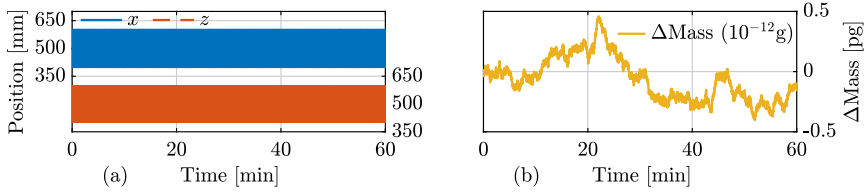


Fig. 5.6: Simulation performed using mass flow formulation of components. (a) Simulated piston positions. (b) Simulated oil-air mixture mass, given as the difference between current mass and initial mass ($\Delta\text{Mass} = \text{current mass} - \text{initial mass}$). Initial mass is 5.065 kg.

5.2 Model Simplifications and Assumptions

Focus is now turned towards modelling the ECD+ system used for actuation of the knuckle boom crane. All parameters used to model the dynamics of the ECD+ system are given in Tab. A.6 on page 257.

The main components of the ECD+ drive system are shown in Fig. 5.7. An electrical supply unit rectifies the grid supplied AC to DC. The DC-link further includes a capacitor to maintain a stable DC-voltage supply as well as a braking resistor to dissipate power if the DC-link voltage increases above a threshold. The latter may happen during braking operation of the electrical motors. As an alternative to dissipate excess power across a braking resistor, electrical energy storage systems such as lithium-ion batteries may be connected to the DC-link. Alternatively a regenerative supply unit capable of supplying power back to the AC grid may be used [109].

The shaft torques generated by the PMSMs are controlled using three phase motor inverters, which modulates the DC-voltage to appropriate motor phase voltages, \mathbf{u}_{ABC} , using field oriented control (FOC) techniques. The PMSMs are used to control the motion of the hydraulic pump units, in turn controlling

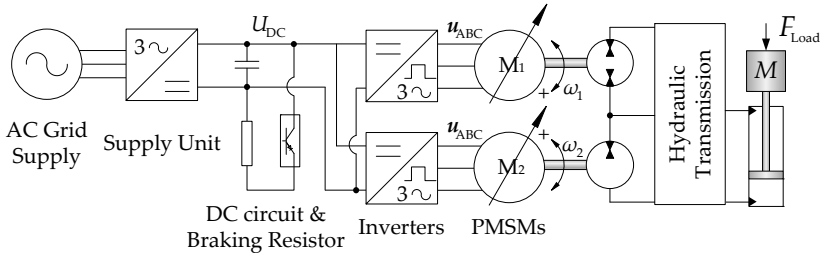


Fig. 5.7: General overview of the complete drive system.

5.2. Model Simplifications and Assumptions

the piston motion and pressure level of the hydraulic cylinder. During model formulation a few simplifications compared to the overview in Fig. 5.7 are introduced. It is assumed that a constant DC-voltage is available, such that the supply unit, capacitor and the braking resistor are not modelled. Even though the electrical grid on ships and offshore platforms currently are predominantly AC-grids, the authors in [110], spot a trend towards electrical DC-grids on ships and drilling rigs in the future. This is motivated by easier integration of variable-speed motor drives and electrical energy storage systems such as lithium-ion batteries, already being utilised on a few marine vessels and drilling rigs [111]. The voltage level of the DC-link is assumed to be $U_{DC} = 750$ V [109]. Furthermore the electrical circuits of the PMSM and the inverters are not modelled in the physical a,b,c -domain, but rather in the dq -domain. As such the modulation of the DC-voltage to the demanded dq -voltages is not considered, meaning that demanded dq -voltages are realised ideally. Fig. 5.8 visualises these simplifications to the electrical sub-models, and shows that model development may conveniently be divided into three main parts: electrical drive models, hydraulic transmission model and model of the load, i.e. the knuckle boom crane. The latter model was presented in Sec. 2.2

From Fig. 5.8 it is furthermore illustrated that the drive system needs only to be supplied with DC-power and shaft speed references. The PMSM shaft torque references are generated by a speed control loop here included in the electrical drive models. Notice that in this work, the control task is to manipulate the hydraulic drive dynamics by a proper shaft speed reference,

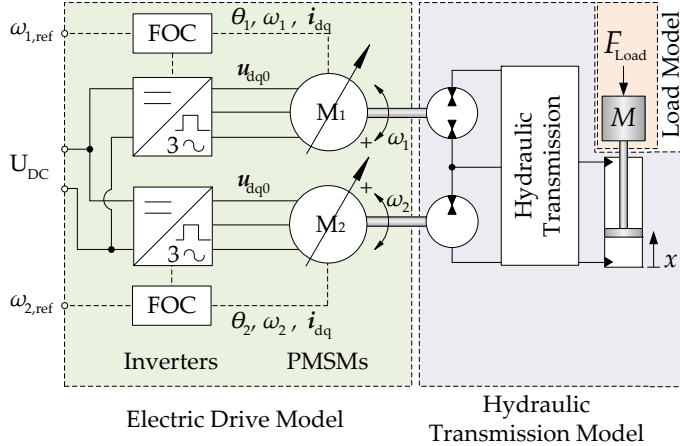


Fig. 5.8: Simplified model structure. During model establishment it is assumed that a constant DC-voltage is available. It is convenient to separate model development into: Electric Drive Model, Hydraulic Transmission Model and Load Model.

i.e. utilizing the conventional speed loop of variable-speed PMSM drive units. Alternatively, so-called secondary control approaches may be considered [64, 92, 112]. Here the conventional speed loop is not utilized, but the system dynamics are manipulated by proper shaft torque references.

The modelling task is thus to establish dynamic equations describing the behaviour of the drive system, when applying shaft speed references. This includes modelling of motion, temperature and pressure states, as well as modelling the power losses, such that energy consumption may be estimated. The outer control loops, i.e. calculating shaft speed references to obtain the desired drive behaviour are established in Chapter 6.

The assumptions made during model development are summarised as:

- DC-voltage is constant and motors are modelled in dq -frame only
- Modulation of DC-voltage to dq -frame is assumed ideal (no switching or modulation is modelled)
- Steady state component loss models are utilised
- Power consumption for valve actuation and sensors are neglected
- Cylinder and external leakages to surroundings are neglected
- Transmission line dynamics and pressure drops are neglected
- Volume changes caused by valve spool/seat movement are neglected
- Dissolved air in fluid is not released (mass ratio of free air is constant)
- Vaporisation of air or fluid are not included in fluid models
- Steady state pump models are used, i.e. no flow ripples are included
- Bootstrap reservoir is assumed to be horizontally oriented
- Heat transfer is assumed to be entirely natural convection and radiation
- Electric machines are thermally isolated from remaining system

5.3 Hydraulic Transmission Model

The modelling of the hydraulic transmission takes offset in the thermo-hydraulic modelling approach derived in Paper F. In this paper two model complexities are compared. The *benchmark* modelling approach was previously developed by the co-authors and documented in [71, 72]. This *benchmark* model, showed accurate results compared to experimentally obtained data. However, the parametrisation of this model requires accurate knowledge about system dimensions, oil flow paths etc. Alternatively, the *reduced* model is based on a coarse discretization of control volumes and assumes that oil temperature is uniform such that all components in contact with the

5.3. Hydraulic Transmission Model

oil are at the same temperature (i.e. infinite forced convection). This leads to a much simpler model structure, because only a single temperature state is needed. In paper F, a comparison shows that the *reduced* model still provided rather accurate results. Due to this and because detailed knowledge of the system dimensions are not available during this investigation phase, the *reduced* modelling approach is utilised in the remainder.

The simplified ECD+ hydraulic schematics used for model derivation is given in Fig. 5.9. Pressure relief valves are not included during model derivation as these are closed during nominal operation of the system.

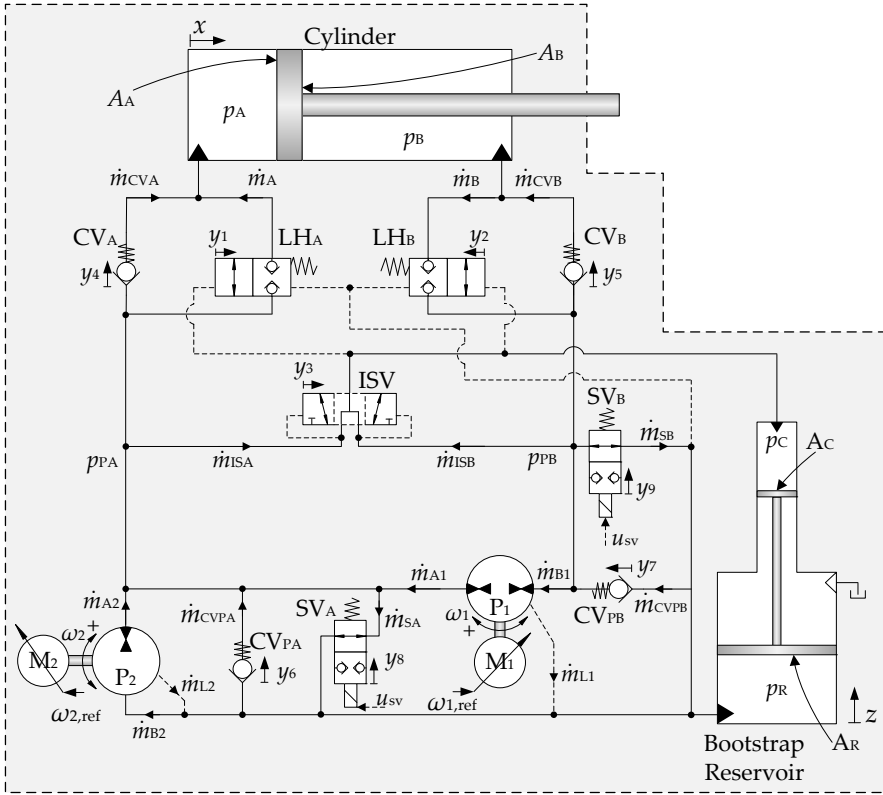


Fig. 5.9: Simplified diagram of the hydraulic transmission. Pressure relief valves are not included.

5.3.1 Pressure and Temperature Dynamics

The pressure and temperature dynamics of a lumped control volume including mechanical elasticity is derived in Paper F, as:

$$\begin{aligned}
 & \underbrace{\frac{\dot{p}V}{\beta}}_{\text{Compression of oil}} - \underbrace{\frac{\dot{m}}{\rho}}_{\text{Volume flow}} + \underbrace{\dot{V}_x}_{\text{Expansion due to movement}} + \underbrace{\dot{V}_x \frac{p-p_0}{\beta_{\text{mech}}}}_{\text{Expansion due to pressurisation of "new" volume}} + \underbrace{\frac{V_x}{\beta_{\text{mech}}} \dot{p}}_{\text{Expansion due to pressure change}} - \underbrace{\alpha V \dot{T}}_{\text{Thermal expansion}} = 0 \\
 & \dot{p} = \underbrace{\left(\frac{\beta \beta_{\text{mech}}}{\beta_{\text{mech}} + \beta \frac{\beta_{\text{mech}}}{\beta_{\text{mech}} + p - p_0}} \right)}_{\beta_{\text{eff}}} \left(\frac{\dot{m}}{\rho V} - \frac{\dot{V}_x}{V_x} + \alpha \dot{T} \right), \quad V = V_x \left(1 + \frac{p-p_0}{\beta_{\text{mech}}} \right) \\
 & \dot{T} = \frac{1}{mc_p} \left(\dot{Q} + \dot{W}_{\text{shaft}} + \sum_i \dot{m}_i (h_i - h) + T \alpha V \dot{p} \right) \quad (5.9)
 \end{aligned}$$

where m , \dot{m} , \dot{Q} , \dot{W}_{shaft} are the fluid mass in the control volume, the net mass flow into the control volume and the net rate of heat flow and shaft work transferred to and done on the control volume. T and p are the temperature and absolute pressure of the control volume, with V_x being the uncompressed volume i.e. the volume at p_0 and V the expanded volume including mechanical elasticity. ρ , α , c_p are the density, the thermal expansion coefficient and the specific heat of the fluid in the control volume. $\sum_i \dot{m}_i (h_i - h)$ is the sum of inlet mass flows times the difference in specific enthalpy of the fluid in the control volume, h , and of the incoming fluid, h_i . i is used to index the number of incoming fluid flows. The specific enthalpy is calculated based on the pressure and temperature as shown in Paper F. β and β_{eff} are visualised in Fig. 5.3b on page 89 and are the bulk modulus of the oil-air mixture and the effective bulk modulus including mechanical compliance. β_{eff} is calculated based on the tuning parameter β_{mech} , where a large value of β_{mech} corresponds to a stiff volume. In this study with $\beta_{\text{mech}} = 2 \text{ GPa}$ is used, corresponding to a volume expansion of 1 % at 200 bar.

As mentioned previously, the current model is based on the *reduced* model formulation in Paper F, and assumes the temperature of the system to be uniform. Only a single temperature state is therefore included, which is conveniently done by neglecting the dynamic coupling of the pressure and temperature dynamics in Eq. 5.9. This may be done without sacrificing much accuracy as shown in [113]. The previously defined fluid density and bulk modulus in Eqs. 5.5 and 5.6 lead to a thermal expansion coefficient of $\alpha = 0$, such that the dynamic couplings are neglected. This simplifies model development significantly, as the number of thermal resistances to consider reduces drastically. However, the price to pay for this simplification, is that the

5.3. Hydraulic Transmission Model

small piston movement of the bootstrap reservoir caused by thermal expansion of the fluid is not modelled. Furthermore, is the individual temperature distribution of the system components and oil volumes not modelled. However both of these are found to be small for the system modelled in Paper F justifying the simplification made here.

Thus, the pressure dynamics of the six control volumes from Fig. 5.9 is:

$$\dot{p}_A = \beta_{\text{eff},A} \left(\frac{\dot{m}_A + \dot{m}_{\text{CVA}}}{\rho_A V_A} - \frac{\dot{x}A_A}{V_{Ax}} \right) \quad V_{Ax} = V_{0A} + xA_A \quad V_A = V_{Ax} \left(1 + \frac{p_A - p_0}{\beta_{\text{mech}}} \right) \quad (5.10)$$

$$\dot{p}_B = \beta_{\text{eff},B} \left(\frac{\dot{m}_{\text{CVB}} - \dot{m}_B}{\rho_B V_B} + \frac{\dot{x}A_B}{V_{Bx}} \right) \quad V_{Bx} = V_{0B} - xA_B \quad V_B = V_{Bx} \left(1 + \frac{p_B - p_0}{\beta_{\text{mech}}} \right) \quad (5.11)$$

$$\dot{p}_C = \beta_{\text{eff},C} \left(\frac{\dot{m}_{\text{ISA}} + \dot{m}_{\text{ISB}}}{\rho_C V_C} + \frac{\dot{z}A_C}{V_{Cx}} \right) \quad V_{Cx} = V_{0C} - zA_C \quad V_C = V_{Cx} \left(1 + \frac{p_C - p_0}{\beta_{\text{mech}}} \right) \quad (5.12)$$

$$\dot{p}_{PA} = \beta_{\text{eff},PA} \left(\frac{\dot{m}_{A1} + \dot{m}_{A2} + \dot{m}_{\text{CVPA}} - \dot{m}_{SA} - \dot{m}_{\text{ISA}} - \dot{m}_{\text{CVA}} - \dot{m}_A}{\rho_{PA} V_{PA}} \right) \quad (5.13)$$

$$\dot{p}_{PB} = \beta_{\text{eff},PB} \left(\frac{\dot{m}_B + \dot{m}_{\text{CVPB}} - \dot{m}_{B1} - \dot{m}_{\text{SB}} - \dot{m}_{\text{ISB}} - \dot{m}_{\text{CVB}}}{\rho_{PB} V_{PB}} \right) \quad (5.14)$$

$$V_{PA} = V_{0PA} \left(1 + \frac{p_{PA} - p_0}{\beta_{\text{mech}}} \right) \quad V_{PB} = V_{0PB} \left(1 + \frac{p_{PB} - p_0}{\beta_{\text{mech}}} \right) \quad (5.15)$$

$$\dot{p}_R = \beta_{\text{eff},R} \left(\frac{\dot{m}_{SA} + \dot{m}_{\text{SB}} + \dot{m}_{L1} + \dot{m}_{L2} - \dot{m}_{B2} - \dot{m}_{\text{CVPA}} - \dot{m}_{\text{CVPB}}}{\rho_R V_R} - \frac{\dot{z}A_z}{V_{Rx}} \right) \quad (5.16)$$

$$V_{Rx} = V_{0R} + zA_R \quad V_R = V_{Rx} \left(1 + \frac{p_R - p_0}{\beta_{\text{mech}}} \right) \quad (5.17)$$

where A_* , \dot{m}_* , V_{0*} are areas, mass flows according to Fig. 5.9 and initial volumes. The temperature dynamics of the uniform system temperature is given as:

$$\dot{T}_{\text{sys}} = \frac{1}{C_{p,\text{sys}}} \left(\dot{Q}_{\text{losses}} - \dot{Q}_{\text{amb}} + \dot{H}_{\text{sys}} \right) \quad C_{p,\text{sys}} = m_{\text{oil}} c_{p,\text{oil}} + m_{\text{steel}} c_{p,\text{steel}} \quad (5.18)$$

where m_{oil} , m_{steel} are the oil and steel mass of the system and $c_{p,\text{steel}}$, $c_{p,\text{oil}}$ the specific heat of steel and oil modelled as linear functions of system temperature as given in Paper F. \dot{Q}_{losses} is the frictional losses of the cylinder and pumps, and \dot{Q}_{amb} is the rate of heat transferred from the system to the ambience by natural convection and radiation. \dot{H}_{sys} is the sum of enthalpy flow rates occurring with the mass transfer to the control volumes. \dot{H}_{sys} inherently accounts for throttling losses, such that these need not to be included in \dot{Q}_{losses} . The modelling of the mass flows (\dot{m}), enthalpy flow rate (\dot{H}_{sys}) and convection and radiation heat flow rate (\dot{Q}_{amb}) is presented in appendix D.

The valve flows are modelled according to the two-regime mass flow model presented in Eqs. 5.4 and 5.8. The pump model is in close resemblances with the model used in Paper F and reuses the steady state losses presented in Fig. 3.2 on page 41. The opening dynamics of the valves is modelled as first order linear systems.

In terms of thermal behaviour it is worth mentioning that it is assumed that the electric motors are thermally isolated from the remaining system. This is done because the selected electric motors are cooled by a fan (forced convection), and are as such dimensioned to stay within its temperature limits for the experienced loadings. This means that neither the motor losses, the heat transfer to the remaining system nor the heat transferred to the ambience by ventilation are included in the temperature dynamics in Eq. 5.18. Additionally, the conductive heat transfer occurring between the system and the crane structure and the forced convection to the ambience caused by movement or wind is not included. As such only natural convection and radiation heat transfer rates from the knuckle boom cylinder, the bootstrap reservoir, the pumps and the hydraulic manifold to the ambience are included in \dot{Q}_{amb} , which is a conservative estimate. To simplify the radiation analysis all surfaces are assumed to be grey diffuse surfaces (emissivity independent of wavelength and direction) with an emissivity of $\epsilon = 0.8$ for all surfaces, as a conservative estimate for coated, varnished or painted surfaces [114].

In further design iterations it may be beneficial to include the effect of the motor fans to guide air flows across the hydraulic manifold, bootstrap reservoir or cylinder to improve the thermal design.

5.3.2 Motion Dynamics and Friction Modelling

The linear force exerted on the crane structure from the knuckle boom cylinder, in Fig. 5.9, is calculated by:

$$F_{\text{cyl2}} = p_A A_A - p_B A_B - p_0 (A_A - A_B) - F_{\text{Fric},x} \quad (5.19)$$

where p_0 is the atmospheric pressure and the cylinder friction $F_{\text{Fric},x}$ is modelled by a Stribeck curve as:

$$F_{\text{Fric},x} = \left(F_{C,x} + (F_{S,x} - F_{C,x}) e^{\frac{-|\dot{x}|}{v_{\text{sw}}}} \right) \tanh(\gamma_F \dot{x}) + B_x \dot{x} \quad (5.20)$$

where $F_{C,x}$, $F_{S,x}$ are Coulomb and static friction parameters, v_{sw} is a Stribeck curve decay parameter, γ_F is a directional switching parameter and B_x is a viscous friction coefficient. The friction parameters $F_{C,x}$, $F_{S,x}$, B_x has been obtained by scaling these linearly with the circumference of the piston and rod from a validated friction model of a smaller cylinder [51].

To utilise the dynamic knuckle boom crane model derived in Sec. 2.2 on page 32, the linear cylinder force is mapped to an external torque by Eq. 2.13 on page 35. Note that only cylinder friction according to Eq. 5.20 is included in the dynamic model. The cylinder position and velocities (x, \dot{x}) used in the continuity equations 5.10 and 5.11 are calculated from the simulated generalised coordinates using the formulae introduced in Sec. 2.2.

The motion dynamics of the bootstrap reservoir pistons is modelled by assuming the bootstrap reservoir to be constantly oriented horizontally, even though orientation changes with the movement of the booms. However, as the mass of the moving bootstrap pistons is small, the gravitational load is small compared to the pressure forces even for a vertically oriented bootstrap reservoir:

$$\ddot{z} = \frac{1}{M_z} (p_R A_R - p_C A_C - p_0 (A_R - A_C) - F_{\text{Fric},z}) \quad (5.21)$$

where M_z , p_0 and $F_{\text{Fric},z}$ are the moving mass, the atmospheric pressure and the friction force. As the bootstrap piston moves with a small velocity and stick-slip phenomenons potentially lead to reservoir pressure oscillations it is desired to use sealing systems optimised for low speed operation. Several manufacturers offer piston sealing solutions featuring *"no stick-slip effect"* [115] and *"minimal break-away and dynamic friction and no stick-slip tendency ensures uniform motion even at low speeds"* [116]. The friction force of the bootstrap reservoir pistons is thus modelled as:

$$F_{\text{Fric},z} = F_{C,z} \tanh(\gamma_F \dot{z}) + B_z \dot{z} \quad (5.22)$$

where $F_{C,z}$ is the Coulomb friction and B_z is a viscous friction coefficient.

5.4 Electrical Drive Models

In the appended papers C, D, E, the electrical motor dynamics is modelled as a linear second order system, without considering physically motivated models. In this dissertation the PMSM is modelled in the dq -reference frame to include the current dynamics and current dependent losses.

The current dynamics is given as [117]:

$$\frac{d}{dt} i_d = \frac{u_d - R i_d + P \omega L_q i_q}{L_d} \quad \frac{d}{dt} i_q = \frac{u_q - R i_q - P \omega (L_d i_d + \lambda_{\text{pm}})}{L_q} \quad (5.23)$$

where u_q , u_d and i_q , i_d are q -axis and d -axis voltages and currents. R is the stator resistance, P is the number of pole pairs, ω is the mechanical rotor speed and λ_{pm} is the flux linkage linking the rotor magnets with the stator. L_q and L_d are q -axis and d -axis inductances respectively.

The electro-magnetic motor torque (τ_{em}) and shaft dynamics is given as:

$$\tau_{em} = \frac{3}{2}P \left(\lambda_{pm} i_q + (L_d - L_q) i_d i_q \right) \quad \dot{\omega} = \frac{\tau_{em} - \tau_L}{J_{shaft}} \quad (5.24)$$

where J_{shaft} is the total shaft inertia and τ_L is the pump load torque.

The dq -currents are controlled by their voltages using PI-controllers as shown in [64]:

$$u_d = \omega_1 L_d e_d + \omega_1 R \bar{e}_d - L_q i_q \omega P \quad \dot{e}_d = e_d = i_{d,ref} - i_d \quad (5.25)$$

$$u_q = \omega_1 L_q e_q + \omega_1 R \bar{e}_q + (L_d i_d + \lambda_{pm}) \omega P \quad \dot{e}_q = e_q = i_{q,ref} - i_q \quad (5.26)$$

The voltages are limited to $\sqrt{u_d^2 + u_q^2} < 0.71 U_{DC}$ according to [118]. The modulation of the DC-voltage to the demanded dq -voltages is not considered, and it is as such assumed these are realised ideally.

In this work a surface mounted PMSM is utilised ($L_q = L_d$) such that the current references are conveniently chosen as in [64]:

$$i_{d,ref} = 0 \quad i_{q,ref} = \frac{2}{3} \frac{\tau_{em,ref}}{P \lambda_{pm}} \quad (5.27)$$

The torque dynamics may be established using the approach from [92] by combining the q -axis current dynamics in Eq. 5.23, the torque relation in Eq. 5.24 the control voltages in Eq. 5.26 and the q -axis current reference in Eq. 5.27:

$$\dot{\tau}_{em} = \frac{3}{2} P \lambda_{pm} \frac{d}{dt} i_q = \frac{3}{2} P \lambda_{pm} \left(\omega_1 e_q + \omega_1 \frac{R}{L_q} \bar{e}_q - \frac{R}{L_q} i_q \right) \quad (5.28)$$

$$\dot{e}_q = i_{q,ref} - i_q = \frac{2}{3 P \lambda_{pm}} \tau_{em,ref} - i_q = \frac{2}{3 P \lambda_{pm}} (\tau_{em,ref} - \tau_{em}) \quad (5.29)$$

By Laplace transforming these linear equations and inserting Eq. 5.29 into Eq. 5.28 a first order linear transfer function relation between the torque reference and the motor torque is found [92]:

$$\frac{\tilde{\tau}_{em}(s)}{\tilde{\tau}_{em,ref}(s)} = \frac{\omega_1}{s + \omega_1} \quad (5.30)$$

where $\tilde{\bullet}$ denotes a change variable of state \bullet and s is the Laplace variable. ω_1 is the desired current/torque bandwidth. This is limited by the bandwidth of which the control voltages may be realised, i.e. limited by the switching frequency of the motor inverter. The switching frequency is typically no less than 4000 Hz (8000π rad/s) [64, 92]. To limit the dynamic impact of

5.4. Electrical Drive Models

the voltage bandwidth ω_l is selected to be a decade below the switching frequency, i.e. $\omega_l = 800\pi$ rad/s (400 Hz) [64, 92]. The dynamics in Eq. 5.30 is only realised in the case of known motor parameters to parameterise the current controller (L_d , L_q , R , λ_{pm} and ω).

The torque reference $\tau_{em,ref}$ is provided by a PI shaft speed controller as:

$$\tau_{em,ref} = K_{\omega P} e_\omega + K_{\omega I} \bar{e}_\omega + \hat{\tau}_L \quad (5.31)$$

$$\dot{\bar{e}}_\omega = e_\omega = \omega_{ref} - \omega \quad \hat{\tau}_L = D_p \Delta p \quad (5.32)$$

where $\hat{\tau}_L$ is the estimated load torque, $K_{\omega P}$, $K_{\omega I}$ are controller parameters and ω_{ref} is the reference shaft speed.

As mentioned in Sec. 5.2, the hydraulic drive dynamics is manipulated by appropriate shaft speed references. To simplify the system analysis and controller design in Chapter 6, the shaft speed dynamics is modelled as a linear first order system. This may be justified by a careful selection of the controller parameters $K_{\omega P}$ and $K_{\omega I}$ [64].

Consider the shaft speed dynamics (Eq. 5.24) including the shaft speed controller (Eq. 5.31) under the assumption that $\tau_{em} \approx \tau_{em,ref}$:

$$\dot{\omega} \approx \frac{\tau_{em,ref} - \tau_L}{J_{shaft}} = \frac{K_{\omega P} e_\omega + K_{\omega I} \bar{e}_\omega + \hat{\tau}_L - \tau_L}{J_{shaft}} \quad (5.33)$$

To parametrise the shaft speed controller, i.e. select parameters $K_{\omega P}$ and $K_{\omega I}$, consider the load torque τ_L being decomposed as:

$$\tau_L = \tau_T + B_{shaft} \omega + \tau_\delta \quad K_{\omega P} = \omega_\omega J_{shaft} \quad K_{\omega I} = \omega_\omega \hat{B}_{shaft} \quad (5.34)$$

where τ_T is the ideal or pressure induced torque ($\tau_T = D_p \Delta p$). B_{shaft} and \hat{B}_{shaft} are the true and estimated shaft viscous friction coefficient, and τ_δ is the additional or non-modelled torque losses. ω_ω is the desired closed loop speed bandwidth. As $\hat{\tau}_L = \tau_T$, the following transfer function relation from shaft speed reference and non-modelled shaft torque to shaft speed is given:

$$\tilde{\omega}(s) = \frac{\omega_\omega s + \omega_{n,\omega}^2}{s^2 + 2\omega_{n,\omega} \zeta_{n,\omega} + \omega_{n,\omega}^2} \tilde{\omega}_{ref}(s) - \frac{\omega_{n,\omega}^2 s}{s^2 + 2\omega_{n,\omega} \zeta_{n,\omega} + \omega_{n,\omega}^2} \frac{\tilde{\tau}_\delta(s)}{\hat{B}_{shaft} \omega_\omega} \quad (5.35)$$

$$\omega_{n,\omega} = \sqrt{\frac{\hat{B}_{shaft} \omega_\omega}{J_{shaft}}} \quad \zeta_{n,\omega} = \frac{J_{shaft} \omega_\omega + B_{shaft}}{2\sqrt{J_{shaft} \hat{B}_{shaft} \omega_\omega}} \quad (5.36)$$

The non-modelled shaft torque may be considered a disturbance to the closed loop shaft speed control loop that dies out eventually. Considering $\tilde{\tau}_\delta(s) = 0$, the simplified shaft dynamics is represented by a linear second order system with a zero placed at $s = -\omega_{n,\omega}^2 / \omega_\omega$. For the second order system it may

be seen that a large value of \hat{B}_{shaft} leads to an increased $\omega_{n,\omega}$ but a smaller damping ratio $\zeta_{n,\omega}$. In the event of $\hat{B}_{\text{shaft}} = B_{\text{shaft}}$, i.e. ideal parameter estimate, the choice of controller parameters in Eq. 5.34 leads to the closed loop shaft dynamics given in the absence of disturbances:

$$\frac{\tilde{\omega}(s)}{\tilde{\omega}_{\text{ref}}(s)} = \frac{\omega_{\omega}}{s + \omega_{\omega}} \quad (5.37)$$

Notice that these dynamics is obtained under the assumption that $\tau_{\text{em,ref}} \approx \tau_{\text{em}}$, which means that the closed loop speed bandwidth must be selected at least 5-10 times smaller than the torque bandwidth, i.e. $10 \omega_{\omega} \leq \omega_1$.

The presented simplifications are used subsequently for controller design purposes and dynamic analysis. For this purpose the simplified dynamics in Eq. 5.37 are represented in state-space form as:

$$\dot{\mathbf{x}}_{\text{u}} = \mathbf{A}_{\text{u}} \mathbf{x}_{\text{u}} + \mathbf{B}_{\text{u}} \mathbf{u}_{\text{ref}}, \quad \mathbf{y}_{\text{u}} = \mathbf{C}_{\text{u}} \mathbf{x}_{\text{u}} = \mathbf{x}_{\text{u}} \quad (5.38)$$

$$\mathbf{x}_{\text{u}} = [\tilde{\omega}_1 \quad \tilde{\omega}_2]^T, \quad \mathbf{u}_{\text{ref}} = [\tilde{\omega}_{1,\text{ref}} \quad \tilde{\omega}_{2,\text{ref}}]^T \quad (5.39)$$

$$\mathbf{A}_{\text{u}} = \begin{bmatrix} -\omega_{\omega} & 0 \\ 0 & -\omega_{\omega} \end{bmatrix}, \quad \mathbf{B}_{\text{u}} = \begin{bmatrix} \omega_{\omega} & 0 \\ 0 & \omega_{\omega} \end{bmatrix} \quad (5.40)$$

5.4.1 Power Losses

The power losses of the motor inverter, P_{inv} , and electric motor is modelled as steady state loss models, according to the procedure and equations used in the steady state modelling of the ECD in Sec. 3.2.2 on page 49.

5.5 Chapter Summary

A simple modelling example showed the importance of using a mass flow description of the fluid flows instead of a volume flow formulation. This eliminates the risk of mass drift causing cylinder piston or reservoir pressures to drift for long term simulations. A dynamic thermo-hydraulic simulation model has been derived, based on a simplified approach where only a single lumped system temperature is modelled as showed in Paper F. Simplified shaft speed dynamics has been established for system analysis and controller design purposes in the next chapter.

Chapter 6

System Analysis and Controller Design

In this chapter the controller structures used to control the ECD+ system are designed. In paper C, a control strategy for a system incorporating the load holding valves but without the bootstrap reservoir is developed. Paper E presents a control strategy for a system including a bootstrap reservoir but without load holding valves. Both strategies are based on controlling virtual states by virtual inputs to deal with the strong dynamic couplings between the physical inputs and the outputs desired to control. This strategy is re-used in this chapter where a unified approach for controlling the ECD+ system including both the load holding valves and a bootstrap reservoir is derived. The approaches in Papers C and E are based on tuning controllers using frequency responses, i.e. a numerical approach. In this chapter however, control laws are defined based on a few fundamental system parameters which for the most cases are easy obtainable. This is inspired by the method presented in [64] and is found to be more versatile and easier to implement and tune for commissioning personnel.

A schematic overview of the control structure is given in Fig. 6.1. Here it is seen that the combined system controller basically consists of four cascaded control loops, e.g. current controllers, shaft speed controllers, pressure controllers, and a motion controller. The two inner control loops, i.e. current and shaft speed controllers are not considered in this chapter, because basic control laws were outlined in Sec. 5.4. This means that the task is to manipulate the ECD+ system using the shaft speed references as inputs. In this dissertation this is done by designing two inner loop pressure controllers, controlling the load pressure and the minimum chamber pressure respec-

tively. Based on measurements of the system states the pressure controller coefficients are updated, but the structure of the controllers does not change. This is in contrast to the approach in paper C where controllers, controlling different outputs are disengaged or engaged depending on the desired operation mode. This is found to cause timing issues during closing and opening of the load holding valves. Another difference between the current approach and the approaches presented in the papers, is that in paper E, the pressure in the bootstrap reservoir chamber is controlled using a virtual weighted sum of the three system pressures. In the current approach the reservoir chamber pressure is controlled indirectly by controlling the pressure in the charge chamber. From the steady state solutions presented in Fig. 4.11 on page 83 this is found to keep the reservoir pressure within allowed limits, provided that the charge chamber pressure is appropriately controlled.

In motion operation mode the load pressure reference is generated by an

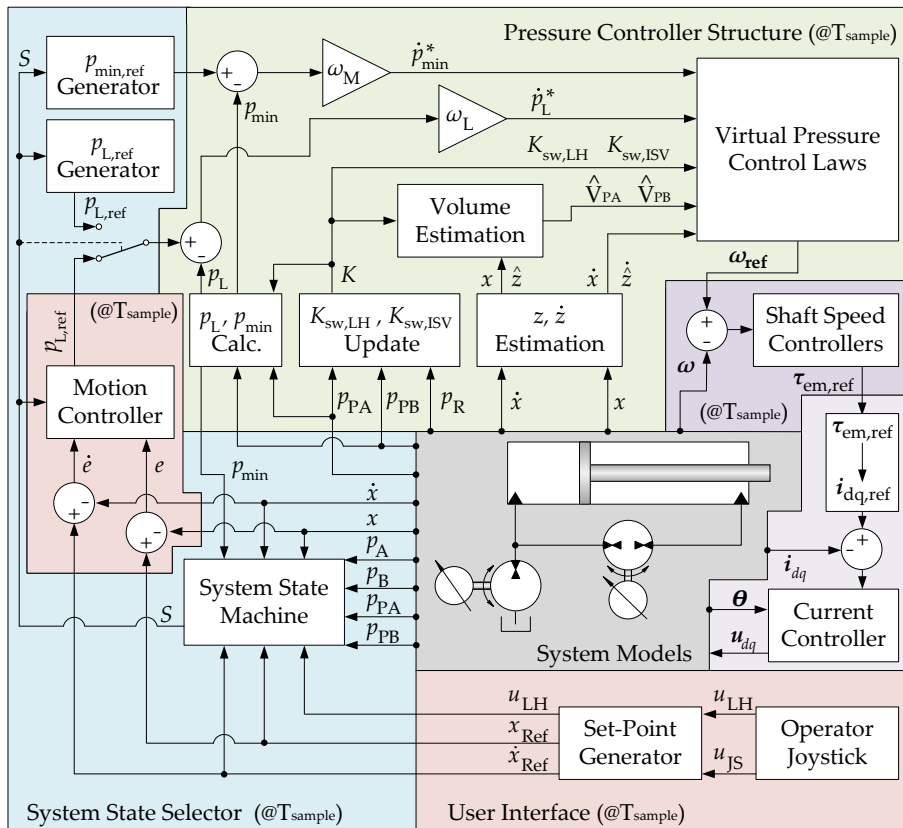


Fig. 6.1: Overview of system control loops.

outer loop motion controller, while the minimum chamber pressure reference is constant. Motion references are generated by filtering the operator joystick position as described in Sec. 3.4.1. The desired operation mode, i.e. motion or self-locking mode is determined based on the state of a switch outputting the binary variable u_{LH} . When engaging or disengaging the self-locking mode, the references to the pressure loop controllers are generated by the $p_{\text{L,ref}}$ and $p_{\text{min,ref}}$ generator blocks in Fig. 6.1. The references are generated to open or close the load holding valves appropriately. A *System State Selector* is designed to ensure smooth transition between operation modes.

In this chapter focus is on designing the *pressure controller structure* and the *motion controller* from Fig. 6.1. The *System State Selector* and associated pressure reference blocks are designed in Sec. 7.2. Fig. 6.1 shows that all control loops and reference generation blocks except the current controller are implemented discretely at the sample rate, T_{sample} . In Sec. 7.2 the controller structures are implemented in the simulation model with $T_{\text{sample}} = 1$ ms, but in this chapter discretization effects are neglected, because the bandwidths of the control loops to be derived are much lower than 1000 Hz.

During controller design it is assumed that all pressure states, the piston position, and piston velocity are available from measurements, in addition to the measurements required for current and shaft speed control. This means that neither the position or velocity of the bootstrap reservoir piston is measured. For practical realisation it may be considered to use proximity limit switches to stop system operation prior to hitting end-stops.

The chapter starts by presenting the simplified modelling equations of the system used throughout the chapter. Based on the simplified model the chapter continues with deriving and tuning the pressure controllers and the motion controller. The chapter is finalised by a numerical investigation of the *local* stability of the system.

6.1 Simplified Modelling Equations

To simplify the controller design and system analysis the modelling equations presented in Chapter 5 are significantly simplified. The electric motor speed dynamics is approximated by a linear first order system as showed in Sec. 5.4 and additionally the following simplifications are imposed on the hydraulic submodels:

- System temperature is constant (i.e. no temperature state included).
- Valve flow gains of load holding and inverse shuttle valves are assumed to be large, such that pressure drops across these valves are neglected. This means that the number of pressure states are reduced by three.

- The state of the load holding and inverse shuttle valves depend discretely on the system states, i.e. valves are either fully open (with no pressure drop) or fully closed (zero flow). Valve dynamics is neglected.
- Pump and valve leakages are neglected.
- Oil-air density is constant and equal in all control volumes (i.e. pump volume flow models are re-introduced)
- The pressure dependency of volumes is neglected
 $(V = V_x (1 + (p - p_0) / \beta_{\text{mech}}) = V_x)$.
- Mechanical elasticity is included in the bulk moduli expressions such that β_{eff} from Sec. 5.3.1 is still utilised.
- Static and Coulomb friction of the cylinder are neglected and thus only viscous friction is included.
- Anti-cavitation check valves are not included. Safety valves (SV_A and SV_B) are energised/closed.
- The equivalent cylinder loads are simplified compared to the model of the knuckle boom crane derived in Sec. 2.2.
 - Loads are evaluated by assuming remaining axes at standstill and zero acceleration.
 - The equivalent mass/inertia (M_{eq}) and gravitational load (F_G) are assumed constant.
 - The velocity dependent forces (denoted C_x) are neglected, due to insignificance compared to the gravitational load.

The simplifications lead to the following simplified modelling equations:

$$M_{\text{eq}}(\mathbf{x}) \ddot{x} = p_A A_A - p_B A_B - F_{\text{vel}}(\mathbf{x}, \dot{x}) \dot{x} - F_G(\mathbf{x}) - F_{\text{fric}}(\dot{x}) \quad \Downarrow \quad (6.1)$$

$$\ddot{x} = \frac{1}{M_{\text{eq}}} ((p_{\text{PA}} A_A - p_{\text{PB}} A_B - F_G) K_{\text{sw,LH}} - B_x \dot{x}) \quad (6.2)$$

$$\ddot{z} = \frac{1}{M_z} (p_R A_R - (K_{\text{sw,ISV}} p_{\text{PB}} + (1 - K_{\text{sw,ISV}}) p_{\text{PA}}) A_C - B_z \dot{z}) \quad (6.3)$$

$$\dot{p}_{\text{PA}} = \frac{\beta_{\text{eff,PA}}}{V_{\text{PA}}} \left(\omega_1 D_{\text{p},1} + \omega_2 D_{\text{p},2} - K_{\text{sw,LH}} \dot{x} A_A + (1 - K_{\text{sw,ISV}}) \dot{z} A_C \right) \quad (6.4)$$

$$\dot{p}_{\text{PB}} = \frac{\beta_{\text{eff,PB}}}{V_{\text{PB}}} \left(-\omega_1 D_{\text{p},1} + K_{\text{sw,LH}} \dot{x} A_B + K_{\text{sw,ISV}} \dot{z} A_C \right) \quad (6.5)$$

$$\dot{p}_R = \frac{\beta_{\text{eff,R}}}{V_R} \left(-\omega_2 D_{\text{p},2} - \dot{z} A_R \right), \quad V_R = V_{\text{OR}} + z A_R \quad (6.6)$$

$$V_{\text{PA}} = V_{\text{OPA}} + K_{\text{sw,LH}} (V_{\text{OA}} + x A_A) + (1 - K_{\text{sw,ISV}}) (V_{\text{OC}} - z A_C) \quad (6.7)$$

$$V_{\text{PB}} = V_{\text{OPB}} + K_{\text{sw,LH}} (V_{\text{OB}} - x A_B) + K_{\text{sw,ISV}} (V_{\text{OC}} - z A_C) \quad (6.8)$$

6.1. Simplified Modelling Equations

M_{eq} and F_G is the equivalent mass and gravitational load working on the cylinder and M_z is the moving mass of the bootstrap reservoir pistons. p_* and A_* are gauge pressures and areas corresponding to Fig. 6.2. B_x and B_z are viscous friction coefficients. $\beta_{eff,*}$ are the effective bulk modulus evaluated for each chamber including mechanical elasticity (refer to Sec. 5.3.1). V_* are chamber volumes calculated without including mechanical elasticity with $V_{0,*}$ being the initial chamber volume. ω_1 and ω_2 are pump shaft speeds. $D_{p,1}$ and $D_{p,2}$ are geometric pump displacements. $K_{sw,LH}$ and $K_{sw,ISV}$ are virtual discrete/binary switching conditions based on the pressure states as:

$$K_{sw,LH} = \begin{cases} 0 & \text{for } \min(p_{PA}, p_{PB}) - p_R < p_{CR,LH} \\ 1 & \text{for } \min(p_{PA}, p_{PB}) - p_R \geq p_{CR,LH} \end{cases} \quad (6.9)$$

$$K_{sw,ISV} = \begin{cases} 0 & \text{for } p_{PA} < p_{PB} \\ 1 & \text{for } p_{PA} \geq p_{PB} \end{cases} \quad (6.10)$$

Notice that $K_{sw,LH}$ and $K_{sw,ISV}$ as such are simple binary representations of the load holding and inverse shuttle valve openings respectively, neglecting valve dynamics and leakage flows. The equations above may therefore represent the system in both motion operation and self-locking mode with either p_{PA}

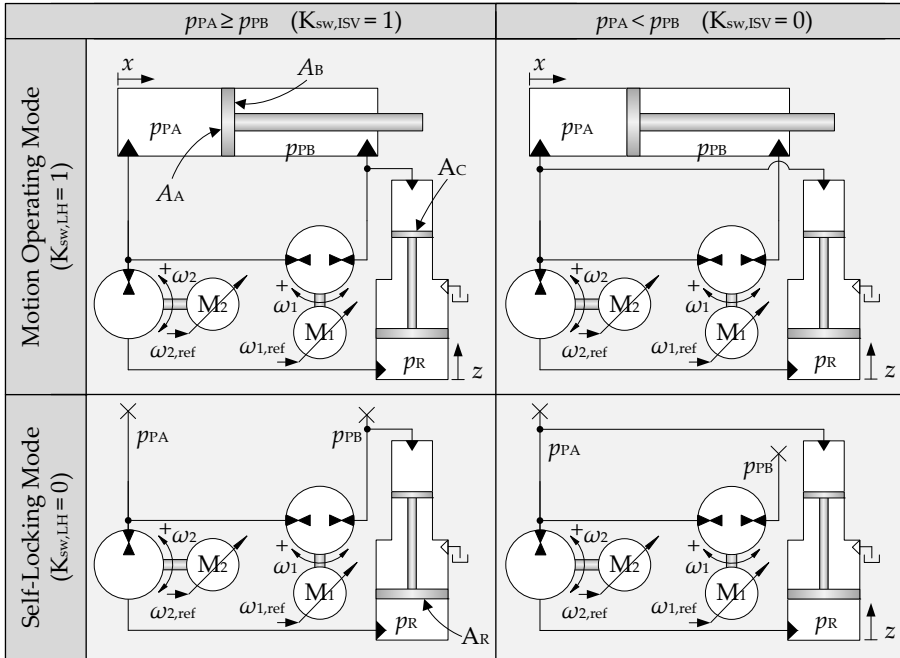


Fig. 6.2: The simplified modelling equations describe the system by four distinct model structures determined by the state of the virtual binary switching variables $K_{sw,LH}$ and $K_{sw,ISV}$.

or p_{PB} being the lower pressure, leading to four distinct model structures as visualised in Fig. 6.2.

Due to the switching of the load holding and the inverse shuttle valves the system is a switched system with state dependent switching events [119]. This is a subclass of hybrid models incorporating both continuous and discrete states. However, the current work is delimited from analysis of the switched system as such. This means that the subsequent analysis is carried out *locally* based individually on the four distinct system structures, without considering the discrete switching behaviour between these structures.

The equivalent mass M_{eq} and the gravitational load F_G are assumed constant during analysis and controller design. The variations for cylinder 2 experienced along the motion trajectory, (Sec. 3.4.1), are illustrated in Fig. 6.3. According to Fig. 6.3 the gravitational load ranges between -333 kN and 901 kN, while the equivalent mass ranges from 176 ton to 835 ton.

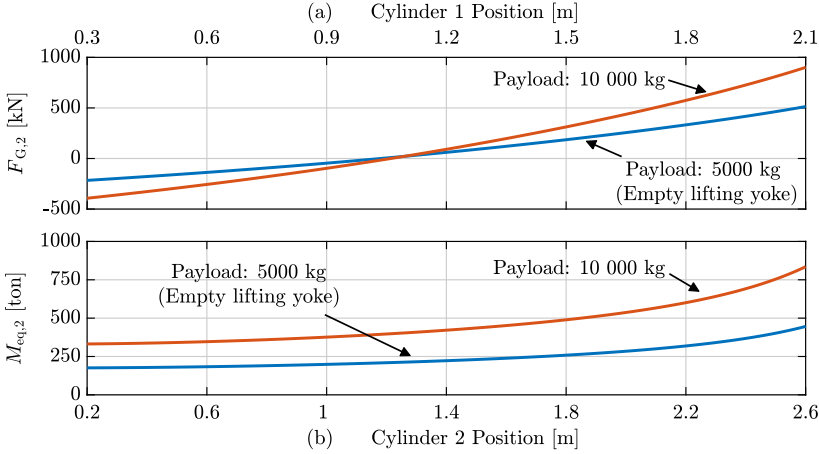


Fig. 6.3: Gravitational load and equivalent mass working on cylinder 2 during the trajectory. Illustrated for a total payload of 5 ton (empty lifting yoke) and 10 ton.

6.1.1 Linear Model

Linear system models are subsequently used to evaluate input-output cross couplings and for local stability analysis. In addition to the mentioned model simplifications, the linear models assume that:

- The effective bulk modulus is constant for each chamber in the considered linearisation point [32].
- The position dependency of volumes are neglected and the chamber volumes are assumed constant in the considered linearisation point [32].

6.1. Simplified Modelling Equations

The linear models are concerned with change variables, here denoted $\tilde{\bullet}$ of state \bullet . By a first order Taylor series expansion the linear counterparts of Eqs. 6.2 to 6.6 may be established:

$$\Delta\ddot{x} = \ddot{x} = \left. \frac{\partial\ddot{x}}{\partial M_{\text{eq}}} \right|_0 (M_{\text{eq}} - M_{\text{eq}0}) + \left. \frac{\partial\ddot{x}}{\partial p_{\text{PA}}} \right|_0 (p_{\text{PA}} - p_{\text{PA}0}) \quad (6.11)$$

$$+ \left. \frac{\partial\ddot{x}}{\partial p_{\text{PB}}} \right|_0 (p_{\text{PB}} - p_{\text{PB}0}) + \left. \frac{\partial\ddot{x}}{\partial F_{\text{G}}} \right|_0 (F_{\text{G}} - F_{\text{G},0}) + \left. \frac{\partial\ddot{x}}{\partial \dot{x}} \right|_0 (\dot{x} - \dot{x}_0) \quad (6.12)$$

$$= \frac{1}{M_{\text{eq}0}} (K_{\text{sw,LH}} (\tilde{p}_{\text{PA}} A_{\text{A}} - \tilde{p}_{\text{PB}} A_{\text{B}}) - B_{\text{x}} \dot{x}) \quad (6.13)$$

$$\ddot{z} = \frac{1}{M_{\text{z}}} (\tilde{p}_{\text{R}} A_{\text{R}} - K_{\text{sw,ISV}} \tilde{p}_{\text{PB}} A_{\text{C}} - (1 - K_{\text{sw,ISV}}) \tilde{p}_{\text{PA}} A_{\text{C}} - B_{\text{z}} \dot{z}) \quad (6.14)$$

$$\dot{\tilde{p}}_{\text{PA}} = \frac{\beta_{\text{eff,PA}0}}{V_{\text{PA}0}} (\tilde{\omega}_1 D_{\text{p},1} + \tilde{\omega}_2 D_{\text{p},2} - K_{\text{sw,LH}} A_{\text{A}} \dot{x} + (1 - K_{\text{sw,ISV}}) A_{\text{C}} \dot{z}) \quad (6.15)$$

$$\dot{\tilde{p}}_{\text{PB}} = \frac{\beta_{\text{eff,PB}0}}{V_{\text{PB}0}} (-\tilde{\omega}_1 D_{\text{p},1} + K_{\text{sw,LH}} A_{\text{B}} \dot{x} + K_{\text{sw,ISV}} A_{\text{C}} \dot{z}) \quad (6.16)$$

$$\dot{\tilde{p}}_{\text{R}} = \frac{\beta_{\text{eff,R}0}}{V_{\text{R}0}} (-\tilde{\omega}_2 D_{\text{p},2} - A_{\text{R}} \dot{z}) \quad (6.17)$$

where $M_{\text{eq}0}$, $\beta_{\text{eff},\bullet 0}$ and $V_{\bullet 0}$ are the equivalent mass, bulk modulus and volume evaluated in the linearisation point. Note that the discrete virtual switching parameters $K_{\text{sw,LH}}$ and $K_{\text{sw,ISV}}$ are evaluated based on the conditions in the linearisation point only. This means that the valves will stay fully open or closed, disregarding how the change variables $\tilde{\bullet}$ are developing.

The linear model of the system without electric motor (actuator) dynamics may be represented in state space form as:

$$\dot{\mathbf{x}}_{\text{p}} = \mathbf{A}_{\text{p}} \mathbf{x}_{\text{p}} + \mathbf{B}_{\text{p}} \mathbf{u}_{\text{p}}, \quad \mathbf{y}_{\text{p}} = \mathbf{C}_{\text{p}} \mathbf{x}_{\text{p}} \quad (6.18)$$

$$\mathbf{A}_{\text{p}} = \quad (6.19)$$

$$\begin{bmatrix} 0 & 1 & 0 & 0 & 0 & 0 \\ 0 & -\frac{B_{\text{x}}}{M_{\text{eq}0}} & 0 & \frac{A_{\text{A}}}{M_{\text{eq}0}} K_{\text{sw,LH}} & -\frac{A_{\text{B}}}{M_{\text{eq}0}} K_{\text{sw,LH}} & 0 \\ 0 & 0 & -\frac{B_{\text{z}}}{M_{\text{z}}} & -\frac{(1-K_{\text{sw,ISV}})A_{\text{C}}}{M_{\text{z}}} & -\frac{K_{\text{sw,ISV}}A_{\text{C}}}{M_{\text{z}}} & \frac{A_{\text{R}}}{M_{\text{z}}} \\ 0 & -\frac{\beta_{\text{eff,PA}0}A_{\text{A}}K_{\text{sw,LH}}}{V_{\text{PA}0}} & \frac{\beta_{\text{eff,PA}0}A_{\text{C}}(1-K_{\text{sw,ISV}})}{V_{\text{PA}0}} & 0 & 0 & 0 \\ 0 & \frac{\beta_{\text{eff,PB}0}A_{\text{B}}K_{\text{sw,LH}}}{V_{\text{PB}0}} & \frac{\beta_{\text{eff,PB}0}A_{\text{C}}K_{\text{sw,ISV}}}{V_{\text{PB}0}} & 0 & 0 & 0 \\ 0 & 0 & -\frac{\beta_{\text{eff,R}0}A_{\text{R}}}{V_{\text{R}0}} & 0 & 0 & 0 \end{bmatrix}$$

$$\mathbf{x}_p = [\tilde{x} \quad \dot{\tilde{x}} \quad \dot{\tilde{z}} \quad \tilde{p}_{PA} \quad \tilde{p}_{PB} \quad \tilde{p}_R]^T, \quad \mathbf{u}_p = [\tilde{\omega}_1 \quad \tilde{\omega}_2]^T \quad (6.20)$$

$$\mathbf{B}_p = \begin{bmatrix} 0 & 0 & 0 & \frac{\beta_{\text{eff},PA0}}{V_{PA0}} D_{p,1} & -\frac{\beta_{\text{eff},PB0}}{V_{PB0}} D_{p,1} & 0 \\ 0 & 0 & 0 & \frac{\beta_{\text{eff},PA0}}{V_{PA0}} D_{p,2} & 0 & -\frac{\beta_{\text{eff},R0}}{V_{R0}} D_{p,2} \end{bmatrix}^T \quad (6.21)$$

The subscript \bullet_p denotes the reduced or simplified *plant* model without actuator dynamics. The output matrix \mathbf{C}_p is used to select the relevant outputs. The linear plant model may be extended with the linear actuator dynamics from Sec. 5.4 according to:

$$\dot{\mathbf{x}}_E = \mathbf{A}_E \mathbf{x}_E + \mathbf{B}_E \mathbf{u}_{\text{ref}}, \quad \mathbf{y}_E = \mathbf{C}_E \mathbf{x}_E, \quad \mathbf{C}_E = [\mathbf{0} \quad \mathbf{C}_p] \quad (6.22)$$

$$\mathbf{x}_E = \begin{bmatrix} \mathbf{x}_u \\ \mathbf{x}_p \end{bmatrix}, \quad \mathbf{A}_E = \begin{bmatrix} \mathbf{A}_u & \mathbf{0} \\ \mathbf{B}_p \mathbf{C}_u & \mathbf{A}_p \end{bmatrix}, \quad \mathbf{B}_E = \begin{bmatrix} \mathbf{B}_u \\ \mathbf{0} \end{bmatrix} \quad (6.23)$$

where the subscript \bullet_E denotes the *extended* linear model.

In appendix E the extended linear model is compared to the nonlinear model defined in Chapter 5 and a full linear model including pump leakages and the three additional pressure states. It is concluded that important dynamics properties such as oscillation frequencies and damping ratios are captured with a satisfactory accuracy, for further analysis and controller development using the presented simplified modelling equations.

Subsequently, numerical evaluations of the linear models are used to evaluate system cross couplings, system responses etc. Unless otherwise noted two linearisation points are used throughout. To evaluate the system in motion operation mode, cylinder 2 (knuckle boom cylinder) moves at 20 mm/s in the linearisation point and the lower chamber pressure is defined to 28.8 bar (absolute). The remaining states in the linearisation point are calculated such that $\dot{\mathbf{x}}_E = 0$, except for the position state \tilde{x} . The position change variable \tilde{x} does not affect the dynamics and is only included in the linear model because a position controller is to be designed subsequently. Note however, that the position x in the linearisation point may severely affect system dynamics due to changed volume evaluations in the linearisation point. Volumes are here evaluated in the center position and the cylinder loads are evaluated with cylinder 1 fully extended and at rest using a payload, m_3 , of 10 ton.

In self-locking mode with load holding valves fully closed, the pressures in the linearisation point are chosen to $p_{PA0} = 5$ bar and $p_{PB0} = 3$ bar. Remaining states are selected such that $\dot{\mathbf{x}}_E = 0$.

6.2 Linear Coupling Analysis

The degree of dynamic cross couplings or interactions between system inputs and outputs are analysed by the concept of the linear Relative Gain Array

6.2. Linear Coupling Analysis

(RGA) [120]. RGA analyses are also performed in Papers C and E.

In a multi-variable system the RGA-number ($\text{RGA}_\#$) can be used to establish if the system can be regarded as a diagonal system, equivalently to indicate the severity of the off-diagonal elements (cross couplings). If a system is diagonal or close to diagonal, decentralised control approaches may yield satisfying results. Therefore an RGA analysis may be used to establish proper input-output pairings.

In the mentioned papers C and E, severe cross couplings between the inputs and the physical states have been identified. For now a linear cross coupling analysis is conducted between the physical inputs and virtual outputs being the load and the minimum chamber pressures:

$$p_L = p_{PA} - \alpha p_{PB} \quad (6.24)$$

$$p_{\min} = \min(p_{PA}, p_{PB}) = (1 - K_{\text{sw,ISV}}) p_{PA} + K_{\text{sw,ISV}} p_{PB} \quad (6.25)$$

By proper definition of the output matrix \mathbf{C}_p , the change variables of the load and minimum pressures \tilde{p}_L and \tilde{p}_{\min} may be analysed:

$$\mathbf{C}_p = \begin{bmatrix} \mathbf{0} & \mathbf{0} & \mathbf{0} & \mathbf{0} & \mathbf{0} & \mathbf{0} \\ 0 & 0 & 0 & 1 & -\alpha & 0 \\ 0 & 0 & 0 & (1 - K_{\text{sw,ISV}}) & K_{\text{sw,ISV}} & 0 \\ 0 & 0 & 0 & 0 & 0 & 0 \end{bmatrix} \quad (6.26)$$

The output of the extended linear model with virtual pressures as outputs is expressed in the Laplace domain by the transfer function matrix:

$$\mathbf{y}_E(s) = \mathbf{G}_E(s) \mathbf{u}_{\text{ref}}(s), \quad \mathbf{G}_E(s) = \mathbf{C}_E (s\mathbf{I} - \mathbf{A}_E)^{-1} \mathbf{B}_E \quad (6.27)$$

Note that due to the definition of \mathbf{C}_p only four entries in the 8×8 transfer function matrix $\mathbf{G}_E(s)$ are non-zero, given by the sub-matrix:

$$\mathbf{G}_{E1} = \begin{bmatrix} G_{\tilde{\omega}_{1,\text{ref}} \rightarrow \tilde{p}_L} & G_{\tilde{\omega}_{2,\text{ref}} \rightarrow \tilde{p}_L} \\ G_{\tilde{\omega}_{1,\text{ref}} \rightarrow \tilde{p}_{\min}} & G_{\tilde{\omega}_{2,\text{ref}} \rightarrow \tilde{p}_{\min}} \end{bmatrix} \quad (6.28)$$

The dynamic cross couplings are evaluated by the Relative Gain Array number ($\text{RGA}_\#$), which for a diagonal input-output pairing is defined in Eq. 6.29. Off-diagonal definition of the RGA-numbers is given by Eq. 6.30, [121]:

$$\text{RGA}_{\# \text{dia}} = \sum_{i,k} \left| \underbrace{\mathbf{G}_{E1}(j\omega) \times \left(\mathbf{G}_{E1}^{-1}(j\omega) \right)^T}_{\text{RGA Elements}} - \begin{bmatrix} 1 & 0 \\ 0 & 1 \end{bmatrix} \right| \quad (6.29)$$

$$\text{RGA}_{\# \text{off}} = \sum_{i,k} \left| \underbrace{\mathbf{G}_{E1}(j\omega) \times \left(\mathbf{G}_{E1}^{-1}(j\omega) \right)^T}_{\text{RGA Elements}} - \begin{bmatrix} 0 & 1 \\ 1 & 0 \end{bmatrix} \right| \quad (6.30)$$

Here \times denotes element-by-element multiplication or Hadamard product. i, k denotes rows and columns in the transfer function matrix. For further details on the RGA and RGA-numbers the references [120] and [121] may be consulted. In this dissertation it suffices to note that for a 2×2 system an ideal diagonal input-output decoupling are indicated by the $\text{RGA}_{\# \text{dia}}$ and $\text{RGA}_{\# \text{off}}$ attaining the values 0 and 4 respectively for all frequencies. For $\text{RGA}_{\# \text{dia}}$ and $\text{RGA}_{\# \text{off}}$ attaining the values 4 and 0 respectively for all frequencies indicates an ideal decoupling utilizing an off-diagonal input-output pairing.

Fig. 6.4a and b show the RGA-numbers for \mathbf{G}_{E1} in motion operation mode and self-locking mode respectively. In motion operation mode, the RGA numbers are showing severe dynamic coupling making a decentralised control approach infeasible using the physical inputs. In self-locking mode close to ideal RGA-numbers are found up to around 35 Hz, which is the eigenfrequency of the bootstrap reservoir piston at this specific operation point. This suggests that decentralised control approaches may be feasible, but this is complicated by the observation that the ideal input-output pairing are changing depending on the position of the inverse shuttle valve.

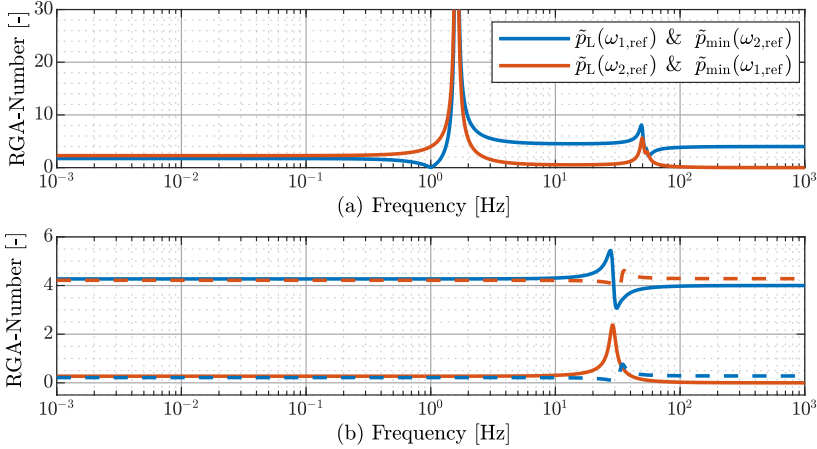


Fig. 6.4: RGA numbers for diagonal and off-diagonal input-output pairings of \mathbf{G}_{E1} . (a) Motion operation mode. (b) Self-locking mode, solid lines are for $p_{\text{PA}} > p_{\text{PB}}$ ($K_{\text{sw,ISV}} = 1$) and dashed lines are for $p_{\text{PA}} < p_{\text{PB}}$ ($K_{\text{sw,ISV}} = 0$).

6.3 Pressure Controller Design

Due to the severe cross couplings a control strategy for controlling the load and minimum pressure is established using virtual system inputs. This is done by properly defining an input mapping between the virtual system inputs and the physical system inputs (shaft speed references).

6.3. Pressure Controller Design

The dynamics of the virtual pressure states p_L and p_{\min} can be found using the dynamics of the physical states in Eqs. 6.4 and 6.5. The desired closed loop virtual pressure dynamics is denoted as \bullet^* :

$$\dot{p}_L = \dot{p}_{PA} - \alpha \dot{p}_{PB} \quad \dot{p}_L^* = \omega_L (p_{L,\text{ref}} - p_L) \quad (6.31)$$

$$\dot{p}_{\min} = (1 - K_{\text{sw,ISV}}) \dot{p}_{PA} - K_{\text{sw,ISV}} \dot{p}_{PB} \quad \dot{p}_{\min}^* = \omega_M (p_{\min,\text{ref}} - p_{\min}) \quad (6.32)$$

where ω_L and ω_M are the desired bandwidths of the closed loop dynamics of the virtual pressures.

Defining two equations as $\dot{p}_L = \dot{p}_L^*$ and $\dot{p}_{\min} = \dot{p}_{\min}^*$ and solving for the two shaft speeds ω_1 and ω_2 yields:

$$\omega_1 = \frac{K_{\text{sw,ISV}} - 1}{\Gamma_1} V_{PB} \dot{p}_L^* + \frac{V_{PB}}{\Gamma_1} \dot{p}_{\min}^* + \frac{K_{\text{sw,LH}} A_B}{D_{p,1}} \dot{x} + \frac{A_C K_{\text{sw,ISV}}}{D_{p,1}} \dot{z} \quad (6.33)$$

$$\begin{aligned} \omega_2 = & \frac{(1 - K_{\text{sw,ISV}}) V_{PB} \beta_{\text{eff,PA}} - K_{\text{sw,ISV}} V_{PA} \beta_{\text{eff,PB}}}{\Gamma_2} \dot{p}_L^* - \frac{V_{PA} \beta_{\text{eff,PB}} \alpha + V_{PB} \beta_{\text{eff,PA}}}{\Gamma_2} \dot{p}_{\min}^* \\ & + \frac{A_A - A_B}{D_{p,2}} K_{\text{sw,LH}} \dot{x} - \frac{A_C}{D_{p,2}} \dot{z} \end{aligned} \quad (6.34)$$

$$\begin{aligned} \Gamma_1 = & ((\alpha - 1) K_{\text{sw,ISV}} - \alpha) D_{p,1} \beta_{\text{eff,PB}}, \quad \Gamma_2 = \beta_{\text{eff,PB}} \beta_{\text{eff,PA}} D_{p,2} ((\alpha - 1) K_{\text{sw,ISV}} - \alpha) \\ V_{PA} = & V_{0PA} + K_{\text{sw,LH}} (V_{0A} + x A_A) + (1 - K_{\text{sw,ISV}}) (V_{0C} - z A_C) \\ V_{PB} = & V_{0PB} + K_{\text{sw,LH}} (V_{0B} - x A_B) + K_{\text{sw,ISV}} (V_{0C} - z A_C) \end{aligned} \quad (6.35)$$

If the shaft speeds satisfy Eqs. 6.33 and 6.34, then the desired closed loop pressure dynamics are obtained. Eqs. 6.33 and 6.34 may therefore be regarded an input mapping from the virtual inputs being the desired virtual pressure dynamics. However, in reality the shaft speeds are realised and limited by the actuator dynamics while the volumes, bulk moduli and z, \dot{z} are not known exactly. This means that estimated quantities are used in a realistic controller [64] given as Eqs. 6.37 to 6.40:

$$\omega_{1,\text{ref}} = \frac{K_{\text{sw,ISV}} - 1}{\hat{\Gamma}_1} \hat{V}_{PB} \dot{p}_L^* + \frac{\hat{V}_{PB}}{\hat{\Gamma}_1} \dot{p}_{\min}^* + \frac{K_{\text{sw,LH}} A_B}{D_{p,1}} \dot{x} + \frac{A_C K_{\text{sw,ISV}}}{D_{p,1}} \dot{z} \quad (6.37)$$

$$\begin{aligned} \omega_{2,\text{ref}} = & \frac{(1 - K_{\text{sw,ISV}}) \hat{V}_{PB} \hat{\beta}_{\text{eff,PA}} - K_{\text{sw,ISV}} \hat{V}_{PA} \hat{\beta}_{\text{eff,PB}}}{\hat{\Gamma}_2} \dot{p}_L^* - \frac{\hat{V}_{PA} \hat{\beta}_{\text{eff,PB}} \alpha + \hat{V}_{PB} \hat{\beta}_{\text{eff,PA}}}{\hat{\Gamma}_2} \dot{p}_{\min}^* \\ & + \frac{A_A - A_B}{D_{p,2}} K_{\text{sw,LH}} \dot{x} - \frac{A_C}{D_{p,2}} \dot{z} \end{aligned} \quad (6.38)$$

$$\begin{aligned} \hat{\Gamma}_1 = & ((\alpha - 1) K_{\text{sw,ISV}} - \alpha) D_{p,1} \hat{\beta}_{\text{eff,PB}}, \quad \hat{\Gamma}_2 = \hat{\beta}_{\text{eff,PB}} \hat{\beta}_{\text{eff,PA}} D_{p,2} ((\alpha - 1) K_{\text{sw,ISV}} - \alpha) \\ \hat{V}_{PA} = & \hat{V}_{0PA} + K_{\text{sw,LH}} (\hat{V}_{0A} + x A_A) + (1 - K_{\text{sw,ISV}}) (\hat{V}_{0C} - \hat{z} A_C) \end{aligned} \quad (6.39)$$

$$\hat{V}_{PB} = \hat{V}_{0PB} + K_{\text{sw,LH}} (\hat{V}_{0B} - x A_B) + K_{\text{sw,ISV}} (\hat{V}_{0C} - \hat{z} A_C) \quad (6.40)$$

Note, it is assumed that pump displacements, piston areas, and state measurements are known exactly. $K_{sw,LH}$ and $K_{sw,ISV}$ are implemented with a hysteresis-band of 1 and 3 bar respectively to avoid oscillations close to the switching conditions according to [122]. The estimated bootstrap piston speed and position are found from the steady state relationship between \dot{x} and \dot{z} , assuming the initial position to be known:

$$\dot{z} = K_{\dot{x} \rightarrow \dot{z}} \dot{x} = -\frac{A_A (1 - \alpha)}{A_R (1 - \alpha_B)} \dot{x} \quad (6.41)$$

6.3.1 State Space Representation

For analysis purposes the linear counterparts of Eqs. 6.37 to 6.40 may be established. This is done by enforcing the mentioned assumptions of constant volumes ($\hat{V}_{PA0}, \hat{V}_{PB0}$), bulk moduli ($\hat{\beta}_{eff,PA}, \hat{\beta}_{eff,PB}$) and switching parameters $K_{sw,ISV}, K_{sw,LH}$ close to the linearisation point. By doing so the controller is linear in the states and the virtual inputs $\tilde{p}_{L,ref}$ and $\tilde{p}_{min,ref}$. Thus the controller may be represented as a state feedback gain matrix \mathbf{K}_{PC} and a pre-filter \mathbf{F}_{PC} , using the physical states and virtual inputs:

$$\mathbf{u}_{ref} = \begin{bmatrix} \tilde{\omega}_{1,ref} \\ \tilde{\omega}_{2,ref} \end{bmatrix} = \mathbf{F}_{PC} \mathbf{u}_{P-ref} - \mathbf{K}_{PC} \mathbf{x}_P, \quad \mathbf{u}_{P-ref} = \begin{bmatrix} \tilde{p}_{L,ref} \\ \tilde{p}_{min,ref} \end{bmatrix} \quad (6.42)$$

$$\mathbf{F}_{PC} = \begin{bmatrix} \frac{(K_{sw,ISV} - 1) \hat{V}_{PB0} \omega_L}{\hat{\Gamma}_{1,0}} & \frac{\hat{V}_{PB0} \omega_M}{\hat{\Gamma}_{1,0}} \\ -\frac{\omega_L (\hat{V}_{PB0} (K_{sw,LH} - 1) \hat{\beta}_{eff,PA} + K_{sw,ISV} \hat{V}_{PA0} \hat{\beta}_{eff,PB})}{\hat{\Gamma}_{2,0}} & -\frac{(\alpha \hat{V}_{PA0} \hat{\beta}_{eff,PB} + \hat{\beta}_{eff,PA} \hat{V}_{PB0}) \omega_M}{\hat{\Gamma}_{2,0}} \end{bmatrix}$$

$$\mathbf{K}_{PC} = \begin{bmatrix} 0 & -\frac{A_C K_{sw,ISV} K_{\dot{x} \rightarrow \dot{z}} + K_{sw,LH} A_B}{D_{p,1}} & 0 & \frac{(K_{sw,ISV} - 1) \hat{V}_{PB0} (\omega_L - \omega_M)}{\hat{\Gamma}_{1,0}} & K_{KP1} & 0 \\ 0 & \frac{(A_B - A_A) K_{sw,LH} + A_C K_{\dot{x} \rightarrow \dot{z}}}{D_{p,2}} & 0 & K_{KP2} & K_{KP3} & 0 \end{bmatrix}$$

$$K_{KP3} = \frac{\left((\hat{V}_{PB0} \omega_L \hat{\beta}_{eff,PA} + \hat{\beta}_{eff,PB} \hat{V}_{PA0} (\omega_L - \omega_M)) \alpha - \hat{V}_{PB0} \hat{\beta}_{eff,PA} \omega_M \right) K_{sw,ISV} - \alpha \hat{V}_{PB0} \hat{\beta}_{eff,PA} \omega_L}{\hat{\Gamma}_{2,0}}$$

$$K_{KP1} = -\frac{((K_{sw,ISV} - 1) \alpha \omega_L - \omega_M K_{sw,ISV}) \hat{V}_{PB0}}{\hat{\Gamma}_{1,0}}, \quad K_{KP2} = \quad (6.43)$$

$$-\frac{\hat{V}_{PB0} (\omega_L - \omega_M) (K_{sw,ISV} - 1) \hat{\beta}_{eff,PA} + \hat{\beta}_{eff,PB} (\alpha (K_{sw,ISV} - 1) \omega_M - K_{sw,ISV} \omega_L) \hat{V}_{PA0}}{\hat{\Gamma}_{2,0}}$$

The linear ECD+ system with closed loop pressure controllers may be repre-

6.3. Pressure Controller Design

sented as:

$$\dot{\mathbf{x}}_{\text{PC}} = \mathbf{A}_{\text{PC}} \mathbf{x}_{\text{PC}} + \mathbf{B}_{\text{PC}} \mathbf{u}_{\text{P-ref}}, \quad \mathbf{y}_{\text{PC}} = \mathbf{C}_{\text{E}} \mathbf{x}_{\text{PC}}, \quad \mathbf{x}_{\text{PC}} = \mathbf{x}_{\text{E}} \quad (6.44)$$

$$\mathbf{A}_{\text{PC}} = \mathbf{A}_{\text{E}} - \mathbf{B}_{\text{E}} \begin{bmatrix} 0 & \mathbf{K}_{\text{PC}} \end{bmatrix}, \quad \mathbf{B}_{\text{PC}} = \mathbf{B}_{\text{E}} \mathbf{F}_{\text{PC}} \quad \mathbf{u}_{\text{P-ref}} = \begin{bmatrix} \tilde{p}_{\text{L,ref}} \\ \tilde{p}_{\text{min,ref}} \end{bmatrix} \quad (6.45)$$

where the subscript \bullet_{PC} denotes the *pressure controlled* linear model.

6.3.2 Linear Couplings in Pressure Controlled System

In Fig. 6.5, the RGA-numbers for the closed loop pressure controlled ECD+ system are shown. Here both a case assuming ideal parameter estimates with actuator dynamics absent and a case including actuator dynamics and with realistic parameter estimates are considered. The realistic parameter estimates here assume the inactive or dead chamber volumes to be estimated 20% larger than the real values. The bulk moduli are estimated to 15000 bar, which is close to the maximum value for the oil itself, disregarding the effect from mechanical elasticity, see. Fig. 5.3 on page 89. This means that the bulk moduli are overestimated compared to the true values.

Fig. 6.5 shows that in the absence of actuator dynamics ($\omega = \omega_{\text{ref}}$) and by assuming ideal parameter estimates, the system is an ideal diagonal system. As such $\tilde{p}_{\text{L,ref}}$ may be used to control \tilde{p}_{L} without introducing any cross coupling effects to \tilde{p}_{min} which is controlled by $\tilde{p}_{\text{min,ref}}$. However when parameters are not known ideally, RGA numbers are deviating from the RGA numbers of an

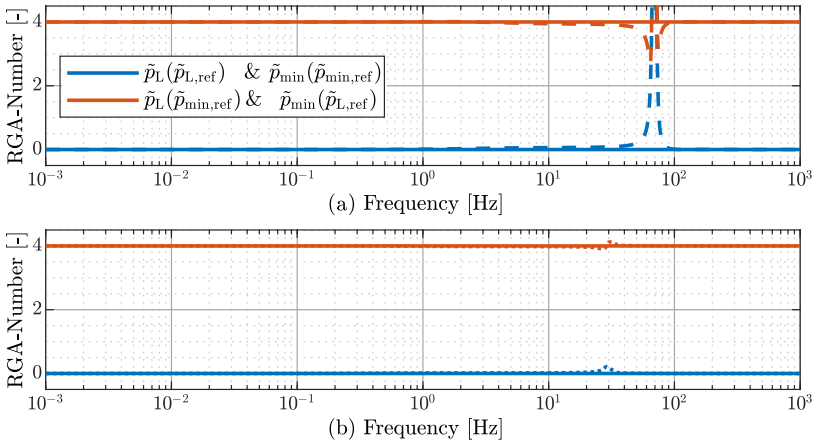


Fig. 6.5: RGA numbers for the system under closed loop pressure control. Solid lines are RGA numbers assuming ideal parameter estimates and no actuator dynamics while dotted lines include actuator dynamics and realistic parameter estimates. (a) Motion operation mode. (b) Self-locking mode.

ideally decoupled system at a frequency corresponding to the eigenfrequency of the bootstrap reservoir pistons. This is found to happen, because the bootstrap reservoir piston velocity is estimated and because the eigenfrequency is above the bandwidth of the actuators (electric motors). To mitigate this effect, the dimensions of the bootstrap reservoir may be changed or its piston mass increased. However, because the cross couplings are introduced at a relatively high frequency and well above the desired bandwidth of the pressure control loops, the cross couplings at high frequencies are accepted.

6.3.3 Time Domain Response

Fig. 6.6 shows an example of the pressure response in the time domain of the pressure controlled system in motion operation mode. As expected, if ideal parameter estimates are utilised and actuator dynamics neglected, the desired first order pressure response is obtained. For realistic estimates, the response is slightly slower than desired and with a small steady state error and cross coupling disturbances. For comparison the nonlinear pressure responses are also shown in Fig. 6.6. Beside small cross coupling disturbances, it is noticeable that steady state errors are present. These are caused by the pump leakages, which have not been included in the linear model.

Fig. 6.7 shows an example of the pressure responses in the time domain of the pressure controlled system in self-locking mode. For ideal parameter estimates no cross coupling effects are present and the desired dynamics are obtained. However, for realistic parameter estimates, the pressure response of the ECD+ system in self-locking mode is found to be sensitive to estimation errors. Note that the estimated bulk moduli are here even lowered to

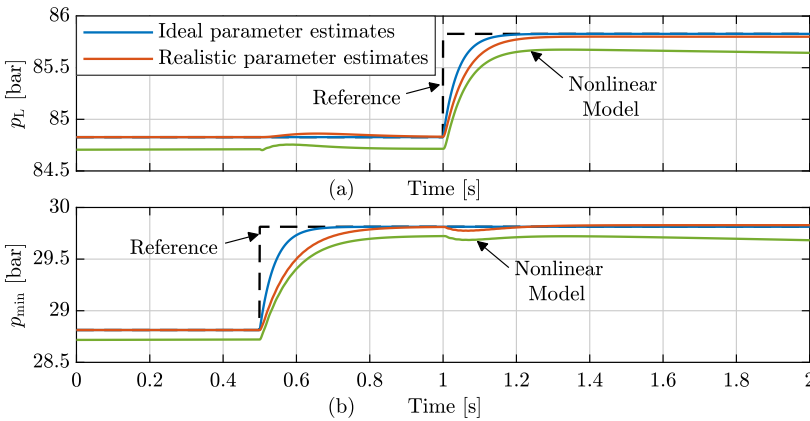


Fig. 6.6: Linear closed loop pressure responses in motion operation mode. For comparison the nonlinear response is included. (a) Load pressure, p_L . (b) Minimum pressure, p_{min} .

6.3. Pressure Controller Design

8000 bar, but this is still much larger than the true values ranging from 800 to 1900 bar in this example. Additionally the volume estimation errors are here relatively larger compared to motion operation mode, as the volumes of the cylinder chambers are not included due to the load holding valves being closed. Finally, the velocity of the bootstrap reservoir piston is estimated to 0, because the main cylinder is stationary. Altogether this means that the pressure response significantly differs from the desired. This is especially true for the nonlinear model, as the pump leakages are here a relatively large contribution compared to the compression flow estimated by the controller.

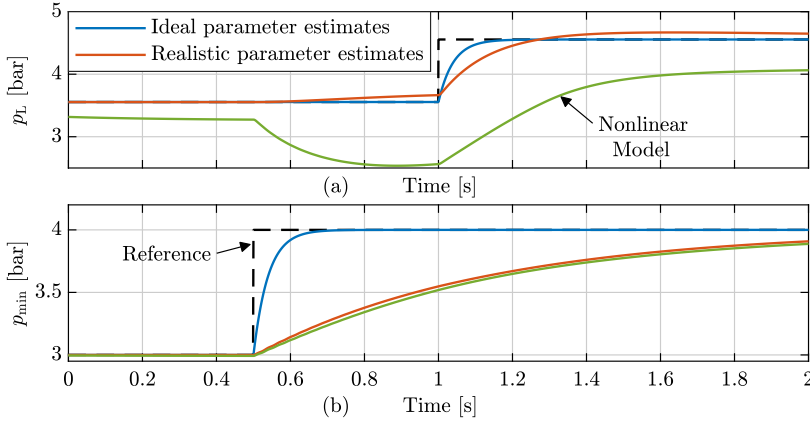


Fig. 6.7: Linear closed loop pressure responses in self-locking mode. For comparison the nonlinear response is included. (a) Load pressure, p_L . (b) Minimum pressure, p_{min} .

6.3.4 Controller Tuning

The tuning of the pressure controllers is related to the selection of the estimated bulk moduli, initial volumes and desired closed loop bandwidths ω_L and ω_M . Note that the pressure controllers assume that $\omega \approx \omega_{ref}$, meaning that $\omega_L, \omega_M \ll \omega_\omega$. The desired closed loop bandwidths are selected 10 times smaller than the closed loop shaft speed bandwidth:

$$10\omega_L = \omega_\omega \quad 10\omega_M = \omega_\omega \quad (6.46)$$

The initial dead volumes are assumed to be known within 20 %, such that the estimated values are 20 % larger than the real values in this study.

Even though the true bulk moduli vary significantly with the pressure levels, the estimated bulk moduli $\hat{\beta}_{eff,PA}$ and $\hat{\beta}_{eff,PB}$ are selected to be constant. Note again, that the pressure controllers assume $\omega \approx \omega_{ref}$, meaning that the selection of the estimated bulk moduli should not turn this assumption invalid, i.e. not result in a higher closed loop bandwidth than specified by ω_L, ω_M . In

[64] it was shown analytically for a simpler SISO system, that this is fulfilled by selecting the estimates equal to the highest expected values. Due to a high order of the considered system (8 states), this has not been solved analytically in this dissertation. Instead Fig. 6.8, shows numerically how the step response of the closed loop system changes when the estimated bulk moduli are varied between 10 % and 200 % of the true values.

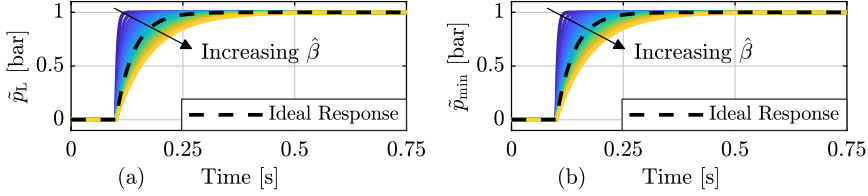


Fig. 6.8: Linear model responses of idealised pressure control loops (no actuator dynamics and known \bar{z}), as the estimated bulk moduli are varied. (a) Change variable of load pressure. (b) Minimum pressure.

Fig. 6.8 shows that choosing $\hat{\beta} < \beta$ results in a higher bandwidth than desired while choosing $\hat{\beta} > \beta$ results in a smaller bandwidth. Ideally both should be avoided, as a high bandwidth renders the system sensitive to measurement noise, and may lead to on-off like behaviour of the control system when considering actuator saturation in the nonlinear model. If the bandwidth is significantly smaller than desired, this may influence the performance of the outer motion control loop, as this is later designed based on the assumption that the pressure loop has the specified bandwidth. However, the conservative choice is to select $\hat{\beta}$ at the maximum expected value, which generally is the bulk modulus of the pure oil. Thus:

$$\hat{\beta}_{\text{eff,PA}} = \hat{\beta}_{\text{eff,PB}} = 15000 \text{ bar} = 1.5 \text{ GPa} \quad (6.47)$$

To sum up, a pressure control strategy able to handle the dynamic cross couplings of the ECD+ system has been proposed. The controller may be tuned easily based on physical parameters and if good parameter estimates are available, decent results can be obtained. However, for realistic parameter estimates, steady state errors, slower responses, and slight cross coupling effects must be accepted. Especially in self-locking mode the performance is sensitive to estimation errors, meaning that fast responses with no steady state errors can not be expected. In Sec. 7.2 the limitations induced by this in terms of closing and opening the load holding valves are discussed. If one is keen on removing pressure steady state errors, integral action may be included in the control laws. This is not considered in the current work. In motion operation mode, the pressure steady state error can be accepted because an outer motion control loop is providing the reference to the control loop. Likewise, small pressure errors of p_{\min} are not considered a problem.

6.4 Motion Controller

The motion controller design is based on the simplified modelling equation of the main piston dynamics (Eq. 6.2). The motion controller is only active when the load holding valves are estimated to be open ($K_{sw,LH} = 1$), leading to the following equation:

$$\ddot{x} = \frac{1}{M_{eq}} (p_{PA} A_A - p_{PB} A_B - F_G - B_x \dot{x}) = \frac{1}{M_{eq}} (p_L A_A - F_G - B_x \dot{x}) \quad (6.48)$$

The motion controller must be a control law calculating the load pressure reference $p_{L,ref}$. $F_G \neq 0$ and $p_{L,ref} \neq 0$ for $x = x_{ref}$, meaning that integral action is required [64]. A sensible control law for the motion controller may therefore be constituted by:

$$p_{L,ref} = K_{\dot{x}} (\dot{x}_{ref} - \dot{x}) + K_{Px} e_x + K_{Ix} \bar{e}_x, \quad \bar{e}_x = e_x = (x_{ref} - x) \quad (6.49)$$

By assuming $p_{L,ref} \approx p_L$ and inserting Eq. 6.49 into Eq. 6.48:

$$\ddot{x} = \frac{1}{M_{eq}} (K_{\dot{x}} (\dot{x}_{ref} - \dot{x}) + K_{Px} e_x + K_{Ix} \bar{e}_x A_A - F_G - B_x \dot{x}) \quad (6.50)$$

By regarding F_G to be a disturbance, the transfer function from $\tilde{x}_{ref} \rightarrow \tilde{x}$ may be derived based on Eq. 6.50:

$$\frac{\tilde{x}}{\tilde{x}_{ref}} = \frac{K_{\dot{x}} s^2 + K_{Px} s + K_{Ix}}{\frac{M_{eq}}{A_A} s^3 + \left(\frac{B_x}{A_A} + K_{\dot{x}} \right) s^2 + K_{Px} s + K_{Ix}} \quad (6.51)$$

Eq. 6.51 is a closed loop system consisting of three poles and two zeros. The control law has three real coefficients that may be selected freely. By selection of these control parameters it is possible to place three of the five poles and zeros where desired. Here it is chosen to control the locations of the three poles to ensure stability and thus accept the resulting locations of the zeros. A natural choice is to place the poles as a pair of complex conjugate poles and a single non-complex pole. By selecting the control parameters as given in Eqs. 6.52 and 6.53 this is achieved. In the case of ideal parameter estimates ($\hat{M}_{eq} = M_{eq}$, $\hat{B}_x = B_x$) and $p_{L,ref} = p_L$ the corresponding closed loop dynamics given in Eq. 6.54 is obtained as:

$$K_{\dot{x}} = \frac{(2\zeta_{xx} \omega_{xx} + \omega_x) \hat{M}_{eq} - \hat{B}_x}{A_A}, \quad K_{Ix} = \frac{\hat{M}_{eq} \omega_x \omega_{xx}^2}{A_A} \quad (6.52)$$

$$K_{Px} = \frac{(2\zeta_{xx} \omega_x + \omega_{xx}) \hat{M}_{eq} \omega_{xx}}{A_A} \Rightarrow \quad (6.53)$$

$$\frac{\tilde{x}}{\tilde{x}_{ref}} = \frac{1}{K_{Ix}} \frac{\omega_x \omega_{xx}^2 (K_{\dot{x}} s^2 + K_{Px} s + K_{Ix})}{(s + \omega_x) (s^2 + 2\zeta_{xx} \omega_{xx} s + \omega_{xx}^2)} \quad (6.54)$$

where ω_x , ω_{xx} , and ζ_{xx} are the desired frequency of the motion control loop poles and damping ratio of the complex conjugated pair of poles.

6.4.1 State Space Representation

The linear ECD+ system including the outer loop motion controller may be represented in state space form by first augmenting the system with an integrator:

$$\begin{bmatrix} \dot{\mathbf{x}}_{\text{PC}} \\ \dot{\tilde{e}}_x \end{bmatrix} = \underbrace{\begin{bmatrix} \mathbf{A}_{\text{PC}} & \mathbf{0} \\ -\mathbf{C}_1 & 0 \end{bmatrix}}_{\mathbf{A}_I} \begin{bmatrix} \mathbf{x}_{\text{PC}} \\ \tilde{e}_x \end{bmatrix} + \underbrace{\begin{bmatrix} \mathbf{B}_{\text{PC}} \\ \mathbf{0} \end{bmatrix}}_{\mathbf{B}_I} \underbrace{\begin{bmatrix} \tilde{p}_{L,\text{ref}} \\ \tilde{p}_{\text{min,ref}} \end{bmatrix}}_{\mathbf{u}_{\text{P-ref}}} + \underbrace{\begin{bmatrix} \mathbf{0} & \mathbf{0} \\ 1 & 0 \end{bmatrix}}_{\mathbf{u}_{\text{MC-ref}}} \underbrace{\begin{bmatrix} \tilde{x}_{\text{ref}} \\ \tilde{p}_{\text{min,ref}} \end{bmatrix}}_{\mathbf{u}_{\text{MC-ref}}} \quad (6.55)$$

$$\mathbf{C}_I = \begin{bmatrix} 0 & 0 & 1 & 0 & 0 & 0 & 0 & 0 \end{bmatrix} \quad (6.56)$$

The motion controller may be represented by the state feedback matrix \mathbf{K}_{MC} , the prefilter \mathbf{F}_{MC} and the derivative input matrix \mathbf{F}_{MCd} , assuming that the derivative $\dot{\tilde{p}}_{\text{min,ref}} = 0$:

$$\begin{bmatrix} \tilde{p}_{L,\text{ref}} \\ \tilde{p}_{\text{min,ref}} \end{bmatrix} = -\mathbf{K}_{\text{MC}} \begin{bmatrix} \mathbf{x}_{\text{PC}} \\ \tilde{e}_x \end{bmatrix} + \mathbf{F}_{\text{MC}} \begin{bmatrix} \tilde{x}_{\text{ref}} \\ \tilde{p}_{\text{min,ref}} \end{bmatrix} + \mathbf{F}_{\text{MCd}} \begin{bmatrix} \dot{\tilde{x}}_{\text{ref}} \\ 0 \end{bmatrix} \quad (6.57)$$

$$\mathbf{K}_{\text{MC}} = \begin{bmatrix} 0 & 0 & K_{\text{Px}} & K_{\dot{x}} & 0 & 0 & 0 & 0 & -K_{\text{Ix}} \\ 0 & 0 & 0 & 0 & 0 & 0 & 0 & 0 & 0 \end{bmatrix} \quad (6.58)$$

$$\mathbf{F}_{\text{MC}} = \begin{bmatrix} K_{\text{Px}} & 0 \\ 0 & 1 \end{bmatrix} \quad \mathbf{F}_{\text{MCd}} = \begin{bmatrix} K_{\dot{x}} & 0 \\ 0 & 0 \end{bmatrix} \quad (6.59)$$

Inserting Eq. 6.57 into Eq. 6.55 yields:

$$\begin{bmatrix} \dot{\mathbf{x}}_{\text{PC}} \\ \dot{\tilde{e}}_x \end{bmatrix} = \underbrace{\begin{bmatrix} \mathbf{A}_I - \mathbf{B}_I \mathbf{K}_{\text{MC}} \end{bmatrix}}_{\mathbf{A}_{\text{MC}}} \begin{bmatrix} \mathbf{x}_{\text{PC}} \\ \tilde{e}_x \end{bmatrix} + \underbrace{\begin{bmatrix} \mathbf{B}_I \mathbf{F}_{\text{MC}} + \begin{bmatrix} \mathbf{0} & \mathbf{0} \\ 1 & 0 \end{bmatrix} \end{bmatrix}}_{\mathbf{B}_0} \begin{bmatrix} \tilde{x}_{\text{ref}} \\ \tilde{p}_{\text{min,ref}} \end{bmatrix} + \underbrace{\mathbf{B}_I \mathbf{F}_{\text{MCd}}}_{\mathbf{B}_1} \begin{bmatrix} \dot{\tilde{x}}_{\text{ref}} \\ 0 \end{bmatrix}$$

To arrive at the final representation the input derivative needs to be eliminated by using an equivalent linear representation. Here the method described in [123] is applicable, assuming that the derivative $\dot{\tilde{p}}_{\text{min,ref}} = 0$:

$$\mathbf{x}_{\text{MC}} = \begin{bmatrix} \mathbf{x}_{\text{PC}} \\ \tilde{\mathbf{e}}_x \end{bmatrix} - \mathbf{B}_1 \begin{bmatrix} \tilde{x}_{\text{ref}} \\ \tilde{p}_{\text{min,ref}} \end{bmatrix}, \quad (6.60)$$

$$\begin{aligned} \dot{\mathbf{x}}_{\text{MC}} &= \mathbf{A}_{\text{MC}} \begin{bmatrix} \mathbf{x}_{\text{PC}} \\ \tilde{\mathbf{e}}_x \end{bmatrix} + \mathbf{B}_0 \begin{bmatrix} \tilde{x}_{\text{ref}} \\ \tilde{p}_{\text{min,ref}} \end{bmatrix} + \mathbf{B}_1 \begin{bmatrix} \dot{\tilde{x}}_{\text{ref}} \\ 0 \end{bmatrix} - \mathbf{B}_1 \begin{bmatrix} \dot{\tilde{x}}_{\text{ref}} \\ 0 \end{bmatrix} \\ &= \mathbf{A}_{\text{MC}} \left(\mathbf{x}_{\text{MC}} + \mathbf{B}_1 \begin{bmatrix} \tilde{x}_{\text{ref}} \\ \tilde{p}_{\text{min,ref}} \end{bmatrix} \right) + \mathbf{B}_0 \begin{bmatrix} \tilde{x}_{\text{ref}} \\ \tilde{p}_{\text{min,ref}} \end{bmatrix} \\ &= \mathbf{A}_{\text{MC}} \mathbf{x}_{\text{MC}} + \underbrace{(\mathbf{A}_{\text{MC}} \mathbf{B}_1 + \mathbf{B}_0)}_{\mathbf{B}_{\text{MC}}} \mathbf{u}_{\text{MC-ref}} = \mathbf{A}_{\text{MC}} \mathbf{x}_{\text{MC}} + \mathbf{B}_{\text{MC}} \mathbf{u}_{\text{MC-ref}} \end{aligned} \quad (6.61)$$

$$\mathbf{y}_{\text{MC}} = \mathbf{C}_{\text{MC}} \begin{bmatrix} \mathbf{x}_{\text{PC}} \\ \tilde{\mathbf{e}}_x \end{bmatrix} = \mathbf{C}_{\text{MC}} \mathbf{x}_{\text{MC}} + \underbrace{\mathbf{C}_{\text{MC}} \mathbf{B}_1}_{\mathbf{D}_{\text{MC}}} \mathbf{u}_{\text{MC-ref}} \quad (6.62)$$

where the subscript \bullet_{MC} denotes the *motion controlled* linear model of the ECD+ system. \mathbf{C}_{MC} is chosen such that the outputs of the linear models are \tilde{x} and \tilde{p}_{min} , leading to $\mathbf{D}_{\text{MC}} = \mathbf{0}$.

6.4.2 Time Domain Response

The step responses of the linear model in Eqs. 6.61 and 6.62 are shown in Fig. 6.9. Notice that the linearisation point is here slightly changed compared to earlier, as the piston velocity in the linearisation point is 0 m/s, ($\dot{x} = 0$). In Fig. 6.9a the response to a position step is shown. Interestingly it is seen that even if the pressure dynamics is neglected ($p_L = p_{L,\text{ref}}$), the response is underdamped caused by the zeros in Eq. 6.54. Furthermore Fig. 6.9a shows that including pressure dynamics and realistic parameter estimates ($\hat{M}_{\text{eq}} = 1.5M_{\text{eq}}$, $\hat{B}_x = 0$) renders the response less damped and with a significant overshoot, i.e. the response is further away from the desired response.

However, even small position steps may lead to high required piston speeds. This means that position step inputs are generally avoided, such that motion references are generated based on filtering the position of the operator's joystick, as described in Sec. 3.4.1. Fig. 6.9b and c show the piston velocity and position response during an acceleration from standstill to maximum speed (40 mm/s).

The three linear model responses in Fig. 6.9b and c are almost similar, and both the velocity and position errors are small. Small position and velocity errors are also found in Fig. 6.10 where the response of the nonlinear model during acceleration phases are shown, using estimated controller parameters. Fig. 6.10a and b shows that the maximum position error is around ± 0.3 mm and the maximum velocity error is less than ± 2.5 mm/s.

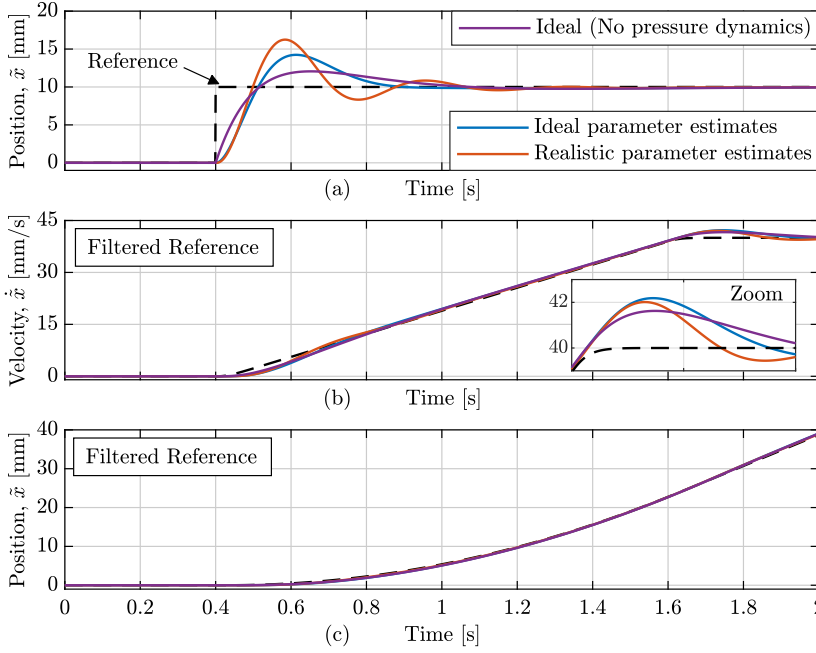


Fig. 6.9: Linear model responses. (a) Position step. (b) and (c) Motion reference generated by filtering the joystick position (Sec. 3.4.1). The ideal model neglects the pressure dynamics ($p_L = p_{L,ref}$). The ideal parameter case neglects the electric motor dynamics. For the realistic parameter case the parameters for the pressure controller are equivalent to Sec. 6.3.3 whereas $\dot{M}_{eq} = 1.5M_{eq}$ and $\hat{B}_x = 0$ is selected for the motion controller.

Fig. 6.10c shows the pressure response of the nonlinear model and the linear model with estimated parameters during the acceleration phase, confirming the findings in the previous section. These include that a small steady state error is present in the nonlinear model. Furthermore minor cross coupling effects caused by actuator dynamics and realistic parameter estimates yield the minimum pressure to deviate ± 0.3 bar from the reference value.

6.4.3 Controller Tuning

The tuning of the motion controller is related to the choice of ω_x , ω_{xx} , ζ_{xx} , \hat{B}_x , and \hat{M}_{eq} . Indeed the dynamics in Eq. 6.54 on page 119 are only obtained if $p_{L,ref} = p_L$ which is unachievable, as the load pressure is ideally obtained with first order dynamics. Therefore the obtained dynamics even in the case of ideal parameter estimates is only approximately equal to Eq. 6.54, if the desired frequency of the motion control loop poles is selected sufficiently below the pressure control bandwidth. Here the following choice is made:

$$5\omega_x = \omega_L, \quad 5\omega_{xx} = \omega_L, \quad \zeta_{xx} = 1 \quad (6.63)$$

6.4. Motion Controller

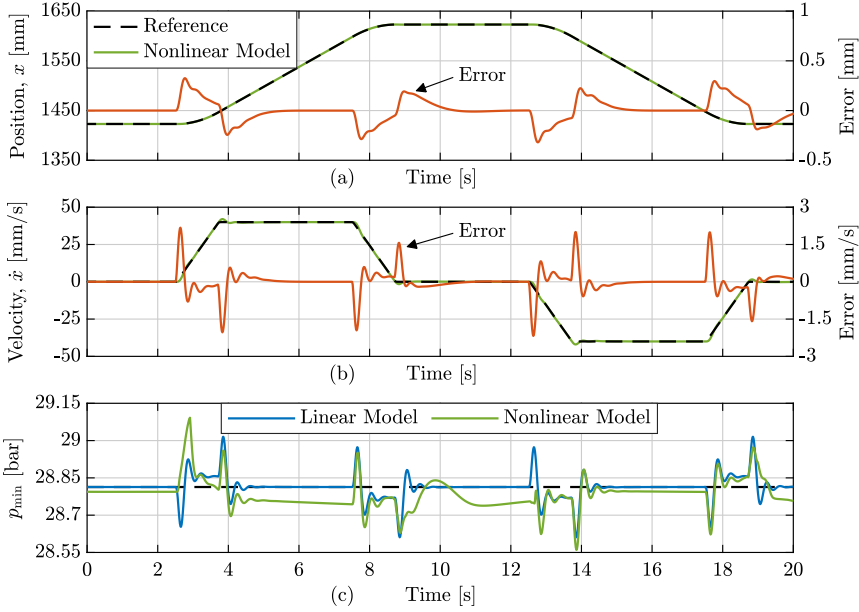


Fig. 6.10: (a) and (b) Simulated position and velocity of nonlinear model. (c) Simulated minimum chamber pressure p_{\min} . The linear model is derived from estimated parameters.

From the controller coefficients in Eqs. 6.52 and 6.53, it is clear that \hat{B}_x has a small influence, due to the high M_{eq} , leading to the choice $\hat{B}_x = 0$. Even though M_{eq} varies significantly along the motion trajectory, as illustrated in Fig. 6.3 on page 108, \hat{M}_{eq} is selected to be constant. A numerical investigation is used to obtain insights into how the selection of \hat{M}_{eq} may affect system response and stability.

Fig. 6.11a shows how the linear closed loop position response changes, in the considered linearisation point, as \hat{M}_{eq} varies between 20 % and 500 % of M_{eq} . Bad estimates lead to oscillating responses. If $\hat{M}_{eq} > M_{eq}$, high frequency os-

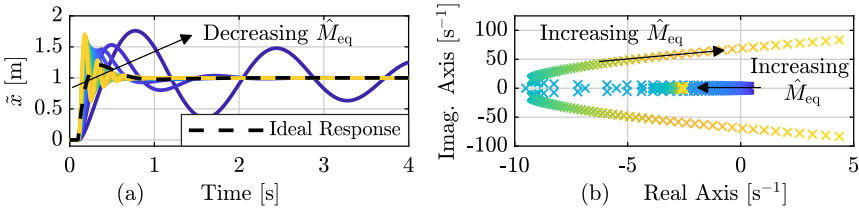


Fig. 6.11: (a) Linear step response for varying \hat{M}_{eq} . (b) Pole locations (closest to the right half plane) for varying \hat{M}_{eq} .

cillations are observed, which may violate $p_{L,ref} \approx p_L$. To be conservative \hat{M}_{eq} should therefore be chosen to be the minimum value experienced through the motion trajectory. However Fig. 6.11b shows that both too low and too high estimates may lead to system instabilities by displaying the eigenvalues of \mathbf{A}_{MC} located closest to the right half plane. Here \hat{M}_{eq} varies between 10 % and 2000 % of M_{eq} . To keep \hat{M}_{eq} within 25 % of the maximum M_{eq} , M_{eq} is chosen to 208.75 ton. This choice leads to $0.25M_{eq} \leq \hat{M}_{eq} \leq 1.2M_{eq}$.

6.5 Local Stability

As mentioned earlier the system may be characterised as a switched linear system, because the system matrix changes discretely depending on the switching variables $K_{sw,LH}$ and $K_{sw,ISV}$. This section contains a simple numerical investigation of the stability of the distinct model structures, i.e only the continuous states are considered. This means that the switching behaviour as such are not included from a stability point of view.

Fig. 6.12 shows the eigenvalues of \mathbf{A}_{MC} located closest to the right half plane, as the cylinder extends through the motion trajectory, utilizing the controller parameters given above. It is seen that for all cylinder positions, the system is stable both considering an empty lifting yoke, $m_3 = 5\text{ton}$, and a full, $m_3 = 10\text{ton}$. Note here that the velocity in the linearisation point is 0 for all considered piston positions, because it is found that the velocity in the linearisation point, only has a minor impact on pole locations.

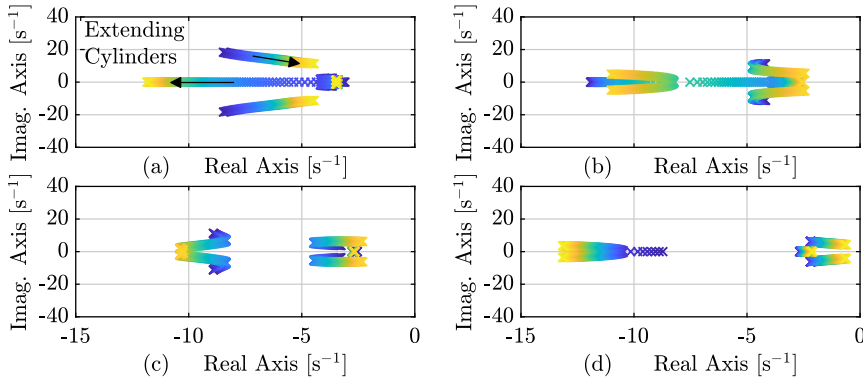


Fig. 6.12: Pole locations (closest to the right half plane) of closed loop motion controlled system for varying piston positions, along the motion trajectory. (a) Pole locations for $K_{sw,ISV} = 0$, $m_3 = 5\text{ ton}$. (b) Pole locations for $K_{sw,ISV} = 1$, $m_3 = 5\text{ ton}$. (c) Pole locations for $K_{sw,ISV} = 0$, $m_3 = 10\text{ ton}$. (d) Pole locations for $K_{sw,ISV} = 1$, $m_3 = 10\text{ ton}$.

Chapter 7

Simulation Results

In this chapter, the work presented in the proceeding chapters are all combined. This includes the ideas developed in Chapter 4 leading to the proposed ECD+ system. From here a dynamic thermo-hydraulic model was presented in Chapter 5, and control laws were derived in the previous chapter. The current chapter presents simulation results for the ECD+ system. This includes the dynamic load model of the knuckle boom crane derived in Sec. 2.2, with the crane performing the motion trajectory from Sec. 3.4.1. The system parameters can be found in Tab. A.6 on page 257. The control parameters are given in Tab. A.7 on page 259. All models have been implemented in MATLAB Simulink and simulated using the ODE45-solver.

7.1 Continuous Controller Implementation

Initially, the conditions for which the control laws were derived are applied. Therefore the control laws are implemented as continuous calculations. This means that the controller calculations are performed with the same sampling frequency as the integration of the physical system states in the MATLAB Simulink environment. Furthermore the measurements are obtained without noise and without including sensor resolutions. During the first simulations, the ECD+ system is kept in motion operation mode, i.e. the load holding valves are kept open and the safety valves SV_A and SV_B are energised/closed.

Fig. 7.1 shows the reference values, actual values and corresponding control errors of the motion and virtual pressure control loops. In Fig. 7.1a and b it is observed that the position and velocity errors during the trajectory are generally larger for the 10 ton load than for the 5 ton load, which is expected

as the estimated mass \hat{M}_{eq} used in the motion control law is closer to the value experienced with the 5 ton load. Furthermore control errors are found to be slightly larger than for the case with a constant load in Fig. 6.10. This is caused by disturbances from motion of the main axis and the swinging payload as well as the varying M_{eq} . During the entire trajectory the position error is kept within ± 3 mm, which according to [37] is within expectations as *"the expected accuracy for hydraulic cranes is typically worse as the maximum position error is frequently higher than 15 mm"*.

The performance of the inner loop pressure controllers are visualised in Fig. 7.1c and d. The load pressure is kept within ± 2.25 bar of the reference, whereas the minimum pressure is kept within ± 1.25 bar of the constant reference. This ensures that the load holding valves are kept fully open and a sufficient charge pressure for the bootstrap reservoir is available.

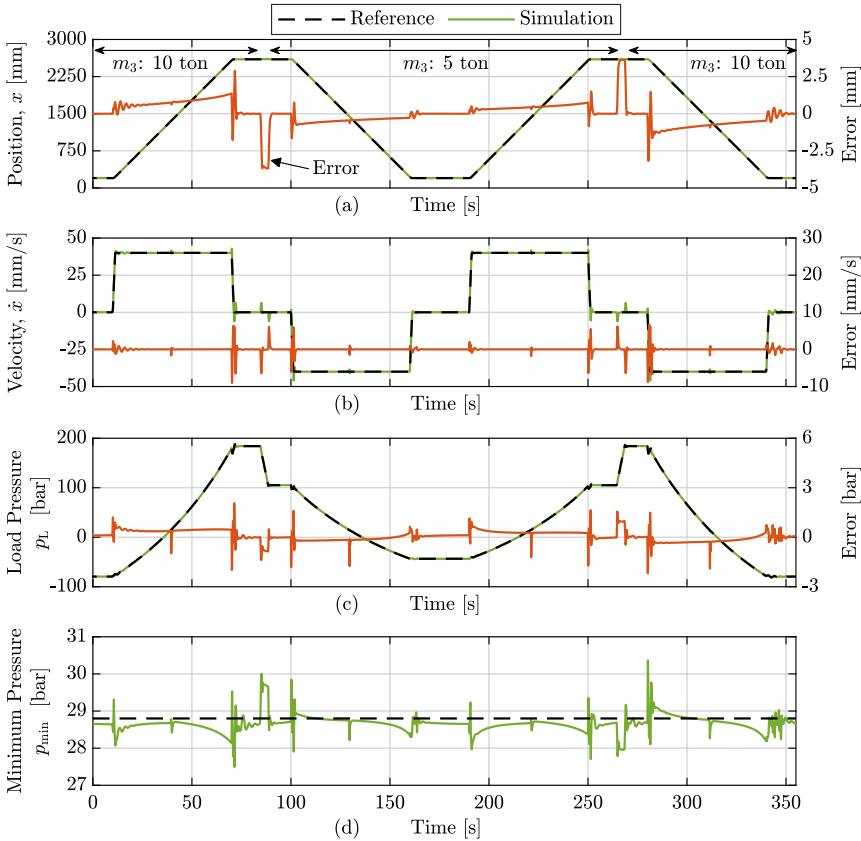


Fig. 7.1: Reference values, actual values and corresponding control errors of the motion and virtual pressure control loops. (a) Position. (b) Velocity. (c) Load pressure. (d) Minimum pressure.

7.1. Continuous Controller Implementation

Fig. 7.2 shows the physical pressures during the trajectory. In Fig. 7.2a the piston and rod chamber pressures are shown. It is clearly seen that the control system is capable of switching between which pressure to be controlled as the minimum chamber pressure. Note that the corresponding p_{PA} and p_{PB} pressures are not shown, because the pressure drop across the load holding valves are less than 0.8 bar.

Fig. 7.2b shows the absolute pressures in the bootstrap reservoir. It may be observed that the reservoir pressure is kept well above the 1.5 bar limit in the entire trajectory. Additionally the reservoir pressure is kept well below the maximum pressure limit of 4 bar, except for short peaks where the reservoir pressure is just at the 4 bar limit. Observing the charge pressure also visualised in Fig. 7.2b shows that this happens because the charge pressure increases well above the reference of 28.8 bar. This happens even though the cylinder chamber pressures are controlled in close vicinity of 28.8 bar. Further examining this issue reveals, that this situation occurs, when the load force changes direction and the velocity of the bootstrap pistons are positive. The former causes a position change of the inverse shuttle valve. This leads to a situation where an insufficient amount of oil are able to leave the charge chamber leading to an increasing pressure. This happens despite the inverse shuttle valve transition occurs with an open center. The open center is mod-

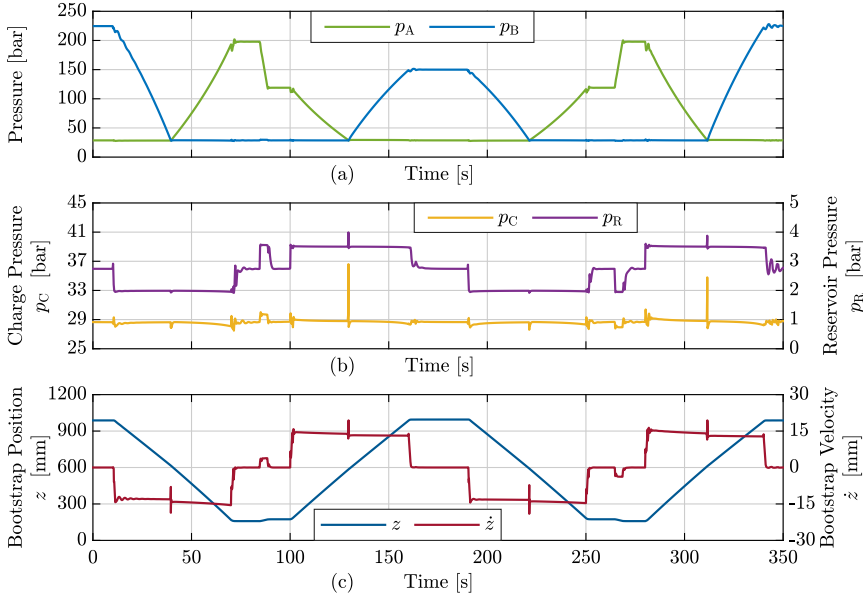


Fig. 7.2: (a) Piston and rod chamber pressures (absolute). (b) Absolute charge and reservoir pressures of the bootstrap reservoir. (c) Bootstrap reservoir motion states during the trajectory.

elled as a leakage flow when the spool position is close to 0. The level of the pressure peak is distinct because this happens at the maximum piston speed. This potential problem may be mitigated by increasing the leakage rate of the inverse shuttle valve during transition. Alternatively a pressure relief valve or pressure compensator between the charge and reservoir chambers may be included as considered in Paper D. Fig. 7.2c shows the motion states of the bootstrap reservoir piston. A position margin of approximately 160 mm to the end-stops (at $z = 0$ mm and $z = 1153$ mm) is present. This corresponds to 12.4 L available compensation volume.

The previous figures confirm that the main control objectives have been met, i.e. a reasonable motion accuracy and a reservoir pressure kept within range. It is equally important to observe how this performance is obtained in terms of requirements or reference commands to the system actuators. Even though accurate and swift performance is obtained regarding the controlled states, this should not lead to large and oscillating actuator references, requiring immense power to obtain the required shaft accelerations. Fig. 7.3 is used to examine this topic. In Fig. 7.3a, the shaft speeds are visualised. The maximum absolute shaft speed is 2750 RPM, leaving a 250 RPM margin to the maximum allowed pump speed of 3000 RPM. Generally, the shaft speeds

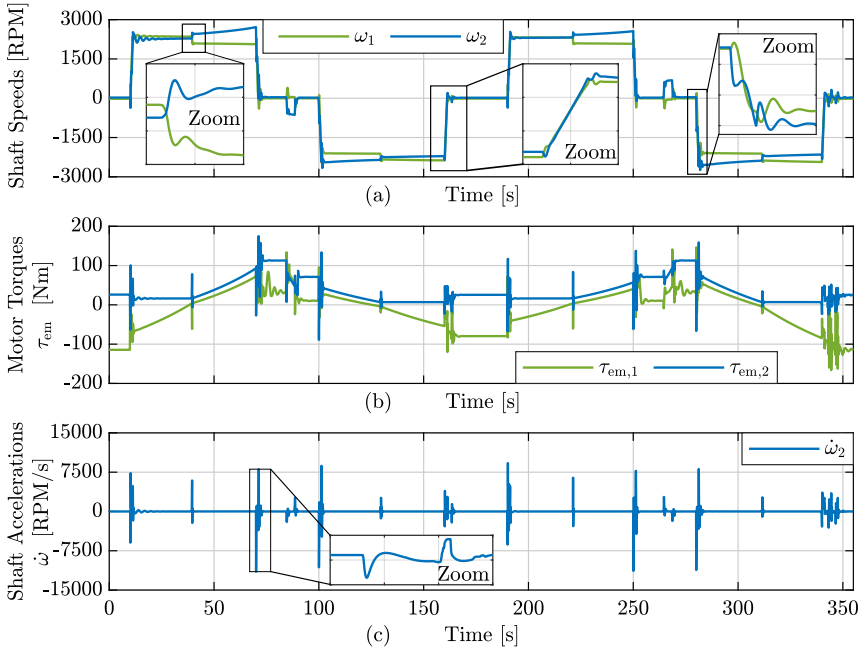


Fig. 7.3: (a) Shaft speeds. (b) Electric motor torques. (c) Shaft accelerations.

7.1. Continuous Controller Implementation

exhibit a well-damped behaviour. Even when the position of the inverse shuttle valve changes, oscillatory behaviour is avoided, as seen in the left-most zoom. This is partly achieved by imposing first order dynamics on $K_{sw,ISV}$, $K_{sw,LH}$. This means that these do not change abruptly, i.e. control law gains do not change instantaneously or jump. During acceleration and deceleration in Fig. 7.3a, some oscillations are present, which are found to origin from rejecting the disturbances caused by motion of the main axis and the payload. These oscillations are not found to be critical, which is confirmed by the motor torques in Fig. 7.3b. The torques are seen to oscillate slightly during acceleration and deceleration, but without resembling on/off behaviour i.e. oscillating between maximum and minimum torque. Finally, Fig. 7.3c shows the shaft accelerations for motor 2 during the trajectory. The acceleration for motor 1 is left out as this resembles the one for motor 2, but with smaller maximum values. The maximum absolute shaft acceleration is approximately 11500 RPM/s, which is far away from the maximum allowed shaft acceleration of 106950 RPM/s (11200 rad/s² [78]) for the pumps.

Fig. 7.4a shows the required power from the DC-link and the cylinder output power or rate of work. The switching of the inverse shuttle valve and

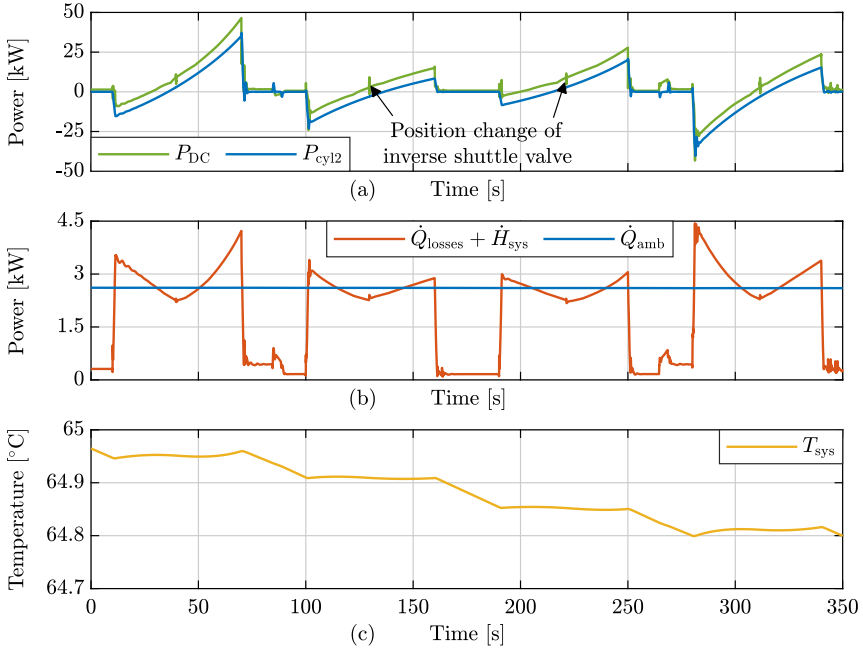


Fig. 7.4: (a) DC-link power required for both motor inverters during the trajectory and cylinder power. (b) Comparison of system losses (friction and sum of enthalpy flow rates) and passive heat transfer rate from the system to the ambience. (c) System temperature.

the associated accelerations of the motor shafts do not require huge power amounts, even though the switching is observable from the power curve as local peaks. Two of these peaks are marked in Fig. 7.4a.

Fig. 7.4b compares $\dot{Q}_{\text{losses}} + \dot{H}_{\text{sys}}$ with the passive heat flow rate from the system to the ambience, \dot{Q}_{amb} . Recall, that \dot{Q}_{losses} includes the frictional losses of the pumps, cylinder and bootstrap reservoir pistons and \dot{H}_{sys} the sum of enthalpy flow rates occurring with the mass transfer *to* the control volumes. As noted in the modelling chapter the losses of the electrical machines are not included in the system temperature dynamics, as the electrical motors are regarded as thermally isolated from the remaining system.

It can be observed in Fig. 7.4b, that the passive heat transfer rate to the ambience at 20 °C is almost constant because the system temperature varies insignificantly. In most of the operating cycle, the heat transfer rate to the ambience is larger than the system losses. However, at large loadings the losses exceed passive heat transfer rates. This means that operation breaks are required to obtain thermal equilibrium at an acceptable oil temperature. Considering the whole motion cycle, the amount of heat transferred to the ambience exceeds the energy losses, meaning that the temperature drops during the motion trajectory. This is confirmed in Fig. 7.4c, where the system temperature decreases from 65 °C to 64.8 °C. The small temperature gradient is related to a large heat capacity of the system. For the given operating conditions and assuming that the system losses are valid at 65 °C the results suggest that passive heat transfer is sufficient. This also assumes that a temperature difference of 45 K to the ambience is present. Note, that if using a VG46 oil, continuous operation of the pumps are allowed within 5 °C and 70 °C [78].

Fig. 7.5 shows the distribution of energy in the dynamic simulation of the ECD+ system. Note that the visualisation of the energy distribution is slightly different than the Sankey diagrams used earlier. The frictional and throttling losses do not *leave* the system as such, but is rather converted to heat and subsequently transferred by passive heat transfer to the ambience.

Compared to the steady state energy consumption, more energy is required from the DC-link (increase of 4.3 % from 606 Wh to 632 Wh), due to dynamic effects such as shaft accelerations and compression flows. The latter is leading to larger shaft speeds causing changed loss behaviour of inverters, electric machines, and pumps. Likewise, the positive output work of the cylinder is slightly larger than for the steady state case. It is observed that the negative cylinder work (available for energy recuperation) is slightly smaller than the positive cylinder work. This difference is originating from disturbance rejection caused by the swinging payload. The energy transferred to the energy storage system (ESS) is larger than for the steady state case meaning that the

7.1. Continuous Controller Implementation

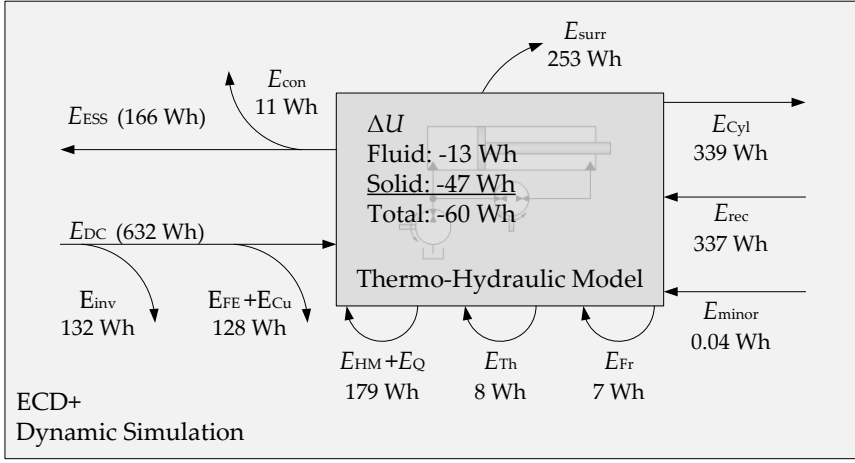


Fig. 7.5: Visualisation of energy distribution for the whole motion trajectory. ΔU is the change in internal energy. Q_{amb} and W_{minor} are heat transferred to the ambience and minor work done on the system respectively.

net amount of energy required from the DC-link is 466 Wh compared to 448 Wh (4 % larger) for the steady state case.

In Fig. 7.5 two energy contributions not observed in the previous Sankey diagrams have been included. These include heat transferred to the ambience by passive heat transfer Q_{amb} and W_{minor} . W_{minor} accounts for work done on the system due to slightly changed conditions by the end of the simulation compared to the initial conditions. This includes smaller shaft speeds (approximately -1 RPM) and slightly changed system pressures. The latter both causes work due to mechanical elasticity and causes a net oil volume needed for fluid compression. This leads to a changing bootstrap position causing a net work to be done on the system.

Finally, Fig. 7.5 shows that the internal energy of the system has decreased by 60 Wh, due to the work and heat transferred to and from the system ($dU = \dot{W} + \dot{Q}$). This has been evaluated as:

$$\text{Solid :} \quad \Delta U = \int_{t_1}^{t_2} \dot{T}_{sys} m_{steel} c_{p,steel} dt \quad (7.1)$$

$$\text{Fluid :} \quad \Delta U = \int_{t_1}^{t_2} \dot{U} dt \quad (7.2)$$

$$\dot{U} = \dot{m}u + m\dot{u} = \dot{m}(h - pv) + m(\dot{h} - \dot{p}v - p\dot{v}) \quad (7.3)$$

$$= \dot{m}h + m\dot{h} - \dot{p}V - p\dot{V} \quad (7.4)$$

The change in internal energy is evaluated for each control volume using the equations above.

7.2 Switching Between Operation Modes

In this section it is investigated how a smooth transition between motion operation mode and self-locking mode may be obtained for the ECD+ system. For this, the motion trajectory previously defined is slightly changed, as the load is kept constant at $m_3 = 5$ ton. The cylinders only extend and retract once, with the system entering self-locking mode whenever the cylinder is at a standstill. All control loops and reference generation blocks except the current controllers are implemented discretely at a sample rate of 1 ms. The control laws have been discretised by emulation of the continuously designed controllers using the bilinear or Tustin's rule.

For a realistic evaluation of the control loops, sensor noise and finite sensor resolutions have been included in this section. The position sensor of the main cylinder, is simulated with a resolution of $5\ \mu\text{m}$. The resolution of the velocity measurement is assumed to $0.1\ \text{mm/s}$. Both of these criteria are met by the magnetostrictive sensors in [124]. Only quantification noise has been included for the position and velocity measurements. The measurements are filtered with a first order low pass filter having a bandwidth 10 times higher than the desired frequency of the motion control loop poles. For the analogue pressure sensors zero mean white noise with a standard deviation of $\sigma=0.1\ \text{bar}$ is added to all pressure sensor measurements. The control loops are found to be sensitive toward noise in the pressure measurements, leading to noise propagation to the shaft speed references causing highly oscillating motor torque references. Therefore the measurements are subsequently filtered with third order low pass filters having a frequency five times larger than the desired bandwidth of the pressure control loops. This is exemplified in Fig. 7.6, where it is seen that the filtered signal, denoted sensor output, adds substantial phase compared to the true state. Filtering the signals is a compromise between adding phase and propagating noise to the control loops. Alternatively more sophisticated filtering techniques may be applied, e.g. Kalman filters as investigated in [125].

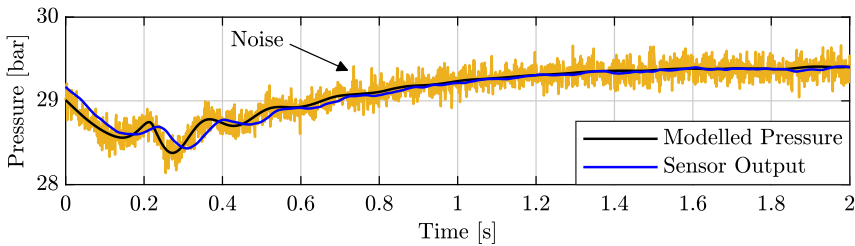


Fig. 7.6: Sensor noise is added to the pressure states in current simulations. The sensor output is obtained using a third order low pass filter.

7.2. Switching Between Operation Modes

To further reduce the impact of the measurement noise to the internal system states it is found beneficial to decrease the desired bandwidth of the pressure control loops while maintaining the desired frequency of the motion loop poles. This leads to:

$$15\omega_L = \omega_\omega, \quad 15\omega_M = \omega_\omega, \quad 3.33\omega_x = \omega_L, \quad 3.33\omega_{xx} = \omega_L \quad (7.5)$$

A local stability analysis equivalent to Sec. 6.5 reveals that this does not lead to system instability.

7.2.1 Switching Logic

The *System State Selector* and pressure generator blocks from Fig. 6.1 on page 104 are designed here. Fig. 7.7 shows a visualisation of the *System State Selector* showing the five distinct states the system may operate within in order to enable smooth transition between motion operation mode (state 3) and self-locking mode (state 0). State 1, 2 and 4 may be regarded as intermediate states.

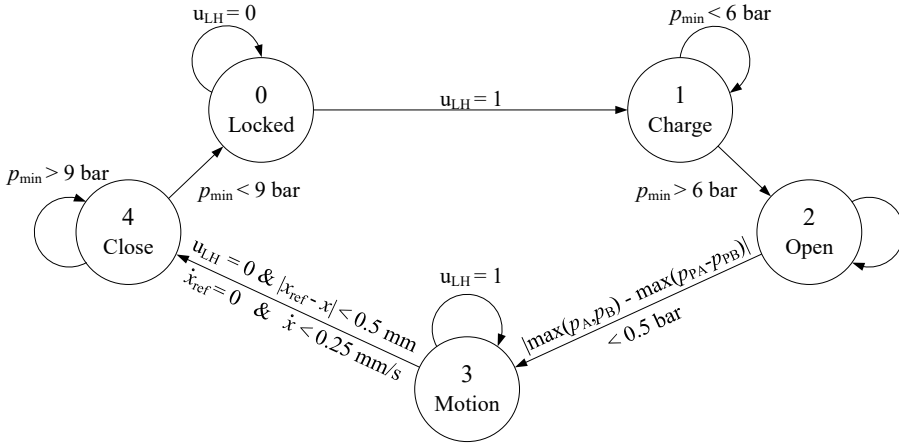


Fig. 7.7: Five states are defined to ensure proper switching between motion operation mode (state 3) and self-locking mode (state 0).

The switching logic illustrated in Fig. 7.7 is elaborated in the following starting from the system being in motion operation mode (state 3):

State 3 (Motion operation mode)

The system remains in motion operation mode as long a *self-locking* switch remains at $u_{LH} = 1$.

State 3 → State 4

When u_{LH} is toggled to $u_{LH} = 0$, the system will attempt to switch to state 4

(closing state). This is only successful if the position error is below 0.5 mm, the velocity reference is 0, i.e. the operator joystick is at neutral position, and the measured velocity is below 0.25 mm/s.

State 4 (Closing)

The closing of the load holding valves are obtained by reducing the minimum pressure reference to 1.01 bar (atmospheric pressure).

The system remains here if the measured minimum pressure is above 9 bar.

State 4 → State 0

When the minimum pressure falls below 9 bar, the load holding valves are estimated to be fully closed, such that the system can safely enter state 0.

State 0 (Self-locking mode)

To decompress the chambers PA and PB quickly the system enters a safe state where the safety valves SV_A and SV_B opens/de-energises. Additionally in this safe state the motion errors are defined to 0 to avoid integrator windup if a small position error is present. Additionally, the motor control references i.e. speed, torque, currents and control voltages are all defined to zero, including their control errors. All integrators are reset to 0. The system remains here as $u_{LH} = 0$.

State 0 → State 1

When the operator toggles $u_{LH} = 1$ the system will enter state 1.

State 1 (Charging)

In this state the safety valves will close and the motor control references are not forced to zero. However, the motion control errors are still defined to zero to maintain motion control integrators inactive. In this state the pressures in the chambers PA and PB are increased to raise reservoir pressure prior to entering the motion operation mode. This is done by increasing the minimum pressure reference, still keeping this below the cracking pressure of the load holding valves. The system remains in this state for $p_{min} < 6$ bar.

State 1 → State 2

When p_{min} increases above 6 bar state 2 is initiated.

State 2 (Opening)

Motion control errors are still defined to zero to maintain integrators inactive. The virtual pressure references are chosen such that the virtual load pressure $p_{PA} - \alpha p_{PB}$ matches the load pressure of the cylinder, i.e. $p_{L,ref} = p_A - \alpha p_B$. The minimum pressure reference is increased to open the load holding valves.

State 2 → State 3

Due to a steady state error (as discussed in Sec. 6.3.3), the obtained load pressure $p_{PA} - \alpha p_{PB}$ will be lower than the reference. Therefore, when the maximum cylinder pressure is within 0.5 bar of the maximum pressure of

7.2. Switching Between Operation Modes

either p_{PA} or p_{PB} this indicates that the load holding valves are open and the system enters state 3.

State 3

As the system re-enters state 3, the load pressure is generated by the motion controller. The initial controller output of the motion controller is chosen to equal the last load pressure reference by adjusting the integrator value.

To obtain smooth pressure references during mode switching, the pressure references are rate limited and filtered by a first order low pass filter. Tab. 7.1 summarises the virtual pressure references and their rate limits.

Table 7.1: Virtual pressure references and rate limits. [†]The rate is selected such that $p_{\min, \text{ref}}$ crosses the opening pressure of the load holding valves as $p_{L, \text{ref}}$ reaches $p_A - \alpha p_B$.

State	$p_{L, \text{ref}}$	$p_{L, \text{ref}}$ rate limit	$p_{\min, \text{ref}}$	$p_{\min, \text{ref}}$ rate limit
0	0 bar	-	1.01 bar	10 bar/s
1	6.15 bar, if $p_A > p_B$ 0 bar otherwise	5 bar/s	8.00 bar	5 bar/s
2	$p_A - \alpha p_B$	75 bar/s	28.80 bar	[†]
3	Motion Controller	-	28.80 bar	15 bar/s
4	Motion Controller	-	1.01 bar	10 bar/s

Note, that for the generation of $p_{L, \text{ref}}$ in state 1, a distinction is made based on which cylinder chamber pressure is largest to ensure that $p_{PA} - p_{PB}$ does not change sign when entering motion operation mode. This ensures no unnecessary position changes of the inverse shuttle valve.

Fig. 7.8 shows the virtual pressure references and how the system states change during the trajectory considered in this section according to Tab. 7.1. Fig. 7.8b shows the active load pressure reference where the red plot is generated by the motion controller and the black plot is from the reference generator. When switching from state 4→0, the non-smooth reference change is acceptable because the system enters a safe state.

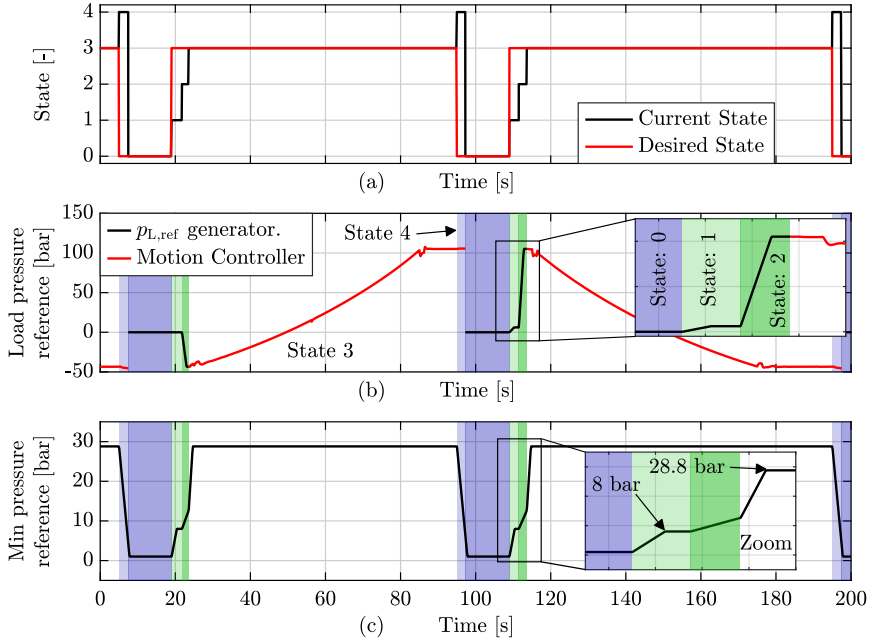


Fig. 7.8: (a) Current and desired system state during the trajectory considered in this section. (b) Load pressure reference. (c) Minimum pressure reference.

7.2.2 Simulation Results

The performance of the system in motion operation mode (state 3) closely resembles the results already presented in the previous section. Therefore focus is on evaluating the system performance during change of operation mode. For convenience a simplified system diagram is given in Fig. 7.9 to keep track of the different states referred to in the following. The locking and unlocking procedure taking place at around 100 s in Fig. 7.8 is used as an example in Fig. 7.10 on page 138 to evaluate the switching logic and the performance of the ECD+ system during mode transition.

The left hand five plots of Fig. 7.10 show the virtual pressure states and their references, the physical pressures and the piston position when switching to self-locking mode. The right hand five plot show the same states when returning to motion operation mode. In Fig. 7.10c it is seen how the minimum pressure slowly decreases to close the load holding valves. When the minimum pressure reaches 9 bar the system switch to state 0 where all pressures reduce quickly due to the opening of the safety valves. Note in Fig. 7.10i how the reduction of the minimum pressure initially creates a small position error of less than 0.1 mm. This is eliminated by the motion controller, before entering the self-locking mode.

7.2. Switching Between Operation Modes

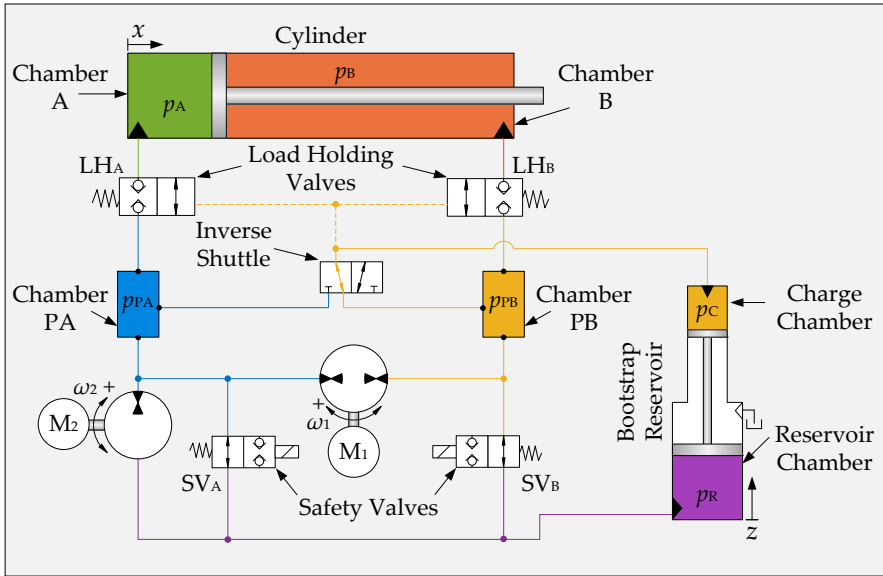


Fig. 7.9: Simplified system diagram intended to be useful for the reader as the simulation results are presented in the following.

When re-entering motion operation mode it is clear how the virtual pressure response is not ideal due to bad parameter estimates as discussed in Sec. 6.3.3. This is especially true in state 1. However as the minimum pressure in Fig. 7.10d reaches more than 6 bar, state 2 is initiated and pressure references are increased. As parameter estimates (bulk moduli) are now closer to the true values caused by the higher pressures, the virtual pressures are realised with smaller errors. In Fig. 7.10b it is clearly seen that a steady state error is present in the load pressure response, in state 2. In this case this means that the physical pressure p_{PA} is smaller than the corresponding cylinder chamber pressure p_A . Despite this, it is possible to obtain a reasonable performance when opening the load holding valves. This is possible because the cylinder chambers are being significantly larger than the chambers PA and PB. This means that if the load holding valves are opened while the pressures differ slightly, the small chambers PA and PB will be pressurised without affecting the cylinder position significantly. This is also seen in Fig. 7.10. As the minimum pressure continues to increase in state 2 (Fig. 7.10d), the load holding valves finally open, which is visible just before entering state 3 as p_{PA} quickly increases to equal p_A . This triggers entering state 3, where the minimum pressure reference rate is increased compared to state 2. In Fig. 7.10j the pressurisation of chambers PA and PB, as the state changes from 2 to 3 and the increase of the minimum pressure in state 3, causes a small

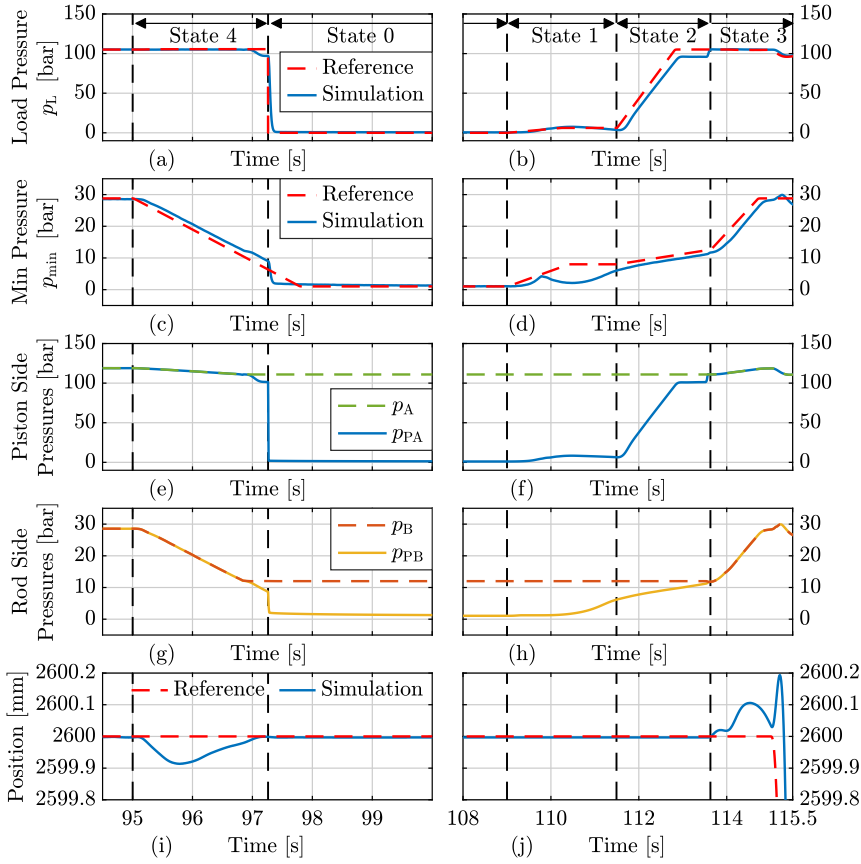


Fig. 7.10: Left hand plots: References and states as the system enters self-locking mode (state 0). Right hand plots: References and states as the system enters motion operation mode (state 3). (a)-(b) Reference and simulated load pressure. (c)-(d) Reference and simulated minimum pressure. (e)-(f) Simulated piston side pressures (g)-(h) Simulated rod side pressures. (i)-(j) Reference and simulated piston position.

piston error (approximately 0.1 mm), before motion is initiated after 115 s.

Altogether Fig. 7.10 confirms that smooth switching of the load holding valves is obtainable by properly controlling the virtual pressure states. Small position errors occur during the locking and unlocking process. These may be reduced by allowing the process to last for longer i.e. smaller pressure reference rates. Faster transition processes on the other hand lead to larger control errors, lower reservoir pressures during transitions (cavitation risk) and larger motor shaft accelerations. The results presented here therefore represent a compromise. The closing of the load holding valves lasts 2.5 s and opening takes around 5 s.

7.2. Switching Between Operation Modes

In the previous section it was shown how the reservoir pressure was kept within the limits of 1.5 to 4 bar in motion operation mode. As the system pressures are reduced to atmospheric pressure during self-locking mode, this is obviously not possible to obtain while changing operation mode. Fig. 7.11a shows the simulated charge and reservoir pressure. It is seen that the reservoir pressure drops to atmospheric pressure in self-locking mode. In the zoomed window of Fig. 7.11a it is even seen how the reservoir pressure drops below atmospheric pressure when returning to motion operation mode. This happens because compression flows are needed in order to increase pressure levels, meaning that the bootstrap reservoir pistons need to retract. This causes a friction force in the same direction as the force generated by the reservoir pressure, leading to pressures below the ambient pressure. Even though the reservoir pressure is kept above 0.85 bar and thus above the minimum allowed suction pressure of the pumps (0.8 bar [78]), this needs further examination. Low pressures may cause severe cavitation problems and thus reduce system reliability. The examination is preferably done through experimental testing, as the magnitude of the modelled friction force is seen to impact the reservoir pressure significantly.

For completeness Fig. 7.11 shows the simulated piston position. It may be observed that there are no significant differences regarding control error compared to the continuous controller implementation case neglecting measurement noise from the previous section.

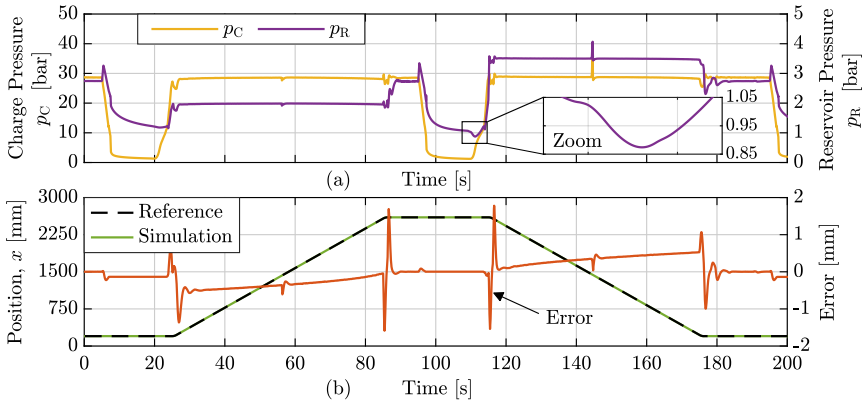


Fig. 7.11: (a) Charge and reservoir pressures. (b) Simulated and reference piston position.

Fig. 7.12 shows how the measurement noise propagates to the actuator references, i.e. shaft speed and torque references. In Fig. 7.12a it may first be observed how mode operation changes require small shaft speeds only. This is the case because the mode switching is fundamentally done by controlling the pressures in the small chambers PA and PB as well as the charge

chamber of the bootstrap reservoir. The maximum speed during transition is roughly 375 RPM. Fig. 7.12a also shows that measurement noise causes the shaft speed references to oscillate with an amplitude of around 10 RPM. The oscillating shaft speed references propagate to oscillating motor torque references of up to 10 Nm as seen in Fig. 7.12b.

Finally, Fig. 7.12c shows the required power from the DC-link, which is oscillating caused by the varying shaft speed and torque references. Fig. 7.12c also clearly demonstrates the advantage of entering self-locking mode in terms of energy consumption. Instead of having a standby consumption of roughly 700-900 W at standstill if load holding valves remain open this may be reduced to 0 W in self-locking mode.

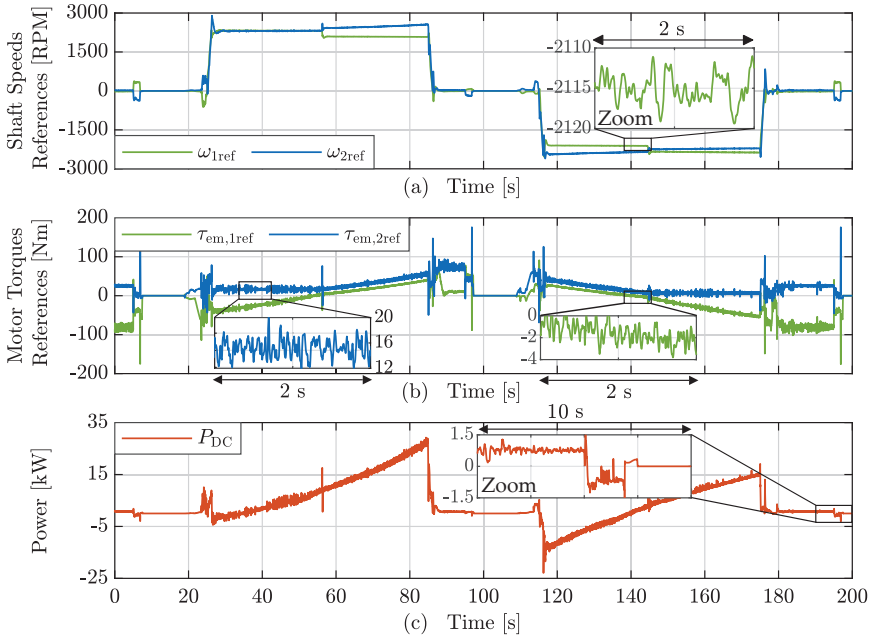


Fig. 7.12: (a) Shaft speed references. (b) Motor torque references. (c) Power required from DC-link.

Chapter 8

Closing Remarks

8.1 Conclusions

This dissertation is motivated by the poor energy efficiency of conventional hydraulic systems. It is concerned with designing and simulating an efficient electro-hydraulic compact drive (ECD), meeting the requirements defined by load carrying applications working in four quadrants, such as cranes and excavators. As a case study a medium sized knuckle boom crane is considered. The specific requirements include the design of a gasless reservoir solution permitting the system to operate in tilted orientations as well as the design of a load holding functionality not preventing the ECD system from recovering potential energy as the crane lowers its load.

To initiate the study, the energy consumption characteristics of a basic ECD system has been compared to a valve-controlled system architecture considering actuation of the knuckle boom crane. This analysis showed a potential for energy savings in the range of 58 % to 75 % for a realistic motion cycle. This is partly achieved by superior energy efficiencies in resistive load quadrants and due to the ability of the ECD to recover energy in aided load quadrants. ECDs may be designed as decentralised compact units integrating the electrical prime mover, hydraulic pumps, reservoir and cylinder. This eliminates the need for hydraulic piping to the cylinder but reduces the static payload capacity. To investigate the specific reduction for the considered crane, a mechanical crane model is established showing that a decentralised location of the ECD reduces the static payload capacity by approximately 3 %.

To meet the requirements in terms of load holding functionality and a gasless oil reservoir a novel system architecture is proposed. This system consists of a self-pressurising reservoir charged by internal system pressures and

a so-called indirectly controlled hydraulic lock. The lock ensures that the cylinder is hydraulically locked in case of power loss or hose burst, but may be unlocked by properly controlling the internal pressure states. Two electrical motor-pump units are included to permit sufficient control possibilities and to increase the scalability properties, thus expanding the application range.

To ensure that the load holding valves are fully open and to keep the reservoir pressure within an allowed range during operation, it is important to maintain a certain minimum pressure level in the cylinder chambers. To enable smooth opening and closing of the load holding valves it is furthermore required that the pressure level may be adjusted during operation. As two electric motor drive units are used as system inputs a multiple-input-multiple-output control system consisting of two virtual pressure control loops and an outer motion control loop have been designed, analysed and simulated in this dissertation. A linear analysis reveals strong dynamic cross couplings between the virtual pressure states and the physical inputs, which are handled by defining an input mapping between desired virtual pressure dynamics and the physical shaft speed references. All designed control loops may be parametrised by a few basic parameters such as chamber volumes, pump displacements, cylinder areas, and equivalent mass. This is assessed to be a versatile approach that is easier to implement and tune for commissioning personnel compared to numerical or frequency response based design and tuning methods. By defining five operation modes for the system, simulation results show that it is possible to control the opening of the load holding valves, as well as obtaining proper motion performance while keeping the reservoir pressure elevated. Thus it is found possible to design and control an ECD system meeting the requirements defined by load carrying applications still offering significantly improved energy characteristics compared to valve-controlled systems.

For the considered motion cycle, a thermo-hydraulic analysis shows that the passive heat transfer from the system to the ambience is sufficient in order to maintain the oil temperature at reasonable levels. This suggest that active cooling may be avoided. This result is based on a thermo-hydraulic modelling method derived within the project and verified using experimental data obtained from a smaller version of an ECD.

The dissertation contributes with knowledge to the research field by suggesting new technical solutions to the load holding and oil reservoir design challenges. Additionally, insights into how the thermal behaviour of ECDs may be simulated are provided. These findings may lead to an expansion of the application range, and thus a wider acceptance of ECDs as a viable energy efficient alternative to conventional valve-controlled hydraulic systems, which is also relevant for safety critical load carrying applications.

8.2 Future Work

As a natural next step, the further studies should include experimental validation of the proposed system architecture and associated control methodology. This includes investigations considering the obtainable energy efficiency, the ability to smoothly engaging and disengaging the hydraulic lock and evaluation of motion tracking performance. Furthermore, the applicability of the bootstrap reservoir must be investigated, with special attention on the friction and leakage characteristics.

Due to practical and economical restrictions, it is beneficial to conduct a first round of experimental tests on a downscaled ECD. For this purpose an ECD with a maximum electrical motor power of 9.7 kW has been designed and manufactured as a part of the project. The ECD has been manufactured without attaching a hydraulic cylinder yet, to facilitate easy changeover between different cylinder sizes and thus applications. The ECD may deliver a piston side flow of up to 21.6 L/min, and is optimised for a cylinder with an area ratio of 2/3 in terms of pump displacement matching.

The designed ECD prototype offers a number of additional configuration

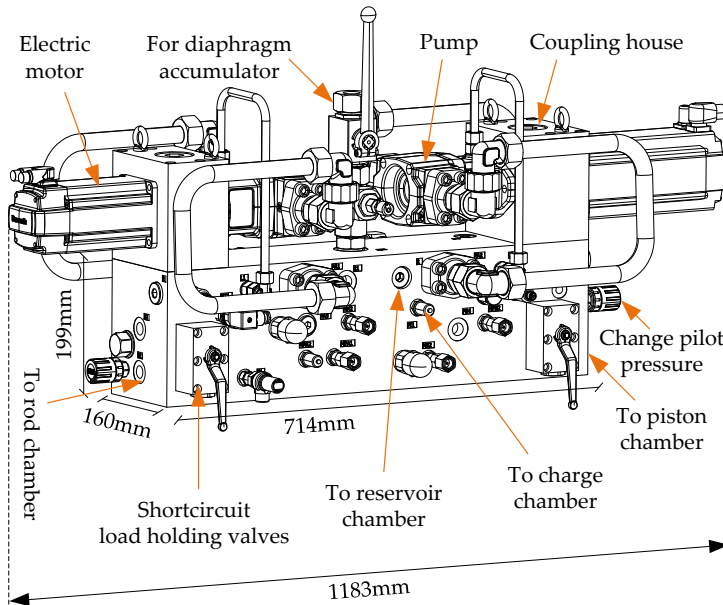


Fig. 8.1: Configurable ECD prototype that has been manufactured within the project to validate the proposed system architecture and derived control methods. Unfortunately it has not been possible to obtain experimental results within the project period and the prototype awaits testing by upcoming PhD students within the SFI Offshore Mechatronics Research Project.

possibilities. Manually controlled ball valves may be adjusted to short-circuit the load holding valves if an application does not require this functionality. Additional directional valves may change the pilot setting of the load holding valves. This enables using the crossport of the cylinder as the pilot pressure (illustrated in section 4.1.2) or using the lowest chamber pressure as investigated in this dissertation. Finally, it is possible to either include a gas-charged accumulator to the system or to utilise a bootstrap reservoir. Fig. 8.1 shows a drawing of the manufactured ECD system. In Fig. 8.2 a bootstrap reservoir prototype capable of delivering a compensation volume of 1.9 L is shown.

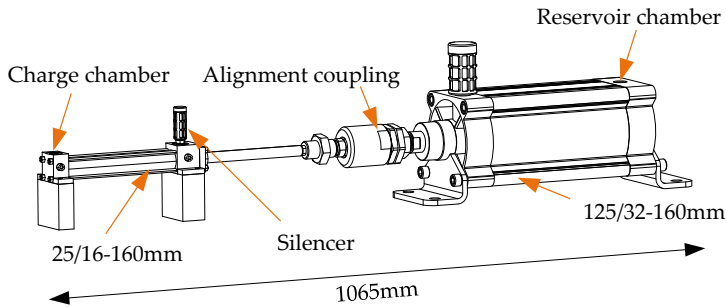


Fig. 8.2: Bootstrap reservoir prototype that has been manufactured within the project.

References

Note: All URL-links have been accessed on February 1st, 2022

- [1] B. Brahmer, "CLDP - Hybrid Drive using Servo Pump in Closed Loop," in *Proceedings of the 8th International Fluid Power Conference*, Dresden, March 26-28, 2012, pp. 93–102.
- [2] C. Williamson, "Power Management for Multi-Actuator Mobile Machines with Displacement Controlled Hydraulic Actuators," Ph.D. dissertation, Purdue University, West Lafayette, Indiana, USA, 2010.
- [3] D. Padovani, M. Rundo, and G. Altare, "The Working Hydraulics of Valve-Controlled Mobile Machines: Classification and Review," *Journal of Dynamic Systems, Measurement, and Control*, vol. 142, no. 7, 2020.
- [4] C. Williamson, J. Zimmerman, and M. Ivantysynova, "Efficiency study of an excavator hydraulic system based on displacement-controlled actuators," in *Proceeding of the ASME/BATH Symposium on Fluid Power and Motion Control*, Bath, UK, September 10-12, 2008, pp. 291–307.
- [5] L. Love, E. Lanke, and P. Alles, "Estimating the Impact (Energy, Emissions and Economics) of the US Fluid Power Industry," Oak Ridge National Laboratory (ORNL), Oak Ridge, TN, United States, Tech. Rep. December, 2012. [Online]. Available: <https://doi.org/10.2172/1061537>
- [6] V. H. Donkov, "Secondary Control of Multi-chamber Cylinders for Low-speed, High-force Offshore Applications," Ph.D. dissertation, Aalborg University, Denmark, 2020.
- [7] D. Fassbender, T. Minav, C. Brach, and K. Huhtala, "Improving the Energy Efficiency of Single Actuators with High Energy Consumption: An Electro-Hydraulic Extension of Conventional Multi-Actuator Load-Sensing Systems," in *Proceedings of the 17th Scandinavian International Conference on Fluid Power*, Linköping, Sweden, May 31 - June 2, 2021.
- [8] V. H. Donkov, T. O. Andersen, M. K. Ebbesen, and H. C. Pedersen, "Applying Digital Hydraulic Technology on a Knuckle Boom Crane,"

References

- in *Proceedings of the Ninth Workshop on Digital Fluid Power*, Aalborg, Denmark, September 7-8, 2017.
- [9] V. Donkov, T. O. Andersen, H. C. Pedersen, and M. K. Ebbesen, "Application of Model Predictive Control in Discrete Displacement Cylinders to Drive a Knuckle Boom Crane," in *Proceedings of the 2018 Global Fluid Power Society PhD Symposium (GFPS)*, Samara, Russia, July 18-20, 2018.
 - [10] P. Achten, Z. Fu, and G. Vael, "Transforming future hydraulics: a new design of a hydraulic transformer," in *Proceedings of the Fifth Scandinavian International Conference on Fluid Power*, Linköping, Sweden, May 28-30, 1997.
 - [11] P. Achten and J.-O. Palmberg, "What a Difference a Hole Makes - The Commercial Value of the Innas Hydraulic Transformer," in *Proceedings of the Sixth Scandinavian International Conference on Fluid Power*, Tampere, Finland, May 26-28, 1999, pp. 873–886.
 - [12] P. Achten, "Fluid power genes and memes - About sharks, mice and a poor albatross chick," Key note speak held at the 16th Scandinavian International Conference on Fluid Power in Tampere, Finland, May 22-24., 2019. [Online]. Available: <https://bit.ly/3KUE5pL>
 - [13] K. Heybroek, "On Energy Efficient Mobile Hydraulic Systems: with Focus on Linear Actuation," Ph.D. dissertation, Linköping University, Sweden, 2017.
 - [14] E. Busquets and M. Ivantysynova, "A Multi-Actuator Displacement-Controlled System with Pump Switching – A Study of the Architecture and Actuator-Level Control," *JFPS International Journal of Fluid Power System*, vol. 8, no. 2, pp. 66–75, 2014.
 - [15] R. Rahmfeld, "Development and Control of Energy Saving Hydraulic Servo Drives for Mobile Systems," Ph.D. dissertation, TU Hamburg-Harburg, Germany, 2002.
 - [16] C. Williamson and M. Ivantysynova, "The Effect of Pump Efficiency on Displacement-Controlled Actuator Systems," in *Proceedings of the 10th Scandinavian International Conference on Fluid Power*, Tampere, Finland, May 21-23, 2007, pp. 301–326.
 - [17] R. Rahmfeld, M. Ivantysynova, and J. Weber, "Displacement Controlled Wheel Loader - a simple and clever Solution," in *Proceedings of the 4th International Fluid Power Conference*, Dresden, Germany, March 25-26, 2004, pp. 183–196.
 - [18] T. Neubert, "Elektro-hydraulische antriebssysteme mit drehzahlveränderbaren Pumpen," in *Proceedings of 1. Internationales Fluidtechnisches Kolloquium*, Aachen, Germany March 17-18, in German, 1998.

References

- [19] I. Rühlicke, “Elektrohydraulische Antriebssysteme mit drehzahlveränderbarer Pumpe,” Ph.D. dissertation, TU Dresden, Germany, in German, 1997.
- [20] B. Kazmeier, “Energieverbrauchsoptimierte Regelung eines elektrohydraulischen Linearantriebs kleiner Leistung mit drehzahlgeregeltem Elektromotor und Verstellpumpe,” Ph.D. dissertation, TU Hamburg-Harburg, Germany, in German, 1998.
- [21] M. Ristic and M. Wahler, “Electrification of Hydraulics Opens New Ways for Intelligent Energy-Optimized Systems,” in *Proceedings of the 11th International Fluid Conference*, Aachen, Germany March 21-23, 2018.
- [22] W. Pawlus, M. Choux, and M. R. Hansen, “Hydraulic vs. Electric: A Review of Actuation Systems in Offshore Drilling Equipment,” *Modeling, Identification and Control: A Norwegian Research Bulletin*, vol. 37, no. 1, pp. 1–17, 2016. [Online]. Available: <https://doi.org/10.4173/mic.2016.1.1>
- [23] Bosch Rexroth AG, “Electromechanical Cylinder EMC-HD,” Product Presentation., 2015. [Online]. Available: <https://bit.ly/39ESk0n>
- [24] Parker Hannifin, “Extreme Force Electromechanical Cylinder – Series XFC.” Product Catalogue HY08-0890-4/NA, 2013. [Online]. Available: <https://prker.co/39DuYbu>
- [25] D. Hagen, W. Pawlus, M. K. Ebbesen, and T. O. Andersen, “Feasibility Study of Electromechanical Cylinder Drivetrain for Offshore Mechatronic Systems,” *Modeling, Identification and Control: A Norwegian Research Bulletin*, vol. 38, no. 2, pp. 59–77, 2017. [Online]. Available: <https://doi.org/10.4173/mic.2017.2.2>
- [26] S. Osterland, L. Müller, and J. Weber, “Influence of Air Dissolved in Hydraulic Oil on Cavitation Erosion,” *International Journal of Fluid Power*, vol. 22, no. 3, 2021.
- [27] S. Kärnell, “Fluid Power Pumps and the Electrification in Load Handling Applications,” Licentiate Thesis, Linköping University, Sweden, 2020.
- [28] S. Michel and J. Weber, “Energy-efficient Electrohydraulic Compact Drives for Low Power Applications,” in *Proceedings of the ASME/BATH Symposium on Fluid Power and Motion Control*, Bath, UK, September 12-14, 2012, pp. 93–107.
- [29] —, “Electrohydraulic Compact-drives for Low Power Applications considering Energy-efficiency and High Inertial Loads,” in *Proceedings of the 7th FPNI PhD Symposium on Fluid Power*, Reggio Emilia, Italy, 2012, pp. 1–18.

References

- [30] D. van den Bossche, "The A380 Flight Control Electrohydrostatic Actuators, Achievements and Lessons Learnt," in *Proceedings of the 25th International Congress of the Aeronautical Sciences (ICAS)*, Hamburg, Germany, September 3-8, 2006.
- [31] J. C. Mare, "Combining Hydraulics and Electrics for Innovation and Performance Improvement in Aerospace Actuation," in *Proceedings of the 12th Scandinavian International Conference on Fluid Power*, Tampere, Finland, May 18-20, 2011, pp. 255–270.
- [32] S. Michel, "Elektrisch-hydrostatische Kompaktantriebe mit Differentialzylinder für die industrielle Anwendung," Ph.D. dissertation, TU Dresden, Germany, in German, 2021.
- [33] Parker Hannifin, "Parker Compact EHA Electro-Hydraulic Actuators," Product catalogue, 2009. [Online]. Available: <https://prker.co/2ZFOzWQ>
- [34] Bucher, "HELAX – The Solution for Decentralized Drive Concepts with High Efficiency," Product sheet, 2020. [Online]. Available: <https://bit.ly/3ui24sQ>
- [35] J. Weber, B. Beck, E. Fischer, R. Ivantysyn, G. Kolks, M. Kunkis, H. Lohse, J. Lübbert, S. Michel, M. Schneider, L. Shabi, A. Sitte, J. Weber, and J. Willkomm, "Novel System Architectures by Individual Drives," in *Proceedings of the 10th International Fluid Power Conference*, Dresden, Germany, March 8-10, 2016, pp. 29–62.
- [36] A. Imam, M. Rafiq, E. Jalayeri, and N. Sepehri, "Design, Implementation and Evaluation of a Pump-Controlled Circuit for Single Rod Actuators," *Actuators*, vol. 6, no. 1, 2017. [Online]. Available: <https://doi.org/10.3390/act6010010>
- [37] D. Padovani, S. Ketelsen, D. Hagen, and L. Schmidt, "A Self-Contained Electro-Hydraulic Cylinder with Passive Load-Holding Capability," *Energies*, vol. 12, no. 2, 2019. [Online]. Available: <https://doi.org/10.3390/en12020292>
- [38] G. K. Costa and N. Sepehri, "Four-Quadrant Analysis and System Design for Single-Rod Hydrostatic Actuators," *Journal of Dynamic Systems, Measurement and Control*, vol. 141, no. 2, 2018.
- [39] H. Çalışkan, T. Balkan, and B. E. Platin, "A Complete Analysis and a Novel Solution for Instability in Pump Controlled Asymmetric Actuators," *Journal of Dynamic Systems, Measurement, and Control*, vol. 137, no. 9, 2015. [Online]. Available: <https://doi.org/10.1115/1.4030544>
- [40] —, "A Complete Analysis for Pump Controlled Single Rod Actuators," in *Proceedings of the 10th International Fluid Power Conference*, Dres-

- den, Germany, March 8-10, 2016, pp. 119–132.
- [41] L. Wang and W. J. Book, "Using Leakage to Stabilize a Hydraulic Circuit for Pump Controlled Actuators," *Journal of Dynamic Systems, Measurement, and Control*, vol. 135, no. 6, 2013. [Online]. Available: <https://doi.org/10.1115/1.4024900>
 - [42] G. K. Costa and N. Sepehri, "A Critical Analysis of Valve-Compensated Hydrostatic Actuators: Qualitative Investigation," *Actuators*, vol. 8, no. 59, 2019. [Online]. Available: <https://doi.org/10.3390/act8030059>
 - [43] P. H. Gøytil, D. Padovani, and M. R. Hansen, "A novel solution for the elimination of mode switching in pump-controlled single-rod cylinders," *Actuators*, vol. 9, no. 1, 2020. [Online]. Available: <https://doi.org/10.3390/act9010020>
 - [44] E. Jalayeri, A. Imam, Z. Tomas, and N. Sepehri, "A throttle-less single-rod hydraulic cylinder positioning system: Design and experimental evaluation," *Advances in Mechanical Engineering*, vol. 7, no. 5, 2015. [Online]. Available: <https://doi.org/10.1177/1687814015583249>
 - [45] L. Quan, Y. Yang, and X. Hou, "Simulation and experimental research on the axial piston pump with series three-windows in valve plate," in *Proceedings of the 2011 International Conference on Fluid Power and Mechatronics*, Beijing, China, August 17-20, 2011, pp. 71–76. [Online]. Available: <https://doi.org/10.1109/FPM.2011.6045732>
 - [46] X. Zhang, L. Quan, Y. Yang, C. Wang, and L. Yao, "Output characteristics of a series three-port axial piston pump," *Chinese Journal of Mechanical Engineering*, vol. 25, no. 3, pp. 498–505, 2012.
 - [47] J. Huang, L. Quan, and X. Zhang, "Development of a dual-acting axial piston pump for displacement-controlled system," *Proceedings of the Institution of Mechanical Engineers, Part B: Journal of Engineering Manufacture*, vol. 228, no. 4, pp. 606–616, 2013. [Online]. Available: <https://doi.org/10.1177/0954405413506196>
 - [48] J. Huang, Z. Hu, L. Quan, and Z. Xiaogang, "Development of an Asymmetric Axial Piston Pump for Displacement-Controlled System," *Institution of Mechanical Engineers, Part C: Journal of Mechanical Engineering Science*, vol. 228, no. 8, pp. 1418–1430, 2013. [Online]. Available: <https://doi.org/10.1177/0954406213508385>
 - [49] T. Minav, S. Panu, and P. Matti, "Direct-Driven Hydraulic Drive Without Conventional Oil Tank," in *Proceedings of the ASME/BATH Symposium on Fluid Power & Motion Control*, Bath, UK, September 10-12, 2014, pp. 1–6.
 - [50] T. Minav, C. Bonato, P. Sainio, and M. Pietola, "Position control of direct

References

- driven hydraulic drive,” in *Proceedings of the 8th FPNI PhD Symposium on Fluid Power*, Lappeenranta, Finland, June 11-13, 2014.
- [51] L. Schmidt, M. Groenkjaer, H. C. Pedersen, and T. O. Andersen, “Position Control of an Over-Actuated Direct Hydraulic Cylinder Drive,” *Control Engineering Practice*, vol. 64, 2017.
- [52] L. Schmidt, D. B. Roemer, H. C. Pedersen, and T. O. Andersen, “Speed-Variable Switched Differential Pump System for Direct Operation of Hydraulic Cylinders,” in *Proceedings of the ASME/BATH Symposium on Fluid Power and Motion Control*, Chicago, Illinois, USA, October 12-14, 2015.
- [53] K. Cleasby and A. Plummer, “A Novel High Efficiency Electro-hydrostatic Flight Simulator Motion System,” in *Proceedings of the ASME/BATH Symposium on Fluid Power and Motion Control*, Bath, UK, September 10-12, 2008, pp. 437–449.
- [54] Bucher Hydraulics, “Decentralized Hydraulic - Electric Linear Axis,” Product sheet, 2020. [Online]. Available: <https://bit.ly/2ZRO9wE>
- [55] H. C. Pedersen, L. Schmidt, T. O. Andersen, and M. H. Brask, “Investigation of New Servo Drive Concept Utilizing Two Fixed Displacement Units,” in *Proceedings of the 9th International Symposium in Fluid Power*, Matsue, Japan, October 28-31, 2014. [Online]. Available: <https://doi.org/10.5739/jfpsij.8.1>
- [56] S. Helduser, “Electric-Hydrostatic Drive Systems and their Application in Injection Moulding Machines,” in *Proceedings of the Forth JHPS International Symposium on Fluid Power*, Tokyo, Japan, November 15-17, 1999, pp. 261–266.
- [57] —, “Electric-hydrostatic drive - An Innovative Energy-Saving Power and Motion Control System,” *Proceedings of the Institution of Mechanical Engineers, Part I: Journal of Systems and Control Engineering*, vol. 213, no. 5, pp. 427–438, 1999.
- [58] Q. Long, T. Neubert, and S. Helduser, “Principle to Closed Loop Control Differential Cylinder with Double Speed Variable Pumps and Single Loop Control Signal,” *Chinese Journal of Mechanical Engineering (English Edition)*, vol. 17, pp. 85–88, 2004.
- [59] P. Gøyttil, D. Padovani, and M. R. Hansen, “On the Energy Efficiency of Dual Prime Mover Pump-Controlled Hydraulic Cylinders,” in *Proceedings of the ASME/BATH Symposium on Fluid Power and Motion Control*, Sarasota, FL, USA, October 7-9, 2019.
- [60] D. Hagen, D. Padovani, and M. Choux, “A Comparison Study of a Novel Self-Contained Electro-Hydraulic Cylinder versus a

- Conventional Valve-Controlled Actuator — Part 2 : Energy Efficiency,” *Actuators*, vol. 78, no. 4, 2019. [Online]. Available: <https://doi.org/10.3390/act8040078>
- [61] P. Casoli, F. Scolari, T. Minav, and M. Rundo, “Comparative Energy Analysis of a Load Sensing System and a Zonal Hydraulics for a 9 - Tonne Excavator,” *Actuators*, vol. 39, no. 9, 2020. [Online]. Available: <https://doi.org/doi:10.3390/act9020039>
- [62] D. Fassbender, V. Zakharov, and T. Minav, “Utilization of electric prime movers in hydraulic heavy-duty-mobile-machine implement systems,” *Automation in Construction*, vol. 132, 2021. [Online]. Available: <https://doi.org/10.1016/j.autcon.2021.103964>
- [63] P. Gøyttil and D. Padovani, “Motion Control of Large Inertia Loads Using Electrohydrostatic Actuation,” in *Proceedings of the IEEE 16th International Workshop on Advanced Motion Control*, Kristiansand, Norway, September 14-16, 2020. [Online]. Available: <https://doi.org/10.1109/AMC44022.2020.9244442>
- [64] L. Schmidt, S. Ketelsen, N. Grønkaer, and K. V. Hansen, “On Secondary Control Principles in Pump Controlled Electro-Hydraulic Linear Actuators,” in *Proceedings of the ASME/BATH Symposium on Fluid Power and Motion Control*, Virtual Conference, September 9-11, 2020, pp. 1–13.
- [65] N. Grønkaer, K. V. Hansen, P. Johansen, and L. Schmidt, “Tribotronics in Electro-Hydraulic Actuator Technology: Improving Durability by Control,” in *In Proceedings of the ASME/BATH Symposium on Fluid Power and Motion Control*, Virtual Conference, September 9-11, 2020.
- [66] S. Qu, D. Fassbender, A. Vacca, and B. Enrique, “Formulation , Design and Experimental Verification of an Open Circuit Electro-Hydraulic Actuator,” in *Proceedings of the IEEE Global Power Society PhD Symposium (GFPS)*, Virtual Conference, October 19-21, 2020.
- [67] S. Qu, D. Fassbender, A. Vacca, B. Enrique, and U. Neumann, “A Closed Circuit Electro-Hydraulic Actuator with Energy Recuperation Capacity,” in *Proceedings of the 12th International Fluid Power Conference*, Virtual Conference, October 12-14, 2020, pp. 89–98.
- [68] R. Mommers, P. Achten, J. Achten, and J. Potma, “Benchmarking the performance of hydrostatic pumps,” in *Proceedings of the 17th Scandinavian International Conference on Fluid Power*, Linköping, Sweden, May 31 - June 2, 2021.
- [69] Bucher Hydraulic, “Fixed Displacement Piston Pumps and Motors - AX Series,” Datasheet, 2021. [Online]. Available: <https://bit.ly/3gcZJHJ>
- [70] S. Michel and J. Weber, “Investigation of Self-Contamination of Electro-

References

- hydraulic Compact Drives,” in *Proceedings of the 10th JFPS International Symposium on Fluid Power*, Fukuoka, Japan, October 24-27, 2017.
- [71] S. Michel, T. Schulze, and J. Weber, “Energy-efficiency and thermo energetic behaviour of electrohydraulic compact drives,” in *Proceedings of the 9th International Fluid Power Conference*, Aachen, Germany, March 24-26, 2014.
- [72] S. Michel and J. Weber, “Prediction of the Thermo-Energetic Behaviour of an Electrohydraulic Compact Drive,” in *Proceedings of the 10th International Fluid Power Conference*, Dresden, Germany, March 8-10, 2016, pp. 219-234.
- [73] S. Qu, D. Fassbender, A. Vacca, and E. Busquets, “Development of a Lumped-Parameter Thermal Model for Electro-Hydraulic Actuators,” in *Proceedings of the 10th International Conference on Fluid Power Transmission and Control (ICFP)*, Hangzhou, China, April 11-13, 2021, pp. 20-31.
- [74] P. Ponomarev, T. Minav, R. Åman, and L. Luostarinen, “Integrated electro-hydraulic machine with self-cooling possibilities for non-road mobile machinery,” *Journal of Mechanical Engineering*, vol. 61, no. 3, 2015. [Online]. Available: <https://doi.org/10.5545/sv-jme.2014.2017>
- [75] J. Siefert and P. Y. Li, “Optimal Control and Energy-Saving Analysis of Common Pressure Rail Architectures: HHEA and STEAM,” in *Proceedings of the BATH/ASME 2020 Symposium on Fluid Power and Motion Control*, Virtual Conference, September 9-11, 2020.
- [76] M. K. Bak, “Model Based Design of Electro-Hydraulic Motion Control Systems for Offshore Pipe Handling Equipment,” Ph.D. dissertation, Univeristy of Agder, Norway, 2014.
- [77] NOV, “Lifting & Handling product portfolio,” 2018. [Online]. Available: <https://bit.ly/3z96KB2>
- [78] Bosch Rexroth, “Axial piston units A10FZO, A10VZO and A10FZG, A10VZG Series 10 for variable-speed drives. RE 91485,” Datasheet, 2016. [Online]. Available: www.bit.ly/3qQy0mm
- [79] —, “Axial Piston Fixed Pump A2FO - RE 91401,” Datasheet, 2012. [Online]. Available: <https://bit.ly/30A8wiC>
- [80] —, “Axial Piston Fixed Pump A4FO - RE 91455,” Datasheet, 2015. [Online]. Available: <https://bit.ly/3kKbBDH>
- [81] —, “Rexroth IndraDyn E - Standard Motors MOT-FC for Frequency Converter Operation - R911343624,” Project Planning Manual, 2015. [Online]. Available: <https://bit.ly/30thmif>
- [82] —, “Rexroth IndraDyn S MSK Synchronous Motors - RE911296289,” Project Planning Manual, 2013. [Online]. Available: <https://bit.ly/3kG>

LD3T

- [83] Eaton, "Hydraulic Cylinders - Heavy Duty Metric Mill Type," Datasheet, 2010. [Online]. Available: <https://eaton.works/3DILudy>
- [84] B. Siciliano and O. Khatib, *Handbook of Robotics*, 1st ed. Berlin, Heidelberg: Springer, 2008. [Online]. Available: <https://doi.org/10.1007/978-3-540-30301-5>
- [85] L. Schmidt, "Robust Control of Industrial Hydraulic Cylinder Drives - with Special Reference to Sliding Mode- & Finite-Time Control," Ph.D. dissertation, Aalborg University, Denmark, 2014.
- [86] M. K. Bak and M. R. Hansen, "Analysis of Offshore Knuckle Boom Crane - Part One: Modeling and Parameter Identification," *Modeling, Identification and Control: A Norwegian Research Bulletin*, vol. 34, no. 4, 2013. [Online]. Available: <http://doi.org/10.4173/mic.2013.4.1>
- [87] J. Zimmerman, "Toward Optimal Multi-Actuator Displacement Controlled Mobile Hydraulic Systems," Ph.D. dissertation, Purdue University, West Lafayette, Indiana, USA, 2012.
- [88] INNAS BV, "Performance of Hydrostatic Machines - Extensive Measurement Report," 2020. [Online]. Available: <https://bit.ly/2Yu8SWr>
- [89] N. H. Pedersen, "Development of Control Strategies for Digital Displacement Units," Ph.D. dissertation, Aalborg University, Denmark, 2018.
- [90] US Department of Energy, "Adjustable Speed Drive Part-Load Efficiency," U.S. Department of Energy, Tech. Rep. November, 2012. [Online]. Available: <https://bit.ly/3CyyVhv>
- [91] J. Willkomm, M. Wahler, and J. Weber, "Potentials of Speed and Displacement Variable Pumps in Hydraulic Applications," in *Proceedings of the 10th International Fluid Power Conference*, Dresden, Germany, March 8-10, 2016, pp. 379–392.
- [92] L. Schmidt, S. Ketelsen, R. Mommers, and P. Achten, "Analogy between hydraulic transformers & variable-speed pumps," in *Proceedings of the ASME/BATH Symposium on Fluid Power and Motion Control*, Virtual Conference, September 9-11, 2020.
- [93] Bosch Rexroth, "MS2N - Synchronous Servomotors - R911347583," Project Planning Manual, 2019. [Online]. Available: <https://bit.ly/3wTacze>
- [94] D. Padovani, S. Ketelsen, and L. Schmidt, "Downsizing the Electric Motors of Energy Efficient Self-Contained Electro-hydraulic Systems by Hybrid Technologies," in *Proceedings of the ASME/BATH Symposium*

References

- on Fluid Power and Motion Control*, Virtual Conference, September 9-11, 2020.
- [95] American Bureau of Shipping, "Certification of Lifting Appliances," 2020. [Online]. Available: <https://bit.ly/3GIJjXS>
 - [96] G. Altare and A. Vacca, "A Design Solution for Efficient and Compact Electro-hydraulic Actuators," *Procedia Engineering*, vol. 106, pp. 8–16, 2015. [Online]. Available: <http://doi.org/10.1016/j.proeng.2015.06.003>
 - [97] K. J. Jensen, M. K. Ebbesen, and M. R. Hansen, "Novel Concept for Electro-Hydrostatic Actuators for Motion Control of Hydraulic Manipulators," *Energies*, vol. 14, no. 6566, 2021. [Online]. Available: <https://doi.org/10.3390/en14206566>
 - [98] M. Schneider, O. Koch, J. Weber, M. Bach, and G. Jacobs, "Green Wheel Loader – Development of an energy efficient drive and control system," in *Proceedings of the 9th International Fluid Power Conference*, Aachen, Germany, March 24-26, 2014.
 - [99] K. Rongjie, J. Zongxia, W. Shaoping, C. Lisha, R. Kang, J. Zongxia, W. Shaoping, and C. Lisha, "Design and Simulation of Electro - hydrostatic Actuator with a Built - in Power Regulator," *Chinese Journal of Aeronautics*, vol. 22, no. 6, pp. 700–706, 2009. [Online]. Available: [https://doi.org/10.1016/S1000-9361\(08\)60161-2](https://doi.org/10.1016/S1000-9361(08)60161-2)
 - [100] Hydac International, "Hose Burst Valve direct-acting flast seat valve, Cartridge - 350 bar," Datasheet. [Online]. Available: <https://bit.ly/HydacBurstValves>
 - [101] Bosch Rexroth, "Bladder-type accumulator. RE 50171," Datasheet, 2016. [Online]. Available: <https://bit.ly/3jDXP4m>
 - [102] Hawe Hydraulic, "Spring accumulator," Webpage, 2021. [Online]. Available: <https://bit.ly/3w5Pqfw>
 - [103] J. Aaltonen, "Interaction of Bootstrap Reservoir and Hydraulic Pump in Aircraft Hydraulic Systems," Ph.D. dissertation, Tampere University of Technology, Finland, 2016.
 - [104] Parker Hannifin, "Bootstrap Hydraulic Reservoirs," Product catalogue, 2009. [Online]. Available: <https://bit.ly/BootstrapRes>
 - [105] A. Ellman and R. Piché, "A Modified Orifice Flow Formula for Numerical Simulation of Fluid Power Systems," *Fluid Power Systems and Technology: Collected Papers*, vol. 3, 1996.
 - [106] R. Åman, H. Handroos, and T. Eskola, "Computationally efficient two-regime flow orifice model for real-time simulation," *Simulation Modelling Practice and Theory*, vol. 16, no. 8, pp. 945–961, 2008.

References

- [107] B. Manhartsgruber, *Simulationsmethoden in der Fluidtechnik*. Issue: March 10, Lectures in "Simulationsmethoden in der Fluidtechnik", Johannes Kepler University Linz, in German, 2014.
- [108] R. Rituraj, A. Vacca, and M. A. Morselli, "Thermal modelling of external gear machines and experimental validation," *Energies*, vol. 13, no. 11, 2020. [Online]. Available: <https://doi.org/10.3390/en13112920>
- [109] Bosch Rexroth AG, "Rexroth IndraDrive Supply Units HMV01 - R911339050," Operating instructions, 2013. [Online]. Available: <https://bit.ly/3cg1dPh>
- [110] K. Kim, K. Park, G. Roh, and K. Chun, "DC-grid system for ships: a study of benefits and technical considerations," *Journal of International Maritime Safety, Environmental Affairs, and Shipping*, vol. 2, no. 1, 2018. [Online]. Available: <https://doi.org/10.1080/25725084.2018.1490239>
- [111] DNV, "Northern Drilling's West Mira first rig to receive DNV GL Battery (Power) Class Notation," Webpage, 2019. [Online]. Available: <https://bit.ly/3tjZakV>
- [112] Z. Chenyang and J. Hongzhou, "Experimental Study of the Direct Drive Hydraulic System with the Torque Mode," *Energies*, vol. 14, no. 941, 2021. [Online]. Available: <https://doi.org/10.3390/en14040941>
- [113] L. Chenggong and J. Zongxia, "Calculation Method for Thermal-Hydraulic System Simulation," *Journal of Heat Transfer*, vol. 130, no. 8, 2008. [Online]. Available: <https://doi.org/10.1115/1.2928006>
- [114] Transmetra GmbH - Messtechnik mit KnowHow, "Table of Emissivity of Various Surfaces," 1999. [Online]. Available: <https://bit.ly/3GbK9aL>
- [115] Trelleborg Sealing Solutions, "Hydraulic seals - linear," Product Catalogue, 2021. [Online]. Available: <https://bit.ly/3nSN6Vv>
- [116] Parker Hannifin GmbH, "Hydraulic Seals," Product Catalogue, 2020. [Online]. Available: <https://prker.co/3wftXAP>
- [117] P. Pillay and R. Krishnan, "Modeling, Simulation, and Analysis of Permanent-Magnet Motor Drives, Part I: The Permanent-Magnet Synchronous Synchronous Motor Drive," *IEEE Transactions on Industry Applications*, vol. 25, no. 2, 1989.
- [118] Bosch Rexroth AG, "ctrlX DRIVE - R911386579," Project planning manual, 2021. [Online]. Available: <https://bit.ly/32Sds3r>
- [119] D. Liberzon, "Switched Systems: Stability Analysis and Control Synthesis," Lecture Notes for HYCON-EECI Graduate School on Control, University of Illinois USA,, 2013. [Online]. Available: <https://bit.ly/32BJW1H>

References

- [120] T. Glad and L. Ljung, *Control Theory - Multivariable and Nonlinear Methods*, 1st ed. Taylor & Francis, 2000. [Online]. Available: <https://doi.org/10.1201/9781315274737>
- [121] S. Skogestad and I. Postlethwaite, *Multivariable Feedback Control - Analysis and Design*, 2nd ed. John Wiley & Sons, 2005.
- [122] S. Kärnell, "Hysteresis Control in Pump-Controlled Systems — A Way to Reduce Mode-Switch Oscillations in Closed and Open Circuits," *Energies*, vol. 15, no. 2, 2022. [Online]. Available: <https://doi.org/10.3390/en15020424>
- [123] B. Shafai, A. Moradmand, and S. Nazari, "Observer-based Controller Design for Systems with Derivative Inputs," in *Proceedings of the 57th Annual Allerton Conference on Communication, Control, and Computing*, Monticello, IL, USA, September 24-27, 2019.
- [124] Balluff, "Magnetostrictive Sensors, BTL7-V50E-M," Users's guide. [Online]. Available: <https://bit.ly/BalluffSensor>
- [125] N. Simonsen, E. M. Sørensen, M. van Binsbergen-Galán, S. F. H. Kleine, M. H. Nielsen, and L. Schmidt, "Noise Attenuation in a Secondary Controlled Electro-Hydraulic Actuator Using an Extended Kalman Filter," in *Proceedings of the ASME/BATH Symposium on Fluid Power and Motion Control*, Virtual Conference, October 19-21, 2021.
- [126] Sun Hydraulics, "Vented Counterbalance Valve - CWGG," Datasheet, 2019. [Online]. Available: <https://www.sunhydraulics.com/model/CWGG>
- [127] MathWorks, "Asynchronous Machine," 2021. [Online]. Available: <https://bit.ly/3ja1CqQ>
- [128] D. Novotny and T. Lipo, *Vector Control and Dynamics Of AC Drives*. New York: Oxford University Press, 1996.
- [129] P. Pillay and R. Krishnan, "Modeling Of Permanent Magnet Motor Drives," *IEEE Transactions on Industrial Electronics*, vol. 35, no. 4, pp. 537–541, 1988.
- [130] ABB, "Low voltage Process Performance Motors," Product catalogue, 2021. [Online]. Available: <https://bit.ly/3j0Nm3p>
- [131] J. Smith, H. Van Ness, and M. Abbott, *Introduction to Chemical Engineering Thermodynamics*, 6th ed. McGraw-Hill, 2001.
- [132] Y. A. Çengel, J. M. Cimbala, and R. H. Turner, *Fundamentals of fluid-thermal sciences*, 5th ed. McGraw-Hill Education, 2017.
- [133] G. Jungnickel, *Simulation des thermischen Verhaltens von Werkzeugmaschinen*. Technische Universität Dresden, in German, 2000.

Part II

Publications

Paper A

Classification and Review of Pump-Controlled Differential Cylinder Drives

Søren Ketelsen, Damiano Padovani, Torben Ole Andersen,
Morten Kjeld Ebbesen and Lasse Schmidt

The paper has been published in
Energies Vol. 12, No. 7, 2019.

© 2019 by the authors

Review

Classification and Review of Pump-Controlled Differential Cylinder Drives

Søren Ketelsen ^{1,*} , Damiano Padovani ² , Torben O. Andersen ¹, Morten Kjeld Ebbesen ² and Lasse Schmidt ¹ 

¹ Fluid Power and Mechatronic Systems, Department of Energy Technology, Aalborg University, 9220 Aalborg, Denmark; toa@et.aau.dk (T.O.A.); lsc@et.aau.dk (L.S.)

² Department of Engineering Sciences, University of Agder, 4879 Grimstad, Norway; damiano.padovani@uia.no (D.P.); morten.k.ebbesen@uia.no (M.K.E.)

* Correspondence: sok@et.aau.dk

Received: 28 February 2019; Accepted: 1 April 2019; Published: 4 April 2019

Abstract: Pump-controlled hydraulic cylinder drives may offer improved energy efficiency, compactness, and plug-and-play installation compared to conventional valve-controlled hydraulic systems and thus have the potential of replacing conventional hydraulic systems as well as electro-mechanical alternatives. Since the late 1980s, research into how to configure the hydraulic circuit of pump-controlled cylinder drives has been ongoing, especially in terms of compensating the uneven flow requirements required by a differential cylinder. Recently, research has also focused on other aspects such as replacing a vented oil tank with a small-volume pressurized accumulator including the consequences of this in terms of thermal behavior. Numerous references describe the advantages and shortcomings of pump-controlled cylinder drives compared to conventional hydraulic systems or electro-mechanical drives. This paper presents a throughout literature review starting from the earliest concepts based on variable-displacement hydraulic pumps and vented reservoirs to newer concepts based on variable-speed electric drives and sealed reservoirs. By classifying these drives into several proposed classes it is found that the architectures considered in the literature reduce to a few basic layouts. Finally, the paper compares the advantages and shortcomings of each drive class and seek to predict future research tasks related to pump-controlled cylinder drives.

Keywords: pump-controlled cylinder drives; direct-driven hydraulics; throttleless hydraulics; valveless hydraulic drive; linear hydraulic actuation

1. Introduction

With an increased industrial focus on energy efficiency, plug-and-play installation, and compactness, conventional valve-controlled hydraulic cylinder drives are increasingly being replaced by electro-mechanical alternatives, such as roller or ball screws [1], especially for small power classes. This happens despite the well-known advantages of hydraulic linear actuation such as large force/power densities, reliability, and robustness. Hydraulic actuation is, however, still the preferred solution for many applications such as industrial presses, large mobile machinery, crane manipulators, primary aircraft control etc. [2–4]. Among other reasons this is due to certain limitations for the electro-mechanical alternatives, such as limited reliability (e.g., shock loads damage), the difficulties of implementing overload/failure protection and/or limited force capabilities [5–7]. To strengthen the position regarding these applications and to make hydraulic cylinder drives competitive with electro-mechanical drives for low power applications, there is a need to enhance both the energy efficiency and the overall flexibility of hydraulic cylinder drives.

The flexibility of a hydraulic system may be related to how power is being distributed between the prime mover and the actuator(s). As illustrated in Figure 1, at least three different power distribution topologies exist: hydraulic, mechanical, and electrical distribution.

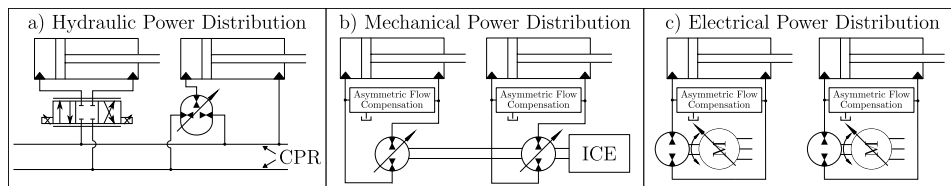


Figure 1. Three different power distribution topologies. In (a) power is distributed hydraulically by common pressure rails (CPR) to a control element controlling each actuator. In (b) power is distributed mechanically by a rotating shaft to multiple rotating hydraulic pumps, each controlling the motion of a cylinder. The shaft may be driven by an internal combustion engine (ICE). In (c) power is electrically distributed, requiring both an electric machine and a hydraulic pump for controlling each cylinder.

In conventional hydraulic systems a centralized hydraulic power unit (HPU) delivers power to all actuators through a common pressure rail (CPR). Each actuator is controlled by a throttling valve, leading to significant losses. To enhance the energy efficiency, the resistive losses associated with throttling must be reduced. A main challenge is to achieve this with preserved controllability at a justifiable cost level. Examples of improving the energy efficiency and maintaining the CPR counts the so-called digital hydraulics where the proportional valve is replaced by multiple on/off valves [8–12] and hydraulic transformers, namely throttleless control devices that replace control valves. The latter is investigated in [13–15], where the variable INNAs floating cup transformer is considered, see Figure 1a. Conversely, for a conventional constant hydraulic transformer unit this is investigated in [16]. Hydraulic transformers can be considered as a retrofit solution to conventional systems, as only the control element is replaced while the hydraulic power supply, the common pressure rail and the cylinder remain unchanged. Because the piping is preserved, the flexibility of the system is not significantly improved and so these systems cannot be considered an alternative to electro-mechanical cylinder drives.

Another approach for reducing throttle related losses is represented by pump-controlled cylinder drives. Here the motion of the cylinder is controlled by varying the flow delivered by the pump. Since the pump is used as the control element, a pump is needed for each actuator, which necessitates a complete redesign of the system architecture but also enables the avoidance of the common pressure rail. If a single prime mover is used to drive multiple variable-displacement pumps each controlling a single actuator, the power distribution may be considered mechanical, see Figure 1b. This approach has been of particular interest in mobile machinery, where the internal combustion engine (ICE) acts as the only prime mover. Because the hydraulic pumps are mounted on the same shaft, substantial piping may still be required to each cylinder.

The highest level of flexibility and compactness is achieved if power is distributed electrically and each cylinder is equipped with an individual pump and electric motor. This is especially the case if the conventional vented oil tank is replaced by a sealed accumulator, meaning that only an electrical and mechanical machine interface is present. This aids to the flexibility and compactness of the solution because hoses and pipes related to having a centralized HPU are avoided. For this reason, some researchers also use the term decentralized or zonal hydraulics. These self-contained or compact electro-hydraulic drives are aiming at combining the energy efficiency and flexibility of electric drives while retaining the reliability and force capabilities of hydraulic drives. Even for applications with no electric grid connection readily available, such as mobile machinery, it may be profitable to either replace the ICE with an electric machine and batteries (full electrification) [17] or even to generate a local electric grid by connecting an electric generator to the ICE [18]. Generally, pump-controlled

systems can recover kinetic or potential energy (e.g., during load lowering). This is a significant difference compared to conventional valve-controlled systems, where energy recovery is generally not possible, due to throttling across the control valve. If a system contains multiple actuators with the ability to share power (e.g., through a common DC-bus), pump-controlled systems may offer increased energy efficiency, not only on an actuator level but also on a system level. The opportunity of sharing power and recovering kinetic and potential energy opens new possibilities for designing “*intelligent energy-optimized systems*” [19]. This may especially be the case if including energy storage technologies such as batteries, super-capacitors, or fly-wheels. By proper energy management this may be used to minimize the power peaks requiring by the DC-supply [19], or to optimize loading of the ICE enabling reduced fuel consumption and/or downsizing of the prime mover’s rated power.

Compact pump-controlled cylinder drives match the ongoing industrial trend of electrification and countless applications would benefit from a decentralized, energy efficient, compact, and flexible hydraulic drive. Numerous references (e.g., [20,21]) focus on which advantages and disadvantages pump-controlled cylinder drives possess compared to conventional valve-controlled hydraulics or electro-mechanical drives. As will be evident, pump-controlled cylinder drives may be configured in different ways but, so far, no references compare these approaches thoroughly. This paper is creating an overview of system architectures for pump-controlled hydraulic differential cylinder drives found in literature and industry and classifies these into several proposed classes. This is done to compare general advantages and shortcomings between the drive classes instead of each individual system architecture.

The paper is organized in the following way: In section 3 the classes used to classify the drive architectures are presented, while Section 4 presents the literature review. Section 5 identifies which research areas are currently in focus. Also, future research topics in order for pump-controlled differential cylinder drives to be valid alternatives to electro-mechanical drives and a valid successor for conventional valve-controlled cylinder drives are proposed. In Section 6 the advantages and shortcomings of the presented classes are summarized and compared. A general introduction to the technology is given in the next section.

2. Overview of Pump-Controlled Differential Cylinder Drives

According to the definition made in this paper, a pump-controlled differential cylinder drive consists of a differential cylinder, a hydraulic supply, an oil reservoir, and auxiliary components which may include valves for safety functions, load-holding, and flow-balancing components. This is illustrated in Figure 2. In the literature these drives are also denoted as self-contained or compact electro-hydraulic/hydrostatic actuators, direct-driven hydraulics, valveless/throttleless actuators etc.

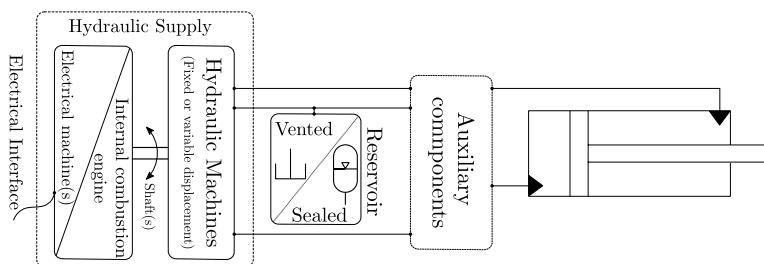


Figure 2. Conceptual illustration showing the subsystems constituting a pump-controlled differential cylinder drive as defined in this text.

For pump-controlled differential cylinder drives to be valid alternatives to both electro-mechanical drives and conventional valve cylinder drives for general applications, capability of four-quadrant operation is required. Figure 3 exemplifies how a compact pump-controlled differential cylinder drive capable of four-quadrant operation may be designed [2,22]. The hydraulic supply consists of a single

fixed-displacement pump connected to a variable-speed electric machine. The reservoir is sealed, and the so-called inverse shuttle valve needed for uneven flow compensation may be regarded as an auxiliary component.

In quadrant Q_1 , the fluid is pumped into the piston side chamber. Due to the asymmetry of the cylinder, a larger flow is required by the piston chamber than the flow leaving the rod side chamber. This differential flow (or rod volume flow) is supplied from a sealed accumulator, through the inverse shuttle valve, which is passively actuated to connect the low-pressure chamber of the cylinder with the accumulator. The accumulator is usually pressurized to a couple of bars (1–3 bar), as a low-pressure leakage line is required for common pump types such as commercially available internal gear pumps [23], external gear pumps [24–26] and axial piston pumps [27,28].

In quadrant Q_3 the piston is retracting under a resistive load, causing the rod side chamber to be at a higher pressure than the piston side chamber. This causes the inverse shuttle valve to change position compared to Q_1 and connects the piston chamber with the accumulator. The additional flow leaving the piston side chamber is thus guided to the accumulator. In Q_1 and Q_3 the load is resistive, so power is being supplied to the drive, while in Q_2 and Q_4 the load is aiding the piston motion. In these quadrants the hydraulic pump works in motoring mode, and a potential of recovering some of the energy supplied by the external load is present.

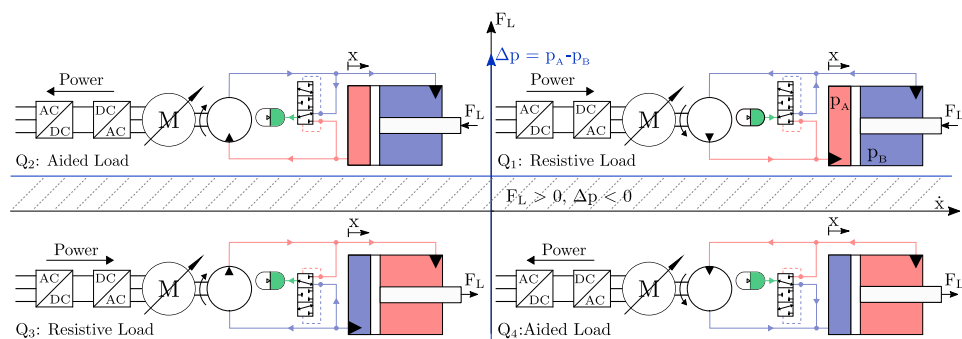


Figure 3. Four-quadrant operation of a pump-controlled differential cylinder drive. This particular architecture consists of a variable-speed electric motor connected to a fixed-displacement pump. The uneven cylinder chamber flow is compensated by a so-called inverse shuttle valve [2,22].

The research emphasis was initially on symmetric actuators controlled by variable-displacement pumps. This concept was already examined by [29] in 1967. The PhD dissertation from [30] from the late 1970s is one of the first references dealing thoroughly with pump-controlled double rod cylinder drives. Initial effort was placed on characterizing the dynamical behavior of variable-displacement pumps, to assess their applicability as primary control elements [31–33]. In [34] these are found to be well suited for primary control tasks, while in [35,36] it was pointed out that the dynamics of variable-displacement pumps is generally inferior compared to a conventional control valve. Later [37] found that pump control bandwidths above 45 Hz are achievable and [38] experimentally found closed loop pump control bandwidths of 80 Hz. These results are confirmed in [39], who also concludes that the “commonly found prejudice that pump-controlled systems suffer from slow dynamics of the servo pump used as a final control element are not justified.” As pointed out in [40] such dynamic behavior is generally reserved for custom-built pumps e.g., used for research purposes or special applications. Commonly used pumps exhibit much slower control dynamics. Displacement-controlled actuators have been investigated intensively in relation to mobile machinery. For example, in [41] it was found that for controlling the working hydraulics in a 5 ton excavator, a pump bandwidth of 15–20 Hz at $\pm 10\%$ displacement is required. This result is generalized to other larger displacement-controlled mobile

applications and it is concluded that a pump bandwidth of 15–20 Hz satisfies even the most strenuous frequency requirements.

The advances within power electronics and electric servo drives enabled using variable-speed electric drives in combination with fixed-displacement pumps for primary control of hydraulic double rod cylinders, which facilitated electrical power distribution instead of hydraulic distribution [42]. Based on thermal considerations, the improved energy efficiency compared to valve-controlled systems, further enhanced the possibility of reducing the oil volume compared to conventional valve cylinder drives. This led to the development of the electro-hydraulic actuator (EHA), characterized by having a pressurized sealed oil reservoir (accumulator) instead of a vented tank. During the 1990s the EHA emerged in the aircraft industry, and are now used for primary flight control in e.g., the Airbus A340 and A380, [2,42].

Due to increased cost and size, the use of double rod cylinders is limited in other industries, where the preferred linear actuator is the differential cylinder [2,43]. Using a single rod cylinder leads to unequal flow rates required by the cylinder chambers. The main focus has therefore been on developing and investigating system architectures capable of compensating this flow difference. A variety of different methods has been proposed. Roughly speaking, the focus on differential cylinders in combination with variable-displacement pumps started in the late 1980s, while the combination of differential cylinders and variable-speed drives can be traced back to the mid-1990s. Compact or self-contained (i.e., using a sealed accumulator) differential cylinder drives emerged around 2010.

Pump-controlled differential cylinder drives have primarily been of interest in the academic community, but recently commercial products have entered the market, e.g., by Parker Hannifin [44], Bosch Rexroth AG [45] and Servi Group [46]. The real industrial breakthrough is however yet to come.

3. Classification of Pump-Controlled Differential Cylinder Drives

As mentioned previously pump-controlled cylinder drives may be able to recover energy, and thus offers new opportunities in terms of designing energy-optimized systems, by incorporating power-sharing and energy storage. It is generally important to recognize that the hydraulic drive is part of a bigger system, meaning that to optimize energy consumption of the system, it may not be sufficient to optimize energy consumption on an individual drive level. It is, therefore, always necessary to take into account in which system the drive is included to select and design the actuator best suited for the task. This paper, however, focuses on classifying and reviewing pump-controlled systems on a drive level, e.g., not considering in which context the cylinder drive or actuator is used. This is done even though the authors recognize that it may not be fair to directly compare pump-controlled hydraulic drives optimized for different applications. On a general level, it is however assessed that main advantages and drawbacks for different circuit architectures is identifiable.

A drive classification may generally be performed on different detail levels. To focus on main functionality and to keep the number of classes reasonable, a high level classification is proposed. As an example a drive may be classified based on whether the used hydraulic pump is a fixed or variable-displacement type (higher level), or more specific which machine topology is used, e.g., axial/radial piston, internal/external gear etc. (lower level). Similarly, a drive may be classified based on whether a constant-speed or variable-speed prime mover is used (higher level), or specifically whether e.g., an asynchronous induction, a switched reluctance or a permanent magnet synchronous machine is used (lower level).

The lower level classification is relevant during the design phase for a specific application, but counterproductive when obtaining an overview concerned with the main functionality. A system classification based on main hardware components and their configuration is therefore proposed. As such, only a classification of the basic system architectures is within the scope of the paper. Such classifications have previously been presented in various publications. In [47] the authors distinguished between valve compensated and pump compensated circuits, while [48] presented a basic classification of architectures using two pumps, based on the configuration of the pumps. In [22] a classification

also including single-pump solutions and different auxiliary components needed for uneven flow compensation was presented. The classification proposed in this paper, is closely related to the one presented in [22], however the type of hydraulic supply (variable-displacement or speed-variable pumps) is included in the following. This extension is made to assess how the chosen type of hydraulic supply affects the performance characteristics of the pump-controlled cylinder drive.

Figure 4 shows the classes emerging when classifying the pump-controlled cylinder drives based on: hydraulic supply (type and number of prime movers and hydraulic pumps), circuit architecture (open or closed) and uneven flow compensation method. A circuit architecture is said to be open if one of the pump ports is always being connected to a reservoir/accumulator. This means that oil leaving a cylinder chamber is not able to enter the other chamber in all four operating quadrants without entering a reservoir first. An open-circuit architecture normally does not require a four-quadrant pump. A closed-circuit architecture requires at least one four-quadrant pump, i.e., some of the oil may be pumped directly from one-cylinder chamber to the other, without passing the reservoir, thus constituting a closed circuit.

The classification is based on the following delimitations:

1. The classes based on variable-speed electric drives combined with variable-displacement hydraulic pumps are omitted in this classification due to the lack of research efforts and the higher cost. It is however likely that a higher energy efficiency is obtainable [42,49,50], meaning that future pump-controlled cylinder drives may be based on this approach.
2. The classification only includes the use of one or two prime movers, as none of the considered publications deal with more prime movers.
3. The classes based on two constant-speed prime movers are not considered because this is only relevant for dimensioning considerations. The general functioning of the drive does not change compared to using a single prime mover, because the control functionality is handled by the variable-displacement pump(s).
4. Classes based on two variable-speed prime movers in combination with a single hydraulic pump are omitted, because this architecture is functionally similar to single variable-speed prime mover and single-pump classes.

Additional components to handle the uneven cylinder flow are needed for the classes based on a single pump (A and E). Some suggestions are shown in the green (functional) classes A.1 to A.3 and E.1 to E.3. For multiple-pump hydraulic supplies (class B, C, D) uneven flow compensation may be realized without the need for additional components.

Based on the hydraulic supply class only, the above considerations lead to five main classes (A to E) and 13 functional sub-classes, shown as green boxes in Figure 4. The classification leads to a limited number of basic system architectures, whereas numerous different varieties of these basic architectures may be derived to obtain specific characteristics needed for a given application (or family of applications). The specific architectures may include auxiliary components such as load-holding and safety valves, oil filter, cooler etc., and the chosen reservoir type (sealed or vented).

Please note that the distinction made between variable-displacement and variable-speed hydraulic supplies increase the functional solution groups compared the e.g., the classification made in [22]. It is however important to emphasize that the solution space for the architectures in e.g., class A is exactly the same as for class E, because the only difference is the method of controlling the pump flow. The same is true for classes B.1, C.1, D.1 and B.2, C.2 and D.2. Some flow compensation methods are however more suitable for some classes. For example, even though the hydraulic transformer solution is only listed for class E, this would also be functional for class A.

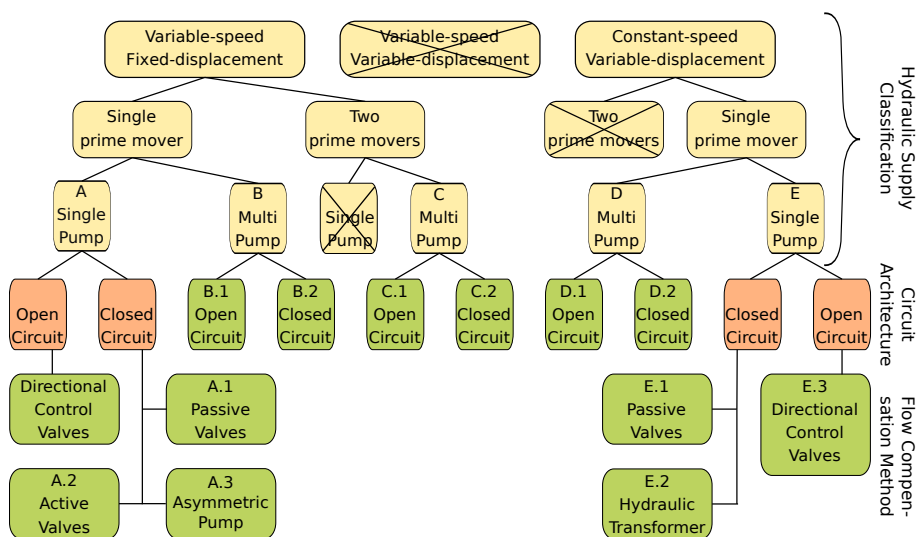


Figure 4. Proposed classification of pump-controlled differential cylinder drives. The green boxes denote classes generally functional in four quadrants: Five main classes (A–E) and 13 sub-classes are proposed.

4. Reviewing and Classifying the State-of-the-Art

In the following sub-sections, a literature review is conducted, and the identified systems are classified into the classes proposed in Figure 4.

4.1. Class A—Single Variable-Speed Prime Mover and Single Pump

Class A drives work by controlling the rotational direction and speed of a variable-speed electric machine connected to a single fixed-displacement pump. As the cylinder chamber flows are uneven, additional components are needed to compensate this difference to avoid cavitation or/and excessive pressure build up. In general, class A drives are characterized by a simple hydraulic circuit only requiring a small number of components and a relatively low control complexity due to a rather constrained system as only a single input is generally present. This also leads to a general inability to control the pressure of the non-load-carrying chamber, resulting in the low-pressure chamber being close to the accumulator/tank pressure. This causes the overall drive stiffness to be low, decreasing the eigenfrequency of the drive which may lead to positioning inaccuracy [51] and unsatisfying dynamic performance of the drive e.g., at impact loads.

The contributions identified in the literature for the sub-classes A.1 to A.3 are presented in the following. Open-circuit variable-speed architectures using directional control valves in the main transmission lines (pump to cylinder) have not been found in the literature. For open-circuit displacement-controlled drives, however, a few examples are shown in Section 4.5.3. These architectures would also be feasible in combination with open-circuit single-pump variable-speed supplies.

4.1.1. A.1—Passive Valves

A simple solution to compensate uneven cylinder flows using a flushing/inverse shuttle valve was patented in [52], see Figure 5a. The inverse shuttle valve connects the low-pressure cylinder chamber to the reservoir to compensate the uneven cylinder flow. In aided load situations, the hydraulic pump and the electric machine work in motoring and generator mode respectively, meaning that a potential for recovering energy exists. Recently the inverse shuttle valve solution has been given renewed attention, possibly because of the appealing simplicity of this configuration consisting of rather few and simple

components [2,22]. The drive however suffers from undesired shuttle valve oscillations (so-called mode oscillations) for certain load cases (switching loads). This rather complicated phenomenon is occurring when the equilibrium point for the system is close to the switching pressure of the inverse shuttle valve. If the system is poorly damped, the valve switching condition is met, while moving towards the equilibrium point. Due to the cylinder asymmetry, this causes the structure of the system to change, in turn causing the equilibrium point to move compared to before the valve switch [53]. The repetition of this process (potentially a limit cycle) is responsible for undesired pressure and piston motion oscillations. Investigation of the mode oscillation issue has been addressed by multiple researchers, see. e.g., [47,54–58].

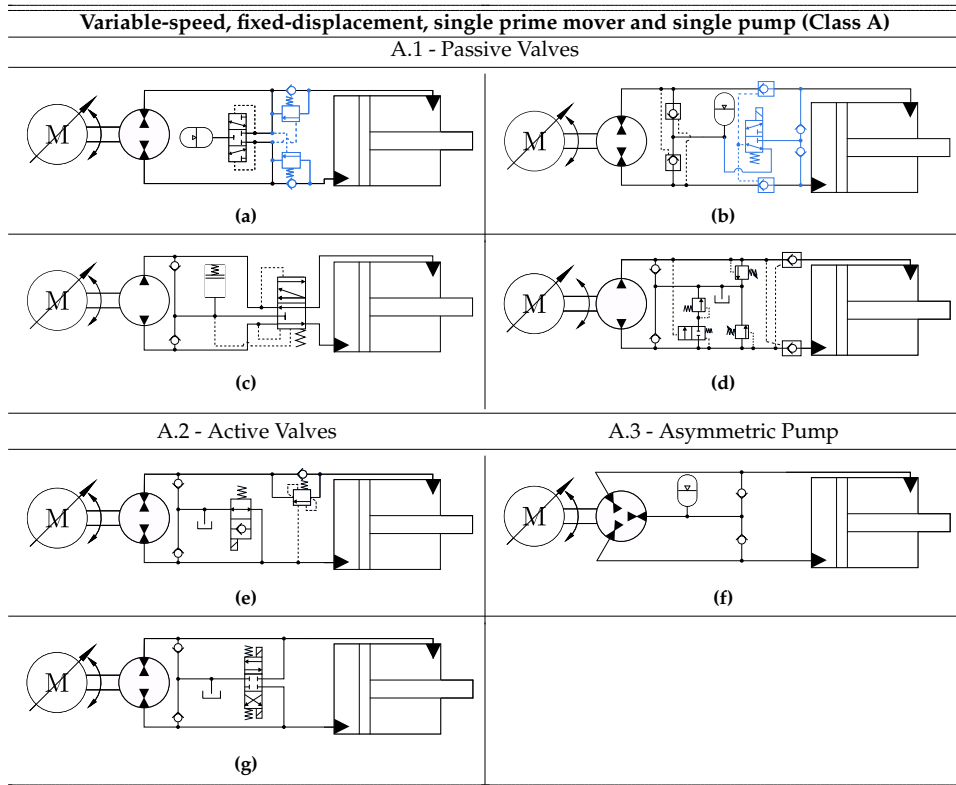


Figure 5. Overview of class A architectures. Only main components are included, whereas e.g., anti-cavitation and pressure-relief valves are omitted for simplicity. Blue components indicate that these components are only included by some researchers. (a) Architecture based on an inverse shuttle valve; (b) Architecture based on pilot-operated check valves; (c) Architecture based on a passively actuated directional valve; (d) EHA concept by Parker Hannifin; (e) Architecture based on actively controlled on/off valve; (f) Architecture based on asymmetric pump; (g) Architecture based on actively controlled directional valve.

One of the proposed solutions to counteract this undesirable behavior, is to use an under-lapped inverse shuttle valve. This has experimentally proved to reduce the tendency of mode oscillation, at the expense of throttling losses, and thus lower energy efficiencies [54,55]. The acceleration limits to avoid mode oscillations for large inertia loads have been investigated in [21], and the authors experimentally showed that these limits may be calculated to avoid oscillatory operation if the load is known.

Another known disadvantage of this drive is the inability to control the pressure of the non-load-carrying chamber, resulting in the low-pressure chamber being close to the accumulator/tank pressure. This causes the overall drive stiffness to be low, which negatively affects the dynamic properties of the drive. An additional charge pump can be used to avoid low-pressure operation [55]. This generally has a negative impact on compactness, flexibility, reliability, and energy efficiency.

In [59] it is proposed to use counter balance valves for load-holding purposes (blue components in Figure 5a), at the expense of not being able to regenerate energy. Compared to the system in Figure 5c [60], simulation results suggest an energy saving of 57% when used to control the position of aircraft seats. The system in Figure 5c also contains load-holding valves not shown in the figure, and uses a passively actuated directional control valve, to guide the additional oil flow from the piston side to the accumulator during retraction.

As an alternative to the inverse shuttle valve, two pilot-operated check valves may be used (Figure 5b), which has been investigated intensively for displacement-controlled actuators (Class E). This system is functionally very similar to the inverse shuttle valve solution, and suffers from the drawbacks regarding mode oscillations and low-pressure operation. Commercial products based on the pilot-operated check valve solution has been introduced lately by Bosch Rexroth AG [45,61]. In [3] the authors proposed to include a passive load-holding subsystem (Blue components in Figure 5b) for actuating a single link crane manipulator. The load-holding subsystem passively holds the load in case of emergency e.g., power shutdown but it may also be enabled by the operator during standstill to enhance energy efficiency. For a given test trajectory an energy efficiency of 60% is obtained experimentally.

To address the mode oscillation issue [40] introduced two counter balance valves and a low-pressure charge pump. By a clever sizing of the counter balance valves, significant throttling losses are only present when the chamber pressure difference is small, which is critical regarding mode oscillation, while the throttling losses are insignificant when the pressure difference is larger. This is experimentally shown to yield oscillation free performance at critical loads, while the energy efficiency is not affected for non-critical loads. The oscillation free operation comes at a cost of an increased energy consumption of 12% for a specific operation cycle.

Another approach for compensating the uneven cylinder chamber flows is used by Parker Hannifin [44] in their commercially available EHA, shown in Figure 5d. The EHA is available in a power range up to 560 W [44]. Dependent on the piston motion, a passively actuated directional control valve guides oil to/from the cylinder whenever the rod side pressure exceeds the piston side pressure. A pressure-relief valve inserted between the reservoir and the directional valve elevates the pressure in the non-load-carrying chamber, (back pressure), to ensure drive stiffness during piston motion. For this reason, Parker Hannifin denotes the combination of the directional valve and the pressure-relief valve a "*back pressure valve*". A closely related concept is also found in [62].

4.1.2. A.2—Active Valves

The pump-controlled drive visible in Figure 5e was investigated in a two-quadrant tote dumper application in [63]. An electrically actuated 2/2-way on/off valve is used to direct oil from the piston side chamber to the vented tank during retraction, while this valve is closed during cylinder extension. Load-holding is achieved using a counter balance valve, which is found to prohibit the circuit to work in motoring mode and thus precludes energy recovery during load lowering. A test showed decreased energy consumption of 21% compared to a valve-controlled system for a given load cycle.

A comprehensive analysis of the mode oscillation issue known from passive valve compensated architectures was conducted in [47]. Based on this analysis a rather simple switching logic for the flow compensating valves counteracting mode oscillation issues is derived. This switching logic may be realized using an actively controlled 4/3-way directional valve as shown in Figure 5g or using architectures based on hydraulically/passively actuated valves. Experimental results for the latter are however not presented. Beside the circuit shown in Figure 5g experimental results for circuits using

an additional pressurized flow supply to elevate chamber pressures and to deliver the compensation flow are presented. The experimental work is conducted on a backhoe loader performing a pendular motion (four-quadrant operation) and the results showed that by using the proposed valve switching logic mode oscillations did not occur independent of the operation condition, i.e., there are no critical regions or critical loads leading to mode oscillations. This solution is not restricted to variable-speed architectures but may also be incorporated in variable-displacement architectures.

4.1.3. A.3—Asymmetric Pump

By redesigning the valve plate of a conventional axial piston pump, an asymmetric unit with three independent ports has been designed and tested [64–67]. This 3-port pump solution was also disclosed in a patent application [68]. The two ports connected to the cylinder chambers may be constructed with a displacement ratio that matches the cylinder area ratio, meaning that no additional components are needed for flow compensation. The third port is connected to a low-pressure line. This is shown in Figure 5f. Fundamentally, the asymmetric pump-controlled cylinder drive is similar to a drive comprising of two fixed-displacement pumps connected on the same shaft. However, there might be a slight advantage in terms of compactness in favor of the asymmetric pump drive. Also, a better energy efficiency of the asymmetric pump drive compared to the double pump solution have been reported, which may be due to reduced frictional losses as only a single pump instead of two needs to be driven [43]. Compared to a separate-meter-in-separate-meter-out (SMISMO) valve-controlled system, energy savings of 75% have been reported for a given load cycle when implemented in a mini excavator [69].

4.2. Class B—Variable-Speed Single Prime Mover with Multiple Pumps

Instead of using auxiliary components to compensate the uneven flow (Class A), a fundamentally different approach is to handle the uneven flow problem by the hydraulic supply itself, i.e., using multiple pumps. Compared to the valve solutions in class A, this approach has the advantage of ideally not requiring the use of additional valves for uneven flow compensation. This is especially advantageous due to the absence of mode oscillations. Class B systems are characterized by using simple hydraulic components in a simple hydraulic architecture. The main drawback is the inherent low-pressure operation.

The usage of two oppositely oriented pumps in an open-circuit configuration (Figure 6a) has been investigated by multiple researchers. Here the uneven cylinder flows are compensated by the pumps, as the displacement ratio of the pumps ideally matches the cylinder area ratio. However, as pointed out by [70], anti-cavitation valves and pressure-relief valves are generally required, because the pressure dependent pump leakages make it impossible to achieve proper matching of the pump displacement ratio and the cylinder area ratio under all operating conditions. To limit a potential pressure increase [70] uses two proportional valves shown as the blue components to bleed off oil to the reservoir. These valves are not included in this setup by other researchers.

For actuating a single link boom [71] reported lifting efficiencies around 55%. The sizing error of the displacement ratio of the pumps related to the cylinder area ratio is assessed to reduce the energy efficiency of the system. To address this, a hydraulic accumulator may be connected to the non-load-carrying chamber. This is found to increase efficiencies as much as 30 percentage points for this two-quadrant lifting/lowering operation [72].

To enhance compactness the conventional oil reservoir has been replaced by a pressurized accumulator by several researchers, e.g., in [1,73,74]. In [75] the authors investigated how to install such a compact hydraulic drive on the links of a small excavator. In particular, the focus is on evaluating how the additional weight originating from the compact drives affect the energy efficiency and the stresses in the boom structure. Simulation results suggested an increased energy consumption of 11–17%. A structural analysis furthermore showed that the original boom structure is safe. In [76] lifting efficiencies ranging from 67% to 77% are simulated for the same excavator.

To avoid low-pressure operation, which is an inherent feature of the double pump configuration [77,78] added a third pump which is only active in the forward direction, see Figure 6c. Using advanced control functionality, it is possible to control the pressure level (i.e., the minimum chamber pressure) and thus the drive stiffness during motion. Experimental verification shows energy efficiencies ranging from 18% to 51% in four-quadrant operation. A simulation study shows an energy saving potential of 60% compared to a conventional valve-controlled system for actuation of a two-link middle-sized knuckle boom crane for a representative load cycle [79].

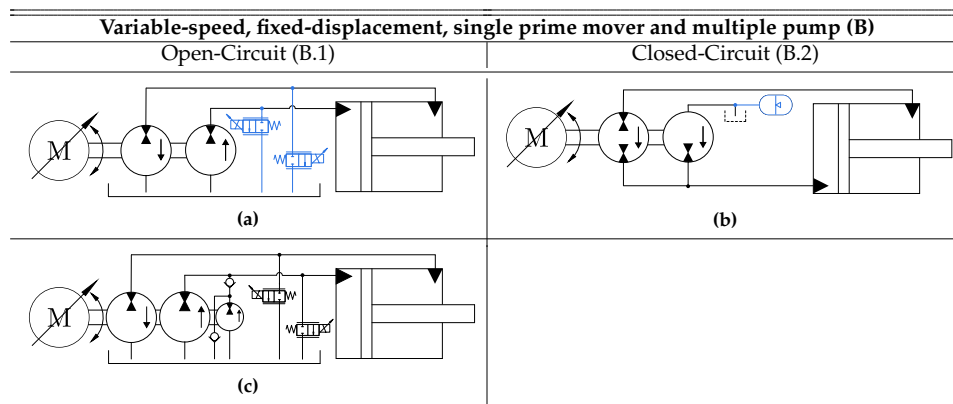


Figure 6. Overview of class B architectures (simplified schematics). The arrow inside the pump symbols denote main flow direction for positive shaft speeds. Blue components indicate that these components are only included by some researchers. (a) Two pump architecture in open-circuit configuration; (b) Two pump architecture in closed-circuit configuration; (c) Architecture based on three pumps in open-circuit configuration.

The two pumps may also be configured in a closed-circuit architecture, as seen in Figure 6b, offering smaller pump sizes compared to open-circuit architectures at the expense of requiring a closed-circuit pump. Early focus on this concept and variable-speed drives in general is found in [51] from 1997. Here the main advantage compared to variable-displacement drives (Class D/E) is pointed out to be improved efficiency especially at part loads and avoidance of an additional pressure source needed to control the variable-displacement pump. For the pumps available at that time it is highlighted that to enhance the reliability these needed to be optimized for low speed operation.

In [51] the investigation was based on a vented tank configuration (Figure 6b) finding that the drive stiffness impacts severely on the positioning accuracy. In [2,22] the vented tank was replaced with a pressurized accumulator and the authors experimentally compared this drive with an electro-mechanical counterpart. This investigation showed similar energy efficiencies and compactness, superior robustness towards impact loads and overload protection but inferiority regarding drive stiffness due to low-pressure operations. This architecture was investigated for actuating the six cylinders of a Stewart platform used for flight simulations in [80]. The evaluated energy consumption was between 25% to 50% of a conventional valve-controlled system. This is partly achieved by connecting an extra accumulator to the rod side, rendering the possibility of passively carrying the static load of the platform by cleverly pre-charging the two accumulators, which ideally results in zero torque on the prime mover's shaft in static situations. This also increases the drive stiffness, but requires an additional charging/discharging circuit [81].

4.3. Class C—Two Variable-Speed Prime Movers and Multiple Pumps

Including a second variable-speed prime mover enables the possibility of controlling an additional state, often chosen to be a pressure state, to avoid low-pressure operations. Beside the possibility

of avoiding low-pressure operations, class C drives are characterized by being highly scalable. This also results in a higher cost, compared to single prime mover classes for the same power output demands. Furthermore, the control complexity generally increases as two independent inputs need to be controlled.

In the closed-circuit architecture (Figure 7b) both prime movers operate simultaneously in motor or generator mode, contrary to the open-circuit architecture (Figure 7a) where one prime mover works as a motor while the other acts as a generator. This means that the closed-circuit architecture is more scalable as larger output powers may be delivered for the same electric motor sizes. The open-circuit solution is briefly presented in [43,51], but neither in-depth analyses nor experimental testing have been published for this architecture.

The closed-circuit architecture (Figure 7b) has been investigated in [82–86], and a 64 kW drive has been experimentally tested in an injection molding machine, with clamping forces up to 1600 kN and max rod velocities of 0.8 m/s (not simultaneously). In [48] this concept is investigated with focus on different multi-variable control concepts and a closed position control loop and closed chamber sum-pressure loop strategy is implemented, yielding a constant chamber sum pressure, to keep the drive stiffness high. The reference speed for the electric machines is a (scaled) sum of the controller output, constituting a static decoupling of the input-output couplings. In this work it is furthermore shown that using a variable-speed, variable-displacement drive does not improve energy efficiency compared to a variable-speed fixed-displacement approach, for a considered injection molding machine case.

Finally, no architectures using more than a single pump connected to each electric machine have been identified.

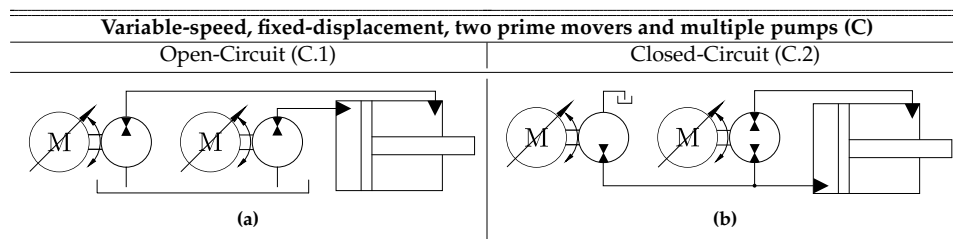


Figure 7. Overview of class C architectures (simplified schematics). (a) Open-circuit configuration; (b) Closed-circuit configuration.

4.4. Class D—Single Constant-Speed Prime Mover and Multiple Pumps

Instead of using variable-speed fixed-displacement drives, variable-displacement constant-speed hydraulic units may be used. This approach is in some sense the predecessor of the variable-speed approach, as the variable-displacement pump was investigated as a primary control element for cylinder drives before variable-speed electric drives were economically and dynamically feasible. The main focus on variable-displacement differential cylinder drives is related to mobile machinery.

Most attention has been given to single-pump displacement-controlled drives (Class E), whereas the focus on using two pumps for each cylinder has been limited. This is probably due to this solution being cost-intensive and requiring advanced control methods, which is infeasible for cost-sensitive applications such as mobile machinery [87].

The open-circuit solution (Figure 8a) has been presented in [81,88] investigated this concept in a 0.6 MN forging press. A decentralized position and rod side pressure chamber control method has been adopted. The positioning accuracy and forging rapidity was found to improve when increasing the rod side chamber pressure (increased drive stiffness). The energy consumption of the press however remained almost unchanged. The high cost of the variable-displacement pumps compared to valve-controlled drives is pointed out to be a challenge for the market penetration of this technology.

The closed-circuit architecture (Figure 8b) is found in [89], where emphasis was placed on investigating suitable control strategies. Two different control methods were suggested, both aiming at controlling the cylinder motion and at keeping a certain pressure level. The first approach only required piston position feedback and included a hydraulically actuated pressure level valve, guiding oil from a charge source to the cylinder chambers if the pressure sum is lower than some preset value. The second approach did not require an additional valve but was based on multi-variable control techniques, thus requiring both piston position and chamber pressure feedback signals.

In [90] the closed-circuit architecture (Figure 8b) was used to actuate a hydraulic broaching machine and reduced the energy consumption with 55% compared to a conventional valve system for a given load cycle. A similar concept is also observed in a patent application [91].

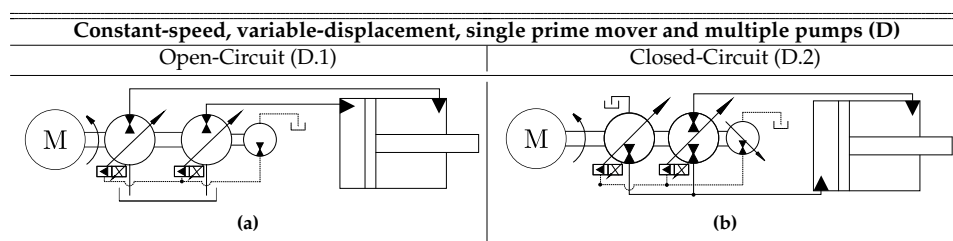


Figure 8. Overview of class D architectures (simplified schematics). (a) Open-circuit configuration; (b) Closed-circuit configuration.

Using three variable-displacement main pumps enables the opportunity to circulate oil, ideally without affecting neither cylinder motion nor pressure levels. This may be advantageous in relation to ensure proper oil filtration and cooling [92]. However, no references concerned with three or more variable-displacement main pumps have been identified, which may be due to this solution being rather expensive.

4.5. Class E—Single Constant-Speed Prime Mover and Single Pump

As mentioned in the previous section the focus on using multiple variable-displacement pumps is limited. Conversely, using a single variable-displacement pump has obtained significant attention. As with the single pump arranged in the variable-speed fixed-displacement configuration (Class A), additional components are needed to handle the uneven cylinder flows. The investigated solutions are quite similar to the methods used for class A, because the fundamental challenge is similar. The differences between class A and E concerns the requirement of a low displacement charge pump, which conventionally is needed to control the displacement setting of the main pump. The charge pump is often also used to elevate the chamber pressures yielding a higher drive stiffness. Including the charge pump and the control circuit for the main pump generally leads to a larger complexity of the hydraulic circuit and to a higher system cost compared to variable-speed drives.

4.5.1. E.1—Passive Valves

Using a pilot-operated check valve for flow compensation in uneven cylinder drives for two-quadrant operation was suggested in [33]. The pilot-operated check valve was used to connect the cylinder chamber with a vented reservoir, which inherently led to low-pressure operation and reduced stiffness. This idea has been modified into the architecture shown in Figure 9a where a charged low-pressure line is connected to the cylinder chambers using pilot-operated check valves [93–96]. The low-pressure line is generated by a fixed-displacement pump and generally needed for controlling the displacement of the main pump, to compensate system leakages, avoiding cavitation at the inlet port of the main pump and recirculating oil for filtration and cooling. Additionally, this increases the chamber pressure levels and thus stiffness. The circuit in Figure 9a has been intensively researched

from the end of the 1990s, especially regarding mobile machinery where a combustion engine is used to drive the working hydraulics. Some varieties in terms of including the load-holding functionality exist. In some references, no load-holding functions are included, in others load-holding is achieved by electrically actuated on/off valves (Figure 9a), while [97] included the load-holding capability using hydraulically actuated logic elements. The main drive functionality however remains the same.

The architecture is especially well suited for multiple actuator mobile machinery because they can share the same low-pressure charge line. In [87,98,99] the drive architecture was implemented on a multi-link mobile crane and on a wheel loader respectively, and in both cases fuel savings of 15% compared to a conventional load sensing system was reported.

Fuel savings of more than 40% have been reported when implemented in a multiple actuator small excavator compared to a conventional load sensing system. This leads to lower working temperature, downsized combustion engines and reduction or potential elimination of the cooling requirements [100–103]. The authors in [104,105] suggested pump sharing between multiple actuators to decrease the overall cost of the hydraulic system. Further activities have been related to mode oscillation (similar to what was seen in Section 4.1.1) [106], active oscillation damping [107,108] and thermal modelling [109,110].

In [56,57] a solution that makes use of an inverse shuttle valve for flow compensation (Figure 9c) was investigated, and special attention was given to investigate mode oscillations. By adding additional leakage using two electrically actuated 2/2-way valves (Figure 9c) mode oscillations are found to be suppressed at the expense of throttling losses across these valves.

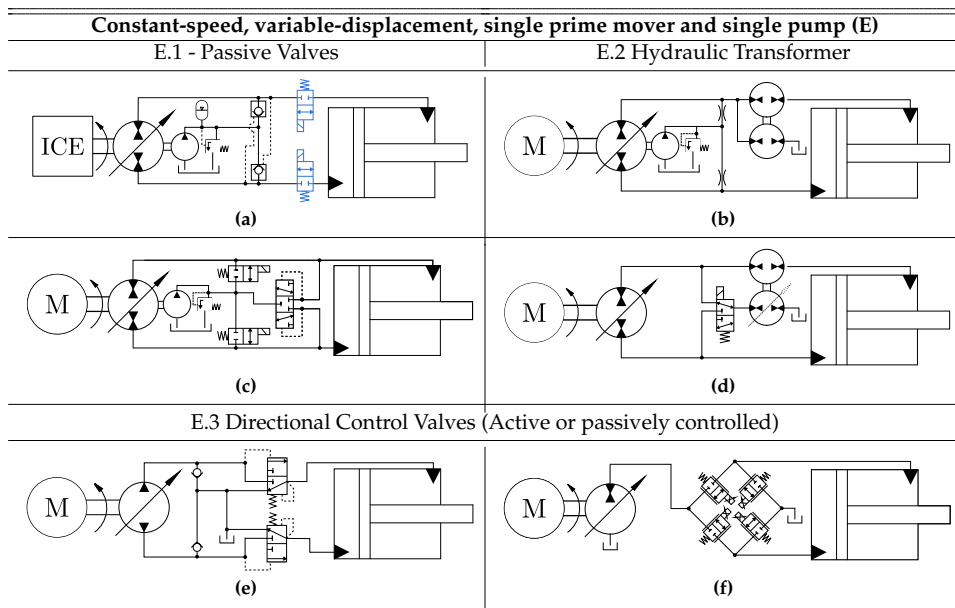


Figure 9. Overview of class E architectures (simplified schematics). Sub-circuits for controlling the displacement of the main pump is not showed in all schematics. (a) Architecture based on pilot-operated check valves; (b) Architecture based on hydraulic transformer; (c) Architecture based on inverse shuttle valve; (d) Architecture based on variable hydraulic transformer; (e) Architecture based on passively actuated directional valves; (f) Open-circuit architecture based on actively controlled proportional valves.

4.5.2. E.2—Hydraulic Transformer

In [33] it is proposed to use a hydraulic transformer to compensate the uneven cylinder flows, as illustrated in Figure 9b. In [89,111] the author investigated the hydraulic transformer as a flow compensation device and derived six feasible ways of connecting the hydraulic transformer with a variable-displacement pump, the cylinder, and the reservoir. Two of these configurations were combined using a switching valve (see Figure 9d) to switch between a high speed and a high force mode. The solution suffers from being unable to match the cylinder flow needs under all operating conditions due to pressure dependent leakage. In [89] it was suggested to use a variable-displacement charge pump in combination with a sum of pressure control valve to address this while [81] recommended involving a variable-displacement transformer (illustrated with a dotted arrow in Figure 9d). As pointed out by [81], since a conventional hydraulic transformer is *“bulky, heavy and complex”*, it makes these solutions *“less appealing when compared to other solutions”*. Innovative transformer technologies may be able to change this, e.g., the variable INNAs floating cup transformer which is significantly more compact, as only a single rotating machine (with three ports in the valve plate) is used instead of two rotating machines [13].

4.5.3. E.3—Directional Control Valves

For single-pump open-circuit architectures, directional valves in the main transmission lines (between pump and cylinder) are needed to accommodate four-quadrant operation. One approach is shown in Figure 9e where the two directional valves connect the cylinder chambers with the reservoir, unless the pressure on the pump side exceeds the chamber pressure. This means oil leaving the cylinder chambers is directed to the reservoir disabling the opportunity for energy recovery. This architecture is briefly presented in [2] without any further examination.

A more elaborate architecture combining the advantages of pump-controlled cylinder drives with the advantages of separate metering valves is shown in Figure 9f. This architecture is characterized by controlling the piston motion in different modes dependent on the positions of the four 2/2 valves. This expands the operating region (force and speed) compared to single-pump closed-circuit solutions [112]. For example, is the cylinder piston retracting speed not limited by the pump size in aided load situations, because oil may also be guided to the other cylinder chamber (differential lowering) or directly to the reservoir (meter out flow control) [113]. This is a significant advantage in relation to some mobile machinery where the lowering speed is often demanded to be twice as high as the lifting speed [114]. Using the proposed architecture, the pump may be downsized compared to equivalent closed-circuit architectures. The challenges for this architecture are related to the control of pump and valves required for smooth transition between operation mode and quadrant [112,115]. In [113] fuel savings of 10% to 20% compared to a conventional load sensing hydraulic system was achieved, when implemented in a wheel loader. Using a closely related architecture in a 300 ton mining excavator [116] investigated a closely related open-circuit concept and simulated fuel savings of 28% compared to a conventional system.

5. Current and Future Research Topics

As mentioned in the introduction the industrial breakthrough for pump-controlled differential cylinder drives is yet to come. For these drives to be attractive compared to both electro-mechanical alternatives and conventional valve cylinder drives the qualities of both these technologies need to be combined. This means that pump-controlled cylinder drives must be comparable to electro-mechanical cylinder drive technologies in relation to:

- Energy efficiency including energy recovery
- Compactness (Self-contained system)
- Only electrical and mechanical (machine) interface

Furthermore, pump-controlled differential cylinder drives must be comparable to conventional valve cylinder drives in relation to:

- Scalability/application range
- Fluid management (cooling, filtration)
- Drive stiffness
- Reliability and durability
- Safety functionality

Based on the literature review research has previously been focused on identifying system architectures capable of compensating uneven cylinder flows and the implementation in specific applications. Architectures meeting all above requirements have not been identified. Therefore, such a system architecture is a natural focus for future research.

When considering compact and sealed hydraulic drives, one of the major challenges is the significantly reduced oil amount compared to conventional systems. This causes the oil filtration and cooling to be handled differently to avoid the conventional use of an additional subsystem connected to the oil tank to manage the fluid condition.

An attractive idea is the complete avoidance of both the cooling and filtration elements. This would enhance compactness of the system, but would also require the energy losses of the system to be balanced only by the passive heat transfer to the surroundings, to keep the oil and component temperature within acceptable ranges. This has led to research concerned with thermal modelling and temperature investigation of pump-controlled cylinder drives [110,117–120]. In [121], experimental results for a compact pump-controlled system equivalent to the system in Figure 5a, reveal oil temperatures above 70 °C, at indoor working conditions if no oil cooler is used. For standard hydraulic components and fluids this may be beyond limits, which may cause reduced durability and reliability. On the contrary [122] tests a pump-controlled system running with oil temperatures below 0 °C, sometimes experienced by mobile machinery in the Scandinavian countries, Canada, Russia etc. The investigation shows drastically decreased efficiencies at lower temperatures. Furthermore, significant differences are observed for the two different types of working fluids included in the study. No investigation into how operating with very low oil temperatures affects the wear and reliability of the system is included.

Investigation and modelling of thermal behavior, sizing and layout of an oil cooling/heating methodology (either passive or active) is therefore an important research area to ensure durability and reliability of pump-controlled cylinder drives.

Another attractive idea is the avoidance of an oil filter, which may be possible due to the sealed nature of a compact drive. As such, only self-contamination will be present in the fluid, as external contamination is ideally absent. Additionally, if oil is treated within design range (e.g., temperature), lifespan oil filling may be possible. For the architecture depicted in Figure 6b, [123] found that after 960 hours of operation, the self-contamination, especially originating from the beginning of the test, resulted in a high particle load. This leads to the observation that operating a compact pump-controlled cylinder drive is currently not recommended without an oil filter, at least when using a standard HLP 46 hydraulic fluid. Another potential research field is therefore investigation of more suitable working fluids (e.g., oils specifically designed for self-contained systems).

As pointed out by [92], most pump types are not able to continuously run at low rotational speeds (<300 RPM). Running at low speed may reduce reliability and durability. None of the considered architectures can circulate oil, without affecting cylinder motion. Therefore, it may be beneficial to consider architectures permitting this function. Oil circulation ability may also be appropriate for filtration and cooling purposes.

6. Classification Summary

From the literature review it is found that research has primarily been focused on classes A, B, and E, compared to the classes with two control elements (i.e., class C and D). Taking the release date of the literature into consideration it seems that the focus on variable-displacement drive architectures is declining and almost exclusively is related to mobile machinery.

The interest for variable-speed and compact architectures is broad-based across both stationary hydraulics and mobile machinery. This is assessed mainly to be related to a lower cost, a better energy efficiency, and a simpler hydraulic circuit compared to variable-displacement drives. Furthermore, no variable-displacement architectures using a sealed, low volume accumulator have been identified in the literature, which may be due to the difficulties of reducing the oil volume due to significant and constant energy losses. This generally affects the applicability of variable-displacement systems compared to variable-speed drives, as a trend towards compact and self-contained solutions is occurring. This tendency may also be explained by the general industrial focus on electrification, as this favors variable-speed technology due to the control functionality being handled by electric components (i.e., frequency converters) instead of hydraulic control valves.

To summarize the findings of the review process, the drive classes are compared based on the eight criteria listed below. Even though cost is an important parameter, it is chosen not to consider this criterion because it is too difficult to assess and compare the cost between the classes as this is heavily affected by the specific components selected to meet the requirements of a given application. The same is true for the experienced acoustic noise levels of the drive classes. The drive acoustics are highly dependent on the chosen pump type and whether an internal combustion engine (only class D and E) or electrical prime mover is used. An advantage for class A, B, and C drives is that significant acoustic noise is only present during motion of the cylinder piston.

Energy efficiency

For all drive classes a significantly reduced energy consumption compared to conventional valve-controlled systems has been reported. In general, variable-speed drives (Class A, B, C) are reported to achieve a better part load efficiency [42,51,82,124] compared to variable-displacement drives. For variable-displacement drives (Class D and E) a small fixed-displacement charge pump is often used, which is assessed to reduce the overall energy efficiency. Using a variable-displacement charge pump may improve energy efficiency but it yields a more complicated and cost-intensive hydraulic system. At piston standstill (i.e., no power output) energy is still consumed by both the variable-displacement and variable-speed approaches due to inherent losses. For the classes based on variable-speed electric drives these losses originate from the torque generated by the fixed-displacement pumps in turn causing electric losses even though the load is kept stationary. Because common fixed-displacement pump types, are not recommended to be operated at low pump speeds, it may be necessary to circulate the oil, i.e., maintain a non-zero pump speed even at cylinder piston standstill, which is associated with losses. To circumvent this, components such as pilot-operated check valves, overcenter valves, or counterbalance valves well known from safety-critical conventional cylinder drives may be used.

Also, for variable-displacement drive classes (Class D and E) significant input energy is required at standstill. Especially the pump losses i.e., volumetric, mechanical, and churning losses accounts for this. The term churning losses are used to describe the losses associated with the rotating components stirring the oil during operation of a piston pump, and they increase with increasing rotational speed [125]. For axial piston pumps published data from the manufacturers Eaton and Parker Hannifin show that the energy consumption at zero delivery / zero stroke conditions for large pressure differences may be over 10% of the input energy required at full flow [126–128].

Ability to control drive stiffness

For classes based on a single variable-speed prime mover (A and B) it is generally not possible to control the drive stiffness/pressure level under all operating conditions. So far, this problem has not been solved without including an additional charge source. The authors in [78] succeeded in controlling the drive stiffness for a single variable-speed prime mover architecture, but only during motion of the cylinder piston. If two prime movers are used (class C), multiple researchers used this additional degree-of-freedom to control a pressure state as well as the cylinder motion to attain a

reasonable drive stiffness. For variable-displacement drives (Class D and E), most solutions use a low-pressure charge pump which maintains chamber pressures at an elevated level.

Ability to handle highly dynamic/switching loads

The ability to keep the drive stiffness at a reasonable level improves the ability to handle highly dynamic loads. Furthermore, transition issues, known as mode oscillations, have been reported for most class A and E drives at certain load cases.

Concerning oscillation reduction and active vibration damping, which are important aspects for modern hydraulic drives, the dynamic performance/control bandwidth of the pump flow is important. As reported by several researchers, e.g., [39] the bandwidth of the pump displacement adjustment system (class D and E), is dominated by the characteristics of the pump-controlled valve and it is possible to achieve small-signal bandwidths above 80 Hz [38]. As mentioned previously, the authors in [40] argues that such bandwidths are reserved for custom-built pumps, and that commonly available pumps exhibit much slower control dynamics. Therefore, the achievable bandwidth is highly dependent on the chosen components.

The same is so to speak true for the variable-speed drive classes (class A, B, and C). An investigation from 2002 [48], shows velocity control bandwidths around 5 Hz (small signal) for standard induction motors controlled by a frequency converter. For other motor types (e.g., switched reluctance or AC servomotors) the small-signal control bandwidth is found to be significantly higher, approximately 30–40 Hz. In [129], a small-signal bandwidth of 120 Hz is experimentally verified for an industrially available permanent magnet synchronous machine controlled by a frequency converter.

Furthermore, achievable bandwidths are assessed to be highly dependent on control components (valves and frequency converters) and controller tuning. The above however shows that high control bandwidths are achievable for all drive classes. The upper limit is assessed to be the highest for custom-built variable-displacement pumps (class D and E), because high-end servo valves with very high dynamic capabilities may be used if necessary.

Drive compactness and flexibility

Drive compactness depends on the number and configuration of the components. Based on the high-level classification considered here, it is difficult to compare compactness for each drive class, as this is heavily affected by the specific components chosen during a design phase. For the same power output, the size of an asynchronous induction machine is generally larger than a comparable permanent magnet synchronous machine. However, it is generally assumed that using two prime movers (class C) reduces the achievable compactness compared to single prime mover classes.

Concerning flexibility of the drive classes, the architectures based on electric machines for each cylinder drive (Class A, B, and C) are assessed to be highly flexible due to the possibility of plug-and-play-installation.

Hydraulic circuit simplicity

It is generally assumed that the multiple-pump classes are simpler than single-pump classes, as additional components and fluid paths are needed to compensate uneven flows. Furthermore, it is assumed that using variable-displacement pumps increases the complexity of the hydraulic circuit, as such pumps conventionally are electro-hydraulically actuated.

Control simplicity

In general, hydraulic drives are characterized by non-linearities and uncertainties, and the control complexity is heavily affected by the requirements set by a specific application. This means that closed loop control structures may be arbitrary involved for all drive classes. However, it may be generally assumed that the control complexity increases as the number of inputs increases. This is justified by a simple observation: It is relatively easy to control the piston motion in single input systems (class A, B and E) in an open loop manner. The operator basically just needs to guide oil

into the cylinder chamber he desires to supply. For the multiple input classes (C and D) this is not sufficient, as the operator must also control the amount of oil leaving the other chamber. Furthermore, optimizing a complex control algorithm is generally more challenging than optimizing a simple one. The performance of architectures requiring complex algorithms may therefore be affected significantly by a poor control design.

Reliability

Long term evaluation of the reliability of pump-controlled drives is limited in the literature. Some investigations were conducted around the year 2000 concerning the reliability of different types of variable-speed pumps [48]. A 1000 h test cycle was performed, and the results indicated that some pump types (i.e., radial piston pump) did not show any significant wear after 1000 h of operating. In fact, the efficiency of the radial piston pump improved after 1000 h of operation [48]. For other pumps types (axial piston pumps and internal gear pumps) the efficiency is seen to be unaffected or slightly decreased. Visual inspection shows some cavitation related damages (e.g., grooves) for both pump types.

Due to the recent increased industrial interest in variable-speed pumps, these may have been improved in relation to variable-speed operation. Therefore, the results in [48] may be outdated. However, data sheet information reveals that some pump types are not recommended for continuous low speed operation. Whether this is due to the manufacturers not having tested the pumps at continuous low speed or if this really implies a reduced reliability is unknown. For constant-speed variable-displacement drives it is however clear that all components are used within recommended range. This also includes oil temperatures and contamination levels as cooling and filtration are done by offline subsystems similar to conventional systems. As mentioned for compact variable-speed pump-controlled cylinder drives, it is challenging to filter and cool the oil sufficiently to keep oil temperature within a prescribed range. Given the information currently available it is assumed that the reliability of variable-displacement drives is expected to be superior compared to the variable-speed drive classes. However, consistent research and industrial focus is needed to assess the reliability thoroughly.

Degree of scalability

The degree of scalability is primarily decided by the available components, rather than by the drive class. For the basic architectures, valves are primarily only used for uneven flow compensation meaning that these are not assessed to limit scalability. As a result, the limiting factor in terms of power is assessed to be either the (electric) prime mover or the pump.

For variable-displacement drives, the prime mover would normally be an internal combustion engine or a synchronous induction machine running at grid frequency, which offer a wide power range. The used pump is normally chosen as a variable piston pump, which also offer a wide power range. Axial piston pumps with power outputs of more than 500 kW can be purchased as standard components.

For variable-speed drive classes, a variety of different options are available, and the component choices rather depend on the application than on the drive class. In general, asynchronous induction machines offer a wider power range than e.g., permanent magnet synchronous machines, while the dynamic capabilities are superior for the latter. Similarly, external gear pumps generally offer a narrower operating range compared to e.g., internal gear units or piston pumps, but they are more cost-effective. If the same type of components is chosen, it is obvious that the dual prime mover class C configured in a closed-circuit architecture offers a larger power output than the single prime mover classes (class A and B).

Table 1 provides a synthesis of the mentioned criteria where each drive class has been graded. The grades are as follows, (- -), (-), (+), (+ +), with (- -) being the worst.

Table 1. The derived drive classes are assessed based on eight criteria. Four different grades are used, ranging from (− −) to (+ +), with (− −) being the worst.

Comparison between the Proposed Drive Classes					
	Class A	Class B	Class C	Class D	Class E
Energy efficiency	+	+	+	−	−
Ability to control drive stiffness	− −	−	++	++	++
Ability to handle highly dynamic/switching loads	− −	+	++	++	−
Drive compactness and flexibility	++	++	+	−	−
Hydraulic circuit simplicity	+	++	++	−	−
Control simplicity	+	+	−	−	+
Reliability	−	−	−	++	++
Degree of scalability	−	−	+	++	++

7. Conclusions

Conventional valve-controlled linear hydraulic actuation systems are notoriously known for large force/power densities, reliability, and robustness. A main drawback is however a low energy efficiency, much lower than electro-mechanical counterparts, such as roller or ball screws. To improve the energy efficiency of hydraulic systems it is, therefore, required to reduce throttling losses. One approach for doing so, is represented by so-called pump-controlled cylinder drives. This paper presents a review of different architectures found in research literature, industrial catalogues, and patent applications. Common for these modern system architectures is that the control valve is omitted and that the motion of the cylinder is controlled directly by the pump flow, thus requiring at least one pump per actuator. To obtain an overview, the identified architectures are classified into several proposed classes, and it is found that if considering main functionality, the architectures considered in literature reduce to a few basic layouts only.

The review reveals that compared to valve-controlled systems, significant energy savings are obtainable. Some references report energy savings up to 75% for specific applications. Furthermore, a trend towards the architectures based on electrical prime movers rather than combustion engines is spotted, which is found to match the industrial focus on electrification well. This is furthermore supported by the observation that pump-controlled cylinder drives are generally able to recover energy and share power between multiple actuators. This facilitate designing energy-optimized systems by incorporating proper energy management on a system level, and thus pump-controlled cylinder drives may play an important role in future hydraulically actuated applications.

The main challenges for the market penetration of the technology and thus obvious focus for future research, is assessed to be related to thermal issues and drive controllability. As such, newer references are focusing on replacing the vented oil tank with a small pressurized accumulator, to enhance compactness. This may give rise to oil temperatures beyond limits, which would negatively impact performance and reliability. Related to drive controllability, some system architectures suffer from a low drive stiffness. This is found to affect positioning accuracy and control bandwidths negatively, thus making these system designs inappropriate for applications requiring high control bandwidths and positioning accuracies.

Author Contributions: Conceptualization, S.K., D.P., L.S. and T.O.A.; methodology, S.K.; investigation, S.K.; resources, S.K., D.P. and L.S.; writing—original draft preparation, S.K.; writing—review and editing, S.K., D.P., L.S., T.O.A., M.K.E.; visualization, S.K.; supervision, L.S., T.O.A., M.K.E.; funding acquisition, T.O.A.

Funding: This research was funded by the Research Council of Norway, SFI Offshore Mechatronics, project number 237896/O30.

Conflicts of Interest: The authors declare no conflict of interest.

References

1. Brahmer, B. CLDP—Hybrid Drive using Servo Pump in Closed Loop. In Proceedings of the 8th International Fluid Power Conference, Dresden, Germany, 26–28 March 2012; pp. 93–102.
2. Weber, J.; Beck, B.; Fischer, E.; Ivantysyn, R.; Kolks, G.; Kunkis, M.; Lohse, H.; Lübbert, J.; Michel, S.; Schneider, M.; Shabi, L.; Sitte, A.; Weber, J.; Willkomm, J. Novel System Architectures by Individual Drives. In Proceedings of the 10th International Fluid Power Conference, Dresden, Germany, 8–10 March 2016; pp. 29–62.
3. Padovani, D.; Ketelsen, S.; Hagen, D.; Schmidt, L. A Self-Contained Electro-Hydraulic Cylinder with Passive Load-Holding Capability. *Energies* **2019**, *12*, 292. [[CrossRef](#)]
4. Frischmeier, S. Electrohydrostatic actuators for aircraft primary flight control-types, modelling and evaluation. In Proceedings of the 5th Scandinavian International Conference on Fluid Power, SICFP '97, Linköping, Sweden, 28–30 May 1997; pp. 1–16. [[CrossRef](#)]
5. van den Bossche, D. The A380 Flight Control Electrohydrostatic Actuators, Achievements and Lessons Learnt. In Proceedings of the ICAS 25TH International Congress of the Aeronautical Sciences, Hamburg, Germany, 3–8 September 2006; pp. 1–8.
6. Mare, J.C. Combining Hydraulics and Electrics for Innovation and Performance Improvement in Aerospace Actuation. In Proceedings of the 12th Scandinavian International Conference on Fluid Power, Tampere, Finland, 18–20 May 2011; pp. 255–270.
7. Hagen, D.; Pawlus, W.; Ebbesen, M.K.; Andersen, T.O. Feasibility Study of Electromechanical Cylinder Drivetrain for Offshore Mechatronic Systems. *Model. Identif. Control A Nor. Res. Bull.* **2017**, *38*, 59–77. [[CrossRef](#)]
8. Hedegaard Hansen, A.; Pedersen, H.C. Optimal configuration of a discrete fluid power force system utilised in the PTO for WECs. *Ocean Eng.* **2016**, *117*, 88–98. [[CrossRef](#)]
9. Hedegaard Hansen, A.; F Asmussen, M.; Bech, M.M. Energy optimal tracking control with discrete fluid power systems using model predictive control. In Proceedings of the Ninth Workshop on Digital Fluid Power, Aalborg, Denmark, 7–8 September 2017.
10. Hedegaard Hansen, A.; F Asmussen, M.; Bech, M.M. Model Predictive Control of a Wave Energy Converter with Discrete Fluid Power Power Take-Off System. *Energies* **2018**, *11*, 635. [[CrossRef](#)]
11. Linjama, M.; Vihtanen, H.P.; Sipola, A.; Vilenius, M. Secondary Controlled Multi-chamber Hydraulic Cylinder. In Proceedings of the 11th Scandinavian International Conference on Fluid Power, Linköping, Sweden, 2–4 June 2009; pp. 1–15.
12. Huova, M.; Aalto, A.; Linjama, M.; Huhtala, K.; Lantela, T.; Pietola, M. Digital hydraulic multi-pressure actuator—the concept, simulation study and first experimental results. *Int. J. Fluid Power* **2017**, *18*, 141–152. [[CrossRef](#)]
13. Achten, P.A.J. What a Difference a Hole Makes—The Commercial Value of the INNAS Hydraulic Transformer. In Proceedings of the Sixth Scandinavian International Conference on Fluid Power, Tampere, Finland, 26–28 May 1999; pp. 873–886.
14. Vael, G.; Achten, P.; Potma, J. Cylinder Control with Floating Cup Hydraulic Transformer. In Proceedings of the Eighth Scandinavian Conference on Fluid Power, Tampere, Finland, 7–9 May 2003; pp. 175–190.
15. Heybroek, K.; Vael, G.; Palmberg, J.O. Towards Resistance-free Hydraulics in Construction Machinery. In Proceedings of the 8th International Fluid Power Conference, Dresden, Germany, 26–28 March 2012; Volume 2, pp. 123–138.
16. Dluzik, K. Entwicklung und Untersuchung energiesparender Schaltungskonzepte für Zylinderantriebe am Drucknetz. Ph.D. Thesis, RWTH Aachen, Aachen, Germany, 1989. (In German)
17. Hassi, T.; Korva, A.; Markkula, S.; Paratanen, T.; Sourander, T.; Kiviluoma, P.; Korhonen, A.; Kuosmanen, P. Improving Energy Efficiency of an Electric Mini Excavator. In Proceedings of the 11th International DAAAM Baltic Conference, Tallinn, Estonia, 20–22 April 2016.
18. Minav, T.; Heikkinen, J.E.; Pietola, M. Direct driven hydraulic drive for new powertrain topologies for non-road mobile machinery. *Electr. Power Syst. Res.* **2017**, *152*, 390–400. [[CrossRef](#)]
19. Ristic, M.; Wahler, M. Electrification of Hydraulics Opens New Ways for Intelligent Energy-Optimized Systems. In Proceedings of the 11th International Fluid Power Conference, Aachen, Germany, 19–21 March 2018.

20. Helbig, A.; Boes, C. Electric Hydrostatic Actuation-modular building blocks for industrial applications. In Proceedings of the 10th International Fluid Power Conference, Dresden, Germany, 8–10 March 2016; pp. 93–102.
21. Michel, S.; Weber, J. Electrohydraulic Compact-drives for Low Power Applications considering Energy-efficiency and High Inertial Loads. In Proceedings of the 7th FPNI PhD Symposium on Fluid Power, Reggio Emilia, Italy, 27–30 June 2012; pp. 1–18.
22. Michel, S.; Weber, J. Energy-efficient electrohydraulic compact drives for low power applications. In Proceedings of the ASME/BATH 2012 Fluid Power and Motion Control, Bath, UK, 12–14 September 2012; pp. 93–107.
23. Rexroth, Bosch AG. Internal Gear Pump PGM Series 4X, RE10235, 2014. Available online: https://md.boschrexroth.com/modules/BRMV2PDFDownload-internet.dll/re10235_2014-09.pdf?db=brmv2&lvid=1182639&mvid=13907&clid=20&sid=77703FE74E26CCE9963705CEDFFFF9EE.borex-tc&sch=M&id=13907,20,1182639 (accessed on 3 April 2019).
24. Rexroth, Bosch AG. External Gear Motors. RE 14026, 2005. Available online: https://md.boschrexroth.com/modules/BRMV2PDFDownload-internet.dll/re14026_2009-05.pdf?db=brmv2&lvid=1143155&mvid=13907&clid=20&sid=77703FE74E26CCE9963705CEDFFFF9EE.borex-tc&sch=M&id=13907,20,1143155 (accessed on 3 April 2019).
25. Rexroth, Bosch AG. External Gear Pump Series B, RE10088, 2013. Available online: https://md.boschrexroth.com/modules/BRMV2PDFDownload-internet.dll/re10088_2019-01.pdf?db=brmv2&lvid=1210039&mvid=13907&clid=20&sid=77703FE74E26CCE9963705CEDFFFF9EE.borex-tc&sch=M&id=13907,20,1210039 (accessed on 3 April 2019).
26. Parker Hannifin. Gear Pumps/Motors Series PGP/PGM Fixed Displacement Pumps, Cast-Iron and Aluminium Designs. Catalogue HY30-3300/UK. Available online: https://www.parker.com/literature/PMDE/Catalogs/Gear_Units/PGP_PGM/HY30-3300-UK.pdf (accessed on 3 April 2019).
27. Rexroth, Bosch AG. Axial Piston Units A10FZO, A10VZO and A10FZG, A10VZG Series 10 for variable-speed drives. RE91485, 2016. Available online: https://md.boschrexroth.com/modules/BRMV2PDFDownload-internet.dll/RE91485_2016-10.pdf?db=brmv2&lvid=1199007&mvid=13907&clid=20&sid=77703FE74E26CCE9963705CEDFFFF9EE.borex-tc&sch=M&id=13907,20,1199007 (accessed on 3 April 2019).
28. Parker Hannifin. Axial Piston Pumps Series PVplus Variable Displacement, Catalogue MSG30- 3245/UK. Available online: http://www.parker.com/Literature/PMDE/Catalogs/Piston_Pumps/PV+/MSG30-3245_UK.pdf (accessed on 3 April 2019).
29. Merritt, H.E. *Hydraulic Control Systems*; Wiley: New York, NY, USA, 1967.
30. Sprockhoff, V. Untersuchungen von Regelungen am hydrostatischen Zylinderantrieb mit Servopumpe. Ph.D. Thesis, RWTH Aachen, Aachen, Germany, 1979. (In German)
31. Backé, W.; Berbuer, J. Neue Schaltungskonzepte für hydrostatische Getriebe. *Ölhydraul. Pneum.* **1987**, *31*, 518–525. (In German)
32. Backé, W. Möglichkeiten zur Energieeinsparung in der Hydraulik. In Proceedings of the 11. Aachener Fluidtechnisches Kolloquium, Aachen, Germany, 8–10 March 1994; pp. 201–235. (In German)
33. Berbuer, J. Neuartige Servoantriebe mit primärer Verdrängersteuerung. Ph.D. Thesis, RWTH Aachen, Aachen, Germany, 1988. (In German)
34. Hahmann, W. Das Dynamische Verhalten hydrostatischer Antriebe mit Servopumpe und ihr Einsatz in Regelkreisen. Ph.D. Thesis, RWTH Aachen, Aachen, Germany, 1973. (In German)
35. Backé, W. Hydraulic Drives With High Efficiency. In Proceedings of the International Mechanical Engineering Congress, Fluid Power Systems and Technology, San Francisco, CA, USA, 12–17 November 1995; Volume 2, pp. 45–73.
36. Backé, W. The present and future of fluid power. *Proc. Inst. Mech. Eng.* **1993**, *207*, 193–212. [CrossRef]
37. Rahmfeld, R.; Ivantysynova, M. New displacement Controlled Linear Actuator Technology—A Suitable Control Element for Active Oscillation Damping. In Proceedings of the Eighth Scandinavian International Conference on Fluid Power, Tampere, Finland, 7–9 May 2003; pp. 1139–1155.
38. Berg, H.; Ivantysynova, M. Design and testing of a robust linear controller for secondary controlled hydraulic drive. *Proc. Inst. Mech. Eng. Part I* **1999**, *213*, 375–386. [CrossRef]
39. Grabbel, J.; Ivantysynova, M. An Investigation of Swash Plate Control Concepts for Displacement Controlled Actuators. *Int. J. Fluid Power* **2005**, *6*, 19–36. [CrossRef]

40. Imam, A.; Rafiq, M.; Jalayeri, E.; Sepehri, N. Design, Implementation and Evaluation of a Pump-Controlled Circuit for Single Rod Actuators. *Actuators* **2017**, *6*, 10. [CrossRef]
41. Rose, J.; Ivantysynova, M. A Study of Pump Control Systems for Smart Pumps. In Proceedings of the 52nd National Conference on Fluid Power, Las Vegas, NV, USA, 23–25 March 2011; pp. 683–692.
42. Kazmeier, B. Energieverbrauchsoptimierte Regelung Eines Elektrohydraulischen Linearantriebs Kleiner Leistung Mit Drehzahlgezieltem Elektromotor Und Verstellpumpe. Ph.D. Thesis, TU Hamburg-Harburg, Hamburg, Germany, 1998. (In German)
43. Quan, Z.; Quan, L.; Zhang, J. Review of energy efficient direct pump controlled cylinder electro-hydraulic technology. *Renew. Sustain. Energy Rev.* **2014**, *35*, 336–346. [CrossRef]
44. Parker Hannifin. Compact EHA—Electro-Hydraulic Actuators for high power density applications, 2011. Available online: <http://www.parker.com/Literature/Hydraulic%20Pump%20Division/Oildyne%20EHA/Compact-EHA-Catalog-HY22-3101E-7-13.pdf> (accessed on 3 April 2019).
45. Bosch Rexroth AG. SHA Servo-Hydraulic Actuator, 2017. Available online: https://dc-corp.resource.bosch.com/media/general_use/products/industrial_hydraulics_1/systems_1/20170915_Kundeninformation_SHA_EN.pdf (accessed on 3 April 2019).
46. Servi Group. Servi Hybrid Drive. Linear Actuator, 2017. Available online: https://www.servi.no/media/documents/Hybrid_Cylinder_1705-1_NO.pdf (accessed on 3 April 2019).
47. Costa, G.K.; Sepehri, N. Four-Quadrant Analysis and System Design for Single-Rod Hydrostatic Actuators. *J. Dyn. Syst. Meas. Control* **2018**, *141*. [CrossRef]
48. Neubert, T. Untersuchungen von drehveränderbaren Pumpen. Ph.D. Thesis, TU Dresden, Dresden, Germany, 2002. (In German)
49. Willkomm, J.; Wahler, M. Potentials of Speed and Displacement Variable Pumps in Hydraulic Applications. In Proceedings of the 10th International Fluid Power Conference, Dresden, Germany, 8–10 March 2016; pp. 379–391.
50. Willkomm, J.; Wahler, M.; Weber, J. Quadratic Programming to Optimize Energy Efficiency of Speed- and Displacement-Variable Pumps. In Proceedings of the 8th FPNi Ph.D Symposium on Fluid Power, Lappeenranta, Finland, 11–13 June 2014. [CrossRef]
51. Rühlicke, I. Elektrohydraulische Antriebssysteme mit Drehzahlveränderbarer Pumpe. Ph.D. Thesis, TU Dresden, Dresden, Germany, 1997. (In German)
52. Hewett, A.J. Hydraulic Circuit Flow Control. U.S. Patent 5,329,767, 19 July 1994.
53. Williamson, C. Power Management for Multi-Actuator Mobile Machines with Displacement Controlled Hydraulic Actuators. Ph.D. Thesis, Purdue University, West Lafayette, IN, USA, 2010.
54. Çalışkan, H.; Balkan, T.; Platin, B.E. A Complete Analysis for Pump Controlled Single Rod Actuators. In Proceedings of the 10th International Fluid Power Conference, Dresden, Germany, 8–10 March 2016; pp. 119–132. [CrossRef]
55. Çalışkan, H.; Balkan, T.; Platin, B.E. A Complete Analysis and a Novel Solution for Instability in Pump Controlled Asymmetric Actuators. *J. Dyn. Syst. Meas. Control* **2015**, *137*. [CrossRef]
56. Wang, L.; Book, W.J.; Huggins, J.D. A Hydraulic Circuit for Single Rod Cylinders. *J. Dyn. Syst. Meas. Control* **2012**, *134*, 011019. [CrossRef]
57. Wang, L.; Book, W.J. Using Leakage to Stabilize a Hydraulic Circuit for Pump Controlled Actuators. *J. Dyn. Syst. Meas. Control* **2013**, *135*, 061007. [CrossRef]
58. Imam, A.; Rafiq, M.; Jalayeri, E.; Sepehri, N. A Pump-Controlled Circuit for Single-Rod Cylinders that Incorporates Limited Throttling Compensating Valves. *Actuators* **2018**, *7*, 13. [CrossRef]
59. Altare, G.; Vacca, A. A Design Solution for Efficient and Compact Electro-hydraulic Actuators. *Procedia Eng.* **2015**, *106*, 8–16. [CrossRef]
60. Altare, G.; Vacca, A.; Richter, C. A Novel Pump Design for an Efficient and Compact Electro- Hydraulic Actuator. In Proceedings of the IEEE Aerospace Conference, Big Sky, MT, USA, 1–8 March 2014. [CrossRef]
61. Bosch Rexroth AG. Advantages of Electrification and Digitalization Technology For Hydraulics, 2018. Available online: <https://www.boschrexroth.com/en/xr/products/product-groups/industrial-hydraulics/the-fitness-program-for-hydraulics> (accessed on 3 April 2019).
62. Olson, M.; Praazak, J. Electro-Hydraulic Actuator. U.S. Patent 2011/0289912 A1, 2011. Available online: <https://patentimages.storage.googleapis.com/11/87/9d/336151787d8fa5/US20110289912A1.pdf> (accessed on 3 April 2019).

63. Jalayeri, E.; Imam, A.; Tomas, Z.; Sepehri, N. A throttle-less single-rod hydraulic cylinder positioning system: Design and experimental evaluation. *Adv. Mech. Eng.* **2015**, *7*. [[CrossRef](#)]
64. Quan, L.; Yang, Y.; Hou, X. Simulation and experimental research on the axial piston pump with series three-windows in valve plate. In Proceedings of the 2011 International Conference on Fluid Power and Mechatronics, Beijing, China, 17–20 August 2011; pp. 71–76. [[CrossRef](#)]
65. Zhang, X.; Quan, L.; Yang, Y.; Wang, C.; Yao, L. Output characteristics of a series three-port axial piston pump. *Chin. J. Mech. Eng.* **2012**, *25*, 498–505. [[CrossRef](#)]
66. Huang, J.; Quan, L.; Zhang, X. Development of a dual-acting axial piston pump for displacement controlled system. *Proc. Inst. Mech. Eng. Part B* **2013**, *228*, 606–616. [[CrossRef](#)]
67. Huang, J.; Zhao, H.; Quan, L.; Zhang, X. Development of an asymmetric axial piston pump for displacement-controlled system. *Proc. Inst. Mech. Eng. Part C* **2013**, *228*, 1418–1430. [[CrossRef](#)]
68. Kenyon, R.L.; Scanderberg, D.; Wilkerson, W.D. Electro-Hydraulic Actuator. European Patent 90304554.0, 26 April 1990.
69. Quan, L.; Ge, L.; Wang, C.; Li, B.; Zhao, B.; Lu, Z. Performance of Speed Variable Asymmetric Pump Controlled Asymmetric Hydraulic Cylinder. In Proceedings of the 10th JFPS International Symposium on Fluid Power, Fukuoka, Japan, 24–27 October 2017; pp. 1–10.
70. Pedersen, H.C.; Schmidt, L.; Andersen, T.O.; H. Brask, M. Investigation of New Servo Drive Concept Utilizing Two Fixed Displacement Units. *JFPS Int. J. Fluid Power Syst.* **2014**, *8*, 1–9. [[CrossRef](#)]
71. Minav, T.; Bonato, C.; Sainio, P.; Pietola, M. Direct Driven Hydraulic Drive. In Proceedings of the 9th International Fluid Power Conference, Aachen, Germany, 24–26 March 2014; pp. 7–11.
72. Järf, A.; Minav, T.; Pietola, M. Nonsymmetrical Flow Compensation Using Hydraulic Accumulator. In Proceedings of the 9th FPNI Ph.D. Symposium on Fluid Power, Florianopolis, Brazil, 26–28 October 2016; pp. 1–6. [[CrossRef](#)]
73. Minav, T.; Panu, S.; Matti, P. Direct-Driven Hydraulic Drive Without Conventional Oil Tank. In Proceedings of the ASME/BATH 2014 Symposium on Fluid Power and Motion Control, Bath, UK, 10–12 September 2014; p. V001T01A022. [[CrossRef](#)]
74. Filatov, D.; Minav, T.; Heikkinen, J.E. Adaptive Control for Direct-Driven Hydraulic Drive. In Proceedings of the 11th International Fluid Power Conference, Aachen, Germany, 19–21 March 2018.
75. Niraula, A.; Zhang, S.; Minav, T.; Pietola, M. Effect of Zonal Hydraulics on Energy Consumption and Boom Structure of a Micro-Excavator. *Energies* **2018**, *11*, 2088. [[CrossRef](#)]
76. Zhang, S.; Minav, T.; Pietola, M. Decentralized Hydraulics for Micro Excavator. In Proceedings of the 15th Scandinavian International Conference on Fluid Power, Linköping, Sweden, 7–9 June 2017; pp. 187–195. [[CrossRef](#)]
77. Schmidt, L.; Roemer, D.B.; Pedersen, H.C.; Andersen, T.O. Speed-Variable Switched Differential Pump System for Direct Operation of Hydraulic Cylinders. In Proceedings of the ASME/BATH 2015 Symposium on Fluid Power and Motion Control, Chicago, IL, USA, 14–16 October 2015.
78. Schmidt, L.; Groenkjaer, M.; Pedersen, H.C.; Andersen, T.O. Position Control of an Over-Actuated Direct Hydraulic Cylinder Drive. *Control Eng. Pract.* **2017**, *64*, 1–14. [[CrossRef](#)]
79. Ketelsen, S.; Schmidt, L.; Donkov, V.H.; Andersen, T.O. Energy Saving Potential in Knuckle Boom Cranes using a Novel Pump Controlled Cylinder Drive. *Model. Identif. Control* **2018**, *39*, 73–89. [[CrossRef](#)]
80. Cleasby, K.; Plummer, A. A novel high efficiency electrohydrostatic flight simulator motion system. In Proceedings of the ASME/BATH 2008 Symposium on Fluid Power and Motion Control, Bath, UK, September 2008; pp. 437–449.
81. Costa, G.K.; Sepehri, N. *Hydrostatic Transmissions and Actuators: Operation, Modelling and Applications*; Wiley: Hoboken, NJ, USA, 2015.
82. Neubert, T. Elektro-hydraulische antriebsysteme mit drehzahlveränderbaren Pumpen. In Proceedings of the 1. Internationales Fluidtechnisches Kolloquium, Aachen, Germany, 17–18 March 1998; pp. 287–300. (In German)
83. Helduser, S. Electric-hydrostatic drive—An innovative energy-saving power and motion control system. *Proc. Inst. Mech. Eng. Part I* **1999**, *213*, 427–437. [[CrossRef](#)]
84. Helduser, S. Electric-Hydrostatic Drive Systems and their Application in Injection Moulding Machines. In Proceedings of the Forth JHPS International Symposium on Fluid Power, Tokyo, Japan, November 1999; pp. 261–266.

85. Cho, S.H.; Helduser, S. Robust motion control of a clamp-cylinder for energy-saving injection moulding machines. *J. Mech. Sci. Technol.* **2008**, *22*, 2445–2453. [[CrossRef](#)]
86. Long, Q.; Neubert, T.; Helduser, S. Principle to Closed Loop Control Differential Cylinder with Double Speed Variable Pumps and Single Loop Control Signal. *Chin. J. Mech. Eng.* **2004**, *17*, 85–88.
87. Rahmfeld, R. Development and Control of Energy Saving Hydraulic Servo Drives for Mobile Systems. Ph.D. Thesis, TU Hamburg-Harburg, Hamburg, Germany, 2002.
88. Yao, J.; Wang, P.; Cao, X.M.; Wang, Z. Independent volume-in and volume-out control of an open circuit pump-controlled asymmetric cylinder system. *J. Zhejiang Univ. Sci. A* **2018**, *19*, 203–210. [[CrossRef](#)]
89. Lodewyks, J. Der Differentialzylinder im Geschlossenen Hydrostatischen Kreislauf. Ph.D. Thesis, RWTH Aachen, Aachen, Germany, 1994. (In German)
90. Feuser, A.; Dantlgraber, J.; Spath, D.; Wilke, O. Servopumpenantriebe für Differentialzylinder. *Ölhydraul. Pneum.* **1995**, *39*, 540–544. (In German)
91. Dantlgraber, J. Hydraulic System for a Differential Piston Type Cylinder. U.S. Patent 5179836, 19 January 1993.
92. Klug, D. Hydraulische Antriebe mit Drehzahlge-regeltem Elektromotor. Ph.D. Thesis, TU Chemnitz, Chemnitz, Germany, 2000. (In German)
93. Rahmfeld, R.; Ivantysynova, M. Energy Saving hydraulic actuators for mobile machines. In Proceedings of the 1st Bratislavian Fluid Power Conference, Častá-Píla, Slovakia, 2–3 June 1998.
94. Ivantysynova, M. Displacement Controlled Linear and Rotary Drives for Mobile Machines with Automatic Motion Control. *SAE Trans. Sect. 2* **2000**, *109*, 125–132.
95. Ivantysynova, M. Die Schrähscheibenmaschine-eine Verdrängereinheit mit großem Entwicklungspotential. In Proceedings of the 1. Internationales Fluidtechnisches Kolloquium, Aachen, Germany, 17–18 March 1998. (In German)
96. Rahmfeld, R.; Ivantysynova, M. Displacement controlled linear actuator with differential cylinder—A way to save primary energy in mobile machines. In Proceedings of the 5th International Conference on Fluid Power Transmission and Control, Hangzhou, China, 4–5 April 2001.
97. Schneider, M.; Koch, O.; Weber, J.; Bach, M.; Jacobs, G. Green Wheel Loader—Development of an energy efficient drive and control system. In Proceedings of the 9th International Fluid Power Conference, Aachen, Germany, 24–26 March 2014.
98. Rahmfeld, R.; Ivantysynova, M.; Weber, J. Displacement Controlled Wheel Loader—A simple and clever Solution. In Proceedings of the 4th International Fluid Power Conference, Dresden, Germany, 23–24 March 2004; pp. 183–196.
99. Schneider, M.; Koch, O.; Weber, J. Green Wheel Loader—Improving fuel economy through energy efficient drive and control concepts. In Proceedings of the 10th International Fluid Power Conference, Dresden, Germany, 8–10 March 2016.
100. Williamson, C.; Zimmerman, J.; Ivantysynova, M. Efficiency study of an excavator hydraulic system based on displacement-controlled actuators. In Proceedings of the ASME/BATH 2008 Symposium on Fluid Power and Motion Control, Bath, UK, 10–12 September 2008; pp. 291–307.
101. Zimmerman, J.D.; Ivantysynova, M. Reduction of Engine and Cooling Power by Displacement Control. In Proceedings of the 6th FPNI PhD Symposium, West Lafayette, IN, USA, 15–19 June 2010; pp. 339–352.
102. Zimmerman, J.; Busquets, E.; Ivantysynova, M. 40% fuel savings by displacement control leads to lower working temperatures—A simulation study and measurements. In Proceedings of the 52nd National Conference on Fluid Power, Las Vegas, NV, USA, 23–25 March 2011; pp. 693–702.
103. Zimmerman, J. Toward Optimal Multi-Actuator Displacement Controlled Mobile Hydraulic Systems. Ph.D. Thesis, Purdue University, West Lafayette, IN, USA, 2012.
104. Busquets, E.; Ivantysynova, M. The World's First Displacement-Controlled Excavator Prototype with Pump Switching—A Study of the Architecture and Control. In Proceedings of the 9th JFPS International Symposium on Fluid Power, Matsue, Japan, 28–31 October 2014.
105. Busquets, E.; Ivantysynova, M. A Multi-Actuator Displacement-Controlled System with Pump Switching—A Study of the Architecture and Actuator-Level Control. *JFPS Int. J. Fluid Power Syst.* **2015**, *8*, 66–75. [[CrossRef](#)]
106. Williamson, C.; Ivantysynova, M. Pump Mode Prediction for Four-Quadrant Velocity Control of Valveless Hydraulic Actuators. In Proceedings of the 7th JFPS International Symposium on Fluid Power, Toyama, Japan, 15–18 September 2008; Volume 2008, pp. 323–328. [[CrossRef](#)]

107. Williamson, C.; Lee, S.; Ivantysynova, M. Active Vibration Damping for an Off-Road Vehicle with Displacement Controlled Actuators. *Int. J. Fluid Power* **2009**, *10*, 5–16. [CrossRef]
108. Williamson, C.; Ivantysynova, M. Stability and Motion Control of Inertial Loads with Displacement Controlled Hydraulic Actuators. In Proceedings of the 6th FPNI PhD Symposium, West Lafayette, IN, USA, 15–19 June 2010; pp. 499–514.
109. Busquets, E. An Investigation of the Cooling Power Requirements for Displacement-Controlled Multi-Actuator Machines. Master's Thesis, Purdue University, West Lafayette, IN, USA, 2013.
110. Busquets, E.; Ivantysynova, M. Temperature Prediction of Displacement Controlled Multi-Actuator Machines. *Int. J. Fluid Power* **2013**, *14*, 25–36. [CrossRef]
111. Lodewyck, J. Differenzialzyliner im geschlossenen hydrostatischen Getriebe. *Ölhydraul. Pneum.* **1993**, *37*, 394–401.
112. Heybroek, K. On Energy Efficient Mobile Hydraulic Systems: with Focus on Linear Actuation. Ph.D. Thesis, Linköping University, Linköping, Sweden, 2017.
113. Heybroek, K.; Palmberg, J.O.; Lillemets, J.; Lugnborg, M.; Ousbäck, M. Evaluating a Pump Controlled Open Circuit Solution. In Proceedings of the 51th National Conference on Fluid Power, Las Vegas, NV, USA, 12–14 March 2008.
114. Heybroek, K.; Larsson, J.; Palmberg, J.O. Open Circuit Solution for Pump Controlled Actuators. In Proceedings of the 4th FPNI PhD Symposium on Fluid Power, Sarasota, FL, USA, 13–17 June 2006; pp. 27–40.
115. Heybroek, K.; Larsson, J.; Palmberg, J.O. Mode Switching and Energy Recuperation in Open-Circuit Pump Control. In Proceedings of the 10th Scandinavian International Conference on Fluid Power, Tampere, Finland, 21–23 May 2007; Volume 3, pp. 197–209.
116. Ivantysyn, R.; Weber, J. Open Circuit Displacement Control in a 300 t Mining Excavator. *ATZoffhighway Worldw.* **2017**, *10*, 48–53. [CrossRef]
117. Michel, S.; Schulze, T.; Weber, J. Energy-efficiency and thermo energetic behaviour of electrohydraulic compact drives. In Proceedings of the 9th International Fluid Power Conference, Aachen, Germany, 24–26 March 2014.
118. Minav, T.; Sainio, P.; Pietola, M. Efficiency of Direct Driven Hydraulic Setup in Arctic Conditions. In Proceedings of the Fourteenth Scandinavian International Conference on Fluid Power, Tampere, Finland, 20–22 May 2015.
119. Minav, T.; Papini, L.; Pietola, M. A Thermal Analysis of Direct Driven Hydraulics. In Proceedings of the 10th International Fluid Power Conference, Dresden, Germany, 8–10 March 2016; pp. 235–247.
120. Karlén, N.; Minav, T.; Pietola, M. Investigation of Thermal Effects in Direct Driven Hydraulic System for Off-Road Machinery. In Proceedings of the 9th FPNI Ph.D. Symposium on Fluid Power, Florianopolis, Brazil, 26–28 October 2016. [CrossRef]
121. Michel, S.; Weber, J. Prediction of the thermo-energetic behaviour of an electrohydraulic compact drive. In Proceedings of the 10th International Fluid Power Conference, Dresden, Germany, 8–10 March 2016; pp. 219–234.
122. Minav, T.; Heikkinen, J.; Schimmel, T.; Pietola, M. Direct Driven Hydraulic Drive: Effect of Oil on Efficiency in Sub-Zero Conditions. *Energies* **2019**, *12*, 219. [CrossRef]
123. Michel, S.; Weber, J. Investigation of Self-Contamination of Electrohydraulic Compact Drives. In Proceedings of the 10th JFPS International Symposium on Fluid Power, Fukuoka, Japan, 24–27 October 2017.
124. Tasner, T.; Les, K.; Tic, V.; Lovrec, D. Energy efficiency of different electrohydraulic drives. In Proceedings of the 9th International Fluid Power Conference, Aachen, Germany, 24–26 March 2014.
125. Bing, X.; Junhui, Z.; Ying, L.; Qun, C. Modeling and analysis of the churning losses characteristics of swash plate axial piston pump. In Proceedings of the 2015 International Conference on Fluid Power and Mechatronics, Harbin, China, 5–7 August 2015; pp. 22–26. [CrossRef]
126. Parker Hannafin. P2/P3 Series Piston Pumps Variable Displacement—Catalog HY28-1559-01/PT , 2003. Available online: https://www.parker.com/literature/Hydraulic%20Pump%20Division/P2_P3-Files/P2-P3%20Series%20Piston%20Pumps%20Variable%20Displacement-HY28-1559-01-PT.pdf (accessed on 3 April 2019).
127. Eaton Vickers. Axial Piston Pumps Fixed and Variable Displacement. Catalog: GB-2379B. Available online: http://www.advancedfluidsystems.com/files/Eaton-Vickers_PVB_Catalog.pdf (accessed on 3 April 2019).

128. Caldwell, N.J. Digital Displacement Hydrostatic Transmission Systems. Ph.D. Thesis, University of Edinburgh, Edinburgh, Scotland, 2007. Available online: <http://www.artemisip.com/wp-content/uploads/2018/05/180518-Dr-Niall-Caldwell-PhD-FINAL.pdf> (accessed on 3 April 2019).
129. Grønkjær, M.; Rahn, H. Control and Experimental Evaluation of Speed-variable Switched Differential Pump Concept. Master's Thesis, Aalborg University, Aalborg, Denmark, 2015. Available online: https://projekter.aau.dk/projekter/files/213881780/Control_and_Experimental_Evaluation_of_Speed_variable_Switched_Differential_Pump_Concept_MCE4_1021.pdf (accessed on 3 April 2019).



© 2019 by the authors. Licensee MDPI, Basel, Switzerland. This article is an open access article distributed under the terms and conditions of the Creative Commons Attribution (CC BY) license (<http://creativecommons.org/licenses/by/4.0/>).

Paper B

Mass Estimation of Self-Contained Linear Electro-Hydraulic Actuators and Evaluation of the Influence on Payload Capacity of a Knuckle Boom Crane

Søren Ketelsen, Torben Ole Andersen, Morten Kjeld Ebbesen
and Lasse Schmidt

The paper has been published in
Proceedings of the ASME/Bath 2019 Symposium on Fluid Power and
Motion Control

© 2019 by American Society of Mechanical Engineers

Paper C

A Self-Contained Cylinder Drive with Indirectly Controlled Hydraulic Lock

Søren Ketelsen, Torben Ole Andersen, Morten Kjeld Ebbesen
and Lasse Schmidt

The paper has been published in
Modeling, Identification and Control Vol. 41, No. 3, pp.185-205, 2020.



A Self-Contained Cylinder Drive with Indirectly Controlled Hydraulic Lock

S. Ketelsen¹ T.O. Andersen¹ M.K. Ebbesen² L. Schmidt¹

¹*Department of Energy Technology, Aalborg University, 9220 Aalborg, Denmark. E-mail: sok@et.aau.dk*

²*Department of Engineering Sciences, University of Agder, Grimstad, Norway*

Abstract

This paper presents a self-contained pump-controlled hydraulic linear drive including an innovative load holding sub-circuit. For safety critical applications such as crane manipulators, locking valves or load holding valves are enforced by legislation, but the load holding functionality may also be used actively to decrease the energy consumption for applications where the load is kept stationary for longer periods of time. The system proposed in this paper is based on a simple hydraulic architecture using two variable-speed electric motors each connected to a fixed-displacement pump. This architecture is well-known in academic literature, but in this paper a novel load holding sub-circuit has been included. To control this load holding functionality, the low chamber pressure needs to be controlled accurately, while still being able to control the motion of the cylinder piston as well. Due to strong cross-couplings between cylinder piston motion and chamber pressures this task is non-trivial. The control for opening the locking valves is indirect in the sense that it is controlled via the chamber pressures, which are actively controlled. The fundamental control strategy presented in this paper is based on transforming the highly coupled physical states to virtual states, significantly reducing cross-couplings.

As a case study, a two link medium sized knuckle boom crane is selected as an application example. Simulation results confirm the applicability of the proposed system. Appropriate position tracking performance has been achieved for the considered motion trajectory, while the low chamber pressure is controlled in a satisfying manner. A smooth transition from motion operating mode to load holding mode is achieved, with the system not requiring any input energy to keep the load stationary when the hydraulic cylinder lock is engaged.

Keywords: Energy efficient hydraulic actuation, pump-controlled cylinder, cylinder direct drive, multi-variable control, load holding, safety functionality, cylinder lock

1 Introduction

Hydraulic linear actuation technology is well-known for its high power and force densities. This often makes the technology the preferred solution for applications characterised by low speed high force operation. Such applications may include large industrial machinery, e.g. presses, test-equipment, construction machines, and cranes. In many industries the preferred linear hydraulic actuator is the standard differential cylinder

(Quan et al., 2014; Weber et al., 2016). Conventionally, several cylinders are supplied from a centralised hydraulic power unit (HPU), and individual valves control the motion of each cylinder by throttling the chamber flows. The resulting pressure loss inherently leads to a poor energy efficiency of conventional hydraulic systems. To improve the energy efficiency, a load sensing HPU is often utilised. Here the supply pressure is adjusted to the needs of the cylinder requiring the

largest pressure, which reduces the throttling losses, especially if the pressure level is similar for all consumers. In situations where a slowly moving consumer requires a high supply pressure, while a fast moving consumer requires a low supply pressure, significant pressure losses are however still present.

To significantly increase the energy efficiency, the throttle based control clearly needs to be eliminated, while preserving controllability, still at a reasonable cost level. An obvious idea is to completely replace the hydraulic technology with a competing technology, such as electro-mechanical drives, e.g. ball or roller screws. Due to low reliability under high load conditions (e.g. shock load damage) and limited force capabilities this technology is not well-suited for all applications (Hagen et al., 2017; Padovani et al., 2019).

Another idea is to stay with the hydraulic technology and the centralised HPU, and replace the control valve with other components. The so-called digital hydraulic technology is one approach for doing so. One branch of digital hydraulics considers multi-chamber cylinders. Here the conventional control valve is replaced by several on/off valves which may be supplied by multiple pressure lines (Hedegaard Hansen et al., 2017; Linjama et al., 2003; Hedegaard Hansen and Pedersen, 2016; Hedegaard Hansen et al., 2018). In Donkov et al. (2017, 2018) a simulation study investigating actuation of a knuckle boom crane using the digital hydraulic technology was conducted. The results show an improved energy efficiency, but an unsatisfying tracking performance due to the discrete valve switching.

Recently, industrial and academic interest into self-contained pump-controlled cylinder drive technology has been increasing. Here the idea is to replace the conventional control valve and the centralised HPU, with one or more electric motors and hydraulic pumps to control each cylinder. This solution holds several benefits compared to conventional control valves. The resistive losses associated with throttling are ideally eliminated, leading to a significantly improved energy efficiency. This is furthermore strengthened because self-contained cylinder drives are generally able to recover energy in aided load situations. Secondly, all components, i.e. cylinder, motors, pumps, pressurised oil tank, hydraulic manifold, are integrated into a single unit, eliminating the need of piping to the centralised HPU.

A general challenge for controlling a differential cylinder directly by the pump flow is to compensate the uneven flow requirements originating from the asymmetry of the cylinder. Two fundamentally different solutions may be found in literature: valve-compensated and pump-compensated architectures (Costa and Sepehri, 2018). A comprehensive

overview of both compensation topologies is given in Ketelsen et al. (2019b).

In valve-compensated architectures a single (symmetric) pump is often used, which requires auxiliary valves to handle cylinder flow asymmetry. In Michel and Weber (2012); Hewett (1994); Çalkan et al. (2015) an inverse shuttle valve is used to always connect the low pressure chamber of the cylinder with the low pressure reservoir. In Rahmfeld and Ivantysynova (2001); Padovani et al. (2019); Schneider et al. (2014) this is achieved using pilot-operated check valves. To avoid oscillatory valve switchings - so-called mode oscillation - for certain load situations, Padovani et al. (2020); Gøytil et al. (2020) suggests using actively controlled on/off valves. A common disadvantage of valve-compensated architectures compared to conventional valve-control, is the fact that the pressure in the low pressure chamber is close to the low pressure reservoir. This lowers the drive stiffness which in turn causes the realisable control bandwidth to decrease, and thus limits the application range of these concepts.

The uneven flow requirement may also be compensated by mounting multiple pumps, typically two, on the same shaft. Here the displacement ratio of the pumps must be matched to the cylinder asymmetry. This strategy has been investigated in Pedersen et al. (2014); Brahmer (2012); Minav et al. (2014); Grønkaer et al. (2020); Schmidt et al. (2020), where the issues of low pressure operation similar to valve-compensated architectures are also present. To avoid low pressure operation Schmidt et al. (2019b,a), suggested to include rectifying check valves in combination with actively controlled proportional valves. This enables controlling the cylinder flow into the cylinder by the pump and flow from the cylinder using proportional valves.

Another approach to avoid low pressure operation is given in Schmidt et al. (2015, 2017). Here a third pump, only active in the forward direction is included. By advanced control efforts, it was proven experimentally possible, to control the pressure in the low pressure chamber and thus maintain a desired drive stiffness, while in motion. In Ketelsen et al. (2018), this drive concept was used for actuation of a middle sized two link knuckle boom crane. Simulation results suggested a significantly improved energy efficiency compared to a conventional load sensing system. For a real life working trajectory the consumed energy was lowered by 60 %.

The drive concept utilised in Ketelsen et al. (2018) lacked the safety functionality often realised by counter-balance-valves (CBV) in conventional systems, i.e. a flow-blocking device ensuring that in case of power shutdown or overrunning loads controllability of the load is not lost. This is done by ensuring that a cer-

tain back pressure is always present during operation. In pump-controlled systems CBV's may be utilised as well. CBV's are however throttling devices, meaning that these typically reduce the achievable energy efficiency and may preclude the opportunity of energy recovery in certain load situations (Imam et al., 2017; Jalayeri et al., 2015).

Cylinder locking or load holding may also be achieved by installing pilot-operated check valves or logic elements in the main transmission lines. As shown in Padovani et al. (2019), this may lead to undesired oscillatory valve openings and piston motion, for some configurations of the pilot-operated check valves. In Hagen et al. (2018) and Schneider et al. (2014) the pilot pressure is controlled using an electrically actuated on/off valve which avoids oscillatory check valve openings.

Due to a desire of keeping safety functionality in hydraulic/mechanical components, without compromising energy efficiency and controllability an innovative load holding concept is presented in this paper. The functionality of this circuit is based upon the requirement that the low chamber pressure may be controlled rather accurately for all operating scenarios. Therefore the triple pump concept, investigated by the authors in Ketelsen et al. (2018) is found infeasible.

Instead a circuit architecture based on two variable-speed electrical prime movers, each connected to a fixed-displacement pump is utilised. This gives the required controllability, being able to control both piston motion and the lower chamber pressure. This

dual variable-speed pump drive is abbreviated DvSP in the following. Using two prime movers increases the scalability of the drive, which may be important for applications requiring large actuator powers, such as crane manipulators (Ketelsen et al., 2019a; Gøytill et al., 2019). The idea of using two variable flow suppliers is not new. For variable-displacement pumps this is found in Dantlgraber (1993); Feuser et al. (1995); Lodewyks (1994). For two variable-speed prime movers this is considered in Helduser (1999); Neubert (2002). However none of the mentioned references consider controlling a load holding device in combination with two prime movers.

This paper is organized in the following order: In the next section the hydraulic system is presented. In section 3 an application example chosen as a knuckle boom crane is presented. The hydraulic architecture has a wide application range, but a knuckle boom crane is found to be a well suited application, due to the requirement of safety/load holding functionality and the need of four quadrant operation including smooth switching between quadrants. In section 4 and 5 non-linear and linear models are derived and an analysis of the input-output cross couplings is presented. Based on the results of the coupling analysis, a control strategy based on state decoupling is derived in section 6 and 7. In section 8 simulation results are presented.

2 Pump-Controlled Cylinder Drive with Self-Locking Ability

The proposed DvSP drive is shown in Fig. 1. The concept consists of a closed-circuit pump, P_1 , which is connected to both cylinder chambers and driven by the variable-speed electric machine M_1 . An open circuit pump P_2 is driven by the variable-speed electric machine M_2 and provides uneven chamber flow compensation. A pressurized accumulator is used for storing the cylinder rod volume, compression volume and thermal expansion volume. To keep the reservoir pressure low, a large gas volume is needed. For the current study a gas volume of 288 L is used. Recently Ketelsen et al. (2020a,b) suggested implementing a gasless reservoir in pump-controlled systems to increase system compactness. For filtering a hydraulic filter is included. Check valves CV_6 and CV_7 ensure uni-directional filter flow. The valves LH_A and LH_B are used to lock the cylinder. These valves are closed unless the pilot pressure is high enough to open the valve against the spring force. The pilot pressure is controlled using the inverse shuttle valve, SV , which is supplying the lowest chamber pressure to the pilot line. To avoid undesired loss of pilot pressure the shuttle valve must switch in open

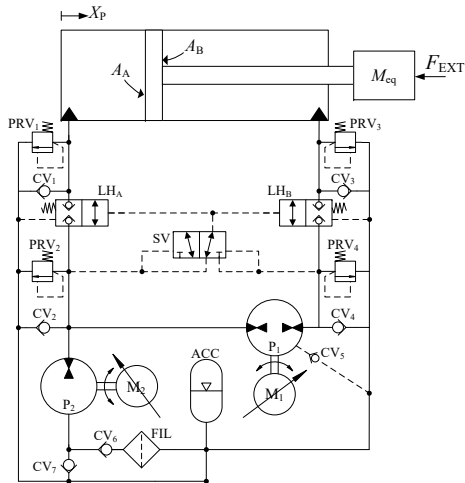


Figure 1: Asymmetric cylinder controlled by the dual variable-speed pump (DvSP) system.

rather than closed transition. If the lowest chamber pressure is controlled appropriately, oscillatory openings of the load holding valves may be avoided. The three valves LH_A , LH_B and SV constitute the cylinder lock/load holding sub-circuit and ensure that the hydraulic cylinder is locked if the lowest pressure is not controlled to be larger than the opening pressure of LH_A , LH_B . In case of hose leak, power cut-off or similar emergency the load is going to move slightly until the volume increase in one of the chambers causes the pressure to decrease, in turn causing the load holding valves to close. This effectively locks the cylinder piston and load. On the other hand, if the lowest chamber pressure is successfully controlled to be larger than the full open pressure of the load holding valves, the cylinder piston is unlocked and controllable. Please note that the load holding valves should be sized, such that the pressure drop at full cylinder flow is small.

2.1 Operation Modes

In Fig. 2 a simplified schematics of the DvSP drive is shown in motion operating mode (a) to (d) and in self-locking/load holding mode (e) and (f). The desired operation modes are described in the following.

2.1.1 Four Quadrant Motion Operation Mode

In the four operating quadrants given in Fig. 2 the lower chamber pressure is controlled to ensure that the load holding valves are fully open. Notice that in the figure, chamber pressures and their adjacent transmission lines are the same color to indicate that the pressure drop across the load holding valves in motion operating mode is considered negligible.

In the first quadrant, Fig. 2a, the external load prescribes the piston side chamber pressure P_A to be larger than the rod side chamber pressure P_B , such that P_B is controlled to ensure the load holding valves are fully open. The cylinder is extending meaning that pump 1 is moving oil from the rod chamber to the piston chamber while pump 2 is delivering fluid from the accumulator to the piston side chamber. Both motors are supplying energy to the system in this quadrant. If the cylinder area ratio is 0.5, the two pumps need to supply the same amount of flow statically.

In the second quadrant Fig. 2b, the cylinder retracts under an assistive load. Both motors act as generators in this operating quadrant and a potential for recovering some of the energy supplied by the load exists.

In the third and fourth quadrant the external load prescribes $P_B > P_A$. An important difference from quadrant 1 and 2, is the fact that the operation mode of the electric machines is not identical. For example in the third quadrant, motor 1 is supplying energy to

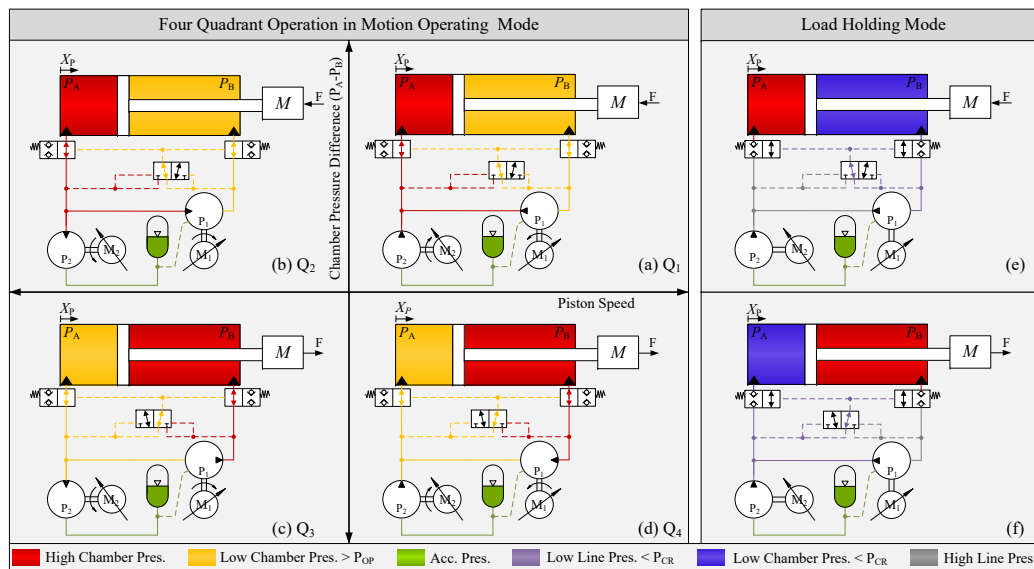


Figure 2: Four quadrant operation schematics of a asymmetric cylinder controlled by the DvSP-system.

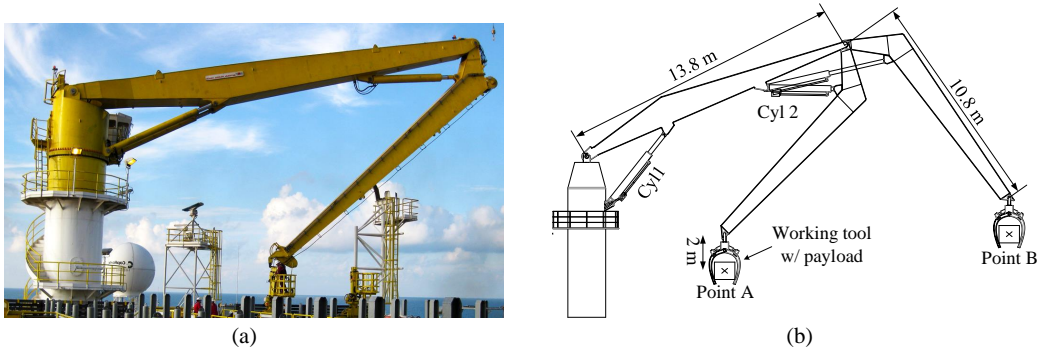


Figure 3: (a) Example of knuckle boom crane with two links provided by National Oilwell Varco ©; (b) Simplified drawing of the knuckle boom crane used as a case study. The considered motion trajectory in tool center space is indicated.

the system while motor 2 is in generator mode. The opposite is true in the fourth quadrant. This situation arises, because the pressure in the low pressure chamber is required to be above the accumulator pressure, to open the load holding valves. If this was not desired, motor 2 would be idling in quadrants 3 and 4. For operation in the third and fourth quadrant, it is beneficial to have a shared DC supply to the frequency converters controlling the motion of the two motors. This would facilitate that the power generated by one motor, may be supplied directly to the other motor.

2.1.2 Load Holding Mode

In load holding mode, Fig. 2e and 2f, the smallest transmission line pressure is below the cracking pressure of the load holding valves, such that these are fully closed. This means that the cylinder piston is hydraulically locked. In the case of emergency i.e. power loss or

hose burst, the lowest chamber pressure cannot be kept above the opening pressure of the load holding valves, meaning that the system enters this operation mode. The load holding mode may also be engaged actively during nominal operation to save energy in stationary situations. In these situations it is obviously beneficial to control the pressure in the transmission lines to equal the accumulator pressure to yield zero torque on the pump shafts.

3 Application Example

A relevant application for studying the DvSP drive is the actuation of crane manipulators. During emergencies e.g. power-shutdown or hose burst, the load needs to be locked passively by hydraulically and/or mechanically actuated components. Furthermore, the power requirements for large crane manipulators may be sub-

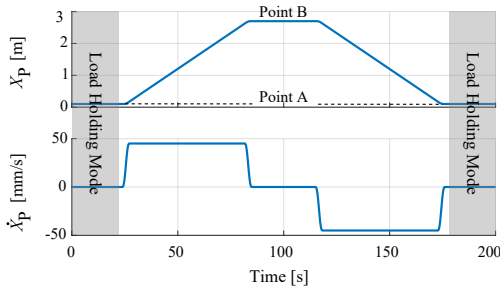


Figure 4: Considered motion trajectory in actuator space.

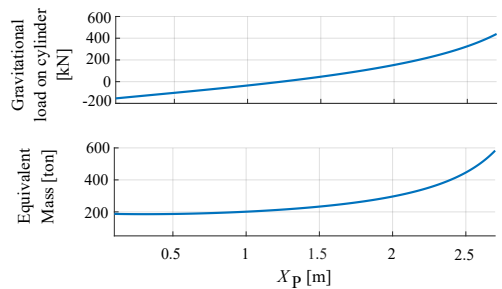


Figure 5: Actuator loads for DvSP system as a function of piston position x_p .

stantial, meaning that sharing this between two electrical prime movers improves the scalability compared to single prime mover architectures.

To show the applicability of the proposed system architecture, a medium sized knuckle boom crane similar to the one shown in Fig. 3 is selected as a case study.

For the study presented in this paper, the knuckle boom actuator (cylinder 2) is considered for actuation by the DvSP drive, while the main actuator (cylinder 1) is kept stationary. This is chosen to keep focus on main functionality and control of the hydraulic architecture, rather than control and performance on the machine level (crane). Using the knuckle boom actuator as a case study is suitable, since this requires operation in all four operating quadrants (see Fig. 2). Furthermore the DvSP drive is commanded to enable load holding mode at point A, meaning that the transition back and forth between motion and load holding mode is tested as well. The considered trajectory in actuator space is given in Fig. 4

Seen from the actuator perspective the trajectory may be considered an *advanced* drive task, due to the four operation quadrants, enabling/disabling of the load holding functionality and the large parameter variations typical for actuating a crane manipulator (See Fig. 5).

For brevity, it has been decided to focus on how the DvSP drive performs under such demanding conditions rather than focusing on modelling/parametrisation of a specific crane. Therefore it has been chosen to use a dynamic mechanical model of the considered crane (Fig. 3b) that was derived by the authors in Ketelsen et al. (2018). Here it suffices to show the equivalent inertia and gravitational load (see Fig. 5) experienced by the knuckle boom actuator, when performing the motion trajectory shown in Fig. 3b and Fig. 4. The velocity dependent forces (e.g. Coriolis forces) are not shown in Fig. 5, due to insignificance compared to the gravitational load.

4 Mathematical Model of the DvSP Drive

During nominal operation of the DvSP drive the pressure relief valves PRV₁ to PRV₄ and the check valves CV₁ to CV₄ in Fig. 1 are closed at all times. By further assuming CV₅ to CV₇ and the filter (FIL) to be ideal the hydraulic schematic in Fig. 1 may be reduced to the one depicted in Fig. 6, and used for deriving the non-linear system model.

Considering Fig. 6, the DvSP system is modelled by Eq. (1)-(18). Cylinder cross port leakage is assumed negligible, and the following definitions are made $V_A =$

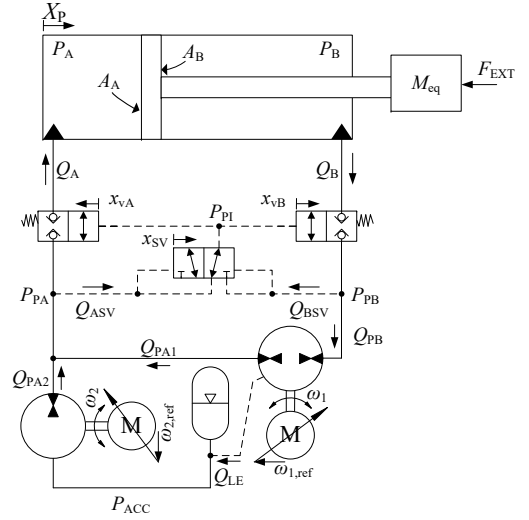


Figure 6: Asymmetric cylinder controlled by DvSP-system.

$V_{0A} + A_A X_P$, $V_B = V_{0B} - A_B X_P$, $\alpha = A_B/A_A$. The volumes V_{PB} , V_{PA} , V_{PI} and V_0 (pipe/hose connection to accumulator) are constant.

$$\ddot{X}_P = \frac{A_A(P_A - \alpha P_B) - \dot{X}_P B_v - F_C \tanh(\gamma \text{sign}(\dot{X}_P)) - f(X_P, \dot{X}_P)}{M_{eq}} \quad (1)$$

$$\dot{P}_A = \frac{\beta_A}{V_A} (Q_A - \dot{X}_P A_A) \quad (2)$$

$$\dot{P}_B = \frac{\beta_B}{V_B} (\dot{X}_P \alpha A_A - Q_B) \quad (3)$$

$$\dot{P}_{PA} = \frac{\beta_{PA}}{V_{PA}} (Q_{PA1} + Q_{PA2} - Q_A - Q_{ASV}) \quad (4)$$

$$\dot{P}_{PB} = \frac{\beta_{PB}}{V_{PB}} (Q_B - Q_{PB} - Q_{BSV}) \quad (5)$$

$$\dot{P}_{PI} = \frac{\beta_{PI}}{V_{PI}} (Q_{ASV} + Q_{BSV}) \quad (6)$$

$$\dot{P}_{ACC} = \frac{Q_{LE} - Q_{PA2}}{\frac{V_{ACC} + V_0 - V_g}{\beta_{ACC}} + \frac{V_g}{\kappa P_{ACC}}} \quad (7)$$

$$V_g = \begin{cases} V_{ACC} & P_{ACC} < p_0 \\ V_{ACC} \left(\frac{p_0}{P_{ACC}} \right)^{\frac{1}{\kappa}} & P_{ACC} > p_0 \end{cases} \quad (8)$$

$$Q_{PA1} = \omega_1 D_1 - K_1(P_{PA} - P_{PB}) - K_1(P_{PA} - P_{ACC}) \quad (9)$$

$$Q_{PB} = \omega_1 D_1 - K_1(P_{PA} - P_{PB}) + K_1(P_{PB} - P_{ACC}) \quad (10)$$

$$Q_{PA2} = \omega_1 D_2 - K_2(P_{PA} - P_{ACC}) \quad (11)$$

$$Q_{LE} = K_1(P_{PA} - P_{ACC}) + K_1(P_{PB} - P_{ACC}) \quad (12)$$

5 Linear Models and Coupling Analysis

$$Q_A = x_{vA} K_{Qv} \sqrt{|P_{PA} - P_A|} \operatorname{sign}(P_{PA} - P_A) \quad (13)$$

$$Q_B = x_{vB} K_{Qv} \sqrt{|P_B - P_{PB}|} \operatorname{sign}(P_B - P_{PB}) \quad (14)$$

$$Q_{ASV} = (1 - x_{sv}) K_{Qsv} \sqrt{|P_{PA} - P_{PI}|} \operatorname{sign}(P_{PA} - P_{PI}) \quad (15)$$

$$Q_{BSV} = x_{sv} K_{Qsv} \sqrt{|P_{PB} - P_{PI}|} \operatorname{sign}(P_{PB} - P_{PI}) \quad (16)$$

$$\ddot{\omega}_1 = \omega_n^2 \omega_{1,\text{ref}} - 2\zeta \omega_n \dot{\omega}_1 - \omega_n^2 \omega_1 \quad (17)$$

$$\ddot{\omega}_2 = \omega_n^2 \omega_{2,\text{ref}} - 2\zeta \omega_n \dot{\omega}_2 - \omega_n^2 \omega_2 \quad (18)$$

$$x_{vA} = x_{vB} = \begin{cases} 0 & \text{for } P_{PI} \leq P_{CR} \\ \frac{P_{PI} - P_{CR}}{P_{OP} - P_{CR}} & \text{for } P_{CR} < P_{PI} < P_{OP} \\ 1 & \text{for } P_{PI} \geq P_{OP} \end{cases} \quad (19)$$

$$x_{sv} = \begin{cases} 0 & \text{for } P_{PA} < P_{PB} \\ 0.5 & \text{for } P_{PA} = P_{PB} \\ 1 & \text{for } P_{PA} > P_{PB} \end{cases} \quad (20)$$

X_P is the cylinder piston position, F_C is a Coulomb friction constant, and γ is a switching parameter. B_v is a viscous friction coefficient and $f(X_P, \dot{X}_P)$ contains the gravitational load and the Coriolis force. P_A , P_B , P_{PA} , P_{PB} , P_{PI} , P_{ACC} are control volume pressures, V_g is the volume of the gas in the accumulator, Q_{PA1} , Q_{PB} , Q_{PA2} and Q_{LE} are pump flows modelled by the Wilson pump model using geometric pump displacements D_1 , D_2 and laminar leakage coefficients K_1, K_2 . Q_A , Q_B , Q_{ASV} and Q_{BSV} are valve flows modelled by the orifice equation, x_{vA} , x_{vB} , x_{sv} are valve poppet positions modelled as quasi static, i.e. no poppet/spool dynamics is included. P_{CR} and P_{OP} are valve cracking and full open pressures respectively. ω_1 and ω_2 are motor shaft speeds, ζ is damping ratio and ω_n is bandwidth used for modelling the dynamics of the electrical motor and drive. K_{Qv} , K_{Qsv} are valve flow gains and the motor shaft reference speeds $\omega_{1,\text{ref}}$, $\omega_{2,\text{ref}}$ are the two system inputs. Finally, the effective bulk modulus of the oil air mixture, β_i , $i = \{A, B, PA, PB, PI, ACC\}$ is modelled being pressure dependent using, (Kim and Murrenhoff, 2012):

$$\beta_i(P_i) = \frac{(1 - \epsilon) \left(1 + \frac{m(P_i - p_{\text{atm}})}{\beta_F} \right)^{-\frac{1}{m}} + \epsilon \left(\frac{p_{\text{atm}}}{P_i} \right)^{\frac{1}{\kappa}}}{\frac{1 - \epsilon}{\beta_F} \left(1 + \frac{m(P_i - p_{\text{atm}})}{\beta_F} \right)^{-\frac{m+1}{m}} + \frac{\epsilon}{\kappa p_{\text{atm}}} \left(\frac{p_{\text{atm}}}{P_i} \right)^{\frac{\kappa+1}{\kappa}}}$$

where ϵ is the volumetric air content at atmospheric pressure (p_{atm}), β_F is the bulk modulus of the pure fluid, m is the pressure dependent bulk modulus gradient of the pure fluid and κ is the poly-tropic constant which is set to 1.4, assuming air to behave as an ideal gas and the compression process to be adiabatic. The effective bulk modulus is limited to 7500 bar, to include some mechanical compliance. All model parameters are listed on page 202.

Two linear models are defined according to the two distinct operation modes, i.e. motion operation mode and load holding mode.

When deriving the linear models, M_{eq} and the accumulator pressure as well as the gravitational load and Coriolis force contained in $f(X_P, \dot{X}_P)$ are assumed constant close to the linearisation point. The bulk modulus are assumed equal and constant (β_0) in all control volumes. Similarly the volume of the cylinder chambers are assumed constant close to the linearisation point, and defined by $V_{A0} = V_A|_{\mathbf{x}_0}$, $V_{B0} = V_B|_{\mathbf{x}_0}$, $\rho = V_B/V_A$, $\rho_0 = V_{B0}/V_{A0}$, with \mathbf{x}_0 being the state vector at the linearisation point.

5.1 Motion Operation Mode

In motion operation mode the load holding valves LH₁ and LH₂ are considered ideal due to high flow gains for these valves in the fully open position, i.e. the pressures on each side of the valve are considered equal. Similarly the pressure dynamics in the pilot chamber is omitted, due to the small volume of this chamber relative to the remaining volumes in the system.

The simplified model structure, under the mentioned assumptions are illustrated in Fig. 7, with lowercase letters representing linear deviation variables.

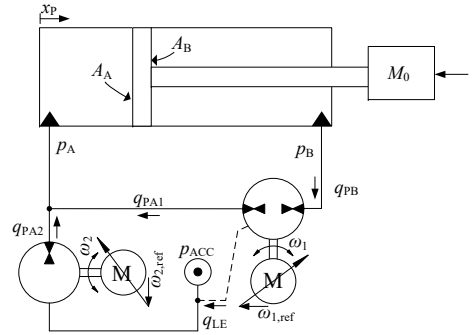


Figure 7: Simplified model structure for deriving linear model of the system in motion operating mode.

The linearised equations are given in Eq. (21) to (23):

$$\ddot{x}_P = M_{\text{eq}0}^{-1} (A_A (p_A - \alpha p_B) - \dot{x}_P B_v) \quad (21)$$

$$\dot{p}_A = \frac{\beta_0}{V_{A0}} (\omega_1 D_1 + \omega_2 D_2 - (2K_1 + K_2) p_A + K_1 p_B - \dot{x}_A A_A) \quad (22)$$

$$\dot{p}_B = \frac{\beta_0}{\rho_0 V_{A0}} (-\omega_1 D_1 - K_1 (2p_B - p_A) + \dot{x}_A A_A) \quad (23)$$

In state space form the dynamics may be represented as:

$$\dot{\mathbf{x}}_M = \mathbf{A}_M \mathbf{x}_M + \mathbf{B}_M \mathbf{u}_M, \quad \mathbf{y}_M = \mathbf{C}_M \mathbf{x}_M \quad (24)$$

$$\mathbf{x}_M = [x_P \quad \dot{x}_P \quad p_A \quad p_B]^T, \quad \mathbf{u}_M = [\omega_1 \quad \omega_2]^T$$

$$\mathbf{A}_M = \begin{bmatrix} 0 & 1 & 0 & 0 \\ 0 & -\frac{B_v}{M_{eq0}} & \frac{A_{A0}}{M_{eq0}} & -\frac{\alpha A_{A0}}{M_{eq0}} \\ 0 & -\frac{\beta_0 A_{A0}}{V_{A0}} & -\frac{\beta_0(2K_1 + K_2)}{V_{A0}} & \frac{\beta_0 K_1}{V_{A0}} \\ 0 & \frac{\beta_0 \alpha A_{A0}}{\rho_0 V_{A0}} & \frac{\beta_0 K_1}{\rho_0 V_{A0}} & -2 \frac{\beta_0 K_1}{\rho_0 V_{A0}} \end{bmatrix}$$

$$\mathbf{B}_M = \begin{bmatrix} 0 & 0 \\ 0 & 0 \\ \frac{\beta_0 D_1}{V_{A0}} & \frac{\beta_0 D_2}{V_{A0}} \\ -\frac{\beta_0 D_1}{\rho_0 V_{A0}} & 0 \end{bmatrix} \quad \mathbf{C}_M = \begin{bmatrix} 1 & 0 & 0 & 0 \\ 0 & 0 & 1 & 0 \\ 0 & 0 & 0 & 1 \end{bmatrix}$$

The subscript _M is used to denote motion operating mode.

5.2 Load Holding Mode

In load holding mode the load holding valves LH_1 and LH_2 are closed and assumed leakage free. Utilizing this assumption the simplified model structure is illustrated in Fig. 8, with lowercase letters representing linear deviation variables.

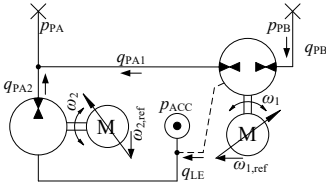


Figure 8: Simplified model system structure in load holding mode, used for deriving linearised model.

The linearised equations are given in Eq. (25) to (26), and represented in state space as:

$$\dot{p}_{\text{PA}} = \frac{\beta_0}{V_{A0}} (\omega_1 D_1 + \omega_2 D_2 - (2K_1 + K_2) p_A + K_1 p_B) \quad (25)$$

$$\dot{p}_{\text{PB}} = \frac{\beta_0}{\rho_0 V_{\text{A0}}} (-\omega_1 D_1 - K_1 (2p_{\text{B}} - p_{\text{A}})) \quad (26)$$

$$\dot{\mathbf{x}}_{\text{LH}} = \mathbf{A}_{\text{LH}} \mathbf{x}_{\text{LH}} + \mathbf{B}_{\text{LH}} \mathbf{u}_{\text{LH}}, \quad \mathbf{y}_{\text{LH}} = \mathbf{C}_{\text{LH}} \mathbf{x}_{\text{LH}} \quad (27)$$

$$\mathbf{x}_{\text{LH}} = [p_{\text{PA}} \quad p_{\text{PB}}]^T, \quad \mathbf{u}_{\text{LH}} = [\omega_1 \quad \omega_2]^T$$

$$\mathbf{A}_{\text{LH}} = \begin{bmatrix} -\frac{\beta_0(2K_1+K_2)}{V_{A0}} & \frac{\beta_0 K_1}{V_{A0}} \\ \frac{\beta_0 K_1}{\rho_0 V_{A0}} & -2\frac{\beta_0 K_1}{\rho_0 V_{A0}} \end{bmatrix}$$

$$\mathbf{B}_{\text{LH}} = \begin{bmatrix} \frac{\beta_0 D_1}{V_{A0}} & \frac{\beta_0 D_2}{V_{A0}} \\ \frac{-\beta_0 D_1}{\rho_0 V_{A0}} & 0 \end{bmatrix} \quad \mathbf{C}_{\text{M}} = \begin{bmatrix} 1 & 0 \\ 0 & 1 \end{bmatrix}$$

The subscript _{LH} is denoting load holding mode.

5.3 Electrical Motor Drive Model

The input to the linearised models are the shaft speeds (ω_1 and ω_2), thus the actuator dynamics has been neglected so far. To include these, a state space representation of the motor, motor drive and motor control dynamics is derived from Eq. (17) and (18):

$$\dot{\mathbf{x}}_{\mathbf{u}} = \mathbf{A}_{\mathbf{u}}\mathbf{x}_{\mathbf{u}} + \mathbf{B}_{\mathbf{u}}\mathbf{u}_{\text{ref}}, \quad \mathbf{y}_{\mathbf{u}} = \mathbf{C}_{\mathbf{u}}\mathbf{x}_{\mathbf{u}} \quad (28)$$

$$\mathbf{x}_u = [\omega_1 \ \omega_2]^T, \quad \mathbf{u}_{\text{ref}} = [\omega_{1,\text{ref}} \ \omega_{2,\text{ref}}]^T$$

$$\mathbf{A}_u = \begin{bmatrix} \mathbf{A}_{EM} & \mathbf{0} \\ \mathbf{0} & \mathbf{A}_{EM} \end{bmatrix} \mathbf{A}_{EM} = \begin{bmatrix} 0 & 1 \\ -\omega_n^2 & -2\zeta\omega_n \end{bmatrix}$$

$$\mathbf{B}_u = \begin{bmatrix} 0 & 0 \\ \omega_n^2 & 0 \\ 0 & 0 \\ 0 & \omega_n^2 \end{bmatrix} \quad \mathbf{C}_u = \begin{bmatrix} 1 & 0 & 0 & 0 \\ 0 & 0 & 1 & 0 \end{bmatrix}$$

5.4 Combined Linear Models

The linear models of the system in motion operating mode and load holding mode may be obtained by combining the respective models with the actuator models according to:

$$\dot{\mathbf{x}}_{\text{cM}} = \mathbf{A}_{\text{cM}} \mathbf{x}_{\text{cM}} + \mathbf{B}_{\text{cM}} \mathbf{u}_{\text{ref}}, \quad \mathbf{y}_{\text{M}} = \mathbf{C}_{\text{cM}} \mathbf{x}_{\text{cM}}$$

$$\mathbf{x}_{\text{cM}} = \begin{bmatrix} \mathbf{x}_{\text{M}} \\ \mathbf{x}_{\text{u}} \end{bmatrix}, \mathbf{A}_{\text{cM}} = \begin{bmatrix} \mathbf{A}_{\text{M}} & \mathbf{B}_{\text{M}}\mathbf{C}_{\text{u}} \\ \mathbf{0} & \mathbf{A}_{\text{u}} \end{bmatrix}$$

$$\mathbf{B}_{\text{cM}} = \begin{bmatrix} \mathbf{0} \\ \mathbf{B}_{\text{u}} \end{bmatrix}, \mathbf{C}_{\text{cM}} = \begin{bmatrix} \mathbf{C}_{\text{M}} & \mathbf{0} \end{bmatrix} \quad (29)$$

$$\dot{\mathbf{x}}_{\text{cLH}} = \mathbf{A}_{\text{cLH}} \mathbf{x}_{\text{cLH}} + \mathbf{B}_{\text{cLH}} \mathbf{u}_{\text{ref}}, \quad \mathbf{y}_{\text{LH}} = \mathbf{C}_{\text{cLH}} \mathbf{x}_{\text{cLH}}$$

$$\mathbf{x}_{\text{cLH}} = \begin{bmatrix} \mathbf{x}_{\text{LH}} \\ \mathbf{x}_{\text{u}} \end{bmatrix}, \quad \mathbf{A}_{\text{cLH}} = \begin{bmatrix} \mathbf{A}_{\text{LH}} & \mathbf{B}_{\text{LH}} \mathbf{C}_{\text{u}} \\ \mathbf{0} & \mathbf{A}_{\text{u}} \end{bmatrix}$$

$$\mathbf{B}_{\text{cLH}} = \begin{bmatrix} \mathbf{0} \\ \mathbf{B}_{\text{u}} \end{bmatrix}, \quad \mathbf{C}_{\text{cLH}} = \begin{bmatrix} \mathbf{C}_{\text{LH}} & \mathbf{0} \end{bmatrix} \quad (30)$$

The subscripts c_M and c_{LH} denote the combined linear models for motion operating mode and load holding mode respectively.

The combined linear models from Eq. (29) and (30) may be expressed by the transfer function matrices Eq. (31) and (32), (Philips and Parr, 2011):

$$\begin{aligned} \mathbf{y}_M(s) &= \mathbf{G}_{cM}(s) \mathbf{u}_{ref}(s) \\ \mathbf{G}_{cM}(s) &= \mathbf{C}_{cM}(s\mathbf{I} - \mathbf{A}_{cM})^{-1} \mathbf{B}_{cM} \end{aligned} \quad (31)$$

$$\begin{aligned} \mathbf{y}_{\text{LH}}(s) &= \mathbf{G}_{\text{cLH}}(s) \mathbf{u}_{\text{ref}}(s) \\ \mathbf{G}_{\text{cLH}}(s) &= \mathbf{C}_{\text{cLH}}(s\mathbf{I} - \mathbf{A}_{\text{cLH}})^{-1} \mathbf{B}_{\text{cLH}} \end{aligned} \quad (32)$$

5.5 Coupling Analysis

To analyse the degree of cross couplings or interactions in the system, the concept of the Relative Gain Array (RGA) is used (Glad and Ljung, 2000). In a multi-variable system the RGA-number may be used to analyse "how close" the system is to being a diagonal system, equivalently to indicate the severity of the off-diagonal elements (cross couplings). If a system is diagonal, a diagonal controller (decentralised control), may yield satisfying results. As such a RGA analysis is often utilised to select proper input/output pairings.

In motion operating mode, three system outputs (x, p_A, p_B) are present. It is not possible to control all three outputs independently, meaning that the cross couplings may be investigated for the following three 2×2 sub-matrices of $\mathbf{G}_{cM}(s)$:

$$\mathbf{G}_{cM1}(s) = \begin{bmatrix} G_{\omega_1+x} & G_{\omega_2+x} \\ G_{\omega_1+p_A} & G_{\omega_2+p_A} \end{bmatrix} \quad (33)$$

$$\mathbf{G}_{cM2}(s) = \begin{bmatrix} G_{\omega_1+x} & G_{\omega_2+x} \\ G_{\omega_1+p_B} & G_{\omega_2+p_B} \end{bmatrix} \quad (34)$$

$$\mathbf{G}_{cM3}(s) = \begin{bmatrix} G_{\omega_1+p_A} & G_{\omega_2+p_A} \\ G_{\omega_1+p_B} & G_{\omega_2+p_B} \end{bmatrix} \quad (35)$$

The transfer function matrix $G_{cLH}(s)$ is a 2×2 matrix, meaning that only one input/output pairing must be investigated:

$$\mathbf{G}_{cLH}(s) = \begin{bmatrix} G_{\omega_1+p_{PA}} & G_{\omega_2+p_{PA}} \\ G_{\omega_1+p_{PB}} & G_{\omega_2+p_{PB}} \end{bmatrix} \quad (36)$$

The Relative Gain Array number ($\text{RGA}_{\#}$) is defined for diagonal input/output pairing in Eq. (37) and off-diagonal pairing in Eq. (38), (Skogestad and Postlethwaite, 2005):

$$\text{RGA}_{\#dia} = \sum_{k,j} \left| \underbrace{\mathbf{G}_i \times (\mathbf{G}_i^{-1})^T}_{\text{RGA Elements}} - \begin{bmatrix} 1 & 0 \\ 0 & 1 \end{bmatrix} \right| \quad (37)$$

$$\text{RGA}_{\#off} = \sum_{k,j} \left| \underbrace{\mathbf{G}_i \times (\mathbf{G}_i^{-1})^T}_{\text{RGA Elements}} - \begin{bmatrix} 0 & 1 \\ 1 & 0 \end{bmatrix} \right| \quad (38)$$

where $i = \{cM1, cM2, cM3, cLH\}$, and \times here denotes element-by-element multiplication or Hadamard product. k, j is the number of row and columns in the transfer function matrix. For further details on the RGA and RGA-number the reader may consult Skogestad and Postlethwaite (2005) or Glad and Ljung (2000). Here it suffices to note that in case of ideal decoupling utilizing a diagonal input/output pairing the $\text{RGA}_{\#dia}$ and $\text{RGA}_{\#off}$ attain the values 0 and 4 respectively for all frequencies, while in case of ideal

decoupling utilizing an off-diagonal input/output pairing the $\text{RGA}_{\#dia}$ and $\text{RGA}_{\#off}$ attain the values 4 and 0 respectively for all frequencies.

The evaluated RGA-numbers for load holding mode and motion operation mode are shown in Fig. 9 and 10. In load holding mode, both RGA-numbers are constantly equal to 2 in the considered frequency range. This means that a proper input/output pairing suited for a decentralised control strategy can not be identified. For motion operating mode, the three pairings in Fig. 10 are all seen to yield RGA-numbers highly above the desired values of 0 and 4 around 2 Hz, which is the eigenfrequency of the drive at this particular linearisation point. For frequencies below the eigenfrequency the RGA-numbers are closer to the desired values. As such the analysis suggests that if decentralised control strategy should be utilised, the closed loop bandwidths need to be well below the system eigenfrequency, and the input/output pairing should be made such that $\omega_{1,ref}$ controls the piston position, while $\omega_{2,ref}$ controls either chamber pressure A or B. However, because the RGA numbers are still rather far from the desired values of 0 and 4, it is found questionable whether using a decentralised control approach directly may yield satisfying results.

For both operation modes the coupling analysis reveals rather strong couplings which may render the performance using decentralised control unsatisfying. Therefore an alternative approach is desirable.

In Schmidt et al. (2017) a concept for decoupling the motion dynamics from the chamber pressure dynamics, by transforming the inputs and output states, are presented. For a pump-controlled system fundamentally different than the one proposed in the current paper, this is shown to effectively decouple the selected transformed/virtual states. As such a simple decentralised control structure may be used to control the transformed states, using conventional linear controllers. This strategy is adopted for the proposed system in the following section.

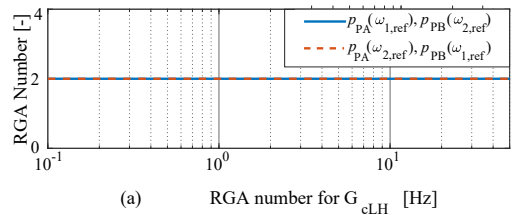


Figure 9: RGA numbers for diagonal and off-diagonal input/output pairings evaluated for the transfer function matrix $\mathbf{G}_{cLH}(s)$.

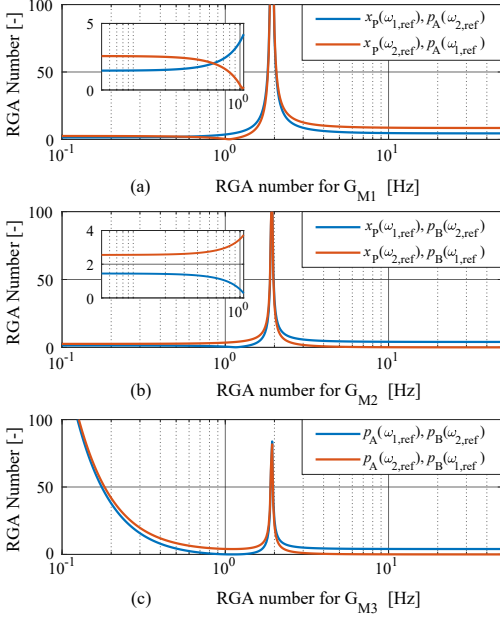


Figure 10: RGA numbers for diagonal and off-diagonal input/output pairings for $\mathbf{G}_{cM1}(s)$, $\mathbf{G}_{cM2}(s)$ and $\mathbf{G}_{cM3}(s)$.

6 Control Strategy

The overall control strategy is to derive a transformed system, where the evaluated RGA-numbers are significantly closer to the desired values of 0 and 4.

The physical input and output variables are transformed using the pre-compensator \mathbf{W}_1 and post-compensator \mathbf{W}_2 (Skogestad and Postlethwaite, 2005). Using these compensators or transformation matrices new virtual states may be defined as: $\tilde{\mathbf{y}} = \mathbf{W}_2 \mathbf{y}$, $\tilde{\mathbf{u}} = \mathbf{W}_1^{-1} \mathbf{u}_{\text{ref}}$.

If defining $\mathbf{G}_M(s)$, $\mathbf{G}_{LH}(s)$ and $\mathbf{G}_u(s)$ to be the transfer function formulation of the dynamic systems represented by Eq. (24), (27) and (28), the following may be written (omitting (s) for brevity), for the system operating in motion mode:

$$\mathbf{u}_M = \mathbf{G}_u \mathbf{u}_{\text{ref}}, \quad \mathbf{u}_{\text{ref}} = \mathbf{W}_{1M} \tilde{\mathbf{u}}_M \Rightarrow \mathbf{u}_M = \mathbf{G}_u \mathbf{W}_{1M} \tilde{\mathbf{u}}_M \quad (39)$$

$$\tilde{\mathbf{y}}_M = \mathbf{W}_{2M} \mathbf{y}_M, \quad \mathbf{y}_M = \mathbf{G}_M \mathbf{u}_M \Rightarrow \tilde{\mathbf{y}}_M = \mathbf{W}_{2M} \mathbf{G}_M \mathbf{u}_M \quad (40)$$

Substituting Eq. (39) into Eq. (40), gives the transformed system as:

$$\tilde{\mathbf{y}}_M = \mathbf{W}_{2M} \mathbf{G}_M \mathbf{G}_u \mathbf{W}_{1M} \tilde{\mathbf{u}}_M = \tilde{\mathbf{G}}_{cM} \tilde{\mathbf{u}}_M, \quad (41)$$

For load holding mode, the transformed system may be described in a similar manner as:

$$\tilde{\mathbf{y}}_{LH} = \mathbf{G}_{LH} \mathbf{G}_u \mathbf{W}_{1LH} \tilde{\mathbf{u}}_{LH} = \tilde{\mathbf{G}}_{cLH} \tilde{\mathbf{u}}_{LH}, \quad (42)$$

Please note, that for the transformed system operating in load holding mode, the output transformation matrix $\mathbf{W}_{2LH} = \mathbf{I}$.

The transformation matrices \mathbf{W}_{1M} , \mathbf{W}_{2M} and \mathbf{W}_{2LH} are chosen as static pre and post compensators. Due to the static gain of \mathbf{G}_u being unity, \mathbf{W}_{1M} , \mathbf{W}_{2M} and \mathbf{W}_{2LH} may be designed by only considering \mathbf{G}_M and \mathbf{G}_{LH} respectively.

6.1 Transformed System in Motion Operation Mode

The task of deriving suitable transformation matrices \mathbf{W}_{1M} , \mathbf{W}_{2M} and \mathbf{W}_{2LH} are divided into subtasks. First the output transformation in motion operation mode, \mathbf{W}_{2M} , is derived.

6.1.1 Output Transformation

Instead of considering the physical pressure states, Schmidt et al. (2017) found it desirable to formulate an output transformation (\mathbf{W}_{2LH}) considering more appropriate pressure states. These appropriate states were selected to be the piston position, the virtual load pressure P_L , and the level pressure P_H :

$$P_L = P_A - \alpha P_B, \quad P_H = P_A + H P_B, \quad (43)$$

The load pressure is proportional to the piston force and as such closely related to the cylinder motion dynamics. The task is to define H , such that the virtual level pressure is decoupled from the piston motion/load pressure. By inserting the non-linear pressure dynamics from Eq. (2) to (5), and assuming $\beta = \beta_A = \beta_B$, the virtual pressure dynamics may be expressed as:

$$\dot{P}_L = \dot{P}_A - \alpha \dot{P}_B \quad (44)$$

$$= \frac{\beta}{\rho V_A} (\rho(Q_{PA1} + Q_{PA2}) + \alpha(Q_{PB} - A_A \dot{X}_P(\alpha^2 + \rho)))$$

$$\dot{P}_H = \dot{P}_A + H \dot{P}_B + \dot{H} P_B \quad (45)$$

$$= \frac{\beta}{\rho V_A} \left(\rho(Q_{PA1} + Q_{PA2}) - H Q_{PB} + \underbrace{A_A \dot{X}_P(\alpha H - \rho)}_{\Psi} \right) + \frac{\dot{H}}{H + \alpha} (P_H - P_L)$$

The assumption of equal bulk modulus in the two control volumes is justified in the fact, that in motion operation mode both chamber pressures are kept at an elevated level (e.g. 30 bar).

The term denoted Ψ in Eq. (45) represents a direct coupling between the piston velocity and the pressure gradient. To decouple the level pressure from the piston motion H is chosen as ρ/α , yielding $\Psi = 0$

The last term in Eq. (45) contains \dot{H} , which by the selection of H in fact creates another \dot{X}_P dependent term. The derivative of H is given as:

$$\dot{H} = \frac{-\dot{X}_P A_A (\alpha + \rho)}{V_A \alpha} \quad (46)$$

By the definition of H , the P_H dynamics is given by:

$$\begin{aligned} \dot{P}_H = & \frac{\beta}{\rho V_A} (\rho(Q_{PA1} + Q_{PA2}) - H Q_{PB}) \\ & - \dot{X}_P \frac{A_A}{V_A} \frac{H+1}{H+\alpha} (P_H - P_L) \end{aligned} \quad (47)$$

Whether the last term in Eq. (47) yields severe cross coupling is not immediately evident. This has to be evaluated when the cross-couplings are analysed for the transformed system in section 6.3. For this purpose a linear representation of the transformed system is required.

The linear virtual pressure dynamics may be obtained by inserting the linearised pump flows and expressing ρ as a function of H and α :

$$\begin{aligned} \dot{p}_L = & \frac{\beta_0}{V_{A0} H_0} (\omega_1 D_1 (H_0 + 1) + \omega_2 D_2 H_0 \\ & - \dot{x}_P A_A (H_0 + \alpha) - \frac{H_0}{H_0 + \alpha} (C_5 p_H - C_6 p_L)) \end{aligned} \quad (48)$$

$$\begin{aligned} \dot{p}_H = & \frac{\beta_0}{V_{A0}} \left(\omega_1 D_1 + \omega_2 D_2 - \frac{\omega_1 D_1}{\alpha} \right. \\ & \left. - \frac{(C_1 + C_2) p_H + (C_3 - C_2) p_L + C_4 \dot{x}_P}{\alpha + H_0} \right) \end{aligned} \quad (49)$$

$$C_1 = \left(2\alpha - 2 + \frac{2}{\alpha} \right) K_1 + \alpha K_2$$

$$C_2 = \frac{\dot{x}_{P0} A_A (H_0 + 1)}{\beta}$$

$$C_3 = \left(2H_0 + 1 - \frac{H_0 + 2}{\alpha} \right) K_1 + H_0 K_2$$

$$C_4 = \frac{A_A (H_0 + 1) (p_{H0} - p_{L0})}{\beta}, \quad C_5 = -\frac{\alpha}{H_0} C_3$$

$$C_6 = \left(2H_0 + 2 + \frac{2}{H_0} \right) K_1 + H_0 K_2$$

The output transformation matrix W_{2M} may be established as:

$$\tilde{\mathbf{y}}_M = \mathbf{W}_{2M} \mathbf{y}_M, \quad \tilde{\mathbf{y}}_M = \begin{bmatrix} x_P \\ p_L \\ p_H \end{bmatrix}, \quad \mathbf{W}_{2M} = \begin{bmatrix} 1 & 0 & 0 \\ 0 & 1 & -\alpha \\ 0 & 1 & H_0 \end{bmatrix}$$

6.1.2 Input Transformation

Virtual inputs, q_H q_L are defined such that the distribution of the motor speeds ω_1 and ω_2 is not directly present in the pressure dynamics. Based on the linear level and load pressure dynamics in Eq. (48) and Eq. (49):

$$q_L = \omega_1 D_1 (H_0 + 1) + \omega_2 D_2 H_0 \quad (50)$$

$$q_H = \omega_1 D_1 + \omega_2 D_2 - \frac{\omega_1 D_1}{\alpha} \quad (51)$$

This leads to the input transformation matrix, \mathbf{W}_{1M} :

$$\begin{aligned} \tilde{\mathbf{u}}_M &= \mathbf{W}_{1M}^{-1} \mathbf{u}_M \\ \tilde{\mathbf{u}}_M &= [q_L \quad q_H]^T, \quad \mathbf{u}_M = [\omega_1 \quad \omega_2]^T \\ \mathbf{W}_{1M}^{-1} &= \begin{bmatrix} D_1 (H_0 + 1) & D_2 H_0 \\ (D_1 - \frac{D_1}{\alpha}) & D_2 \end{bmatrix} \\ \mathbf{W}_{1M} &= \begin{bmatrix} \frac{\alpha}{D_1 (H_0 + \alpha)} & -\frac{\alpha H_0}{D_1 (H_0 + \alpha)} \\ \frac{1 - \alpha}{(H_0 + \alpha) D_2} & \frac{H_0 \alpha + \alpha}{D_2 (H_0 + \alpha)} \end{bmatrix} \end{aligned}$$

6.2 Transformed System in Load Holding Mode

In load holding mode only an input transformation matrix, \mathbf{W}_{1LH} is derived. This is done by defining virtual inputs directly from the linear pressure dynamics of p_{PA} and p_{PB} in Eq. (25) and (26), such that the distribution of the individual motor speeds is not present in the pressure dynamics:

$$q_A = D_1 \omega_1 + D_2 \omega_2 \quad (52)$$

$$q_B = -D_1 \omega_1 \quad (53)$$

$$\begin{aligned} \tilde{\mathbf{u}}_{LH} &= \mathbf{W}_{1LH}^{-1} \mathbf{u}_{LH} \\ \tilde{\mathbf{u}}_{LH} &= [q_A \quad q_B]^T, \quad \mathbf{u}_{LH} = [\omega_1 \quad \omega_2]^T \\ \mathbf{W}_{1LH} &= \begin{bmatrix} 0 & -\frac{1}{D_1} \\ \frac{1}{D_2} & \frac{1}{D_2} \end{bmatrix} \end{aligned} \quad (54)$$

6.3 Coupling Analysis of Transformed Systems

To evaluate the cross couplings in the transformed systems, linear state space representations, without actuator dynamics may be established as:

$$\begin{aligned} \dot{\mathbf{x}}_{T,M} &= \mathbf{A}_{T,M} \mathbf{x}_{T,M} + \mathbf{B}_{T,M} \mathbf{u}_{T,M}, \quad \mathbf{y}_{T,M} = \mathbf{C}_{T,M} \mathbf{x}_{T,M} \\ \mathbf{x}_{T,M} &= [x_P \quad \dot{x}_P \quad p_L \quad p_H]^T, \quad \mathbf{u}_{T,M} = [q_L \quad q_H]^T \\ C_7 &= \frac{\beta_0}{V_{A0} (H_0 + \alpha)} \end{aligned}$$

$$\mathbf{A}_{T,M} = \begin{bmatrix} 0 & 1 & 0 & 0 \\ 0 & -\frac{B_v}{M_{eq0}} & \frac{A_A}{M_{eq0}} & 0 \\ 0 & -\frac{\beta_0 A_A (H_0 + \alpha)}{V_{A0} H_0} & -C_6 C_7 & C_5 C_7 \\ 0 & -C_4 C_7 & -(C_3 - C_2) C_7 & -(C_1 + C_2) C_7 \end{bmatrix}$$

$$\mathbf{B}_{T,M} = \begin{bmatrix} 0 & 0 \\ 0 & 0 \\ \frac{\beta_0}{H_0 V_{A0}} & 0 \\ 0 & \frac{\beta_0}{V_{A0}} \end{bmatrix} \quad \mathbf{C}_{T,M} = \begin{bmatrix} 1 & 0 & 0 & 0 \\ 0 & 0 & 0 & 1 \end{bmatrix}$$

The subscripts T,M denote the transformed system in motion operating mode. From the above a 2×2 transfer function matrix may be derived, and used to evaluate cross couplings and for controller design.

The transformed system in load holding mode is denoted with the subscript T,LH , and is shown as a state space representation below:

$$\begin{aligned} \dot{\mathbf{x}}_{T,LH} &= \mathbf{A}_{T,LH} \mathbf{x}_{T,LH} + \mathbf{B}_{T,LH} \mathbf{u}_{T,LH}, \\ \mathbf{y}_{T,LH} &= \mathbf{C}_{T,LH} \mathbf{x}_{T,LH} \\ \mathbf{x}_{T,LH} &= [p_{PA} \ p_{PB}]^T, \quad \mathbf{u}_{T,LH} = [q_{PA} \ q_{PB}]^T \\ \mathbf{A}_{T,LH} &= \begin{bmatrix} -\frac{\beta_0 (2K_1 + K_2)}{V_{A0}} & \frac{\beta_0 K_1}{V_{A0}} \\ \frac{\beta_0 K_1}{\rho_0 V_{A0}} & -2 \frac{\beta_0 K_1}{\rho_0 V_{A0}} \end{bmatrix} \\ \mathbf{B}_{T,LH} &= \begin{bmatrix} \frac{\beta_0}{V_{A0}} & 0 \\ 0 & \frac{\beta_0}{H_0 \alpha V_{A0}} \end{bmatrix} \quad \mathbf{C}_{T,LH} = \begin{bmatrix} 1 & 0 \\ 0 & 1 \end{bmatrix} \end{aligned}$$

A 2×2 transfer function matrix may be derived to evaluate cross couplings and for control design purposes. By including the actuator dynamics (Eq. (28)),

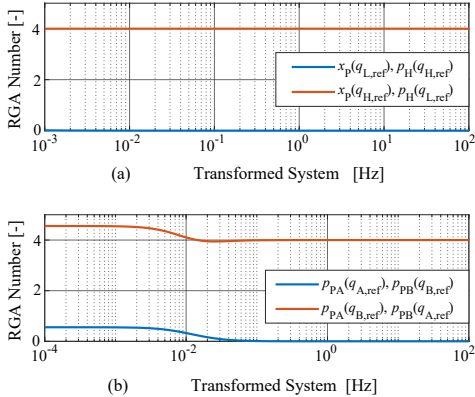


Figure 11: (a) RGA-numbers for the transformed system in motion operating mode. (b) RGA-numbers for the system operated in load holding mode.

the RGA numbers are evaluated for the transformed systems and shown in Fig. 11.

For the transformed system in motion operating mode a close to ideal decoupling in the entire frequency range may be observed. By varying the linearization point, and updating H accordingly, it is found that the RGA analysis yields results equivalent to the RGA-numbers shown in Fig. 11. This means that the proposed decoupling method, is independent of the operating point, if H is updated. The analysis shows that the transfer function matrix of the transformed system is close to diagonal, independently of operating point, and may thus be controlled by a diagonal controller (decentralised control), by neglecting the system cross-couplings (off-diagonal elements). The piston position is to be controlled by $q_{L,ref}$ while p_H is paired with $q_{H,ref}$.

For the transformed system in load holding mode, utilizing the input transformation matrix \mathbf{W}_{1LH} , results in a significantly more decoupled system compared to the original system (Fig. 9). However, at low frequencies the RGA-numbers are not indicating an ideally decoupled system. All-together by Fig. 11b it is still easy to find that p_{PA} must be paired with $q_{A,ref}$ and p_{PB} with $q_{B,ref}$. For now this is done by accepting the minor cross couplings observed at low frequencies.

To sum up, it is assessed reasonable to control the transformed system in both motion operating mode and load holding mode using a decentralised control approach. The control strategy is summed up in Fig. 12. Note that H is updated during operation, to obtain proper decoupling as the cylinder moves (H changes). Also note that for the position control loop, velocity feedforward and pressure feedback have been included. The velocity feedforward gain is H dependent (see. section 7.2), effectively yielding a feedback of the piston position. The consequence of this may be included in a linear analysis similar to the one presented in section 6.

7 Controller Design

From Fig. 12 seven blocks need to be designed for the system to be operational. These include: level pressure reference generator, level pressure controller, pressure feedback filter, position controller, velocity feedforward gain, P_{PA} controller and finally P_{PB} controller.

Generally the controller design procedure is approached in a simple manner in this paper, as the main purpose is to illustrate the basic working principle of the drive, and the decoupling control strategy. The design procedure of the linear controllers follows the same pattern. First the most conservative design point is chosen by sweeping through different linearisation points and considering relative stability

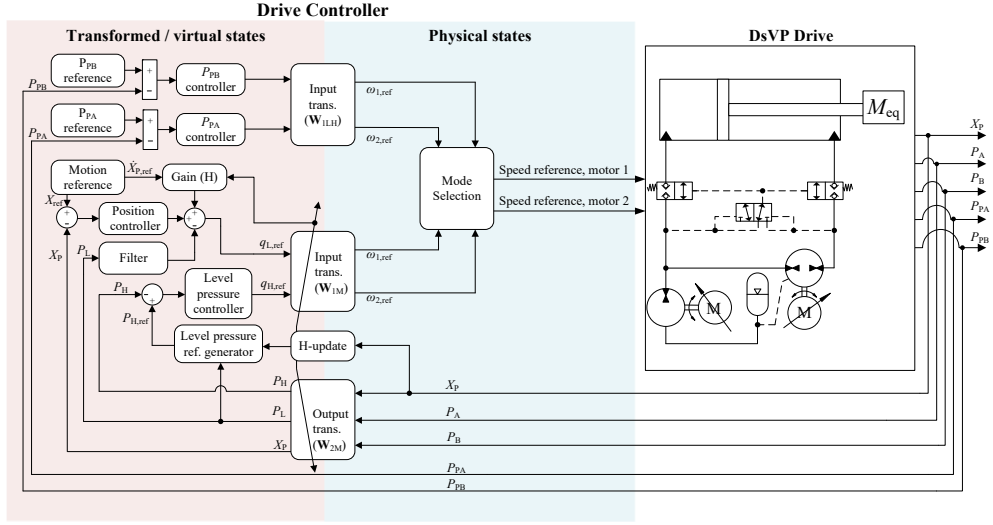


Figure 12: Schematic of the control structure for the proposed system.

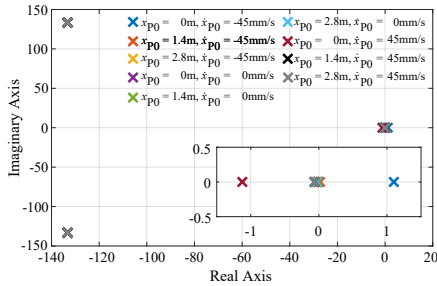
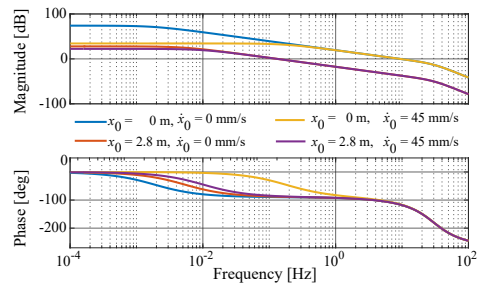
margins. Even though this procedure ensures stability in the entire operating range, it may also yield unsatisfying performance due to large parameter variations (e.g. inertia) for the considered crane. For improved performance it may be beneficial to consider control structures, that include these parameters variations, such as gain scheduling or adaptive controllers. When a design point is chosen, linear controllers are designed based on desired stability margins.

7.1 Level Pressure Controller

The design of the level pressure controller is based on the transfer function $\frac{p_H}{q_{H,ref}}$, assuming that the cross

coupling from $\frac{p_H}{q_{L,ref}}$ is negligible. The pressure in the low pressure chamber is defined as 30 bar, while the pressure in the load-carrying chamber is defined based on the crane load at a specific piston position.

By varying the piston position in the entire stroke length (0m to 2.8m) and the piston speed between minimum and maximum velocity (-45mm/s to 45 mm/s), the position of the open loop poles as a function of different linearisation points are found. This is illustrated in Fig. 13, where it is found that the placement of the pole close to origin is of special interest. It is found that the combination of large retraction velocities and small piston strokes yield this pole to be placed in the right half of the complex plane.

Figure 13: Variation of open loop poles for the transfer function $\frac{p_H}{q_{H,ref}}$.Figure 14: Open loop uncompensated Bode plot for the transfer function $\frac{p_H}{q_{H,ref}}$.

By investigating the root locus of the system at 0m and -45 mm/s, it is evident that a P-controller is able to stabilize the closed loop system. Utilizing the Routh-Hurwitz stability criterion (Philips and Parr, 2011), it is found that the controller gain must be chosen between $0.02 \frac{\text{L}}{\text{min Bar}} < K_p < 4.4 \frac{\text{L}}{\text{min Bar}}$.

To choose an appropriate controller gain within this range, the frequency response for different linearisation points (excluding those yielding a non-minimum phase system) are given in Fig. 14. The lowest relative stability margin is occurring at the fully retracted position, meaning that this is chosen as a conservative design point. A proportional gain of $K_P = 2.3 \frac{\text{L}}{\text{min Bar}}$ is selected to yield a gain margin of 6 dB and a phase margin of 30 deg.

7.1.1 Level Pressure Reference Generator

The level pressure control loop controls a virtual pressure state. For this to be sensible also for the physical states, an appropriate level pressure reference must be generated. It is desired that neither P_A nor P_B decreases below a set pressure p_{set} , which is set to 30 bar. Which of the physical pressures P_A or P_B is to be controlled depends on the force working on the piston, i.e. the pressure in the load carrying-chamber should not be controlled directly. Therefore a load pressure dependent switching condition, $p_{L,s}$, can be defined as the situation when both chamber pressures equal the set pressure, (Schmidt et al., 2017):

$$p_A = p_B = p_{\text{set}} \Rightarrow p_{L,s} = p_{\text{set}} (1 - \alpha) \quad (55)$$

Assuming the lower chamber pressure to equal p_{set} the chamber pressures may be described by:

$$p_L > p_{L,s} \Rightarrow p_B = p_{\text{set}}, p_A = p_L + \alpha p_{\text{set}} \quad (56)$$

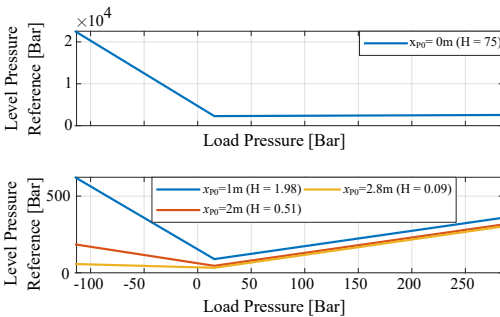


Figure 15: Examples of level pressure reference values as a function of load pressure evaluated using Eq. (58) for different piston positions.

$$p_L \leq p_{L,s} \Rightarrow p_A = p_{\text{set}}, p_B = \frac{p_{\text{set}} - p_L}{\alpha} \quad (57)$$

From the definition of p_H in Eq. (43) a load pressure reference may be calculated as:

$$p_{H,\text{ref}} = \begin{cases} p_L + (\alpha + H)p_{\text{set}} & \text{for } p_L > p_{L,s} \\ p_{\text{set}} + H \left(\frac{p_{\text{set}} - p_L}{\alpha} \right) & \text{for } p_L \leq p_{L,s} \end{cases} \quad (58)$$

The level pressure reference is thus a function of the load and set pressure as well as H . Examples of the load pressure reference values are shown in Fig. 15.

By controlling the pressure in the low pressure chamber using a virtual level pressure instead of the chamber pressure directly, it is not necessary to define which physical pressure to control. This is taken care of by the construction of the level pressure. This ensures smooth transition between operating quadrants (e.g direction of load force).

7.2 Motion Controller

The design of the motion controller is based on the transfer function $\frac{x}{q_{L,\text{ref}}}$. Similarly to the design of the level pressure controller, the linearisation point is varied to identify a conservative design point, using the open loop frequency response. It is found that the influence of varying the piston speed is insignificant, meaning that it suffices to vary the piston position. In Fig. 16 the frequency responses at different piston positions are shown.

It is seen that the relative stability margins are smallest at the linearisation point, yielding the lowest eigenfrequency. Due to the increased inertia load for increasing piston position, the design point is selected at the fully extended position.

The system is observed to be poorly damped. To increase the damping of the system, the load pressure

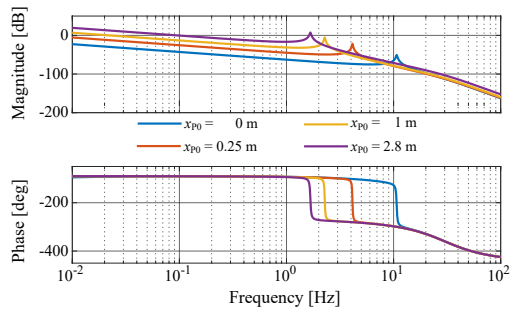


Figure 16: Open loop frequency response at different linearisation points for the transfer function $x_p/q_{L,\text{ref}}$. M_{eq} is included.

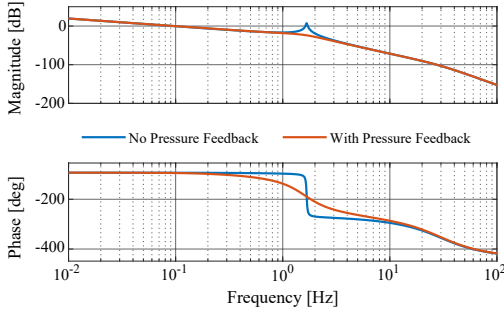


Figure 17: Comparison of frequency responses for the transfer function $x_p/q_{L,ref}$ (blue) and $x_p/q_{L,ref}^*$ (red).

is fed back through a high pass filter (Pedersen and Andersen, 2018):

$$q_{L,ref} = q_{L,ref}^* - p_L G_{c,PF}(s) \quad (59)$$

$$G_{c,PF}(s) = K_{PF} \frac{s}{s + \omega_{PF}} \quad (60)$$

The pole of the high pass filter, $G_{c,PF}$, is placed one decade lower than the lowest system eigenfrequency and K_{PF} has been adjusted to yield a damping ratio of approximately 0.5. To avoid propagation of measurement noise, a low pass filter may be added in the pressure feedback path. The cut-off frequency of this filter, should be selected above the system eigenfrequency and below the frequency of the measurement noise. This is not considered in the current simulation study, as measurement noise has not been included. The effect of including the pressure feedback is clearly illustrated in Fig. 17, where the damping ratio of the system is seen to be significantly increased.

Based on the transfer function $\frac{x_p}{q_{L,ref}^*}$, a PI controller has been designed to yield (minimum) relative stability margins of 6 dB and 45 deg for the considered conservative linearisation point:

$$G_{c,M}(s) = \frac{K_P s + K_I}{s} \quad (61)$$

The controller coefficients are found to $K_P = 6.3 \frac{L}{\min \text{ mm}}$, $K_I = 6.1 \frac{L}{\min \text{ mm s}}$, placing the controller zero approximately one decade lower than the lowest system eigenfrequency.

To improve the position tracking ability, velocity feedforward as illustrated in Fig. 12 is implemented. The feedforward flow reference $q_{L,FF}$, is calculated by combining Eq. (48) and (50) and setting the pressure

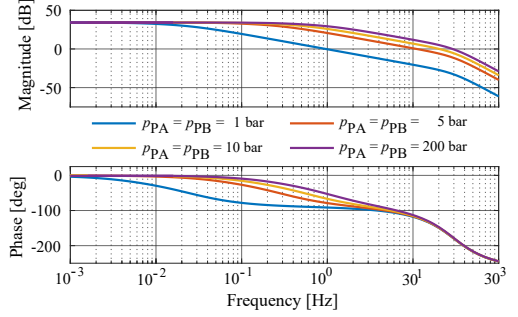


Figure 18: Open loop frequency responses for $\frac{p_{PA}}{q_{A,ref}}$ at different linearisation points.

gradient $\dot{p}_L = 0$:

$$q_{L,FF} = A_A(H + \alpha) \dot{X}_{P,ref} \quad (62)$$

7.3 Pressure Controller

The pressure controllers when operating in load holding mode are chosen as PI controllers (Eq. (61)), because it is crucial that no steady state pressure error is present during transition between operation modes, to avoid load dropping.

The controllers are designed based on the transfer functions $\frac{p_{PA}}{q_{A,ref}}$ and $\frac{p_{PB}}{q_{B,ref}}$ respectively. In Fig. 18 the open loop frequency response for the former is shown at different linearisation points (varying line pressures). It is seen that the conservatively chosen design point must be selected as the linearisation point with the largest line pressures. The same may be shown for $\frac{p_{PB}}{q_{B,ref}}$, which is left out for brevity.

Based on the transfer functions evaluated at the maximum allowed system pressure, PI controllers have been designed yielding stability margins of 8 dB and 40 deg for both pressure control loops.

8 Simulation Results

The performance of the proposed DvSP system and the derived control structure is evaluated by solving the non-linear dynamic equations from section 4 and the derived control structure. For this purpose a MatLAB/Simulink environment has been used in this study.

8.1 Motion Operating Mode

In Fig. 19 the performance of the system performing the motion trajectory in section 3 is presented. Note

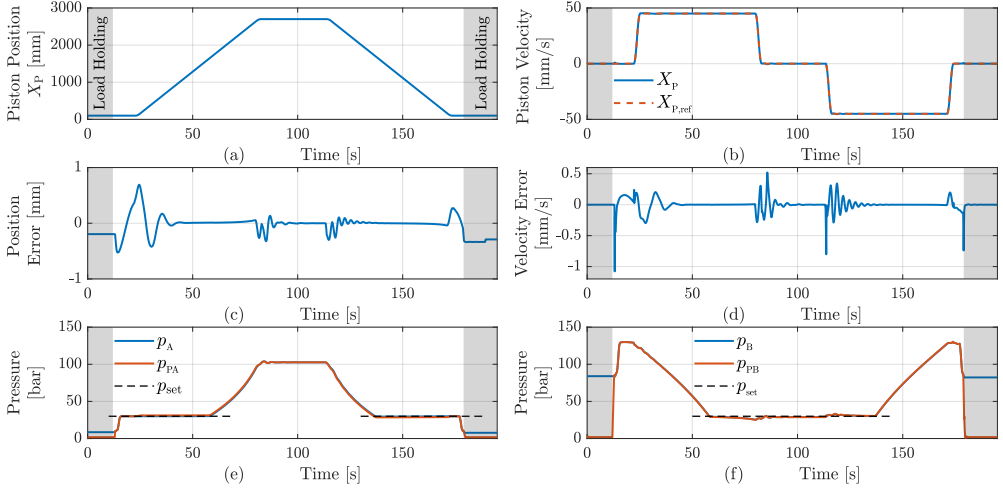


Figure 19: Performance of the proposed DvSP system performing the trajectory presented in section 3. The grey areas indicate that the system is operated in load holding mode, while being controlled in motion operation mode between these. (a) Piston position; (b) Piston velocity and reference; (c) Piston position error; (d) Piston velocity error; (e) Pressure in the piston chamber and adjacent transmission line; (f) Pressure in the rod chamber and adjacent transmission line.

that in the first and last approximately 20 s in Fig. 19 (grey areas), the system is controlled in load holding mode, while it is controlled in motion operating between these.

In Fig. 19a to Fig. 19d the motion tracking performance is visualised. Generally, rather accurate motion tracking is present in the entire trajectory, where the maximum position error is kept well within $\pm 1\text{mm}$. The largest position/velocity errors are present during the acceleration phase, where low frequency and amplitude velocity oscillations are also seen to be present. These oscillations are found to originate from a swinging payload. The oscillations are suppressed at a slow rate ($\approx 20\text{s}$), meaning that a room for improvement in terms of re-designing the active oscillation damping is present.

Regarding the level pressure control, it is found that the low pressure chamber is successfully controlled to the vicinity of the set pressure (30 bar). Deviations of a few bar from the set pressure is observed, especially as the piston position is increased. This is related to the conservative controller design approach leading to the level pressure being designed for the fully retracted position. The level pressure control is of secondary importance compared to the motion performance and therefore the small pressure deviations are not a concern. Most importantly, the level pressure control en-

sures that the load holding valves remains fully open as desired. Also note that even at full speed the differences between pressures P_A , P_{PA} and P_B , P_{PB} respectively are small, i.e. the pressure drops across the load holding valves in the fully open position are small. This is essential for energy-efficient operation.

A last thing to note from Fig. 19 is that the concept of controlling the level pressure, yields a smooth transition between operation quadrants.

8.2 Load Holding Mode and Mode Transition

In load holding mode two important operations are required:

1. Elevate the transmission line pressures to equal the chamber pressures during transition between load holding mode and mode operation mode. This is needed to avoid load drop and non smooth transition.
2. Reduce energy consumption when load is stationary.

Fig. 20 is a zoomed-in version of Fig. 19, where the transition between the two operation modes is highlighted.

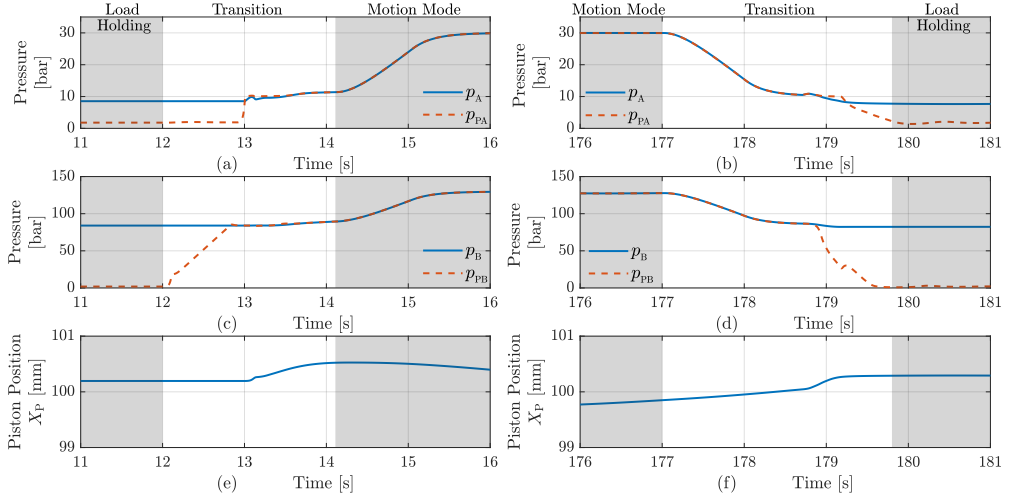


Figure 20: Transition between operation modes. (a) P_A and P_{PA} in transition between load holding and motion operating mode; (b) P_A and P_{PA} in transition between motion operating and load holding mode; (c) P_B and P_{PB} in transition between load holding and motion operating mode; (d) P_B and P_{PB} in transition between motion operating and load holding mode; (e) Piston position in transition between load holding and motion operating mode; (f) Piston position in transition between motion operating and load holding mode.

In Fig. 20a, 20c and 20e the focus is on the transition between load holding mode to motion operation mode. During transition (from 12 s to 14 s), the pressure in the transmission line adjacent to the load-carrying chamber, in this case P_{PB} , is controlled to equal the pressure in the cylinder chamber, P_B . The load holding valves are still fully closed. When P_{PB} has settled at P_B , P_A is increased in order to open the load holding valves. When the pressures P_A and P_{PA} are slightly larger than the cracking pressure (≈ 1 bar) of the load holding valves, the operating mode is changed to motion mode. In motion mode the lowest chamber pressure is further increased, to a value well above the full open pressure of the load holding valves. In Fig. 20e it may be seen that the piston position is steady until the lowest pressure has reached the cracking pressure of the load holding valve. During the transition period, the piston position is uncontrolled, leading to a slight drift in piston position. This is corrected as the system enters motion operation mode.

In Fig. 20b, 20d and 20f the focus is on the transition between motion operating mode and load holding mode. In the transition period (177s to 180 s) the pressure in the low pressure chamber is reduced to the cracking pressure of the load holding valves. When this pressure is reached, the system is operated in load

holding mode and the transmission lines pressures are actively controlled to equal the accumulator pressure in order to reduce the energy consumption. In Fig. 20f it is observed that during the transition period, the piston position drifts approximately 0.5 mm. Because the cylinder is locked in load holding mode, this cannot be corrected. The position drift of 0.5 mm results in

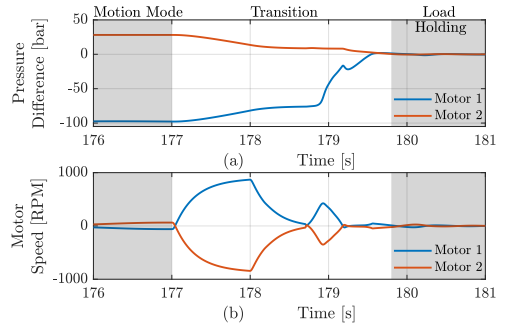


Figure 21: (a) Pressure difference across pumps during mode transition and in load holding mode. (b) Shaft speeds during mode transition and in load holding mode.

a movement of up 5.2 mm of the tool-center, for the crane considered in this investigation. To reduce this, further investigation into handling this mode transition is needed.

The active utilization of the load holding mode to decrease energy consumption, i.e. the load holding valves are not only a safety measure, requires that the pump torque is reduced in load holding mode. This is done by setting the reference pressures for the transmission line control to equal the current accumulator pressure. As illustrated by Fig. 21, this reduces the pressure difference across both pumps to ≈ 0 bar, reducing shaft torques, in turn reducing current losses in the motor. From Fig. 21 the shaft speed is seen to decrease to 0 RPM, when the load is carried by the load holding valves, reducing the shaft power to 0 W.

9 Conclusion

In this paper a self-contained pump-controlled cylinder drive with a pressure controlled hydraulic lock is proposed. A simple hydraulic architecture based on two variable-speed electrical motors each connected to a fixed-displacement hydraulic pump, with an innovative load holding sub-circuit is presented. The functionality of the load holding sub-circuit requires that the lowest cylinder chamber pressure is controlled accurately, without affecting the motion performance of the cylinder piston, which is found non-trivial due to severe cross couplings in the system. Therefore a control strategy aiming on state decoupling is derived based on input/output transformations. An analysis shows that the cross couplings in the transformed system are significantly decreased, and a simple decentralised control strategy is adopted for controlling the transformed system. Simulation results confirm the applicability of the drive architecture and the proposed decoupling strategy. Good position tracking performance and pressure control as well as smooth transition between operation quadrants are demonstrated. Furthermore, a close to bump-less transition between load holding and motion mode are seen, showing that a potential for utilising the load holding functionality actively to reduce energy consumption when the load is to be kept stationary, is present. The simulation results suggest a potential for future load carrying applications to be based on the proposed concept.

Acknowledgments

The research in this paper has received funding from The Research Council of Norway, SFI Offshore Mechatronics, project number 237896/O30.

Key Parameter List

	Description	Value
α	Cylinder area ratio	0.48 [-]
β_F	Bulk modulus of pure fluid	15000 bar
ϵ	Volumetric air content in oil	0.75 %
γ	Switching parameter	5000 [-]
κ	Poly-tropic constant	1.4 [-]
ω_n	Bandwidth, el. motor	30 Hz
ζ	Damping ratio, el. motor	0.7 [-]
A_A	Piston Area	491 cm ²
A_B	Rod Area	236 cm ²
B_v	Viscous friction constant	40000 $\frac{Ns}{m}$
D_1	Geometric displacement	26 $\frac{cm^3}{rev}$
D_2	Geometric displacement	28 $\frac{cm^3}{rev}$
F_C	Coulomb friction constant	5000 N
K_1	Leakage coefficient, pump 1	5.4 $\frac{mL}{minbar}$
K_2	Leakage coefficient, pump 2	11.4 $\frac{mL}{minbar}$
K_{Qv}	Flow gain, LH ₁ and LH ₂	127 $\frac{L}{min\sqrt{bar}}$
K_{Qsv}	Flow gain, shuttle valve	0.3 $\frac{L}{min\sqrt{bar}}$
m	Bulk modulus gradient	11.4 [-]
P_0	Accumulator precharge pres.	1.1 bar
P_{CR}	Cracking pressure	10 bar
P_{OP}	Full open pressure	20 bar
V_{0A}	Initial volume	2.0 L
V_{0B}	Initial volume	72.3 L
V_{PA}	Line PA-volume	0.5 L
V_{PB}	Line PB-volume	0.5 L
V_{PI}	Pilot Line volume	0.1 L
V_{ACC}	Accumulator volume	288.0 L
V_0	Accumulator line volume	1.0 L

References

- Brahmer, B. CLDP - Hybrid Drive using Servo Pump in Closed Loop. In *Proceedings of the 8th International Fluid Power Conference, Dresden, Germany, March 26-28*. pages 93–102, 2012.
- Çalkan, H., Balkan, T., and Platin, B. E. A Complete Analysis and a Novel Solution for Instability in Pump Controlled Asymmetric Actuators. *Journal of Dynamic Systems, Measurement, and Control*, 2015. 137(9). doi:[10.1115/1.4030544](https://doi.org/10.1115/1.4030544).

- Costa, G. K. and Sepehri, N. Four-Quadrant Analysis and System Design for Single-Rod Hydrostatic Actuators. *Journal of Dynamic Systems, Measurement, and Control*, 2018. 141(2). doi:10.1115/1.4041382.
- Dantlgraber, J. Hydraulic System for a Differential Piston Type Cylinder. 1993. URL <https://patentimages.storage.googleapis.com/b1/da/49/ce4d84ab1ec11c/US5179836.pdf>. United States Patent, Patent Number: 5179836, Company: Mannesmann Rexroth GmbH.
- Donkov, V., Andersen, T. O., and Pedersen, H. C. Applying Digital Hydraulic Technology on a Knuckle Boom Crane Applying Digital Hydraulic Technology on a Knuckle Boom Crane. *The Ninth Workshop on Digital Fluid Power, September 7-8, 2017, Aalborg, Denmark*, 2017.
- Donkov, V. H., Andersen, T. O., Pedersen, H. C., and Ebbesen, M. K. Application of Model Predictive Control in Discrete Displacement Cylinders to Drive a Knuckle Boom Crane. *Global Fluid Power Society PhD Symposium*, 2018. doi:10.1109/GFPS.2018.8472363.
- Feuser, A., Dantlgraber, J., Spath, D., and Wilke, O. Servopumpenantriebe für Differentialzylinder. *Ölhydraulik und Pneumatik*, 1995. 39:540–544.
- Glad, T. and Ljung, L. *Control Theory - Multivariable and Nonlinear Methods*. Taylor & Francis, 2000.
- Gøystil, P., Padovani, D., and Hansen, M. R. On the Energy Efficiency of Dual Prime Mover Pump-Controlled Hydraulic Cylinders. In *Proceedings of the ASME/BATH 2019 Symposium on Fluid Power and Motion Control, Sarasota, Florida, USA, October 7-9*. 2019.
- Gøystil, P. H., Padovani, D., and Hansen, M. R. A novel solution for the elimination of mode switching in pump-controlled single-rod cylinders. *Actuators*, 2020. 9(1). doi:10.3390/act9010020.
- Grønkær, N., Hansen, K. V., Johansen, P., and Schmidt, L. Tribotronics in Electro-Hydraulic Actuator Technology: Improving Durability by Control. In *Proceedings of ASME/BATH 2020 Symposium on Fluid Power and Motion Control*. pages 1–9, 2020.
- Hagen, D., Padovani, D., and Ebbesen, M. K. Study of a Self-Contained Electro-Hydraulic Cylinder Drive. *Global Fluid Power Society PhD Symposium*, 2018. pages 1–7. doi:10.1109/GFPS.2018.8472360.
- Hagen, D., Pawlus, W., Ebbesen, M. K., and Andersen, T. O. Feasibility Study of Electromechanical Cylinder Drivetrain for Offshore Mechatronic Systems. *Modeling, Identification and Control: A Norwegian Research Bulletin*, 2017. 38(2):59–77. URL <http://www.mic-journal.no/ABS/MIC-2017-2-2.asp>, doi:10.4173/mic.2017.2.2.
- Hedegaard Hansen, A., F Asmussen, M., and Bech, M. M. Energy optimal tracking control with discrete fluid power systems using model predictive control. In *Proceedings of the Ninth Workshop on Digital Fluid Power, Aalborg, Denmark, September 7-8*. 2017.
- Hedegaard Hansen, A., F Asmussen, M., and Bech, M. M. Model Predictive Control of a Wave Energy Converter with Discrete Fluid Power Power Take-Off System. *Energies*, 2018. 11(3):635. doi:10.3390/en11030635.
- Hedegaard Hansen, A. and Pedersen, H. C. Optimal configuration of a discrete fluid power force system utilised in the PTO for WECs. *Ocean Engineering*, 2016. 117:88–98. doi:10.1016/j.oceaneng.2016.03.032.
- Helduser, S. Electric-hydrostatic drive an innovative energy-saving power and motion control system. *Proceedings of the Institution of Mechanical Engineers, Part I: Journal of Systems and Control Engineering*, 1999. 213(5):427–437. URL <http://journals.sagepub.com/doi/10.1243/0959651991540250>, doi:10.1243/0959651991540250.
- Hewett, A. J. Hydraulic Circuit Flow Control. 1994. United States Patent, Patent Number: 5329767.
- Imam, A., Rafiq, M., Jalayeri, E., and Sepehri, N. Design, Implementation and Evaluation of a Pump-Controlled Circuit for Single Rod Actuators. *Actuators*, 2017. 6. doi:10.3390/act6010010.
- Jalayeri, E., Imam, A., Tomas, Z., and Sepehri, N. A throttle-less single-rod hydraulic cylinder positioning system: Design and experimental evaluation. *Advances in Mechanical Engineering*, 2015. 7(5). doi:10.1177/1687814015583249.
- Ketelsen, S., Andersen, T. O., Ebbesen, M. K., and Schmidt, L. Mass Estimation of Self-contained Linear Electro-Hydraulic Actuators and Evaluation of the Influence on Payload Capacity of a Knuckle Boom Crane. In *Proceedings of the ASME/BATH 2019 Symposium on Fluid Power and Motion Control, Sarasota, Florida, USA, October 7-9*. 2019a.

- Ketelsen, S., Kolks, G., Andersen, T. O., Schmidt, L., and Weber, J. Bootstrap Reservoir Concepts for Electro-hydraulic Compact Cylinder Drives. In *Proceedings of the 12th International Fluid Power Conference*. 2020a.
- Ketelsen, S., Padovani, D., Andersen, T., Ebbesen, M., and Schmidt, L. Classification and Review of Pump-Controlled Differential Cylinder Drives. *Energies*, 2019b. 12(7):1293. doi:[10.3390/en12071293](https://doi.org/10.3390/en12071293).
- Ketelsen, S., Padovani, D., Ebbesen, M. K., Andersen, T. O., and Schmidt, L. A Gasless Reservoir Solution for Electro-Hydraulic Compact Drives with Two Prime Movers. In *Proceedings of ASME/BATH 2020 Symposium on Fluid Power and Motion Control*. 2020b.
- Ketelsen, S., Schmidt, L., Donkov, V. H., and Andersen, T. O. Energy Saving Potential in Knuckle Boom Cranes using a Novel Pump Controlled Cylinder Drive. *Modeling, Identification and Control*, 2018. 39(2):73–89. doi:[10.4173/mic.2018.2.3](https://doi.org/10.4173/mic.2018.2.3).
- Kim, S. and Murrenhoff, H. Measurement of Effective Bulk Modulus for Hydraulic Oil at Low Pressure. *Journal of Fluids Engineering*, 2012. 134(2):021201. doi:[10.1115/1.4005672](https://doi.org/10.1115/1.4005672).
- Linjama, M., Laamanen, A., and Vilenius, M. Is it Time for Digital Hydraulics? *Proceedings of the 8th Scandinavian International Conference on Fluid Power, SICFP, Vol1*, 2003. (March):347–366.
- Lodewyckx, J. *Der Differentialzylinder im geschlossenen hydrostatischen Kreislauf*. Ph.D. thesis, RWTH Aachen, 1994.
- Michel, S. and Weber, J. Energy-efficient electrohydraulic compact drives for low power applications. In *Proceedings of the ASME/BATH 2012 Fluid Power and Motion Control, Bath, United Kingdom, September 12–14*. pages 93–107, 2012.
- Minav, T., Bonato, C., Sainio, P., and Pietola, M. Direct Driven Hydraulic Drive. In *Proceedings of the 9th International Fluid Power Conference, Aachen, Germany, March 24–26*. pages 7–11, 2014.
- Neubert, T. *Untersuchungen von drehveränderbaren Pumpen*. Ph.D. thesis, TU Dresden, 2002.
- Padovani, D., Ketelsen, S., Hagen, D., and Schmidt, L. A Self-Contained Electro-Hydraulic Cylinder with Passive Load-Holding Capability. *Energies*, 2019. 12(2):292. doi:[10.3390/en12020292](https://doi.org/10.3390/en12020292).
- Padovani, D., Ketelsen, S., and Schmidt, L. Downsizing the Electric Motors of Energy Efficient Self-Contained Electro-hydraulic Systems by Hybrid Technologies. In *Proceedings of the ASME/BATH Symposium on Fluid Power and Motion Control*. pages 1–10, 2020.
- Pedersen, H. C. and Andersen, T. O. Pressure Feedback in Fluid Power Systems - Active Damping Explained and Exemplified. *IEEE Transactions on Control Systems Technology*, 2018. 26(1):102–113. doi:[10.1109/TCST.2017.2650680](https://doi.org/10.1109/TCST.2017.2650680).
- Pedersen, H. C., Schmidt, L., Andersen, T. O., and H. Brask, M. Investigation of New Servo Drive Concept Utilizing Two Fixed Displacement Units. *JFPS International Journal of Fluid Power System*, 2014. 8(1):1–9. doi:[10.5739/jfpsij.8.1](https://doi.org/10.5739/jfpsij.8.1).
- Phillips, C. and Parr, J. *Feedback Control Systems, 5th Edition*. Pearson, fifth edit edition, 2011. ISBN: 978-93-325-0760-9.
- Quan, Z., Quan, L., and Zhang, J. Review of energy efficient direct pump controlled cylinder electro-hydraulic technology. *Renewable and Sustainable Energy Reviews*, 2014. 35:336–346. doi:[10.1016/j.rser.2014.04.036](https://doi.org/10.1016/j.rser.2014.04.036).
- Rahmfeld, R. and Ivantysynova, M. Displacement controlled linear actuator with differential cylinder - A way to save primary energy in mobile machines. In *Proceedings of the 5th International Conference on Fluid Power Transmission and Control, Hangzhou, China, April 4–5*. 2001.
- Schmidt, L., Groenkaer, M., Pedersen, H. C., and Andersen, T. O. Position Control of an OverActuated Direct Hydraulic Cylinder Drive. *Control Engineering Practice*, 2017. 64:1–14. doi:[10.1016/j.conengprac.2017.04.003](https://doi.org/10.1016/j.conengprac.2017.04.003).
- Schmidt, L., Ketelsen, S., Brask, M. H., and Mortensen, K. A. A Class of Energy Efficient Self-Contained Electro-Hydraulic Drives with Self-Locking Capability. *Energies*, 2019a. 12(10):1866. doi:[10.3390/en12101866](https://doi.org/10.3390/en12101866).
- Schmidt, L., Ketelsen, S., Grønkær, N., and Hansen, K. V. On Secondary Control Principles in Pump Controlled Electro-Hydraulic Linear Actuators. In *Proceedings of ASME/BATH 2020 Symposium on Fluid Power and Motion Control*. pages 1–13, 2020.
- Schmidt, L., Ketelsen, S., Padovani, D., and Mortensen, K. A. Improving the Efficiency and Dynamic Properties of a Flow Control Unit in a Self-Locking Compact Electro-Hydraulic Cylinder Drive.

- In *Proceedings of the ASME/BATH 2019 Symposium on Fluid Power and Motion Control, Sarasota, Florida, USA, October 7-9*. 2019b.
- Schmidt, L., Roemer, D. B., Pedersen, H. C., and Andersen, T. O. Speed-Variable Switched Differential Pump System for Direct Operation of Hydraulic Cylinders. In *Proceedings of the ASME/BATH 2015 Symposium on Fluid Power and Motion Control, Chicago, USA, October 14-16*. 2015.
- Schneider, M., Koch, O., Weber, J., Bach, M., and Jacobs, G. Green Wheel Loader - Development of an energy efficient drive and control system. In *Proceedings of the 9th International Fluid Power Conference, Aachen, Germany, March 24-26*. 2014.
- Skogestad, S. and Postlethwaite, I. *Multivariable Feedback Control - Analysis and Design*. Wiley, 2. edition, 2005.
- Weber, J., Beck, B., Fischer, E., Ivantysyn, R., Kolks, G., Kunkis, M., Lohse, H., Lübbert, J., Michel, S., Schneider, M., Shabi, L., Sitte, A., Weber, J., and Willkomm, J. Novel System Architectures by Individual Drives. In *In Proceedings of the 10th International Fluid Power Conference, Dresden, Germany, March 8-10*. pages 29–62, 2016.

Paper D

Bootstrap Reservoir Concepts For Electro-Hydraulic Compact Cylinder Drives

Søren Ketelsen, Giacomo Kolks, Torben Ole Andersen, Lasse
Schmidt and Jürgen Weber

The paper has been published in
Proceedings of the 12th International Fluid Power Conference, Dresden, 2020.

©2020 by the IFK Organization
The layout has been revised

Paper E

A Gasless Reservoir Solution for Electro-Hydraulic Compact Drives with Two Prime Movers

Søren Ketelsen, Damiano Padovani, Morten Kjeld Ebbesen,
Torben Ole Andersen and Lasse Schmidt

The paper has been published in
*Proceedings of the BATH/ASME 2020 Symposium on Fluid Power and Motion
Control*

© 2020 by American Society of Mechanical Engineers

Paper F

Thermo-Hydraulic Modelling and Experimental Validation of an Electro-Hydraulic Compact Drive

Søren Ketelsen, Sebastian Michel, Torben Ole Andersen,
Morten Kjeld Ebbesen, Jürgen Weber and Lasse Schmidt





The paper has been published in
Energies Vol. 14, No. 9, 2021.

© 2021 by the authors

Typos have been corrected and are marked with a footnote

Article

Thermo-Hydraulic Modelling and Experimental Validation of an Electro-Hydraulic Compact Drive

Søren Ketelsen ^{1,*} , Sebastian Michel ², Torben O. Andersen ¹, Morten Kjeld Ebbesen ³ , Jürgen Weber ²  and Lasse Schmidt ¹ 

¹ Department of Energy Technology, Aalborg University, 9220 Aalborg, Denmark; toa@et.aau.dk (T.O.A.); lsc@et.aau.dk (L.S.)

² Institute of Fluid Power (IFD), Technische Universität Dresden, 01069 Dresden, Germany; sebastian.michel@tu-dresden.de (S.M.); fluidtronik@mailbox.tu-dresden.de (J.W.)

³ Department of Engineering Sciences, University of Agder, 4879 Grimstad, Norway; morten.k.ebbesen@uia.no

* Correspondence: sok@et.aau.dk; Tel.: +45-28-25-32-58

Abstract: Electro-hydraulic compact drives (ECDs) are an emerging technology for linear actuation in a wide range of applications. Especially within the low power range of 5–10 kW, the plug-and-play capability, good energy efficiency and small space requirements of ECDs render this technology a promising alternative to replace conventional valve-controlled linear drive solutions. In this power range, ECDs generally rely on passive cooling to keep oil and system temperatures within the tolerated range. When expanding the application range to larger power classes, passive cooling may not be sufficient. Research investigating the thermal behaviour of ECDs is limited but indeed required for a successful expansion of the application range. In order to obtain valuable insights into the thermal behaviour of ECDs, thermo-hydraulic simulation is an important tool. This may enable system design engineers to simulate thermal behaviour and thus develop proper thermal designs during the early design phase, especially if such models contain few parameters that can be determined with limited information available. Our paper presents a lumped thermo-hydraulic model derived from the conservation of mass and energy. The derived model was experimentally validated based on experimental data from an ECD prototype. Results show good accuracy between measured and simulated temperatures. Even a simple thermal model containing only a few thermal resistances may be sufficient to predict steady-state and transient temperatures with reasonable accuracy. The presented model may be used for further investigations into the thermal behaviour of ECDs and thus toward proper thermal designs required to expand the application range.

Keywords: thermal modelling; energy efficient fluid power; direct driven hydraulic drives; pump-controlled cylinder; electro-hydraulic compact drives; self-contained cylinder drive



Citation: Ketelsen, S.; Michel, S.; Andersen, T.O.; Ebbesen, M.K.; Weber, J.; Schmidt, L. Thermo-Hydraulic Modelling and Experimental Validation of an Electro-Hydraulic Compact Drive. *Energies* **2021**, *14*, 2375. <https://doi.org/10.3390/en14092375>

Academic Editor: Davide Barater

Received: 21 March 2021

Accepted: 14 April 2021

Published: 22 April 2021

Publisher's Note: MDPI stays neutral with regard to jurisdictional claims in published maps and institutional affiliations.



Copyright: © 2021 by the authors. Licensee MDPI, Basel, Switzerland. This article is an open access article distributed under the terms and conditions of the Creative Commons Attribution (CC BY) license (<https://creativecommons.org/licenses/by/4.0/>).

1. Introduction

Electro-hydraulic compact drives (ECDs) represent a promising alternative to conventional valve-controlled hydraulics as well as to electro-mechanical linear drive solutions [1–3]. By combining the robustness (including overload protection), high force density and high achievable transmission ratios of conventional hydraulic drives with the plug-and-play capabilities, better energy-efficiency and small space requirements of electro-mechanical linear drives, ECDs may be a competitive alternative in applications previously dominated by conventional technologies. As illustrated in Figure 1, ECDs basically consist of a variable-speed electric motor driving a fixed-displacement hydraulic pump. The pump outlets are connected to a differential cylinder, without any throttling elements, thus avoiding the associated immense power losses and enabling ECDs to recover energy in aided load situations. To balance the asymmetric cylinder flows, a low-pressure accumulator is often utilised to ensure appropriate suction conditions for the hydraulic pump. As opposed to valve-controlled drive solutions, the energy losses of ECDs are governed

by the energy efficiency of the components, as no inherent losses (i.e., valve throttling) are associated with the actuation principle.

During recent decades, the main research focus has been placed on identifying and investigating architectures that are able to connect the accumulator with the remaining circuit to facilitate operating in four quadrants. Two main topologies can be identified in research literature [4,5]. In valve-compensated architectures (Figure 1a), either hydraulically or electrically actuated valves are used to connect the low pressure cylinder chamber with the accumulator [6–8]. For pump-compensated architectures (Figure 1b), two or more pumps are matched to the areas of the differential cylinder to balance asymmetric flow without the need of valves [9–13]. To enable the ideal matching of pump displacements to the cylinder areas, independent of operating conditions, circuit architectures using two variable-speed electric motors (Figure 1c) are also being investigated [14,15]. A recent review highlighting the advantages and disadvantages of the considered architectures may be found in [16].

Some common drawbacks of the ECD technology potentially limiting its application range are currently being addressed by the research community. These include reliability and energy efficiency limitations in the low speed range of conventional hydraulic units [17–20], the challenge of incorporating load holding devices not affecting the ability of recovering energy in aided load situations [21–25] and identifying alternatives to the rather bulky gas-loaded accumulator [26,27]. The former challenge is also addressed by designing new types of hydraulic units, such that these are capable of low-speed operation at good efficiencies. The newly introduced AX series pump from Bucher Hydraulics is an example of such [28].

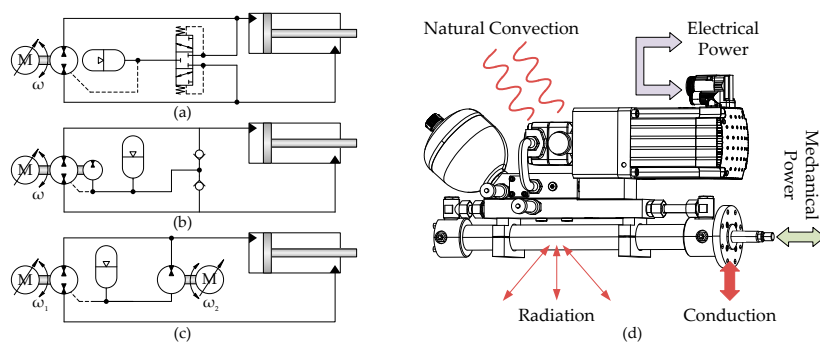


Figure 1. (a) Valve-compensated ECD. (b) Pump-compensated ECD. (c) ECD with two electric motors. (d) ECDs may rely solely on passive cooling.

The reported energy-efficiency of ECDs ranges from 50% up to 80% [29–31], but depends heavily on the working conditions. Nevertheless this is much higher than the energy efficiency of valve-controlled hydraulics, which features an average efficiency of 21% according to [32]. As opposed to conventional valve-controlled hydraulics where cooling devices are needed, the improved energy efficiency of ECDs may permit these systems to rely solely on passive cooling. This is illustrated in Figure 1d. The power losses of the system equals the passive heat transfer to the surroundings at an allowable equilibrium temperature. Passive cooling may be sufficient in the smaller power range of 5–10 kW, but for a higher power range it is unlikely that passive cooling suffices. Applications requiring larger power outputs, may among many other applications, include the actuation of large crane manipulators, where ECD architectures up to 80 kW or even bigger have been investigated by simulation studies in [33–35]. These studies however did not include thermal considerations. In the design phase of an ECD, it would be beneficial to understand the thermal behaviour of the system and to estimate to what extent cooling efforts are needed, prior to system realization. Nevertheless, research aiming at understanding and analysing the thermal behaviour of ECDs is limited. The authors in [36] measure

and compare efficiencies of a pump-compensated ECD, showing drastically reduced efficiencies at ambient temperatures below 0 °C. In [37,38], a thermo-hydraulic model is formulated in the commercially available software Simulation X, but compares this with measurements for a limited period of time, making it difficult to determine the accuracy of the model. In [39] a simple first order thermal model is proposed and used to actively control the average temperature of the system. It is unclear if the accuracy of the proposed thermal model is sufficient for system design purposes as well. In [40,41], a Simulation X model is formulated, and a good accuracy between measurements and simulation results is demonstrated. The parametrisation of the thermal model is elaborate, however, as a high number of solid thermal capacities are included. The current paper can be viewed as the continuation of the work in [40,41], as this paper investigates the trade-off between model complexity and accuracy based on the ECD system and experimental results presented in these references. The paper investigates two different thermal model complexities—the *benchmark* and the *reduced* model. The *benchmark* model is based on a relatively fine meshed discretization of the solid thermal capacities leading to an elaborate thermal submodel. On the other hand the *reduced* model features a more coarse discretization, leading to a simpler thermal model structure, making this suitable for design purposes.

The paper contributes to the research field by deriving the necessary equations, including descriptions of the fluid properties, needed to model the pressure and temperature dynamics of an ECD. Both of the considered model complexities were simulated using the equations derived in this paper to ensure comparability and full transparency. Note that the simulation results obtained in [40,41] are therefore not reused in this paper. To validate the derived models, these are compared to the experimental data obtained in [40,41].

For the mentioned references, the models are commonly based on a lumped parameter approach, which is also the case for this paper. This means that appropriate control volumes are defined assuming pressure and temperature to be homogeneous within the control volume [42]. This approach reduces the model complexity and needed computational effort greatly compared to finite element or computational fluid dynamics (CFD) methods, which are assessed to be too elaborate for system design purposes. Note that a system designer is desiring to roughly anticipate the system temperatures, and to do this with minimal effort and prior information.

The paper is organised as follows: In Section 2 the temperature and pressure dynamics of a lumped control volume are derived from first principles physics and in Section 3 consistent fluid properties of the oil–air mixture are derived. Section 4 presents the ECD prototype used for verification of the derived thermo-hydraulic model and Section 5 formulates the two thermal model complexities of the ECD prototype denoted the *benchmark* and *reduced* model. In Section 6, examples of calculating heat transfer resistances for basic geometries are given and used to parametrise the *reduced* model. Section 7 concludes the modelling part of the paper by deriving mass and enthalpy flow component models. Section 8 finally compares the simulation results of the two model complexities with experimental data. In the Nomenclature (Appendix A), the symbols used in the paper are listed.

2. Control Volume Dynamics

In this section, the pressure and temperature dynamics for a lumped control volume are derived from first principles physics, i.e., conservation of mass and energy. For a general control volume (CV), as seen in Figure 2, the continuity equation and the first law of thermodynamics may be written as Equations (1) and (2), respectively [43]:

$$\frac{\partial}{\partial t} \int_{cv} \rho dV + \int_{cs} \rho \mathbf{\hat{V}} \cdot \mathbf{\hat{n}} dA = 0 \quad (1)$$

$$\frac{\partial}{\partial t} \int_{cv} \left(u + \frac{\hat{V}^2}{2} + gz \right) \rho dV + \int_{cs} \left(u + \frac{\hat{V}^2}{2} + gz \right) \rho \mathbf{\hat{V}} \cdot \mathbf{\hat{n}} dA = \dot{Q} + \dot{W} \quad (2)$$

ρ is the fluid density, $\hat{\mathbf{V}}$ is the velocity vector of the fluid leaving the control volume across the control surface (CS) with normal vector $\hat{\mathbf{n}}$. Thus, the mass flow leaving the control volume is positive. u is specific internal energy, $\hat{V}^2/2$ and gz are kinetic energy and potential energy per unit mass, respectively. \dot{Q} and \dot{W} are heat flow transferred to and net rate of work done on the system, respectively.

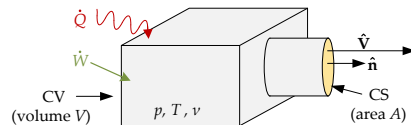


Figure 2. Illustration of a lumped control volume. Pressure, temperature and specific volume are assumed to be homogeneous. Mass transfer may occur across the control surface (CS).

2.1. Lumped Pressure Dynamics

Consider Equation (1), and assume that the density is homogeneous in the CV and on the CS. Allowing for mass exchange to occur across multiple control surfaces leads to the following simplification of the continuity equation in Equation (1):

$$\frac{\partial}{\partial t}(\rho V) + \sum_k \dot{m}_k - \sum_i \dot{m}_i = 0 \quad \Leftrightarrow \quad \dot{m} = \sum_i \dot{m}_i - \sum_k \dot{m}_k \quad \Leftrightarrow \quad \dot{\rho}V + \rho\dot{V} = \dot{m} \quad (3)$$

where V is the volume of the CV, and the index i is used to sum over incoming mass flows while k denotes leaving mass flows, such that $\dot{m} = \sum_i \dot{m}_i - \sum_k \dot{m}_k$. The density is an intensive property and may, by the state postulate, be expressed as a function of two independent intensive properties e.g., temperature and pressure. A change in density may be established by the total differential [44]:

$$\rho = f(p, T) \quad \Rightarrow \quad d\rho = \left(\frac{\partial \rho}{\partial p}\right)_T dp + \left(\frac{\partial \rho}{\partial T}\right)_p dT \quad \Rightarrow \quad \dot{\rho} = \left(\frac{\partial \rho}{\partial p}\right)_T \dot{p} + \left(\frac{\partial \rho}{\partial T}\right)_p \dot{T} \quad (4)$$

The partial derivatives in Equation (4) may be expressed using material properties, recognizing that the isothermal bulk modulus β and the isobaric expansion coefficient α are defined as [45,46]:

$$\beta = -V \left(\frac{\partial p}{\partial V}\right)_T = \rho \left(\frac{\partial p}{\partial \rho}\right)_T = \frac{\rho}{\left(\frac{\partial \rho}{\partial p}\right)_T} \quad \alpha = \frac{1}{v} \left(\frac{\partial v}{\partial T}\right)_p = -\frac{1}{\rho} \left(\frac{\partial \rho}{\partial T}\right)_p \quad (5)$$

where v is the specific volume ($v = \rho^{-1}$). Substituting Equation (4) into Equation (3) combined with the material properties from Equation (5), and isolating for \dot{p} yield:

$$\left(\frac{\rho}{\beta} \dot{p} - \alpha \rho \dot{T}\right) V + \rho \dot{V} = \dot{m} \quad \Leftrightarrow \quad \dot{p} = \frac{\beta}{V} \left(\frac{\dot{m}}{\rho} - \dot{V} + \alpha V \dot{T}\right) \quad (6)$$

Hence, the pressure dynamics of a lumped control volume is given by Equation (6).

2.1.1. Mechanical Elasticity

To include mechanical elasticity, i.e., expanding hoses or pipes for increasing pressures, the volume in Equation (6) is calculated as:

$$V = V_x \left(1 + \frac{p - p_0}{\beta_{\text{mech}}}\right) \quad \Rightarrow \quad \dot{V} = \dot{V}_x \left(\frac{p - p_0}{\beta_{\text{mech}}}\right) + \frac{V_x}{\beta_{\text{mech}}} \dot{p} + \dot{V}_x \quad (7)$$

where V_x is the volume at p_0 , and may include a fixed volume as well as a time dependent volume, e.g., a stoke dependent volume if the control volume is a cylinder chamber. β_{mech} is

a tuning parameter such that a high value of β_{mech} corresponds to a stiff volume, whereas a low value corresponds to an elastic volume. Inserting Equation (7) into Equation (6) yields:

$$\dot{p} = \underbrace{\left(\frac{\beta \beta_{\text{mech}}}{\beta_{\text{mech}} + \beta \frac{\beta_{\text{mech}}}{\beta_{\text{mech}} + p - p_0}} \right)}_{\beta_{\text{eff}}} \left(\frac{\dot{m}}{\rho V} - \frac{\dot{V}_x}{V_x} + \alpha \dot{T} \right) \quad (8)$$

where β_{eff} is the effective bulk modulus, including the effect of mechanical elasticity. If β_{mech} approaches infinity, β_{eff} approaches β and V_x approaches V , such that Equation (8) approaches Equation (6).

2.1.2. Diaphragm and Bladder Accumulators

Control volumes contained in a gas-loaded diaphragm or bladder accumulator are modelled without including mechanical elasticity. This is appropriate because nitrogen is much more compliant than the mechanical structures. For ECDs, the accumulator is operated at low pressures and room temperatures, i.e., far away from the critical point [46], justifying nitrogen to be modelled as an ideal gas. The volume and \dot{V} of the oil in the accumulator control volume are therefore found as:

$$V = V_{\text{acc}} + V_x - V_{\text{gas}} \quad \dot{V} = \dot{V}_x - \dot{V}_{\text{gas}} \quad (9)$$

$$V_{\text{gas}} = \frac{V_{\text{acc}} p_{\text{acc0}} T_{\text{gas}}}{T_{\text{acc0}} p} \quad \dot{V}_{\text{gas}} = \frac{V_{\text{gas}}}{T_{\text{gas}}} \dot{T}_{\text{gas}} - \frac{V_{\text{gas}}}{p} \dot{p} \quad (10)$$

where V_{acc} is the accumulator volume (constant), V_{gas} is the gas volume, and V_x is the oil volume outside the accumulator shell, which may include a fixed volume or a volume changing in time. T_{gas} is the gas temperature and finally p_{acc0} and T_{acc0} are the precharge pressure and temperature, respectively. Assuming the gas and oil pressure to be equal, and by combining Equation (10) with Equation (6) yield \dot{p} as:

$$\dot{p} = \frac{p\beta}{pV + \beta V_{\text{gas}}} \left(\frac{\dot{m}}{\rho} - \dot{V}_x + \alpha V \dot{T} + \frac{V_{\text{gas}}}{T_{\text{gas}}} \dot{T}_{\text{gas}} \right) \quad (11)$$

Note that T is the oil temperature and T_{gas} is the gas temperature. It can be seen that if the accumulator is removed ($V_{\text{acc}} = 0$) Equation (11) equals Equation (6).

The gas temperature may be assumed to equal the temperature of the accumulator shell, by assuming the gas compression to be an isothermal process. However, to include temperature changes due to compression, consider the first law of thermodynamics in Equation (2). Assume the density to be homogeneous within the control volume, the kinetic and potential energies to be negligible and acknowledge that mass is not exchanged across the control surfaces:

$$\dot{m}_{\text{gas}} = \dot{U} = \dot{Q} + \dot{W} \quad , \quad U(p, V) \Rightarrow \quad (12)$$

$$dU = \left(\frac{\partial U}{\partial T_{\text{gas}}} \right)_V dT_{\text{gas}} + \left(\frac{\partial U}{\partial V_{\text{gas}}} \right)_T dV_{\text{gas}} = m_{\text{gas}} c_v dT_{\text{gas}} + \left(T_{\text{gas}} \left(\frac{\partial p}{\partial T_{\text{gas}}} \right)_V - p \right) dV_{\text{gas}} \Rightarrow$$

$$\dot{U} = m_{\text{gas}} c_v \dot{T}_{\text{gas}} + \left(\beta \alpha T_{\text{gas}} - p \right) \dot{V}_{\text{gas}} \xrightarrow{\text{Ideal Gas}} \dot{U} = m_{\text{gas}} c_v \dot{T}_{\text{gas}} \quad (13)$$

where U is internal energy of the gas, m_{gas} is the mass of the gas and c_v is the isochoric specific heat. Equation (13) originates from the state postulate by taking the total differential of the internal energy as a function of pressure and volume and expressing the partial derivatives using fluid properties [47]. For ideal gasses $\beta = p$ and $\alpha = T^{-1}$ leading to

$\dot{U} = m_{\text{gas}} c_v \dot{T}$. Recognizing the rate of work done on the gas is by compression ($\dot{W} = -p\dot{V}_{\text{gas}}$) and combining Equations (12) and (13) yield the gas temperature dynamics as:

$$\left. \begin{aligned} \dot{T}_{\text{gas}} &= \frac{1}{m_{\text{gas}} c_v} (\dot{Q} - p\dot{V}_{\text{gas}}) \\ \dot{Q} &= hA(T_{\text{acc}} - T_{\text{gas}}) = \frac{m_{\text{gas}} c_v}{\tau} (T_{\text{acc}} - T_{\text{gas}}) \end{aligned} \right\} \Rightarrow \dot{T}_{\text{gas}} = \frac{(T_{\text{acc}} - T_{\text{gas}})}{\tau} - \frac{p}{m_{\text{gas}} c_v} \dot{V}_{\text{gas}} \quad (14)$$

Instead of calculating the transferred heat \dot{Q} using the convection heat transfer coefficient h and the surface area A , \dot{Q} is modelled using a fixed thermal time constant defined as $\tau = \frac{m_{\text{gas}} c_v}{hA}$ [48–50]. T_{acc} is the temperature of the accumulator shell.

2.2. Lumped Temperature Dynamics

For hydrostatic transmission systems kinetic and potential energies are small compared to internal energy and flow work (enthalpy) and thus neglected [41,51] in the first law of thermodynamics in Equation (2). Additionally, the assumptions given in Section 2.1 are imposed, i.e., assuming uniform density and specific internal energy distribution in the control volume and on the control surfaces. By allowing mass transfer to occur from several control surfaces Equation (2) simplifies to:

$$\frac{\partial}{\partial t}(\rho V u) - \sum_i \dot{m}_i u_i + \sum_k \dot{m}_k u = \dot{Q} + \dot{W} \quad (15)$$

$$\dot{m}u + m\dot{u} - \sum_i \dot{m}_i u_i + \sum_k \dot{m}_k u = \dot{Q} + \dot{W} \quad (16)$$

$$\sum_i \dot{m}_i u - \sum_k \dot{m}_k u + m\dot{u} - \sum_i \dot{m}_i u_i + \sum_k \dot{m}_k u = \dot{Q} + \dot{W} \quad (17)$$

$$\sum_i \dot{m}_i (u - u_i) + m\dot{u} = \dot{Q} + \dot{W} \quad (18)$$

Defining specific enthalpy as $h = u + pv$, the term $m\dot{u}$ can be rewritten to $m\dot{u} = m(\dot{h} - \dot{p}v - \dot{v}p)$. \dot{h} is expressed as a function of temperature and pressure [52]:

$$dh = \left(\frac{\partial h}{\partial T} \right)_p dT + \left(\frac{\partial h}{\partial p} \right)_T dp = c_p dT + \left(v - T \left(\frac{\partial v}{\partial T} \right)_p \right) dp \quad (19)$$

$$= c_p dT + v(1 - T\alpha)dp \quad \Rightarrow \quad \dot{h} = c_p \dot{T} + (1 - T\alpha)v\dot{p} \quad (20)$$

The partial derivatives are rewritten using material properties based on [47,52,53]. Inserting Equation (20) into $m\dot{u} = m(\dot{h} - \dot{p}v - \dot{v}p)$ leads to:

$$m\dot{u} = m(\dot{h} - \dot{p}v - \dot{v}p) = m(c_p \dot{T} + (1 - T\alpha)v\dot{p} - \dot{p}v - \dot{v}p) = mc_p \dot{T} - m\dot{v}p - T\alpha V\dot{p} \quad (21)$$

\dot{W} in Equation (18) has the form of either rate of shaft work, rate of moving boundary work (MBW) or rate of flow work [54]:

$$\begin{aligned} \dot{W} &= \dot{W}_{\text{shaft}} - \underbrace{p\dot{V}}_{\text{MBW}} + \underbrace{\sum_i p_i A_i \dot{V}_i - \sum_k p A_k \dot{V}_k}_{\text{flow work}} = \dot{W}_{\text{shaft}} - \underbrace{m\dot{v}p - \dot{m}vp}_{\text{MBW}} + \underbrace{\sum_i \dot{m}_i p_i v_i - \sum_k \dot{m}_k pv}_{\text{flow work}} \\ &= \dot{W}_{\text{shaft}} - m\dot{v}p - \left(\sum_i \dot{m}_i - \sum_k \dot{m}_k \right) vp + \sum_i \dot{m}_i p_i v_i - \sum_k \dot{m}_k pv \end{aligned} \quad (22)$$

$$= \dot{W}_{\text{shaft}} - m\dot{v}p + \sum_i \dot{m}_i (p_i v_i - pv) \quad (23)$$

Inserting Equations (21) and (23) in Equation (18), and isolating for the temperature derivative:

$$\sum_i \dot{m}_i (u - u_i) + mc_p \dot{T} - T\alpha V \dot{p} - m\dot{v}p = \dot{Q} + \dot{W}_{\text{shaft}} + \sum_i \dot{m}_i (p_i v_i - pv) - m\dot{v}p \quad (24)$$

$$\sum_i \dot{m}_i (h - h_i) + mc_p \dot{T} - T\alpha V \dot{p} = \dot{Q} + \dot{W}_{\text{shaft}} \quad (25)$$

$$\dot{T} = \frac{1}{mc_p} \left(\dot{Q} + \dot{W}_{\text{shaft}} + \sum_i \dot{m}_i (h_i - h) + T\alpha V \dot{p} \right) \quad (26)$$

Thus, the temperature dynamic of a lumped control volume is given by Equation (26).

3. Fluid Properties

The pressure and temperature dynamics in the previous section were derived from the conservation of mass and energy. For this to be upheld during a numerical simulation, the material properties need to fulfil the relationships stated in Equation (5). One approach for doing so is to use a density description as the starting point for deriving the remaining mass/volume related properties. The oil density, ρ_F is modelled as a function of pressure and temperature and approximated by a first order Taylor series expansion:

$$\rho_F = \rho_{F0} \left(1 + \frac{p - p_0}{\beta_0} - \alpha_0 (T - T_0) \right) \quad (27)$$

where ρ_{F0} , β_0 and α_0 are oil properties at $T_0 = 288.15$ K and $p_0 = 101,325$ Pa. Especially at low pressures, free air present in the oil affects the fluid properties. To include this, the density of the free air ρ_A is modelled as an ideal gas, compressed during a polytropic process [46]:

$$\rho_A = \frac{p}{RT_1} \quad T_1 = \left(\frac{p_0}{p} \right)^{\frac{1-\kappa}{\kappa}} T \quad (28)$$

where R is the gas constant for air, T_1 is the air temperature at the current pressure p , assuming polytropic compression from p_0 with polytropic coefficient κ . T is the lumped temperature of the oil–air mixture. The density of the oil–air mixture is found as:

$$\rho = \frac{m}{V} = \frac{V_{A0}\rho_{A0} + V_{F0}\rho_{F0}}{V_A + V_F} = \frac{V_{A0}\rho_{A0} + V_{F0}\rho_{F0}}{\frac{m_A}{\rho_A} + \frac{m_F}{\rho_F}} = \frac{V_{A0}\rho_{A0} + V_{F0}\rho_{F0}}{\frac{V_{A0}\rho_{A0}}{\rho_A} + \frac{V_{F0}\rho_{F0}}{\rho_F}} \quad (29)$$

where ρ_{A0} , V_{A0} and V_{F0} are the air density and the volumes occupied by air and oil at p_0 and T_0 , respectively. ϵ is defined as the volumetric ratio of air in the mixture at p_0 and T_0 , such that Equation (29) rewrites to:

$$\left. \begin{aligned} V_{A0} &= \epsilon V_0 \\ V_{F0} &= (1 - \epsilon) V_0 \end{aligned} \right\} \Rightarrow \rho = \frac{\epsilon V_0 \rho_{A0} + (1 - \epsilon) V_0 \rho_{F0}}{\frac{\epsilon V_0 \rho_{A0}}{\rho_A} + \frac{(1 - \epsilon) V_0 \rho_{F0}}{\rho_F}} = \frac{\epsilon \rho_{A0} + (1 - \epsilon) \rho_{F0}}{\frac{\epsilon \rho_{A0}}{\rho_A} + \frac{(1 - \epsilon) \rho_{F0}}{\rho_F}} \quad (30)$$

The mixture density can thus be written as a function of pressure and temperature:

$$\rho = \frac{C_1 f_1}{p_0^{\frac{1}{\kappa}} p^{-\frac{1}{\kappa}} T f_1 \epsilon + (\epsilon - 1) \beta_0 T_0} \quad \begin{aligned} C_1 &= T_0 (\rho_{F0} + (\rho_{A0} - \rho_{F0}) \epsilon) \\ f_1 &= (\alpha_0 (T - T_0) - 1) \beta_0 - p + p_0 \end{aligned} \quad (31)$$

The bulk modulus β , and expansion coefficient α of the mixture are found from the definitions in Equation (5):

$$\beta = \frac{\rho}{\left(\frac{\partial \rho}{\partial p}\right)_T} = \frac{f_1 \kappa p \left(p_0^{\frac{1}{\kappa}} T \epsilon f_1 + p^{\frac{1}{\kappa}} \beta_0 T_0 (\epsilon - 1) \right)}{T p_0^{\frac{1}{\kappa}} \epsilon f_1^2 - T_0 \kappa \beta_0 (\epsilon - 1) p^{\frac{1+\kappa}{\kappa}}} \quad (32)$$

$$\alpha = \frac{f_1 p_0^{\frac{1}{\kappa}} \left(\epsilon^2 T p_0^{\frac{1}{\kappa}} f_1^2 - T_0 \beta_0 p^{\frac{1}{\kappa}} (\epsilon^2 - \epsilon) (T \alpha_0 \beta_0 - f_1) \right) - \alpha_0 T_0^2 \beta_0^3 (\epsilon - 1)^2 p^{\frac{2}{\kappa}}}{\left(\epsilon T p_0^{\frac{1}{\kappa}} f_1 + p^{\frac{1}{\kappa}} \beta_0 T_0 (\epsilon - 1) \right)^2 f_1} \quad (33)$$

The specific heat, c_p , is considered only for the oil due to a small mass fraction of air in the mixture. A volume fraction of air of 10% ($\epsilon = 0.1$) at atmospheric pressure yields a mass fraction of air less than 0.2%. The specific heat is assumed to be only a function of temperature, and is given for a HLP32 oil in [55] as:

$$c_p = c_{p0} + K_{cp} T \quad (34)$$

c_{p0} and K_{cp} are modelling parameters found in Appendix B. The specific enthalpy of the oil–air mixture is approximated by the differential equation in Equation (19) as a finite difference [56]:

$$\Delta h \cong \bar{c}_p \Delta T + \frac{1 - \bar{\alpha} \bar{T}}{\bar{\rho}} \Delta p \quad \Rightarrow \quad h \cong \bar{c}_p (T - T_0) + \frac{1 - \bar{\alpha} \left(\frac{T_0 + T_1}{2} \right)}{\bar{\rho}} (p - p_0) \quad (35)$$

where the notation $\bar{\bullet}$ denotes material properties evaluated at the mean temperature and pressure. The specific enthalpy equals 0 J/kg at $T_0 = 288.15$ K, and $p_0 = 101325$ Pa.

In order to calculate the thermal resistances in Section 6, additional fluid properties are needed, including the dynamic viscosity, μ , and thermal conductivity, k . These are modelled as oil properties, i.e., without considering the air in the mixture. The dynamic viscosity of an HM46 oil is modelled by the Vogel–Barus model [57], and the thermal conductivity is calculated as a first order polynomial using fluid properties extracted as a function of temperature from the Equation Engineering Solver (EES, V10.836) library:

$$\mu = a_{\mu 1} e^{\left(\frac{a_{\mu 2}}{T - a_{\mu 3}} \right)} e^{\left(\frac{p}{a_{\mu 4} + a_{\mu 5} (T - 273.15)} \right)} \quad k = a_{k1} - a_{k2} T \quad (36)$$

where a_{\bullet} are modelling coefficients that are given in Appendix B.

3.1. Temperature Independent Density

The temperature and pressure dynamics derived in Section 2 (Equations (6) and (26)), are coupled via the thermal expansion coefficient α . As the numerical value of α is small (≈ 0.0007 K⁻¹), the coupling between the pressure and temperature dynamics may be neglected without sacrificing much accuracy in terms of the main dynamics [56]. To simplify the model formulation, it is profitable to decouple pressure and temperature dynamics by assuming $\alpha = 0$. However for mass to be conserved, the remaining volume and mass related properties (ρ and β) must be consistent with this assumption. This can be obtained by assuming the density of oil and air only being pressure dependent, such that:

$$\tilde{\rho}_F = \tilde{\rho}_{F0} \left(1 + \frac{p - p_0}{\beta_0} \right) \quad \tilde{\rho}_A = \frac{p}{RT_0} \quad (37)$$

where the notation \bullet denotes properties assumed to be temperature independent. By Equation (37), the temperature independent properties can be expressed as:

$$\tilde{\rho} = \frac{(\tilde{\rho}_{F0} + (\tilde{\rho}_{A0} - \tilde{\rho}_{F0})\epsilon)(\beta_0 + p - p_0)p}{(p_0 - \beta_0)(p - p_0)\epsilon + \beta_0 p} \quad (38)$$

$$\tilde{\beta} = \frac{p((p_0 - \beta_0)(p - p_0)\epsilon + \beta_0 p)(\beta_0 + p - p_0)}{(p_0^2 - (\beta_0 + 2p)p_0 + p^2)(p_0 - \beta_0)\epsilon + \beta_0 p^2} \quad (39)$$

The definitions in Equations (38) and (39) yield $\tilde{\alpha} = 0$, as desired.

3.2. Comparing Modelled and Measured Fluid Properties

In [55], the density of an HLP 32 oil was measured as a function of temperature and pressure. These measurements are used to fit the parameters of ρ_{F0} , β_0 and α_0 in Equation (27). In Figure 3a, a good fit between the modelled density and the measurements from [55] is observed. In the plot, the density of the oil–air mixture is also shown. The bulk modulus and thermal expansion coefficients are shown in Figure 3b,c. Figure 3b includes the effective bulk modulus, β_{eff} , considering mechanical elasticity, as introduced in Equation (8). Introducing mechanical elasticity lowers the bulk modulus compared to just considering the oil–air mixture.

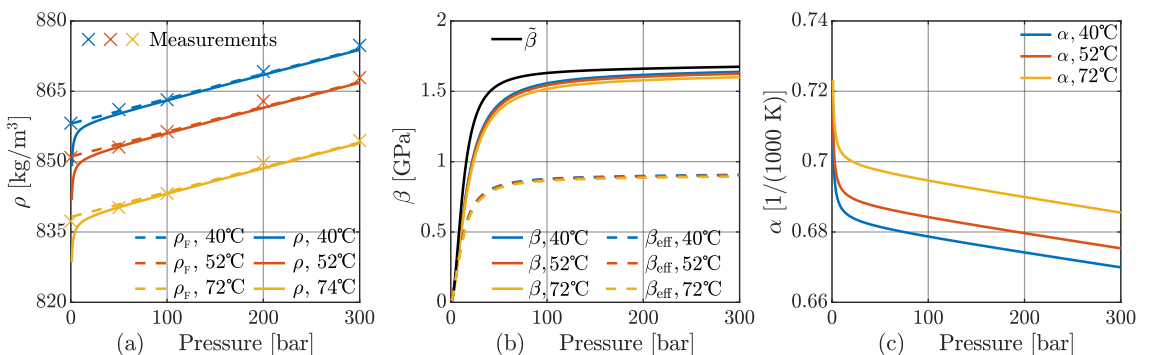


Figure 3. Fluid properties evaluated with a volumetric air content of 1%. (a) Dashed lines are modelled oil densities and solid lines are oil–air mixture densities. Measurements are obtained from [55]. (b) Modelled oil–air mixture bulk moduli. Dashed lines include the effect of mechanical elasticity with $\beta_{\text{mech}} = 2$ GPa. $\tilde{\beta}$ is the temperature independent bulk modulus. (c) Modelled thermal expansion coefficient of oil–air mixture.

This concludes the derivation of the lumped thermo-hydraulic model, including definition of consistent fluid properties. Models of the heat, mass and enthalpy flows entering the control volumes are defined subsequently. The ECD prototype used for experimental investigation is introduced next.

4. Electro-Hydraulic Compact Drive Prototype

The ECD prototype shown in Figure 4 was manufactured and tested at the Technical University of Dresden, Germany. The cylinder of the prototype was flanged on a general purpose test-rig, with the rod being connected to a load cylinder capable of loading the ECD with varying load forces. The ECD was connected with the load cylinder via an inertia mass of 110 kg, which is not shown in Figure 4. On the cylinder, a manifold was mounted, which connects the cylinder chambers with the pump and a diaphragm accumulator using an inverse shuttle valve for flow balancing. The pump was driven by a brushless DC motor. The pump and motor shafts were connected through the adapter plate. The adapter plate and accumulator were mounted on the manifold, such that the ECD forms a self-contained and compact drive system. The hydraulic diagram showing the main components of the

is defined. This thermal network was developed in previous publications [40,41], and is used here as a benchmark for model validation and for comparison with a simpler model complexity, i.e., the *reduced* model.

In the *reduced* model, a significantly coarser discretization is utilised. In [40,41], the forced convection resistances were found to be negligible, as the thermal behaviour was governed by natural convection and radiation from the system to the surroundings. Therefore, the *reduced* model investigates, among other things, how model accuracy is affected by neglecting forced convection resistances. Neglecting the forced convection resistances may be done in several ways. If commercial simulation software is used, arbitrary small forced convection resistances may be defined to maintain the number of lumped temperatures. Alternatively, the temperature dynamics of multiple fluid and solid control volumes may be lumped together, thus reducing the number of temperature states in the model. The latter approach is featured here. As the temperature dynamics of multiple fluid volumes are lumped together, it is beneficial to neglect the coupling between the temperature and pressure dynamics by utilising temperature independent fluid properties, as given in Section 3.1.

Table 1 compares the two model complexities.

Table 1. Comparison of the two model complexities.

	Model Complexity	
	Benchmark	Reduced
Fluid Properties	Temperature Dependent (Equations (31)–(33))	Temperature Independent $\tilde{\alpha} = 0$ and Equations (38) and (39)
Number of Thermal Capacities	3 Oil Capacities 18 Solid Capacities	1 Combined Oil/Solid Capacity 1 Oil Capacity & 1 Solid Capacity
Number of Thermal Resistances	18 Natural Convection & Radiation 21 Conduction Resistances 23 Forced Convection Resistances	5 Natural Convection & Radiation 1 Conduction Resistance 1 Forced Convection Resistance

The reason for dealing with two model complexities is to investigate how much information and accuracy are lost when reducing the model complexity. As seen from Table 1, the current study especially investigates the needed level of detail for the thermal submodels, including the number of thermal resistances used to model heat transfers in the system. The *benchmark* model demonstrated a good ability to provide accurate temperature simulations for most of the thermal capacities in [41]. However, parametrising the 62 thermal resistances present in the *benchmark* model is both a time-consuming and tedious task. In addition, for instance, the forced convection resistances occurring in the flow channels of a custom made manifold requires detailed knowledge about the construction of this to parametrise the resistances. Such detailed information may not be available during the design phase, where a design engineer desires to estimate the operating temperature for a given ECD under some loading conditions. To address the potential challenges of the *benchmark* model, a drastically reduced model, which requires limited information for parametrisation, was investigated. This includes cylinder and accumulator dimensions as well as approximate dimensions of manifold, pump and electric motor. As such, the current investigation may be regarded as a natural next step toward a simple but yet sufficiently accurate model level. The authors claim that if a thermo-hydraulic model should be useful for a design engineer, it should be relatively easy to parametrise even though this may decrease the accuracy. By the end of the day, approximate estimations or rough ideas are more useful than very accurate simulations that are never carried out due to time-consuming model development or parameters unknown during the design phase. Estimating the operating temperature is important to determine to what extent cooling is required, i.e., to obtain a proper thermal design. This may include the addition of a fan, heat pipes mounted in the manifold, an oil cooler or a water cooled manifold.

The following sections show the derivation of the two model complexities, with an offset in the system diagram in Figure 5b.

5.1. Benchmark Model

The pressure dynamics of the *benchmark* model are formulated as:

$$\dot{p}_A = \frac{\beta_A \beta_{\text{mech}}}{\beta_{\text{mech}} + \beta_A \frac{\beta_{\text{mech}}}{\beta_{\text{mech}} + p_A - p_0}} \left(\frac{\dot{m}_A}{\rho_A V_A} - \frac{\dot{x} A_A}{V_{\text{Ax}}} + \alpha_A \dot{T}_A \right), \quad \begin{matrix} V_{\text{Ax}} = V_{A0} + x A_A \\ V_A = V_{\text{Ax}} \left(1 + \frac{p_A - p_0}{\beta_{\text{mech}}} \right) \end{matrix} \quad (40)$$

$$\dot{p}_B = \frac{\beta_B \beta_{\text{mech}}}{\beta_{\text{mech}} + \beta_B \frac{\beta_{\text{mech}}}{\beta_{\text{mech}} + p_B - p_0}} \left(\frac{-\dot{m}_B - \dot{m}_C}{\rho_B V_B} + \frac{\dot{x} A_B}{V_{\text{Bx}}} + \alpha_B \dot{T}_B \right), \quad \begin{matrix} V_{\text{Bx}} = V_{B0} + (L_s - x) A_B \\ V_B = V_{\text{Bx}} \left(1 + \frac{p_B - p_0}{\beta_{\text{mech}}} \right) \end{matrix} \quad (41)$$

$$\dot{p}_C = \frac{p_C \beta_C}{p_C V_C + \beta_C V_{\text{gas}}} \left(\frac{\dot{m}_L + \dot{m}_C}{\rho_C} + \alpha_C V_C \dot{T}_C + \frac{V_{\text{gas}}}{T_{\text{gas}}} \dot{T}_{\text{gas}} \right), \quad \begin{matrix} V_C = V_{\text{Acc}} + V_{C0} - V_{\text{gas}} \\ V_{\text{gas}} = \frac{V_{\text{Acc}} p_{\text{acc0}} T_{\text{gas}}}{T_{\text{acc0}} p_C} \end{matrix} \quad (42)$$

The subscripts {A, B, C} in Equations (40)–(42) refer to the piston chamber, the rod side chamber and the accumulator, respectively, according to Figure 5b.

The gas temperature is modelled using Equation (14). The temperature dynamics of the oil control volumes are modelled from Equation (26) as:

$$\dot{T}_A = \frac{1}{V_A \rho_A c_{p,A}} \left(\dot{Q}_A + \dot{H}_{A,\text{pump}} + T_A \alpha_A V_A \dot{p}_A \right) \quad (43)$$

$$\dot{T}_B = \frac{1}{V_B \rho_B c_{p,B}} \left(\dot{Q}_B + \dot{H}_{B,\text{pump}} + \dot{H}_C^- + T_B \alpha_B V_B \dot{p}_B \right) \quad (44)$$

$$\dot{T}_C = \frac{1}{V_C \rho_C c_{p,C}} \left(\dot{Q}_C + \dot{H}_C^+ + \dot{H}_{L,\text{pump}} + T_C \alpha_C V_C \dot{p}_C \right) \quad (45)$$

where \dot{Q}_A , \dot{Q}_B and \dot{Q}_C are the sum of heat flows to the control volumes, $\dot{H}_{A,\text{pump}}$, $\dot{H}_{B,\text{pump}}$ and $\dot{H}_{L,\text{pump}}$ are the pump enthalpy flows to the control volumes. \dot{H}_C^+ and \dot{H}_C^- are the enthalpy flow through the orifice. The enthalpy flows are modelled in Section 7.

The *benchmark* model discretises the system into 18 solid thermal capacities each associated with an individual temperature. The temperature dynamics of a solid capacity is modelled as:

$$\dot{T}_j = \frac{\sum_i \dot{Q}_{j,i}}{m_j c_{p,j}} \quad \dot{Q}_i = \frac{\Delta T_i}{R_{\text{th},i}} \quad (46)$$

where j is indexing the 18 solid capacities and i the heat transfer to the solid capacity. $\sum_i \dot{Q}_{j,i}$ is the net sum of heat flow into capacity j , m_j is the mass of the solid capacity and $c_{p,j}$ is the specific heat for the given solid material modelled as a function of the temperature. Specific heats as a function of temperature are obtained from the library of EES, and implemented as 1D lookup tables. The heat flow is described using the concept of thermal resistances, R_{th} . Analogous to an electric circuit, the temperature (voltage) may be described as the product of heat flow (current) and the thermal resistance [K/W]. $\sum_i \dot{Q}_{j,i}$ is thus the sum of all heat flows through the thermal resistances connected to the capacity, and ΔT_i is the temperature difference across the thermal resistance. The heat flows to oil and solid capacities may be visualised by a thermal resistance network. The resistance network for both the *benchmark* and the *reduced* model are presented in Section 6.

5.2. Reduced Model

The pressure dynamics of the *reduced* model are similar to the dynamics from Equations (40)–(42), except that temperature independent fluid properties, \bar{p} , $\bar{\beta}$ and $\bar{\alpha}$, are utilised. This entails that the temperature coupling term ($\alpha V \dot{T}$) vanishes.

Whereas the *benchmark* model includes 18 solid thermal capacities, the *reduced* model only includes five. These are the electric motor and adapter plate, the cylinder barrel, the manifold, the pump and the accumulator. In Figure 6a, these are illustrated as basic geometries, which are used for heat transfer calculations. These include cubes (blue), horizontal cylinders (green) and spheres (yellow). For comparison, Figure 6b shows 15 of the 18 considered solid thermal capacities approximated as basic geometries used in the *benchmark* model.

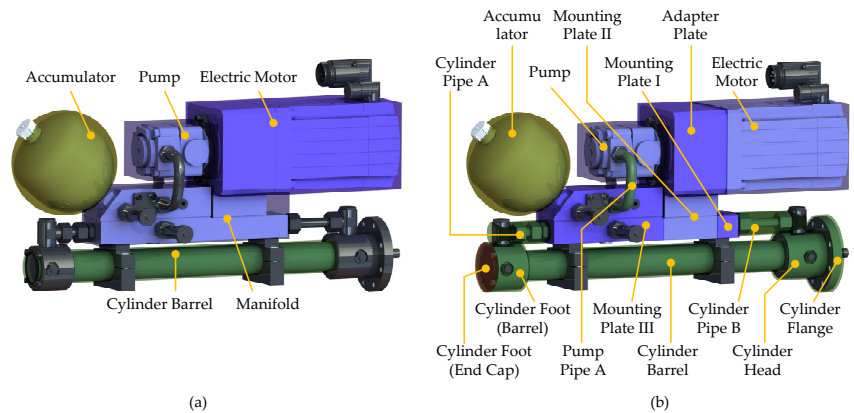


Figure 6. (a) In the *reduced* model, natural convection and radiation to the surroundings are modelled to occur from five shapes. (b) In the *benchmark* model, natural convection and radiation are modelled to occur from 18 shapes (three not shown).

As noted in [40], the thermal behaviour of the system is governed by the natural convection and radiation resistances on the outer surfaces as these are considerably larger than the forced convection resistances between the oil and the solid materials on the inner surfaces. Taking the cylinder barrel as an example, the combined natural convection and radiation resistance is more than nine times higher than the forced convection resistance. In the *reduced* model, this observation is exploited by neglecting all forced convection resistances, except the forced convection between oil and accumulator, and thus reducing the number of thermal resistances significantly.

This has the implication that all solids being in contact with oil (accumulator not included) are modelled to have the same temperature. This leads to a further simplification compared to the *benchmark* model, as contact and conduction resistances between solid thermal capacities are omitted. However, as a consequence, only three distinct temperatures are modelled in the *reduced* model. These include the oil temperature in the accumulator T_C , the accumulator shell temperature T_{acc} and the lumped system temperature, T_{sys} , combining the thermal capacity of the oil in the A and B chamber with the cylinder barrel, pump, manifold, electric motor and adapter plate capacities. Even though the electric motor and adapter plate are not in contact with the oil, these are included in the lumped system temperature due to large contact areas with the pump and manifold, thus assuming the contact resistance to be small. All other thermal capacities, such as pipes, cylinder flanges, etc., are not included in the *reduced* model. This means that only approximate dimensions of the main system components are needed to parametrise the thermal resistance network.

The temperature dynamics of the three control volumes of the *reduced* model are given as:

$$\begin{aligned} \dot{T}_{\text{sys}} &= \frac{\dot{Q}_{\text{losses}} + \dot{H}_{A,\text{pump}} + \dot{H}_{B,\text{pump}} + \dot{H}_C^- - \dot{Q}_{\text{th}}}{V_A \bar{\rho}_A c_{p,A} + V_B \bar{\rho}_B c_{p,B} + m_{\text{steel}} c_{p,\text{steel}} + m_{\text{alu}} c_{p,\text{alu}}}, \quad \dot{T}_C = \frac{\dot{H}_{L,\text{pump}} + \dot{H}_C^+ - \dot{Q}_{\text{VII}}}{V_A \bar{\rho}_A c_{p,A} + V_C \bar{\rho}_C} \quad (47) \\ \dot{T}_{\text{acc}} &= \frac{\dot{Q}_{\text{VII}} - \dot{Q}_V}{m_{\text{acc}} c_{p,\text{acc}}}, \quad \dot{Q}_{\text{losses}} = \dot{Q}_{L,\text{HM}} + \dot{Q}_{L,\text{Cyl}} + \dot{Q}_{L,\text{EM}}, \quad \dot{Q}_{\text{th}} = \dot{Q}_I + \dot{Q}_{II} + \dot{Q}_{III} + \dot{Q}_{IV} + \dot{Q}_{VI} \end{aligned}$$

\dot{Q}_I to \dot{Q}_{VII} are heat flows through the thermal resistances defined in the next section. m_{steel} and m_{alu} are the mass of steel and aluminium with temperature dependent specific heats $c_{p,\text{steel}}$ and $c_{p,\text{alu}}$, respectively. $\dot{Q}_{L,\text{HM}}$, $\dot{Q}_{L,\text{Cyl}}$ and $\dot{Q}_{L,\text{EM}}$ are hydro-mechanical pump losses, cylinder friction losses and losses of the electric machine, respectively. These are modelled in Section 7 along with the enthalpy flows \dot{H} .

6. Thermal Resistance Networks

In this section, the heat flows to the control volumes and the solid capacities for both model complexities are presented. As mentioned, the heat flows are calculated based on the temperature differences across thermal resistances. This may beneficially be visualised using a thermal resistance network. The thermal resistance network for the *benchmark* model was derived in [41] and is shown in Figure 7.

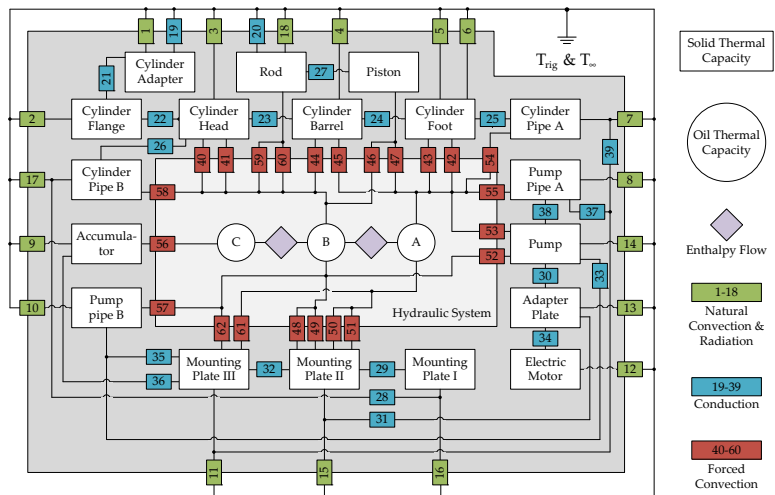


Figure 7. Thermal resistance network for the *benchmark* model. The thermal network was developed in [40,41]. Contact resistance is included in the conduction resistances.

The 62 thermal resistances in Figure 7 were computed in [40,41]. Examples of how to calculate thermal resistances for different geometries and flow conditions are given in Section 6, when calculating resistances for the *reduced* model.

In addition to heat exchanged through thermal resistances, heat is also ascribed as the consequence of energy losses of the components. The power loss due to cylinder friction is entirely added to the cylinder barrel, 25% of the pump friction losses are added to each of the oil control volumes A and B and the remaining 50% are added to the pump housing. Finally, the electric motor power losses are added to the solid capacity of the electric motor. Leakage and valve throttling losses are ascribed inherently by the enthalpy flows.

The thermal resistance network for the *reduced* model is given in Figure 8. In addition to natural convection and radiation from the five basic shapes in Figure 6a, forced convec-

tion between oil and accumulator as well as heat conduction (contact resistance included) from the cylinder barrel through the cylinder head and flange to the test-rig are included.

The seven thermal resistances from Figure 8 are found as either conduction, convection or radiation resistances given as [46]:

$$R_{\text{cond}} = \frac{L}{kA}, R_{\text{cont}} = \frac{1}{h_c A}, R_{\text{conv}} = \frac{1}{hA_s}, R_{\text{rad}} = \frac{1}{A_{s,\text{Eff}} \epsilon \sigma (T_s^2 + T_\infty^2) (T_s + T_\infty)} \quad (48)$$

where R_{cond} is the conduction resistance (here for a plane wall example) modelling the heat transfer through a material. L is the length of which the heat transfer occurs, k is the thermal conductivity of the material and A is the cross-section area. R_{cont} is the contact resistance, with h_c being the contact conductance. R_{conv} is forced or natural convection resistance. Forced convection occurs between oil and solid elements, whereas natural convection takes place at the outer surfaces of the system, as no fan is incorporated in the system. h is the convective heat transfer coefficient. A_s is the surface area. R_{rad} is radiation resistance, with $A_{s,\text{Eff}}$ being the effective radiation surface area. ϵ is the surface emissivity and σ is the Stefan–Boltzmann constant. T_s and T_∞ are the surface temperature and the ambient temperature, respectively.

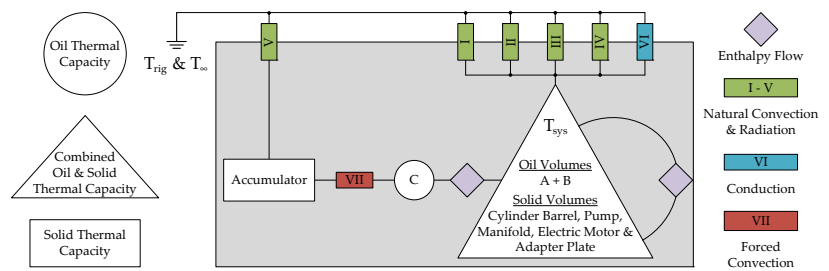


Figure 8. Thermal resistance network for the *reduced* model. The natural convection and radiation resistance are found as a parallel connection of the convection and radiation resistances.

6.1. Heat Conduction

Only heat conduction from the cylinder barrel through the cylinder head and flange to the test-rig is included in the *reduced* model. The test-rig is considered as a thermal reservoir, thus remaining at a constant temperature. The heat transfer is modelled as a serial connection of two conduction and two contact resistances (R_{cond} and R_{cont} in Equation (48)). The apparent contact areas for calculation of the contact resistances are given in Figure 9a as A_1 and $(A_1 + A_2)$. The conduction resistances are modelled with areas $(A_1 + A_2)$, $(A_1 + A_2 + A_3)$ and lengths L_1 , L_2 .

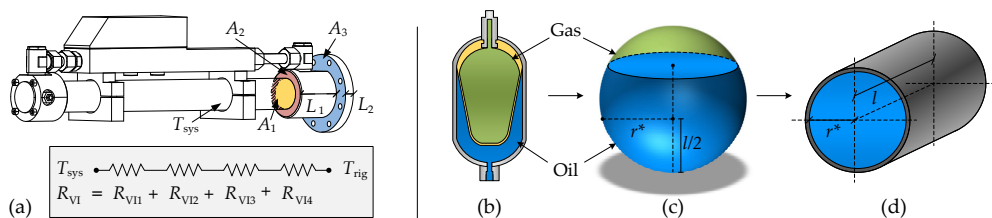


Figure 9. (a) The heat conduction from the cylinder barrel to the test-rig is modelled as a serial connection of two conduction and two contact resistances. (b) Bladder type gas-loaded accumulator. (c) The bladder accumulator is approximated as a sphere when calculating the natural convection heat transfer from the outer surface. (d) Forced convection on the inner surface is approximated as internal pipe flow, with the length of the pipe being the oil height in the virtual sphere and the pipe radius being evaluated as the radius of the spherical cap at $l/2$.

6.2. Convection

The convective heat transfer coefficient, h in Equation (48), may be determined from the average Nusselt number (Nu). The Nusselt number is a function of the Reynolds (Re) and Prandtl (Pr) numbers for forced convection problems, and the Rayleigh (Ra) and Prandtl numbers for natural convection problems.

$$\text{Nu}(\text{Re or Ra, Pr}) = \frac{hL_c}{k} \quad \text{Re} = \frac{\hat{V}L_c\rho}{\mu} \quad \text{Pr} = \frac{\mu c_p}{k} \quad \text{Ra} = \frac{g\alpha L_c^3 \rho^2 c_p \Delta T}{\mu k} \quad (49)$$

where L_c is the geometry dependent characteristic length, \hat{V} is the mean flow speed and g is the gravitational acceleration. For natural convection problems, the fluid properties of the ambient air are calculated at the reference temperature $\bar{T} = 0.5(T_s + T_\infty)$, i.e., at the mean temperature between surface and surroundings. Fluid properties for forced convection problems are evaluated at the lumped pressure and temperature of the oil control volume using the expressions derived in Section 3.

The Nusselt number depends on geometry, and the methodology utilised here is to identify an appropriate approximation of the considered shape, such that well-known methodologies and formulas valid for basic shapes may be applied. This is done in Figure 6a, where the outer surfaces of the ECD prototype is approximated using the basic shapes of a cube (electric motor and adapter plate, pump and manifold), horizontal cylinder (cylinder barrel) and sphere (accumulator).

To illustrate this approach further, consider the accumulator, which is approximated by a sphere for calculation of the natural convection resistance, as seen in Figure 9b,c. The forced convection between the oil and the accumulator shell is modelled by approximating the flow as an internal pipe flow. The length and diameter of this pipe are updated according to the oil level in the accumulator, which is illustrated in Figure 9c,d. The fluid height present in the virtual sphere is calculated dependent on the oil volume in the accumulator, and is used as the pipe length when calculating the Nusselt number. The pipe diameter is approximated as the diameter of the spherical cap containing the oil at half the oil height, as illustrated in Figure 9c.

Table 2 shows the expressions for calculation of the Nusselt numbers for the geometries and flow conditions considered in the *reduced* model, obtained from [59,60]:

Table 2. Nusselt numbers for convective heat transfer problems in the *reduced* model. A_{proj} is the projected area of the cube on a horizontal flat surface below the cube. d_i is internal diameter. The Nusselt number for internal pipe flow is valid for laminar flows during hydrodynamic and thermal flow development.

Geometry		Nusselt Number	Prandtl Function	L_c
Natural	Horizontal Cylinder	$\text{Nu} = (0.752 + 0.387(\text{Ra} f(\text{Pr}))^{1/6})^2$	$f(\text{Pr}) = \left(1 + \left(\frac{0.559}{\text{Pr}}\right)^{9/16}\right)^{-16/9}$	$L_c = \frac{1}{2}\pi d$
	Sphere	$\text{Nu} = 0.56 \left(\left(\frac{\text{Pr}}{0.846 + \text{Pr}}\right) \text{Ra}\right)^{1/4} + 2$	-	$L_c = d$
	Cube	$\text{Nu} = 5.748 + 0.752 \left(\frac{\text{Ra}}{f(\text{Pr})}\right)^{0.252}$	$f(\text{Pr}) = \left(1 + \left(\frac{0.492}{\text{Pr}}\right)^{9/16}\right)^{16/9}$	$L_c = \frac{A}{d}$ $d = \sqrt{4 \frac{A_{\text{proj}}}{\pi}}$
Forced	Internal Pipe Flow	$\text{Nu} = (49.37 + (f_1 - 0.7)^3 + f_2^3)^{1/3}$	$f_1 = 1.615 \left(\text{RePr} \frac{d_i}{L}\right)^{1/3}$	$L_c = d_i$
			$f_2 = \left(\frac{2}{1 + 22\text{Pr}}\right)^{1/6} \left(\text{RePr} \frac{d_i}{L}\right)$	

The heat transfer coefficients for natural convection calculated based on the Nusselt numbers given in Table 2 are valid for idealised conditions. In technical environments such as workshops, factories, etc., the heat transfer coefficients can be assumed to be up

to 20% larger than the theoretical values, according to [61]. This is due to ambient air flow occurring from windows, doors, people walking around, etc. In [41], experiments identified that the ambient conditions caused the natural heat transfer coefficients to be 16% larger than the theoretical values. For a fair comparison between the *benchmark* and *reduced* model, all natural convection heat transfer coefficients used in this paper have been increased by 16% compared to their theoretically obtained counterparts.

6.3. Radiation

All bodies above 0 K emit thermal radiation. However, for the current study, radiation heat transfer is assumed to only occur between the solid elements and the surroundings, and not internally between the solid elements. As seen in Equation (48) the effective radiation surface, $A_{s, \text{Eff}}$, is utilised instead of the actual surface area A_s , acknowledging that solid elements may be shadowing each other. This means that the effective radiation area is smaller than the actual surface area. This effect is included in the *benchmark* model, however, the *reduced* model assumes $A_{s, \text{Eff}} = A_s$, as the shadowing effect is difficult to determine without accurate knowledge of the relative placement of the solid components.

6.4. Thermal Resistances in the Reduced Model

In Table 3, the seven thermal resistances of the *reduced* model are exemplarily calculated. The resistances have been evaluated at oil and solid temperatures of 60 °C, an ambient temperature of 20 °C, fluid velocities present for a piston speed of 150 mm/s and at the initial oil level in the accumulator. As mentioned, the heat transfer coefficients have been increased by 16% compared to the idealised values to reflect the ambient flow conditions. Please note that the resistances are updated during the simulation, and the values given in Table 3 are only given as an example to illustrate the order of magnitude.

Table 3. Thermal resistances, according to Figure 8, evaluated at oil and solid temperatures of 60 °C, an ambient temperature of 20 °C and for fluid velocities present for a piston speed of 150 mm/s.

Natural Convection & Radiation									
ID	Geometry	A_s	A_{proj}	L_c	ϵ	h_{conv}	h_{rad}	h_{comb}	R_{th}
I	Horizontal Cylinder	980 cm ²	-	79 mm	0.92	$7.1 \frac{\text{W}}{\text{m}^2\text{K}}$	$6.4 \frac{\text{W}}{\text{m}^2\text{K}}$	$13.5 \frac{\text{W}}{\text{m}^2\text{K}}$	$0.76 \frac{\text{K}}{\text{W}}$
II	Cube (Manifold)	1341 cm ²	221 cm ²	799 mm	0.26	$5.0 \frac{\text{W}}{\text{m}^2\text{K}}$	$1.8 \frac{\text{W}}{\text{m}^2\text{K}}$	$6.8 \frac{\text{W}}{\text{m}^2\text{K}}$	$1.1 \frac{\text{K}}{\text{W}}$
III	Cube (Electric Motor)	2268 cm ²	469 cm ²	928 mm	0.69	$4.8 \frac{\text{W}}{\text{m}^2\text{K}}$	$4.8 \frac{\text{W}}{\text{m}^2\text{K}}$	$9.6 \frac{\text{W}}{\text{m}^2\text{K}}$	$0.46 \frac{\text{K}}{\text{W}}$
IV	Cube (Pump)	614 cm ²	120 cm ²	497 mm	0.92	$5.7 \frac{\text{W}}{\text{m}^2\text{K}}$	$6.4 \frac{\text{W}}{\text{m}^2\text{K}}$	$12.1 \frac{\text{W}}{\text{m}^2\text{K}}$	$1.34 \frac{\text{K}}{\text{W}}$
V	Sphere (Accumulator)	707 cm ²	-	150 mm	0.92	$5.9 \frac{\text{W}}{\text{m}^2\text{K}}$	$6.4 \frac{\text{W}}{\text{m}^2\text{K}}$	$12.4 \frac{\text{W}}{\text{m}^2\text{K}}$	$1.14 \frac{\text{K}}{\text{W}}$
Heat Conduction to Test-Rig									
ID	Geometry	A_1	A_2	A_3	L_1	L_2	k [46]	h_c [40]	R_{th}
VI	Plane Wall	20 cm ²	28 cm ²	75 cm ²	73 mm	16 mm	$63.9 \frac{\text{W}}{\text{mK}}$	$6.5 \frac{\text{kW}}{\text{m}^2\text{K}}$	$0.37 \frac{\text{K}}{\text{W}}$
Forced Convection (Oil to Accumulator)									
ID	Geometry	A_s	l	d_i	\hat{V}	Re		h_{conv}	R_{conv}
VII	Internal Pipe Flow	243 cm ²	51.6 mm	113 mm	$7.6 \frac{\text{mm}}{\text{s}}$	28		$51 \frac{\text{W}}{\text{m}^2\text{K}}$	$0.80 \frac{\text{K}}{\text{W}}$

$$\ddot{x} = \frac{1}{M_L} (p_A A_A - p_B A_B - (A_A - A_B) p_0 - F_L - F_F) \quad \dot{Q}_{L,Cyl} = F_F \dot{x} \quad (50)$$

$$F_F = \left(F_c + (F_s - F_c) e^{\frac{-|\dot{x}|}{\dot{x}_{sw}}} + K_p |p_A - p_B| \right) \tanh(\gamma \dot{x}) + B_L \dot{x} \quad (51)$$

The term $(A_A - A_B) p_0$ includes the force from the surroundings on the rod and is included because the modelled pressures are absolute. F_L is the load force and F_F is cylinder friction modelled as a Stribeck characteristic curve including a pressure dependent friction term [62,63]. F_c is the Coulomb friction, F_s is the static friction, \dot{x}_{sw} is the Stribeck velocity, K_p is the pressure dependent friction coefficient and B_L is the viscous friction coefficient.

The mass and enthalpy flows of the inverse shuttle valve/orifice are modelled according to Figure 10b as [52]:

$$\dot{m}_c = A_o C_d \sqrt{2\bar{p} |p_B - p_C|} \operatorname{sign}(p_B - p_C) \quad (52)$$

$$\dot{H}_c^+ = \begin{cases} \dot{m}_c (h_B - h_C) & , \dot{m}_c \geq 0 \\ 0 & , \dot{m}_c < 0 \end{cases} \quad \dot{H}_c^- = \begin{cases} 0 & , \dot{m}_c \geq 0 \\ -\dot{m}_c (h_C - h_B) & , \dot{m}_c < 0 \end{cases} \quad (53)$$

where A_o is the orifice area and C_d is the discharge coefficient.

7.2. Electric Motor

The dynamics of the electric motor is omitted in the model, i.e., the shaft speed equals the reference speed. Thus, only the loss behaviour of the motor is modelled. The losses of the electric motor are measured for varying motor speeds and torques and implemented as a 2D lookup table. The losses are assumed to be temperature independent and identical in both generator and motor operation mode. For a visualisation of the loss behaviour of the motor, the measured efficiency map is shown in Figure 11a.

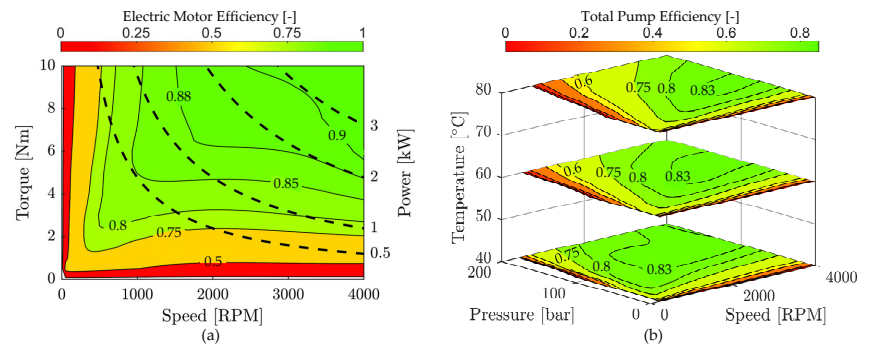


Figure 11. (a) Measured efficiency map of the electric motor, as a function of torque and speed. Dotted lines are power levels. (b) Measured efficiency map of the pump as a function of pressure difference, speed and temperature.

7.3. Pump

A pump model expressing the static relationship between the inputs (i.e., the pump speed, pressure difference across the pump and inlet temperature) and the outputs is needed. The outputs include the mass and enthalpy flows as well as the shaft torque. This is visualised in Figure 10c. Here, it may also be seen that external leakage is modelled to only occur from the high pressure chamber.

In addition to the mentioned model inputs, loss information or loss models are required, which may either be an analytical model or simply measured loss quantities,

implemented as look-up tables. The latter approach is used here. Figure 11b shows the measured efficiency map of the pump. Losses are assumed to be equivalent in both motor and pump operation modes. The actual pumping process is modelled as an ideal process, with losses/irreversibilities added subsequently. E.g., leakage losses may be regarded as variable orifices surrounding the ideal pump process (as visualised in Figure 10c). From Figure 10c, it is important to note that the inlet pressure and temperature to the ideal pump equal the states of the delivering chamber (rotation direction dependent), and the outlet pressure equals the pressure in the receiving chamber. The output temperature, however, is calculated by assuming an isentropic compression process, as [47]:

$$S = f(T, p) \quad \Rightarrow \quad dS = \left(\frac{\partial S}{\partial T} \right)_p dT + \left(\frac{\partial S}{\partial p} \right)_T dp = \frac{c_p}{T} dT - \alpha v dp \quad (54)$$

$$\xrightarrow{dS=0} \quad dT = \frac{\alpha T}{\rho c_p} dp \quad \xrightarrow{\text{Approximation}} \quad T_{\text{out}} \cong T_{\text{in}} + \frac{\bar{\alpha} T_{\text{in}}}{\bar{c}_p \bar{\rho}} (p_{\text{out}} - p_{\text{in}}) \quad (55)$$

S is the entropy modelled as a function of temperature and pressure, p_{in} and p_{out} is either p_A or p_B depending on the direction of rotation. Likewise, the inlet temperature is either T_A or T_B . $\bar{\bullet}$ denotes fluid properties evaluated at $\frac{p_{\text{in}} + p_{\text{out}}}{2}$ and T_{in} . The enthalpy change of the fluid may be found by inserting the isentropic temperature change from Equation (55) in Equation (19):

$$dh = c_p dT + v(1 - T\alpha)dp = c_p \left(\frac{\alpha T}{\rho c_p} dp \right) + v(1 - T\alpha)dp = \frac{1}{\rho} dp \quad (56)$$

$$\xrightarrow{\text{Approximation}} \quad \Delta h \cong \frac{1}{\bar{\rho}} (p_{\text{out}} - p_{\text{in}}) \quad (57)$$

where $\bar{\rho}$ is the fluid density evaluated at $\frac{p_{\text{in}} + p_{\text{out}}}{2}$ and $\frac{T_{\text{in}} + T_{\text{out}}}{2}$. The ideal mass flow, \dot{m}_T , the mass leakage flow, \dot{m}_L and the theoretical pump torque are modelled as:

$$\dot{m}_T = \omega D_p \bar{\rho} \quad \dot{m}_L = \frac{1}{2} Q_L \bar{\rho} \quad \tau_T \omega = \dot{m}_T \Delta h \quad \Rightarrow \quad \tau_T = D_p (p_{\text{out}} - p_{\text{in}}) \quad (58)$$

where D_p is the geometric displacement of the pump and Q_L is the measured volumetric flow loss. Note that τ_T ends up being the familiar torque equation for incompressible fluids. To include the compressibility of the fluid, somewhat more elaborate models are available, i.e., from [64], but are not considered here. The calculation of the mass and enthalpy flows, defined in Figure 10c, depend on the operating quadrant, i.e., the direction of pump rotation and the pressure difference across the pump. Likewise, the actual shaft torque τ must be calculated based on the operation quadrant by including the measured torque loss τ_L .

The relevant expressions for the four operating quadrants are given in Table 4:

Table 4. Pump torque, mass and enthalpy flows based on operation quadrant. $\Delta P = (p_A - p_B)$. * Only valid for $\dot{m}_A > 0$,
[†] Only valid for $\dot{m}_B < 0$.

Pump Model Outputs						
Quadrant	τ	\dot{m}_A	\dot{m}_B	\dot{H}_A	\dot{H}_B	\dot{H}_L
I ($\omega \geq 0$) ($\Delta P \geq 0$)	$\tau_T + \tau_L$	$\dot{m}_T - 2\dot{m}_L$	$\dot{m}_T - \dot{m}_L$	$\dot{m}_A(h_B + \Delta h - h_A)^*$	$\dot{m}_L \Delta h^*$	$\dot{m}_L(h_B + \Delta h - h_C)^*$
II ($\omega < 0$) ($\Delta P > 0$)	$-\tau_T - \tau_L$	$\dot{m}_T - 2\dot{m}_L$	$\dot{m}_T - \dot{m}_L$	0	$\frac{\dot{m}_L(h_A - h_B) - \dot{m}_T(h_A + \Delta h - h_B)}{}$	$\dot{m}_L(h_A - h_C)$
III ($\omega < 0$) ($\Delta P < 0$)	$-\tau_T - \tau_L$	$\dot{m}_T + \dot{m}_L$	$\dot{m}_T + 2\dot{m}_L$	$\dot{m}_L \Delta h^{\dagger}$	$-\dot{m}_B(h_A + \Delta h - h_B)^{\dagger}$	$\dot{m}_L(h_A + \Delta h - h_C)^{\dagger}$
IV ($\omega > 0$) ($\Delta P < 0$)	$\tau_T + \tau_L$	$\dot{m}_T + \dot{m}_L$	$\dot{m}_T + 2\dot{m}_L$	$\frac{\dot{m}_L(h_B - h_A) - \dot{m}_T(h_B + \Delta h - h_A)}{}$	0	$\dot{m}_L(h_B - h_C)$

8. Results

The ECD prototype presented in Section 4 was tested in the laboratory by controlling it to follow a sinusoidal position reference with a frequency of 0.4 Hz ($t_{\text{cycle}} = 2.5$ s), reaching maximum cylinder and motor speeds of ± 300 mm/s and ± 3600 RPM, respectively. A constant load force of 5 kN is requested by the load cylinder, but due to friction and load dynamics, this is found to be varying between 3.9 kN and 5.7 kN. The test continued for a period of three hours until thermal equilibrium was reached. Oil temperatures were measured using four thermocouples (see position in Figure 10a) with an accuracy of ± 0.5 K. The surface temperatures of the prototype were monitored by a thermo-graphic camera having an accuracy of ± 1.5 K. The measured load force and the position reference were used as the simulation inputs. The derived governing equations were simulated in MatLAB Simulink using the ODE45-solver, with a maximum stepsize of $1/5000$ s. Using a laptop with an Intel i7-10610 1.8 GHz processor, a 10 min simulation of the *benchmark* model was completed within 20 min, whereas the simulation of the *reduced* model was completed within 13 min.

8.1. Loss Behaviour

As illustrated in the previous section, the modelled temperature is rather sensitive towards inaccuracies between actual and modelled heat losses. Therefore, the simulated and measured loss behaviour is compared in Figure 12.

Figure 12b,d,f show a good coherence between the measured and simulated pressure in all control volumes. For the pressure in the piston chamber (p_A), the oscillation frequency is modelled fairly accurately while the measured damping is slightly larger than the modelled damping. Interestingly, it is found that there are no noticeable differences between the pressures modelled in the *benchmark* and the *reduced* models, even though the dynamic pressure–temperature coupling is neglected in the *reduced* model.

No noticeable differences are found between the two model complexities for any of the quantities visualised in Figure 12, expect for the accumulator pressure. Here small deviations of approximately 0.05 bar can be seen.

Figure 12a shows a good coherence between the measured and simulated position. Combined with the accurately modelled chamber pressures, this leads to the cylinder power being modelled accurately, as seen in Figure 12c.

Slight deviations exist between the modelled and estimated shaft torque and power during cylinder retraction, at ~ 2 s and ~ 4.5 s in Figure 12e. On average, it is found that the input power to the hydraulic system and the output power are modelled with an acceptable accuracy. This means that the losses are established with a sufficient degree of accuracy for anticipating the thermal behaviour. In other words, deviations between modelled and simulated temperatures are assessed to originate from inaccurate heat transfer models rather than loss model deviations.

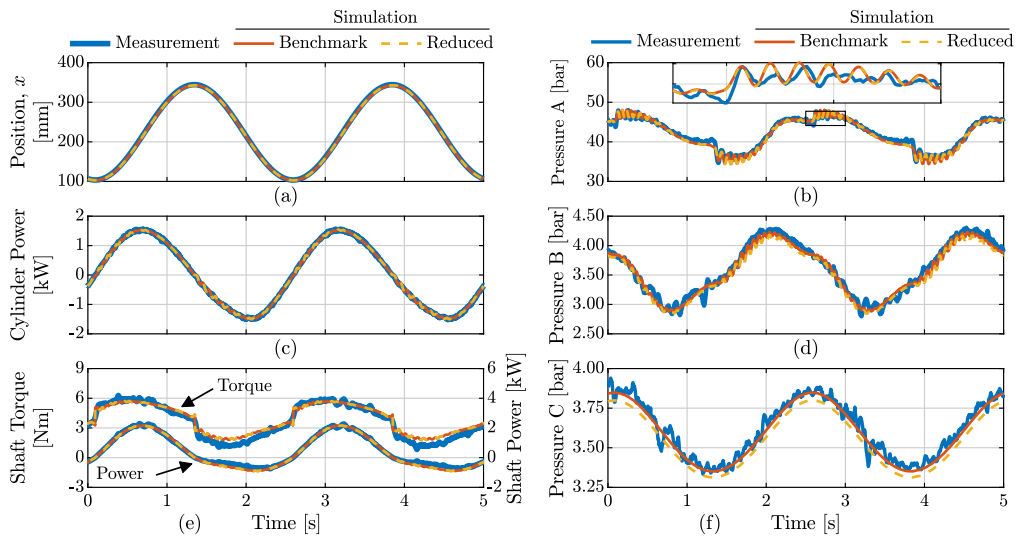


Figure 12. (a) Measured and simulated piston position. (b) Measured and simulated pressure in the piston chamber p_A . (c) Measured and simulated mechanical output power ($\dot{W} = \dot{x}F_{cyl}$). (d) Measured and simulated pressure in the rod chamber p_B . (e) Measured and simulated shaft torque and shaft power ($\dot{W} = \omega\tau$). (f) Measured and simulated accumulator pressure.

8.2. Static Temperatures

Even though the derived models are dynamic models, the transient temperature development is not important in some applications. If a system is going to perform the same task 24 h a day for 20 years, it is not important if static temperatures are reached after 10 min or 10 h. In this situation, only the static temperatures are relevant to ensure that the oil temperature stays within limits.

Figure 13a compares the *benchmark* modelled oil and surface temperatures with the measured values. Regarding the surface temperatures, the high number of simulated thermal capacities in the *benchmark* model pays off in terms of the ability to fairly accurately model the qualitative temperature distribution, e.g., the model predicts that the motor is warmer than the pump and that the cylinder head is colder than the cylinder barrel. This information is lost in the *reduced* model due to the simplification of only including three thermal capacities. As seen in Figure 13b, only two different surface temperatures are modelled, i.e., the surface temperature of the accumulator and the lumped temperature of the remaining system.

The *benchmark* model in Figure 13a models all surface temperatures within ± 5.5 K. Furthermore the oil temperatures are estimated within approximately ± 1.5 K, except for the oil temperature in the rod side chamber, which is overestimated with approximately 3 K. This is assessed to be satisfactorily accurate for analysis purposes, e.g., to analyse the effect of changing certain parameters such as areas and emissivities on the thermal behaviour.

As mentioned, the *reduced* model in Figure 13b is not formulated such that it is capable of predicting the individual temperature distribution of the system. This is because all system components, except the accumulator, are lumped in a single thermal capacity. This was chosen to avoid parametrising a high number of forced convection and conduction resistances. The modelled surface temperature of the system components are somewhat in-between the highest system temperature of the motor and the lowest system temperature of the cylinder barrel. Given the reduced complexity of the model, this is the expected result, but it leads to deviations up to 6.4 K, considering the surface temperatures.

In terms of the modelled oil temperatures in the *reduced* model, these are overestimated by 1.4 K to 6.8 K. However, all modelled oil temperatures are larger than the measured, meaning that the simulated temperatures are conservative estimates, which is desired in terms of design tool applicability. For comparison, it can be noted that if the natural convection resistances have not been corrected for the ambient flow conditions, i.e., the idealised values are used, the modelled temperatures would be approximately 2 K larger, than the ones given in Figure 13b.

A trade-off between modelling complexity and accuracy is identified in the comparison between the *benchmark* and the *reduced* model. Due to the simple thermal network, which may be parametrised relatively easy, this is much more applicable in the design phase, compared to the *benchmark* model. Furthermore, the *reduced* model produces reasonably accurate and conservative temperature estimates, which may be valuable to have available in the design phase. In this manner, important choices related to the thermal design of the system can be made on a fairly informed basis.

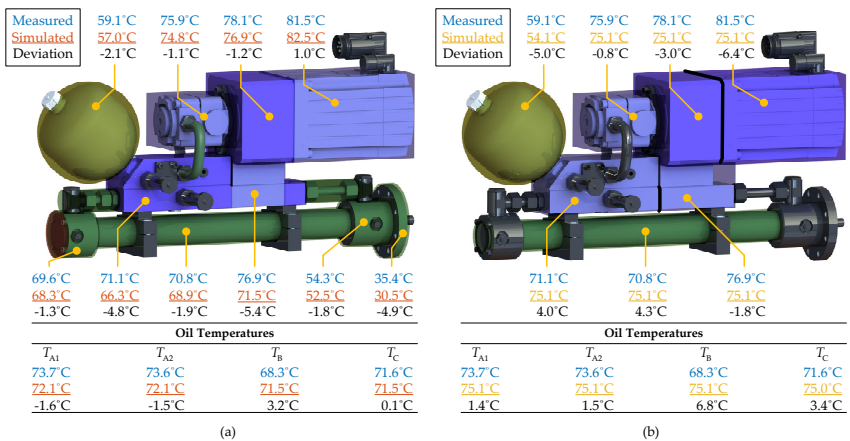


Figure 13. (a) Simulated steady state temperatures of the *benchmark* model compared to the measured static temperatures of the ECD prototype. (b) Simulated steady state temperatures of the *reduced* model compared to the measured static temperatures of the ECD prototype.

8.3. Transient Temperature

In applications where actuators are used on an on/off basis, i.e., the actuator is working for a limited time with cooling breaks in between the operating cycles, transient temperature behaviour may be relevant to optimise the thermal design. Figure 14 compares the simulated transient temperature responses of the two model complexities and the measurements.

A general thing to observe from Figure 14 is that the *benchmark* model for most of the thermal capacities predicts the transient temperature more accurately than the *reduced* model. The *reduced* model heats up too slowly during the first 45 min, which can be explained by all system components being lumped together. This means that the transient temperature response is governed by the components with large heat capacities. In this case, this is the motor and the mounting plates (Figure 14d,f,g). A reasonably transient fit is seen for these components in the *reduced* model.

To illustrate how neglecting the dynamic pressure–temperature coupling in the *reduced* model influences the transient temperature, consider Figure 14a, where the oil temperature in the piston chamber, T_A , is shown. In the *benchmark* model, temperature oscillations of ~ 0.2 K are seen, and is due to pressure oscillations and the dynamic coupling by the thermal expansion coefficient α . In the *reduced* model, the same pressure oscillations are present, as shown in Figure 12b, but this does not result in any temperature oscillations,

as the dynamic coupling is neglected. The temperature oscillations of the *benchmark* model are, however, insignificant with respect to the dominating dynamics; thus, it is found that neglecting the dynamic coupling i.e., defining $\tilde{\alpha} = 0$ is recommendable, as it enables a decoupled simulation of pressure and temperature dynamics.

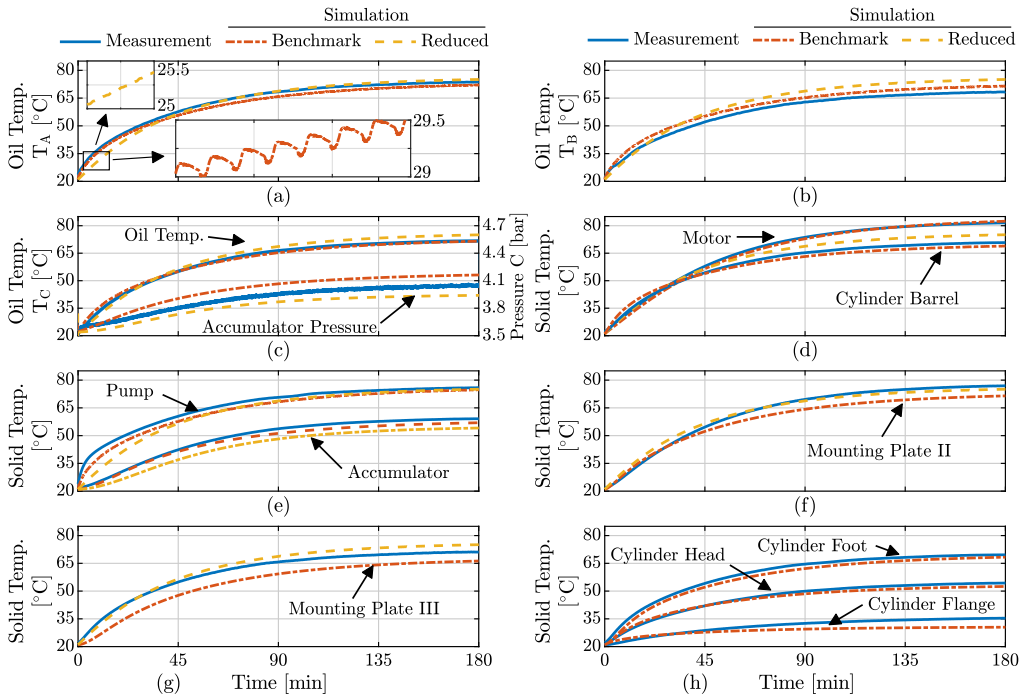


Figure 14. (a) Measured and simulated oil temperature in the piston chamber T_A . (b) Measured and simulated oil temperature in the rod chamber T_B . (c) Measured and simulated oil temperature and pressure in the accumulator T_C and p_C . (d) Measured and simulated surface temperatures of the motor and cylinder barrel. (e) Measured and simulated surface temperatures of the pump and accumulator shell. (f) Measured and simulated surface temperatures of mounting plate II. (g) Measured and simulated surface temperatures of mounting plate III. (h) Measured and simulated surface temperatures of the cylinder head, flange and foot. This is only available for the *benchmark* model, as these components are not included in the *reduced* model.

Another difference arising as a result of neglecting the pressure–temperature coupling is visible in Figure 14c, where the average accumulator pressure for one operating cycle is plotted. As the thermal expansion of the oil is defined as zero in the *reduced* model, the accumulator pressure only increases due to thermal expansion of the gas in the accumulator. For the *benchmark* model, the accumulator must contain a larger oil volume as the oil temperatures increase, resulting in a higher pressure compared to the *reduced* model. However, both model complexities predicts the measured pressure within ± 0.15 bar, which is fairly accurate.

To sum up the presentation of the modelling results, it is found that there is a trade-off in terms of accuracy and thermal modelling complexity. Both model complexities, however, predict the temperature with an accuracy found to be reasonable for design purposes. Note that this is partly possible because the losses of the ECD prototype was modelled with a high degree of accuracy. For most applications, the relatively small differences in terms of modelled temperatures cannot justify the formulation of the elaborate thermal network of the *benchmark* model compared with the *reduced* model. Note that the number of resistances

are reduced from 62 in the *benchmark* model to 7 in the *reduced* model. More importantly the seven resistances can be parametrised fully based on cylinder, motor, accumulator and manifold dimensions. These are available with some accuracy in the design phase of the system, thus making the *reduced* modelling framework a valuable tool for proper thermal design. To fully utilise the framework as a design tool, the modelling accuracy when including various heat transfer enhancing designs must be investigated. This may be the effect of including a fan, an oil cooler, heat pipes in the manifold or even a water cooled manifold.

9. Conclusions

In this paper, a lumped thermo-hydraulic model for electro-hydraulic compact drives (ECDs) was derived and experimentally verified. To investigate the trade-off between accuracy and modelling complexity, the paper presents two model complexities. It is found that neglecting the dynamic pressure–temperature coupling does not affect the main pressure and temperature dynamics significantly. Therefore, it is recommended to neglect this coupling as it simplifies model development. Additionally, it is found that an elaborate thermal resistance network predicts the oil and surface temperatures of an ECD prototype slightly more accurately than a significantly simplified model structure. For most applications, the small differences in terms of modelled temperatures cannot justify the formulation of the elaborate thermal network compared to the simplified network. The findings in the paper may lead to the acceptance of simplified thermo-hydraulic model structures that are applicable in the early design phase where only limited information about the system is available. This may be an important contribution toward proper thermal design of ECDs needed to expand the application range of the technology.

Author Contributions: Conceptualization: S.K., S.M. and L.S.; methodology: S.K., S.M. and L.S.; software: S.K.; experimental work: S.M.; data analysis: S.K. and S.M.; writing—original draft preparation: S.K.; review: S.M., L.S. and M.K.E.; editing: S.K.; supervision: L.S., M.K.E., T.O.A. and J.W.; project administration: M.K.E. and T.O.A.; funding acquisition: M.K.E. and T.O.A.. All authors have read and agreed to the published version of the manuscript.

Funding: This research was funded by the Research Council of Norway, SFI Offshore Mechatronics, project number 237896/O30.

Institutional Review Board Statement: Not applicable.

Informed Consent Statement: Not applicable.

Data Availability Statement: Not applicable.

Conflicts of Interest: The authors declare no conflict of interest.

Abbreviations

The following abbreviations are used in this manuscript:

CFD	Computational Fluid Dynamics
CV	Control Volume
ISV	Inverse Shuttle Valve
RPM	Revolutions per Minute
CS	Control Surface
ECD	Electro-Hydraulic Compact Drives
MBW	Moving Boundary Work

Appendix A. Nomenclature

Symbol	Description	Unit	Symbol	Description	Unit
α	Isobaric expansion coefficient	K^{-1}	\dot{H}	Enthalpy Flow	W
$\beta, \beta_{\text{eff}}, \beta_{\text{mech}}$	Isothermal, Effective and Mechanical Bulk Modulus	Pa	k	Thermal Conductivity	W/mK
ϵ	Emissivity	-	L_c	Characteristic Length	m
μ	Dynamic Viscosity	Ns/m ²	\dot{m}	Mass Flow	
ν	Specific Volume	m ³ /kg	\hat{n}	Normal Vector	
ρ, ρ_A, ρ_F	Mixture, Air, Oil density	kg/m ³	p	Pressure	Pa
ω	Shaft Speed	rad/s	\dot{Q}	Heat Flow	W
τ, τ_L, τ_T	Shaft Torque, Torque Losses, Theoretical Torque	Nm	R_{th}	Thermal Resistance	K/W
$\bar{\bullet}$	Property evaluated at average conditions		S	Entropy	J/K
$\bar{\bullet}$	Temperature Independent Property		T_s, T	(Surface) Temperature	K
$\bullet_A, \bullet_B, \bullet_C$	Quantify evaluated in CV A, B or C		u	Specific Internal Energy	J/kg
A, A_s	Area & Surface Area	m ²	U	Internal Energy	J
c_p, c_v	Isobaric & Isochoric Specific Heat	J/kgK	\hat{V}, \hat{V}	Fluid Speed & Velocity Vector	m/s
d, d_i	Diameter, Internal Diameter	m	V, V_x	Volume & Volume at p_0	m ³
F_L, F_F	Load & Cylinder Friction Force	N	\dot{W}	Rate of Work	W
h	Convection Heat Transfer Coefficient	W/m ² K	x	Piston Position	m
h	Specific Enthalpy	J/kg	z	Height in Gravitational Field	m

Appendix B. Modelling Parameters

Symbol	Description	Value	Symbol	Description	Value
α_0	Expansion Coefficient at p_0, T_0	0.00067 K ⁻¹	B_L	Cylinder Viscous Friction	285 Ns/m
β_0	Bulk Modulus at p_0, T_0	1.65 GPa	C_d	Orifice Discharge Coefficient	0.7
β_{mech}	Mechanical Bulk Modulus	0.3 GPa	c_{p0}	Oil Specific Heat Parameter	657 J/kgK
ϵ	Volumetric Air Ratio	0.01	D_p	Pump Displacement	6.3 cm ³ /rev
κ	Polytropic process coefficient	1.4	F_s	Static Friction	90 N
ρ_{F0}	Oil Density at p_0, T_0	873 kg/m ³	F_c	Coulomb Friction	15 N
σ	Stefan-Boltzmann Constant		g	Gravitational Acceleration	9.82 m/s ²
τ	Thermal Time Constant	3.5 s			
A_A	Cylinder Piston Area	12 cm ²	K_{sp}	Oil Specific Heat Parameter	4.21 J/kgK ²
A_B	Rod Chamber Area	8.8 cm ²	K_F	Friction Parameter	0.9 N/bar
A_o	Orifice Area	14 mm ²	M_L	Load Mass	112.5 kg

Symbol	Description	Value	Symbol	Description	Value
a_{k1}	Conductivity Parameter	0.17 W/mK	p_0	Atmospheric Pressure	1.01 bar
a_{k2}	Conductivity Parameter	97 $\mu\text{W/mK}^2$	p_{acc0}	Precharge Pressure	2.4 bar
$a_{\mu1}$	Viscosity Model Parameter	63 Ns/mm ²	R	Air Gas Constant	287 J/kgK
		bar			
$a_{\mu2}$	Viscosity Model Parameter	880 K	T_0	Reference Temperature	288.15 K
$a_{\mu3}$	Viscosity Model Parameter	178 K	T_{acc0}	Precharge Temperature	288.15 K
$a_{\mu4}$	Viscosity Model Parameter	334 bar	$T_{\text{rig}}, T_{\text{inf}}$	Test-rig & Ambient Temp.	296.15 K
$a_{\mu5}$	Viscosity Model Parameter	3.26 bar/K	V_{acc}	Volume of Accumulator	1.4 L

References

- Michel, S.; Weber, J. Energy-efficient Electrohydraulic Compact Drives for Low Power Applications. In Proceedings of the ASME/BATH Symposium on Fluid Power & Motion Control, Bath, UK, 12–14 September 2012.
- Wiens, T.; Deibert, B. A low-cost miniature electrohydrostatic actuator system. *Actuators* **2020**, *9*, 130. [\[CrossRef\]](#)
- Fassbender, D.; Minav, T. Finding the Perfect Match: Different Heavy-Duty Mobile Applications Call for Different Actuators. In Proceedings of the 1st International Electronic Conference on Actuator Technology (IeCAT 2020), Online, 23–27 November 2020.
- Costa, G.K.; Sepehri, N. Four-Quadrant Analysis and System Design for Single-Rod Hydrostatic Actuators. *J. Dyn. Syst. Meas. Control* **2018**, *141*. [\[CrossRef\]](#)
- Costa, G.K. A Critical Analysis of Valve-Compensated Hydrostatic Actuators: Qualitative Investigation. *Actuators* **2019**, *8*, 59. [\[CrossRef\]](#)
- Göytil, P.H.; Padovani, D.; Hansen, M.R. A novel solution for the elimination of mode switching in pump-controlled single-rod cylinders. *Actuators* **2020**, *9*, 20. [\[CrossRef\]](#)
- Imam, A.; Rafiq, M.; Jalayeri, E.; Sepehri, N. A Pump-Controlled Circuit for Single-Rod Cylinders that Incorporates Limited Throttling Compensating Valves. *Actuators* **2018**, *7*, 13. [\[CrossRef\]](#)
- Çalışkan, H.; Balkan, T.; Platin, B.E. A Complete Analysis and a Novel Solution for Instability in Pump Controlled Asymmetric Actuators. *J. Dyn. Syst. Meas. Control* **2015**, *137*, 091008. [\[CrossRef\]](#)
- Minav, T.; Panu, S.; Matti, P. Direct-Driven Hydraulic Drive Without Conventional Oil Tank. In Proceedings of the ASME/BATH Symposium on Fluid Power & Motion Control, Bath, UK, 10–12 September 2014; pp. 1–6. [\[CrossRef\]](#)
- Schmidt, L.; Roemer, D.B.; Pedersen, H.C.; Andersen, T.O. Speed-Variable Switched Differential Pump System for Direct Operation of Hydraulic Cylinders. In Proceedings of the ASME/BATH Symposium on Fluid Power & Motion Control, Chicago, IL, USA, 12–14 October 2015.
- Schmidt, L.; Groenkaer, M.; Pedersen, H.C.; Andersen, T.O. Position Control of an Over-Actuated Direct Hydraulic Cylinder Drive. *Control Eng. Pract.* **2017**, *64*, 1–14. [\[CrossRef\]](#)
- Brahmer, B. Hybrid Drive using Servo Pump in Closed Loop. In Proceedings of the 8th International Fluid Power Conference, Dresden, Germany, 26–28 March 2012; pp. 93–102.
- Cleasby, K.; Plummer, A.; Company, T. A novel high efficiency electrohydrostatic flight simulator motion system. In Proceedings of the ASME/BATH Symposium on Fluid Power & Motion Control, Bath, UK, 10–12 September 2008; pp. 437–449.
- Neubert, T. Elektro-hydraulische antriebssysteme mit drehzahlveränderbaren Pumpen. In Proceedings of the Internationales Fluidtechnisches Kolloquium, Aachen, Germany, 17–18 March 1998. (In German)
- Göytil, P.; Padovani, D.; Hansen, M.R. On the Energy Efficiency of Dual Prime Mover Pump-Controlled Hydraulic Cylinders. In Proceedings of the ASME/BATH Symposium on Fluid Power & Motion Control, Longboat Key, FL, USA, 7–9 October 2019.
- Ketelsen, S.; Padovani, D.; Andersen, T.O.; Ebbesen, M.K.; Schmidt, L. Classification and Review of Pump-Controlled Differential Cylinder Drives. *Energies* **2019**, *12*, 1293. [\[CrossRef\]](#)
- Grönkær, N.; Hansen, K.V.; Johansen, P.; Schmidt, L. Tribotronics in Electro-Hydraulic Actuator Technology: Improving Durability by Control. In Proceedings of the ASME/BATH Symposium on Fluid Power & Motion Control, Virtual, Online, 9–11 September 2020.
- Qu, S.; Fassbender, D.; Vacca, A.; Busquets, E. Formulation, Design and Experimental Verification of an Open Circuit Electro-Hydraulic Actuator. In Proceedings of the 2020 IEEE Global Fluid Power Society PhD Symposium (GFPS), Online, 19–21 October 2020.
- Qu, S.; Fassbender, D.; Vacca, A.; Busquets, E.; Neumann, U. A Closed Circuit Electro-Hydraulic Actuator with Energy Recuperation Capacity. In Proceedings of the 12th International Fluid Power Conference, Dresden, Germany, 12–14 October 2020; pp. 89–98.
- Zagar, P.; Kogler, H.; Scheidl, R.; Winkler, B. Hydraulic switching control supplementing speed variable hydraulic drives. *Actuators* **2020**, *9*, 129. [\[CrossRef\]](#)
- Schmidt, L.; Ketelsen, S.; Brask, M.H.; Mortensen, K.A. A Class of Energy Efficient Self-Contained Electro-Hydraulic Drives with Self-Locking Capability. *Energies* **2019**, *12*, 1866. [\[CrossRef\]](#)

22. Schmidt, L.; Ketelsen, S.; Padovani, D.; Mortensen, K.A. Improving the Efficiency and Dynamic Properties of a Flow Control Unit in a Self-Locking Compact Electro-Hydraulic Cylinder Drive. In Proceedings of the ASME/BATH Symposium on Fluid Power & Motion Control, Longboat Key, FL, USA, 7–9 October 2019.
23. Padovani, D.; Ketelsen, S.; Hagen, D.; Schmidt, L. A Self-Contained Electro-Hydraulic Cylinder with Passive Load-Holding Capability. *Energies* **2019**, *12*, 292. [\[CrossRef\]](#)
24. Ketelsen, S.; Andersen, T.O.; Ebbesen, M.K.; Schmidt, L. A Self-Contained Cylinder Drive with Indirectly Controlled Hydraulic Lock. *Model. Identif. Control.* **2020**, *41*, 185–205. [\[CrossRef\]](#)
25. Hagen, D.; Padovani, D.; Choux, M. A Comparison Study of a Novel Self-Contained Electro-Hydraulic Cylinder versus a Conventional Valve-Controlled Actuator—Part 1 : Motion Control. In *Actuators*; Multidisciplinary Digital Publishing Institute: Basel, Switzerland, 2019.
26. Ketelsen, S.; Kolks, G.; Andersen, T.O.; Schmidt, L.; Weber, J. Bootstrap Reservoir Concepts for Electro-hydraulic Compact Cylinder Drives. In Proceedings of the 12th International Fluid Power Conference, Dresden, Germany, 12–14 October 2020.
27. Ketelsen, S.; Padovani, D.; Ebbesen, M.K.; Andersen, T.O.; Schmidt, L. A Gasless Reservoir Solution for Electro-Hydraulic Compact Drives with Two Prime Movers. In Proceedings of the ASME/BATH Symposium on Fluid Power & Motion Control, Online, 9–11 September 2020.
28. Bucher Hydraulic. *AX Series Piston Pumps and Motors*; Bucher Hydraulic: Klettgau, Germany, 2019.
29. Hagen, D.; Padovani, D.; Choux, M. A Comparison Study of a Novel Self-Contained Electro-Hydraulic Cylinder versus a Conventional Valve-Controlled Actuator—Part 2: Energy Efficiency. In *Actuators*; Multidisciplinary Digital Publishing Institute: Basel, Switzerland, 2019.
30. Qu, S.; Fassbender, D.; Vacca, A.; Busquets, E. A High-Efficient Solution for Electro-Hydraulic Actuators with Energy Regeneration Capability. *Energy* **2021**, *216*, 119291. [\[CrossRef\]](#)
31. Minav, T.; Bonato, C.; Sainio, P.; Pietola, M. Position control of direct driven hydraulic drive. In Proceedings of the 9th International Fluid Power Conference, Aachen, Germany, 24–26 March 2014. [\[CrossRef\]](#)
32. Love, L.; Lanke, E.; Alles, P. *Estimating the Impact (Energy, Emissions and Economics) of the US Fluid Power Industry*; Technical Report December; Oak Ridge National Laboratory (ORNL): Oak Ridge, TN, USA, 2012. [\[CrossRef\]](#)
33. Ketelsen, S.; Schmidt, L.; Donkov, V.; Andersen, T. Energy saving potential in knuckle boom cranes using a novel pump controlled cylinder drive. *Model. Identif. Control* **2018**, *39*. [\[CrossRef\]](#)
34. Ketelsen, S.; Andersen, T.O.; Ebbesen, M.K.; Schmidt, L. Mass Estimation of Self-Contained Linear Electro-Hydraulic Actuators and Evaluation of the Influence on Payload Capacity of a Knuckle Boom Crane. In Proceedings of the ASME/BATH Symposium on Fluid Power & Motion Control, Longboat Key, FL, USA, 7–9 October 2019.
35. Padovani, D.; Ketelsen, S.; Schmidt, L. Downsizing the Electric Motors of Energy Efficient Self-Contained Electro-hydraulic Systems by Hybrid Technologies. In Proceedings of the ASME/BATH Symposium on Fluid Power & Motion Control, Online, 9–11 September 2020.
36. Minav, T.; Sainio, P.; Pietola, M. Efficiency of Direct Driven Hydraulic Setup in Arctic Conditions. In Proceedings of the Fourteenth Scandinavian International Conference on Fluid Power, Tampere, Finland, 20–22 May 2015.
37. Minav, T.; Papini, L.; Pietola, M. A Thermal Analysis of Direct Driven Hydraulics. In Proceedings of the 10th International Fluid Power Conference, Dresden, Germany, 8–10 March 2016; pp. 235–247.
38. Minav, T.; Pietola, M. A study on thermal behavior of pump-controlled actuator. In Proceedings of the 15th Scandinavian International Conference on Fluid Power, Linköping, Sweden, 7–9 June 2017. [\[CrossRef\]](#)
39. Grønkræ, N.; Nielsen, L.N.; Nielsen, F.Ø.; Ketelsen, S.; Schmidt, L. Multi-Objective Control of a Self-Contained Compact Electro-Hydraulic Cylinder Drive. In Proceedings of the 12th International Fluid Power Conference, Dresden, Germany, 12–14 March 2020.
40. Michel, S.; Schulze, T.; Weber, J. Energy-efficiency and thermo energetic behaviour of electrohydraulic compact drives. In Proceedings of the 9th International Fluid Power Conference, Aachen, Germany, 24–26 March 2014.
41. Michel, S.; Weber, J. Prediction of the thermo-energetic behaviour of an electrohydraulic compact drive. In Proceedings of the 10th International Fluid Power Conference, Dresden, Germany, 8–10 March 2016; pp. 219–234.
42. Sidders, J.A.; Tilley, D.G.; Chappie, P.J. Thermal-Hydraulic Performance Prediction in Fluid Power Systems. *Proc. Inst. Mech. Eng. Part I J. Syst. Control Eng.* **1996**, *210*, 231–242. [\[CrossRef\]](#)
43. Munson, B.R.; Young, D.F.; Okiishi, T.H.; Huebsch, W.W. *Fundamentals of Fluid Mechanics*, 6th ed.; John Wiley & Sons: Hoboken, NJ, USA, 2010.
44. Cengel, Y.A.; Boles, M.A. *Thermodynamics: An Engineering Approach*, 5th ed.; McGraw-Hill: New York, NY, USA, 2006.
45. Knežević, D. Analysis of Changes of Bulk Modulus of Mineral Oil. In Proceedings of the 12th International Conference on Tribology, Kragujevac, Serbia, 11–13 May 2011.
46. Cengel, Y.A.; Cimbala, J.M.; Turner, R.H. *Fundamentals of Thermal-Fluid Sciences*, 4th ed.; McGraw-Hill: New York, NY, USA, 2012; p. 1083.
47. Smith, J.; Van Ness, H.; Abbott, M. *Introduction to Chemical Engineering Thermodynamics*, 6th ed.; McGraw-Hill: New York, NY, USA, 2001.

48. Brun Hansen, H.; Windfeld Rasmussen, P. Modeling Hydraulic Accumulators for use in Wind Turbines. In Proceedings of the 13th Scandinavian International Conference on Fluid Power, Linköping, Sweden, 3–5 June 2013; Volume 92, pp. 327–334. [\[CrossRef\]](#)
49. Liniger, J. Design of Reliable Fluid Power Pitch Systems for Wind Turbines. Ph.D. Thesis, Aalborg University, Aalborg, Denmark, 2018.
50. Liniger, J.; Sepehri, N.; Soltani, M.; Pedersen, H.C. Signal-based gas leakage detection for fluid power accumulators in wind turbines. *Energies* **2017**, *10*, 331. [\[CrossRef\]](#)
51. Busquets, E.; Ivantysynova, M. Temperature prediction of displacement controlled multi-actuator machines. *Int. J. Fluid Power* **2013**, *14*, 25–36. [\[CrossRef\]](#)
52. Rituraj, R.; Vacca, A.; Morselli, M.A. Thermal modelling of external gear machines and experimental validation. *Energies* **2020**, *13*, 2920. [\[CrossRef\]](#)
53. Pfeffer, A.; Glück, T.; Kemmetmüller, W.; Kugi, A. Mathematical modelling of a hydraulic accumulator for hydraulic hybrid drives. *Math. Comput. Model. Dyn. Syst.* **2016**, *22*, 397–411. [\[CrossRef\]](#)
54. Moran, M.; Shapiro, H. *Fundamentals of Engineering Thermodynamics*, 5th ed.; John Wiley & Sons: Hoboken, NJ, USA, 2006.
55. Oppermann, M. A new approach for failure prediction in mobile hydraulic systems. Ph.D. Thesis, Hamburg University of Technology, Hamburg, Germany, 2007.
56. Chenggong, L.; Zongxia, J. Calculation Method for Thermal-Hydraulic System Simulation. *J. Heat Transf.* **2008**, *130*. [\[CrossRef\]](#)
57. Knežević, D.; Savić, V. Mathematical Modelling of Changing of Dynamic Viscosity, as a Function of Temperature and Pressure of Mineral Oils for Hydraulic Systems. *Mech. Eng.* **2006**, *4*, 27–34.
58. Michel, S.; Weber, J. Electrohydraulic Compact-drives for Low Power Applications considering Energy-efficiency and High Inertial Loads. In Proceedings of the 7th FPNI PhD Symposium on Fluid Power, Reggio Emilia, Italy, 27–30 June 2012; pp. 1–18.
59. Verein Deutscher Ingenieure. *VDI Heat Atlas*, 2nd ed.; VDI-Verlag GmbH: Dusseldorf, Germany, 2010. [\[CrossRef\]](#)
60. Verein Deutscher Ingenieure. *VDI-Wärmeatlas*, 11th ed.; Springer: Berlin/Heidelberg, Germany, 2013.
61. Jungnickel, G. *Simulation des Thermischen Verhaltens von Werkzeugmaschinen*; TU-Dresden: Dresden, Germany, 2010.
62. Ruderman, M. Full- and Reduced-order Model of Hydraulic Cylinder for Motion Control. In Proceedings of the IECON 2017-43rd Annual Conference of the IEEE Industrial Electronics Society, 29 October–1 November 2017.
63. Ottestad, M.; Hansen, N.; Hansen, M.R. Reducing the Static Friction in Hydraulic Cylinders by Maintaining Relative Velocity Between Piston and Cylinder. In Proceedings of the 12th International Conference on Control, Automation and Systems, Jeju Island, Korea, 17–21 October 2017.
64. Li, P.; Barkei, J.H. Hydraulic Effort and the Efficiencies of Pump and Motor with Compressible Fluid. In Proceedings of the ASME/BATH Symposium on Fluid Power & Motion Control, Online, 9–11 September 2020.

Part III

Appendices

Appendix A

Parameter List

Parameters used in Chapter 2

For convenience a figure showing the kinematics of the knuckle boom crane is repeated in Fig. A.1

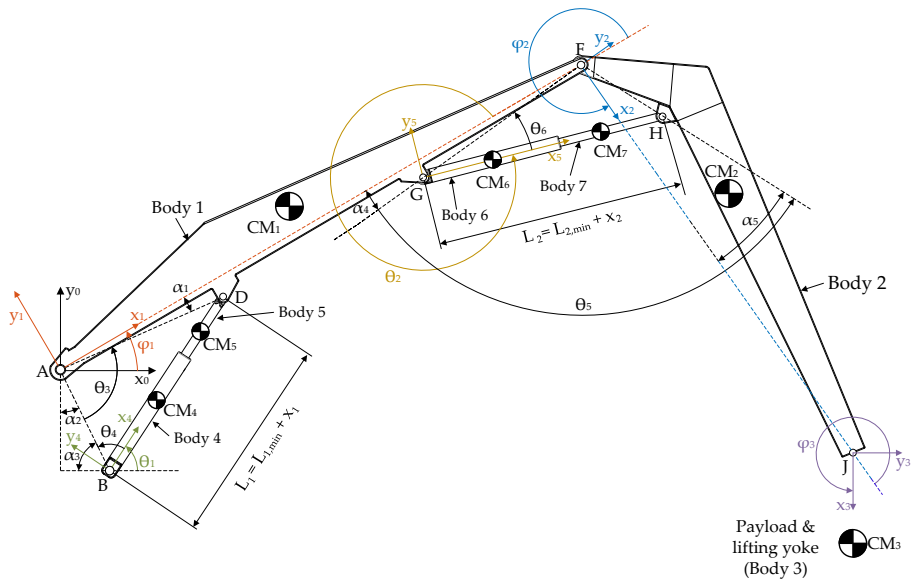


Fig. A.1: Sketch showing the knuckle boom crane and the relevant quantities used for derivation of the crane kinematics.

Appendix A. Parameter List

Table A.1: Mechanical parameters for knuckle boom crane model in Sec. 2.2

Parameter	Description	Value
\mathbf{s}_{A-CM1}	2D-vector from point A to CM_1	$\begin{bmatrix} 6.30 & 0.31 \end{bmatrix}^T \text{ m}$
\mathbf{s}_{A-F}	2D-vector from point A to F	$\begin{bmatrix} 13.76 & 0.00 \end{bmatrix}^T \text{ m}$
\mathbf{s}_{F-CM2}	2D-vector from point F to CM_2	$\begin{bmatrix} 4.43 & 1.08 \end{bmatrix}^T \text{ m}$
\mathbf{s}_{F-J}	2D-vector from point F to J	$\begin{bmatrix} 10.80 & 0.00 \end{bmatrix}^T \text{ m}$
\mathbf{s}_{J-CM3}	2D-vector from point J to CM_3	$\begin{bmatrix} 2.00 & 0.00 \end{bmatrix}^T \text{ m}$
\mathbf{s}_{A-B}	2D-vector from point A to B	$\begin{bmatrix} 1.12 & -2.30 \end{bmatrix}^T \text{ m}$
\mathbf{s}_{B-CM4}	2D-vector from point B to CM_4	$\begin{bmatrix} 1.73 & 0.00 \end{bmatrix}^T \text{ m}$
\mathbf{s}_{A-D}	2D-vector from point A to D	$\begin{bmatrix} 4.04 & -0.45 \end{bmatrix}^T \text{ m}$
\mathbf{s}_{D-CM5}	2D-vector from point D to CM_5	$\begin{bmatrix} -1.17 & 0.00 \end{bmatrix}^T \text{ m}$
\mathbf{s}_{A-G}	2D-vector from point A to G	$\begin{bmatrix} 9.36 & -0.41 \end{bmatrix}^T \text{ m}$
\mathbf{s}_{G-CM6}	2D-vector from point G to CM_6	$\begin{bmatrix} 1.70 & 0.00 \end{bmatrix}^T \text{ m}$
\mathbf{s}_{F-H}	2D-vector from point F to H	$\begin{bmatrix} 2.03 & 0.87 \end{bmatrix}^T \text{ m}$
\mathbf{s}_{H-CM7}	2D-vector from point H to CM_7	$\begin{bmatrix} -1.42 & 0.00 \end{bmatrix}^T \text{ m}$
α_1	Angle	0.110 rad, 6.31°
α_2	Angle	0.453 rad, 25.96°
α_3	Angle	1.118 rad, 64.04°
α_4	Angle	0.092 rad, 5.26°
α_5	Angle	0.403 rad, 23.11°
m_1	Mass of main boom	6000 kg
m_2	Mass of knuckle boom	3300 kg
m_3	Mass of payload	5000 kg and 10000 kg
m_4	Mass of main cylinder barrel	1535 kg
m_5	Mass of main cylinder rod	549 kg
m_6	Mass of knuckle boom cylinder barrel (Benchmark/VCD)	1186 kg
m_6	Mass of knuckle boom cylinder barrel including mass of actuator	2144 kg
m_7	Mass of knuckle boom cylinder rod	525 kg
J_1	Inertia of body 1 about CM_1	68289 kg m ²
J_2	Inertia of body 2 about CM_2	24954 kg m ²
J_3	Inertia of body 3 about CM_3	500/1000 kg m ²
J_4	Inertia of body 3 about CM_4	1561 kg m ²
J_5	Inertia of body 3 about CM_5	250 kg m ²
J_6	Inertia of body 3 about CM_6	2095 kg m ²
J_6	Inertia of body 3 about CM_6 (Benchmark/VCD)	1159 kg m ²
J_7	Inertia of body 3 about CM_7	355 kg m ²

Table A.1: Mechanical parameters for knuckle boom crane model in Sec. 2.2

Parameter	Description	Value
$L_{1,\min}$	Minimum length of cylinder 1	3.460 m
$L_{2,\min}$	Minimum length of cylinder 2	3.396 m
$L_{s,1}$	Stroke of cylinder 1	2.333 m
$L_{s,2}$	Stroke of cylinder 2	2.846 m
g	Gravitational acceleration	9.82 m/s ²
B_{CM3}	Viscous friction coefficient	25000 Nms/rad

Parameters used in Chapter 3

Table A.2: Steady state simulation parameters for benchmark actuation system in Sec. 3.1

Parameter	Description	Value
$\Delta p_{PCCV,nom}$	Nominal valve pressure drop	10 bar
Δp_{CV}	Valve pressure drop	3 bar
ϵ_{asynch}	Ratio of sheet metal	0.5 [-]
ω_{Fe}	Reference speed for loss calculation	50 Hz
ω_s	Synchronous angular velocity	60 Hz
A_{A1}	Piston area	616 cm ²
A_{A2}	Piston area	491 cm ²
A_{B1}	Rod side area	302 cm ²
A_{B2}	Rod side area	236 cm ²
$D_{p,max}$	Maximum pump displacement	250 cm ³ /rev
$D_{p,ref}$	Pump displacement of reference unit	28 cm ³ /rev
L_s	Stator inductance	9.61 mH
L_r	Rotor inductance	9.61 mH
L_m	Mutual/Magnetizing inductance	9.42 mH
$p_{CR,CBV}$	Valve cracking pressure	358 bar
$p_{LS,margin}$	Load sensing margin pressure	35 bar
$p_{OP,CBV}$	Valve fully open pressure	558 bar
p_T	Tank pressure, gauge	0 bar
P	Number of pole pairs (induction motor)	2 [-]
$K_{q,CBV}$	Valve flow gain	$60 \frac{L}{\min \text{ bar}^{0.5}}$
K_{Fe}	Parameter for power loss calculation	4 W/kg
m_{asynch}	Motor mass	1220 kg
$Q_{A,nom}$	Nominal valve flow	240 L/min
$Q_{B,nom}$	Nominal valve flow	130 L/min
R_{CBV}	Valve area ratio	5 [-]
R_s	Resistance of stator winding	18.18 mΩ

Appendix A. Parameter List

Table A.2: Steady state simulation parameters for benchmark actuation system in Sec. 3.1

Parameter	Description	Value
R_r	Resistance of rotor winding	9.96 m Ω
U_n	Nominal line-to-neutral voltage (RMS-value)	265 V

Table A.3: Steady state simulation parameters for ECD system in Sec. 3.2

Parameter	Description	Value
ϵ_{PMSM}	Ratio of sheet metal	0.5 [-]
λ_{pm}	Flux linkage	0.372 Wb
ω_{Fe}	Reference speed for loss calculation	50 Hz
A_{A1}	Piston area	616 cm ²
A_{A2}	Piston area	491 cm ²
A_{B1}	Rod side area	302 cm ²
A_{B2}	Rod side area	236 cm ²
$D_{\text{p},11}$	Pump displacement	26 cm ³ /rev
$D_{\text{p},12}$	Pump displacement	28 cm ³ /rev
$D_{\text{p},21}$	Pump displacement	26 cm ³ /rev
$D_{\text{p},22}$	Pump displacement	28 cm ³ /rev
$D_{\text{p,ref}}$	Pump displacement of reference unit	28 cm ³ /rev
K_{Fe}	Parameter for power loss calculation	4 W/kg
L_d	d -axis inductance	3 mH
L_q	q -axis inductance	3 mH
m_{PMSM11}	Motor mass	127 kg
m_{PMSM12}	Motor mass	127 kg
m_{PMSM21}	Motor mass	127 kg
m_{PMSM22}	Motor mass	127 kg
p_{set}	Pressure set-point, gauge	30 bar
p_{T}	Tank pressure, gauge	0 bar
P	Number of pole pairs (PMSM)	3 [-]
$P_{\text{inv,rated}}$	Rated inverter power	40 kW
R	Stator resistance of PMSM	46 m Ω

Table A.4: Simulation parameters for reference generation filter in Sec. 3.4.1

Parameter	Description	Value
ζ_{ref}	Damping ratio of reference filter	1 [-]
ω_{ref}	Eigenfrequency of reference filter	10 Hz
$\dot{x}_{1,\text{max}}$	Maximum allowed reference velocity	30 mm/s
$\dot{x}_{2,\text{max}}$	Maximum allowed reference velocity	40 mm/s

Table A.4: Simulation parameters for reference generation filter in Sec. 3.4.1

Parameter	Description	Value
$\ddot{x}_{1,\max}$	Maximum allowed reference acceleration	25 mm/s ²
$\ddot{x}_{2,\max}$	Maximum allowed reference acceleration	33 mm/s ²

Parameters used in Chapter 5

Table A.5: Parameters used for the dynamic simulation of simplified system, used to show the importance of mass flow simulations in Sec. 5.1.

Parameter	Description	Value
β_{0F}	Oil bulk modulus at p_0	16480 bar
Δp_{nom}	Nominal valve pressure drop	7 bar
ϵ	Volumetric content of free air at p_0	1 %
ρ_{0F}	Oil density at p_0	850 kg/m ³
ρ_{0G}	Air density at p_0	1.23 kg/m ³
A_A	Piston area	19.64 cm ²
B	Viscous damping coefficient	5000 Nm/s
D_p	Pump displacement	5 cm ³ /rev
F_{ext}	External Load	1500 N
K_x	Controller parameter	10000 rad/m/s
$K_{\dot{x}}$	Feedforward gain (A_A/D_p)	2467 rad/m
M	Load Mass	1000 kg
p_0	Atmospheric pressure	101325 Pa
p_t	Transition pressure	0.2 bar
Q_{nom}	Nominal valve flow	375 L/min
V_0	Initial chamber volume	1 L

Table A.6: Parameters used for the dynamic model of the ECD+ system in Chapter 5 and Appendix D. The ECD+ system is simulated in Chapter 7.

Parameter	Description	Value
β_{0F}	Oil bulk modulus at p_0	16480 bar
β_{mech}	Mechanical elasticity parameter	20000 bar
γ	Shaft friction directional parameter	2 s/rad
γ_F	Friction directional switching parameter	2000 s/m
$\Delta p_{CV,\text{nom}}$	Nominal valve pressure drop	0.8 bar
$\Delta p_{ISV,\text{nom}}$	Nominal valve pressure drop	3.5 bar
$\Delta p_{LH,\text{nom}}$	Nominal valve pressure drop	7 bar
$\Delta p_{SV,\text{nom}}$	Nominal valve pressure drop	13 bar

Appendix A. Parameter List

Table A.6: Parameters used for the dynamic model of the ECD+ system in Chapter 5 and Appendix D. The ECD+ system is simulated in Chapter 7.

Parameter	Description	Value
ϵ	Volumetric content of free air at p_0	1 %
ϵ	Surface emissivity	0.8 [-]
λ_{PM}	Flux Linkage	0.37 Wb
$\rho_{0\text{F}}$	Oil density at p_0	850 kg/m ³
$\rho_{0\text{G}}$	Air density at p_0, T_0	1.23 kg/m ³
σ	Stefan-Boltzmann constant	5.68 · 10 ⁻⁸ kg/s ³ /K ⁴
ω_ω	Desired shaft speed bandwidth	40 Hz
ω_{Fe}	Reference speed for loss calculation	50 Hz
ω_1	Desired bandwidth, current control	400 Hz
$\omega_{\text{V,CV}}$	Valve bandwidth	50 Hz
$\omega_{\text{V,ISV}}$	Valve bandwidth	50 Hz
$\omega_{\text{V,LH}}$	Valve bandwidth	20 Hz
$\omega_{\text{V,SV}}$	Valve bandwidth	20 Hz
A_{A}	Piston area	491 cm ²
A_{B}	Rod side area	236 cm ²
A_{C}	Area of charge piston	50 cm ²
A_{R}	Area of reservoir piston	804 cm ²
B_{x}	Viscous friction coefficient	1075 Ns/m
B_{z}	Viscous friction coefficient	1000 Ns/m
\hat{B}_{shaft}	Estimated viscous friction coefficient	0.01 Nms/rad
$D_{\text{p},1}$	Pump displacement	25 cm ³ /rev
$D_{\text{p},2}$	Pump displacement	28 cm ³ /rev
$D_{\text{p},\text{ref}}$	Pump displacement of reference unit	28 cm ³ /rev
$F_{\text{C,x}}$	Coulomb friction coefficient	310 N
$F_{\text{C,z}}$	Coulomb friction coefficient	6032 N
$F_{\text{S,x}}$	Static friction coefficient	1795 N
J_{shaft}	Total shaft inertia	0.1 kg m ²
K_{Fe}	Parameter for power loss calculation	4 W/kg
K_{Leak}	Valve leakage parameter	0.19 L/min/bar
$L_{\text{d}}, L_{\text{q}}$	PMSM inductance	3mH
m_{oil}	System oil mass	136 kg
m_{PMSM}	Mass of PMSM	127 kg
m_{steel}	System steel mass	2265 kg
M_{z}	Mass of bootstrap pistons and rod	49 kg
p_0	Atmospheric pressure	101325 Pa
$p_{\text{CR,CV}}$	Valve cracking pressure	0.2 bar
$p_{\text{CR,ISV}}$	Valve cracking pressure	0 bar
$p_{\text{CR,LH}}$	Valve cracking pressure	10 bar

Table A.6: Parameters used for the dynamic model of the ECD+ system in Chapter 5 and Appendix D. The ECD+ system is simulated in Chapter 7.

Parameter	Description	Value
$p_{OP,CV}$	Fully open valve pressure	0.3 bar
$p_{OP,ISV}$	Fully open valve pressure	0.5 bar
$p_{OP,LH}$	Fully open valve pressure	20 bar
p_t	Transition pressure	0.2 bar
P	Number of pole pairs	3 [-]
$P_{inv,rated}$	Rated inverter power	40 kW
$Q_{ISV,nom}$	Nominal valve flow	53 L/min
$Q_{LH,nom}$	Nominal valve flow	375 L/min
$Q_{CV,nom}$	Nominal valve flow	65 L/min
$Q_{SV,nom}$	Nominal valve flow	60 L/min
R	Stator resistance	46 mΩ
R	Gas constant for air	287 J/kg/K
T_0	Constant temperature for evaluation of fluid properties	15 °C
T_{amb}	Ambient temperature	20 °C
U_{DC}	DC-link voltage	750 V
v_{sw}	Stribeck curve decay parameter	7.5 mm/s
V_{0A}	Initial chamber volume	0.9 L
V_{0B}	Initial chamber volume	70.2 L
V_{0C}	Initial chamber volume	6.3 L
V_{0PA}	Initial chamber volume	0.5 L
V_{0PB}	Initial chamber volume	0.3 L
V_{0R}	Initial chamber volume	0.9 L
y_{leak}	Leakage flow switching parameter	0.025 [-]

Parameters used in Chapter 7

Table A.7: Control parameters used for the dynamic simulation of the ECD+ system.

Parameter	Description	Value
$\hat{\beta}_{eff,A}, \hat{\beta}_{eff,B}$	Estimated bulk moduli	15000 bar
ζ_{xx}	Desired damping ratio of motion loop.	1 [-]
ω_L	Desired pressure loop bandwidth	4 Hz
ω_L	Desired bandwidth, discrete implementation	2.67 Hz
ω_M	Desired pressure loop bandwidth	4 Hz
ω_M	Desired bandwidth, discrete implementation	2.67 Hz
ω_x, ω_{xx}	Desired motion loop dynamics frequency	0.8 Hz

Appendix A. Parameter List

Table A.7: Control parameters used for the dynamic simulation of the ECD+ system.

Parameter	Description	Value
\hat{B}_x	Estimated viscous friction coefficient	0 Ns/m
\hat{M}_{eq}	Estimated equivalent mass	208.75 ton
T_{sample}	Controller sample time	1 ms
\hat{V}_{0A}	Estimated initial volume	1.08 L
\hat{V}_{0B}	Estimated initial volume	70.7 L
\hat{V}_{0C}	Estimated initial volume	6.4 L
\hat{V}_{0PA}	Estimated initial volume	0.62 L
\hat{V}_{0PB}	Estimated initial volume	0.38 L

Parameters used in Appendix C

Table A.8: Simulation parameters for steady state simulation model of ECD+ system

Parameter	Description	Value
ϵ_{PMSM}	Ratio of sheet metal	0.5 [-]
$\Delta p_{ISV,nom}$	Nominal valve pressure drop	3.5 bar
$\Delta p_{LH,nom}$	Nominal valve pressure drop	7 bar
λ_{pm}	Flux linkage	0.372 Wb
ω_{Fe}	Reference speed for loss calculation	50 Hz
A_A	Piston area	491 cm ²
A_B	Rod side area	236 cm ²
A_C	Area of charge piston	50 cm ²
A_R	Area of reservoir piston	804 cm ²
B_z	Viscous friction coefficient	1000 Ns/m
$D_{p,1}$	Pump displacement	25 cm ³ /rev
$D_{p,2}$	Pump displacement	28 cm ³ /rev
$F_{C,z}$	Coulomb friction coefficient	6032 N
K_{Fe}	Parameter for power loss calculation	4 W/kg
L_d	d -axis inductance	3 mH
L_q	q -axis inductance	3 mH
m_{PMSM}	Motor mass	127 kg
p_{set}	Pressure set-point, gauge	27.8 bar
p_T	Tank pressure, gauge	0 bar
P	Number of pole pairs (PMSM)	3 [-]
$P_{inv,rated}$	Rated inverter power	40 kW
$Q_{ISV,nom}$	Nominal valve flow	53 L/min
$Q_{LH,nom}$	Nominal valve flow	375 L/min
R	Stator resistance of PMSM	46 m Ω

Appendix B

Steady State Model of Benchmark System

In Sec. 3.1 on page 39 the benchmark system or valve-controlled actuation system is used to assess the energy saving potential of the ECD system. Fig. B.1 repeats the schematic of this system.

The steady state hydraulic equations describing the benchmark system or valve-controlled actuation system used is given as:

$$\dot{p}_{A1}^0 = \left(Q_{A1} - \dot{x}_{1,\text{ref}} A_{A1} \right) \frac{\beta_{A1}}{V_{A1}} \Rightarrow \quad (\text{B.1})$$

$$Q_{A1} = \dot{x}_{\text{ref},1} A_{A1} \quad , \quad Q_{B1} = \dot{x}_{\text{ref},1} A_{B1} \quad (\text{B.2})$$

$$Q_{A2} = \dot{x}_{\text{ref},2} A_{A2} \quad , \quad Q_{B2} = \dot{x}_{\text{ref},2} A_{B2} \quad (\text{B.3})$$

$$F_{\text{req},1} = p_{A1} A_{A1} - p_{B1} A_{B1} \quad (\text{B.4})$$

$$F_{\text{req},2} = p_{A2} A_{A2} - p_{B2} A_{B2} \quad (\text{B.5})$$

where $\dot{x}_{1,\text{ref}}$, $\dot{x}_{2,\text{ref}}$ are desired cylinder speeds, $F_{\text{req},1}$ and $F_{\text{req},2}$ required cylinder forces and Q_{\bullet} , A_{\bullet} volume flows and areas defined in Fig. B.1. β_{A1} and V_{A1} are the bulk modulus of the oil-air mixture in chamber A1 and the chamber volume. These do not affect the steady state solution. Note that in this steady state analysis gauge pressures are utilised, meaning that p_T is equal 0 Pa (atmospheric pressure). Note that cylinder frictions are not included in this comparison, as it is assumed to be equivalent for both the VCD and ECD system.

The pressure drops across the pressure compensated proportional valves are calculated using the orifice equation, assuming the pressure compensator as

Appendix B. Steady State Model of Benchmark System

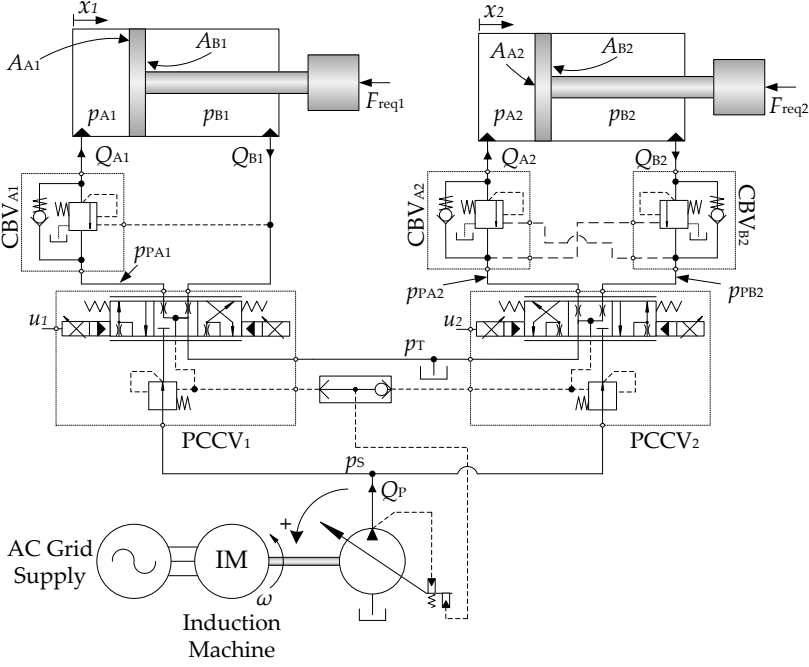


Fig. B.1: Schematic of the hydraulic actuation system used as a benchmark. The left cylinder is actuating the main boom, while the right cylinder is actuating the knuckle boom.

ideal, such that the input flow is a linear scaling of the control input u :

$$Q_{A1} = \begin{cases} Q_{A, \text{nom}} u_1 & \text{for } \dot{x}_{\text{ref},1} \geq 0 \\ u_1 \frac{Q_{A, \text{nom}}}{\sqrt{\Delta p_{\text{PCCV}, \text{nom}}}} \sqrt{p_{PA1} - p_T} & \text{for } \dot{x}_{\text{ref},1} < 0 \end{cases} \quad (\text{B.6})$$

$$Q_{B1} = \begin{cases} u_1 \frac{Q_{B, \text{nom}}}{\sqrt{\Delta p_{\text{PCCV}, \text{nom}}}} \sqrt{p_{B1} - p_T} & \text{for } \dot{x}_{\text{ref},1} \geq 0 \\ Q_{B, \text{nom}} u_1 & \text{for } \dot{x}_{\text{ref},1} \leq 0 \end{cases} \quad (\text{B.7})$$

$$Q_{A2} = \begin{cases} Q_{A, \text{nom}} u_2 & \text{for } \dot{x}_{\text{ref},2} \geq 0 \\ u_2 \frac{Q_{A, \text{nom}}}{\sqrt{\Delta p_{\text{PCCV}, \text{nom}}}} \sqrt{p_{PA2} - p_T} & \text{for } \dot{x}_{\text{ref},2} \leq 0 \end{cases} \quad (\text{B.8})$$

$$Q_{B2} = \begin{cases} u_2 \frac{Q_{B, \text{nom}}}{\sqrt{\Delta p_{\text{PCCV}, \text{nom}}}} \sqrt{p_{PB2} - p_T} & \text{for } \dot{x}_{\text{ref},2} \geq 0 \\ Q_{B, \text{nom}} u_2 & \text{for } \dot{x}_{\text{ref},2} \leq 0 \end{cases} \quad (\text{B.9})$$

where u_1 and u_2 are the inputs to the pressure compensated control valves, which in this steady state analysis equals the normalised valve opening ranging from -1 to 1. $Q_{A, \text{nom}}$, $Q_{B, \text{nom}}$ are nominal valve flows and $\Delta p_{\text{PCCV}, \text{nom}}$ nominal pressure drop. p_{\bullet} are pressures defined in Fig. B.1.

The pressure drops across the counter balance valves (CPV) are assumed to be constant (Δp_{CV} [126]) when flow is flowing into a cylinder chamber, i.e. through the check valve. When oil is leaving the chamber the pressure drop is calculated by the orifice equation:

$$Q_{A1} = -K_{q,CBV} y_{CBV,A1} \sqrt{p_{A1} - p_{PA1}} \quad \text{for } u_1 < 0 \quad (B.10)$$

$$Q_{A2} = -K_{q,CBV} y_{CBV,A2} \sqrt{p_{A2} - p_{PA2}} \quad \text{for } u_2 < 0 \quad (B.11)$$

$$Q_{B2} = K_{q,CBV} y_{CBV,B2} \sqrt{p_{B2} - p_{PB2}} \quad \text{for } u_2 > 0 \quad (B.12)$$

where $K_{q,CBV}$ is the flow gain and y_{\bullet} is the normalised valve opening. The normalised valve openings (y_{\bullet}) are calculated by:

$$y_{CBV,A1} = \begin{cases} 0 & \text{for } p_{A1} + p_{B1} R_{CBV} \leq p_{CR,CBV} \\ \frac{p_{A1} + p_{B1} R_{CBV} - p_{CR,CBV}}{p_{OP,CBV} - p_{CR,CBV}} & \text{for } p_{CR,CBV} < p_{A1} + p_{B1} R_{CBV} \leq p_{OP,CBV} \\ 1 & \text{for } p_{A1} + p_{B1} R_{CBV} > p_{OP,CBV} \end{cases} \quad (B.13)$$

$$y_{CBV,A2} = \begin{cases} 0 & \text{for } p_{A2} + p_{PB2} R_{CBV} \leq p_{CR,CBV} \\ \frac{p_{A2} + p_{PB2} R_{CBV} - p_{CR,CBV}}{p_{OP,CBV} - p_{CR,CBV}} & \text{for } p_{CR,CBV} < p_{A2} + p_{PB2} R_{CBV} \leq p_{OP,CBV} \\ 1 & \text{for } p_{A2} + p_{PB2} R_{CBV} > p_{OP,CBV} \end{cases} \quad (B.14)$$

$$y_{CBV,B2} = \begin{cases} 0 & \text{for } p_{B2} + p_{PA2} R_{CBV} \leq p_{CR,CBV} \\ \frac{p_{B2} + p_{PA2} R_{CBV} - p_{CR,CBV}}{p_{OP,CBV} - p_{CR,CBV}} & \text{for } p_{CR,CBV} < p_{B2} + p_{PA2} R_{CBV} \leq p_{OP,CBV} \\ 1 & \text{for } p_{B2} + p_{PA2} R_{CBV} > p_{OP,CBV} \end{cases} \quad (B.15)$$

where $p_{CR,CBV}$ and $p_{OP,CBV}$ are the cracking pressure of the CBV and the pressure at which the CBV is fully open respectively. R_{CBV} is the area ratio of the pilot. Note that the vent pressure of pilot is not included in the above equations, as these are vented to tank ($p_T=0$). The nonlinear system of the 16 equations given in Eqs. B.2 to B.15 is solved for the seven unknown pressures, the four volume flows, and the five valve openings (u_1 , u_2 , $y_{CBV,A1}$, $y_{CBV,A2}$, $y_{CBV,B2}$).

From this solution the steady state pump flow Q_p and the pump outlet pressure p_s can be found as ($p_{Ls,margin}$ is the pressure margin of the pressure con-

trolled pump) :

$$Q_P = Q_1 + Q_2 \quad (\text{B.16})$$

$$Q_1 = \begin{cases} Q_{A1} & \text{for } u_1 \geq 0 \\ |Q_{B1}| & \text{for } u_1 < 0 \end{cases} \quad Q_2 = \begin{cases} Q_{A2} & \text{for } u_2 \geq 0 \\ |Q_{B2}| & \text{for } u_2 < 0 \end{cases} \quad (\text{B.17})$$

$$p_s = \max(p_1, p_2) + p_{\text{LS,margin}} \quad (\text{B.18})$$

$$p_1 = \begin{cases} p_{\text{PA1}} & \text{for } u_1 \geq 0 \\ p_{\text{B1}} & \text{for } u_1 < 0 \end{cases} \quad p_2 = \begin{cases} p_{\text{PA2}} & \text{for } u_2 \geq 0 \\ p_{\text{PB2}} & \text{for } u_2 < 0 \end{cases} \quad (\text{B.19})$$

B.1 Steady State Model of Induction Motor

By calculating the required pump flow and pump outlet pressure, the required shaft torque, the shaft speed and the pump displacement may be calculated based on a dq -model of a electric induction machine connected in the star/ wye configuration [127]:

$$U_{qs} = R_s I_{qs} + \frac{d\phi_{qs}}{dt} + \omega_s \phi_{ds} \quad , \quad U_{qr} = R_r I_{qr} + \frac{d\phi_{qr}}{dt} + (\omega_s - \omega_r) \phi_{dr} \quad (\text{B.20})$$

$$U_{ds} = R_s I_{ds} + \frac{d\phi_{ds}}{dt} - \omega_s \phi_{qs} \quad , \quad U_{dr} = R_r I_{dr} + \frac{d\phi_{dr}}{dt} - (\omega_s - \omega_r) \phi_{qr} \quad (\text{B.21})$$

$$\phi_{qs} = L_s I_{qs} + L_m I_{qr} \quad , \quad \phi_{ds} = L_s I_{ds} + L_m I_{dr} \quad (\text{B.22})$$

$$\phi_{qr} = L_r I_{qr} + L_m I_{qs} \quad , \quad \phi_{dr} = L_r I_{dr} + L_m I_{ds} \quad (\text{B.23})$$

where U_{qs} , U_{ds} , U_{qr} , U_{dr} are the q -axis stator, d -axis stator, q -axis rotor and d -axis rotor voltages respectively and I_\bullet are the corresponding currents. L_s , L_r , L_m are the stator, rotor and magnetizing/mutual inductances, R_s , R_r the stator and rotor resistances and ω_s , ω_r are the synchronous electrical angular velocity and the angular electrical velocity of the rotor. Note that the rotor quantities are referred to the stator side, i.e. after turns ratio transformation [128].

By assuming the a, b, c voltages of the grid to be balanced, it is straightforward to show by using the Park transformation [129], that $U_{qs} = 0$ and U_{ds} equals the amplitude or maximum value of the a, b, c voltages (line-to-neutral). Additionally, the rotor windings are short circuited. By further assuming steady state Eqs. B.20 and B.21 reduces to:

$$U_{qs} = 0 = R_s I_{qs} + \omega_s (L_m I_{dr} + L_s I_{ds}) \quad (\text{B.24})$$

$$U_{ds} = \sqrt{2} U_n = R_s I_{ds} - \omega_s (L_m I_{qr} + L_s I_{qs}) \quad (\text{B.25})$$

$$U_{qr} = 0 = R_r I_{qr} + (\omega_s - \omega_r) (L_m I_{ds} + L_r I_{dr}) \quad (\text{B.26})$$

$$U_{dr} = 0 = R_r I_{dr} - (\omega_s - \omega_r) (L_m I_{qs} + L_r I_{qr}) \quad (\text{B.27})$$

B.1. Steady State Model of Induction Motor

U_n is the line-to-neutral voltage of the grid (RMS-value). The synchronous angular velocity (ω_s) is also defined by the grid, such that Eqs. B.24 to B.27 represent four equations with five unknowns ($I_{qs}, I_{ds}, I_{qr}, I_{dr}, \omega_r$). The last equation is found using the torque equation as [127]:

$$\tau_{\text{Asynch}} = \frac{3}{2}P \left(\phi_{ds} I_{qs} - \phi_{qs} I_{ds} \right) = \frac{3}{2}PL_m \left(I_{qs} I_{dr} - I_{ds} I_{qr} \right)$$

where τ_{Asynch} is the electromagnetic torque generated by the induction machine and P is the number of pole pairs. τ_{Asynch} is assumed to be equal to the pump load torque τ_L , i.e. the frictional losses of the motor has been neglected as these are assumed to be small compared to frictional losses of the pump and the pump load torque. In steady state, Newtons second law of motion may therefore be rewritten to:

$$\overset{0}{\omega} = \frac{\tau_{\text{Asynch}} - \tau_L}{J_{\text{shaft}}} \Rightarrow \tau_L = \frac{3}{2}PL_m \left(I_{qs} I_{dr} - I_{ds} I_{qr} \right) \quad (\text{B.28})$$

The mechanical angular velocity of the rotor shaft ω is linked to the electrical rotor velocity (ω_r) by the number of pole pairs as: $\omega P = \omega_r$. Utilising this and Eqs. B.24 to B.28, it is possible to solve for the shaft speed ω , as well as the four motor currents for a required τ_L . Equivalently it is possible to solve for the motor currents and τ_L for a given shaft speed ω . The closed form expressions for this is left out for brevity.

In the current study a 200 HP (approximately 150 kW) squirrel cage induction motor with two pole pairs and a rated line-to-line voltage of 460 V (RMS-value) is used and connected to the grid with a grid frequency of 60 Hz, i.e. $\omega_s = 60$ Hz. The remaining parameters, i.e. resistances and inductances have been exported from the library of the MathWorks SimScape software. Note that this software package is used solely for the purpose of extracting motor parameters. The parameters can be found in Tab. A.2 on page 255. The steady state speed/torque curve derived from Eq. B.24 to B.28 for this motor is seen in Fig. B.2.

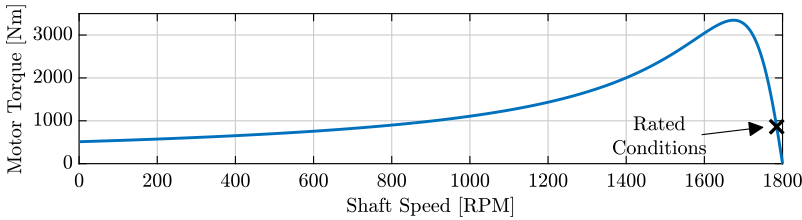


Fig. B.2: Torque characteristic as a function of shaft speed for the induction motor used in the theoretical study.

B.2 Loss Models of Induction Motor

The power input required by the induction motor (P_{asynch}) includes the output shaft power as well as copper and iron losses [91].

$$P_{\text{asynch}} = \tau_L \omega + P_{\text{Cu}} + P_{\text{Fe}} \quad (\text{B.29})$$

where P_{Cu} is the current dependent copper losses and P_{Fe} is the speed dependent iron/core losses caused by eddy currents and magnetic hysteresis [91]. These are modelled as [92]:

$$P_{\text{Cu}} = \frac{3}{2} R_s (I_{\text{ds}}^2 + I_{\text{qs}}^2) + \frac{3}{2} R_r (I_{\text{dr}}^2 + I_{\text{qr}}^2) \quad (\text{B.30})$$

$$P_{\text{Fe}} = K_{\text{Fe}} \underbrace{m_{\text{asynch}} \epsilon_{\text{asynch}}}_{m_{\text{Fe}}} \left(\frac{P \omega}{\omega_{\text{Fe}}} \right)^{3/2} \quad (\text{B.31})$$

where K_{Fe} is a loss model constant of 4 W per kilo sheet metal at an electrical angular velocity of ω_{Fe} . ϵ_{asynch} is the ratio of sheet metal relative to the total motor mass m_{asynch} .

The calculated induction motor efficiency ($\eta_{\text{asynch}} = \omega \tau_L / P_{\text{asynch}}$) is shown as a function of the motor torque in Fig. B.3.

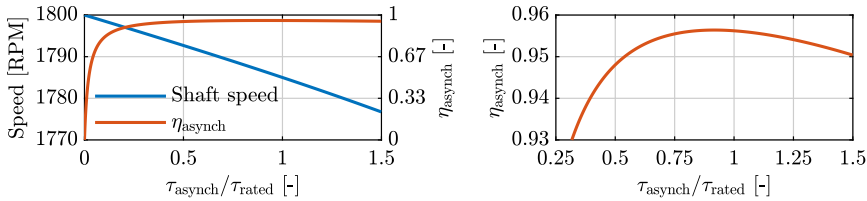


Fig. B.3: (a) Induction motor shaft speed and efficiency as a function of shaft torque. Rated torque is 861 Nm. (b) Induction motor efficiency as a function of shaft torque.

From Fig. B.3a it is seen that increasing the motor torque from 0 to 1.5 times the rated torque, i.e. from 0 Nm to 1291 Nm, only decreases shaft speed (increases motor slip) from 1800 RPM to 1776 RPM (1.3 %). Fig. B.3b, shows the efficiency from 25 % to 150% of the rated load. The peak efficiency is found to be 95.6% at 790 Nm (92% of rated torque) and 1786 RPM. For comparable sizes of induction machines, [81] states efficiencies of 94.1%, 94.9% and 94% for loadings of 50%, 75% and 100% of rated torque respectively. In [130] the efficiencies are stated to 95.9 %, 96.4% and 96.4% for the same loading. In Fig. B.3 those numbers are 94.8, 95.5%, 95.6%, showing that even the coarse loss models given in Eqs. B.30 and B.31 yield results which are rather accurate compared to the datasheet efficiencies.

Appendix C

Steady State Model of ECD+ System

The steady state solution to the modelling equations of the proposed ECD+ system incorporating both load holding valves and a bootstrap reservoir is derived. The ECD+ system was developed in Chapter, 4, and in sections 4.4.3 and 4.4.4, the steady solution is used to assess energy efficiency characteristics of ECD+ system. The simplified system schematics are shown in Fig. C.1.

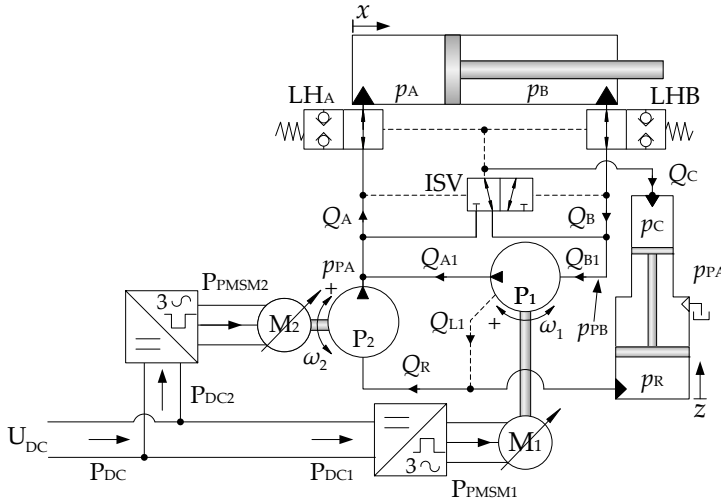


Fig. C.1: Simplified schematics of ECD+ system for knuckle boom cylinder system.

The steady state solution is found based on a required piston speed (\dot{x}_{ref}) and a required force (F_{req}), equivalently to the approach in Chapter 3. However note that the subscripts {1,2} used to denote the main and knuckle boom cylinder systems are omitted here, as only a steady state model for the knuckle boom cylinder is derived.

$$Q_A = \dot{x}_{\text{ref}} A_A \quad , \quad Q_B = \dot{x}_{\text{ref}} A_B \quad , \quad Q_{B1} = \begin{cases} Q_B - Q_C & \text{for } p_{PA} \geq p_{PB} \\ Q_B & \text{for } p_{PA} < p_{PB} \end{cases} \quad (\text{C.1})$$

$$Q_C = -A_C \dot{z} \quad , \quad Q_R = Q_{L1} - A_R \dot{z} \quad , \quad Q_{L1} = Q_{AL1} + Q_{BL1} \quad (\text{C.2})$$

$$p_A = \begin{cases} \frac{F_{\text{req}} + p_B A_B}{A_A} & \text{for } F_{\text{req}} \geq p_{\text{set}} (A_A - A_B) \\ p_{\text{set}} & \text{for } F_{\text{req}} < p_{\text{set}} (A_A - A_B) \end{cases} \quad (\text{C.3})$$

$$p_B = \begin{cases} p_{\text{set}} & \text{for } F_{\text{req}} \geq p_{\text{set}} (A_A - A_B) \\ \frac{p_A A_A - F_{\text{req}}}{A_B} & \text{for } F_{\text{req}} < p_{\text{set}} (A_A - A_B) \end{cases} \quad (\text{C.4})$$

$$p_{PA} = p_A + \frac{Q_A^2 \Delta p_{\text{nom,LH}}}{Q_{\text{nom,LH}}^2} \text{sign}(Q_A) \quad , \quad p_{PB} = p_B - \frac{Q_B^2 \Delta p_{\text{nom,LH}}}{Q_{\text{nom,LH}}^2} \text{sign}(Q_B)$$

$$p_C = \min(p_{PA}, p_{PB}) - \frac{Q_C^2 \Delta p_{\text{nom,ISV}}}{Q_{\text{nom,ISV}}^2} \text{sign}(Q_C) \quad (\text{C.5})$$

$$p_R = \frac{p_C A_C + F_{C,z} \text{sign}(\dot{z}) + B_z \dot{z}}{A_R} \quad , \quad \dot{z} = -\frac{1 - \alpha}{1 - \alpha_B} \frac{A_A}{A_R} \dot{x}_{\text{ref}} \quad (\text{C.6})$$

where Q_{\bullet} and p_{\bullet} are volume flows and chamber pressures (gauge) according to Fig. C.1. Q_{AL1} and Q_{BL1} are external pump leakages of pump 1 from the PA and PB chambers respectively. p_{set} is the controlled lower chamber pressure, here $p_{\text{set}} = 27.8$ bar (gauge). A_A , A_B are the piston and rod side areas of the cylinder respectively and A_R , A_C are the reservoir and charge chamber piston areas respectively. α , α_B are the area ratios of the cylinder and bootstrap reservoir. $Q_{\text{nom},\bullet}$ and $\Delta p_{\text{nom},\bullet}$ are the nominal flows and pressure drops across the load holding valves and inverse shuttle valve. $F_{C,z}$, B_z is the Coulomb friction and viscous friction coefficient for the bootstrap reservoir pistons. All parameters used for this steady state study is found in Tab. A.8 on page 260.

The required shaft speeds of the pumps are calculated based on the required flows and the pump leakage losses. The leakage losses are based on the losses of a reference unit, equivalently to the approach in Chapter 3.

Based on Fig. 3.7 on page 47 the shaft speeds and torques are calculated based the geometric pump flow ($Q_T = \omega D_p$) and the external leakage flows

$(Q_{BL1}, Q_{AL1}, Q_{AL2})$ and torque losses as:

$$Q_{B1} = Q_{T1} + Q_{BL1} = \omega_1 D_{p,1} + \lambda_1^2 Q_{\text{loss,ref}}(\omega_{\text{ref}\lambda 1}, p_{PB}) \Rightarrow \quad (\text{C.7})$$

$$\omega_1 = \frac{Q_{B1} - \lambda_1^2 Q_{\text{loss,ref}}(\omega_{\text{ref}\lambda 1}, p_{PB})}{D_{p,1}} \quad (\text{C.8})$$

$$Q_R = Q_{T2} - Q_{AL2} = Q_{L1} - A_R \dot{z} \quad (\text{C.9})$$

$$= \omega_2 D_{p,2} - \lambda_2^2 Q_{\text{loss,ref}}(\omega_{\text{ref}\lambda 2}, p_{PA}) = Q_{L1} - A_R \dot{z} \Rightarrow \quad (\text{C.10})$$

$$\omega_2 = \frac{Q_{L1} + \lambda_2^2 Q_{\text{loss,ref}}(\omega_{\text{ref}\lambda 2}, p_{PA}) - A_R \dot{z}}{D_2} \quad (\text{C.11})$$

$$Q_{L1} = \lambda_1^2 Q_{\text{loss,ref}}(\omega_{\text{ref}\lambda 1}, p_{PA}) + \lambda_1^2 Q_{\text{loss,ref}}(\omega_{\text{ref}\lambda 1}, p_{PB}) \quad (\text{C.12})$$

$$\tau_1 = D_{p,1} (p_{PA} - p_{PB}) + \lambda_1^3 \tau_{\text{loss,ref}}(\omega_{\text{ref}\lambda 1}, p_{PA} + p_{PB}) \text{sign}(\omega_1) \quad (\text{C.13})$$

$$\tau_2 = D_{p,2} (p_{PA} - p_R) + \lambda_2^3 \tau_{\text{loss,ref}}(\omega_{\text{ref}\lambda 2}, p_{PA} + p_R) \text{sign}(\omega_2) \quad (\text{C.14})$$

where ω_1, ω_2 are shaft speeds according to Fig. C.1. $D_{p,1}, D_{p,2}$ are the pump displacements for pump 1 and 2. λ_i is a scaling factor used to scale pump losses of a reference unit evaluated at the reference pump speed $\omega_{\text{ref}\lambda,i}$ [87]. The leakage and torque losses of the reference unit is equivalent to the ones used for the VCD and ECD systems in Chapter 3 as showed in Fig. 3.2 on page 41. The scaling factors λ_i and reference speeds are found by [87]:

$$\lambda_i = \sqrt[3]{\frac{D_{p,i}}{D_{p,\text{ref}}}} \quad , \quad \omega_{\text{ref}\lambda,i} = \lambda_i |\omega_i| \quad , \quad i = \{1, 2\} \quad (\text{C.15})$$

Note, that absolute value of the shaft speed is used evaluate the losses of the reference unit, as data is only available for positive shaft speeds, and when working as a pump. Losses are assumed equivalent for all operation quadrants, and always defined positively.

Based on the above equations it is straightforward to calculate the chamber pressures for the required cylinder forces. The shafts speed however both depends on the required output pump flows and the leakage losses which also depends on shaft speed. As the leakage losses are only available as look up tables, the shaft speeds are found by solving the equations iteratively.

The power losses of the inverter and permanent magnet synchronous machines are modelled according to the loss models elucidated in Sec. 3.2.2.

Appendix D

Dynamic Model Derivation

This appendix presents the component models of the ECD+ system modelled in Chapter 5. This includes mass and enthalpy flow rate models and models of the heat transfer to the ambience.

D.1 Mass and Enthalpy Flow Rates

Mass and enthalpy flow rate models are presented in this section.

D.1.1 Pump Model

A pump model expressing the steady state relationship between modelling inputs and outputs is needed. The inputs are the shaft speed and the states in the control volumes adjacent to the pump, i.e. pressure, temperature and specific enthalpy. Model outputs include the mass and enthalpy flow rates and the shaft torque, according to the schematic in Fig. D.1. Such a model has been derived in Paper F. The model has been slightly modified for modelling of the four quadrant pump to account for external leakages occurring from both lines PA and PB to the pump housing (p_R) in Fig. D.1, where the closed circuit pump is used as an example here, and internal leakage is neglected.

Information or measurements of the loss behaviour of the pump is required. Steady-state loss measurements of a reference pump with displacement $D_{p,ref}$ is scaled to the desired pump displacement D_p . The considered drive system has been dimensioned using the Bosch Rexroth A10 FZO and FZG pump

Appendix D. Dynamic Model Derivation

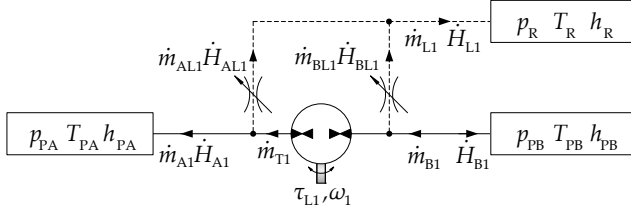


Fig. D.1: Schematic visualising the pump modelling approach. Model inputs are the shaft speed and the states, i.e. pressure, temperature and specific enthalpy in the control volumes adjacent to the pump. Model outputs are the shaft torque, mass and enthalpy flow rates.

series. Loss information for this specific pump has not been available. As an alternative loss measurements for an 28 cm³/rev Bosch Rexroth A4FO pump is available in [88], and used as a reference pump. This information was also used in the steady state modelling section, and visualisations of the pump losses (leakage and torques losses) can be found in Fig. 3.2 on page 41. As both the Bosch Rexroth A10 and the A4 pumps are slipper type axial piston pumps with nine pistons, the loss behaviour are assumed to be comparable for these pump types.

In Paper F, the isentropic temperature increase during the pumping process is included. As the current model assumes the thermal expansion coefficient to be 0, $\alpha = 0$, the pumping process is in fact isothermal, as [131]:

$$S = f(T, p) \quad \Rightarrow \quad dS = \left(\frac{\partial S}{\partial T} \right)_p dT + \left(\frac{\partial S}{\partial p} \right)_T dp = \frac{c_p}{T} dT - \alpha v dp \quad (D.1)$$

$$\xrightarrow{dS=0} \quad dT = \frac{\alpha^0 T}{\rho c_p} dp = 0 \quad (D.2)$$

S is the entropy modelled as a function of temperature and pressure. p_{in} and p_{out} is either of the adjacent chamber pressures depending on the direction of pump rotation.

The change in specific enthalpy of the fluid undergoing a pressure change in the pump is given by:

$$dh = c_p dT^0 + v \left(1 - T \alpha^0 \right) dp = \frac{1}{\rho} dp \quad \xrightarrow{\text{Approximation}} \quad (D.3)$$

$$\Delta h \cong \frac{1}{\bar{\rho}} (p_{out} - p_{in}) \quad (D.4)$$

where $\bar{\rho}$ is the average density of the fluid in adjacent chambers.

The expressions for modelling the closed circuit pump (pump 1) is exemplified next. It is straightforward to use these for modelling the open circuit

D.1. Mass and Enthalpy Flow Rates

pump (pump 2) as well, but for brevity these expressions are not shown.

The ideal mass flow, \dot{m}_{T1} , the mass leakage flows, \dot{m}_{L1} , the chamber mass flows, \dot{m}_{A1} , \dot{m}_{B1} , the ideal pump torque, τ_{T1} , and the torque loss, $\tau_{\text{loss},1}$ for pump 1 are modelled as:

$$\dot{m}_{T1} = \omega_1 D_{p,1} \bar{\rho}_{\text{PA-PB}} \quad \dot{m}_{L1} = \dot{m}_{\text{AL1}} + \dot{m}_{\text{BL1}} \quad (\text{D.5})$$

$$\dot{m}_{\text{AL1}} = \lambda_1^2 Q_{\text{loss,ref}}(\omega_{\text{ref}\lambda 1}, p_{\text{PA}}) \bar{\rho}_{\text{PA-R}} \quad \dot{m}_{\text{BL1}} = \lambda_1^2 Q_{\text{loss,ref}}(\omega_{\text{ref}\lambda 1}, p_{\text{B}}) \bar{\rho}_{\text{PB-R}} \quad (\text{D.6})$$

$$\dot{m}_{A1} = \dot{m}_{T1} - \dot{m}_{\text{AL1}} \quad \dot{m}_{B1} = \dot{m}_{T1} + \dot{m}_{\text{BL1}} \quad (\text{D.6})$$

$$\tau_{T1} \omega_1 = \dot{m}_{T1} \Delta h_1 \quad \Rightarrow \quad \tau_{T1} = D_{p,1} (p_{\text{out}} - p_{\text{in}}) \quad (\text{D.7})$$

$$\tau_{\text{loss},1} = \lambda_1^3 \tau_{\text{loss,ref}}(\omega_{\text{ref}\lambda 1}, p_{\text{A}} + p_{\text{B}}) \quad (\text{D.8})$$

$$\lambda_1 = \sqrt[3]{\frac{D_{p,1}}{D_{p,\text{ref}}}} \quad \omega_{\text{ref}\lambda 1} = \lambda_1 |\omega_1| \quad (\text{D.9})$$

where ω_1 is the shaft speed, $D_{p,1}$ the geometric pump displacement and $\bar{\rho}_\bullet$ is the average fluid density. $Q_{\text{loss,ref}}$ and $\tau_{\text{loss,ref}}$ are the leakage flow and torque loss of the reference unit as a function of pressure and shaft speed shown in Fig. 3.2 on page 41. These losses are scaled from the reference pump with displacement $D_{p,\text{ref}}$ to the desired pump displacement, using the scaling factor λ_1 [87]. For the measurements obtained in [88], used to construct the loss maps in Fig. 3.2, the reference unit was operated in pump mode, with a supply pressure of 6 bar. As no information is available concerning how the leakage losses changes for changing supply pressures, the evaluation of the leakage losses is done separately for each chamber (\dot{m}_{AL1} and \dot{m}_{BL1}). The external leakage from the 6 bar supply line to the pump housing, occurring during the experiments is therefore included as leakage from the high pressure chamber, as the measured leakage is fully ascribed to the high pressure line when constructing the leakage map. Equivalently, no information is available concerning how the torque losses changes for changing supply pressures. As an conservative estimate the torque losses are evaluated using the sum of chamber pressures. The losses are assumed always positive and equivalent in all operation quadrants [37].

The shaft torque is calculated by including the scaled torque losses from Eq. D.8, according to:

$$\tau_{L1} = \begin{cases} \tau_{T1} + \tanh(\gamma \omega_1) \tau_{\text{loss},1} & \text{if } \omega_1 \geq 0 \\ -\tau_{T1} + \tanh(\gamma \omega_1) \tau_{\text{loss},1} & \text{if } \omega_1 < 0 \end{cases} \quad (\text{D.10})$$

The calculation of enthalpy flow rates, defined in Figure D.1, depend on the operation quadrant, i.e. the direction of pump rotation and the pressure difference across the pump. The enthalpy flow rates \dot{H}_{A1} , \dot{H}_{B1} , \dot{H}_{AL1} , \dot{H}_{BL1} and

\dot{H}_{L1} is calculated according to:

$$\dot{H}_{A1} = \begin{cases} \dot{m}_{A1}(h_{PB} + \Delta h_1 - h_{PA}) & \text{if } \dot{m}_{A1} \geq 0 \\ 0 & \text{if } \dot{m}_{A1} < 0 \end{cases} \quad (D.11)$$

$$\dot{H}_{B1} = \begin{cases} |\dot{m}_{B1}|(h_{PA} + \Delta h_1 - h_{PB}) & \text{if } \dot{m}_{B1} \leq 0 \\ 0 & \text{if } \dot{m}_{B1} > 0 \end{cases} \quad (D.12)$$

$$\dot{H}_{AL1} = \begin{cases} \dot{m}_{AL1}(h_{PB} + \Delta h_1 - h_R) & \text{if } \dot{m}_{T1} \geq \dot{m}_{AL1} \text{ and } \dot{m}_{T1} \geq 0 \\ \dot{m}_{T1}(h_{PB} + \Delta h_1 - h_R) + (\dot{m}_{AL1} - \dot{m}_{T1})(h_{PA} - h_R) & \text{if } \dot{m}_{T1} < \dot{m}_{AL1} \text{ and } \dot{m}_{T1} \geq 0 \\ \dot{m}_{AL1}(h_{PA} - h_R) & \text{if } \dot{m}_{T1} < 0 \end{cases} \quad (D.13)$$

$$\dot{H}_{BL1} = \begin{cases} \dot{m}_{BL1}(h_{PA} + \Delta h_1 - h_R) & \text{if } |\dot{m}_{T1}| \geq \dot{m}_{BL1} \text{ and } \dot{m}_{T1} \leq 0 \\ |\dot{m}_{T1}|(h_{PA} + \Delta h_1 - h_R) + (\dot{m}_{BL1} - |\dot{m}_{T1}|)(h_{PB} - h_R) & \text{if } |\dot{m}_{T1}| < \dot{m}_{BL1} \text{ and } \dot{m}_{T1} \leq 0 \\ \dot{m}_{BL1}(h_{PB} - h_R) & \text{if } \dot{m}_{T1} > 0 \end{cases} \quad (D.14)$$

D.1.2 Valve Models

The valve mass flows for the check valves, load holding valves and the safety valves are calculated based on the two-regime flow model presented in Eqs. 5.4 and 5.8 on page 88 and 91 respectively. Note that the safety valves are normally open, i.e. the flow path are fully open at $y_{SV} = 0$, such that the valve opening for flow calculations are found as $y = 1 - y_{SV}$.

To model the *open transition behaviour* of the inverse shuttle valve, i.e. the flow occurring as the spool passes the zero-position, laminar leakage flow has been added to the two-regime flow model. The mass flows, \dot{m}_{ISA} and \dot{m}_{ISB} are thus modelled as:

$$\dot{m}_{ISA} = \underbrace{-\bar{\rho}_{PA-C} y_3 \left(\begin{cases} \frac{Q_{ISV,nom}}{\sqrt{\Delta p_{ISV,nom}}} \sqrt{|p_{PA} - p_C|} \text{sign}(p_{PA} - p_C), p_{PA} - p_C \geq p_t \\ \left(\frac{3 Q_{ISV,nom}(p_{PA} - p_C)}{2\sqrt{\Delta p_{ISV,nom}} p_t} - \frac{Q_{ISV,nom}(p_{PA} - p_C)|p_{PA} - p_C|}{2\sqrt{\Delta p_{ISV,nom}} p_t^3} \right), p_{PA} - p_C < p_t \end{cases} \right)}_{\text{Two Regime Flow Model. For } y_3 \leq 0} + \underbrace{\bar{\rho}_{PA-C} K_{Leak} (p_{PA} - p_C) e^{\frac{-|y_3|}{y_{leak}}}}_{\text{Leakage Flow Model}} \quad (D.15)$$

D.1. Mass and Enthalpy Flow Rates

$$\dot{m}_{\text{ISB}} = \bar{\rho}_{\text{PB-C}} y_3 \left(\underbrace{\left(\begin{cases} \frac{Q_{\text{ISV,nom}}}{\sqrt{\Delta p_{\text{ISV,nom}}}} \sqrt{|p_{\text{PB}} - p_{\text{C}}|} \text{sign}(p_{\text{PB}} - p_{\text{C}}), p_{\text{PB}} - p_{\text{C}} \geq p_{\text{t}} \\ \left(\frac{3 Q_{\text{ISV,nom}} (p_{\text{PB}} - p_{\text{C}})}{2 \sqrt{\Delta p_{\text{ISV,nom}} p_{\text{t}}}} - \frac{Q_{\text{ISV,nom}} (p_{\text{PB}} - p_{\text{C}}) |p_{\text{PB}} - p_{\text{C}}|}{2 \sqrt{\Delta p_{\text{ISV,nom}} p_{\text{t}}^3}} \right), p_{\text{PB}} - p_{\text{C}} < p_{\text{t}} \end{cases} \right)}_{\text{for } y_3 > 0} \right) + \bar{\rho}_{\text{PB-C}} K_{\text{Leak}} (p_{\text{PB}} - p_{\text{C}}) e^{\frac{-|y_3|}{y_{\text{leak}}}} \quad (\text{D.16})$$

where K_{leak} is a leakage coefficient and y_{leak} is the normalised spool position for which the leakage is 36.8% of the maximum leakage (at $y_3=0$).

The opening dynamics for all valves are modelled as linear first order systems according to:

$$\dot{y}_i = \omega_{\text{V},i} (y_{\text{ref},i} - y_i) \quad , \quad i = 1..9 \quad (\text{D.17})$$

The reference valve position y_{ref} for the load holding valves and the inverse shuttle valve are calculated as:

$$y_{\text{ref},i} = \begin{cases} 0 & p_{\text{C}} - p_{\text{R}} \leq p_{\text{CR,LH}} \\ \frac{p_{\text{C}} - p_{\text{R}} - p_{\text{CR,LH}}}{p_{\text{OP,LH}} - p_{\text{CR,LH}}} & p_{\text{CR,LH}} < p_{\text{C}} - p_{\text{R}} \leq p_{\text{OP,LH}} \\ 1 & p_{\text{C}} - p_{\text{R}} > p_{\text{OP,LH}} \end{cases} \quad i = \{1, 2\} \quad (\text{D.18})$$

$$y_{\text{ref},3} = \begin{cases} 0 & |p_{\text{PA}} - p_{\text{PB}}| \leq p_{\text{CR,ISV}} \\ \text{sign}(p_{\text{PA}} - p_{\text{PB}}) \frac{|p_{\text{PA}} - p_{\text{PB}}| - p_{\text{CR,ISV}}}{p_{\text{OP,ISV}} - p_{\text{CR,ISV}}} & p_{\text{CR,ISV}} < |p_{\text{PA}} - p_{\text{PB}}| \leq p_{\text{OP,ISV}} \\ \text{sign}(p_{\text{PA}} - p_{\text{PB}}) & |p_{\text{PA}} - p_{\text{PB}}| > p_{\text{OP,ISV}} \end{cases} \quad (\text{D.19})$$

The reference valve position for the check valves are found based on the pressure difference across the valve (Δp), where a positive Δp works to open the check valve.

$$y_{\text{ref},i} = \begin{cases} 0 & \Delta p \leq p_{\text{CR,CV}} \\ \frac{\Delta p - p_{\text{CR,CV}}}{p_{\text{OP,CV}} - p_{\text{CR,CV}}} & p_{\text{CR,CV}} < \Delta p \leq p_{\text{OP,CV}} \\ 1 & \Delta p > p_{\text{OP,CV}} \end{cases} \quad , \quad i = \{4, 5, 6, 7\} \quad (\text{D.20})$$

The reference valve position for the safety valves ($y_{\text{ref},8}, y_{\text{ref},9}$) equals the valve input u_{SV} , i.e. either 0 or 1.

D.1.3 Enthalpy Flow Rates

The considered thermo-hydraulic model only includes a single uniform temperature state. This simplifies the calculation of the enthalpy flow rate \dot{H}_{sys} ,

because the direction of enthalpy flow does not matter. In other words, there is no need to distinguish between which chamber the enthalpy flow enters. Thus, \dot{H}_{sys} is simply calculated as:

$$\begin{aligned} \dot{H}_{\text{sys}} = & \underbrace{\dot{H}_{A1} + \dot{H}_{B1} + \dot{H}_{AL1} + \dot{H}_{B1}}_{\text{Pump 1}} + \underbrace{\dot{H}_{2A} + \dot{H}_{2B} + \dot{H}_{2AL}}_{\text{Pump 2}} \\ & + \dot{m}_A (h_{PA} - h_A) + \dot{m}_B (h_B - h_{PB}) + \dot{m}_{ISA} (h_{PA} - h_C) + \dot{m}_{ISB} (h_{PB} - h_C) \\ & + \dot{m}_{CVA} (h_{PA} - h_A) + \dot{m}_{CVB} (h_{PB} - h_B) + \dot{m}_{CVPA} (h_R - h_{PA}) + \dot{m}_{CVPB} (h_R - h_{PB}) \\ & + \dot{m}_{SA} (h_{PA} - h_R) + \dot{m}_{SB} (h_{PB} - h_R) \end{aligned} \quad (\text{D.21})$$

D.2 Heat Transfer to Ambience

The heat transfer rate to the ambience, \dot{Q}_{amb} , are modelled as natural convection and radiation. This means that heat conduction to the crane structure and forced convection due to wind or motion of the crane relative to the surroundings are neglected. Additionally, heat transfer from the electric motor to the ambience or the remaining system has been neglected.

In this simulation study, heat transfer to the ambience from the two pumps, the knuckle boom cylinder barrel, the two cylinder barrels of the bootstrap reservoir and the hydraulic manifold have been included. The heat transfer is calculated by approximating the mentioned components as basic shapes, here cylinders and cubes. The calculation of Nusselt numbers for calculating the convective heat transfer coefficient are done according to the procedure in Paper F, i.e. the orientation of the shapes are horizontal and not changing with the motion of the crane. The properties of the ambient air are evaluated at the reference temperature $T_{\text{ref}} = 0.5 (T_{\text{sys}} + T_{\text{amb}})$. From the Nusselt number, the convective heat transfer rate may be calculated as [132]:

$$\dot{Q}_{\text{conv}} = A_s h_{\text{conv}} (T_{\text{sys}} - T_{\text{amb}}) \quad \text{Nu} = \frac{h_{\text{conv}} L_c}{k} \quad (\text{D.22})$$

T_{sys} and T_{amb} are the system and ambient temperatures respectively, where the latter is assumed constant. A_s is the surface area of the geometry, h_{conv} the heat transfer coefficient, L_c the geometry dependent characteristic length and k the thermal conductivity for air at the reference temperature.

For the calculation of the heat transfer by radiation, all surfaces are assumed to be grey diffuse surfaces (emissivity independent of wavelength and direction) with an emissivity of $\epsilon = 0.8$ for all surfaces. This is a conservative estimate for coated, varnished or painted surfaces [114]. Additionally, the radiation from all surfaces are assumed to radiate freely to the ambience, i.e. radiation between the system surfaces is neglected. Thus, the heat transfer

D.2. Heat Transfer to Ambience

rate by radiation is calculated as [132]:

$$\dot{Q}_{\text{rad}} = \epsilon \sigma A_s (T_{\text{sys}}^4 - T_{\text{amb}}^4) = h_{\text{rad}} A_s (T_{\text{sys}} - T_{\text{amb}}) \quad (\text{D.23})$$

$$h_{\text{rad}} = \epsilon \sigma \frac{T_{\text{sys}}^4 - T_{\text{amb}}^4}{T_{\text{sys}} - T_{\text{amb}}} = \epsilon \sigma (T_{\text{sys}}^2 + T_{\text{amb}}^2) (T_{\text{sys}} + T_{\text{amb}}) \quad (\text{D.24})$$

where ϵ , σ is the surface emissivity and the Stefan-Boltzmann constant, h_{rad} is the equivalent heat transfer coefficient for radiation.

Tab. D.1 on page 278 shows exemplarily the values of the thermal resistances, calculated at $T_{\text{sys}} = 60^\circ\text{C}$ and $T_{\text{amb}} = 20^\circ\text{C}$. Convective heat transfer coefficients are increased by 20% compared to their theoretical counterparts, to account for non-idealised conditions according to [133].

In Tab. D.1, A_{proj} is the projected surface area which is used to calculate the Nusselt number for the convective heat transfer of a cube according to the formulae presented in Paper F. R_{th} is the thermal resistance towards heat transfer between the component and the ambience. This is found as the parallel connection of a convective and a radiation thermal resistance. The thermal resistance, heat transfer coefficient and the heat transfer rate \dot{Q} is related as:

$$\dot{Q} = \frac{\Delta T}{R_{\text{th}}} = h_{\text{comb}} A_s \Delta T \quad \Rightarrow \quad R_{\text{th}} = \frac{1}{h_{\text{comb}} A_s} \quad (\text{D.25})$$

where ΔT is the temperature difference across the thermal resistance and h_{comb} is the combined heat transfer coefficient found as $h_{\text{conv}} + h_{\text{rad}}$.

The total heat transfer rate from the system to the ambience are simply found by adding the rate of heat transferred across the six convective and radiation thermal resistances in Tab. D.1:

$$\dot{Q}_{\text{amb}} = \Delta T \left(\frac{1}{R_{\text{th1}}} + \frac{1}{R_{\text{th2}}} + \frac{1}{R_{\text{th3}}} + \frac{1}{R_{\text{th4}}} + \frac{1}{R_{\text{th5}}} + \frac{1}{R_{\text{th6}}} \right) = \frac{T_{\text{sys}} - T_{\text{amb}}}{R_{\text{eq}}} \quad (\text{D.26})$$

$$R_{\text{eq}} = \left(\frac{1}{R_{\text{th1}}} + \frac{1}{R_{\text{th2}}} + \frac{1}{R_{\text{th3}}} + \frac{1}{R_{\text{th4}}} + \frac{1}{R_{\text{th5}}} + \frac{1}{R_{\text{th6}}} \right)^{-1}$$

R_{eq} is the equivalent thermal resistance between the system and the ambience, found as a parallel connection of the six thermal resistances.

From Tab. D.1, $R_{\text{eq}} = 0.0177 \text{ K/W}$, or equivalently $h = 11.2 \text{ W/m}^2/\text{K}$. This means that the modelled passive heat transfer rate is 2260 W at a system temperature of 60 °C and an ambient temperature of 20 °C.

Table D.1: Thermal resistances evaluated at a system temperature of 60 °C and an ambient temperature of 20 °C. *The surface emissivities are assumed to $\epsilon = 0.8$ for all surfaces.

Natural Convection & Radiation								
ID	Geometry	A _s	A _{proj}	L _c	h _{conv}	h _{rad} [*]	h _{comb}	R _{th}
1	Horizontal Cylinder (Transmission Cylinder)	2.24 m ²	-	393 mm	5.93 $\frac{W}{m^2K}$	5.59 $\frac{W}{m^2K}$	11.5 $\frac{W}{m^2K}$	0.039 $\frac{K}{W}$
2	Horizontal Cylinder (Reservoir Barrel)	1.16 m ²	-	503 mm	5.81 $\frac{W}{m^2K}$	5.59 $\frac{W}{m^2K}$	11.4 $\frac{W}{m^2K}$	0.076 $\frac{K}{W}$
3	Horizontal Cylinder (Charge Chamber Barrel)	0.29 m ²	-	126 mm	6.77 $\frac{W}{m^2K}$	5.59 $\frac{W}{m^2K}$	12.4 $\frac{W}{m^2K}$	0.28 $\frac{K}{W}$
4	Cube (Pump 1)	1424 cm ²	289 cm ²	743 mm	5.25 $\frac{W}{m^2K}$	5.59 $\frac{W}{m^2K}$	10.8 $\frac{W}{m^2K}$	0.647 $\frac{K}{W}$
5	Cube (Pump 2)	1424 cm ²	289 cm ²	743 mm	5.25 $\frac{W}{m^2K}$	5.59 $\frac{W}{m^2K}$	10.8 $\frac{W}{m^2K}$	0.647 $\frac{K}{W}$
6	Cube (Manifold)	1.12 m ²	0.3 m ²	1812 mm	4.12 $\frac{W}{m^2K}$	5.59 $\frac{W}{m^2K}$	9.72 $\frac{W}{m^2K}$	0.092 $\frac{K}{W}$

Appendix E

Linear Models and Model Reduction

In this appendix the nonlinear model derived in Chapter 5 is simplified and linearised. To justify the simplifications, the responses of the nonlinear and linear model are compared. To reduce the complexity of the linear model used for controller design in Chapter 6 further, insignificant states are subsequently removed from the linear model to arrive at the final reduced linear model used further on.

E.1 Full Linear Model

Compared to the nonlinear model the following simplifications are made for the linear model:

- System temperature is constant (i.e. no temperature state included).
- Density is constant and equal in all control volumes.
- The bulk modulus is assumed constant for each chamber in the considered linearisation point [32], including mechanical elasticity.
- The position and pressure dependency of volumes are neglected and the chamber volumes are assumed constant in the considered linearisation point [32].
- Static and Coulomb friction of the cylinder is neglected and thus only viscous friction is included [32].
- Leakage flow of valves are neglected and the two-regime flow model is not utilized (i.e. linearised orifice equation is used).

- Valve dynamics are neglected and valves are considered either fully closed or fully open.
- Anti-cavitation check valves are not included.
- The equivalent cylinder loads are simplified compared to the model of the knuckle boom crane derived in Sec. 2.2
 - Loads are evaluated by assuming remaining axes at standstill and zero acceleration.
 - The equivalent mass/inertia (M_{eq}) and gravitational load (F_G) is assumed constant in the linearisation point.
 - The velocity dependent forces (denoted C_x) are neglected.

Given the simplifications listed above, the linear equations of the ECD+ system expressed in change variables $\tilde{\bullet}$ are given as:

$$\ddot{\tilde{x}} = \frac{1}{M_{eq0}} \left(\tilde{p}_A A_A - \tilde{p}_B A_B - \cancel{F_{vel,2}(\dot{x}, \dot{x}_2)} \dot{x}_2 - B_x \dot{\tilde{x}} \right) \quad (E.1)$$

$$\ddot{\tilde{z}} = \frac{1}{M_z} (\tilde{p}_R A_R - \tilde{p}_C A_C - B_z \dot{\tilde{z}}) \quad (E.2)$$

$$\dot{\tilde{p}}_A = \frac{\beta_{eff,A0}}{V_{A0}} (K_{QLHA} (\tilde{p}_{PA} - \tilde{p}_A) - \dot{\tilde{x}} A_A) \quad (E.3)$$

$$\dot{\tilde{p}}_B = \frac{\beta_{eff,B0}}{V_{B0}} (\dot{\tilde{x}} A_B - K_{QLHB} (\tilde{p}_B - \tilde{p}_{PB})) \quad (E.4)$$

$$\dot{\tilde{p}}_{PA} = \frac{\beta_{eff,PA0}}{V_{PA0}} [-K_{QLHA} (\tilde{p}_{PA} - \tilde{p}_A) - K_{ISVA} (\tilde{p}_{PA} - \tilde{p}_C) + \quad (E.5)$$

$$\tilde{\omega}_1 (D_{p,1} - K_{\omega 1}) - K_{P1} (\tilde{p}_{PA} - \tilde{p}_R) + \quad (E.6)$$

$$\tilde{\omega}_2 (D_{p,2} - K_{\omega 2}) - K_{P2} (\tilde{p}_{PA} - \tilde{p}_R)] \quad (E.7)$$

Linear pump model including leakage

$$\dot{\tilde{p}}_{PB} = \frac{\beta_{eff,PB0}}{V_{PB0}} [K_{QLHB} (\tilde{p}_B - \tilde{p}_{PB}) - K_{ISVB} (\tilde{p}_{PB} - \tilde{p}_C) + \quad (E.8)$$

$$- \tilde{\omega}_1 (D_{p,1} + K_{\omega 1}) - K_{P1} (\tilde{p}_{PB} - \tilde{p}_R)] \quad (E.9)$$

$$\dot{\tilde{p}}_C = \frac{\beta_{eff,C0}}{V_{C0}} (K_{ISVA} (\tilde{p}_{PA} - \tilde{p}_C) + K_{ISVB} (\tilde{p}_{PB} - \tilde{p}_C) + \dot{\tilde{z}} A_C) \quad (E.10)$$

$$\dot{\tilde{p}}_R = \frac{\beta_{eff,R0}}{V_{R0}} [-\tilde{\omega}_2 (D_{p,2} - K_{\omega 2}) + K_{P2} (\tilde{p}_{PA} - \tilde{p}_R) + \tilde{\omega}_1 K_{\omega 1} + \quad (E.11)$$

$$K_{P1} (\tilde{p}_{PA} + \tilde{p}_{PB} - 2\tilde{p}_R) - \dot{\tilde{z}} A_R] \quad (E.12)$$

where M_{eq0} , $\beta_{eff,\bullet 0}$ and $V_{\bullet 0}$ is the equivalent mass, bulk moduli and volumes evaluated in the linearisation point. A_A , A_B , A_R , A_C are piston areas, B_x

E.1. Full Linear Model

and B_z are viscous friction coefficients. K_{p1} , K_{p2} are linear or laminar pump leakage coefficients and $K_{\omega1}$, $K_{\omega2}$ are speed dependent leakage coefficients, which are all found from a linear curve-fit of the available pump leakage data. K_{QLHA} , K_{QLHB} , K_{ISVA} , K_{ISVB} are linearisation constants calculated as:

$$K_{QLHA} = \begin{cases} \left. \frac{\partial Q_A}{\partial p_{PA}} \right|_{\mathbf{x}_{F0}} = - \left. \frac{\partial Q_A}{\partial p_A} \right|_{\mathbf{x}_{F0}} & \text{for } p_C - p_R > p_{CR,LH} \\ 0 & \text{for } p_C - p_R \leq p_{CR,LH} \end{cases} \quad (E.13)$$

$$K_{QLHB} = \begin{cases} \left. \frac{\partial Q_B}{\partial p_B} \right|_{\mathbf{x}_{F0}} = - \left. \frac{\partial Q_B}{\partial p_{PB}} \right|_{\mathbf{x}_{F0}} & \text{for } p_C - p_R > p_{CR,LH} \\ 0 & \text{for } p_C - p_R \leq p_{CR,LH} \end{cases} \quad (E.14)$$

$$K_{ISVA} = \begin{cases} 0 & \text{for } p_{PA} \geq p_{PB} \\ \left. \frac{\partial Q_{ISA}}{\partial p_{PA}} \right|_{\mathbf{x}_{F0}} = - \left. \frac{\partial Q_{ISA}}{\partial p_C} \right|_{\mathbf{x}_{F0}} & \text{for } p_{PA} < p_{PB} \end{cases} \quad (E.15)$$

$$K_{ISVB} = \begin{cases} \left. \frac{\partial Q_{ISB}}{\partial p_{PB}} \right|_{\mathbf{x}_{F0}} = - \left. \frac{\partial Q_{ISB}}{\partial p_C} \right|_{\mathbf{x}_{F0}} & \text{for } p_{PA} \geq p_{PB} \\ 0 & \text{for } p_{PA} < p_{PB} \end{cases} \quad (E.16)$$

where Q_{\bullet} are valve volume flows evaluated using the orifice equation, for a fully open valve and \mathbf{x}_{F0} the state vector at the linearisation point. The linearisation constants are defined to 0 when the valves are closed in the linearisation point to include both the motion operation mode and the self-locking mode in the linear model. The valves will stay fully open or closed, disregarding how the change variables $\tilde{\bullet}$ are developing.

The linear model of the system without electric motor, i.e. without actuator dynamics is represented in state space form as:

$$\dot{\mathbf{x}}_F = \mathbf{A}_F \mathbf{x}_F + \mathbf{B}_F \mathbf{u}_F, \quad \mathbf{y}_F = \mathbf{C}_F \mathbf{x}_F = \mathbf{x}_F \quad (E.17)$$

$$\mathbf{x}_F = [\dot{\tilde{x}} \quad \dot{\tilde{z}} \quad \tilde{p}_A \quad \tilde{p}_{PA} \quad \tilde{p}_B \quad \tilde{p}_{PB} \quad \tilde{p}_C \quad \tilde{p}_R]^T \quad \mathbf{u}_F = [\tilde{\omega}_1 \quad \tilde{\omega}_2]^T \quad (E.18)$$

$$\mathbf{B}_F = \begin{bmatrix} 0 & 0 & 0 & \frac{\beta_{\text{eff},PA0} (D_{p,1} - K_{\omega1})}{V_{PA0}} & 0 & \frac{\beta_{\text{eff},PB0} (-D_{p,1} - K_{\omega1})}{V_{PB0}} & 0 & \frac{\beta_{\text{eff},R0} K_{\omega1}}{V_{R0}} \\ 0 & 0 & 0 & \frac{\beta_{\text{eff},PA0} (D_{p,2} - K_{\omega2})}{V_{PA0}} & 0 & 0 & 0 & \frac{\beta_{\text{eff},R0} (K_{\omega2} - D_{p,2})}{V_{R0}} \end{bmatrix}^T$$

Appendix E. Linear Models and Model Reduction

$$\mathbf{A}_F = \begin{bmatrix} -\frac{B_x}{M_{eq0}} & 0 & \frac{A_A}{M_{eq0}} & 0 & -\frac{A_R}{M_{eq0}} & 0 & 0 & 0 \\ 0 & -\frac{B_z}{M_z} & 0 & 0 & 0 & 0 & -\frac{A_C}{M_z} & \frac{A_R}{M_z} \\ -\frac{\beta_{eff,A0} A_A}{V_{A0}} & 0 & -\frac{\beta_{eff,A0} K_{QLHA}}{V_{A0}} & \frac{\beta_{eff,A0} K_{QLHA}}{V_{A0}} & 0 & 0 & 0 & 0 \\ 0 & 0 & \frac{\beta_{eff,PA0} K_{QLHA}}{V_{PA0}} & C_1 & 0 & 0 & \frac{\beta_{eff,PA0} K_{ISVA}}{V_{PA0}} & \frac{\beta_{eff,PA0} (K_{P1} + K_{P2})}{V_{PA0}} \\ \frac{\beta_{eff,B0} A_B}{V_{B0}} & 0 & 0 & 0 & -\frac{\beta_{eff,B0} K_{QLHB}}{V_{B0}} & \frac{\beta_{eff,B0} K_{QLHB}}{V_{B0}} & 0 & 0 \\ 0 & 0 & 0 & 0 & \frac{\beta_{eff,PB0} K_{QLHB}}{V_{PB0}} & C_2 & \frac{\beta_{eff,PB0} K_{QISVB}}{V_{PB0}} & \frac{\beta_{eff,PB0} K_{P1}}{V_{PB0}} \\ 0 & \frac{\beta_{eff,C0} A_C}{V_{C0}} & 0 & \frac{\beta_{eff,C0} K_{ISVA}}{V_{C0}} & 0 & \frac{\beta_{eff,C0} K_{ISVB}}{V_{C0}} & C_3 & 0 \\ 0 & -\frac{\beta_{eff,R0} A_R}{V_{R0}} & 0 & C_4 & 0 & \frac{\beta_{eff,R0} K_{P1}}{V_{R0}} & 0 & \frac{\beta_{eff,R0} (-2K_{P1} - K_{P2})}{V_{R0}} \end{bmatrix}$$

$$C_1 = \frac{\beta_{eff,PA0} (-K_{P1} - K_{P2} - K_{QISVA} - K_{QLHA})}{V_{PA0}} \quad C_4 = \frac{\beta_{eff,R0} (K_{P1} + K_{P2})}{V_{R0}} \quad (\text{E.19})$$

$$C_3 = \frac{\beta_{eff,C0} (-K_{ISVA} - K_{ISVB})}{V_{C0}} \quad C_2 = \frac{\beta_{eff,PB0} (-K_{P1} - K_{QISVB} - K_{QLHB})}{V_{PB0}} \quad (\text{E.20})$$

The subscript \bullet_F denotes the *full* plant model without actuator dynamics opposed to the *reduced* linear model introduced subsequently.

The linear full plant model may be extended with the linear actuator dynamics from Sec. 5.4 according to:

$$\dot{\mathbf{x}}_{EF} = \mathbf{A}_{EF} \mathbf{x}_{EF} + \mathbf{B}_{EF} \mathbf{u}_{ref}, \quad \mathbf{y}_{EF} = \mathbf{C}_{EF} \mathbf{x}_{EF}, \quad \mathbf{C}_{EF} = [\mathbf{0} \quad \mathbf{C}_F] \quad (\text{E.21})$$

$$\mathbf{x}_{EF} = \begin{bmatrix} \mathbf{x}_u \\ \mathbf{x}_F \end{bmatrix}, \quad \mathbf{A}_{EF} = \begin{bmatrix} \mathbf{A}_u & \mathbf{0} \\ \mathbf{B}_F \mathbf{C}_u & \mathbf{A}_F \end{bmatrix}, \quad \mathbf{B}_{EF} = \begin{bmatrix} \mathbf{B}_u \\ \mathbf{0} \end{bmatrix} \quad (\text{E.22})$$

where the subscript \bullet_{EF} denotes the *extended* and *full* linear model. The output of the full extended linear model may also be represented in the Laplace domain by the transfer function matrix:

$$\mathbf{y}_{EF}(s) = \mathbf{G}_{EF}(s) \mathbf{u}_{ref}(s), \quad \mathbf{G}_{EF}(s) = \mathbf{C}_{EF} (s\mathbf{I} - \mathbf{A}_{EF})^{-1} \mathbf{B}_{EF} \quad (\text{E.23})$$

The eight outputs (\mathbf{x}_F) represented by the transfer function matrix $\mathbf{G}_{EF}(s)$ in Eq. E.23 are compared to the nonlinear model in Fig. E.1. The cylinder loads are evaluated with the cylinder fully extended and cylinder 2 in the center position using a payload (m_3) of 10 ton. Cylinder 1 is at standstill with zero acceleration. In the linearisation point cylinder 2 moves at 20 mm/s, and the acceleration is 0. The remaining states at the linearisation point are calculated such that $\dot{\mathbf{x}}_{EF} = 0$, with the lower chamber pressure defined to 28.8 bar (absolute). Note that cylinder loads in the nonlinear models are also assumed constant such that the model comparison are concerned with evaluating the effect of the assumptions made with regard to the hydraulic model and not the varying load. Static and Coulomb friction are included in the nonlinear model.

The comparison in Fig. E.1 shows a good coherence between the nonlinear and linear model close to the chosen linearisation point. It is concluded that

important dynamics properties such as oscillation frequencies and damping ratios are captured with a satisfactory accuracy, for further analysis using the simplifications listed on page 279 and 280.

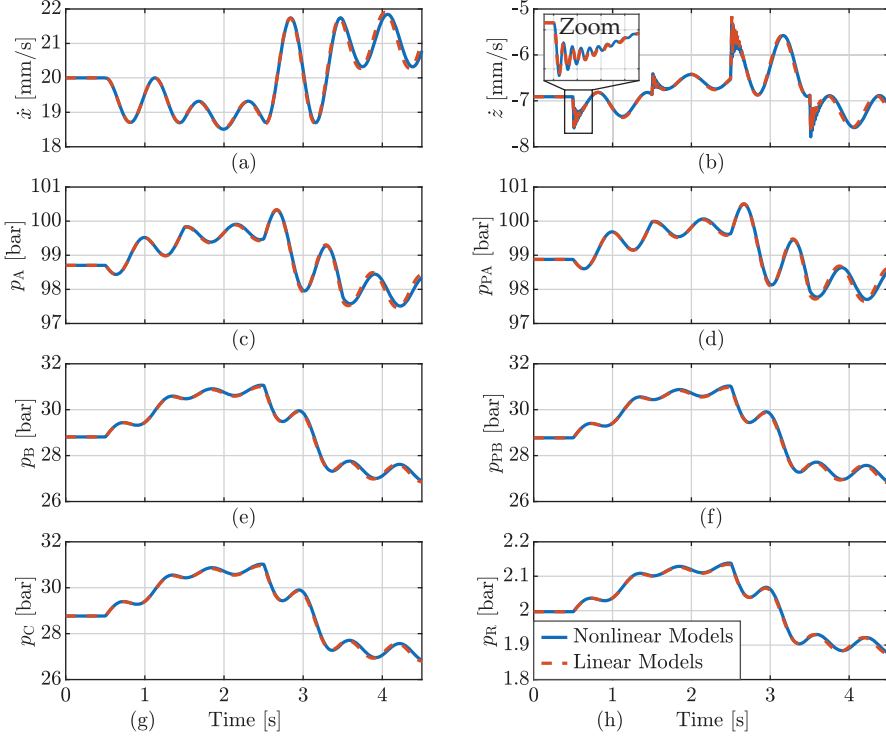


Fig. E.1: Comparison of nonlinear and linear models. Step inputs are given at 0.5 s ($\dot{\omega}_{1,\text{ref}} = -0.02 \omega_{\text{max}}$), at 1.5 s ($\dot{\omega}_{2,\text{ref}} = -0.02 \omega_{\text{max}}$), at 2.5 s ($\dot{\omega}_{1,\text{ref}} = 0.04 \omega_{\text{max}}$) and finally at 3.5 s ($\dot{\omega}_{2,\text{ref}} = 0.04 \omega_{\text{max}}$). $\omega_{\text{max}} = 3000$ RPM.

E.2 Reduced Linear Model

In addition to the simplifications listed on page 279 and 280 a *reduced* linear model is formulated by further assuming:

- Valve flow gains of load holding and inverse shuttle valves are assumed to be large, such that pressure drops across these valve are neglected. This means that the number of pressure states are reduced by three.
- The state of the load holding and inverse shuttle valves depend discretely on the system states, i.e. valves are either fully open (with no pressure drop) or fully closed (zero flow). No valve dynamics or leakage flows are included.

- Pump leakages are neglected.

The reduced linear model is derived in Sec. 6.1.1, and may be represented in state space form not including electric motor dynamics as:

$$\dot{\mathbf{x}}_p = \mathbf{A}_p \mathbf{x}_p + \mathbf{B}_p \mathbf{u}_p, \quad \mathbf{y}_p = \mathbf{C}_p \mathbf{x}_p \quad (\text{E.24})$$

$$\mathbf{x}_p = [\tilde{x} \quad \dot{\tilde{x}} \quad \ddot{\tilde{x}} \quad \tilde{p}_{PA} \quad \tilde{p}_{PB} \quad \tilde{p}_R]^T, \quad \mathbf{u}_p = [\tilde{\omega}_1 \quad \tilde{\omega}_2]^T \quad (\text{E.25})$$

$$\mathbf{B}_p = \begin{bmatrix} 0 & 0 & 0 & \frac{\beta_{\text{eff},PA0}}{V_{PA0}} D_{p,1} & -\frac{\beta_{\text{eff},PB0}}{V_{PB0}} D_{p,1} & 0 \\ 0 & 0 & 0 & \frac{\beta_{\text{eff},PA0}}{V_{PA0}} D_{p,2} & 0 & -\frac{\beta_{\text{eff},R0}}{V_{R0}} D_{p,2} \end{bmatrix}^T \quad (\text{E.26})$$

$$\mathbf{A}_p = \quad (\text{E.27})$$

$$\begin{bmatrix} 0 & 1 & 0 & 0 & 0 & 0 \\ 0 & -\frac{B_x}{M_{\text{eq0}}} & 0 & \frac{A_A}{M_{\text{eq0}}} K_{\text{sw,LH}} & -\frac{A_B}{M_{\text{eq0}}} K_{\text{sw,LH}} & 0 \\ 0 & 0 & -\frac{B_z}{M_z} & -\frac{(1-K_{\text{sw,ISV}})A_C}{M_z} & -\frac{K_{\text{sw,ISV}}A_C}{M_z} & \frac{A_R}{M_z} \\ 0 & -\frac{\beta_{\text{eff},PA0}A_A K_{\text{sw,LH}}}{V_{PA0}} & \frac{\beta_{\text{eff},PA0}A_C(1-K_{\text{sw,ISV}})}{V_{PA0}} & 0 & 0 & 0 \\ 0 & \frac{\beta_{\text{eff},PB0}A_B K_{\text{sw,LH}}}{V_{PB0}} & \frac{\beta_{\text{eff},PB0}A_C K_{\text{sw,ISV}}}{V_{PB0}} & 0 & 0 & 0 \\ 0 & 0 & -\frac{\beta_{\text{eff},R0}A_R}{V_{R0}} & 0 & 0 & 0 \end{bmatrix}$$

The subscript \bullet_p denotes the reduced or simplified *plant* model without actuator dynamics. The output matrix \mathbf{C}_p is used to determine the relevant outputs. Note, that a position state of the main cylinder x , is included in the reduced model. The linear plant model may be extended with the linear actuator dynamics from Sec. 5.4 according to:

$$\dot{\mathbf{x}}_E = \mathbf{A}_E \mathbf{x}_E + \mathbf{B}_E \mathbf{u}_{\text{ref}}, \quad \mathbf{y}_E = \mathbf{C}_E \mathbf{x}_E, \quad \mathbf{C}_E = [\mathbf{0} \quad \mathbf{C}_p] \quad (\text{E.28})$$

$$\mathbf{x}_E = \begin{bmatrix} \mathbf{x}_u \\ \mathbf{x}_p \end{bmatrix}, \quad \mathbf{A}_E = \begin{bmatrix} \mathbf{A}_u & \mathbf{0} \\ \mathbf{B}_p \mathbf{C}_u & \mathbf{A}_p \end{bmatrix}, \quad \mathbf{B}_E = \begin{bmatrix} \mathbf{B}_u \\ \mathbf{0} \end{bmatrix} \quad (\text{E.29})$$

where the subscript \bullet_E denotes the *extended* linear model.

E.3 Comparison of Frequency Responses

The two linear model complexities are compared based on their frequency responses in order to assess the extent to which the additional simplifications made to the reduced *plant* model affect this.

To compare the input directional gain dependency the singular values of the two linear systems are compared in Figs. E.2 and E.3. The singular values

E.3. Comparison of Frequency Responses

are evaluated using the command *sigma()* in MATLAB¹.

In Fig. E.2 the linearisation point of the linear models are chosen according to the point used in Fig. E.1, with the outputs being the cylinder speed \dot{x} and the lower pressure p_{PB} .

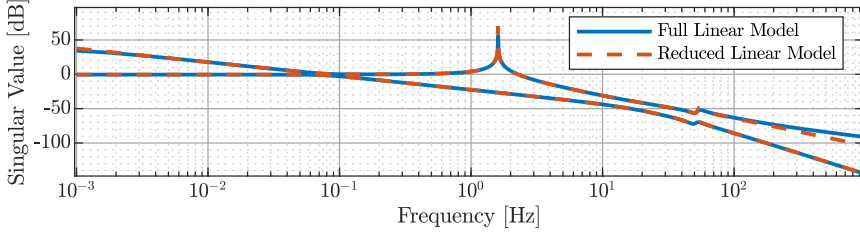


Fig. E.2: Comparison of singular values between full and reduced linear model in motion operation mode. Model outputs are the cylinder speed \dot{x} and the lower pressure p_{PB} .

Fig. E.3 compares the singular values for the case where the load holding valves are closed ($K_{sw,LH} = 0$) and the outputs being the pressures p_{PA} and p_{PB} , with the linearisation point chosen to $p_{PA0} = 5$ bar and $p_{PB0} = 3$ bar.

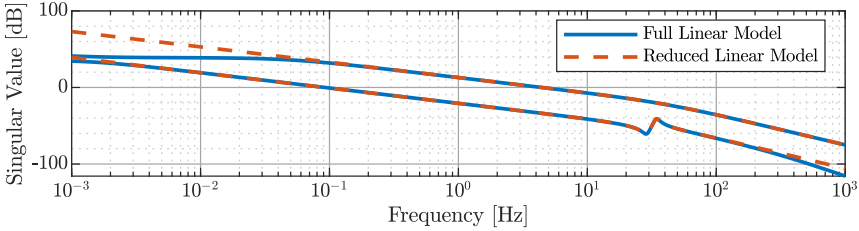


Fig. E.3: Comparison of singular values between full linear and reduced linear model in self-locking mode. Model outputs are the pressures p_{PA} and p_{PB} .

The individual frequency responses from one input, while the other input is zero (i.e. cross couplings are not included) are shown as Bode plots in Fig. E.4 and E.5. Fig. E.4 shows frequency responses between the two inputs and the cylinder speed \dot{x} in motion operation mode and E.5 shows the frequency response in self-locking mode between the two inputs and p_{PA} . The comparison of singular values and Bode plots shows that for motion operation mode the two model complexities are in close coherence. At high frequencies (above 750 Hz) small deviations are seen. Furthermore, the resonance peaks of the reduced model are slightly higher compared to the full model (visi-

¹Systems are normalized prior to evaluation of singular values based on their maximum expected output values.

Appendix E. Linear Models and Model Reduction

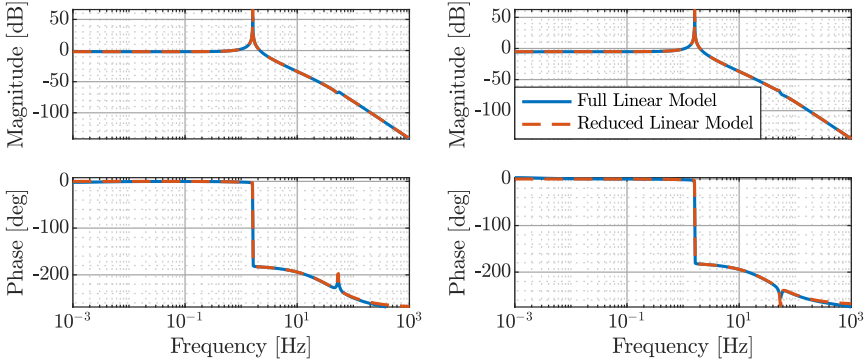


Fig. E.4: Comparison of frequency responses between full linear and reduced linear model in motion operation mode, with \hat{x} being the model output and $\hat{\omega}_{1,ref}$ (left), $\hat{\omega}_{2,ref}$ (right) inputs.

ble if zooming in), due to increased damping (valve pressure loss and pump leakage).

For self-locking mode clear deviations are evident at small frequencies, which are found to be a result of the neglected pump leakage in the simplified model. For the simplified model in self-locking mode the pressure response is an integrator, while this is not the case for the full model due to leakage.

Despite the differences between the model complexities at small frequencies, the simplified model is used for further analysis and for controller design in Chapter 6, as the pump leakage is generally assumed to be small and a varying and uncertain parameter. This means that if a zero steady state pressure

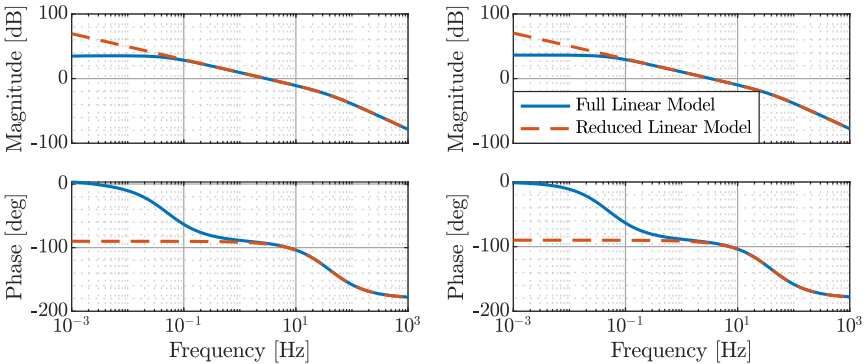


Fig. E.5: Comparison of frequency responses between full linear and reduced linear model in motion operation mode, with p_{PA} being the model output and $\hat{\omega}_{1,ref}$ (left), $\hat{\omega}_{2,ref}$ (right) inputs.

E.3. Comparison of Frequency Responses

error is sought by control efforts, integral action should be included in the controller structure, even though the simplified model complexity suggests this not to be necessary.

To sum up this appendix Fig. E.6 and E.7 compares the model output of the nonlinear and simplified linear model with actuator dynamics. This shows a good coherence between the nonlinear and linear model, close to the chosen linearisation points. In self-locking mode (Fig. E.7), discrepancies are evident, caused by highly nonlinear bulk modulus and a high relative impact of pump leakage in this operation mode. It is however concluded that important dynamics properties such as oscillation frequencies and damping ratios are captured with a satisfactory accuracy for controller design and analysis purposes, especially in motion operation mode.

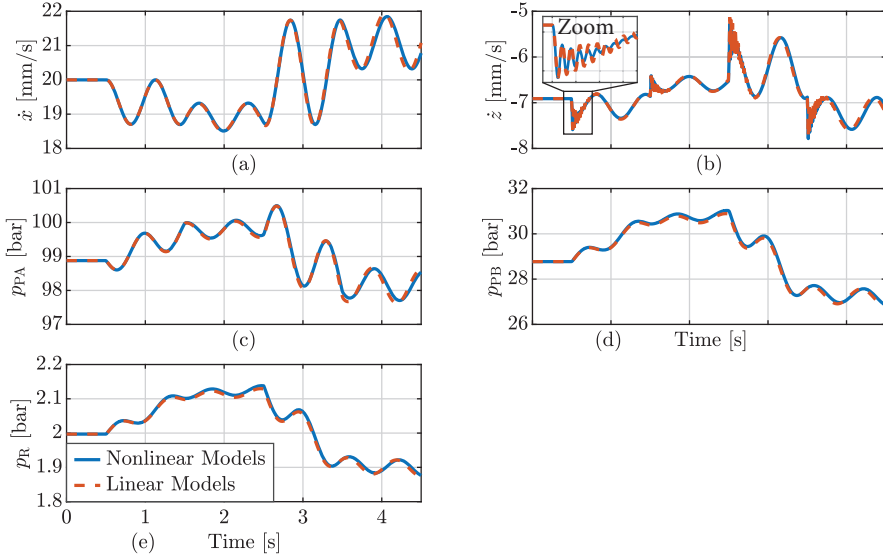


Fig. E.6: Comparison of nonlinear and simplified linear models in motion operation mode. Step inputs are given at 0.5 s ($\tilde{\omega}_{1,\text{ref}} = -0.02 \omega_{\text{max}}$), at 1.5 s ($\tilde{\omega}_{2,\text{ref}} = -0.02 \omega_{\text{max}}$), at 2.5 s ($\tilde{\omega}_{1,\text{ref}} = 0.04 \omega_{\text{max}}$) and finally at 3.5 s ($\tilde{\omega}_{2,\text{ref}} = 0.04 \omega_{\text{max}}$). $\omega_{\text{max}} = 3000$ RPM.

Appendix E. Linear Models and Model Reduction

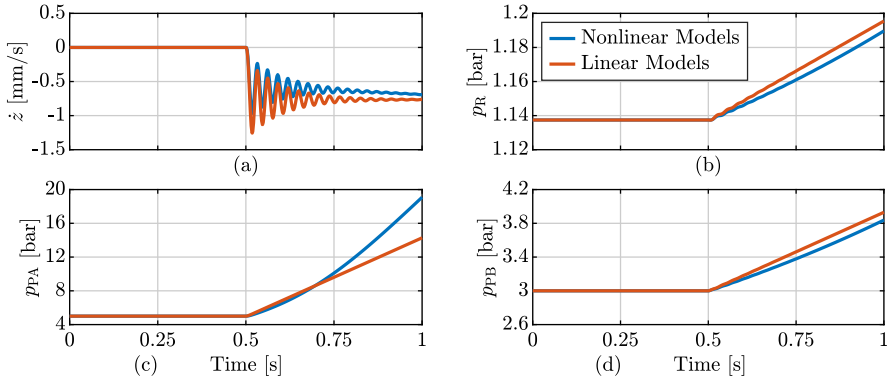


Fig. E.7: Comparison of nonlinear and simplified linear models in self-locking operation mode. Step inputs are given at 0.5 s ($\tilde{\omega}_{1,\text{ref}} = -0.01 \omega_{\text{max}}$ and $\tilde{\omega}_{2,\text{ref}} = 0.0125 \omega_{\text{max}}$), $\omega_{\text{max}} = 3000$ RPM.

ISSN (online): 2446-1636
ISBN (online): 978-87-7573-906-6

AALBORG UNIVERSITY PRESS